Christian Beck Editor

LECTURE NOTES IN PHYSICS 818

Clusters in Nuclei

Volume 1



Lecture Notes in Physics

Volume 818

Founding Editors

- W. Beiglböck
- J. Ehlers
- K. Hepp
- H. Weidenmüller

Editorial Board

- R. Beig, Vienna, Austria
- W. Beiglböck, Heidelberg, Germany
- W. Domcke, Garching, Germany
- B.-G. Englert, Singapore
- U. Frisch, Nice, France
- F. Guinea, Madrid, Spain
- P. Hänggi, Augsburg, Germany
- W. Hillebrandt, Garching, Germany
- R. L. Jaffe, Cambridge, MA, USA
- W. Janke, Leipzig, Germany
- R. A. L. Jones, Sheffield, UK
- H. v. Löhneysen, Karlsruhe, Germany
- M. Mangano, Geneva, Switzerland
- J.-M. Raimond, Paris, France
- M. Salmhofer, Heidelberg, Germany
- D. Sornette, Zurich, Switzerland
- S. Theisen, Potsdam, Germany
- D. Vollhardt, Augsburg, Germany
- W. Weise, Garching, Germany
- J. Zittartz, Köln, Germany

For further volumes: http://www.springer.com/series/5304

The Lecture Notes in Physics

The series Lecture Notes in Physics (LNP), founded in 1969, reports new developments in physics research and teaching—quickly and informally, but with a high quality and the explicit aim to summarize and communicate current knowledge in an accessible way. Books published in this series are conceived as bridging material between advanced graduate textbooks and the forefront of research and to serve three purposes:

- to be a compact and modern up-to-date source of reference on a well-defined topic
- to serve as an accessible introduction to the field to postgraduate students and nonspecialist researchers from related areas
- to be a source of advanced teaching material for specialized seminars, courses and schools

Both monographs and multi-author volumes will be considered for publication. Edited volumes should, however, consist of a very limited number of contributions only. Proceedings will not be considered for LNP.

Volumes published in LNP are disseminated both in print and in electronic formats, the electronic archive being available at springerlink.com. The series content is indexed, abstracted and referenced by many abstracting and information services, bibliographic networks, subscription agencies, library networks, and consortia.

Proposals should be sent to a member of the Editorial Board, or directly to the managing editor at Springer:

Christian Caron Springer Heidelberg Physics Editorial Department I Tiergartenstrasse 17 69121 Heidelberg/Germany christian.caron@springer.com Christian Beck Editor

Clusters in Nuclei

Volume 1



Editor
Christian Beck
Institut de Recherches Subatomiques
Université de Strasbourg,
CNRS-IN2P3, UMR 7500
rue du Loess 23
67037 Strasbourg CX 02
France

ISSN 0075-8450

e-ISSN 1616-6361

ISBN 978-3-642-13898-0

e-ISBN 978-3-642-13899-7

DOI: 10.1007/978-3-642-13899-7

Springer Heidelberg Dordrecht London New York

Library of Congress Control Number: 2010932330

© Springer-Verlag Berlin Heidelberg 2010

This work is subject to copyright. All rights are reserved, whether the whole or part of the material is concerned, specifically the rights of translation, reprinting, reuse of illustrations, recitation, broadcasting, reproduction on microfilm or in any other way, and storage in data banks. Duplication of this publication or parts thereof is permitted only under the provisions of the German Copyright Law of September 9, 1965, in its current version, and permission for use must always be obtained from Springer. Violations are liable to prosecution under the German Copyright Law.

The use of general descriptive names, registered names, trademarks, etc. in this publication does not imply, even in the absence of a specific statement, that such names are exempt from the relevant protective laws and regulations and therefore free for general use.

Cover design: eStudio Calamar, Berlin/Figueres

Printed on acid-free paper

Springer is part of Springer Science+Business Media (www.springer.com)

Preface

A great deal of research work has been performed in the field of alpha clustering since the pioneering discovery, by D. A. Bromley and co-workers half a century ago, of molecular resonances in the excitation functions for ¹²C + ¹²C scattering. The aim of this new series of *Lecture Notes in Physics* entitled **Clusters in Nuclei** is to deepen our knowledge of this field of nuclear molecular physics whose history was so well recounted in 1995 by W. Greiner, J. Y. Park and W. Scheid in their famous book on **Nuclear Molecules** (World Scientific Publishing Co.). Nuclear clustering remains, however, one of the most fruitful domains of nuclear physics, and faces some of the greatest challenges and opportunities in the years ahead.

The conference Cluster '94 as well as the Theoretical Winter School on Clusters in Nuclei were held in Strasbourg in 1994 and 2005, respectively. In recent years, alongside the traditional Cluster Conference series (Cluster '03, held in Nara, Japan, and Cluster '07 held in Stratford-upon-Avon, UK), other more informal workshops have been organised with relatively limited numbers of participants in Rostock (2003, 2004 and 2005), and in Munich and Osaka in 2006. The subjects treated in these recent meetings concentrated mainly on alpha-particle condensates in nuclear systems. But a couple of years ago the Workshop on the **State Of The Art in Nuclear Cluster Physics** (SOTANCP2008) held in Strabourg, France, was open to more diverse aspects of clustering in nuclei.

The purpose of this volume of *Lecture Notes in Physics*, the first in this new series of lectures, is to promote the exchange of ideas and to discuss new developments in Clustering Phenomena in Nuclear Physics and Nuclear Astrophysics both from a theoretical and from an experimental point of view. It is aimed at retaining the pedagogical nature of our earlier Theoretical Winter School, and should provide a useful resource for young researchers entering the field and wishing to get a feel for contemporary research in a number of areas.

The main topics in this first volume of **Clusters in Nuclei** are divided amongst seven chapters, each highlighting an area where new ideas have emerged over recent years:

vi Preface

- Cluster Radioactivity
- Cluster States and Mean Field Theories
- Alpha Clustering and Alpha Condensates
- Clustering in Neutron-rich Nuclei
- Di-neutron Clustering
- Collective Clusterization in Nuclei
- Giant Nuclear Molecules

The first Chapter entitled **Cluster Radioactivity** by Poenaru and Greiner shows how clustering aspects in nature are so important, as for instance in a new type of natural radioactivity predicted in 1980 by Sandulescu, Poenaru and Greiner. Considerable experimental and theoretical progress has been achieved since the discovery in 1984 of the ¹⁴C decay of ²²³Ra by Rose and Jones in Oxford, and further confirmed in Orsay and Argonne. Now, very neutron-rich Ne, Mg and Si isotopes are also known to be emitted through a cluster-radioactivity process that might be considered as super-asymmetric fission.

The second chapter, by Horiuchi, on Coexistence of Cluster States and Mean-Field-type States connects the phenomenological aspect of the two-center shell model with cluster-type microscopic dynamics. For the first time, the coexistence of cluster structures and superdeformation found in light alpha-particle nuclei, using large γ -ray multidetector arrays such as Euroball and/or Gammasphere, can be explained within the framework of a single theoretical approach: the Anty-symmetrized Molecular Dynamics model (AMD).

Alpha-cluster Condensations in Nuclei and Experimental Approaches for their Studies are discussed in Chapter 3 by von Oertzen, who argues that alpha clustering can result in the formation of Bose–Einstein condensates in nuclear physics. While its theoretical background will be reviewed in the second volume, the experimental observation of the decay of such condensed alpha-particle states is proposed here to lead to the coherent emission of several correlated alpha-particles in certain reactions.

Chapter 4 entitled Cluster Structure of Neutron-rich nuclei studied with Antisymmetrized Molecular Dynamics Model, and prepared by Kanada-En'yo and Kimura, shows how light, neutron-rich nuclei can be successfully described by the microscopic AMD approach. As the domain of cluster physics has been extended rapidly toward unstable nuclei, the authors propose new perspectives of clustering phenomena and discuss the role of valence neutrons in very light neutron-rich nuclei.

Ikeda and his collaborators attempt in Chapter 5 (**Di-neutron Clustering and Deuteron-like Tensor Correlation in Nuclear Structure focusing on ¹¹Li)** to reconcile the standard shell model with an effective-interaction approach, using a realistic nucleon–nucleon force. Di-neutron clustering is a new concept found to be a general phenomenon in the neutron-skin and neutron-halo nuclei, that are now experimentally studied more and more, worldwile, exploiting newly-available Radioactive Ion Beams (RIB) facilities.

Preface vii

Chapter 6 is dedicated to Collective Clusterization in Nuclei and Excited Compound Systems: The Dynamical Cluster-decay Model. Gupta analyses heavier nuclei with Relativistic Mean Field (RMF) theories. The concept of preformed clusters in nuclei is discussed in terms of the dynamical cluster-decay model and is shown to be supported by RMF calculations relying on rigorous basic assumptions.

Finally, the last Chapter **Giant Nuclear Systems of Molecular Type**, presented by Zagrebaev and Greiner, attempts to extend Bromley's nuclear molecule concept for ¹²C + ¹²C to the superheavy elements (SHE) that might be produced through the decay of giant nuclear molecules created in heavy-ion collisions. Clustering phenomena arising from shell effects play an important role in the low-energy dynamics of heavy nuclear systems, and new experimental perspectives are proposed for the next generation of RIB facilities.

Forthcoming volumes in this series will contain lectures covering a wider range of topics—not only from nuclear cluster theory but also from experiment and applications—that have gained a renewed interest with the availability of RIB facilities and modern detection techniques. We stress that the contributions in this volume and the following ones are not standrad review articles. They are not intended to contain all of the latest results or to provide an exhaustive coverage of the field but are written instead in the spirit of graduate lectures having a longer-term usefulness to research groups in this field.

The editing of this book would not have been possible without stimulating discussions with Profs. Greiner, Horiuchi, Schuck, Dufour and Rowley. Our appreciation goes to all of our lecturers for their valuable contributions. We thank also all of the referees for their informative comments on the chapters included in this volume. I would like here to thank, more particularly, Prof. Poenaru for his constant, helpful suggestions throughout. Special thanks go to Dr. Christian Caron and to all the members of his Springer-Verlag team for their help, fruitful collaboration and continued support for this ongoing project.

Strasbourg, France, May 2010

Christian Beck

Contents

Clus	ster Ra	dioactivity	1
1.1	1 Introduction		
1.2			3
	1.2.1	Surface Parametrization	4
	1.2.2	Mass Defect and the Q-Values	5
	1.2.3	Liquid Drop Model	6
	1.2.4		8
	1.2.5	Single Particle Shell Model	11
	1.2.6	Shell and Pairing Corrections	16
	1.2.7		18
	1.2.8		20
1.3	Nucle		26
	1.3.1		27
	1.3.2		30
1.4	Analy	e e e e e e e e e e e e e e e e e e e	34
	1.4.1	± •	35
	1.4.2		37
	1.4.3		38
	1.4.4	•	
			41
1.5	Unive		42
	1.5.1		42
	1.5.2		43
1.6	Fine S		44
1.7			45
1.8			46
	1.8.1		
			47
	1.8.2		48
			51
Refe			52
	1.1 1.2 1.3 1.4 1.5 1.6 1.7 1.8	1.1 Introd 1.2 Macro 1.2.1 1.2.2 1.2.3 1.2.4 1.2.5 1.2.6 1.2.7 1.2.8 1.3 Nucle 1.3.1 1.3.2 1.4 Analy 1.4.1 1.4.2 1.4.3 1.4.4 1.5 Unive 1.5.1 1.5.2 1.6 Fine 8 1.7 Terna 1.8 Stabil 1.8.1 1.8.2 1.8.3	1.2 Macroscopic—Microscopic Method. 1.2.1 Surface Parametrization. 1.2.2 Mass Defect and the Q-Values. 1.2.3 Liquid Drop Model. 1.2.4 Phenomenological Yukawa-Plus-Exponential. 1.2.5 Single Particle Shell Model. 1.2.6 Shell and Pairing Corrections. 1.2.7 Potential Energy Surfaces. 1.2.8 Saddle-Point Shapes. 1.3 Nuclear Dynamics. 1.3.1 Werner—Wheeler Approximation. 1.3.2 Cranking Inertia. 1.4 Analytical Superasymmetric Fission Model. 1.4.1 The Model. 1.4.2 Systematic Search for Cluster Decay Modes. 1.4.3 Experimental Confirmations. 1.4.4 Unified Approach of Cold Fission, Cluster Decay and α-Decay. 1.5 Universal Curves. 1.5.1 Preformation Probability in a Fission Model. 1.5.2 Universal Law. 1.6 Fine Structure. 1.7 Ternary and Multicluster Fission. 1.8 Stability of Metallic Atomic Clusters. 1.8.1 Liquid Drop Model of a Neutral Metallic Hemispheroidal Atomic Cluster. 1.8.2 New Single-Particle Shell Model.

x Contents

2	Coe	xistenc	e of Cluster States and Mean-Field-Type States	57
	2.1	Introd	luction	57
	2.2	AMD	Theory	58
		2.2.1	AMD Wave Function	58
		2.2.2	Hartree–Fock-Type Orbits	60
	2.3	Coexi	stence of Cluster Structure and Deformed	
		Mean-	-Field-Type Structure in <i>p</i> -Shell and Light <i>sd</i> -Shell Nuclei.	60
		2.3.1	⁸ Be Case	61
		2.3.2	¹² C Case	68
		2.3.3	¹⁶ O Case	75
		2.3.4	²⁰ Ne Case	82
	2.4	stence of Cluster Structure and Superdeformation		
		in Hea	avy sd-Shell and Light pf-Shell Nuclei	91
		2.4.1	⁴⁴ Ti Case	91
		2.4.2	³² S Case	96
	2.5		ure Change Between Cluster States and	
			-Field-Type States	
		2.5.1		99
		2.5.2	E0 Transitions Between Ground State and Cluster States	
			in ^{16}O and ^{12}C	101
	2.6		nary	105
	Refe	erences		106
•	41.1			
3	_		ter Condensations in Nuclei and Experimental	109
	3.1		s for their Studies	109
	3.1		Formation of Alpha Condensates	111
	3.2	3.2.1	Second Order Phase Transition	111
	3.3		imental Observables.	117
	3.3	3.3.1	Inelastic Scattering, Radial Extensions, Form Factors	117
		3.3.2	Compound Nucleus Decay, Correlated Emission	11/
		3.3.2	of Alpha's	119
		3.3.3	Compound States with Multi-α Decays	120
		3.3.4	Inelastic Excitation and Fragmentation	120
		3.3.5	α - α Correlations	126
				120
	3.4	Concl		126
	3.4 Refe		usions	126 127
				126 127
4	Refe	erences	usions	
4	Refe	erences ster Str	usions	
4	Refe	erences ster Str Antisy Introd	ructure of Neutron-Rich Nuclei Studied symmetrized Molecular Dynamics Model	127
4	Refe Clus with	erences ster Str Antisy Introd	ructure of Neutron-Rich Nuclei Studied ymmetrized Molecular Dynamics Model	127 129
4	Clus with 4.1	erences ster Str Antisy Introd	ructure of Neutron-Rich Nuclei Studied symmetrized Molecular Dynamics Model	127 129 129
4	Clus with 4.1	ster Str Antisy Introd Antisy	ructure of Neutron-Rich Nuclei Studied ymmetrized Molecular Dynamics Model ymmetrized Molecular Dynamics	127 129 129 129

Contents xi

		4.2.4	Parity and Angular-Momentum Projection	132
		4.2.5	Hamiltonian and Energy Variation	133
		4.2.6	GCM in AMD	134
		4.2.7	Variation After Parity and Angular-Momentum Projections	136
		4.2.8	HF Single-Particle Orbits in an AMD Wave Function	137
		4.2.9	Projection and Variation	137
	4.3	Proper	rties of Low-Lying States in Light Nuclei	139
		4.3.1	Structure Changes in Li, Be, B, C Isotopes	139
		4.3.2	Magnetic Moments of Li and B Isotopes	141
	4.4	Proper	rties of Nuclei in the Island of Inversion	144
		4.4.1	Deformation, Particle-Hole Configuration and Spectrum .	145
		4.4.2	Probing the Particle Hole Configuration	147
	4.5	Cluste	er Structure in Excited States	148
		4.5.1	Be Isotopes	148
		4.5.2	F and Ne Isotopes	154
	4.6	Concl	usions	161
	Refe	rences		161
5	Di-N	Veutron	Clustering and Deuteron-like Tensor Correlation	
		uclear	Structure Focusing on ¹¹ Li	165
	5.1		ble Nuclei and the Halo Structure of ¹¹ Li	165
		5.1.1	Experimental Facts on ^{9,10} Li and ¹¹ Li	166
		5.1.2	Theoretical Studies on the Halo Structure in ¹¹ Li	169
		5.1.3	Nucleon-Nucleon Interaction and the Deuteron	
			and the Di-Neutron System	170
		5.1.4	Wave Functions for ^{9,10} Li and ¹¹ Li	172
	5.2		utron Clustering and the Hybrid-VT Model	173
		5.2.1	Formulation of Hybrid-VT Model	175
		5.2.2	Application of the Hybrid-VT Model to ⁶ He	179
		5.2.3	Hybrid-VT Model on Di-Neutron Clustering in ¹¹ Li	181
	5.3		nuum and Resonance States in Complex Scaling Method	184
		5.3.1	Formulation of CSM	185
		5.3.2	Three Body Resonance and Continuum States in ⁶ He	189
	5.4		ron-like Tensor Correlation and Tensor Optimized	
			Model (TOSM)	192
		5.4.1	Formulation of TOSM	194
		5.4.2	Formulation of UCOM	197
		5.4.3	Numerical Results of TOSM for ⁴ He	200
	5.5		utron Clustering and Deuteron-like Tensor Correlation	
		in Li	Isotopes	204
		5.5.1	Model of Li Isotopes	205
		5.5.2	Effective Interactions	208
		5.5.3	⁹ Li	210
		5.5.4	Pauli-Blocking Effect in ¹¹ Li	211
		5.5.5	¹⁰ Li	212

xii Contents

	5.6 Refe	5.5.6 ¹¹ Li 5.5.7 Electromagnetic Properties of Li Isotopes Conclusion	213 216 218 219
6		ective Clusterization in Nuclei and Excited	222
		npound Systems: The Dynamical Cluster-Decay Model	223
	6.1	Introduction	223
	6.2	Clustering in Light, Medium-Mass, Heavy, Super-Heavy,	224
		and Super-Superheavy Nuclei: Mean Field Approach 6.2.1 Relativistic Mean Field Method	224
		6.2.2 Applications of the RMF Model	229
	6.3	The Preformed-Cluster Based Dynamical Cluster-DecayModel	229
	0.5	for the Decay of Hot and RotatingCompound Nucleus	237
		6.3.1 The Preformed Cluster Model for Exotic Cluster	231
		Radioactivity	249
		6.3.2 Applications of the DCM Using Nuclear Proximity	,
		Potential	257
	6.4	Conclusions	261
	Refe	erences	262
_	G:	AND CARREST TO	267
7		nt Nuclear Systems of Molecular Type	267
	7.1	Introduction	267 268
	7.2	Potential Energy of Heavy Nuclear System	268
		7.2.2 Adiabatic Potential Energy and the Two-Center	
		Shell Model	273
		7.2.3 Two-core Approximation for Adiabatic Potential	277
		7.2.4 "Cold Valleys" within the Potential Energy Surface	279
	7.3	Local Potential Minima and Shape Isomeric States	282
	7.4	Cluster (Shell) Effects in Low EnergyHeavy-Ion Collisions	283
		7.4.1 Equations of Motion	284
		7.4.2 Shell Effects in Low-Energy Damped Collisions	288
		7.4.3 Production of New Heavy Neutron Rich Nuclei	202
	7.5	at the "North-East" Part of Nuclear Map	292
	7.5	Low-Energy Collisions of Heavy Actinide Nuclei	200
		and Giant Nuclear Systems of Molecular Type	296
		7.5.1 Production of Superheavy Elements in Collisions	200
		of Actinide Nuclei	296
		7.5.2 Giant Nuclear Systems of Molecular Type	201
	76	and Spontaneous Positron Formation	301
	7.6 7.7	Three-Cluster Configurations of Giant Nuclear Systems Conclusion	305 310
		erences	310
	Neit	AUIICO	.) 1 2

Chapter 1 Cluster Radioactivity

Dorin N. Poenaru and Walter Greiner

1.1 Introduction

The first informations about the atomic nucleus were obtained at the beginning of the twentieth century by studying radioactivity, which lead in fact to the fields of Nuclear Physics, Particle Physics, Radiochemistry as well as to many applications in Medicine, Biology, and Industry. The radioactivity (term coined by Marie Curie) was not known until Antoine Henri Becquerel, trying to see a connection between Wilhelm Conrad Roentgen's X-rays with fluorescence phenomena, discovered in 8 November 1895 a "mysterious" radiation of an uranium salt. Marie and Pierrre Curie found that Th also emits this radiation, and the new elements Ra and Po they discovered were the strong emitters. Ernest Rutherford deflected the charged particles (he named alpha and beta rays) in magnetic and electric field and from scattering experiments he deduced that atomic particles consisted primarily of empty space surrounding a well-defined central core called nucleus. He was the first to artificially transmute one element into another and to elucidate the concepts of the half-life and decay constant. By bombarding nitrogen with α particles, Rutherford demonstrated the production of a different element, oxygen. The atomic nucleus was discovered around 1911.

In 1911 Geiger and Nuttal gave a semi-empirical relationship of the α -decay half-life versus the range of α -particles in the air. It was explained by Gamow [25] by tunnelling the α -particle through the barrier—the first application of quantum theory to nuclei. The liquid drop model (LDM) was introduced earlier by John

D. N. Poenaru (\subseteq)

Horia Hulubei National Institute of Physics and Nuclear Engineering, PO Box MG-6, 077125, Bucharest-Magurele, Romania

e-mail: Dorin.Poenaru@nipne.ro

D. N. Poenaru and W. Greiner

Frankfurt Institute for Advanced Studies, J. W. Goethe University, Ruth-Moufang-Str. 1, 60438, Frankfurt am Main, Germany

e-mail: greiner@fias.uni-frankfurt.de

1

William Strutt, Lord Rayleigh, in a series of papers treating e.g. liquid droplets charged with electricity and the capillarity instability of an infinite jet of fluid [115].

By using the LDM, Gamow attempted to calculate in 1930 the nuclear binding energy. This prestigious work was accomplished by von Weizsäcker in 1935. The LDM published by Niels Bohr in 1936 was used by Lise Meitner and Otto Frisch to explain the induced fission, discovered by Otto Hahn and Fritz Strassman in 1939. Otto Frisch borrowed the name *fission* from biology of cell division. The classical paper by Bohr and Wheeler [6] explained many properties of the fission process, stating that fission was more likely to occur with ²³⁵U than ²³⁸U. Presently, we use as a macroscopic model either the variant of the LDM [76] or the Yukawa-plus-exponential model (Y+EM) [63].

For a long period of time only three kinds of nuclear decay modes (α , β and γ) have been known. They illustrate three of the fundamental interactions in nature: strong; weak, and electromagnetic. Spontaneous fission became popular soon after its discovery in 1940 by Petrzhak and Flerov owing to both military and peaceful applications of the neutron-induced fission, employing the large amount of energy released during the process.

Other decay modes like various kinds of proton radioactivity were predicted in 1960 by Goldansky. Karnaukhov et al. [61] discovered the β -delayed proton radioactivity, and Hofmann et al. observed the proton radioactivity from the ground state (gs for the following) [45, 46]. In 1998 the α and 10 Be accompanied (ternary) cold fission decays have been discovered [114]. The shape isomers and the mass asymmetry of fission fragments could be explained by using the macroscopic—microscopic approach [129] in which the shell and pairing corrections are calculated by using a single-particle shell model like the two center shell model [67, 74].

In 1984 Rose and Jones from Oxford University reported their experiment on ¹⁴C radioactivity of ²²³Ra [118] which we had predicted together with Sandulescu [120]. Several chapters in books and multi-authored books have been published, e.g. [38, 83, 84, 97, 104]. A key role in experiments on cluster decay modes performed in Berkeley, Orsay, Dubna and Milano played Buford Price [112], Eid Hourany and Michel Hussonnois [49, 50], Svetlana Tretyakova [132], and Bonetti [8] and their coworkers. Rose and Jones, as well as Ogloblin's team [1] did their experiments with a rather modest equipment; they had to wait for 6 months to get 11 events! Nevertheless, the experiments were well done; the following measurements confirmed the data. With modern magnetic spectrometers (SOLENO and Enge-split pole), at Orsay [24, 49, 51] and Argonne National Laboratory [43, 64], a very strong source could be used, so that results were obtained in a run of few hours.

The 233 Ra source used in the first experiment is a member of the 235 U natural radioactive family. One can see in Fig. 1.1 how a lighter nucleus, like 209 Pb, can be reached in a single cluster decay (e.g. 14 C decay of 233 Ra), compared to several successive α - or β ⁻-decays. When the daughter (209 Pb or 231 Tl) is not stable, it decays via β ⁻ into 209 Bi or 207 Pb, respectively. We shall mention in Sect. 1.6 the possibility to obtain direct spectroscopic information about 209 Pb by using this

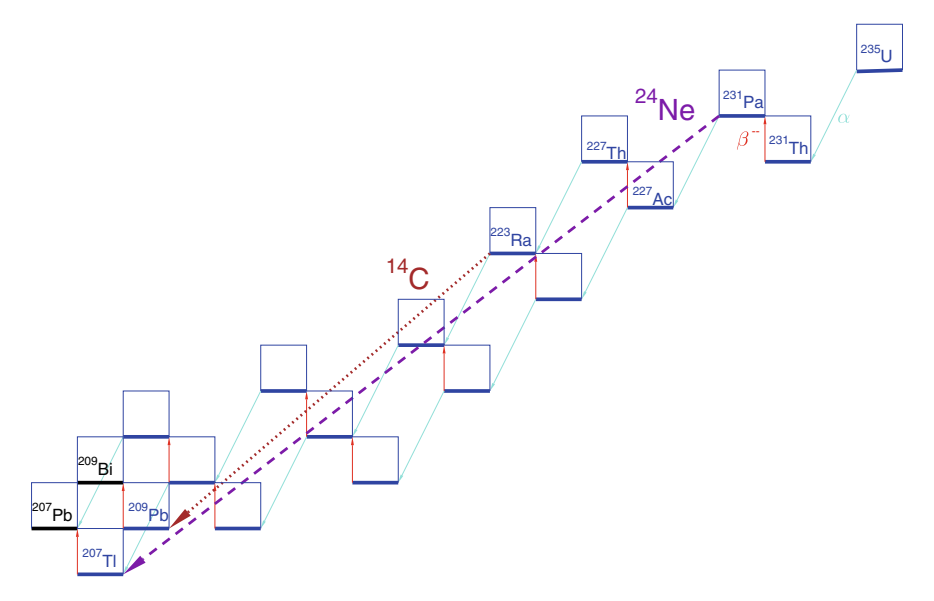


Fig. 1.1 The 235 U natural radioactive family with two cluster decay modes: 14 C from 233 Ra and 24 Ne from 231 Pa

property. Some related topics are discussed in Chap. 7 [142] and Chap. 6 [143] of the present book.

1.2 Macroscopic-Microscopic Method

Many nuclear properties can be explained by assuming that the nucleus is a system of independent particles, moving in an average potential created by all nucleons [23, 39]. This idea of a single-particle motion is the opposite of the collectivity hypothesis governing the LDM. In the framework of LDM, or of a similar macroscopic model, all nuclei have spherical shapes in the gs, and the fission fragment mass distributions of the actinides are perfectly symmetric, in contrast to the reality. Permanent nuclear deformations and fission fragment mass asymmetry can be explained by combining the collective (liquid drop-like) and single particle properties in the framework of macroscopic—microscopic method [129].

The small correction added to the LDM energy is calculated on the basis of single-neutron and single-proton energy levels of some deformed shell models. One single-particle model may be different by another one due to the average potential felt by the single nucleons. This can be either of finite depth (generalized Woods-Saxon or folded Yukawa) or of infinite depth (modified harmonic potential or the two-center shell model (TCSM)). By using the TCSM for describing the single-particle states, one can follow the shell structure all the way from the

original nucleus, over the potential barriers, up to the final stage of individual well separated fragments. Within fragmentation theory [39] all kinds of fission fragment mass distributions experimentally observed (symmetric, asymmetric, superasymmetric) have been explained.

According to the macroscopic–microscopic method the deformation energy of a nucleus, $E_{\rm def}$, is calculated as a sum of two terms coming from a phenomenological (e.g. Yukawa-plus exponential (Y+E)) model, $E_{\rm macro} = E_{\rm Y+E}$, and a small shell-plus-pairing correction, $E_{\rm micro} = \delta E$:

$$E_{\text{def}} = E_{\text{Y+E}} + \delta E \tag{1.1}$$

We calculate the microscopic corrections with the Strutinsky prescription based on the level schemes of protons (subscript $_p$) and neutrons (subscript $_n$) within a single-particle TCSM. This part of the calculations need to performed at every mesh point, therefore these calculations are very time-consuming; one has to diagonalize very large matrices of the Hamiltonian, including the spin–orbit term allowing to reproduce the experimentally determined magic numbers of nucleons.

1.2.1 Surface Parametrization

The permanent distortion from a sphere of a given nucleus in its gs or the change of the deformation during a nuclear process (fission, fusion, heavy ion reactions, etc.) may be described in terms of collective coordinates by using a function with a number of parameters as low as possible, which at the same time allows to determine all the possible shapes of the nuclear surface. It is also desirable to choose deformation coordinates which have simple physical significance. For the fission process one can select the separation distance of the fragments, the radius of the neck between fragments, the mass asymmetry, the charge asymmetry, the deformation of each fragment, etc.

The simplest shapes are spherical fragments. Two spheres of radii R_1 , R_2 are smoothly joined by a neck surface generated when a circle with a radius R_3 and the center coordinates (z_3, ρ_3) rotates around the axis of symmetry connecting the two centers $(z_1, 0)$ and $(z_2, 0)$. One deformation coordinate remains the separation distance $R = z_1 - z_2$. In addition we can define the charge and mass asymmetries of the final products

$$\eta_A = \frac{A_1 - A_2}{A_1 + A_2}, \quad \eta_Z = \frac{Z_1 - Z_2}{Z_1 + Z_2}$$
(1.2)

where A_1 and A_2 denote the mass, and Z_1 and Z_2 the atomic numbers of the fission fragments or of the fusing nuclei. Alternatively, we used to denote the heavy fragment by daughter nucleus (subscript d instead of 1), and the light one by the emitted cluster (subscript e instead of 2).

The nuclear surface is described by the following equation:

$$\rho(z) = \begin{cases} \sqrt{R_1^2 - (z - z_1)^2} & z_1 - R_1 \le z \le z_{c1} \\ \rho_3 - s_3 \sqrt{R_3^2 - (z - z_3)^2} & z_{c1} \le z \le z_{c2} \\ \sqrt{R_2^2 - (z - z_2)^2} & z_{c2} \le z_2 + R_2 \end{cases}$$
(1.3)

where z_{c1} , z_{c2} are the positions of intersection planes of two spheres with the neck surface. By imposing the volume conservation condition, the surface can be perfectly determined by three shape degrees of freedom: elongation (R), mass asymmetry $(\eta_A \text{ or } R_2)$ and the neck parameter (R_3) . Initially $R = R_i = R_0 - R_2$, where R_0 is the radius of the parent nucleus. The touching point configuration is obtained at $R = R_t = R_{1f} + R_{2f}$ when $R_3 = 0$. The subscript f labels final values. In Fig. 1.3 there is a plot of a similar surface with spheroidally deformed fragments and a smoothed neck.

1.2.2 Mass Defect and the Q-Values

The nuclear masses [136, 141] in atomic units (1u = 931493.86 \pm 0.06 keV) are very close to the mass number A = Z + N. This is the reason why usually the mass excess (or the mass defect) Δ is used

$$\Delta(A,Z) = [M(A,Z) - A]c^2 \tag{1.4}$$

where c is the speed of light. The mass of an atom is smaller than the combined masses of its constituent nucleons and electrons. The binding energy, B, accounts for the stability of a nucleus:

$$B(A,Z) = ZM_p + NM_n - M(A,Z) = Z\Delta(1,1) + N\Delta(1,0) - \Delta(A,Z)$$
 (1.5)

It is a positive quantity for any bound state, but the mass excess could be either positive (for light and heavy nuclei) or negative (for intermediate mass nuclei). $\Delta(1, 1) = 7.288969$ MeV and $\Delta(1, 0) = 8.071323$ MeV. The proton and the neutron have no binding energy, B(1, 1) = B(1, 0) = 0. The fact that B/A is maximal at $A \simeq 60$ and decreases both toward smaller and higher mass numbers is crucial for energy production by fusion of two light nuclei or by fission of a heavy nucleus.

The energy needed to remove a nucleon is called separation energy

$$S_n(A,Z) = M(A-1,Z) + M_n - M(A,Z)$$

$$S_p(A,Z) = M(A-1,Z-1) + M_p - M(A,Z)$$
(1.6)

The neutron drip line is defined by $S_n = 0$. A negative value, $S_p < 0$, characterizes a proton radioactive nucleus.

In a nuclear reaction with two bodies in the initial and final states $A + a \rightarrow B + b$, the released energy Q is given by

$$Q = (M_A + M_a) - (M_B + M_b) (1.7)$$

The main trends in binding energy can be understood in terms of a simple, semiempirical mass formula [137] containing volume, surface, Coulomb, symmetry, pairing, and Wigner contributions. Within Myers–Swiatecki's LDM [76], the mass equation of a spherical nucleus is given by

$$M = M_p Z + M_n N - a_V (1 - \kappa_V I^2) A + a_s (1 - \kappa I^2) A^{2/3}$$

+ $a_c Z^2 A^{-1/3} - a_d Z^2 / A + E_p + E_W$ (1.8)

where I = (N-Z)/A, $a_c = 3e^2/(5r_0)$, $a_d = \pi^2 e^2 d^2/(2r_0^3)$, d = 0.5461 fm. The pairing term is

$$E_p = \begin{cases} -11/\sqrt{A} & \text{MeV for even-even} \\ 0 & \text{for odd-}A \\ +11/\sqrt{A} & \text{MeV for odd-odd} \end{cases}$$
 (1.9)

and the Wigner term is given by

$$E_W = -7 \exp(-6|I|) \text{ MeV}.$$
 (1.10)

From a fit with experimental data on nuclear masses, quadrupole moments, and fission barriers, the following values of the parameters have been obtained: $a_V = 15.4941$ MeV; $a_s = 17.9439$ MeV; $\kappa_V = \kappa = 1.7826$; $a_c = 0.7053$ MeV; $a_d = 1.1530$ MeV, where the last two constants correspond to $r_0 = 1.2249$ fm, and $d/r_0 = 0.444$.

1.2.3 Liquid Drop Model

The shape-dependent terms in the LDM are the surface energy due to the strong interactions, tending to hold the nucleons together, and the electrostatic (Coulomb) energy, acting in the opposite direction. By requesting zero deformation energy for a spherical shape, the deformation energy is defined as

$$E_{\text{def}} = (E_s - E_s^0) + (E_c - E_c^0) = E_s^0 [B_s - 1 + 2X(B_c - 1)]$$
(1.11)

where $E_s^0 = a_s(1 - \kappa I^2)A^{2/3}$ and $E_c^0 = a_c Z^2 A^{-1/3}$ are the respective energies corresponding to spherical shape. The relative surface and Coulomb energies $B_s = E_s/E_s^0$, $B_c = E_c/E_c^0$ are only functions of the nuclear shape. The dependence on the neutron and proton numbers is contained in E_s^0 and in the fissility parameter $X = E_c^0/(2E_s^0)$.

The relative surface energy is proportional to the surface area. By expressing the equation for the nuclear surface in cylindrical coordinates $\rho = \rho(z, \phi)$, one has

$$B_{s} = \frac{1}{4\pi R_{0}^{2}} \int_{z'}^{z''} dz \int_{0}^{2\pi} \rho \left[1 + \left(\frac{\partial \rho}{\partial z} \right)^{2} + \left(\frac{1}{\rho} \frac{\partial \rho}{\rho \partial \varphi} \right)^{2} \right]^{1/2} d\varphi$$
 (1.12)

where z', z'' are the intersection points of the nuclear surface with Oz axis.

The electrostatic energy of a charge distribution with a density ρ_e in the nuclear volume V_n is given by

$$E_c = \frac{1}{8\pi} \int_{V_{\infty}} \mathbf{E}^2(\mathbf{r}) d^3 r = \frac{1}{2} \int_{V_{\infty}} \rho_e(\mathbf{r}) V(\mathbf{r}) d^3 r$$
 (1.13)

Here **E** is the electric field produced in the whole space by this distribution of the charges. The electrostatic potential V is a solution of the Poisson differential equation $\Delta V(\mathbf{r}) = -4\pi\rho_e(\mathbf{r})$, where Δ is the Laplacian differential operator. By substituting the expression of V as a solution of Poisson equation, one has

$$E_c = \frac{1}{2} \int_{V_c} \int \frac{\rho_e(\mathbf{r}) \rho_e(\mathbf{r}_1) d^3 r d^3 r_1}{|\mathbf{r} - \mathbf{r}_1|}$$
(1.14)

The Coulomb energy [21], (1.14), and the nuclear energy defined in (1.15), are both expressed as double-volume integrals. These sixfold integrals lead to analytical relationships when the nuclear shape is particularly simple; usually one needs to perform numerical quadratures. Fortunately the double-volume integrals can be transformed into double-surface integrals. By reducing the number of integrations from six to four, the computer running time necessary to achieve the required accuracy (more than five significant digits) becomes substantially shorter.

At the Businaro–Gallone fissility ($X_{\rm BG} = 0.396$ within LDM), a transition to unstable shapes with respect to mass asymmetry occurs. Calculated fission barriers corresponding to the conditional saddle points with constrained mass asymmetry plotted versus η at a given fissility $X \ge X_{\rm BG}$, show a minimum at $\eta = 0$ and a maximum at a value of $\eta_{\rm BG}$ which increases with X, but for $X < X_{\rm BG}$ the fission barrier always decreases with increasing asymmetry.

According to Moretto [71] the distinction between evaporation and fission for $X > X_{\rm BG}$ is given by the Businaro–Gallone peaks $\eta_{\rm BG}$: at a given fissility the fission process ranges from $\eta = 0$ to $\eta_{\rm BG}$, and the evaporation from $\eta_{\rm BG}$ to $\eta = 1$. Below the Businaro–Gallone fissility ($X < X_{\rm BG} = 0.396$ for zero angular momentum l, and smaller for larger l values) there is no distinction between (disappearing) fission and the evaporation extending from $\eta = 0$ to $\eta = 1$.

1.2.4 Phenomenological Yukawa-Plus-Exponential Model

The leptodermous expansion assumed in the LDM is only valid if all dimensions of the drop are large compared to the surface thickness, condition not satisfied for strongly necked-in configurations. Other deficiencies of the LDM surface energy are: the absence of attraction between separated nuclei at a small distance within the range of nuclear forces and the neglect of the surface diffusivity. To overcome these difficulties, the surface energy [63, 121] has been first replaced by a folded Yukawa and later on by a folded Yukawa-plus-exponential potential (Y+E):

$$E_Y = -\frac{a_2}{8\pi^2 r_0^2 a^4} \int_{V_n} \int \left(\frac{r_{12}}{a} - 2\right) \frac{\exp(-r_{12}/a)}{r_{12}/a} d^3 r_1 d^3 r_2$$
 (1.15)

where $r_{12} = |\mathbf{r}_1 - \mathbf{r}_2|$, a is the diffusivity parameter, and $a_2 = a_s(1 - \kappa I^2)$. For a spherical shape one has

$$E_Y^0 = a_2 A^{2/3} \{ 1 - 3x^2 + (1 + 1/x)[2 + 3x(1+x)] \exp(-2/x) \}$$
 (1.16)

in which $x = a/R_0$.

The Coulomb interaction energy of a system of *two spherical nuclei*, separated by a distance R between centers, is $E_{c12} = e^2 Z_1 Z_2 / R$. Within LDM there is no contribution of the surface energy to the interaction of the separated fragments; the barrier has a maximum at the touching point configuration. The proximity forces acting at small separation distances (within the range of strong interactions) give rise in the Y+EM to an interaction term expressed as follows

$$E_{Y12} = -4\left(\frac{a}{r_0}\right)^2 \sqrt{a_{21}a_{22}} \left[g_1 g_2 \left(4 + \frac{R}{a}\right) - g_2 f_1 - g_1 f_2 \right] \frac{\exp(-R/a)}{R/a}$$
 (1.17)

$$g_k = \frac{R_k}{a} \cosh\left(\frac{R_k}{a}\right) - \sinh\left(\frac{R_k}{a}\right); \quad f_k = \left(\frac{R_k}{a}\right)^2 \sinh\left(\frac{R_k}{a}\right)$$
 (1.18)

The interaction energy is maximum at a certain distance $R_m > R_t$.

Generally speaking the ratio of neutron to proton number of the emitted nucleus, N_e/Z_e , is different from that of the parent N/Z, when we consider beta-stable nuclei. The Green approximation [35] for the line of β -stability

$$N_g - Z = 0.4A^2/(200 + A) \tag{1.19}$$

allows us to find approximately which mass number, A, or neutron number, N_g , corresponds to a given proton number, Z, for a β -stable nucleus. It was shown that deformation energy could be underestimated if the condition $\eta_Z \neq \eta_A$ is ignored.

The Y+EM has been extended [105] to binary systems with different charge densities. One can take into consideration the difference in charge densities by assuming uniformity in each of the two fragments. In this way the nuclear volume

 $V=V_1+V_2$ is divided into two parts, each of them being homogeneously charged with a density ρ_{1e} and ρ_{2e} , respectively. The expression of the Coulomb energy is the same, both in LDM and Y+EM. Only the numerical value of the radius constant varies from one model to the other. The double-volume integral in (1.14) can be split into four parts, two of them being equal to each other, hence

$$E_c = \frac{\rho_{1e}^2}{2} \int_{V_1} d^3 r_1 \int_{V_1} \frac{d^3 r_2}{r_{12}} + \rho_{1e} \rho_{2e} \int_{V_2} d^3 r_1 \int_{V_2} \frac{d^3 r_2}{r_{12}} + \frac{\rho_{2e}^2}{2} \int_{V_2} d^3 r_1 \int_{V_2} \frac{d^3 r_2}{r_{12}}$$
(1.20)

The first and last term represent the self-energies of the two fragments, and the intermediate one is their interaction energy. By dividing with the Coulomb energy of a spherical nucleus with the same volume, one obtains the relative energy

$$B_c = \frac{E_c}{E_c^0} = \left(\frac{\rho_{1e}}{\rho_{0e}}\right)^2 B_{c1} + \frac{\rho_{1e}\rho_{2e}}{\rho_{0e}^2} B_{c12} + \left(\frac{\rho_{2e}}{\rho_{0e}}\right)^2 B_{c2}$$
 (1.21)

where the explicit expressions for the relative energies B_{ci} and B_{c12} will be given below. The Coulomb energy of a spherical nucleus is $E_c^0 = 3e^2Z^2/(5r_0A^{1/3})$ with $r_0 = 1.16$ fm for Y+EM.

We assume that nuclear matter is homogeneously distributed in the two fragments ($\rho_1 = \rho_2 = \rho_0$). From the general expression of the double-folded Y+EM nuclear energy, (1.15), we get three terms, in a way similar with the Coulomb energy:

$$B_Y = \frac{E_Y}{E_Y^0} = \frac{a_{21}}{a_{20}} B_{Y1} + \frac{\sqrt{a_{21}a_{22}}}{a_{20}} B_{Y12} + \frac{a_{22}}{a_{20}} B_{Y2}$$
 (1.22)

The volume conservation condition is a consequence of the low compressibility of nuclear matter. By assuming $\eta_Z = (Z_1 - Z_2)/Z = \eta_A = (A_1 - A_2)/A$ in the usual LDM, the volume energy has no variation with the deformation. For $\eta_Z \neq \eta_A$, there is a nonzero contribution $E_V = E_{V_1} + E_{V_2} - E_{V_0}$; $E_{V_i} = -a_V(1 - \kappa_V I_i^2)$ which is due to the symmetry energy.

For binary systems with different charge densities [105] and axially-symmetric shapes, one obtains

$$B_{c1} = b_c \int_{-1}^{x_c} dx \int_{-1}^{x_c} dx' F(x, x'); B_{c2} = b_c \int_{x_c}^{1} dx \int_{x_c}^{1} dx' F(x, x')$$
 (1.23)

$$B_{c12} = b_c \int_{-1}^{x_c} dx \int_{x_c}^{1} dx' F(x, x')$$
 (1.24)

where $b_c = 5d^5/8\pi$, $d = (z'' - z')/2R_0$, and x_c is the position of separation plane between fragments with -1, +1 intercepts on the symmetry axis (surface equation y = y(x) or $y_1 = y(x')$). The integrand reads

$$F(x,x') = \left\{ yy_1 \frac{K - 2D}{3} \left[2(y^2 + y_1^2) - (x - x')^2 + \frac{3}{2}(x - x') \left(\frac{dy_1^2}{dx'} - \frac{dy^2}{dx} \right) \right] + K \left\{ \frac{y^2 y_1^2}{3} + \left[y^2 - \frac{x - x'}{2} \frac{dy^2}{dx} \right] \left[y_1^2 - \frac{x - x'}{2} \frac{dy_1^2}{dx'} \right] \right\} \right\} a_\rho^{-1}$$
(1.25)

K and K' are the complete elliptic integrals of the first and second kind, respectively:

$$K(k) = \int_{0}^{\pi/2} (1 - k^2 \sin^2 t)^{-1/2} dt; K'(k) = \int_{0}^{\pi/2} (1 - k^2 \sin^2 t)^{1/2} dt$$
 (1.26)

and $a_{\rho}^2 = (y + y_1)^2 + (x - x')^2$, $k^2 = 4yy_1/a_{\rho}^2$, $D = (K - K')/k^2$. In our computer program the elliptic integrals are calculated by using the Chebyshev polynomial approximation. For x = x' the function F is not determined. In this case, after removing the indetermination, we get $F(x, x') = 4y^3/3$.

The relative nuclear Y+EM energies are expressed by triple integrals

$$B_{Y1} = b_Y \int_{-1}^{x_c} dx \int_{-1}^{x_c} dx' \int_{0}^{1} dw F_1 F_2 Q_Y; B_{Y2} = b_Y \int_{x_c}^{1} dx \int_{x_c}^{1} dx' \int_{0}^{1} dw F_1 F_2 Q_Y$$

$$(1.27)$$

$$B_{Y12} = b_Y \int_{-1}^{x_c} dx \int_{x_c}^{1} dx' \int_{0}^{1} dw F_1 F_2 Q_Y$$
 (1.28)

in which $b_Y = -d^4(r_0/2a^2)a_2R_0A/E_Y^0$ and

$$F_1 = y^2 + yy_1 \cos \varphi - \frac{x - x'}{2} \frac{dy^2}{dx},$$
 (1.29)

$$Q_Y = \{ [\sqrt{P}(\sqrt{P} + 2a/R_0d) + b] \exp(-R_0\sqrt{P}d/a) - b\}/P^2.$$
 (1.30)

where $b=2a^2/(R_0d)^2$. F_2 is obtained from F_1 by replacing dy^2/dx with dy_1^2/dx' . In the above equations $P=y^2+y_1^2-2yy_1\cos\varphi+(x-x')^2$ and $w=\varphi/2\pi$. The integrals are computed numerically by Gauss-Legendre quadratures. The following values of the parameters [70] were determined: a=0.68, $a_s=21.18466$ MeV, $a_V=16.00126$ MeV, $\kappa_S=2.345$, $\kappa_V=1.9224$, $r_0=1.16$ fm.

1.2.5 Single Particle Shell Model

The complex many-body problem is very much simplified by considering one single-particle in the mean field produced by all other particles.

1.2.5.1 Three-Dimensional Spheroidal Harmonic Oscillator

For spheroidal equipotential surfaces, generated by a potential with cylindrical symmetry, the states of the nucleons (or of the valence electrons for atomic clusters) can be found by using an effective single-particle Hamiltonian with a potential

$$V = \frac{M\omega_0^2 R_0^2}{2} \left[\rho^2 \left(\frac{2+\delta}{2-\delta} \right)^{2/3} + z^2 \left(\frac{2-\delta}{2+\delta} \right)^{4/3} \right]$$
 (1.31)

The deformation δ is defined [17] by expressing the dimensionless two semi-axes, in units of the radius R_0 of a sphere with the same volume, as

$$a = \left(\frac{2-\delta}{2+\delta}\right)^{1/3}; c = \left(\frac{2+\delta}{2-\delta}\right)^{2/3}$$
 (1.32)

We use dimensionless cylindrical coordinates ρ and z. Volume conservation leads to $a^2c = 1$. One can separate the variables in the Schrödinger equation, $H\Psi = E\Psi$. As a result the wave function may be written [134] as

$$\Psi(\eta, \xi, \varphi) = \psi_{n_x}^m(\eta) \Phi_m(\varphi) Z_{n_z}(\xi)$$
 (1.33)

where each component is orthonormalized, $\eta=R_0^2\rho^2/\alpha_\perp^2$, $|m|=(n_\perp-2i)$ with i=0,1,... up to $(n_\perp-1)/2$ for an odd n_\perp or to $(n_\perp-2)/2$ for an even n_\perp , $n_r=(n_\perp-|m|)/2$, $\alpha_\perp=\sqrt{\hbar/M\omega_\perp}$. We are interested in the z-component

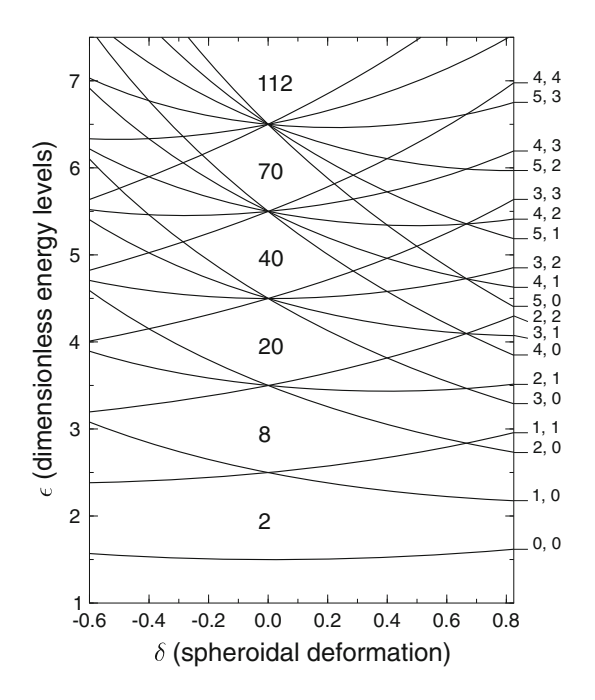
$$Z_{n_z}(\xi) = N_{n_z} e^{-\xi^2/2} H_{n_z}(\xi); N_{n_z} = \frac{1}{(\alpha_z \sqrt{\pi} 2^{n_z} n_z!)^{1/2}}$$
(1.34)

where $\xi = R_0 z/\alpha_z$, $\alpha_z = \sqrt{\hbar/M\omega_z}$, and the main quantum number $n = n_\perp + n_z = 0, 1, 2, \ldots$ The parity of the Hermite polynomials $H_{n_\perp z}(\xi)$ is given by $(-1)^{n_z}$. The eigenvalues are $E_n = \hbar \omega_\perp (n_\perp + 1) + \hbar \omega_z (n_z + 1/2)$, or in units of $\hbar \omega_0$, $\varepsilon_n = E_n/(\hbar \omega_0)$,

$$\varepsilon_n = \frac{2}{(2-\delta)^{1/3}(2+\delta)^{2/3}} \left[n + \frac{3}{2} + \delta \left(n_{\perp} - \frac{n}{2} + \frac{1}{4} \right) \right]$$
 (1.35)

For a prolate spheroid, $\delta > 0$, at $n_{\perp} = 0$ the energy level decreases with deformation except for n = 0, but when $n_{\perp} = n$ it increases. The low lying energy

Fig. 1.2 Energy levels in units of $\hbar\omega_0$ versus the deformation parameter δ of a spheroidal harmonic oscillator. Each level is labelled by n, n_{\perp} quantum numbers shown at the right-hand side, and is $(2n_{\perp} + 2)$ -fold degenerate



levels can be seen in the Fig. 1.2 Each level, labelled by n_{\perp} , n, may accommodate $2n_{\perp}+2$ particles. One has $2\sum_{n_{\perp}=0}^{n}(n_{\perp}+1)=(n+1)(n+2)$ nucleons in a completely filled shell characterized by n, and the total number of states of the low-lying n+1 shells is $\sum_{n=0}^{n}(n+1)(n+2)=(n+1)(n+2)(n+3)/3$ leading to the magic numbers 2, 8, 20, 40, 70, 112, 168, ... for a spherical shape. Besides the important degeneracy at a spherical shape ($\delta=0$), one also has degeneracies at some superdeformed shapes, e.g. for prolate shapes at the ratio $c/a=(2+\delta)/(2-\delta)=2$ i.e. $\delta=2/3$.

1.2.5.2 Two Center Shell Model

The importance of an adequate description of cold fission, cluster radioactivities and alpha decay in terms of an asymmetric and deformed single particle shell model (DTCM) with more realistic shapes during fission and fusion processes was repeatedly stressed [37, 67, 96]. The TCSM has been developed by the Frankfurt school [48, 39]. We shall use a new variant [27, 28, 29], for which the nuclear surface is an equipotential, and which is able to give solutions even for extremely large mass asymmetry. The main part of the potential consists of two spheroidally deformed oscillators. Any change in the axially symmetric nuclear surface shape is reflected in a corresponding modification of the four oscillator frequencies along the symmetry axis and perpendicular to it. A microscopic potential is associated to a spherically matching neck region of the nuclear shape. The spin–orbit and

squared angular momentum operators are calculated by using potential-dependent formulae $\mathbf{ls} = (\nabla V \times \mathbf{p})\mathbf{s}$, and $\mathbf{l}^2 = (\nabla V \times \mathbf{p})^2$ and the potential follows exactly the nuclear shape.

Figure 1.3 shows the main geometrical parameters defining the axially symmetric shape family. Two spheroids (the deformed fragments) with semiaxes a_1 , b_1 and a_2 , b_2 are separated at a distance R between the two centers O_1 and O_2 . A sphere centered in O_3 with radius R_3 is rolling around the symmetry axis, being tangent all the time to the two spheroids. The necking region is generated in this way. Thus we have five independent parameters defining the deformation space: two fragment deformations $\chi_1 = b_1/a_1$, $\chi_2 = b_2/a_2$; mass asymmetry $\eta = (A_1 - A_2)/A$; the neck radius R_3 and the distance between the centers R. This set is available for every parent nucleus A, Z with its own semiaxes ratio $\chi = b/a$.

The equations for shape surfaces described above can be written in cylindrical coordinates (due to axial symmetry) as:

$$\rho(z) = \begin{cases}
\rho_1(z) = [b_1^2 - \chi_1^2 z^2]^{1/2} & -a_1 \le z \le z_{c1} \\
\rho_g(z) = \rho_3 - [R_3^2 - (z - z_3)^2]^{1/2}, & z_{c1} \le z \le z_{c2} \\
\rho_2(z) = [b_2^2 - \chi_2^2 (z - R)^2]^{1/2}, & z_{c2} \le z \le R + a_2
\end{cases}$$
(1.36)

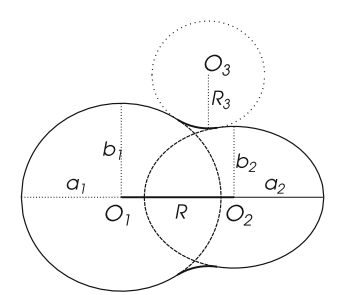
where the origin is placed in the center of the heavy fragment O_1 . Neck sphere center coordinates are (z_3, ρ_3) , and z_{c1} and z_{c2} are the two tangent points of the neck sphere with the two ellipsoids.

The oscillator potential corresponding to the two-center shapes must have the same value on the nuclear surface, e.g. for spheres $V_0 = m_0 \omega_i^2 R_i^2/2$, where R_i is the radius of a nucleus with atomic mass A_i . Since $\hbar \omega_i = 41A^{-1/3}$ and $R_i = r_0 A^{1/3}$, $r_0 = 1.16$ fm, then $V_0 \simeq 27.25$ MeV. For the surface of spheroidal shapes $m_0 \omega_{z_i}^2 a_i^2/2 = m_0 \omega_{\rho_i}^2 b_i^2 = V_0$, the frequencies ω_{z_i} , $\omega_{\rho i}$ are defined along the symmetry axis and respectively perpendicular to it, as functions of the two spheroid semiaxes.

For an arbitrary origin, placed on the symmetry axis, the spheroids surface equations read:

$$\frac{\rho^2}{\frac{2V_0}{m_0\omega_{\rho_1}^2}} + \frac{(z+z_1)^2}{\frac{2V_0}{m_0\omega_{z_1}^2}} = 1; \frac{\rho^2}{\frac{2V_0}{m_0\omega_{\rho_2}^2}} + \frac{(z-z_2)^2}{\frac{2V_0}{m_0\omega_{z_2}^2}} = 1$$
(1.37)

Fig. 1.3 Nuclear shape and deformation parameters for necked-in intersected spheroids. The four geometrical parameters which vary are the two ratios of the spheroid semiaxes, b_1/a_1 and b_2/a_2 , the neck sphere radius R_3 and the distance between the fragment centers R



where z_1 and z_2 are the absolute values of each of the two centers coordinates. Consequently for deformed fragments one has:

$$V^{(r)}(\rho,z) = \begin{cases} V_1(\rho,z) = \frac{1}{2}m_0\omega_{\rho_1}^2\rho^2 + \frac{1}{2}m_0\omega_{z_1}^2(z+z_1)^2 &, v_1 \\ V_2(\rho,z) = \frac{1}{2}m_0\omega_{\rho_2}^2\rho^2 + \frac{1}{2}m_0\omega_{z_2}^2(z-z_2)^2 &, v_2 \end{cases}$$
(1.38)

where v_1 and v_2 are the space regions where the two potentials are acting. The frequencies are shape dependent: from the volume conservation condition we have: $a_i b_i^2 = R_i^3$, where R_i is the radius of the spherical nucleus with the same volume. The shape dependence of the frequencies is given by

$$m_0 \omega_{\rho_i}^2 = (a_i/b_i)^{2/3} \cdot m_0 \omega_{0i}^2 = (a_i/b_i)^{2/3} \cdot 54.5/R_i^2$$

$$m_0 \omega_{\tau_i}^2 = (b_i/a_i)^{4/3} \cdot m_0 \omega_{0i}^2 = (b_i/a_i)^{4/3} \cdot 54.5/R_i^2$$
(1.39)

In this way the two center oscillator potential for fusion like shapes follows the changes of the two spheroidal partner deformations. The ratio $\chi_i = b_i/a_i$, i = 1,2, changes as:

$$\chi_{1,2} = \chi_0 + (\chi_{10,20} - \chi_0) \frac{R - R_f}{kAR}$$
 (1.40)

where ΔR is the step width in R (e.g. 0.1 fm) and k is the number of steps. For k=1 we have $R=R_f$ and $\chi_{1,2}=\chi_0$. The value of χ_{10} and χ_{20} are those taken by the partners at the first step ($k=k_{\rm max}$), immediately after the overlap begins.

By adding the neck-dependent potential the deformed oscillator potential part becomes:

$$V_{\text{DTCSM}}(\rho, z) = \begin{cases} V_1(\rho, z), & v_1 \\ V_g(\rho, z) = \begin{cases} V_{g1}(\rho, z), & v_{g1} \\ V_{g2}(\rho, z) = V_0, & v_{g2} \end{cases}$$
 (1.41)

Here v_1 , v_{g1} , v_{g2} and v_2 are the spatial regions where the corresponding potentials are acting. The deformation-dependent part of the neck contribution is given by

$$V_{g1}(\rho, z) = 2V_0 - \left[\frac{1}{2}m_0\omega_g^2(\rho - \rho_3)^2 + \frac{1}{2}m_0\omega_g^2(z - z_3)^2\right]$$
(1.42)

The angular momentum operator is shape-dependent; we shall avoid confusions by using a different notation for the spin-orbit and the square of the angular momentum terms, namely $V_{\Omega s}$ and V_{Ω^2} . The total two-center Hamiltonian

$$H_{\text{DTCSM}} = -\frac{\hbar^2}{2m_0} \Delta + V_{\text{DTCSM}}(\rho, z) + V_{\Omega s} + V_{\Omega^2}$$
 (1.43)

is not separable. A separable Hamiltonian is obtained if one takes $\omega_{\rho_1} = \omega_{\rho_2} = \omega_1$, and ignores spin–orbit and the other term

$$V^{(d)}(\rho,z) = \begin{cases} V_1^{(d)}(\rho,z) = \frac{1}{2}m_0\omega_1^2\rho^2 + \frac{1}{2}m_0\omega_1^2(z+z_1)^2, & z \le 0 \\ V_2^{(d)}(\rho,z) = \frac{1}{2}m_0\omega_1^2\rho^2 + \frac{1}{2}m_0\omega_2^2(z-z_2)^2, & z \ge 0 \end{cases}$$
(1.44)

This is a two-center potential for a sphere $(z \le 0)$ intersected with a vertical spheroid. The origin (z = 0) is the intersection plane. As a result of variable separation, three known differential equations are obtained for harmonic functions, Laguerre polynomial and Hermite function dependent solutions. With the standard notation for the quantum numbers $n_0 m$, v the diagonalization basis is given by

$$\Phi_{m}(\phi) = \frac{1}{\sqrt{2\pi}} \exp(im\phi)$$

$$R_{n_{\rho}}^{|m|}(\rho) = \sqrt{\frac{2\Gamma(n_{\rho}+1)\alpha_{1}^{2}}{\Gamma(n_{\rho}+|m|+1)}} \exp\left(-\frac{\alpha_{1}^{2}\rho^{2}}{2}\right) (\alpha_{1}^{2}\rho^{2})^{\frac{|m|}{2}} L_{n_{\rho}}^{|m|}(\alpha_{1}^{2}\rho^{2})$$

$$Z_{\nu}(z) = \begin{cases}
C_{\nu_{1}} \exp\left[-\frac{\alpha_{1}^{2}(z+z_{1})^{2}}{2}\right] H_{\nu_{1}}[-\alpha_{1}(z+z_{1})], & z < 0 \\
C_{\nu_{2}} \exp\left[-\frac{\alpha_{2}^{2}(z-z_{2})^{2}}{2}\right] H_{\nu_{2}}[\alpha_{2}(z-z_{2})], & z \ge 0
\end{cases}$$
(1.45)

where Γ is the gamma function, L_n^m is the m-order Laguerre polynomial, C_1 and C_2 the normalization constants, v_1 , v_2 the quantum numbers along the symmetry axis, and H_v is the Hermite function. The eigenvalues for the diagonalized Hamiltonian with the potential $V^{(d)}$ are the oscillator energy levels for the sphere + spheroid system:

$$E_{\rm osc}^{(d)} = \hbar\omega_1(2n_\rho + |m| + 1) + \hbar\omega_{z_1}(v_1 + 0.5)$$
(1.46)

By using this basis one has to calculate the nondiagonal matrix elements of the total Hamiltonian.

The general expression of the matrix elements of the Hamiltonian may be written as:

$$\langle i|H_{\rm DTCSM}|j\rangle = E_{\rm osc}^{(d)} + \langle i|\Delta V_1|j\rangle + \langle i|\Delta V_2|j\rangle + \langle i|V_g|j\rangle + \langle i|V_{\Omega s}|j\rangle + \langle i|V_{\Omega^2}|j\rangle$$
(1.47)

where the first term was given above, ΔV_1 is the difference $V_1(\rho, z) - V^{(d)}(\rho, z)$ within the volume v_1 , ΔV_2 is the similar quantity for v_2 and V_g corresponds to the neck region.

In order to assure Hermiticity for the spin–orbit kind of operator terms (l s and l^2) one uses anticomutators of the types

$$\left\{\frac{\hbar}{m_0\omega_{01}}\kappa_1(\rho,z), (\nabla V \times \mathbf{p})\mathbf{s}\right\}; \left\{\frac{\hbar}{m_0^2\omega_{01}^3}\kappa_1\mu_1(\rho,z), (\nabla V \times \mathbf{p})^2\right\}$$
(1.48)

where one should not forget that

$$\mathbf{ls} \to \frac{1}{2}(\Omega^{+}\mathbf{s}^{-} + \Omega^{-}\mathbf{s}^{+}) + \Omega_{z}\mathbf{s}_{z}; \mathbf{l}^{2} \to \Omega^{2} = \frac{1}{2}(\Omega^{+}\Omega^{-} + \Omega^{-}\Omega^{+}) + \Omega_{z}^{2}$$
 (1.49)

As an example one can write

$$\Omega^{+}(v_{1}) = -e^{i\varphi} \left[\frac{\partial V_{1}(\rho, z)}{\partial \rho} \frac{\partial}{\partial z} - \frac{\partial V_{1}(\rho, z)}{\partial z} \frac{\partial}{\partial \rho} - \frac{i}{\rho} \frac{\partial V_{1}(\rho, z)}{\partial z} \frac{\partial}{\partial \varphi} \right]
= -e^{i\varphi} \left[m_{0} \omega_{\rho_{1}}^{2} \rho \frac{\partial}{\partial z} - m_{0} \omega_{z_{1}}^{2}(z + z_{1}) \frac{\partial}{\partial \rho} - \frac{i}{\rho} m_{0} \omega_{z_{1}}^{2}(z + z_{1}) \frac{\partial}{\partial \varphi} \right]$$
(1.50)

$$\Omega^{-}(v_{1}) = e^{-i\varphi} \left[\frac{\partial V_{1}(\rho, z)}{\partial \rho} \frac{\partial}{\partial z} - \frac{\partial V_{1}(\rho, z)}{\partial z} \frac{\partial}{\partial \rho} + \frac{i}{\rho} \frac{\partial V_{1}(\rho, z)}{\partial z} \frac{\partial}{\partial \varphi} \right]
= e^{-i\varphi} \left[m_{0} \omega_{\rho_{1}}^{2} \rho \frac{\partial}{\partial z} - m_{0} \omega_{z_{1}}^{2}(z + z_{1}) \frac{\partial}{\partial \rho} + \frac{i}{\rho} m_{0} \omega_{z_{1}}^{2}(z + z_{1}) \frac{\partial}{\partial \varphi} \right]$$
(1.51)

$$\Omega_{z}(v_{1}) = -\frac{i}{\rho} \frac{\partial V_{1}}{\partial \rho} \frac{\partial}{\partial \varphi} = -im_{0} \omega_{\rho_{1}}^{2} \frac{\partial}{\partial \varphi}$$

$$(1.52)$$

The strength parameters κ and μ , allowing to reproduce the experimentally determined magic numbers, are continuously changed from the parent to the fragments by requesting

$$\kappa = \kappa_i + \frac{R - R_i}{R_f - R_i} (\kappa_f - \kappa_i) \tag{1.53}$$

Detailed relationships are given in the Appendix of the Ref. [27]. The diagonalization of the Hamiltonian for proton and neutrons leads to the level scheme of two partially overlapping spheroids for a given distance R between centers and intermediary (independent) ratios of the semiaxes of the target and projectile nuclei $\chi_T = b_T/a_T$ and $\chi_P = b_P/a_P$. Here (b_T, a_T) and (b_P, a_P) are the spheroid semiaxes.

The energy level diagram shows the final states of the heavy fragment and of the light one. The light fragment has a separation energy between two shells higher than the heavy one, because $\hbar\omega_H = 41A_H^{-1/3}$ and $\hbar\omega_L = 41A_L^{-1/3}$. At the scission separation distance, the low-lying levels are degenerate, reflecting the development of a barrier between fragments, but around Fermi energy the levels are still splitted, suggesting quasimolecular kind of states where the valence nucleon properties are important for the final stages of the fission process.

1.2.6 Shell and Pairing Corrections

We would like to outline the calculations of the shell, δU , and pairing, δP , corrections leading to the total deformation energy in the framework of the macroscopic–microscopic method

$$E_{\text{def}} = E_{Y+E} + \delta E_{sh+p} \tag{1.54}$$

in which E_{Y+E} is the macroscopic Yukawa-plus-exponential term and $\delta E_{sh+p} = \delta U + \delta P$. More details are given elsewhere [96].

The TCSM [27] gives at every pair of coordinates (R, η) the sequence of doubly degenerate discrete energy levels $\varepsilon_i = E_i/\hbar\omega_0^0$ in units of $\hbar\omega_0^0 = 41A^{-1/3}$, arranged in order of increasing energy. The smoothed-level distribution density is obtained by averaging the actual distribution over a finite energy interval $\Gamma = \gamma\hbar\omega_0^0$, with $\gamma \simeq 1$,

$$\tilde{g}(\varepsilon) = \left\{ \sum_{i=1}^{n_m} [2.1875 + y_i(y_i(1.75 - y_i/6) - 4.375)]e^{-y_i} \right\} (1.77245385\gamma)^{-1}$$
(1.55)

where $y = x^2 = [(\varepsilon - \varepsilon_i)/\gamma]^2$. The summation is performed up to the level n_m fulfilling the condition $|x_i| \ge 3$. The Fermi energy, $\tilde{\lambda}$, of this distribution is given by

$$N_p = 2 \int_{-\infty}^{\tilde{\lambda}} \tilde{g}(\varepsilon) d\varepsilon \tag{1.56}$$

with $N_p = Z$ for proton levels and $N_p = A - Z$ for neutron levels, leading to a non-linear equation in $\tilde{\lambda}$, solved numerically. The total energy of the uniform level distribution is given by

$$\tilde{u} = \tilde{U}/\hbar\omega_0^0 = 2\int_{-\infty}^{\tilde{\lambda}} \tilde{g}(\varepsilon)\varepsilon \, d\varepsilon \tag{1.57}$$

In units of $\hbar\omega_0^0$ the shell corrections are calculated for each pair (R, η) :

$$\delta u(n, R, \eta) = \sum_{i=1}^{n} 2\varepsilon_i(R, \eta) - \tilde{u}(n, R, \eta)$$
 (1.58)

 $n = N_p/2$ particles. Then $\delta u = \delta u_p + \delta u_n$.

Similarly, for pairing corrections we take the doubly degenerate levels $\{\varepsilon_i\}$ in units of $\hbar\omega_0^0$. Z/2 levels are occupied with n levels below and n' above Fermi energy contributing to pairing, $n=n'=\Omega\tilde{g_s}/2$. The cutoff energy, $\Omega\simeq 1\gg\tilde{\Delta}=12/\sqrt{\Lambda}\hbar\omega_0^0$. The gap Δ and the Fermi energy λ are solutions of the BCS system of two equations [10]:

$$0 = \sum_{k_i}^{k_f} \frac{\varepsilon_k - \lambda}{\sqrt{(\varepsilon_k - \lambda)^2 + \Delta^2}}; \frac{2}{G} = \sum_{k_i}^{k_f} \frac{1}{\sqrt{(\varepsilon_k - \lambda)^2 + \Delta^2}}$$
(1.59)

where $k_i = Z/2 - n + 1$, $k_f = Z/2 + n'$, and

$$\frac{2}{G} \simeq 2\tilde{g}(\tilde{\lambda}) \ln \left(\frac{2\Omega}{\tilde{\Delta}}\right) \tag{1.60}$$

As a consequence of the pairing correlation, the levels below the Fermi energy are only partially filled, while those above the Fermi energy are partially empty. The occupation probability by a quasiparticle (v_k^2) or hole (u_k^2) is given by $v_k^2 = [1 - (\varepsilon_k - \lambda)/E_k]/2$; $u_k^2 = 1 - v_k^2$. The quasiparticle energy is expressed as $E_v = \sqrt{(\varepsilon_v - \lambda)^2 + \Delta^2}$.

The pairing correction $\delta p = p - \tilde{p}$, represents the difference between the pairing correlation energies for the discrete level distribution and for the continuous level distribution

$$p = \sum_{k=k}^{k_f} 2v_k^2 \varepsilon_k - 2 \sum_{k=k}^{Z/2} \varepsilon_k - \frac{\Delta^2}{G}; \quad \tilde{p} = -(\tilde{g}\tilde{\Delta}^2)/2 = -(\tilde{g}_s\tilde{\Delta}^2)/4$$
 (1.61)

Compared to shell correction, the pairing correction is out of phase and smaller leading for R = constant to a smoother total curve $\delta e (\eta) = \delta u (\eta) + \delta p (\eta)$ where $\delta p = \delta p_p + \delta p_n$.

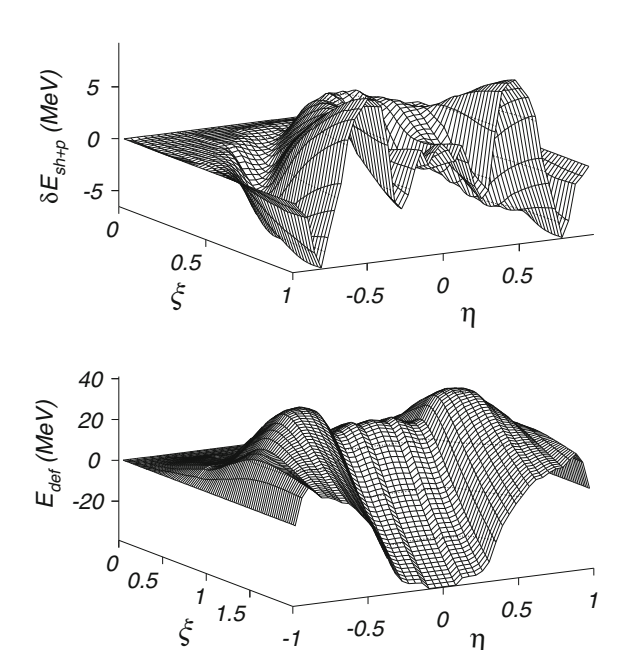
1.2.7 Potential Energy Surfaces

We study a binary fission process ${}^{A}Z \rightarrow {}^{A_{d}}Z_{d} + {}^{A_{e}}Z_{e}$ by taking into account the difference between charge and mass asymmetry. Calculations have been recently outlined [94, 108, 109]. An alternative notation for the emitted cluster or light fragment is ${}^{A_{2}}Z_{2}$ and for the daughter or the heavy fragment is ${}^{A_{1}}Z_{1}$.

The macroscopic part of the deformation energy has a rather smooth variation with ξ and η . The valleys are produced by the proton and neutron shell and pairing corrections, which have a negative value when the nucleon number is magic. Consequently in principle, at least one of the four nucleon numbers Z_d , N_d , Z_e , and N_e should be magic in order to contribute with negative energy corrections, digging a valley into the energy surface. In practice one has to have two magic numbers simultaneously, because the valley becomes much deeper in this way. This rule is clearly fulfilled by the example given in Fig.1.4. The more pronounced two valleys result from the presence of doubly magic nuclei $^{132}_{50} \mathrm{Sn}_{82}$ and $^{208}_{82} \mathrm{Pb}_{126}$ as heavy fragments (daughter nuclei) in the output channel.

In Fig. 1.4 we plotted two energy surfaces versus $\xi = (R - R_i)/(R_t - R_i)$ and $\eta = (A_1 - A_2)/(A_1 + A_2)$ for a heavy cluster emitter with Z = 88 (Ra) and A = 222. The valleys due to the doubly magic fragments ²⁰⁸Pb and ¹³²Sn are shown. Such cold valleys were used in the 1960s by Greiner to motivate the search for superheavies, and the development of Heavy Ion Physics in Germany (where GSI was built) and worldwide. A shell-stabilizing property characteristic for the superheavy nuclei is present in the heaviest elements known to date. The strong

Fig. 1.4 Shell and pairing corrections $\delta E_{\rm sh+p} = \delta U +$ δP (top) and total deformation energy $E_{\text{def}} = E_{\text{Y+EM}} +$ δE (bottom) versus the separation distance $\xi = (R - R_i)/$ $(R_t - R_i)$ and the mass asymmetry $\eta = (A_1 - A_2)/A$ for ²²²Ra. There is a shallow valley not far from symmetry due to a cold fission process with 132Sn as heavy fragment and ⁹⁰Sr as light fragment. Much deeper are two other valleys at n = 0.87 for ¹⁴C radioactivity and 208Pb as the daughter nucleus and near $\eta = 0.36$ for asymmetric fission with $^{70}_{28}\text{Ni}_{42}$ as the light fragment and 152Nd as the daughter nucleus

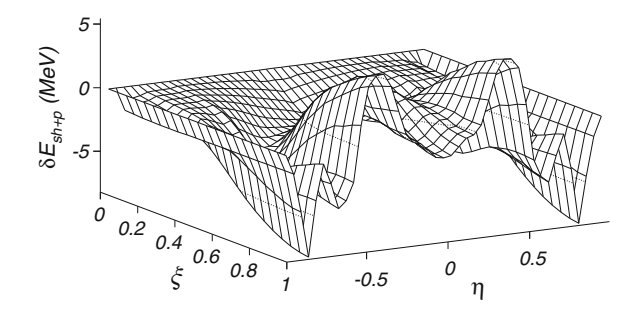


shell effects of the doubly magic daughter ²⁰⁸Pb are responsible for bringing the half-lives of the majority of cluster decay modes into the measurable range, as we shall illustrate below. In particular the ²²²Ra, with the PES shown in Fig. 1.4, has the shortest half-life for ¹⁴C emission.

The potential barrier shape similar to that we considered within the ASAF model was recently calculated by using the macroscopic-microscopic method [94], as a cut through the PES at a given mass asymmetry, usually the ²⁰⁸Pb valley or not far from it.

For one of the lightest α -emitter, ^{106}Te , we give in Fig. 1.5 the shell and pairing corrections, showing the deep minimum at $\eta \simeq 0.92$ due to the almost doubly magic daughter ^{102}Sn . One can see the three valleys: cold-fission (almost symmetrical); ^{16}O radioactivity, and α -decay. The nucleus ^{106}Te has been experimentally produced and studied long ago [117].

Fig. 1.5 Shell and pairing corrections surface of 106 Te. The α -valley around $\eta \simeq 0.92$ is very deep due to the almost doubly magic daughter 102 Sn. Another valley appears at $\eta \simeq 0.69$ with fragments 90 Ru + 16 O



 $^{258} Fm$ is known for its symmetrical distribution of the fission fragment mass yield [44]. $^{264} Fm$ is the neutron-rich parent predicted [31, 104] to be the best cold fissioning nucleus (with cold fission more probable than α decay), owing to its doubly magic identical fragments $^{132} Sn$. The deepest α valley is that of $^{106} Te$, and the deepest cold fission valley is that of $^{264} Fm$ [89], because in these examples both fragments are doubly magic or almost doubly magic nuclei.

1.2.8 Saddle-Point Shapes

In order to determine the saddle point shapes of heavy nuclei e.g. for fissility parameter X = 0.60, 0.70, 0.82 (170 Yb, 204 Pb, 252 Cf nuclei) we developed a method [88] obtained by solving an integro-differential equation (Euler–Lagrange equation minimizing the deformation energy). It was also used to show qualitatively that the mass asymmetry of fission fragments is the result of shell effects.

Let us consider a nuclear system with a shape specified by a set of n generalized coordinates $\{q_i\}$. For an equilibrium (ground-state or saddle-point) shape [21, 131] the deformation energy $E = E(q_1, q_2, ..., n)$ has an extremum, defined by $\partial E/\partial q_i = 0$, (i = 1, 2, ..., n).

In a LDM the gs, characterized by the lowest minimum of the potential energy, always corresponds to a spherical shape. One may define a fission valley on the potential energy surface in a multidimensional space of deformation parameters, as a conditional minimum $\partial E/\partial q_k=0$, (i=1,2,...,k-1,k+1,...,n) with the constraint $q_k=q_k^0$ for different values q_k^0 . The maximum value on this minimum energy determines the saddle-point position, at which all eigenvalues of the symmetric curvature matrix

$$K_{ij} = \frac{\partial^2 E(q)}{\partial a_i \partial a_i} \tag{1.62}$$

have a positive sign, except one.

The potential energy versus one deformation parameter along the fission path is a smooth curve with a minimum at the gs and a maximum at the saddle point. Then it decreases continuously going through the scission point, down to the self energy of the fragments at infinite separation distance. By representing this quantity for a heavy nucleus vs. the mass asymmetry coordinate in a transverse direction at the saddle point we also get a smooth curve with a minimum between two maxima, called Businaro–Gallone mountains [15]. The saddle point is lying at the bottom of the valley separating these mountains.

A conditional saddle point is defined by adding to the above equations one or several constraints. Of particular interest in fission is the constraint of a given mass asymmetry, $\eta = \eta_0$. If η is one of the generalized coordinates the problem is simplified because one takes $\eta = \text{constant}$. In general η depends on q, and the generalization of the variational equation to the equilibrium with constraints leads to

$$\frac{\partial E}{\partial q_i} + \lambda \frac{\partial \eta}{\partial q_i} = 0, \quad i = 1, 2, \dots, n$$
 (1.63)

where λ being a Lagrange multiplier.

There is no need to consider any reflection asymmetry or nonaxiality in the calculation of saddle point shapes within the LDM, because the energy increases in the presence of both kinds of deviations from symmetry. Cohen and Swiatecki [18] have used the parametrization of Legendre polynomial expansion with even order deformation parameters α_{2n} up to the order 18. For low fissility, X, the saddle point shapes are very similar to two tangent spheres, which it is more difficult to be described with a small number of deformation coordinates. By increasing fissility a neck develops between the two symmetrical fragments. The length increases up to X = 0.67 and at the same time the neck radius becomes larger. For even larger values of X the length decreases and there is no neck if X > 0.67. The best accuracy was obtained at larger fissilities, close to X = 1, for which the saddle point shapes are not very different from a single sphere. The cylinder-like shapes of heavy nuclei with 0.67 < X < 1 have been called Bohr-Wheeler family of shapes, and the necked-in dumbell-like shapes for lighter nuclei (0 < X < 0.67) are called Frankel-Metropolis family. Slightly different saddle point shapes (with larger neck radius and shorter length) are found within Y+EM.

Both LDM and Y+EM predict about the same fission barrier height (saddle point energy relative to the ground-state minimum) of heavy nuclei (A > 200). For lighter nuclides ($A \simeq 100$) the LDM fission barrier is about 10 MeV higher than that obtained by Y+EM, which reproduces well the experimental data. At the Businaro–Gallone fissility ($X_{\rm BG} = 0.396$ within LDM), a transition to unstable shapes with respect to mass asymmetry occurs. Calculated fission barriers corresponding to the conditional saddle points with constrained mass asymmetry plotted versus η at a given fissility $X \ge X_{BG}$, show a minimum at $\eta = 0$ and a maximum at a value of $\eta_{\rm BG}$ which increases with X, but for $X < X_{\rm BG}$ the fission barrier always decreases with increasing asymmetry.

Fission of highly excited nuclei in the intermediate mass region is dominated by the liquid drop properties of nuclear matter. A unified approach of light particle evaporation and fission decay modes of highly excited compound nuclei well above the barrier height, was developed by Moretto [71, 72] who applied the transition state formalism used in fission for the light particle evaporation. According to this theory the distinction between evaporation and fission for $X > X_{\rm BG}$ is given by the Businaro–Gallone peaks $\eta_{\rm BG}$: at a given fissility, the fission process ranges from $\eta = 0$ to $\eta_{\rm BG}$, and evaporation from $\eta_{\rm BG}$ to $\eta = 1$. Bellow the Businaro–Gallone fissility ($X < X_{\rm BG} = 0.396$ for zero angular momentum l, and smaller for larger l values) there is no distinction between (disappearing) fission and the evaporation extending from $\eta = 0$ to $\eta = 1$. It was shown experimentally [127] that the topological transition expected at $X = X_{\rm BG}$, takes place around A = 100 (between 85 and 145).

The statical approach was widely used [18, 128] for finding the saddle point shapes within a LDM. Usually the equilibrium nuclear shapes are obtained by

minimizing the energy functional on a certain class of trial functions representing the surface equation. Such an approach shows the importance of taking into account a large number of deformation coordinates (it seems that 5 coordinates are frequently needed) [69]. The parametrization according to Legendre polynomial expansion with even order deformation parameters α_{2n} up to n=18 was employed [18] to describe various saddle point shapes including those very similar to two tangent spheres.

The integro-differential equation [88] allows to find a general reflection symmetrical or asymmetrical saddle point shape without a shape parametrization a priori introduced. This equation is derived as a Euler-Lagrange relationship associated to the variational problem of minimizing the potential energy with constraints (constant volume and given deformation parameter). The axially-symmetrical surface shape minimizing the liquid drop energy, $E_{\rm LDM} = E_s + E_C$, is straightforwardly obtained. Minima of the saddle point deformation energy appear at finite values of the mass-asymmetry parameter as soon as the shell corrections, δE , are taken into account [99, 102].

We are looking for a function $\rho = \rho(z)$ expressing in cylindrical coordinates the nuclear surface equation with axial symmetry around the z axis and the tips z_1 and z_2 . The dependence on the neutron, N, and proton, Z, numbers is contained in the surface energy of a spherical nucleus, E_s^0 , in the fissility parameter X, as well as in the shell correction of the spherical nucleus δE^0 . E_C^0 is the Coulomb energy of the spherical shape for which the radius is $R_0 = r_0 A^{1/3}$. The radius constant is $r_0 = 1.2249$ fm, and $e^2 = 1.44$ MeV·fm is the square of electron charge. The lengths are given in units of the radius, R_0 , and the Coulomb potential at the nuclear surface, $V_s = (R_0/Ze)\phi_s$, in units of Ze/R_0 . The surface tension and the charge density are denoted by σ and ρ_e respectively. The nuclear surface equation we are looking for should minimize the functional of potential energy of deformation

$$E_s + E_C = 2\pi\sigma R_0^2 \int_{z_1}^{z_2} \rho(z) \sqrt{1 + \rho'^2} dz + \frac{2\pi R_0^2 Ze \rho_e}{5} \int_{z_1}^{z_2} \left(\rho^2 - \frac{z \partial \rho^2}{2 \partial z}\right) V_s dz \quad (1.64)$$

with two constraints: volume conservation and a given deformation parameter

$$V = \pi R_0^3 \int_{z_1}^{z_2} \rho^2(z) dz = \frac{4\pi R_0^3}{3}; \quad \alpha = \frac{\pi R_0^3}{V} \int_{z_1}^{z_2} F(z, \rho) \rho^2 dz$$
 (1.65)

where α is assumed to be an adiabatic variable.

We denote with F_1 , F_2 , F_3 , F_4 , the integrands one needs to write the Euler–Lagrange equation:

$$\sigma F_1 = \sigma \rho (1 + \rho'^2)^{1/2}; \frac{R_0 \rho_e \phi_s}{5} F_2 = \frac{R_0 \rho_e \phi_s}{5} (\rho^2 - z \rho \rho'); F_3 = \rho^2; F_4 = \rho^2 F$$
(1.66)

The derivatives are easily obtained

$$\frac{\partial F_1}{\partial \rho} = \left(1 + \rho^2\right)^{1/2} \tag{1.67}$$

$$\frac{d}{dz}\frac{\partial F_1}{\partial \rho'} = \frac{d}{dz}\left[\frac{\rho \rho'}{(1+\rho'^2)^{1/2}}\right] = \frac{\rho'^2 + \rho \rho''}{(1+\rho'^2)^{1/2}} - \frac{\rho \rho'^2 \rho''}{(1+\rho'^2)^{3/2}}$$
(1.68)

$$\frac{\partial F_2}{\partial \rho} = 2\rho - z\rho'; \frac{d}{dz} \frac{\partial F_2}{\partial \rho'} = \frac{d}{dz} (-z\rho) = -\rho - z\rho'; \tag{1.69}$$

$$\frac{\partial F_3}{\partial \rho} = 2\rho; \frac{\partial F_4}{\partial \rho} = 2\rho \left(F + \frac{\rho}{2} \frac{\partial F}{\partial \rho} \right) = 2\rho f \tag{1.70}$$

where we denoted $f(z, \rho) = F(z, \rho) + (\rho/2)(\partial F/\partial \rho)$. Consequently the Euler–Lagrange equation can be written as

$$\sigma\left(\frac{\partial F_1}{\partial \rho} - \frac{d}{dz}\frac{\partial F_1}{\partial \rho'}\right) + \frac{Ze\rho_e V_s}{5}\left(\frac{\partial F_2}{\partial \rho} - \frac{d}{dz}\frac{\partial F_2}{\partial \rho'}\right) + \rho\left(2\lambda_1'' + 2\lambda_2''f\right) = 0 \tag{1.71}$$

leading to

$$\rho \rho'' - \rho'^2 - (\lambda_1 + \lambda_2 |z| + 6XV_s)\rho (1 + \rho'^2)^{3/2} - 1 = 0$$
 (1.72)

if we choose F=|z| (hence f=|z|) and express $3Ze\rho_e/(5\sigma)$ as 6X because the Coulomb and surface energy of a spherical nucleus within LDM are given by $E_C^0=(3Z^2e^2)/(5R_0)$ and $E_s^0=4\pi R_0^2\sigma$, respectively. Alternatively one has

$$2\sigma K + 3\rho_e \phi_s / 5 + \lambda_1' + \lambda_2' |z| = 0 \tag{1.73}$$

where λ_1' and λ_2' are Lagrange multipliers and K is the mean curvature [13] with \mathcal{R}_1 and \mathcal{R}_2 the principal radii of curvature

$$K = (\mathcal{R}_1^{-1} + \mathcal{R}_2^{-1})/2; \quad \mathcal{R}_1 = R_0 \tau \rho \quad \mathcal{R}_2 = -R_0 \tau^3 / \rho'' \quad \tau^2 = 1 + \rho'^2 \quad (1.74)$$

where $\rho' = d\rho/dz$ and $\rho'' = d^2\rho/dz^2$. In the absence of an electric charge, the condition of stable equilibrium at the surface of a fluid [65] is given by the Laplace formula equating the difference of pressures with the product $2\sigma K$.

By choosing the deformation coordinate as the distance between the centers of mass of the left and right fragments, $\alpha = |z_L^c| + |z_R^c|$, one can reach all intermediate stages of deformation from one parent nucleus to two fragments by a continuous variation of its value. Also a possible dynamical study, for which the center of mass treatment is very important [106], may conveniently use this definition of the deformation parameter. The position of the separation plane between fragments, z=0, is given by the condition $(d\rho/dz)_{z=0}=0$, which defines the median plane for a usually spherical, ellipsoidal, or "diamond" shape in the gs, or the middle of the neck for an elongated reflection symmetrical shape on the fission path. For this choice of the function $F(z,\rho)$ one has f=|z|.

The equation to be solved numerically is obtained from (1.72) after changing the variable and function.

$$u(v) = \Lambda^2 \rho^2 [z(v)]; \quad z(v) = z_p - v/\Lambda$$
 (1.75)

By calculating the derivatives and substituting into (72) one gets

$$u'' - 2 - \frac{1}{u} \left[u'^2 + \left(\frac{3XV_s}{2\Lambda} + \frac{\lambda_1 + \lambda_2 z_p}{4\Lambda} - \frac{\lambda_2 v}{4\Lambda^2} \right) (4u + u'^2)^{3/2} \right] = 0$$
 (1.76)

A linear function of v is introduced by adding and subtracting a + bv to $3XV_s/2\Lambda$. The quantity V_{sd} is defined as the deviation of Coulomb potential at the nuclear surface from a linear function of v

$$V_{sd} = \frac{3X}{2\Lambda}V_s - a - vb; a = \frac{3X}{2\Lambda}V_s(v = 0); b = \left[\frac{3X}{2\Lambda}V_s(v = v_p) - a\right] / v_p \quad (1.77)$$

where $v_p = \Lambda z_p$. The constant a is chosen to give $V_{sd}(v = 0) = 0$. Consequently one has

$$u'' - 2 - \frac{1}{u} \left\{ u'^2 + \left[\left(\frac{\lambda_1 + \lambda_2 z_p}{4\Lambda} + a \right) + v \left(b - \frac{\lambda_2}{4\Lambda^2} \right) + V_{sd} \right] (4u + u'^2)^{3/2} \right\} = 0$$
(1.78)

By equating with 1 the coefficient of v, one can establish the following link between Λ and the Lagrange multiplier $\lambda_2\Lambda^2 = \lambda_2/4(b-1)$. In this way u(v) is to be determined by the equation

$$u'' - 2 - \frac{1}{u} \left[u'^2 + (v - d + V_{sd})(4u + u'^2)^{3/2} \right] = 0$$
 (1.79)

where the role of a Lagrange multiplier is played by the quantity d which is taken to be constant instead of α . The value of the deformation coordinate α is calculated after obtaining a convergent solution. To the tip $z=z_p$, at which $\rho(z_p)=0$, corresponds v=0, hence $u(0)=\Lambda^2\rho^2(z_p)=0$, as can be seen from (1.75). By multiplying with u (1.79), introducing v=0, and using the relationship $V_{sd}(v=0)=0$, it follows that u'(0)=1/d. Consequently the boundary conditions for u(v) are:

$$u(0) = 0, \quad u'(0) = 1/d$$
 (1.80)

To z=0, at which $\rho'(0)=0$ (the middle of the neck for elongated shapes), corresponds $v_p=\Lambda z_p$ and $u'(v_p)=-2\Lambda\rho(0)\rho'(0)=0$. The point $v=v_p$ in which $u'(v_{pn})=0$ is determined by interpolation from two consecutive values of v_p leading to opposite signs of u'(v). The number n of changes of signs is equal to the number of necks plus one given in advance, e.g. for a single neck (binary fission) one has n=2 and for two necks (ternary fission) one has n=3, etc.

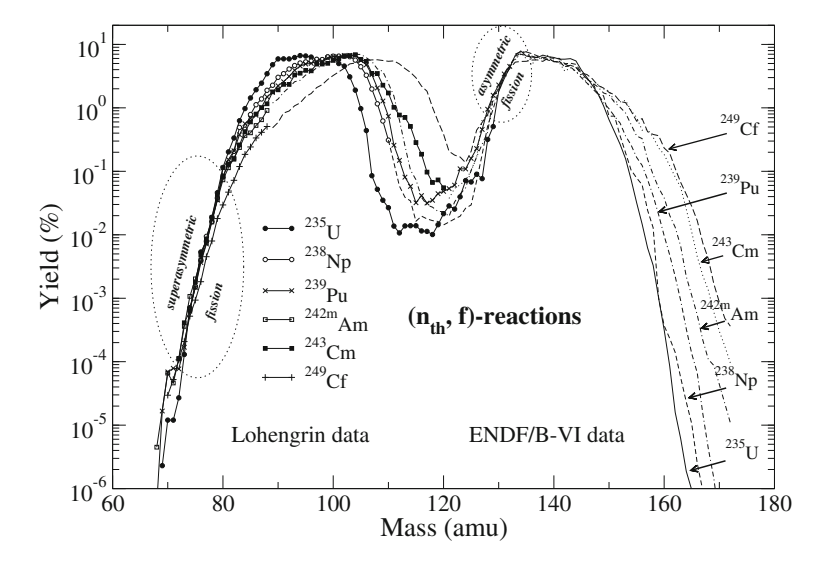


Fig. 1.6 Mass yields in thermal neutron induced fission of the compound nuclei 239 Np* [133], 236 U*, 240 Pu*, 243 Am*, 246 Cm*, and 250 Cf* (courtesy Prof. F. Gönnenwein)

In order to find the shape function u(v) we solve (1.79) with given boundary conditions. One starts with given values of the constants d and n. For reflection symmetric shapes $d_L = d_R$ and $n_L = n_R$. In the first iteration one obtains the solution for a Coulomb potential at the nuclear surface assumed to be a linear function of v, i.e. for $V_s = 0$. Then one calculates the parameters Λ , a, and b, which depend on the Coulomb potential and its deviation V_{sd} from a linear function, and the deformation energy corresponding to the nuclear shape [105]. The quantity V_{sd} determined in such a way is introduced in (1.79) and the whole procedure is repeated until the deformation energy is obtained with the desired accuracy. In every iteration step the equation is solved numerically with the Runge–Kutta method.

One can calculate for different values of deformation α (in fact for a given d_L and d_R) the deformation energy $E_{\text{def}}(\alpha)$. The particular value α_s for which $dE_{\text{def}}(\alpha_s)/d\alpha=0$ corresponds to the extremum, i.e. the shape function describes the saddle point, and the unconditional extremum of the energy is the fission barrier. The other surfaces (for $\alpha \neq \alpha_s$) are extrema only with the condition $\alpha=$ constant. In this way one can compute the deformation energy versus $d_L=d_R$. The saddle point corresponds to the maximum of deformation energy.

For nuclei 170 Yb, 204 Pb and 252 Cf with X = 0.60, 0.70, and 0.82 we obtained [88] the saddle-point shapes in good agreement with [18]. By including shell effects we could explain [99] the asymmetry in the fission fragment mass distribution.

A new superasymmetric peak was observed in the fission yield of ²⁵²No calculated by using the fragmentation theory and the two center shell model developed by the Frankfurt school [119, 120)].

A "shoulder" was experimentally measured in the superasymmetric region of the fission fragment mass distributions of lighter nuclei, e.g. ²²⁰Ra, ^{205,207,209}Bi,

^{208,210,212}Po, ²⁰⁴Pb, ²¹³At, ²⁰¹Tl [57–59, 111]. There are also other very interesting experiments for heavier nuclei U, Np, Pu, Am, Cm and Cf [133] which clearly show superasymmetric fission. In Fig. 1.1 of that paper the experimental evidence for superasymmetric fission as a general phenomenon in low energy fission of actinides came into view. A modified plot is shown in Fig. 1.6 were the superasymmetric shoulder is clearly seen.

1.3 Nuclear Dynamics

By studying fission dynamics [96] one can estimate the value of the disintegration constant λ of the exponential decay law expressing the variation in time of the number of decaying nuclei. The probability of decay may be expressed in terms of its *half-life*, T, the time in which only half of the initial quantity remains. By assuming a disintegration rate independent on the past history of the individual decaying nuclei the variation of the number $\mathcal{N}(t)$ of radioactive nuclei at a time t, during the time dt must be proportional to $\mathcal{N}(t)$ and to dt: $d\mathcal{N} = -\lambda \mathcal{N} dt$. After integration we get the exponential decay law:

$$\mathcal{N}(t) = \mathcal{N}(0) \exp(-t/\tau) \tag{1.81}$$

where the time constant $\tau = 1/\lambda$ defines the life-time of the parent nucleus, and λ is the disintegration constant. The partial decay half-life, T, is defined by $\mathcal{N}(t) = \mathcal{N}(0)/2$, hence $T = \tau \ln 2 = 0.693147/\lambda$.

Our extensive study of one-, two-, and three-dimensional fission dynamics for a wide range of mass asymmetry allowed us to find the nuclear shapes during the deformation process. Some confusions and errors have been made in this field, e.g. when the center of mass motion was not taken into account in the calculation of nuclear inertia within Werner–Wheeler approximation.

The potential energy surface in a multidimensional hyperspace of deformation parameters $\beta_1\beta_2$, ..., β_n gives the generalized forces acting on the nucleus. The information concerning how the system reacts to these forces is contained in a tensor of inertial coefficients, or the effective mass parameters $\{B_{ij}\}$. In contrast to the potential energy $E=E(\beta)$, which only depends on the nuclear shape, the kinetic energy

$$E_k = \frac{1}{2} \sum_{i,j=1}^n B_{ij}(\beta) \frac{d\beta_i d\beta_j}{dt \ dt}$$
 (1.82)

also includes the change in time of this shape. B_{ij} is the *tensor of nuclear inertia*. In a phenomenological approach based on incompressible irrotational flow, the value of an effective mass B^{ir} is usually close to the reduced mass $\mu = (A_1A_2/A)m$ in the exit channel of the binary system. Here m is the nucleon mass. By choosing the distance between fragments as deformation

coordinate, this value of the effective mass is indeed exactly obtained at the touching point of the two fragments.

1.3.1 Werner-Wheeler Approximation

By assuming an irrotational hydrodynamic flow, the effective masses B^{ir} are always greater or equal to the reduced mass μ defined above. As an approximation to incompressible irrotational flow, one can use the Werner-Wheeler method [22]. For pure spheroidal deformation, the flow produced by using Werner-Wheeler approximation is exactly irrotational. It allows analytical results to be obtained for two parametrizations of intersected spheres: the ASAF model "cluster-like" ($R_2 = \text{constant}$) and the more compact (fragment volumes = constant) shapes.

The kinetic energy of a non-viscous fluid due to a shape change is written as

$$E_k = \frac{\sigma}{2} \left[\int_V \mathbf{v}^2 d^3 r - \left(\int_V \dot{z} d^3 r \right)^2 \middle/ \int_V d^3 r \right]$$
 (1.83)

if the system possesses a cylindrical symmetry relative to the z-axis. V is the volume assumed to be conserved, $\sigma = 3m/(4\pi r_o^3)$ is the mass density, \mathbf{v} is the velocity; the nuclear radius constant $r_o = 1.16$ fm within Y+EM.

By assuming irrotational motion $(\nabla \times \mathbf{v} = rot \ \mathbf{v} = 0)$, the velocity field may be derived from a scalar velocity potential φ , i.e. $\mathbf{v} = \nabla \varphi$. From the continuity equation of an incompressible fluid $(D\sigma /Dt = 0)$ it follows that the Laplace equation, $\nabla^2 \varphi = \Delta \varphi = 0$, should be satisfied with kinematical boundary conditions

$$\frac{DF}{\partial t} = \mathbf{v}\nabla F + \frac{\partial F}{\partial t} = 0 \tag{1.84}$$

where the surface equation for axially symmetric shapes in cylindrical coordinates (ρ, φ, z) is written as $F(r, t, \beta) = \rho - \rho_s(z, t, \beta) = 0$ in which ρ_s is the value of ρ on the surface. The velocity components, $\dot{z} = \partial \varphi / \partial z$ and $\dot{\rho} = \partial \varphi / \partial \rho$, are both functions of z and ρ .

In the Werner–Wheeler approximation the flow is considered to be a motion of circular layers of fluid, \dot{z} is independent of ρ , and $\dot{\rho}$ is linear in ρ :

$$\dot{z} = \sum_{i} X_{i}(z, \beta) \dot{\beta}_{i}; \quad \dot{\rho} = (\rho/\rho_{s}) \sum_{i} Y_{i}(z, \beta) \dot{\beta}_{i}$$
 (1.85)

A vanishing total (convective) time derivative of the fluid volume to the right (or left) side of an arbitrary plane normal to the *z*-axis leads to

$$X_{il} = -\rho_s^{-2} \frac{\partial}{\partial \beta_i} \int_{z_{\min}}^{z} \rho_s^2 dz, \quad X_{ir} = \rho_s^{-2} \frac{\partial}{\partial \beta_i} \int_{z}^{z_{\max}} \rho_s^2 dz$$
 (1.86)

By requiring a vanishing normal component of the velocity at the surface, one has

$$Y_{ir(l)} = -\frac{\rho_s}{2} \frac{\partial}{\partial z} X_{ir(l)} \tag{1.87}$$

from which the functions X_i and Y_i are found as a sum of two terms for the left (l) and right (r) side of the shape.

After substitution in the relationship for the kinetic energy and comparison with the initial equation for E_k we find the following relationships for the components of the inertia tensor:

$$B_{ij} = \pi \sigma \int_{z_{\min}}^{z_{\max}} \rho_s^2 \left(X_i X_j + \frac{1}{2} Y_i Y_j \right) dz + B_{ij}^c$$
 (1.88)

$$B_{ij}^{c} = -(\pi^{2}\sigma/V) \int_{z_{min}}^{z_{max}} \rho_{s}^{2} X_{i} dz \int_{z_{min}}^{z_{max}} \rho_{s}^{2} X_{j} dz$$

$$(1.89)$$

where $\rho_s = \rho_s(z)$ is the nuclear surface equation in cylindrical coordinates, with z_{min} , z_{max} intercepts on the z-axis. The correction term for the center of mass motion B_{ij}^c is different from zero if the origin of z is not placed in the center of mass.

For another set of deformation parameters $\{p\}$ describing the same shape,

$$B_{kl}(p) = \sum B_{ij}(q) \frac{\partial q_i}{\partial p_k} \frac{\partial q_j}{\partial p_l}$$
(1.90)

We studied the dynamics of two intersected spheres [30, 31, 106] for the general case of two independent variables R and R_2 . By expressing all lengths in units of the radius of the parent nucleus, $R_0 = r_0 A^{1/3}$, we have obtained the three components of the inertia tensor:

$$\frac{1}{m}B_{RR} = A\left\{\frac{H_1^2}{4}F_1 + \frac{3}{4\pi}V_2 - \frac{9}{16}\left[\frac{H_1}{2}(R_1 + D_1)^2 + \frac{V_2}{\pi}\right]^2\right\}$$
(1.91)

$$\frac{1}{m}B_{RR_2} = AR_2(R_2 + D_2) \left\{ \frac{H_1}{2(R_1 + D_1)} F_1 + \frac{3}{4}(R_2 + D_2) - \frac{9}{16} \left[\frac{H_1}{2} (R_1 + D_1)^2 + \frac{V_2}{\pi} \right] (R + R_1 + R_2) \right\}$$
(1.92)

$$\frac{1}{m}B_{R_2R_2} = AR_2^2 \left[\left(\frac{R_2 + D_2}{R_1 + D_1} \right)^2 F_1 + F_2 - \frac{9}{16} (R_2 + D_2)^2 L^2 \right]$$
 (1.93)

where $L = R + R_1 + R_2$ and

$$F_1 = -2.625D_1 - 3.375R_1 + 1.5\frac{R_1^2}{H_1} + 4.5R_1 \ln \frac{2R_1}{H_1}$$
 (1.94)

$$F_2 = -2.625D_2 - 3.375R_2 + 1.5\frac{R_2^2}{H_2} + 4.5R_2 \ln \frac{2R_2}{H_2}$$
 (1.95)

 V_2 is the volume of the emitted fragment and the involved geometrical quantities are defined below.

The above mentioned one-dimensional parametrizations (compact and cluster-like) are obtained as particular cases. For compact shapes:

$$\frac{B(R)}{m}\Big|_{V_{2}=\text{const.}} = A \left[\left(\frac{H_{1} R_{2} + D_{2}}{2 R + R_{1} + R_{2}} \right)^{2} K_{1} + \left(\frac{H_{2} R_{1} + D_{1}}{2 R + R_{1} + R_{2}} \right)^{2} K_{2} - \frac{3}{4} \frac{H_{2}(R_{1} + D_{1})(R_{2} + D_{2})^{2}}{R + R_{1} + R_{2}} \right] + \mu_{A}$$
(1.96)

where $\mu_A = A_e A_d / A$ is the reduced mass number.

For cluster-like shapes

$$\frac{B(R)}{m} = \frac{B_{RR}}{m} \Big|_{R_2 = \text{ct.}} = \frac{A}{4} \left\{ H_1^2 K_1 + \frac{3V_2}{\pi} - \frac{9A}{4} \left[\frac{H_1}{2} (R_1 + D_1)^2 + \frac{V_2}{\pi} \right]^2 \right\}$$
(1.97)

In this case R is varied from R_i to R_t and R_1 is determined numerically by solving a fourth degree algebraic equation which is derived from the volume conservation and matching conditions in the separation plane. Then we can find $D_1 = R/2 + (R_1^2 - R_2^2)/(2R)$, $H_1 = R_1 - D_1$, $D_2 = R - D_1$, and $H_2 = R_2 - D_2$.

When studying more compact shapes it is convenient to use H_1 as independent variable. It decreases from H_i (equal to h_i) at $R=R_i$ to zero at $R=R_i$. The heavy fragment volume conservation condition allows to obtain an equation of third degree in R_1 . Then $D_1=R_1-H_1$ and the square of the neck radius $\rho_n^2=H_1(R_1+D_1)$. H_2 is found as a solution of another equation obtained from the volume conservation of the small fragment and the matching condition. It follows that $R_2=(H_2+\rho_n^2/H_2)/2$, $D_2=R_2-H_2$, and $R=D_1+D_2$. Here $D_1=z_s-z_1$, $D_2=z_2-z_s$, $H_i=R_i-D_i$, z_s is the position of the intersection plane of the spheres, z_i are the geometrical centers of the spheres.

By changing the shape coordinate from R to z_m (the distance between mass centers of the fragments), the inertia becomes :

$$B(z_m) = B(R) \left(\frac{dR}{dz_m}\right)^2 \tag{1.98}$$

For cluster-like shapes, both B(R) and $B(z_m)$ are increasing functions of the respective variable. On the contrary, $B(z_m)$ decreases but B(R) increases for the more compact shapes. When the motion of the center of mass is not taken into

account, the inertia are much higher; the ratio of wrong to correct value of inertia may be as high as 30/4. A good accuracy test of the computations is obtained at the touching point configurations, where $B = \mu$ —the reduced mass.

1.3.2 Cranking Inertia

The microscopic (cranking) model introduced by Inglis [23, 39, 54–56] leads to much larger values of the inertia compared to the phenomenological ones. By assuming the adiabatic approximation the shape variations are slower than the single-particle motion. According to the cranking model, after including the BCS pairing correlations [3], the inertia tensor [10] is given by

$$B_{ij} = 2\hbar^2 \sum_{\nu\mu} \frac{\langle \nu | \partial H / \partial \beta_i | \mu \rangle \langle \mu | \partial H / \partial \beta_j | \nu \rangle}{(E_{\nu} + E_{\mu})^3} (u_{\nu} v_{\mu} + u_{\mu} v_{\nu})^2 + P_{ij}$$
 (1.99)

where H is the single-particle Hamiltonian allowing to determine the energy levels and the wave functions $|v\rangle$, u_v , v_v are the BCS occupation probabilities, E_v is the quasiparticle energy, and P_{ij} gives the contribution of the occupation number variation when the deformation is changed (terms including variation of the gap parameter, Δ , and Fermi energy, λ , $\partial \Delta/\partial \beta_i$ and $\partial \lambda/\partial \beta_i$):

$$P_{ij} = \frac{\hbar^{2}}{4} \sum_{v} \frac{1}{E_{v}^{5}} \left[\Delta^{2} \frac{\partial \lambda}{\partial \beta_{i}} \frac{\partial \lambda}{\partial \beta_{j}} + (\varepsilon_{v} - \lambda)^{2} \frac{\partial \Delta}{\partial \beta_{i}} \frac{\partial \Delta}{\partial \beta_{j}} + \Delta(\varepsilon_{v} - \lambda) \left(\frac{\partial \lambda}{\partial \beta_{i}} \frac{\partial \Delta}{\partial \beta_{j}} + \frac{\partial \lambda}{\partial \beta_{j}} \frac{\partial \Delta}{\partial \beta_{i}} \right) \right.$$

$$\left. - \Delta^{2} \left(\frac{\partial \lambda}{\partial \beta_{i}} \langle v | \partial H / \partial \beta_{j} | v \rangle + \frac{\partial \lambda}{\partial \beta_{j}} \langle v | \partial H / \partial \beta_{i} | v \rangle \right) \right.$$

$$\left. - \Delta(\varepsilon_{v} - \lambda) \left(\frac{\partial \Delta}{\partial \beta_{i}} \langle v | \partial H / \partial \beta_{j} | v \rangle + \frac{\partial \Delta}{\partial \beta_{j}} \langle v | \partial H / \partial \beta_{i} | v \rangle \right) \right]$$

$$(1.100)$$

Like the shell corrections, the total inertia is a sum of proton and neutron contributions. The denominator is minimal for levels near the Fermi surface. When the level density at the Fermi surface is large, the inertia is large too, and viceversa.

The cranking approach allows to obtain analytical relationships of the nuclear inertia [87] if we consider a single-particle model of a spheroidal harmonic oscillator without spin-orbit interaction. The shape of a spheroid with semiaxes a, c (c is the semiaxis along the symmetry) expressed in units of the spherical radius $R_0 = r_0 A^{1/3}$ may be determined by a single deformation coordinate which can be the quadrupolar deformation [77] $\varepsilon = 3(c-a)/(2c+a)$. The two oscillator frequencies are expressed as:

$$\omega_{\perp}(\varepsilon) = \omega_0 \left(1 + \frac{\varepsilon}{3} \right); \quad \omega_z(\varepsilon) = \omega_0 \left(1 - \frac{2\varepsilon}{3} \right)$$
 (1.101)

and by taking into account the condition of the volume conservation $\omega_{\perp}^2\omega_z=(\omega_0^0)^3$, where $\hbar\omega_0^0=41A^{-1/3}$ MeV, the eigenvalues [96] in units of $\hbar\omega_0^0$ are given by

$$\varepsilon_i = [N + 3/2 + \varepsilon(n_{\perp} - 2N/3)][1 - \varepsilon^2(1/3 + 2\varepsilon/27)]^{-1/3}$$
 (1.102)

in which the quantum numbers n_{\perp} and n_z are nonnegative integers. Their summation gives the main quantum number $N = n_{\perp} + n_z$.

In a system of cylindrical coordinates (ρ, φ, z) the wave function [20, 23, 134] can be written as a product of the eigenfunctions

$$\psi_{n_r}^m(\rho) = \frac{\sqrt{2}}{\alpha_\perp} N_{n_r}^m \eta_r^{\frac{|m|}{2}} e^{-\frac{\eta}{2}} L_{n_r}^{|m|}(\eta) = \frac{\sqrt{2}}{\alpha_\perp} \psi_{n_r}^m(\eta)$$
 (1.103)

$$\psi_{n_z}(z) = \frac{1}{\sqrt{\alpha_z}} N_{n_z} e^{-\frac{\xi^2}{2}} H_{n_z}(\xi) = \frac{1}{\sqrt{\alpha_z}} \psi_{n_z}(\xi); \quad \Phi_m(\varphi) = \frac{1}{\sqrt{2\pi}} e^{im\varphi}$$
 (1.104)

where $L_{n_r}^{|m|}$ are the associated (or generalized) Laguerre polynomials and H_{n_z} are the Hermite polynomials. The variables η and ξ are defined by $\eta=\rho^2/\alpha_\perp^2$, $\xi=z/\alpha_z$, where $\alpha_\perp=\sqrt{\hbar/M\omega_\perp}\approx A^{1/6}\sqrt{\omega_0^0/\omega_\perp}$, $\alpha_z=\sqrt{\hbar/M\omega_z}\approx A^{1/6}\sqrt{\omega_0^0/\omega_z}$. The normalization constants

$$(N_{n_r}^m)^2 = \frac{n_r!}{(n_r + |m|)!}; \quad (N_{n_z})^2 = \frac{1}{\sqrt{\pi} 2^{n_z} n_z!}$$
 (1.105)

are obtained from the orthonormalization conditions.

By ignoring the spin-orbit coupling the Hamiltonian of the harmonic spheroidal oscillator contains the kinetic energy and the potential energy term, *V*:

$$V = \frac{1}{2}\hbar\omega_{\perp}\eta + \frac{1}{2}\hbar\omega_{z}\xi^{2} = \frac{\hbar\omega_{0}^{0}[(3+\varepsilon)\eta + (3-2\varepsilon)\xi^{2}]}{2[27-\varepsilon^{2}(9+2\varepsilon)]^{1/3}}$$
(1.106)

Now we are making some changes in (1.99). First of all we are replacing the deformation β by ε . One may assume [10, 20] that only the leading term of the Hamiltonian, namely the potential denoted above, contributes essentially to the derivative,

$$\frac{dH}{d\varepsilon} \simeq \frac{dV}{d\varepsilon} \tag{1.107}$$

The contribution of P_{ij} , denoted by P_{ε} for a system with one deformation coordinate, sometimes assumed to be negligible small, will be discussed later on. The derivative is written as

$$\frac{1}{\hbar\omega_0^0} \frac{dV}{d\varepsilon} = \frac{3}{2} \left[f_1(\varepsilon) \eta + f_2(\varepsilon) \xi^2 \right]$$
 (1.108)

in which

$$f_1 = \frac{\varepsilon(\varepsilon + 6) + 9}{\left[27 - \varepsilon^2(9 + 2\varepsilon)\right]^{4/3}}; \quad f_2 = 2\frac{\varepsilon(2\varepsilon + 3) - 9}{\left[27 - \varepsilon^2(9 + 2\varepsilon)\right]^{4/3}}$$
(1.109)

For a single deformation parameter the inertia tensor becomes a scalar B_{ε} with a summation in (1.99) performed for all states v, μ taken into consideration in the pairing interaction. In order to solve the problem of the pairing interaction we follow the procedure outlined in Sect. 1.2.6.

The following relationship allows to calculate the effective mass, in units of $\hbar^2/(\hbar\omega_0^0)$

$$\frac{\hbar\omega_0^0}{\hbar^2}B_{\varepsilon} = \frac{9}{2} \sum_{\nu\mu} \frac{\langle \nu | f_1 \eta + f_2 \xi^2 | \mu \rangle \langle \mu | f_1 \eta + f_2 \xi^2 | \nu \rangle}{(E_{\nu} + E_{\mu})^3} (u_{\nu} v_{\mu} + u_{\mu} v_{\nu})^2$$
(1.110)

The matrix elements are calculated by performing some integrals

$$\langle n'_{z}n'_{r}m'|f_{1}(\varepsilon)\eta + f_{2}(\varepsilon)\xi^{2}|n_{z}n_{r}m\rangle = \delta_{m'm}N_{n'_{r}}^{m}N_{n_{r}}^{m}N_{n'_{z}}N_{n_{z}}$$

$$\times \left[f_{1}\int_{0}^{\infty}d\eta\eta^{|m|+1}e^{-\eta}L_{n'_{r}}^{|m|}(\eta)L_{n_{r}}^{|m|}(\eta)\int_{-\infty}^{\infty}d\xi e^{-\xi^{2}}H_{n'_{z}}(\xi)H_{n_{z}}(\xi) \right]$$

$$+ f_{2}\int_{0}^{\infty}d\eta\eta^{|m|}e^{-\eta}L_{n'_{r}}^{|m|}(\eta)L_{n_{r}}^{|m|}(\eta)\int_{-\infty}^{\infty}d\xi\xi^{2}e^{-\xi^{2}}H_{n'_{z}}(\xi)H_{n_{z}}(\xi)$$

$$(1.111)$$

Next we can use the relationships from [13] leading eventually to an important diagonal contribution

$$\frac{\hbar\omega_0^0}{\hbar^2}B_{\varepsilon 1} = \frac{9}{4}\delta_{n'_r n_r}\delta_{m'm}\sum_{\nu=k_z}^{k_f} \left[f_1(2n_r + |m| + 1) + f_2\left(n_z + \frac{1}{2}\right)\right]^2 \frac{(u_\nu v_\nu)^2}{E_\nu^3}\delta_{n'_z n_z} \quad (1.112)$$

and two nondiagonal terms

$$\frac{\hbar\omega_0^0}{\hbar^2}B_{\varepsilon 2} = \frac{9}{4}\delta_{n_r'n_r}\delta_{m'm}\sum_{\nu\neq\mu}\frac{f_2^2}{2}(n_z+1)(n_z+2)\frac{(u_\nu\nu_\mu + u_\mu\nu_\nu)^2}{(E_\nu + E_\mu)^3}\delta_{n_z'n_z+2}$$
(1.113)

$$\frac{\hbar\omega_0^0}{\hbar^2}B_{\varepsilon 3} = \frac{9}{4}\delta_{n'_r n_r}\delta_{m'm}\sum_{\nu\neq\mu}\frac{f_2^2}{2}(n_z-1)n_z\frac{(u_\nu \nu_\mu + u_\mu \nu_\nu)^2}{(E_\nu + E_\mu)^3}\delta_{n'_z n_z - 2}$$
(1.114)

In order to perform the summations of the nondiagonal terms for a state with a certain v (specifying the quantum numbers n_z n_r m) one has to consider only the

states with $\mu \neq v$ and $n'_r = n_r$; m' = m for which $n'_z = n_z + 2$ or $n'_z = n_z - 2$ respectively. Finally one arrives at the nuclear inertia in units of \hbar^2/MeV by adding the three terms and dividing by $\hbar\omega_0^0$.

There are several hydrodynamical formulae [126] for the mass parameters. For a spherical liquid drop with a radius $R_0 = 1.2249A^{1/3}$ fm one has

$$B_{irr}(0) = \frac{2}{15} MAR_0^2 = 0.0048205 A^{5/3} \frac{\hbar^2}{\text{MeV}}$$
 (1.115)

When the spheroidal deformation is switched on it becomes

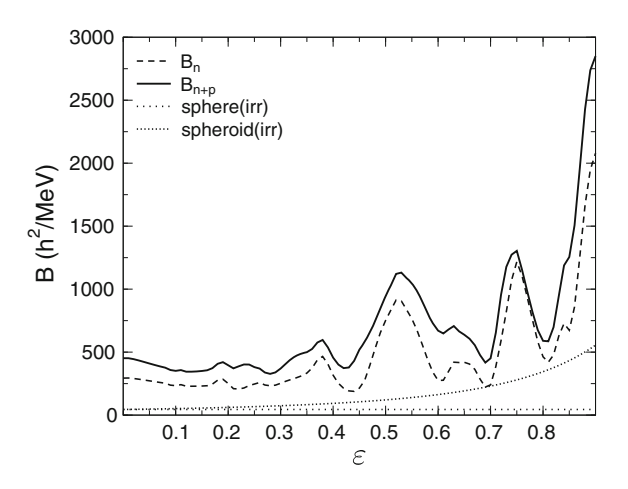
$$B_{\varepsilon}^{ir}(\varepsilon) = B_{irr}(0) \frac{81}{\left[27 - \varepsilon^2 (9 + 2\varepsilon)\right]^{4/3}} \frac{9 + 2\varepsilon^2}{\left(3 - 2\varepsilon\right)^2}$$
(1.116)

The main result of this subsection is represented by (1.112–1.114), which could be used to test complex computer codes developed for realistic single-particle levels, for which it is not possible to obtain analytical relationships.

The nuclear inertia for 240 Pu, calculated with the (1.115) for a spherical liquid drop and with (1.116) for spheroidal shapes is illustrated in Fig. 1.7. The irrotational value $B_{\varepsilon}^{ir}(\varepsilon)$ monotonously increases with the spheroidal deformation parameter ε . Due to the fact that in this single center model the nucleus only became longer without developing a neck and never arriving at a scission configuration when the deformation is increased, the reduced mass is not reached as it should be in a two center model [30].

The cranking inertia of the spheroidal harmonic oscillator calculated by using the analytical relationships (1.112–1.114) and the correction given below shows very pronounced fluctuations which are correlated to the shell corrections. The correction term is given by

Fig. 1.7 Comparison of the effective mass (in units of \hbar^2/MeV) calculated by using the cranking model for the proton plus neutron level schemes, only for neutrons, as well as for the irrotational spheroidal and spherical shapes of ^{240}Pu



$$P_{\varepsilon} = \frac{2\hbar^{2}}{8} \sum_{\nu} \frac{1}{E_{\nu}^{5}} \left[\left(\Delta \frac{d\lambda}{d\varepsilon} \right)^{2} + (\varepsilon_{\nu} - \lambda)^{2} \left(\frac{d\Delta}{d\varepsilon} \right)^{2} + 2\Delta(\varepsilon_{\nu} - \lambda) \frac{d\lambda d\Delta}{d\varepsilon d\varepsilon} - 2\Delta^{2} \frac{d\lambda}{d\varepsilon} \langle \nu | dV / d\varepsilon | \nu \rangle - 2\Delta(\varepsilon_{\nu} - \lambda) \frac{d\Delta}{d\varepsilon} \langle \nu | dV / d\varepsilon | \nu \rangle \right]$$

$$(1.117)$$

The results from [87] are showing the important contribution of the neutron level scheme, $P_{\varepsilon n}$, reflecting the larger density of states at the Fermi energy, compared to the proton term $P_{\varepsilon p}$. Their sum is a positive quantity, contributing to an increase of the nuclear inertia. In a dynamical investigation using the quasiclassical WKB approximation, the quantum tunnelling penetrability depends exponentially on the action integral, in which the integral contains a square root of the product of the mass parameter and the deformation energy. This exponential dependence amplifies significantly any variation of the inertia. Consequently, the term P_{ij} must be considered in calculations. A similar conclusion was drawn [123] from a study based on the two-center shell model.

1.4 Analytical Superasymmetric Fission Model

Any theory of cluster radioactivities with predictive power should give an answer to the following questions. Are these phenomena physically allowed? Can they be measured? In which region of parent nuclei can they be found? Which are the most probable emitted clusters? What is the order of magnitude of the emission rate? Four theoretical models answering at least some of these questions, have been reviewed in 1980 [120], namely: fragmentation theory; penetrability calculations like in traditional theory of α -decay; numerical (NuSAF)- and analytical (ASAF) superasymmetric fission models.

A new superasymmetric peak, experimentally confirmed as a "shoulder", has been obtained in the ²⁵²No fission fragment mass distribution calculation, based on the fragmentation theory and the two center shell model developed by the Frankfurt school. See also other details on superasymmetric fission fragment mass distribution at the end of the Sect. 1.2.8.

One of the eight decay modes by cluster emission, predicted in 1980 by calculating the penetrability, from 16 even—even parents, has been ¹⁴C decay of ^{222,224}Ra. Three variants of the numerical superasymmetric fission (NuSAF) models were developed since 1979 by adding to the macroscopic deformation energy of binary systems with different charge densities a phenomenological shell correction term, and by performing numerical calculations within Wentzel–Kramers–Brillouin (WKB) approximation. In this way we obtained good

agreement with experimental half-lives for 58 even—even α -emitters over a range of 24 orders of magnitude.

A very large number of combinations parent-emitted cluster has to be considered in a systematic search for new decay modes. In order to check the metastability of more than 2,000 nuclides with measured masses against about 200 isotopes of the elements with $Z_e = 2$ –28, this number is of the order of 10^5 . The numerical calculation of three-fold integrals involved in the models mentioned above are too time-consuming. The large amount of computations can be performed in a reasonable time by using an analytical relationship for the halflife. Since 1980, we developed our ASAF model to fulfil this requirement. We started with Myers–Swiatecki LDM [76] adjusted with a phenomenological correction accounting for the known overestimation of the barrier height and for the shell and pairing effects in the spirit of Strutinsky method [129].

1.4.1 The Model

The half-life of a parent nucleus AZ against the split into a cluster A_e Z_e and a daughter A_d Z_d

$$T = [(h \ln 2)/(2E_v)] \exp(K_{ov} + K_s)$$
 (1.118)

is calculated by using the WKB quasiclassical approximation, according to which the action integral is expressed as

$$K = \frac{2}{\hbar} \int_{R_a}^{R_b} \sqrt{2B(R)E(R)} dR \tag{1.119}$$

with $B = \mu$, $K = K_{ov} + K_s$, and E(R) replaced by $[E(R) - E_{corr}] - Q$. E_{corr} is a correction energy similar to the Strutinsky [129] shell correction, also taking into account the fact that Myers–Swiatecki's LDM [76] overestimates fission barrier heights, and the effective inertia in the overlapping region is different from the reduced mass. The turning points of the WKB integral are:

$$R_a = R_i + (R_t - R_i)[(E_v + E^*)/E_b^0]^{1/2}$$
(1.120)

$$R_b = R_t E_c \{ 1/2 + \left[1/4 + (Q + E_v + E^*) E_l / E_c^2 \right]^{1/2} \} / (Q + E_v + E^*)$$
 (1.121)

where E^* is the excitation energy concentrated in the separation degree of freedom, $R_i = R_0 - R_e$ is the initial separation distance, $R_t = R_e + R_d$ is the touching point separation distance, $R_j = r_0 A_j^{1/3} (j=0,e,d; r_0=1.2249 \,\mathrm{fm})$ are the radii of parent, emitted and daughter nuclei, and $E_b^0 = E_i - Q$ is the barrier height before correction. The interaction energy at the top of the barrier, in the presence of a nonnegligible angular momentum, $l\hbar$, is given by:

$$E_i = E_c + E_l = e^2 Z_e Z_d / R_t + \hbar^2 l(l+1) / (2\mu R_t^2)$$
(1.122)

The two terms of the action integral K, corresponding to the overlapping (K_{ov}) and separated (K_s) fragments, are calculated by analytical formulas (approximated for K_{ov} and exact for K_s in case of separated spherical shapes within the LDM):

$$K_{ov} = 0.2196(E_b^0 A_e A_d / A)^{1/2} (R_t - R_i) \left[\sqrt{1 - b^2} - b^2 \ln \frac{1 + \sqrt{1 - b^2}}{b} \right]$$
 (1.123)

$$K_s = 0.4392[(Q + E_v + E^*)A_eA_d/A]^{1/2}R_bJ_{rc}; b^2 = (E_v + E^*)/E_b^0$$
 (1.124)

$$J_{rc} = (c) \arccos \sqrt{(1-c+r)/(2-c)} - \left[(1-r)(1-c+r) \right]^{1/2} + \sqrt{1-c} \ln \left[\frac{2\sqrt{(1-c)(1-r)(1-c+r)} + 2 - 2c + cr}{r(2-c)} \right]$$
(1.125)

where $r = R_t/R_b$ and $c = rE_c/(Q + E_v + E^*)$. In the absence of the centrifugal contribution (l = 0), one has c = 1.

We took $E_{\nu}=E_{\rm corr}$ in order to get a smaller number of parameters. It is evident that, owing to the exponential dependence, any small variation of $E_{\rm corr}$ induces a large change of T, and thus plays a more important role compared to the preexponential factor variation due to E_{ν} . Shell and pairing effects are included in $E_{\rm corr}=a_i(A_e)Q$ (i=1,2,3,4 for even-even, odd-even, even-odd, and odd-odd parent nuclei). For a given cluster radioactivity we have four values of the coefficients a_i , the largest for even-even parent and the smallest for the odd-odd one (see Fig. 1 of [110]). The shell effects for every cluster radioactivity is implicitly contained in the correction energy due to its proportionality with the Q value, which is maximum when the daughter nucleus has a magic number of neutrons and protons.

With only few exceptions, in the region of nuclei far from stability, measured α -decay partial half-lives are not available. In principle we can use the ASAF model to estimate these quantities. Nevertheless, slightly better results can be obtained by using our semiempirical formula [103].

The potential barrier shape similar to that we considered within the ASAF model was recently calculated by using the macroscopic-microscopic method [94], as a cut through the PES at a given mass asymmetry, usually the ²⁰⁸Pb valley or not far from it.

Before any other model was published, we had estimated the half-lives for more than 150 decay modes, including all cases experimentally confirmed until now. A comprehensive table was produced by performing calculations within that model. Subsequently, the numerical predictions of the ASAF model have been improved by taking better account of the pairing effect in the correction energy, deduced from systematics in four groups of parent nuclei (even—even, odd—even, even—odd and odd—odd). In a new table, published in 1986, cold fission as cluster emission has been included. The systematics was extended in the region of heavier

emitted clusters (mass numbers $A_e > 24$), and of parent nuclei far from stability and superheavies. Since 1984, the ASAF model results have been used to guide the experiments and to stimulate other theoretical works.

1.4.2 Systematic Search for Cluster Decay Modes

Our calculations "indicating the possibility of a new type of decay of heavy nuclei" have been mentioned in the New Encyclopaedia Britannica [130]. In [120] we employed several models to predict cluster radioactivities: theory of fragmentation and the asymmetric two center shell model; an α -decay like theory; the numerical superasymmetric fission (NuSAF) model, and the ASAF model [38, 85, 84, 104].

We use the experimental masses. The latest compilation for 2,931 masses of nuclei measured or determined from systematics was published in 2003 [2].

In a systematic search for new nuclear decay modes we calculated with the ASAF model the half-lives of all combinations (about 10^5) of pair of fragments $^{A_e}Z_e,^{A_d}Z_d$ with $2 < Z_d \le 28$ for every parent nucleus AZ . An example of the time spectra obtained for different clusters emitted from the parent nuclei 222,223 Ra and 232 U are given in Fig. 1.8 versus the neutron and proton numbers of the light fragment. The shortest half-lives correspond to α -decay and 14 C, or 24 Ne radioactivity. Comprehensive tables have been published (see [110] and the references therein). The chart of cluster emitters from Fig. 1.9 is obtained by associating to each emitter only the most probable emitted cluster. By selecting the measurable

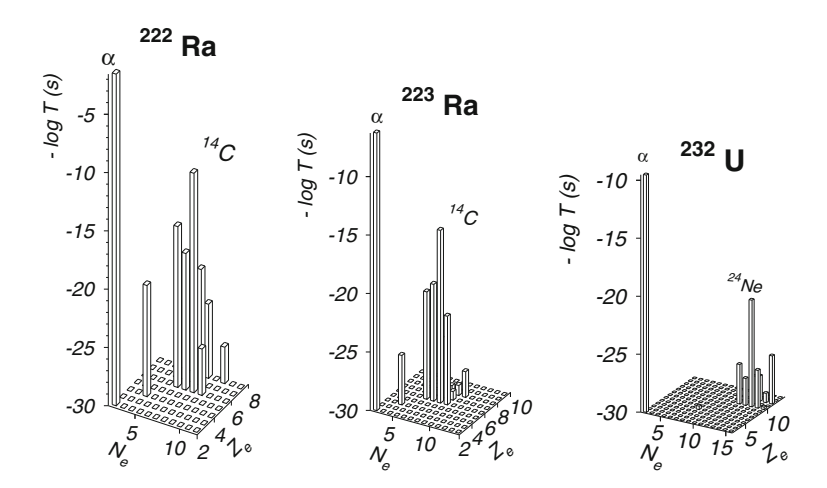


Fig. 1.8 Decimal logarithm of the half-lives for cluster radioactivities of two Ra isotopes and of 232 U versus the number of neutrons and protons of the emitted cluster. The minus sign allows to view the strong decay modes as higher bars in this lego plot. The shortest half-lives correspond to α -decay and to 14 C for Ra isotopes, and to α -decay and to 24 Ne radioactivity for 232 U

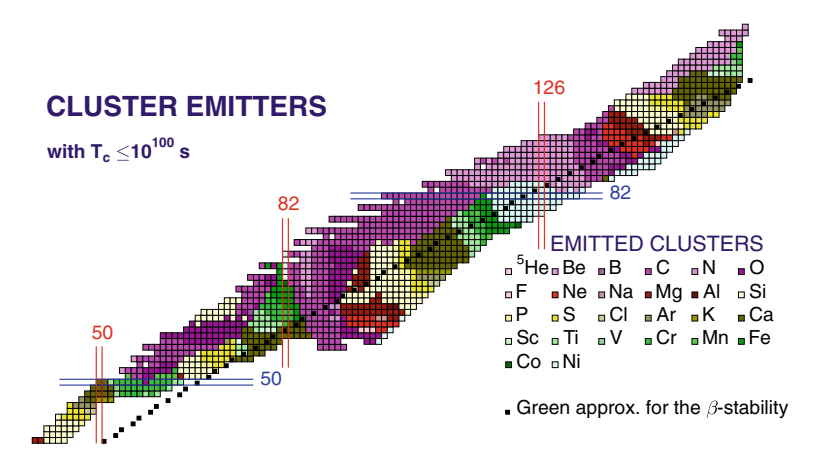
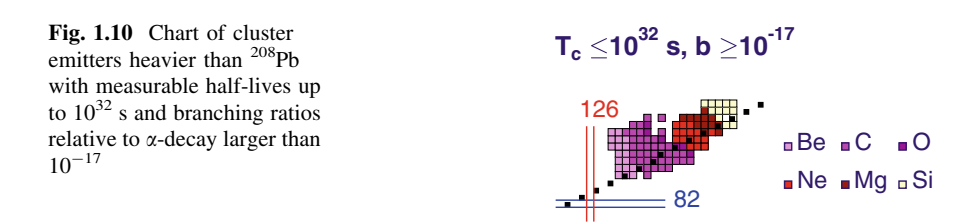


Fig. 1.9 Chart of cluster emitters with half-lives up to 10^{100} s



half-lives shorter than 10^{32} s and branching ratios with respect to α -decay $b \ge 10^{-17}$ we obtain three islands for cluster radioactivity: above 100 Sn, above N=82, and the main island with daughter nuclei in the vicinity of 208 Pb. The last one is given in Fig. 1.10. In 1990, when we submitted the comprehensive tables [110] to be published, there were very few measured masses in the superheavy region of nuclei. Consequently we used different calculated masses to determine the Q-values and the corresponding half-lives. As can be seen from the tables, usually the most probable cluster emitted in this region could be a light one as 8 Be and 12 C or a heavy Ni isotope. Even with a reasonable low half-life of $10^{10}-10^{14}$ s there is no real chance to measure cluster radioactivity of superheavies since the main decay mode is α -decay and the total number of synthesized nuclei is of the order of few units.

1.4.3 Experimental Confirmations

The main quantities experimentally determined are the partial halflife, T, and the kinetic energy of the emitted cluster $E_k = QA_d/A$. This equation is a direct consequence of the "cold" character of this decay mode—the total kinetic energy of

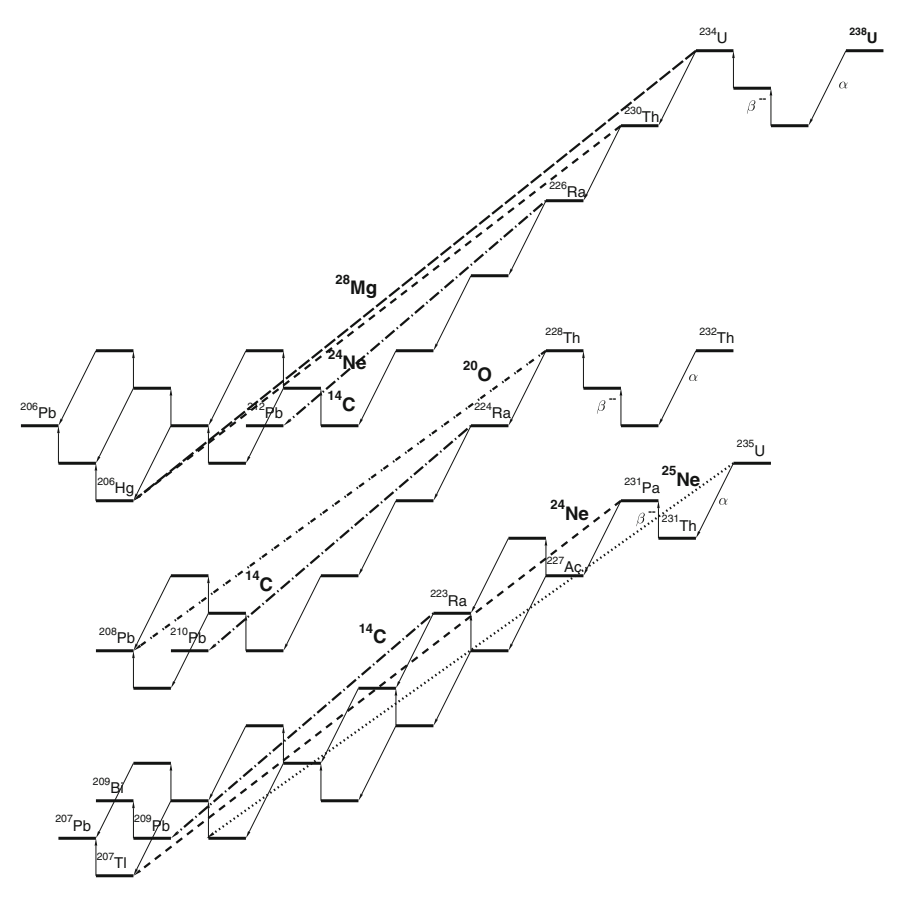


Fig. 1.11 The natural radioactive families. There are several sequences of α and β^- disintegrations ending up with a stable nucleus. Heavy cluster radioactivities with 28 Mg, 24 Ne, 14 C, 20 O, 25 Ne, as emitted cluster allow to reach a stable nucleus, like $^{206\text{-}208}$ Pb or 209 Bi in one decay. When the daughter is a short-lived nucleus (209,210 Pb, 207 Tl or 206 Hg) the cluster decay is followed by one or two β^- -decays

the two fragments practically exhausts the released energy Q, which is shared between the two fragments. The experimental techniques are presented elsewhere [81]. Several experiments have been performed with radioactive sources which are members of one of the three natural radioactive families (see Fig. 1.11).

Our earlier predictions, and those given in 1986, after taking properly into account the even-odd effects, are compared in Fig. 1.12 with the experimental data available until now in an island of trans-francium parent nuclei, where the daughter nucleus is the doubly magic ²⁰⁸Pb or some of its neighbours.

Besides the usual experiment with one cluster emitted by a given parent nucleus, there are results showing two different clusters, e.g. both Ne + Mg from 234 U, Mg + Si from 238 Pu, and F + Ne from 231 Pa. The measured half-lives are represented by points, and our predictions by lines. Only upper limits have been

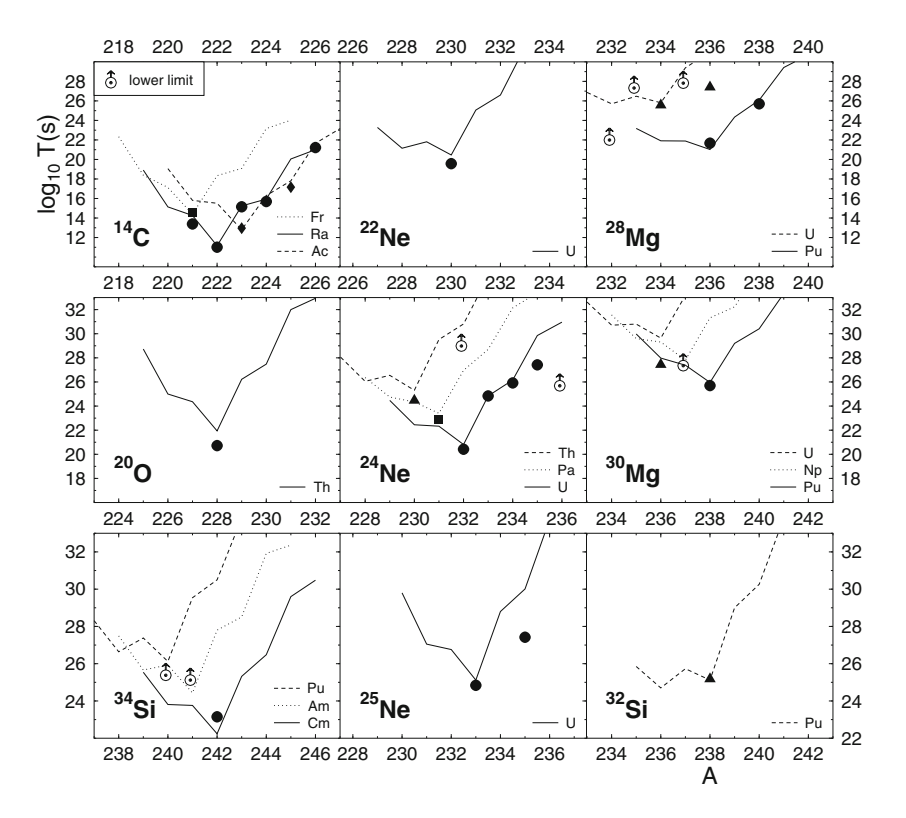


Fig. 1.12 Systematics of experimentally determined half-lives (points) and lower limits of cluster radioactivities compared to the ASAF predictions (lines). Heavy lines correspond to a daughter with magic number of protons, $Z_d = 82$. Two decay modes are not presented: ²³F of ²³¹Pa with $\log_{10} T_{exp}(s) = 26.02$ and ²⁶Ne of ²³⁴U with $\log_{10} T_{exp}(s) = 25.92$

determined for some of the points (e.g. for ²⁸Mg emission from ²³⁵U, ³⁰Mg decay of ²³⁷Np, and ³⁴Si decays of ²⁴⁰Pu and ²⁴¹Am).

The measured half-lives are in good agreement with the ASAF model predictions. The strong shell effect of the doubly magic daughter ²⁰⁸Pb, shortening the half-lives, is evident. Except for the ²⁸Mg radioactivity of ²³⁶U, were none of the proton and neutron numbers of the fragments are magic, in all other 27 successful experiments there are one, two, or three magic numbers involved.

We observed [107] that still this property was not fully exploited so that we suggested a whole list of experiments that could be successfully performed in the future: ^{220,222,223}Fr, ²²⁴Ac, and ²²⁵Th as ¹⁴C emitters; ²²⁹Th for ²⁰O radioactivity; ²²⁹Pa for ²²Ne decay mode; ^{230,232}Pa, ²³¹U, and ²³³Np for ²⁴Ne radioactivity; ²³⁴Pu for ²⁶Mg decay mode; ^{234,235}Np and ^{235,237}Pu as ²⁸Mg emitters; ^{238,239}Am and ²³⁹⁻²⁴¹Cm for ³²Si radioactivity, and ³³Si decay of ²⁴¹Cm. One of the candidates was ²²³Ac emitting ¹⁴C, and in 2007 it was indeed reported [41].

The attempts to detect 12 C radioactivity of 114 Ba, which is proton-rich and far from stability, have not been successful [40]. Nevertheless, the α -decay could be

observed [60, 68]: $Q_{\alpha}=3$, 540 \pm 40 keV and $\log_{1}0T_{\alpha}(s)=1.68$ can be obtained from the total half-life of $0.43^{+0.30}_{-0.15}$ s due to β -decay and a branching ratio $b_{\alpha}=0.9~\pm~0.3\%$.

In conclusion the ASAF model predictions have been confirmed. The magicity of the daughter ²⁰⁸Pb was not fully exploited so that new experimental searches can, hopefully, be successfully performed.

1.4.4 Unified Approach of Cold Fission, Cluster Decay and α-Decay

In the usual fission process a fraction of the released energy (20–40 MeV from about 250 MeV) is spent to deform and excite the fragments. They reach the final gs by neutron evaporation and γ -ray emission. Only the remaining part of the Q-value gives the total kinetic energy (TKE) of the fragments. Another process, called *cold fission* [125], in which the TKE practically exhausts the Q value (no excitation energy and compact shapes at the scission point), has been experimentally observed in two regions of nuclei: U, Np, Pu isotopes, as well as for Fm, Md, No and other trans-fermium nuclei. While the new mechanism is very rare in the first group of nuclei, it is rather strong into the second one, giving rise to the *bimodal* character [53] of the fission phenomena for some trans-fermium nuclei.

The unified approach of the three groups of decay modes (cold fission, cluster radioactivities and α -decay) within the ASAF model is best illustrated by the example of ^{234}U nucleus [96] for which all these processes have been measured. Also in the region of superheavy nuclei the α -decay half-lives can be successfully calculated using the ASAF-model, the universal curve (see below), and a semi-empirical formula, taking into account the shell effects [108, 109].

The theory was extended to cold ternary [85] and to multicluster fission including quaternary (two-particle accompanied) fission [101]. In that paper we stressed the expected enhanced yield of two alpha accompanied fission compared to other combinations of two light particles; it was indeed experimentally confirmed [33, 34].

Also we have studied many other cold- and bimodal fission processes viewed as cluster decays. For instance, since 1986 we payed particular attention to the cold fission of 264 Fm. According to our calculations, performed within the ASAF model, the cold fission mechanism could be the main decay mode of this neutron-rich nucleus, which has not been produced until now. It also should give the most pronounced symmetrical distribution of fission fragments [89], owing to the doubly magic character of 132 Sn fragments. The half-life of 5.7 μ s for a "new fission path" with compact shapes calculated by Möller and Nix in 1994 is not very far from our log_{10} T(s) = -5.6. It would be very interesting to synthesize the neutron-rich 264 Fm in the near future. For alpha-decay, we estimate the following half-lives: log_{10} T(s) = 10.77, 11.00, 12.49, 12.67, 12.86, 13.75, and 14.32, which correspond to $Q_{\alpha} = 5.905$, 5.865, 5.615, 5.585, 5.555, 5.415, and 5.330 MeV,

obtained by taking the masses of the parent 264 Fm and of the daughter 260 Cf, from the mass tables calculated by various authors. The cold fission process should be several orders of magnitude stronger than the α -decay.

1.5 Universal Curves

We developed a new method to estimate the preformation probability, S, as a penetrability through the internal part of the barrier within a fission theory and derived a universal curve [95] which can be used to estimate the half-lives against any kind of heavy particle radioactivity or α -decay including superheavy [108, 109] emitters.

1.5.1 Preformation Probability in a Fission Model

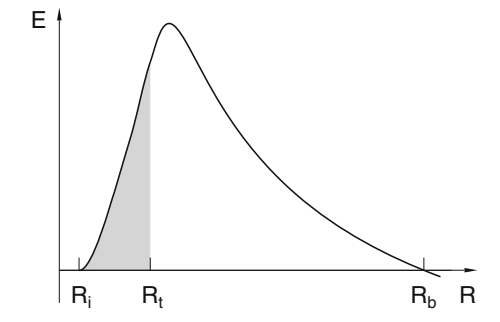
The (measurable) decay constant $\lambda = \ln 2/T$, characterising the well known exponential law $e^{-\lambda t}$ (variation in time of the number of parent nuclei) can be expressed in both alpha-like [4, 5] or fission-like theories, as a product of three (model dependent) quantities

$$\lambda = vSP_s \tag{1.126}$$

where v is the frequency of assaults on the barrier per second, S is the preformation probability of the cluster at the nuclear surface, strongly dependent on the nuclear structure, and P_s is the quantum penetrability of the external potential barrier (Fig. 1.13).

Not every quantity appearing in the above equation plays an important role; usually the penetrability dominates the half-life variation with A. The frequency ν remains practically constant. The preformation differs from one decay mode to another one but it is not changed very much for a given radioactivity, while the general trend of penetrability follows closely that of the half-life. This means that

Fig. 1.13 A schematic example of potential barrier showing the internal part (overlapping fragments) form the initial, R_i , to the touching point separation distance, R_i , and the external part (separated fragments) from R_i to the turning point R_b



for cluster radioactivity and α -decay as well, the external part of the barrier, essentially of Coulomb nature, is much wider than the internal part. Consequently, both fission-like and α -like models, which take into consideration the external part of the barrier in the same manner, can provide a successful explanation for the measured half-lives.

In a model derived from a many-body approach of α -decay, S is expressed as an overlap integral of the wave functions of the three partners (parent and two fragments). According to our new method, developed in 1990, the preformation probability can be calculated within a fission model as a penetrability of the internal part of the barrier,

$$S = \exp(-K_{ov}); \quad K_{ov} = \frac{2}{\hbar} \int_{R_{ov}}^{R_{t}} \sqrt{2B(R)E(R)} dR$$
 (1.127)

where R_a is the internal turning point $(E(R_a) = 0)$, $R_t = R_1 + R_2$ is the separation distance of two fragments at the touching point configuration, B(R) is the nuclear inertia, and E(R) is the deformation energy from which the Q-value was subtracted.

1.5.2 Universal Law

In a first approximation, one may assume the following linear dependence for the preformation probability in the range of emitted clusters already measured:

$$\log S = \frac{(A_e - 1)}{3} \log S_{\alpha} \tag{1.128}$$

where the preformation probability of the α particle S_{α} may be determined by fitting with experimental data.

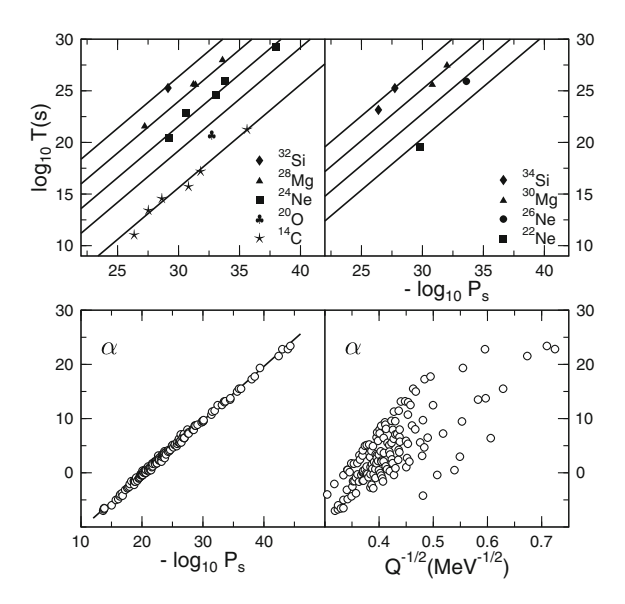
On this basis we have found a single universal curve $\log T = f(\log P_s)$, for each kind of cluster radioactivity of even—even parent nuclei. This has been done by making the further assumption that the frequency v is independent of the emitted cluster and the daughter nucleus $v(A_e, Z_e, A_d, Z_d) = \text{constant}$. From a fit of experimental data we got [95] $S_\alpha = 0.0160694$ and $v = 10^{22.01} \text{ s}^{-1}$, leading to

$$\log T = -\log P_s - 22.169 + 0.598(A_e - 1) \tag{1.129}$$

This equation represents a straight line for a given A_e , with a slope equal to unity. The vertical distance between two universal curves corresponding to A_{e1} and A_{e2} is $0.598(A_{e2}-A_{e1})$. For any combination of fragments A_eZ_e , A_dZ_d one can calculate easily

$$-\log P_s = 0.22873 (\mu_A Z_d Z_e R_b)^{1/2} \left[\arccos \sqrt{r} - \sqrt{r(1-r)}\right]$$
 (1.130)

Fig. 1.14 Universal curves for cluster radioactivities (top left and right) and α -decay (bottom left). In a typical "Geiger–Nuttal" [26] plot for α -decay (bottom right) one can see many scattered data points



where $r = R_t/R_b$, $R_t = 1.2249(A_d^{1/3} + A_e^{1/3})$, $R_b = 1.43998Z_dZ_e/Q$, and $\mu_A = A_dA_e/A$ is the reduced mass number. The up to now even-even half-life measurements are well reproduced (within a ratio 3.86, or rms = 0.587 orders of magnitude).

As far back as in 1911, Geiger and Nuttal [26] have found a simple dependence of the α -decay partial half-life on the α -particle range in air. Nowadays, very often a diagram of $\log T$ versus $Q^{-1/2}$ (see the bottom of Fig. 1.14) for α emission or cluster radioactivity is called Geiger–Nuttal plot. In this kind of systematics the experimental or calculated points are considerably scattered.

1.6 Fine Structure

The superconducting spectrometer SOLENO, at I. P. N. Orsay has been employed since 1984 to detect and identify the ¹⁴C clusters spontaneously emitted from ^{222, 223, 224, 226}Ra parent nuclei. Moreover, its good energy resolution has been exploited in 1989 to discover [12] a "fine structure" in the kinetic energy spectrum of ¹⁴C emitted by ²²³Ra. Cluster emission leading to excited states of the final fragments have been considered for the first time in 1986 by Martin Greiner and Werner Scheid [36]. These important predictions should still be experimentally verified in detail.

When the fine structure of 14 C radioactivity of 223 Ra has been discovered it was shown that the transition toward the first excited state of the daughter nucleus is stronger than that to the gs. In other words, like in spontaneous fission of odd-mass nuclei, or in fine structure of α -decay, one has a hindered and a favoured transition, respectively.

The physical explanation relies on the single-particle spectra of neutrons or/and protons. If the uncoupled nucleon is left in the same state both in parent and heavy fragment, the transition is favoured. Otherwise the difference in structure leads to a large hindrance $H = T^{\rm exp}/T_{e-e}$, where $T^{\rm exp}$ is the measured partial half-life for a given transition, and T_{e-e} is the corresponding quantity for a hypothetical eveneven equivalent, estimated either from a systematics (log T versus $Q^{-1/2}$ for example) or from a model. A transition is favoured if $H \simeq 1$, and it is hindered if H > 5.

Unlike in α -decay, where the initial and final states of the parent and daughter are not so far one from the other, in cluster radioactivities of odd-mass nuclides, one has a unique possibility to study a transition (see Fig. 1.11) from a well deformed parent nucleus with complex configuration mixing, to a spherical nucleus with a rather pure shell model wave function. One can get direct spectroscopic information on spherical components of deformed states. The most accurate experiment has been performed by Hourany *et al.* [52] with SOLENO using high quality 223 Ra sources implanted at ISOLDE CERN. The interpretation given by Sheline and Ragnarsson, according to which the main spherical component of the deformed parent wave function has a $i_{11/2}$ character, has been confirmed. A transition with an excited state of 14 C predicted [36] in 1986 was not yet observed. This is, indeed, a really novel process and should be experimentally addressed!

1.7 Ternary and Multicluster Fission

From time to time (at best once per about 1,000 fision events) a spontaneous (or induced) fission of a nucleus (A,Z) leads to three fragments, usually one light particle (A₁,Z₁) (which is frequently ⁴He or some Be, C, or O isotope) and two fragments (A₂,Z₂), (A₃,Z₃) of sizes not very different from those resulting from binary fission. Even less probable is a process in which the three fragments are almost identical. Since 1946, when "long-range" α particles accompanying fission were observed for the first time, progress made in the field of ternary fission has been reviewed many times (for example Refs [75, 135]).

A renewed interest in such phenomena is motivated on the one hand by the successful synthesis of the heaviest nuclei [47, 73, 78–80] and study of their decay properties, and on the other hand by the new measurements of spontaneous cold fission of 252 Cf [42] and of 242 Pu using large γ -ray detector arrays.

We also consider the Q_3 value for fragmentation into three identical or nearly identical fragments. In spite of having quite large Q values, however, this "true ternary fission" is a rather weak process; the strongest phenomenon remains α -particle-accompanied fission [75].

In 1958 it was theoretically shown on the basis of the liquid drop model [76] that for increasingly heavier nuclei, fission into three, then four and even five fragments becomes energetically more favourable than binary fission. We can

take, as an approximation of the Q value, the energy difference between the sum of Coulomb and surface energies for the parent (superscript 0) and n identical fission fragments (superscript i)

$$Q_n \simeq (E_C^0 + E_s^0) - \sum_{i=1}^n (E_C^i + E_s^i)$$
 (1.131)

where n=2 for binary fission, n=3 for ternary fission, etc. A linear dependence of Q_n on the (binary) fissility parameter, $X=E^0_{C}/(2E^0_{s})$, of the form

$$Q_n/E_s^0 \simeq 1 - n^{1/3} + 2X(1 - n^{-2/3})$$
 (1.132)

has been obtained by Swiatecki. As the fissility parameter increases, fission into more than two equal fragments becomes energetically favored.

Calculated Q values for the cold splitting of even—even nuclei into three particles of equal size, as well as for various fission processes accompanied by light-particle emission are listed for nuclides with Z=90–116 [100]. The released energy gives a good indication about the competition between different emitted particles.

We predicted the multicluster fission [98, 101]. In particular we have stressed that two- α accompanied fission (a type of quaternary fission) has a good chance to be experimentally observed, as the *Q*-value and potential barrier is similar to ⁸Beaccompanied fission. It was indeed discovered by Goennenwein et al. [33, 34].

Pyatkov et al. in JINR Dubna [113] are pursuing experiments on true ternary fission [86] of ²⁵²Cf which they interprets as a collinear cluster tripartition.

1.8 Stability of Metallic Atomic Clusters

The similarity between atomic nuclei and metallic atomic clusters is based on the fact that both systems consists of fermions moving freely in a confined space. The electronic shell structure in monovalent free-electron metal clusters [62] has shown a strong analogy with the single-particle states of atomic nuclei, despite gross differences in the physical forces binding the two systems. Moreover, the delocalized electrons of a metallic cluster may be considered to form a Fermi liquid like the atomic nucleus. Consequently several theories and computation techniques from nuclear physics can be adapted to atomic clusters [122].

We used the LDM and the macroscopic-microscopic method to investigate neutral spheroidal [32] and hemispheroidal atomic clusters deposited on a surface [90, 91, 93]. Such shapes were observed in experiments using atomic force microscope [7, 14, 82, 124]. Analytical relationships for the deformation-dependent LDM energies of oblate and prolate hemispheroidal atomic clusters have been obtained. A superdeformed prolate hemispheroid was found to be the most stable shape within the LDM. It is also the shape with maximum degeneracy of quantum

states of the hemispheroidal harmonic oscillator used to compute the shell and pairing corrections.

We developed [92] a new shell model (quantum harmonic semi-spheroidal oscillator) with striking properties of symmetry, which exhibits the maximum degeneracy at a super-deformed prolate deformation (ratio of semiaxes 1/2). Also we found the maximum LDM stability at the same deformation [90, 91]. By using scanning probe microscopy (SPM) or atomic force microscopy (AFM) it is possible to observe how the shapes of such clusters are distorted after remaining on the surface. The final shape of some of them [7, 14, 124] may be approximated in first order by a hemispheroid. Consequently we developed a shell model accepting a hemispheroidal shape as an equipotential surface of the chosen Hamiltonian. Another argument relies on the 2D measurement [16] of the strong magicity at the number equal to 6, which can be approximated as a limiting case of an extremely large oblate deformation in our model. Also one has to consider the possibility to solve the problem analytically within such an idealization. The advantage of an analytical relationship is not only a very short computational time but also an easier interpretation of the results.

When we compare the LDM PES with the shell and pairing corrections for nuclei we always have the minimum energy of $E_{\rm LDM}$ at a zero mass asymmetry $\eta=0$ but the minima of δE are usually obtained at different mass asymmetry determined by the occurrence of magic numbers of nucleons. It was experimentally proven that the most important yield in fission of charged metallic atomic clusters is usually obtained when the light fragment is a singly charged trimer (the analog of an α -particle with magic number of delocalized electrons $n_e=2$). Our calculations for charged alkali clusters [89] are showing that both the $E_{\rm LDM}$ and δE energies are possessing local minima at the same mass asymmetry corresponding to this " α -cluster".

1.8.1 Liquid Drop Model of a Neutral Metallic Hemispheroidal Atomic Cluster

The surface equation of the hemispheroid from Fig. 1.15 with the symmetry z-axis perpendicular on the surface plane, is given by

Fig. 1.15 Prolate hemispheroidal shape (with semiaxes a < c)

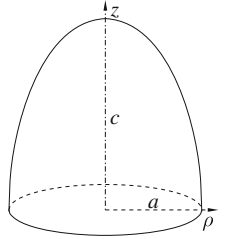
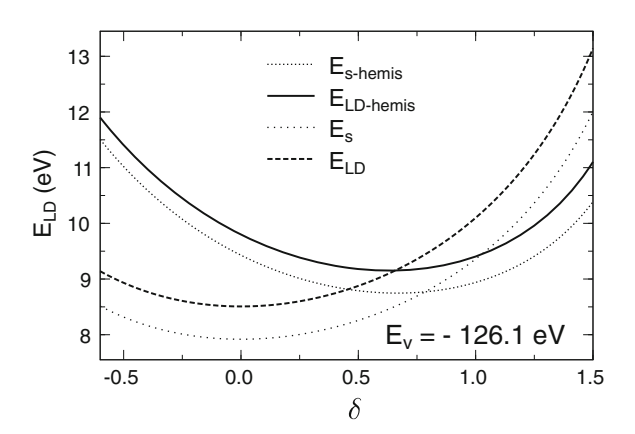


Fig. 1.16 LDM deformation energy of a hemispheroidal cluster Na_{56} compared to the same quantities for a spheroidal shape



$$\rho^2 = \begin{cases} (a/c)^2 (c^2 - z^2) & z \ge 0\\ 0 & z < 0 \end{cases}$$
 (1.133)

If c > a one has a prolate shape; otherwise (c < a) it is oblate. The volume of the spherical cluster with the same number of atoms is $V_{ol}^0 = 4\pi a^2 c R_0^3/3$. When the cluster is a hemisphere $V_{ol}^s = 2\pi a^2 c R_s^3/3$, hence $R_s = 2^{1/3} R_0$. The deformation energy

$$E - E^{s0} = E_s^{s0} (B_{\text{surf}}^s - 1) + E_c^{s0} (B_{\text{curv}}^s - 1)$$
 (1.134)

is for a hemisphere

$$E_s^{s0} = (3/4^{2/3})E_s^0; \quad E_c^{s0} = E_{\text{curv}}^0/4^{1/3}$$
 (1.135)

Surface and curvature deformation energies of an oblate (a > c) hemispheroid with eccentricity $e^2 = a^2/c^2 - 1$ are given by

$$B_{\text{surf}}^{s} = \frac{a}{3} \left[2a + \frac{c}{e} \ln\left(e + \frac{a}{c}\right) \right]; \quad B_{\text{curv}}^{s} = \frac{c}{2} + \frac{a^2}{2ce} \arctan e$$
 (1.136)

When the hemispheroid is prolate, $e^2 = 1 - a^2/c^2$ and

$$B_{\text{surf}}^{s} = \frac{a}{3} \left(2a + \frac{c}{e} \arcsin e \right); \quad B_{\text{curv}}^{s} = \frac{c}{2} + \frac{a^{2}}{4ce} \ln \left| \frac{1+e}{1-e} \right|$$
 (1.137)

For the example of the Na₅₆ cluster, shown in Fig. 1.16, one can see that the minimum of the deformation energy is around the superdeformed prolate shape with $\delta = 0.65(c/a = 1.96)$, unlike for a spheroid ($\delta = 0$).

1.8.2 New Single-Particle Shell Model

The spheroidal harmonic oscillator has been used in various branches of Physics. The famous single-particle Nilsson model [77] is very successful in Nuclear

Physics. Its variants [17, 62, 116] are of particular interest for atomic clusters [19]. Major spherical-shells N = 2, 8, 20, 40, 58, 92 have been found [62] in the mass spectra of sodium clusters of N atoms per cluster, and the Clemenger's shell model [17] was able to explain this sequence of spherical magic numbers.

We derived the analytical expressions for the energy levels of a hemispheroidal harmonic oscillator and used it to study atomic clusters deposited on planar surfaces. It may be used as a reliable approximation of a realistic single-particle shell model for small magic numbers, giving the input data for shell correction calculations [11, 17, 62, 66, 129, 138–140].

In all studies using an harmonic oscillator published since 1955, the maximum degeneracy of the quantum states was reached for a spherical shape, explaining the high stability of the doubly magic nuclei or of the metal clusters with spherical closed shells. To our surprise the maximum stability of the hemispheroidal quantum harmonic oscillator occurs at a superdeformed prolate shape (semiaxes ratio a/c = 1/2), a shape which is also the most stable one within the LDM [91].

We begin with the Hamiltonian containing the potential of (31) and neglect for the moment an additional term proportional to $(\mathbf{l}^2 - \langle \mathbf{l}^2 \rangle_n)$. In a second step further on we investigate its influence. We use dimensionless two semiaxes in units of the radius of a hemisphere with the same volume, $R_s = 2^{1/3}R_0 = 2^{1/3}r_sN^{1/3}$, where r_s is the Wigner-Seitz radius, 2.117 Å for Na [9, 139].

The surface equation was written in the previous subsection. We give ρ , z, a, c in units of R_s instead of R_0 , so that again $a^2c = 1$. The definition of δ_s is the same as that of δ in (32), but now a and c are expressed in terms of R_s instead of R_0 .

The potential along the symmetry axis, $V_z(z)$, has a wall of an infinitely large height at z=0, and ranges only over positive values of z, implying opacity of the surface:

$$V_z = \begin{cases} \infty & z \le 0\\ M R_s^2 \omega_z^2 z^2 / 2 & z > 0 \end{cases}$$
 (1.138)

In this case the wave functions should vanish at the origin, where the potential wall is infinitely high, so that only negative parity Hermite polynomials (n_z odd) should be taken into consideration.

Equation (1.35) of the harmonic oscillator, in units of $\hbar\omega_0$ is still valid, but one should only allow the values of n and n_{\perp} for which $n_z = n - n_{\perp} \ge 1$ are odd numbers.

The shell gap for an atomic cluster [17] is given by

$$\hbar\omega_0(N) = \frac{13.72 \text{ eV Å}^2}{r_s R_s} \left[1 + \frac{t}{r_s N^{1/3}} \right]^{-2}$$
 (1.139)

Since we consider solely monovalent elements, N in this equation is the number of atoms, and t denotes the electronic spillout for the neutral cluster. The striking result is that the maximum degeneracy is obtained at a superdeformed prolate shape ($\delta_s = 2/3$). The magic numbers are those of the spherical shape ($\delta = 0$) of the spheroidal harmonic oscillator: 2, 8, 20, 40, 70, 112, 168, ...

By including a term proportional to $(\mathbf{l}^2 - \langle \mathbf{l}^2 \rangle_n)$ in the Hamiltonian

$$\hat{H} = -\frac{\hbar^2 \Delta}{2M} + \frac{M\omega_0^2 R_0^2}{2} \left(\frac{\rho^2}{a^2} + \frac{z^2}{c^2} \right) - \hbar \omega_0 U(\mathbf{l}^2 - \langle \mathbf{l}^2 \rangle_n)$$
 (1.140)

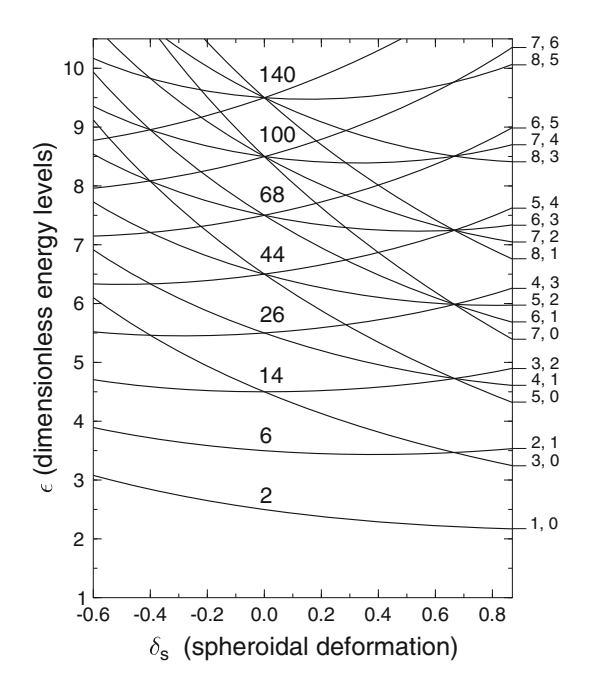
with the dimensionless quantity U = 0.04 and $\langle \mathbf{l}^2 \rangle_n = n(n+3)/2$ like in Ref. [17] for the spheroidal oscillator, we obtain again an analytical relationship for the energy levels:

$$\varepsilon_n = \frac{E_n}{\hbar \omega_0} = \frac{n_{\perp} + 1}{a} + \frac{n_z + 1/2}{c} - \frac{Um^2}{4a^4} + \frac{Un(n+3)}{2}$$
 (1.141)

The terms proportional to U are both diagonal; the first one $-Um^2/(4a^4)$ representing the contribution of the \hat{l}_z^2 part of the angular momentum operator. The possible nondiagonal terms coming from $(\hat{l}^+\hat{l}^-+\hat{l}^-\hat{l}^+)/2$ are not present since their contribution vanishes due to the selection rules excluding even values of the quantum number n_z . As mentioned above, the quantum number $m=(n_\perp-2i)$ with i=0,1,..., so that for $n_\perp=0$ one has m=0—the energy level is not changed. When $n_\perp=1$, $m=\pm 1$ the energy is changed but the degeneracy of 4 remains. For $n_\perp=2$, $m=\pm 2$, 0 one has a split leading to one level with m=0 and the degeneracy 2, and another level with $m=\pm 2$ and the degeneracy 4, etc.

The level scheme which was obtained in this way is different from the scheme plotted in Fig. 1.17. Nevertheless, for the lower levels (say up to 10 closed shells), the sequence of the magic numbers with maximum degeneracy, taking place at the

Fig. 1.17 Energy levels of the hemispheroidal harmonic oscillator in units of $\hbar\omega_0$ vs. the deformation parameter δ . Each level is labelled by n, n_\perp quantum numbers shown at the right-hand side, and is $(2n_\perp + 2)$ -fold degenerate. $n_z = n - n_\perp = 1, 3, 5, \ldots$



superdeformed prolate shape $\delta = 2/3$, remain the same: N = 2, 8, 20, 40, 70, 112, 168. Another remarkable fact is that for very large oblate deformations, leading to "pan-cake" shapes approximating a 2D situation, one of the magic numbers is 6, in agreement with the experiments [16].

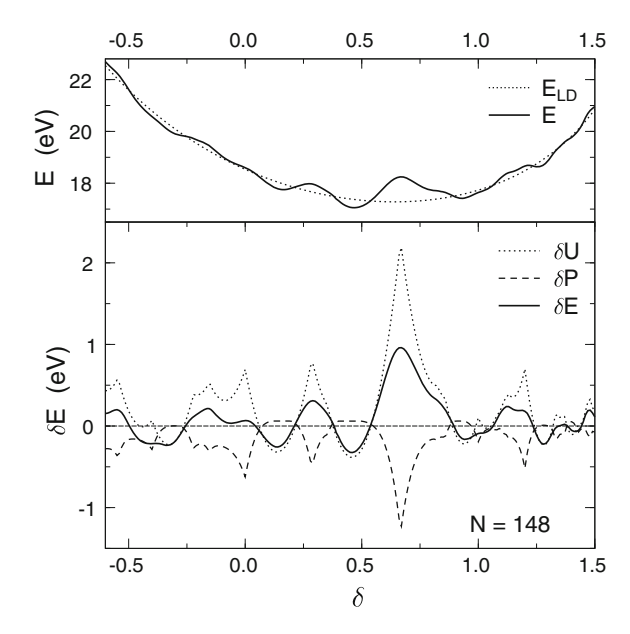
1.8.3 Macroscopic-microscopic deformation energy

The gs and isomeric state deformation of clusters of various sizes depends on the interplay between the minima of LDM and shell correction energies. The deformation energy in the framework of the macroscopic–microscopic method is given by

$$E_{\text{def}} = E_{\text{LDM}} + \delta E = E_{\text{LDM}} + \delta U + \delta P \tag{1.142}$$

Compared to the shell correction, the pairing correction is out of phase and smaller, as may be seen at the bottom of Fig. 1.18 for the example of the hemispheroidal Na₁₄₈ cluster. As a result of taking into account the pairing corrections, δP , the total shell and pairing corrections, $\delta E = \delta U + \delta P$, are smoother as compared to δU . The gs deformation of the Na₁₄₈ cluster, $\delta_{GS} = 0.47$, is given by the minimum value of total deformation energy; the shell and pairing correction contribution shifted this deformation from that of the liquid drop model, $\delta = 0.64$, to the smaller value because not far from $\delta = 0.64$, at $\delta = 0.67$ the shell correction reaches its maximum. The first isomeric state of this cluster has a

Fig. 1.18 Top Liquid drop model deformation energy, $E_{\rm LD} = E_s + E_{\rm curv}$, and the total deformation energy including shell and pairing corrections, $E = E_{LD} + \delta E$, for semi-spheroidal harmonic oscillator energy levels using the deformation parameter δ . A cluster of Na with 148 atoms is considered. The volume energy $E_{\nu} = E_{\nu}^{0} = -333 \text{ eV was}$ not included in $E_{\rm LD}$. The ground state shape prolate deformation $\delta_{GS} = 0.47$. Bottom The shell correction, δU , the pairing correction, δP , and $\delta E = \delta U + \delta P$ for the same cluster



hyperdeformed prolate shape, $\delta_{is1} = 0.93$, while the second one is prolate with a low deformation parameter, $\delta_{is2} = 0.20$.

We expect that the present results will get further support from the experiments in which the ultrasensitive microscopy (e.g. SPM (scanning probe microscopy) or AFM (atomic force microscopy)) is used. In particular for a large range of atomic numbers the increased stability of the prolate superdeformed hemispheroidal shapes may be seen for deposited clusters on planar surfaces with high opacity.

Acknowledgments This work was supported by Deutsche Forschungsgemeinschaft (DFG) and partially within IDEI Programme under contracts 123/01.10.2007 and 124/01.10.2007 with UEFISCSU, Bucharest. One of us (DNP) is grateful to DFG for the Mercator Guest Professorship.

References

- D.V. Aleksandrov, A.F. Belyatski, Y.A. Glukhov, E.Y. Nikolski, B.G. Novatski, A.A. Ogloblin, D.N. Stepanov, JETP Lett. 40, 909 (1984)
- 2. G. Audi, A.H. Wapstra, C. Thibault, Nucl. Phys. A 729, 337 (2003)
- 3. J. Bardeen, L. Cooper, J. Schrieffer, Phys. Rev. 108, 1175 (1957)
- 4. R. Blendowske, T. Fliessbach, H. Walliser, in *Nuclear Decay Modes*, Chap. 7, ed. by D.N. Poenaru (IOP Publishing, Bristol, 1996), pp. 337
- 5. R. Blendowske, T. Fliessbach, H. Walliser, Phys. Rev. Lett. 61, 1930 (1988)
- 6. N. Bohr, J. Wheeler, Phys. Rev. 56, 426 (1939)
- 7. B. Bonanni, S.J. Cannistraro, Nanotech. Online 1, 1 (2005).
- 8. R. Bonetti, A. Guglielmetti, Rom. Rep. Phys. 59, 301 (2007)
- 9. M. Brack, Phys. Rev. B 39(6), 3533 (1989)
- M. Brack, J. Damgaard, A. Jensen, H.C. Pauli, V.M. Strutinsky, G.Y. Wong, Rev. Mod. Phys. 44, 320 (1972)
- 11. C. Bréchignac, P. Cahuzac, F. Carlier, M. de Frutos, Phys. Rev. B 49, 2825 (1994)
- L. Brillard, A.G. Elayi, E. Hourani, M. Hussonnois, J.F. Le Du, L.H. Rosier, L.C.R. Stab, Acad. Sci. Paris 309, 1105 (1989)
- 13. I.N. Bronshtein, K.A. Semendyaev, Handbook of Maths. (Van Nostrand, New York, 1985)
- 14. Brown, S.A.: Private communication (2008)
- 15. U.L. Businaro, S. Gallone, Nuovo Cimento 1, 1277 (1955)
- Y.P. Chiu, L.W. Huang, C.M. Wei, C.S. Chang, T.T. Tsong, Phys. Rev. Lett. 97, 165504 (2006)
- 17. K.L. Clemenger, Phys. Rev. B 32, 1359 (1985). Ph.D. Thesis, University of California, Berkeley
- 18. S. Cohen, W.J. Swiatecki, Ann. Phys. (N. Y.) 22, 406 (1963)
- 19. J.P. Connerade, A.V. Solov'yov, W. Greiner, Europhys. News 33(6), 200 (2002)
- 20. J. Damgaard, H.C. Pauli, V.V. Pashkevich, V.M. Strutinski, Nucl. Phys. A 135, 432 (1969)
- 21. K.T.R. Davies, A.J. Sierk, J. Comput. Phys. 18, 311 (1975)
- 22. K.T.R. Davies, A.J. Sierk, J.R. Nix, Phys. Rev. C 13, 2385 (1976)
- J.M. Eisenberg, W. Greiner, Nuclear Theory, vol. I: Nuclear Models, vol. II: Nuclear Excitations, vol. III: Microscopic Theory. (North-Holland, Amsterdam, 1987, 1988, 1986)
- S. Gales, E. Hourani, M. Hussonnois, J.P. Schapira, L. Stab, M. Vergnes, Phys. Rev. Lett. 53, 759 (1984)
- 25. G. Gamow, Z. Phys. 51, 204 (1928)
- 26. H. Geiger, J.M. Nuttal, Phil. Mag. 22, 613 (1911)

- 27. R.A. Gherghescu, Phys. Rev. C 67, 014309 (2003)
- 28. R.A. Gherghescu, W. Greiner, Phys. Rev. C 68, 044314 (2003)
- 29. R.A. Gherghescu, W. Greiner, Phys. Rev. C 68, 054314 (2003)
- 30. R.A. Gherghescu, W. Greiner, D.N. Poenaru, Phys. Rev. C 52, 2636 (1995)
- 31. R.A. Gherghescu, D.N. Poenaru, W. Greiner, Z. Phys. A 354, 367 (1996)
- R.A. Gherghescu, D.N. Poenaru, A.V. Solov'yov, W. Greiner, Int. J. Mod. Phys. B 22, 4917 (2008)
- F. Gönnenwein, P. Jesinger, M. Mutterer, W.H. Trzaska, G. Petrov, A.M. Gagarski,
 V. Nesvizhevski, P. Geltenbort, Heavy Ion Phys. 18, 419 (2003)
- 34. F. Gönnenwein, M. Mutterer, Y. Kopatch, Europhys. News 36, 11 (2005)
- 35. A.E.S. Green, Nuclear Physics. (McGraw-Hill, New York, 1955)
- 36. M. Greiner, W. Scheid, J. Phys. G: Nucl. Phys. 12, L229 (1986)
- 37. W. Greiner, Int. J. Mod. Phys. E 5, 1 (1996)
- 38. W. Greiner, M. Ivaşcu, D.N. Poenaru, A. Săndulescu, in *Treatise on Heavy Ion Science*, vol. 8, ed by D.A. Bromley (Plenum, New York, 1989), p. 641
- 39. W. Greiner, J.A. Maruhn, Nuclear Models. (Springer, Berlin, 1996)
- A. Guglielmetti, R. Bonetti, G. Poli, R. Collatz, Z. Hu, R. Kirchner, E.R.N. Gunn, P.B. Price, B.A. Weaver, A. Westphal, J. Szerypo, Phys. Rev C 56, R2912 (1997)
- A. Guglielmetti, D. Faccio, R.Bonetti, S.Shishkin, S. Tretyakova, S. Dmitriev, A. Ogloblin, G.Pik-Pichak, N. van der Meulen, G. Steyn, T. van der Walt, C. Vermeulen, D. McGee, J. Phys.: Conf. Series 111, 012050 (2008)
- J.H. Hamilton, A.V. Ramayya, S.J. Zhu, G.M.Ter-Akopian, Y.T. Oganessian, J.D. Cole,
 J.O. Rasmussen, M.A. Stoyer, Prog. Part. Nucl. Phys. 35, 635 (1995)
- 43. W. Henning, W. Kutschera, in *Particle Emission from Nuclei*, vol. II, chap. 7 (CRC Press, Boca Raton, 1989), p. 188
- 44. D.C. Hoffman, T.M. Hamilton, M.R. Lane, in *Nuclear Decay Modes*, chap. 10 (IOP, Bristol, 1996), p. 393
- 45. S. Hofmann, In: Nuclear Decay Modes, chap. 3. (IOP, Bristol, 1996), p. 143
- S. Hofmann, W. Reisdorf, G. Münzenberg, F.P. Heßberger, J.R.H. Schneider, P. Armbruster, Z. Phys. A 305, 111 (1982)
- 47. S. Hofmann, G. Münzenberg, Rev. Mod. Phys. **72**, 733 (2000)
- 48. P. Holzer, U. Mosel, W. Greiner, Nucl. Phys. A 138, 241 (1969)
- 49. E. Hourani, M. Hussonnois, in *Particle Emission from Nuclei*, vol. II, chap. 6. (CRC Press, Boca Raton, 1989), p. 171
- 50. E. Hourani, M. Hussonnois, D.Z. Poenaru, Annales de Physique (Paris) 14, 311–345 (1989)
- 51. E. Hourany, in Nuclear Decay Modes, chap. 8 (IOP Publishing, Bristol, 1996), p. 350
- E. Hourany, G. Berrier-Ronsin, A. Elayi, P. Hoffmann-Rothe, A.C. Mueller, L. Rosier, G. Rotbard, G. Renou, A. Liebe, D.N. Poenaru, H.L. Ravn, Phys. Rev. C 52, 267 (1995)
- E.K. Hulet, J.F. Wild, R.J. Dougan, R.W. Lougheed, J.H. Landrum, A.D. Dougan, M. Schädel, R.L. Hahn, P.A. Baisden, C.M. Hendersson, R.L. Dupzyk, K. Sümmerer, G.R. Bethune, Phys. Rev. Lett. 56, 313 (1986)
- 54. D.R. Inglis, Phys. Rev. 96, 1059 (1954)
- 55. D.R. Inglis, Phys. Rev. 97, 701 (1955)
- 56. D.R. Inglis, Phys. Rev. 103, 1786 (1956)
- 57. M.G. Itkis, V.N. Okolovich, A.Y. Rusanov, G.N. Smirenkin, Z. Phys. A 320, 433 (1985)
- 58. M.G. Itkis, V.N. Okolovich, A.Y. Rusanov, G.N. Smirenkin, Sov. J. Part. Nucl. 19, 301 (1988)
- 59. M.G. Itkis, V.N. Okolovich, G.N. Smirenkin, Nucl. Phys. A 502, 243c (1989)
- Z. Janas, A. Plochocki, J. Szerypo, R. Collatz, Z. Hu, H. Keller, R. Kirchner, O. Klepper, E. Roeckl, K. Schmidt, R. Bonetti, A. Guglielmetti, G. Poli, A. Piechaczek, Nucl. Phys. A 627, 119 (1997)
- 61. V.A. Karnaukhov, G.M. Ter-Akopyan, L.A. Petrov, V.G. Subbotin, JETF 45, 1280 (1963).
- W.D. Knight, K. Clemenger, W.A. de Heer, W.A. Saunders, M.Y. Chou, M.L. Cohen, Phys. Rev. Lett. 52, 2141 (1984). Errata vol. 53, p. 510

- 63. H.J. Krappe, J.R. Nix, A.J. Sierk, Phys. Rev. C 20, 992 (1979)
- 64. W. Kutschera, I. Ahmad, S.G. Armato III, A.M. Friedman, J.E. Gindler, W. Henning, T. Ishii, M. Paul, K.E. Rehm, Phys. Rev. C 32, 2036 (1985)
- 65. H. Lamb, *Hydrodinamics*. (Cambridge Mathematical Library, New York, 1932)
- 66. T.P. Martin, Phys. Rep. 273, 199 (1996)
- 67. J.A. Maruhn, W. Greiner, Z. Phys. **251**, 431 (1972)
- 68. C. Mazzocchi, Z. Janas, L. Batist, V. Belleguic, J. Doring, M. Gierlik, M. Kapica, R. Kirchner, G.A. Lalazissis, H. Mahmud, E. Roeckl, P. Ring, K. Schmidt, P.J. Woods, J. Zylicz, Phys. Lett. B 532, 29 (2002)
- 69. P. Möller, D.G. Madland, A.J. Sierk, A. Iwamoto, Nature 409, 785 (2001)
- 70. P. Möller, J.R. Nix, W.D. Myers, W.J. Swiatecki, At. Data Nucl. Data Tab. 59 185 (1995)
- 71. L.G. Moretto, Nucl. Phys. A **247**, 211 (1975)
- 72. L.G. Moretto, G.J. Wozniak, Prog. Part. Nucl. Phys. 21, 1 (1988)
- K. Morita, K. Morimoto, D. Kaji, T. Akiyama, S. Goto, H. Haba, E. Ideguchi, R. Kanungo, K. Katori, H. Koura, H. Kudo, T. Ohnishi, A. Ozawa, T. Suda, K. Sueki, H. Xu, T. Yamaguchi, A. Yoneda, A. Yoshida, Y. Zhao, J. Phys. Soc. Jpn. 73, 2593 (2004)
- 74. U. Mosel, W. Greiner, Z. Phys. 222, 261 (1969)
- 75. M. Mutterer, J.P. Theobald, in Nuclear Decay Modes, chap. 12 (IOP, Bristol, 1996), p. 487
- 76. W.D. Myers, W.J. Swiatecki, Nucl. Phys. A 81, 1 (1966)
- 77. S.G. Nilsson, Dan. Mat. Fys. Medd. 29(16), 1 (1955)
- 78. Y.T. Oganessian, Nature **413**, 122 (2001)
- 79. Y.T. Oganessian, J. Phys. G: Nucl. Part. Phys. 34, R165 (2007)
- Y.T. Oganessian, V.K. Utyonkov, Y.V. Lobanov, F.S. Abdullin, A.N. Polyakov, R.N. Sagaidak, I.V. Shirokovsky, Y.S. Tsyganov, A.A. Voinov, A.N. Mezentsev, V.G. Subbotin, A.M. Sukhov, K. Subotic, V.I. Zagrebaev, S.N. Dmitriev, R.A. Henderson, K.J. Moody, J.M. Kenneally, J.H. Landrum, D.A. Shaughnessy, M.A. Stoyer, N.J. Stoyer, P.A. Wilk, Phys. Rev. C 79, 024603 (2009)
- 81. P. Papka, C. Beck, in *Clusters in Nuclei, Lecture Notes in Physics*, ed by C. Beck. (Springer, Berlin, 2010)
- J.G. Partridge, R. Reichel, A. Ayesh, D.M.A.Mackenzie, S.A. Brown, Phys. Stat. Sol. (A) 203(6), 1217 (2006)
- 83. D. Poenaru, W. Greiner (eds.), Handbook of Nuclear Properties (Clarendon, Oxford, 1996)
- 84. D.N. Poenaru (ed.), Nuclear Decay Modes (Institute of Physics Publishing, Bristol, 1996)
- 85. D.N. Poenaru, W. Greiner, et al. J. Phys. G: Nucl. Part. Phys. 26, L97 (2000)
- 86. D.N. Poenaru, R.A. Gherghescu, W. Greiner, Heavy Ion Phys. 18, 409 (2003)
- 87. D.N. Poenaru, R.A. Gherghescu, W. Greiner, Eur. Phys. J. A 24, 355 (2005)
- 88. D.N. Poenaru, R.A. Gherghescu, W. Greiner, Nucl. Phys. A 747, 182 (2005)
- D.N. Poenaru, R.A. Gherghescu, W. Greiner, J. Phys. G: Nucl. Part. Phys. 36, 125101 (2009)
- D.N. Poenaru, R.A. Gherghescu, I.H. Plonski, A.V. Solov'yov, W. Greiner, Eur. Phys. J. D 47 379 (2008)
- D.N. Poenaru, R.A. Gherghescu, A.V.Solov'yov, W. Greiner, Europhys. Lett. 79, 63001 (2007)
- D.N. Poenaru, R.A. Gherghescu, A.V. Solov'yov, W. Greiner, Phys. Lett. A 372, 5448 (2008)
- 93. D.N. Poenaru, R.A. Gherghescu, A.V. Solov'yov, W. Greiner, Europhys. Lett. 88, 23002 (2009)
- 94. D.N. Poenaru, R.A. Gherghescu, W. Greiner, Phys. Rev. C 73, 014608 (2006)
- 95. D.N. Poenaru, W. Greiner, Phys. Scripta 44, 427 (1991)
- 96. D.N. Poenaru, W. Greiner, in Nuclear Decay Modes, chap. 6 (IOP, Bristol, 1996), pp. 275
- 97. D.N. Poenaru, W. Greiner (eds.), *Experimental Techniques in Nuclear Physics* (Walter de Gruyter, Berlin, 1997)
- 98. D.N. Poenaru, W. Greiner, J. Phys. G: Nucl. Part. Phys. 25, L7 (1999)
- 99. D.N. Poenaru, W. Greiner, Europhys. Lett. **64**, 164 (2003)

- 100. D.N. Poenaru, W. Greiner, R.A. Gherghescu, At. Data Nucl. Data Tab. 68, 91 (1998)
- D.N. Poenaru, W. Greiner, J.H. Hamilton, A.V. Ramayya, E. Hourany, R.A. Gherghescu, Phys. Rev. C 59, 3457 (1999)
- D.N. Poenaru, W. Greiner, Y. Nagame, R.A. Gherghescu, J. Nucl. Radiochem. Sci. Jpn. 3, 43 (2002)
- D.N. Poenaru, E. Hourany, W. Greiner, In: Nuclear Decay Modes, chap. 4, p. 204. IOP, Bristol, UK (1996)
- 104. D.N. Poenaru, M. Ivaşcu, W. Greiner, in *Particle Emission from Nuclei*, vol. III, chap. 7 (CRC Press, Boca Raton, 1989), p. 203
- 105. D.N. Poenaru, M. Ivaşcu, D. Mazilu, Comp. Phys. Commun. 19, 205 (1980)
- D.N. Poenaru, J.A. Maruhn, W. Greiner, M. Ivaşcu, D. Mazilu, I. Ivaşcu, Z. Phys. A 333, 291 (1989)
- D.N. Poenaru, Y. Nagame, R.A. Gherghescu, W. Greiner, Phys Rev C 65, 054308 (2002).
 Erratum vol. 66, 049902
- D.N. Poenaru, I.H. Plonski, R.A. Gherghescu, W.J. Greiner, Phys. G: Nucl. Part. Phys. 32, 1223 (2006)
- 109. D.N. Poenaru, I.H. Plonski, W. Greiner, Phys. Rev. C 74, 014312 (2006)
- 110. D.N. Poenaru, D. Schnabel, W. Greiner, D. Mazilu, R. Gherghescu, At. Data Nucl. Data Tab. 48, 231 (1991)
- 111. I.V. Pokrovsky, L. Calabretta, M.G. Itkis, N.A. Kondratiev, E.M. Kozulin, C. Maiolino, E.V. Prokhorova, A.Y. Rusanov, S.P. Tretyakova, Phys. Rev. C 60, 041304 (1999)
- 112. P.B. Price, Ann. Rev. Nucl. Part. Sci. 39, 19 (1989)
- 113. Y. Pyatkov, D.V. Kamanin, W.H. Trzaska, W. von Oertzen, S.R. Yamaletdinov, A.N. Tjukavkin, V. Tishchenko, V.G. Lyapin, Y. Penionzhkevich, A.A. Alexandrov, S.V. Khlebnikov, Rom. Rep. Phys. 59, 569 (2007)
- 114. A.V. Ramayya, J.K. Hwang, J.H. Hamilton, A. Sandulescu, A. Florescu, G.M. Ter-Akopian, A.V. Daniel, Y.T. Oganessian, G.S. Popeko, W. Greiner, J.D. Cole, Phys. Rev. Lett. 81, 947 (1998)
- 115. J.W.S. Rayleigh Lord, Proc. Lond. Math. Soc. **10**, 4 (1879)
- 116. S.M. Reimann, M. Brack, K. Hansen, Z. Phys. D. 28, 235 (1993)
- 117. E. Roeckl, in Nuclear Decay Modes (IOP, Bristol, 1996), p. 237
- 118. H.J. Rose, G.A. Jones, Nature 307, 245 (1984)
- 119. A. Sandulescu, H.J. Lustig, J. Hahn, W. Greiner, J. Phys. G: Nucl. Phys. 4, L279 (1978)
- 120. A. Sandulescu, D.N. Poenaru, W. Greiner, Sov. J. Part. Nucl. 11, 528 (1980)
- 121. W. Scheid, W. Greiner, Z. Phys. A 226, 364 (1969)
- R. Schmidt, R.L. Jaffe, R.M. Dreizler, J. Ehlers, K. Hepp (eds.), *Nuclear Physics Concepts in the Study of Atomic Cluster Physics*, vol. 404. Lecture Notes in Physics (Springer, Berlin, 1992)
- 123. W. Schneider, J.A. Maruhn, W. Greiner, Z. Phys. A 323, 111 (1986)
- 124. K. Seeger, R.E. Palmer, Appl. Phys. Lett. **74**, 1627 (1999)
- 125. C. Signarbieux, M. Montoya, M. Ribrag, C. Mazur, C. Guet, P. Perrin, M. Maurel, J. Phys. Lett. 42, L437 (1981)
- 126. A. Sobiczewski, Sov. J. Part. Nucl. 10, 1170 (1979)
- L.G. Sobotka, M.A. MacMahan, R.J. McDonald, C. Signarbieux, G.J. Wozniak, M.L. Padgett, J.H. Gu, Z.H. Liu, Z.Q. Yao, L.G. Moretto, Phys. Rev. Lett. 53, 2004 (1984)
- 128. V.M. Strutinski, Sov. Phys. JETP **15**, 1091 (1962)
- 129. V.M. Strutinsky, Nucl. Phys. A 95, 420 (1967)
- 130. The New Encyclopaedia Britannica, 15th edn (1995), vol. 15, p. 371. Encyclopaedia Britannica Online, http://www.britannica.com/EBchecked/topic/465998/ (2009)
- 131. K. Thomas, K.T.R. Davies, A.J. Sierk, Phys. Rev. C 31, 915 (1985)
- 132. S.P. Tretyakova, Sov. J. Part. Nucl. 23, 156 (1992)
- I. Tsekhanovich, H.-O. Denschlag, M. Davi, Z. Buyukmumcu, F. Goennenwein, S. Oberstedt, H.R. Faust, Nucl. Phys. A 688, 633 (2001)
- 134. D. Vautherin, Phys. Rev. C 7, 296 (1973)

- 135. C. Wagemans, in *Particle Emission from Nuclei*, vol. III, chap. 3 (CRC Press, Boca Raton 1989), p. 63
- 136. A.H. Wapstra, in Handbook of Nuclear Properties, chap. 1 (Clatrendon, Oxford, 1996), p. 1
- 137. C.F. von Weizsäcker, Z. Phys. **96**, 431 (1935)
- 138. C. Yannouleas, U. Landman, Phys. Rev. B 48, 8376 (1993)
- 139. C. Yannouleas, U. Landman, Phys. Rev. B 51, 1902 (1995)
- 140. C. Yannouleas, U. Landman, Phys. Rev. Lett. 78, 1424 (1997)
- 141. N. Zeldes, in *Handbook of Nuclear Properties*, chap. 2 (Clarendon, Oxford, 1996), p. 12
- 142. V.I. Zagrebaev, W. Greiner, in *Clusters in Nuclei*, chap. 7. Lecture Notes in Physics, ed. by C. Beck (Springer, Berlin, 2010)
- 143. R.K. Gupta, in *Clusters in Nuclei*, chap. 6. Lecture Notes in Physics, ed. by C. Beck (Springer, Berlin, 2010)

Chapter 2 Coexistence of Cluster States and Mean-Field-Type States

Hisashi Horiuchi

2.1 Introduction

The saturation property of binding energy and density of the nucleus means that nucleons are easy to assemble and disassemble. If we regard nuclear clustering as being the physics of dynamical assembling and disassembling of nucleons, clustering is a basic nuclear dynamics and appears abundantly in many problems of nuclear structure and reactions [1, 2]. We can say that the formation of clusters is a fundamental aspect of nuclear many body dynamics together with the formation of mean field.

The omnipresence of cluster dynamics in nuclei has long been reported in various phenomena as has been discussed in many conferences and many review papers [3–8]. One of the most impressive manifestations of the omnipresence of clustering has recently been obtained through the studies of neutron-rich unstable nuclei. We now know that neutron-rich nuclei present us with novel types of cluster structure which are composed of clusters and many valence neutrons. Participation of excess neutrons as basic constituents of cluster structure gives rise to quite different features from the cluster structure in stable nuclei.

The coexistence of two structures, the cluster structure and the mean-field-type structure, which are very different to each other, is a unique feature of nuclear system. The coexistence implies that the nuclear many-body physics contains the physics of the structure change between two very distinct structures. We need to clarify what is the relation between two different structures and how one type of structure changes into the other type of structure.

H. Horiuchi (⊠)

Research Center for Nuclear Physics, Osaka University,

Osaka 567-0047, Japan

e-mail: horiuchi@rcnp.osaka-u.ac.jp

International Institute for Advanced Studies, Kizugawa 619-0225, Japan 58 H. Horiuchi

The purpose of this lecture is to discuss two fundamental problems of nuclear cluster physics: (1) how are the coexistence features of cluster states and mean-field-type states in nuclei?, (2) how does nuclear structure change from shell-model-like ground state to cluster states? Our discussion in this lecture is, however, restricted only to stable nuclei. Namely, we do not discuss the dynamics due to the excess neutrons in this lecture.

In this lecture I first review some of the present understandings of the first problem, which is the main purpose of this lecture. This review is made in two parts. In the first part I discuss the relation of cluster structure and deformed mean-field-type structure in p-shell and light sd-shell nuclei. In the second part I discuss the coexistence of cluster structure and superdeformation in sd-shell and light pf-shell nuclei. Specifically, in the first part I discuss the coexistence features of mean-field-type structure and typical cluster structures in 8 Be, 12 C, 16 O, and 20 Ne. In the second part, I discuss the coexistence features in 44 Ti and 32 S. The investigation in 32 S suggests strong interrelation of 16 O + 16 O molecular states and superdeformed states. For the discussions of 20 Ne, 44 Ti and 32 S systems, I utilize the results of the detailed studies with antisymmetrized molecular dynamics (AMD).

I then discuss the second problem, the mechanism of the structure-change between cluster structure and mean-field-type structure. The discussion is made on the basis of the studies of the above two subjects about the coexistence features. I argue that the structure change and the resulting coexistence come from the dual nature of nuclear wave functions which have both characters of cluster wave function and mean-field-type wave function. This argument is shown to be supported by the analyses of the electric monopole (*E*0) transitions between cluster states and the ground state which are reported recently in the cases of ¹⁶O and ¹²C.

2.2 AMD Theory

Since in this lecture we often use the results of AMD calculations, we give here a brief explanation of the AMD model.

2.2.1 AMD Wave Function

The basic building block of the AMD wave function is a Slater determinant

$$\Phi_{\text{int}} = \frac{1}{\sqrt{A!}} \det{\{\varphi_1, \varphi_2, \cdots, \varphi_A\}}, \tag{2.1}$$

$$\varphi_i(r) = \phi_i(r)\chi_i\xi_i, \quad \phi_i(r) \propto \exp\left\{-\sum_{\sigma=x,y,z} v_\sigma(r_\sigma - Z_{i\sigma})^2\right\},$$
(2.2)

$$\chi_i = \alpha_i \chi_\uparrow + \beta_i \chi_\downarrow, \quad |\alpha_i|^2 + |\beta_i|^2 = 1, \quad \xi_i = \text{proton or neutron.}$$
 (2.3)

The parameter $\{Z_{i\sigma}\}$ is a complex vector whose real part $\operatorname{Re}(Z_{i\sigma})$ gives the spatial position of the Gaussian wave packet $\phi_i(r)$ while imaginary part $\operatorname{Im}(Z_{i\sigma})$ gives the momentum of the packet. The imaginary part of $Z_{i\sigma}$ is important to take into account of the effect of the two-nucleon spin-orbit interaction. The size parameter v_{σ} can take different values for different spatial directions $\sigma=x,\ y,\ z$ but takes common value for all the nucleons usually. The Slater determinant $\Phi_{\rm int}$ remains unchanged for any linear transformation of single nucleon wave functions, $\{\varphi_1,\varphi_2,\cdots,\varphi_A\}\to \{\varphi'_1,\varphi'_2,\cdots,\varphi'_A\}$ with $\varphi'_i=\sum_{j=1}^A T_{ij}\varphi_j;$ namely $\Phi_{\rm int}(\{\varphi_i\})=\det\{T\}\Phi_{\rm int}(\{\varphi'_i\}).$ Therefore, for example, we can replace φ_1 and φ_2 by $(\varphi_1+\varphi_2)$ and $(\varphi_1-\varphi_2)$ by keeping $\Phi_{\rm int}$ unchanged. If two wave packets φ_1 and φ_2 are located at almost the same spatial positions $\operatorname{Re}(Z_{1\sigma})\approx\operatorname{Re}(Z_{2\sigma})$ with zero momenta $\operatorname{Im}(Z_{1\sigma})=\operatorname{Im}(Z_{2\sigma})=0,\ (\varphi_1+\varphi_2)$ and $(\varphi_1-\varphi_2)$ are almost equal to the 0s and 0p wave functions, respectively, around the spatial position $\operatorname{Re}(Z_{1\sigma})\approx\operatorname{Re}(Z_{2\sigma}).$ From this argument, we know that the AMD Slater determinant can be almost equal to various kinds of shell model wave functions.

The wave function Φ_{int} is always projected to a good-parity wave function Φ^{\pm} ,

$$\Phi^{\pm} = (1 \pm P)\Phi_{\text{int}}.\tag{2.4}$$

The parameters of Φ^{\pm} , v_{σ} , $Z_{i\sigma}$, α_i , and β_i , are determined by energy variation under the constraint of the given value of the quadrupole deformation parameter β_0 , and such wave function Φ^{\pm} is denoted as $\Phi^{\pm}(\beta_0)$. From $\Phi^{\pm}(\beta_0)$, we project out goodspin wave functions which are denoted as $\Phi^{J\pm}_{MK}$,

$$\Phi_{MK}^{J\pm}(\beta_0) = P_{MK}^J \Phi^{\pm}(\beta_0)
= \int_0^{2\pi} d\alpha \int_0^{\pi} d\beta \sin\beta \int_0^{2\pi} d\gamma (D_{MK}^J(\alpha, \beta, \gamma))^*
\times \exp(-i\alpha J_z) \exp(-i\beta J_y) \exp(-i\gamma J_z) \Phi^{\pm}(\beta_0),$$
(2.5)

where $D_{MK}^{J}(\alpha, \beta, \gamma)$ is Wigner's D function given as

$$D_{MK}^{I}(\alpha, \beta, \gamma) = \langle JM | \exp(-i\alpha J_z) \exp(-i\beta J_y) \exp(-i\gamma J_z) | JK \rangle. \tag{2.6}$$

The AMD wave function $\Phi_n^{J\pm}$ is obtained by superposing $\Phi_{MK}^{J\pm}(\beta_0)$ with various values of β_0 ,

$$\Phi_n^{J\pm} = c_n \Phi_{MK}^{J\pm}(\beta_0) + c_n' \Phi_{MK}^{J\pm}(\beta_0') + \cdots.$$
 (2.7)

The superposition coefficients, c_n, c'_n , and so on, are determined by energy variation.

60 H. Horiuchi

2.2.2 Hartree–Fock-Type Orbits

From the intrinsic wave function of AMD $\Phi_{\rm int}$, we can extract the single nucleon orbits of Hartree–Fock type by which we can study mean-field character of the AMD wave function [9, 10]. First we orthonormalize the single nucleon wave packets φ_i ,

$$\hat{\varphi}_{\alpha} = \frac{1}{\sqrt{\mu_{\alpha}}} \sum_{j=1}^{A} d_{j\alpha} \varphi_{j}, \quad \sum_{j=1}^{A} \langle \varphi_{i} | \varphi_{j} \rangle d_{j\alpha} = \mu_{\alpha} d_{i\alpha}. \tag{2.8}$$

Next we construct the Hartree–Fock single nucleon Hamiltonian h by this orthonormalized basis, which takes the following form when the inter-nucleon interaction consists of only two-body force \hat{v}

$$h_{\alpha\beta} = \langle \hat{\varphi}_{\alpha} | \hat{t} | \hat{\varphi}_{\beta} \rangle + \sum_{\gamma} \langle \hat{\varphi}_{\alpha} \hat{\varphi}_{\gamma} | \hat{v} | \hat{\varphi}_{\beta} \hat{\varphi}_{\gamma} - \hat{\varphi}_{\gamma} \hat{\varphi}_{\beta} \rangle. \tag{2.9}$$

The single nucleon orbit ψ_p and its single nucleon energy e_p of Hartree–Fock type are obtained by diagonalizing $h_{\alpha\beta}$ as

$$\psi_p = \sum_{\alpha} g_{\alpha p} \hat{\varphi}_{\alpha}, \quad \sum_{\beta} h_{\alpha \beta} g_{\beta p} = e_p g_{\alpha p}.$$
 (2.10)

Since the Hartree–Fock type orbits $\{\psi_1, \psi_2, \dots, \psi_A\}$ are obtained by linear transformation of $\{\varphi_1, \varphi_2, \dots, \varphi_A\}$, we have

$$\frac{1}{\sqrt{A!}}\det\{\boldsymbol{\psi}_1,\boldsymbol{\psi}_2,\cdots,\boldsymbol{\psi}_A\} \propto \frac{1}{\sqrt{A!}}\det\{\boldsymbol{\varphi}_1,\boldsymbol{\varphi}_2,\cdots,\boldsymbol{\varphi}_A\} = \boldsymbol{\Phi}_{\text{int}}.$$
 (2.11)

2.3 Coexistence of Cluster Structure and Deformed Mean-Field-Type Structure in *p*-Shell and Light *sd*-Shell Nuclei

Coexistence features of cluster states and mean-field-type states have been studied in many nuclei. In this lecture I review representative examples of such studies in two parts. In this section I discuss the first part which is for the relation of cluster structure and deformed mean-field-type structure in p-shell and light sd-shell nuclei specifically in ${}^8\text{Be}$, ${}^{12}\text{C}$, ${}^{16}\text{O}$, and ${}^{20}\text{Ne}$. In the next section I will discuss the second part which is for the coexistence of cluster structure and superdeformation in sd-shell and light pf-shell nuclei, specifically in ${}^{44}\text{Ti}$ and ${}^{32}\text{S}$. In the cases of discussions of ${}^{20}\text{Ne}$, ${}^{44}\text{Ti}$, and ${}^{32}\text{S}$, I utilize the results of the detailed AMD calculations of the coexistence features.

2.3.1 ⁸Be Case

2.3.1.1 Brink Wave Function and its Telation to Shell-Model Wave Function

The $\alpha + \alpha$ structure of ⁸Be has long been investigated by many authors as the most fundamental two-cluster structure. The intrinsic wave function of the Brimk model [11] for ⁸Be with $\alpha + \alpha$ structure is given as

$$\Psi(d) = n_0(d) \mathcal{A} \left\{ \psi \left(\alpha_1, \frac{d}{2} e_z \right) \psi \left(\alpha_2, -\frac{d}{2} e_z \right) \right\}$$

$$= \frac{n_0(d)}{\sqrt{4!4!}} \det \left\{ g \left(r_1 - \frac{d}{2} e_z, v \right) \chi_{\uparrow} \xi_p \times \dots \times g \left(r_4 - \frac{d}{2} e_z, v \right) \chi_{\downarrow} \xi_n \right. \quad (2.12)$$

$$\times g \left(r_5 + \frac{d}{2} e_z, v \right) \chi_{\uparrow} \xi_p \times \dots \times g \left(r_8 + \frac{d}{2} e_z, v \right) \chi_{\downarrow} \xi_n \right\},$$

$$\psi(\alpha_k, a) = \frac{1}{\sqrt{4!}} \det \left\{ (g(r - a, v))^4 \right\} \quad (r = r_{k_0 + 1} \sim r_{k_0 + 4})$$

$$= \frac{1}{\sqrt{4!}} \det \left\{ g(r_{k_0 + 1} - a, v) \chi_{\uparrow} \xi_p \times \dots \times g(r_{k_0 + 4} - a, v) \chi_{\downarrow} \xi_n \right\},$$

$$\{k_0 = 4(k - 1)\}$$

$$g(r,\gamma) = \left(\frac{2\gamma}{\pi}\right)^{3/4} \exp(-\gamma r^2), \tag{2.14}$$

where \mathscr{A} is the antisymmetrizing operator of nucleons belonging to different α clusters, $n_0(d)$ is the normalization constant and e_z is a unit vector along the z-direction. $n_0(d)$ is calculated by the relation

$$1 = \langle \Psi(d) | \Psi(d) \rangle$$

$$= \left(\frac{n_0(d)}{\sqrt{4!4!}}\right)^2 8! \left(1 - \langle g(r - \frac{d}{2}e_z, v) | g(r + \frac{d}{2}e_z, v) \rangle^2\right)^4, \tag{2.15}$$

which gives us

$$n_0(d) = \sqrt{\frac{4!4!}{8!}} \frac{1}{v^2 d^4 + O(d^6)}.$$
 (2.16)

In the limit of zero inter- α distance d, $\Psi(d)$ becomes equivalent to the intrinsic wave function of the SU(3) shell model with $(\lambda, \mu) = (4, 0)$;

$$\lim_{d \to 0} \Psi(d) = \frac{1}{\sqrt{8!}} \det\{(0, 0, 0)^4 (0, 0, 1)^4\},\tag{2.17}$$

where (n_x, n_y, n_z) stands for the single particle wave function of the harmonic oscillator model

$$(n_x, n_y, n_z) = \boldsymbol{\varphi}_{n_x}(x, v) \boldsymbol{\varphi}_{n_y}(y, v) \boldsymbol{\varphi}_{n_z}(z, v), \qquad (2.18)$$

$$\varphi_n(x, v)$$
 = one dimensinal harmonic oscillator function with
 n quanta and size parameter $\mathbf{v} = \mathbf{m}\omega/2\hbar$. (2.19)

The relation of Eq. (2.17) can be proved by using the expansion of $g(r + (d/2)e_z, v)$ around $g(r - (d/2)e_z, v)$. We introduce the notation $(n_x, n_y, n_z)'$ and $(n_x, n_y, n_z)''$ to express the Cartesian harmonic oscillator function (n_x, n_y, n_z) around the spatial position $(d/2)e_z$ and $-(d/2)e_z$, respectively. Then we have $g(r + (d/2)e_z, v) = (0, 0, 0)''$ and $g(r - (d/2)e_z, v) = (0, 0, 0)'$. We can easily prove the relation

$$(0,0,0)'' = \exp\left(-\frac{1}{2}vd^2\right)\left\{(0,0,0)' - \sqrt{v}d(0,0,1)' + O(d^2)\right\},\tag{2.20}$$

where $O(d^2)$ expresses the terms of d^2 and higher order terms of d than d^2 . The insertion of this relation together with Eq. (2.16) into $\Psi(d)$ gives us the proof of Eq. (2.17).

2.3.1.2 Bayman-Bohr Theorem

A useful way to relate the Brink wave function $\Psi(d)$ to the shell-model wave function is given by expressing $\Psi(d)$ in terms of internal α -cluster wave function $\phi(\alpha)$ and inter-cluster relative wave function $\Gamma(r_{\alpha\alpha},d)$,

$$\Psi(d) = n_0(d) \mathcal{A} \left\{ \psi(\alpha_1, \frac{d}{2} e_z) \psi\left(\alpha_2, -\frac{d}{2} e_z\right) \right\}
= n_0(d) \mathcal{A} \left\{ \Gamma(r_{\alpha\alpha}, d) \phi(\alpha_1) \phi(\alpha_2) \right\} g(X_G, 8v),$$
(2.21)

$$\Gamma(r_{\alpha\alpha}, d) = g(r_{\alpha\alpha} - de_z, 2v) = \left(\frac{4v}{\pi}\right)^{3/4} \exp(-2v(r_{\alpha\alpha} - de_z)^2), \tag{2.22}$$

$$g(X_G, 8\nu) = \left(\frac{16\nu}{\pi}\right)^{3/4} \exp(-8\nu(X_G)^2), \tag{2.23}$$

$$r_{\alpha\alpha} = X_1 - X_2, \quad X_G = \frac{1}{2}(X_1 + X_2) = \frac{1}{8} \sum_{i=1}^{8} r_i,$$
 (2.24)

$$X_1 = \frac{1}{4} \sum_{i=1}^{4} r_i, \quad X_2 = \frac{1}{4} \sum_{i=5}^{8} r_i.$$
 (2.25)

Here we used the relation

$$\psi(\alpha_k, a) = \left(\frac{8\nu}{\pi}\right)^{3/4} \exp(-4\nu(X_k - a)^2)\phi(\alpha_k). \tag{2.26}$$

The actual form of the inter- α relative wave function $\Gamma(r_{\alpha\alpha},d)$ deviates from the Gaussian wave packet due of the effect of the antisymmetrization. The effect of the antisymmetrization is well reflected in the following relation,

$$\mathscr{A}\left\{X_{(n_x,n_y,n_z)}(r_{\alpha\alpha},2\nu)\phi(\alpha_1)\phi(\alpha_2)\right\} = 0, \quad \text{for} \quad n_x + n_y + n_z < 4, \tag{2.27}$$

where $X_{(n_x,n_y,n_z)}(r,\gamma)$ stands for the Cartesian harmonic oscillator function defined as $X_{(n_x,n_y,n_z)}(r,\gamma) = \varphi_{n_x}(x,\gamma)\varphi_{n_y}(y,\gamma)\varphi_{n_z}(z,\gamma)$. It is to be noted that, for $\gamma = \nu$, $X_{(n_v,n_v,n_z)}(r,\gamma)$ is equal to (n_x, n_y, n_z) defined before. Eq. (2.27) is easy to understand. We first notice the following relation

$$N_{\text{op}} \mathscr{A} \Big\{ X_{(n_{x},n_{y},n_{z})}(r_{\alpha\alpha},2\nu)\phi(\alpha_{1})\phi(\alpha_{2}) \Big\} X_{(0,0,0)}(X_{G},8\nu)$$

$$= (n_{x}+n_{y}+n_{z}) \mathscr{A} \Big\{ X_{(n_{x},n_{y},n_{z})}(r_{\alpha\alpha},2\nu)\phi(\alpha_{1})\phi(\alpha_{2}) \Big\} X_{(0,0,0)}(X_{G},8\nu),$$
(2.28)

where $X_{(0,0,0)}(X_G, 8\nu) = (16\nu/\pi)^{3/4} \exp(-8\nu(X_G)^2) = g(X_G, 8\nu)$ and N_{op} stands for the total number operator of harmonic oscillator quanta. Eq. (2.28) is verified to hold by noting the following relation

$$(N_{\rm op})_{\sigma} = \sum_{i=1}^{8} (N_{\rm op}(i))_{\sigma} = (N_{\rm op}(\alpha_1))_{\sigma} + (N_{\rm op}(\alpha_2))_{\sigma} + (N_{\rm op}(r_{\alpha\alpha}))_{\sigma} + (N_{\rm op}(X_G))_{\sigma},$$
(2.29)

$$(N_{\rm op}(\alpha_1))_{\sigma} = \sum_{i=1}^{4} (N_{\rm op}(i))_{\sigma} - (N_{\rm op}(X_1))_{\sigma}, \quad = \sum_{i=5}^{8} (N_{\rm op}(i))_{\sigma} - (N_{\rm op}(X_2))_{\sigma},$$
(2.30)

$$(N_{\rm op}(X_1))_{\sigma} + (N_{\rm op}(X_2))_{\sigma} = (N_{\rm op}(r_{\alpha\alpha}))_{\sigma} + (N_{\rm op}(X_G))_{\sigma}$$
(2.31)

$$(N_{\rm op}(i))_{\sigma} \! = \! N((r_i)_{\sigma}, m), \ (N_{\rm op}(r_{\alpha\alpha}))_{\sigma} \! = \! N(r_{\alpha\alpha})_{\sigma}, 2m), \ (N_{\rm op}(X_G))_{\sigma} \! = \! N(X_G)_{\sigma}, 8m),$$

$$(N_{\text{op}}(X_k))_{\sigma} = N((X_k)_{\sigma}, 4m) \ X_1 = \frac{1}{4} \sum_{i=1}^{4} r_i, \ X_2 = \frac{1}{4} \sum_{i=5}^{6} r_i,$$

$$(2.32)$$

$$N(r,\mu) = \frac{1}{\hbar\omega} \left(\frac{-\hbar^2}{2\mu} \left(\frac{\partial}{\partial r} \right)^2 + \frac{\mu\omega^2}{2} r^2 \right) - \frac{3}{2},\tag{2.33}$$

$$\begin{split} N_{\rm op} &= \sum_{\sigma = x, y, z} (N_{\rm op})_{\sigma}, \ N_{\rm op}(i) = \sum_{\sigma = x, y, z} (N_{\rm op}(i))_{\sigma}, \ N_{\rm op}(r_{\alpha\alpha}) = \sum_{\sigma = x, y, z} (N_{\rm op}(r_{\alpha\alpha}))_{\sigma}, \\ N_{\rm op}(X_G) &= \sum_{\sigma = x, y, z} (N_{\rm op}(X_G))_{\sigma}, \ N_{\rm op}(\alpha_k) = \sum_{\sigma = x, y, z} (N_{\rm op}(\alpha_k))_{\sigma}. \end{split}$$

$$(2.34)$$

Since $N_{\rm op}(\alpha)\phi(\alpha)=N_{\rm op}(X_G)X_{(0,0,0)}(X_G,8\nu)=0$, there holds Eq. (2.28). Now, the shell model teaches us that the lowest number of the total oscillator quanta of ⁸Be is 4, which is given by $\det\{(0s)^4(0p)^4\}$. Therefore we have

$$\mathscr{A}\left\{X_{(n_x,n_y,n_z)}(r_{\alpha\alpha},2\nu)\phi(\alpha_1)\phi(\alpha_2)\right\}g(X_G,8\nu) = 0, \quad \text{for} \quad n_x + n_y + n_z < 4, \ (2.35)$$

from which there follows Eq. (2.27).

By using the expansion of $\Gamma(r_{\alpha\alpha}, d)$ with the harmonic oscillator basis functions, $\Gamma(r_{\alpha\alpha}, d) = \exp(-vd^2) \sum_{n=0}^{\infty} \{(\sqrt{2v}d)^n/\sqrt{n!}\} X_{(0,0,n)}(r_{\alpha\alpha}, 2v)$, we obtain

$$\begin{split} \Psi(d) &= n_0(d) \mathcal{A} \{ \Gamma(r_{\alpha\alpha}, d) \phi(\alpha_1) \phi(\alpha_2) \} g(X_G, 8\nu) \\ &= n_0(d) \exp(-\nu d^2) \left\{ \frac{(\sqrt{2\nu} d)^4}{\sqrt{4!}} \mathcal{A} \{ X_{(0,0,4)}(r_{\alpha\alpha}, 2\nu) \phi(\alpha_1) \phi(\alpha_2) \} + O(d^6) \right\} \\ &\times g(X_G, 8\nu), \end{split}$$
(2.36)

where we used Eq. (2.27). From this relation we obtain

$$\lim_{d \to 0} \Psi(d) = C_0 \mathscr{A} \{ X_{(0,0,4)}(r_{\alpha\alpha}, 2\nu) \phi(\alpha_1) \phi(\alpha_2) \} g(X_G, 8\nu), \tag{2.37}$$

where $C_0 = 4\sqrt{4!/8!} = 1/\sqrt{7!!}$. By combining this with Eq. (2.17) we obtain

$$\frac{1}{\sqrt{8!}} \det\{(0,0,0)^4(0,0,1)^4\}
= C_0 \mathscr{A}\{X_{(0,0,4)}(r_{\alpha\alpha},2\nu)\phi(\alpha_1)\phi(\alpha_2)\}g(X_G,8\nu).$$
(2.38)

This relation is known as an example of the relations of Bayman–Bohr theorem [12] which says that the SU(3) shell model wave function of the ground state is in most cases equivalent to the cluster model wave function. Eq. (3.38) can be proved more directly by noticing that both the left-side and right-side wave functions are the eigenstates of $(N_{\rm op})_x$, $(N_{\rm op})_y$, and $(N_{\rm op})_z$ with eigenvalues 0, 0, 4, respectively. Since it is evident that there is only one wave function of ⁸Be which is an eigenstate of $(N_{\rm op})_x$, $(N_{\rm op})_y$, and $(N_{\rm op})_z$ with eigenvalues 0, 0, 4, respectively. the right-side cluster wave function of Eq. (3.38) is necessarily equal to the left-side wave function. By applying the angular momentum projection to Eq. (3.38), we get the Bayman–Bohr theorem written in the form of good angular momentum states,

$$|(0s)^{4}(0p)^{4}, (\lambda, \mu) = (4, 0)LM\rangle = C_{0} \mathcal{A} \{R_{N=4,L}(r_{\alpha\alpha}, 2\nu)Y_{LM}(\hat{r}_{\alpha\alpha})\phi(\alpha_{1})\phi(\alpha_{2})\}g(X_{G}, 8\nu),$$
(2.39)

where $R_{N,L}(r, \gamma)$ stands for the radial harmonic oscillator function with the size parameter γ and with the number of oscillator quanta N namely with the number of nodes n = (N - L)/2.

2.3.1.3 α - α Interaction and Spatial Localization of α Cluster

If the SU(3) shell model description is good for 8 Be, it means that the inter- α relative wave function in the intrinsic 8 Be wave function is well descrived by the harmonic oscillator function $X_{(0,0,4)}(r_{\alpha\alpha}, 2\nu)$. If the inter- α interaction is strongly attractive, the inter- α relative wave function should express the most compact state allowable by the Pauli principle and hence it is given by $X_{(0,0,4)}(r_{\alpha\alpha}, 2\nu)$. Therefore whether the SU(3) shell model description is good or not for 8 Be can be studied by the investigation of the inter- α interaction. The microscopic study of the α - α interaction has a long history [3–5, 13–17]. The essential feature of the α - α interaction is described by the theory of the orthogonality condition model (OCM) which is an approximation of the RGM (resonating group method) approach. The RGM gives us the α - α relative wave function $\chi(r_{\alpha\alpha})$ as the solution of the integrodifferential equation

$$\langle \phi(\alpha_1)\phi(\alpha_2)|(H-E)|\mathscr{A}\{\chi(r_{\alpha\alpha})\phi(\alpha_1)\phi(\alpha_2)\}\rangle = 0, \tag{2.40}$$

$$H = \sum_{q=1}^{8} T_q - T_G + \sum_{q < q'}^{8} V_{q,q'}^{(2)}, \tag{2.41}$$

where T_G is the kinetic energy of the total center of mass. The OCM equation of motion which is aimed at describing essential feature of the RGM equation of motion is written as

$$\Lambda \left(\frac{-\hbar^2}{2(2m)} \left(\frac{\partial}{\partial r_{\alpha\alpha}} \right)^2 + V_{\alpha\alpha}(r_{\alpha\alpha}) - (E - 2E_{\alpha}) \right) \Lambda \hat{\chi}(r_{\alpha\alpha}) = 0, \qquad (2.42)$$

where E_{α} stands for the binding energy of α particle and Λ is the projection operator given as

$$\Lambda = 1 - \sum_{n_x + n_y + n_z < 4} |X_{(n_x, n_y, n_z)}(r_{\alpha\alpha}, 2\nu)\rangle\langle X_{(n_x, n_y, n_z)}(r_{\alpha\alpha}, 2\nu)|$$

$$= 1 - \sum_{N < 4, L,M} |R_{N,L}(r_{\alpha\alpha}, 2\nu)Y_{LM}(\hat{r}_{\alpha\alpha})\rangle\langle R_{N,L}(r_{\alpha\alpha}, 2\nu)Y_{LM}(\hat{r}_{\alpha\alpha})|.$$
(2.43)

The wave functions $X_{(n_x,n_y,n_z)}(r_{\alpha\alpha},2\nu)$ with $n_x+n_y+n_z<4$ and $R_{N,L}(r_{\alpha\alpha},2\nu)$ $Y_{LM}(\hat{r}_{\alpha\alpha})$ with N<4 are called the Pauli-forbidden states because they satisfy the relation of Eq. (2.27) and

$$\mathscr{A}\left\{R_{N,L}(r_{\alpha\alpha}, 2\nu)Y_{LM}(\hat{r}_{\alpha\alpha})\phi(\alpha_1)\phi(\alpha_2)\right\} = 0, \quad \text{for} \quad N < 4, \tag{2.44}$$

respectively. The operator Λ projects the relative wave function onto the functional space orthogonal to the Pauli-forbidden states. The local potential $V_{\alpha\alpha}(r_{\alpha\alpha})$ is close to the double folding potential and hence it is deep. Because of Eqs. (2.27) and (2.44), Λ satisfies the relation, $\mathscr{A}\{[\Lambda\chi(r_{\alpha\alpha})]\phi(\alpha_1)\phi(\alpha_2)\}=\mathscr{A}\{\chi(r_{\alpha\alpha})\phi(\alpha_1)\phi(\alpha_2)\}$. The wave function $\hat{\chi}(r_{\alpha\alpha})$ is related to $\chi(r_{\alpha\alpha})$ as

$$\hat{\chi}(r_{\alpha\alpha}) = \sqrt{N_K} \, \chi(r_{\alpha\alpha}), \tag{2.45}$$

where N_K is defined by

$$\langle \phi(\alpha_1)\phi(\alpha_2)|\mathscr{A}\{\chi(r_{\alpha\alpha})\phi(\alpha_1)\phi(\alpha_2)\}\rangle = N_K \chi(r_{\alpha\alpha}). \tag{2.46}$$

 N_K and Λ satisfy the relations, $\Lambda N_K = N_K \Lambda = N_K \Lambda \sqrt{N_K} = \sqrt{N_K} \Lambda = \sqrt{N_K}$. In the $\alpha-\alpha$ system, $\sqrt{N_K}$ is close to Λ and hence $\hat{\chi}(r_{\alpha\alpha})$ is close to $\chi(r_{\alpha\alpha})$. The OCM equation of Eq. (2.42) implies that the essential effect of the Pauli principle is expressed by the orthogonalization of the relative wave function to the Pauli-forbidden states. Namely, OCM equation says that the relative wave function is obtained by the deep potential $V_{\alpha\alpha}(r_{\alpha\alpha})$ similar to the double folding potential under the condition of the orthogonality to the Pauli-forbidden states. It was shown that the OCM equation reproduces well the $\alpha-\alpha$ relative wave function $\chi(r_{\alpha\alpha})$ and the $\alpha-\alpha$ scattering phase-shifts given by the RGM equation [13, 14].

The calculated relative wave function $\chi(r_{\alpha\alpha})$ has characteristic features [13–16]. The radial part of $\gamma(r_{\alpha\alpha})$ for low energy has (4-L)/2 nodes in the interaction region which are almost energy-independent and its amplitude is fairly small compared with the amplitude in the outer region. The outermost node is at about 2 fm for both L=0 and 2. The existence of nodal points is due to the orthogonality of the relative wave function to the Pauli-forbiden states. The oscillatory behavior of the radial relative wave function in the inner region causes the large amount of the kinetic energy of the relative motion. The small amplitude of the radial relative wave function in the inner region is caused in order to make the contribution of the kinetic energy from the inner region small as much as possible. If the amplitude of the radial relative wave function in the inner region is large, it can gain energy from the deep attractive potential $V_{\alpha\alpha}(r_{\alpha\alpha})$. Therefore the small amplitude of the radial relative wave function in the inner region means that that the repulsive effect due to the orthogonality to the Pauli-forbiden states is larger than the attractive effect of the potential $V_{\alpha\alpha}(r_{\alpha\alpha})$. The small amplitude of the radial relative wave function in the inner region is always obtained so far as the good reproduction of the α - α scattering phase-shifts is to be guaranteed and this feature remains the same in the ground band resonance states of ⁸Be. Since the function $R_{N=4,L}(r_{\alpha\alpha}, 2\nu)$ which the SU(3) shell model assigns as the radial α - α relative wave function has even larger amplitude in the inner region than in the outer region, we observe that the SU(3) description of the ⁸Be ground band states is not compatible with the α - α scattering data.

2.3.1.4 α-Gas Like Nature of ⁸Be

Recently the 2α structure of ${}^8\text{Be}$ which is the most fundamental two-cluster structure was cast new light [18]. The 0^+ wave function Φ_{0^+} obtained by the GCM (generator coordinate method) calculation, $\Phi_{0^+} = \sum_j f_j P_{J=0} \mathscr{A} \{ \Gamma(r_{\alpha\alpha}, d_j) \phi(\alpha_1) \phi(\alpha_2) \}$, was shown to be almost 100% equivalent to a single 2α wave function $\Phi^{2\alpha \text{THSR}}(\gamma_0)$ which is called 2α THSR wave function [37] and is defined as

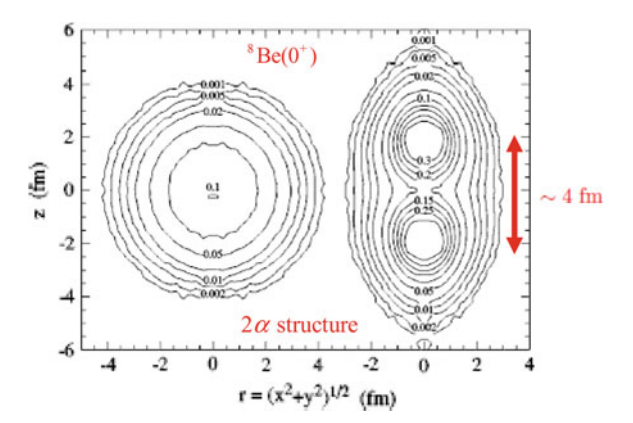
$$\Phi^{2\alpha \text{THSR}}(\gamma_0) = \mathscr{A}\left\{\exp\left(-2\gamma_0\sum_{k=1}^2(X_k - X_G)^2\right)\phi(\alpha_1)\phi(\alpha_2)\right\}. \tag{2.47}$$

Here $P_{J=0}$ is projection operator of angular momentum onto J=0 and the size parameter γ_0 is much smaller than ν . Since the width parameters γ_0 is much smaller than ν , α clusters in the THSR wave function are distributed widely in space. By noting that the orthogonality of the α - α relative wave function to Pauli-forbidden states removes the spatially compact components from the relative wave function, we know that the THSR wave function has a very small staying probability of two α clusters in short relative distance region. Small staying probability in the inner region and long tail probability in the outer region of two α clusters is nothing but what the 2α RGM (or OCM) relative wave function $\gamma(r_{\alpha\alpha})$ describes.

2.3.1.5 Ab Initio Calculation of ⁸Be

A remarkably important progress in theoretical study of ${}^8\text{Be}$ structure was recently achieved by Wiringa et al [19]. They showed that the wave function of ${}^8\text{Be}$ obtained by their ab initio method with realistic nuclear force has a clear $\alpha + \alpha$ structure with inter- α separation around 4 fm as shown in Fig. 2.1. According to Ref. [19], the net energy contribution from the tensor force to the ${}^8\text{Be}$ binding energy is nearly twice that to ${}^4\text{He}$ binding energy. This result is very plausible for the $\alpha + \alpha$ structure where each α cluster wave function is almost the same as the

Fig. 2.1 Density distribution of ⁸Be obtained by ab initio calculation (variational Monte Carlo method) [19]



free ⁴He wave function with large D-state mixture. It is important to check whether mean-field type wave function can reproduce or not such energy contribution from the tensor force.

2.3.2 ¹²C Case

2.3.2.1 From Linear-Chain Structure to Gas-Like Structure of 3α for the Hoyle State

The second 0^+ state of 12 C is located near the 3α breakup threshold. It is called the Hoyle state [20, 21] in honor of astrophysicist Fred Hoyle who predicted the existence of this state which plays an astrophysically crucial role for the synthesis of 12 C in the universe. From the viewpoint of nuclear structure, this state is well known as one of the mysterious 0^+ states in light nuclei. The understanding of its structure has been actually one of the most difficult and challenging problems of nuclear structure. Its small excitation energy of 7.66 MeV has been regarded to be difficult to explain by the shell model. The no-core shell model which is the most advanced modern shell model approach at present has so far not succeeded to reproduce it [22, 23].

More than 40 years ago Morinaga proposed the assignment of 3α linear-chain structure to this Hoyle state [24, 25]. The 3α linear-chain structure is intimately related to the deformed mean-field structure with 4 particle jump from 0p shell to 1s0d shell;

$$\lim_{d\to 0} m_0(d) \mathcal{A}\{\psi(\alpha_1, de_z)\psi(\alpha_2, 0)\psi(\alpha_3, -de_z)\}
= \frac{1}{\sqrt{12!}} \det\{(0, 0, 0)^4(0, 0, 1)^4(0, 0, 2)^4\},$$
(2.48)

where $m_0(d)$ is the normalization constant. However the observed reduced α decay width of the Hoyle state is larger than the Wigner limit value and therefore it is contradictory to the linear-chain structure which gives small reduced width. The linear chain structure necessarily contains high partial waves between ⁸Be and α clusters in spite of the fact that only the S wave contributes to the α decay because of the small Q value. The 3α linear-chain structure can thus give at most only one third of the Wigner limit value [26]. The reduced α decay width $\theta^2(a)$ deduced from the width $\Gamma_{\rm exp}=8.7$ eV of the Hoyle state is given in Table 2.1. The definition of $\theta^2(a)$ is as follows,

Table 2.1 Experimental value of $\theta^2(a)$ of the Hoyle state

	I	. ()	- 7		
a	4.4	4.8	5.2	5.6	6.0
$\theta^2(a)$	2.7	2.2	1.6	1.2	0.9

Channel radius a is in unit of fm

 $R_{\alpha\alpha}$ 4.0 1.0 2.0 3.0 $\theta^2(a)$ 0.29 0.32 0.35 0.37

Table 2.2 Calculated value of $\theta^2(a)$ when 3α linear-chain structure is assumed for the Hoyle

 $R_{\alpha\alpha}$ is the inter- α distance of the chain state, and is in unit of fm

$$\Gamma = 2P_{\ell=0}\theta^{2}(a)\gamma_{W}^{2}(a), \quad P_{\ell} = \frac{ka}{G_{\ell}^{2}(a) + F_{\ell}^{2}(a)}, \quad \gamma_{W}^{2}(a) = \frac{3\hbar^{2}}{2\mu a^{2}}, \tag{2.49}$$

where a is channel radius, μ reduced mass, and F_{ℓ} and G_{ℓ} are regular and irregular Coulomb functions. In terms of reduced width amplitude y(r), we can express $\theta^2(a)$ as $\theta^2(a) = (1/3)a^3v^2(a)$. Note that, in the case of v(r) = constant(a > r > 0), $\theta^2(a) = 1$. In Table 2.2 we show the calculated value of $\theta^2(a)$ when 3α linear-chain structure is assumed for the Hoyle state, which is taken from Ref. [26].

The observed large α -decay reduced width of the Hoyle state in the ${}^{8}\text{Be}(0_{1}^{+}) + \alpha$ channel was successfully reproduced by a full three-body OCM calculation [27, 28]. The wave function $\hat{\chi}(\hat{\xi}_1,\hat{\xi}_2)$ of the 3α OCM which should be totally symmetric with respect to the particle permutation is obtained by solving the following equation of motion

$$\left[-\frac{\hbar^2}{2M_{\alpha}} \sum_{i=1}^{3} \left(\frac{\partial}{\partial x_i} \right)^2 - \hat{T}_G + \sum_{i>j}^{3} V_{2\alpha}(|x_i - x_j|) - E \right] \hat{\chi}(\hat{\xi}_1, \hat{\xi}_2) = 0, \tag{2.50}$$

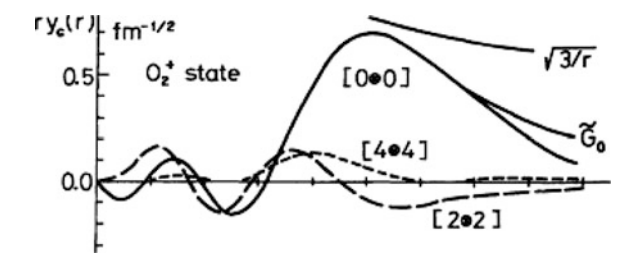
$$\hat{\xi}_1 = x_1 - \frac{1}{2}(x_2 + x_3), \hat{\xi}_2 = x_2 - x_3,$$
 (2.51)

$$\langle \chi^F(x_i - x_i) | \hat{\chi}(\hat{\xi}_1, \hat{\xi}_2) \rangle = 0, (1 \le j < i \le 3).$$
 (2.52)

The coordinate x_i is the position vector of the *i*th α cluster. \hat{T}_G is the kinetic energy of the total center of mass. The 2α wave functions γ^F stand for the Pauli forbidden states of the 2α relative motion which we explained in the previous subsection. Namely, χ^F satisfy $\mathscr{A}[\chi^F(X_i - X_i)\phi(\alpha_i)\phi(\alpha_i)] = 0$, with $X_i = (1/4)$ $\sum_{k=I(i)+1}^{I(i)+4} r_k, I(i) = 4(i-1)$, where r_k stands for kth nucleon coordinate. The numbers of Pauli-forbidden states are two and one for S and D waves, respectively. The structure of the Hoyle state obtained by this 3α OCM calculation has, as the dominant component of the Hoyle state, the ${}^{8}\text{Be}(0_{1}^{+}) + \alpha$ structure with relative S wave between two clusters, ${}^{8}\text{Be}(0_{1}^{+})$ and α . Since ${}^{8}\text{Be}(0_{1}^{+})$ consists of two α clusters weakly coupled in relative S wave, the Hoyle state was concluded to have a weakly coupled 3α structure in relative S waves with large spatial extent. Namely it was regarded as being a gas-like structure of α clusters.

A few years later, this understanding of the structure of the Hoyle state was reported to be confirmed by fully microscopic 3α calculations by two groups, namely the 3α RGM calculations by Kamimura et al. [29, 30] and the 3α GCM calculations by Uegaki et al. [31–33]. The wave functions of the 3α RGM

Fig. 2.2 Reduced width amplitudes of $[L \otimes L]$ channels ($^8\text{Be}(L) + \alpha(\ell = L)$ channels) of the 0_2^+ state of ^{12}C [31–33]



and GCM have the form, $\Phi_J(^{12}\mathrm{C}) = \mathscr{A}\{\chi_J(\xi_1,\xi_2)\phi(\alpha_1)\phi(\alpha_2)\phi(\alpha_3)\}$ with $\xi_1 = X_1 - \frac{1}{2}(X_2 + X_3)$, and $\xi_2 = X_2 - X_3$. The 3α relative wave function $\chi_J(\xi_1, \xi_2)$ satisfies the following equation of motion

$$\langle \phi(\alpha_1)\phi(\alpha_2)\phi(\alpha_3)|(H-E)|\mathscr{A}\{\chi_I(\xi_1,\xi_2)\phi(\alpha_1)\phi(\alpha_2)\phi(\alpha_3)\}\rangle = 0, \qquad (2.53)$$

$$H = \sum_{q=1}^{12} T_q - T_G + \sum_{q < q'}^{12} V_{q,q'}^{(2)}, \tag{2.54}$$

where T_G is the kinetic energy of the total center of mass. It is to be noted that, due to the Bayman–Bohr theorem, the SU(3) shell model wave function $|(0s)^4(0p)^8, (\lambda, \mu) = (04)J = 0\rangle$ can be expressed by the 3α cluster wave function,

$$|(0s)^{4}(0p)^{8}, (\lambda, \mu) = (04)J = 0\rangle$$

$$= N_{0} \mathscr{A} \left\{ R_{4,0}(\xi_{1}, (8/3)\nu) R_{4,0}(\xi_{2}, 2\nu) \phi(\alpha_{1}) \phi(\alpha_{2}) \phi(\alpha_{3}) \right\}$$

$$\times g(X_{G}, 12\nu). \tag{2.55}$$

Figure 2.2 shows that the obtained wave function supports the dominance of ${}^{8}\text{Be}(0_{1}^{+}) + \alpha$ (*S* wave) structure of the Hoyle state. The reduced width amplitude $y_{c}(r)$ in this figure is defined as

$$y_{c=(L,\ell)}(r) = \sqrt{\frac{12!}{4!8!}} \left\langle \frac{\delta(\xi_1 - r)}{r^2} \left[\phi_L(^8 \text{Be}) Y_{\ell}(\hat{\xi}_1) \right]_J \phi(\alpha_1) | \Phi_J(^{12}\text{C}) \right\rangle.$$
(2.56)

These calculations nicely reproduced not only the energy position of the Hoyle state but also other experimental properties including inelastic electron form factor and E0 and E2 transition properties. In Table 2.3 we show the good reproduction of the 12 C data by 3α calculation.

2.3.2.2 AMD and FMD + UCOM Calculations

About 20 years later after the 3α calculations of Refs. [29, 30] and [31–33], the results by these microscopic 3α cluster model calculations were confirmed by the antisymmetrized molecular dynamics (AMD) calculation [34] which does not

Table 2.3 Reproduction of the 12 C data by 3α calculation of Ref. [29, 30]

	Exp.	Theor.
Excitation energy (0 ₂ ⁺) (MeV)	7.65	7.74
Width (0_2^+) (eV)	8.7 ± 2.7	7.7
$M(0_2^+ \to 0_1^+)(\text{fm}^2)$	5.4 ± 0.2	6.7
$B(E2:0_2^+ \to 2_1^+)(e^2 \text{fm}^4)$	13 ± 4	5.6
$B(E2: 2_1^+ \to 0_1^+)(e^2 \text{fm}^4)$	7.8	9.3
$R_{\rm rms}(0_1^+)$ (fm)	2.43	2.4
$R_{\rm rms}(0_2^+)$ (fm)		3.37

assume the alpha clustering. Figure 2.3 shows the energy spectra and density distributions of obtained states by AMD. Furthermore recently the fermionic molecular dynamics (FMD) calculations [35, 36] gave us quite similar results as the AMD results. This FMD approach which also does not assume the alpha clustering starts from a realistic bare N-N force by using the unitary correlation operator method (UCOM) technique. Since both AMD and FMD+UCOM do not assume alpha clustering but build up wave functions totally on nucleonic degrees of freedom, the obtained wave functions contain components with broken spatial symmetry. Table 2.4 shows the good reproduction by the AMD calculation of the observed β ⁺ decay strengths to 12 C states from the ground $^{1+}$ state of 12 N which are due to the components with broken spatial symmetry of 12 C wave function.

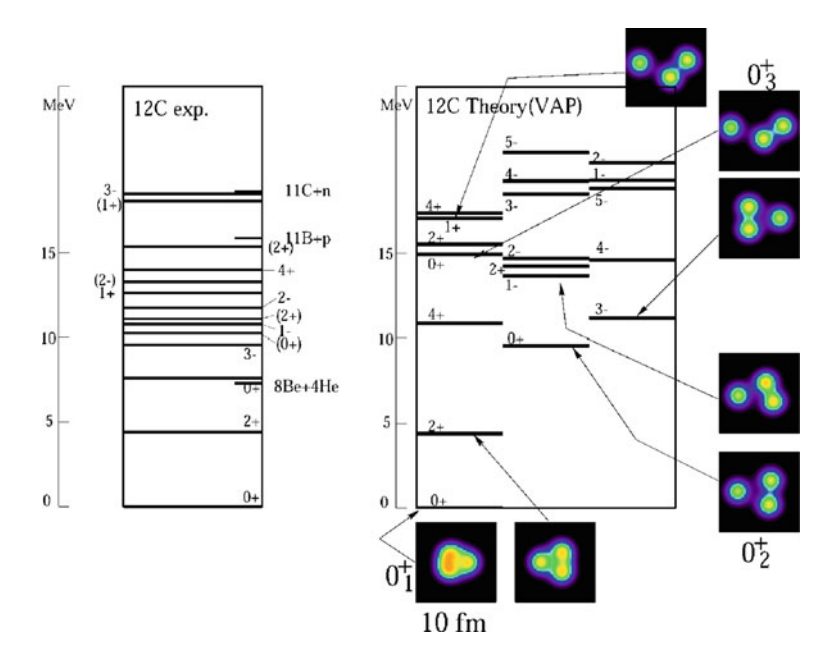


Fig. 2.3 Energy spectra and density distributions of ¹²C by AMD [34]

Table 2.4 The experimental data for β decays $^{12}N(\beta^+)^{12}C$ compared with the AMD results

States in ¹² C (MeV)	J^\pm	$(\log ft)_{\rm exp}$	$(\log ft)_{\text{AMD}} (J_f^{\pm})$
0	0+	4.120 ± 0.003	3.8
4.44	2+	5.149 ± 0.007	$4.8 (2_1^+)$
7.65	0^{+}	4.34 ± 0.06	$4.0 (0_2^+)$
10.3	(0^{+})	4.36 ± 0.17	$4.7 (0_3^+)$
12.71	1+	3.52 ± 0.14	3.8 (11)

2.3.2.3 3α-BEC-Like Structure of the Hoyle State

Almost 30 years after the first proposal of the ${}^8\text{Be}(0^+_1) + \alpha$ structure for the Hoyle state, this state was reconsidered in a new light in Ref. [37]. The authors of this paper presented, for the description of the Hoyle state, the following new model wave function $\Phi^{3\alpha\text{THSR}}(B)$ which is called the 3α THSR wave function :

$$\begin{split} \varPhi^{3\alpha \text{THSR}}(B) &= \mathscr{A} \bigg\{ \exp \bigg[-\frac{2}{B^2} (X_1^2 + X_2^2 + X_3^2) \bigg] \phi(\alpha_1) \phi(\alpha_2) \phi(\alpha_3) \bigg\} \\ &= \exp \bigg(-\frac{6}{B^2} \xi_3^2 \bigg) \mathscr{A} \bigg\{ \exp \bigg(-\frac{4}{3B^2} \xi_1^2 - \frac{1}{B^2} \xi_2^2 \bigg) \phi(\alpha_1) \phi(\alpha_2) \phi(\alpha_3) \bigg\}, \end{split}$$
(2.57)

where $\xi_3 = \frac{1}{3}(X_1 + X_2 + X_3)$. As shown in Eq. (2.57), the THSR wave function can be regarded as expressing the cluster structure where the α_1 cluster and a $^8\text{Be}(0^+_1)$ -like cluster $\mathscr{A}\{\exp(-(1/B^2)\xi_2^2)\phi(\alpha_2)\phi(\alpha_3)\}$ couple via S-wave with inter-cluster wave function $\exp(-(4/3B^2)\xi_1^2)$. On the other hand, Eq. (2.57) shows that the THSR wave function represents the state where three α clusters occupy the same single 0S-orbit $\exp(-(2/B^2)X^2)$, namely a 3α -condensate-like state which is the finite size counterpart of the macroscopic α -particle Bose–Einstein condensation (BEC) in infinite nuclear matter at low density [38]. If the parameter B is so large that the antisymmetrization operator $\mathscr A$ has no effect, the 3α THSR wave function of Eq. (2.57) actually represents the simple product state where three α particles occupy the same single 0S-orbit $\exp(-(2/B^2)X^2)$. On the other hand, in the limit where the parameter B takes its smallest value B = b with b standing for the single-nucleon size parameter of ϕ (α) ($\nu = 1/(2b^2)$), the normalized 3α THSR wave function is equivalent to the shell model wave function;

$$\lim_{B \to b} N(B) \Phi^{3 \text{¢THSR}}(B) = |(0s)^4 (0p)^8, (0,4)J = 0\rangle, \tag{2.58}$$

where N(B) is normalization constant. When we calculate the energy curve by the THSR wave function, we have only one energy minimum corresponding to a compact shell-model-like structure and no energy minimum at a large value of B corresponding to the dilute 3α -condensate-like state. Therefore in order to

study the 3α -condensate-like state, we need to perform the GCM calculation by adopting the parameter B as the generator coordinate. In Ref. [37], this GCM calculation with respect to the parameter B was performed for $n\alpha$ systems with n=3 and 4,

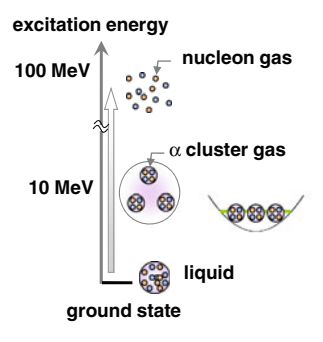
$$\Psi_k(n\alpha) = \sum_j f_j^k \mathscr{A} \left\{ \exp\left[-\frac{2}{B_j^2} \sum_{i=1}^n X_i^2 \right] \phi(\alpha_1) \cdots \phi(\alpha_n) \right\}, \quad (2.59)$$

This GCM calculation gave excited 0^+ state with very large radius in the vicinity of the $n\alpha$ breakup threshold in each $n\alpha$ system (n = 3 and 4).

The results of the calculated 0_2^+ state for 3α system were found to be very similar to those of the previous microscopic 3α calculations of Refs. [29–33]. Actually it was soon discovered [39] that the microscopic 3α wave functions of both of Refs. [29–33] have overlaps of more than 95% with a single 3α THSR wave function with a large size parameter B. This result is very striking since the microscopic 3α wave functions of the 0_2^+ state were obtained by solving very complicated integro-differential three-body equation of motion. This striking fact reported in Ref. [39] means without doubt that the Hoyle state structure has a strong relation with the α condensation physics in dilute infinite nuclear matter [38].

The α -particle condensate-like state is the lowest energy state of the α -particle gas-like state. In nuclear physics, gas-like state of nucleons has been an important subject of study for a long time. Such a state has a very high excitation energy and therefore has been a subject of nuclear matter and nuclear reaction rather than nuclear structure. On the other hand, the gas-like state of clusters, if it exists, is not a so highly excited state, and can be a discrete state accessible spectroscopically. This situation is shown in Fig. 2.4. Gas-like state of clusters is a new concept of nuclear structure and this concept was first proposed for the Hoyle state of ^{12}C in 1970s. However, the discussion at that time was confined only for the Hoyle state. Now in 2000s, gas like state of clusters is expected to be universal and is studied in many nuclei both theoretically and experimentally.

Fig. 2.4 Excitation energies of α-cluster gas state and nucleon gas state in the case of ¹²C



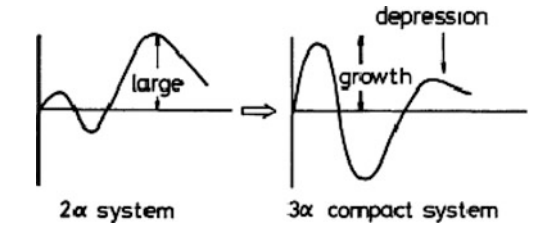
2.3.2.4 Structure Change from the Ground State to the Hoyle State

The energy curve by the 3α THSR wave function shows no local minimum point which corresponds to the Hoyle state and the Hoyle state needs to be obtained by the GCM calculation. When we draw the energy curve by the wave function $(1-|0_1^+\rangle\langle 0_1^+|)\varPhi^{3\alpha\text{THSR}}(B)$ with $|0_1^+\rangle$ standing for the GCM ground state, the energy curve has a minimum point whose wave function is very close to the 0_2^+ state by the GCM calculation [39]. This fact means that the 3α structure of the Hoyle state is largely related to the orthogonality of the Hoyle state to the ground state.

The important role of the orthogonality to the ground state for the formation of the 3α structure of the Hoyle state was discussed already in Ref. [6] from the viewpoint of the 3α dynamics with the α - α interaction described by the OCM. As we explained in the Sect. 2.3.1 on ⁸Be, the OCM says that the α - α interaction is composed of two main factors, one is the local attractive potential of the foldingpotential type and the other is the orthogonality condition of the α - α relative motion to the Pauli-forbidden states. In the 2α system, because of the orthogonality condition to the Pauli-forbidden states, the relative wave function should have nodes, two nodes for S-wave and one node for D-wave, which means that the relative wave function has the oscillatory behavior in the interaction region. The positions of the nodal points are almost fixed unless we are not treating the high energy motion. The oscillatory behavior of the relative wave function gives rise to a large amount of the kinetic energy. Thus in order to avoid the large kinetic energy, the amplitude of the oscillatory part of the relative wave function becomes small. Small amplitude of the inner part of the relative wave function means that the Pauli-forbidden states act like a repulsive core potential. Actually the radius of the repulsive core of the phenomenological α - α potential like the Ali-Bodmer potential [40] is about 2 fm which is the same as the outermost nodal point.

When the same α - α interaction acts in the 3α system, it is to be noted that the attractive interaction between two α 's becomes effectively stronger than in the 2α system because the attractive interaction via the third α cluster strengthen the α - α attraction in the average by factor 1.5. This point can be explained also in the following way. The 3α Hamiltonian can be written as $H = \sum_{i=1}^{3} T_i +$ $\sum_{ij}^{3} V_{ij} = (2/3) \sum_{ij}^{3} [T_{ij} + 1.5V_{ij}]$, where T_{ij} and V_{ij} are the kinetic and interaction operators between ith and jth α clusters. This effectively strengthened $\alpha-\alpha$ attraction drastically changes the inter- α wave function in the interaction region. Namely now the α - α attraction overwhelms the large relative kinetic energy in the inner region, and therefore the amplitude of the relative wave function in the inner region becomes large in order to gain the attractive potential energy. This leads to the formation of the compact ground state of the 3α system (see Fig. 2.5). The formation of the compact ground state affects largely the inter- α relative motion in the excied 0⁺ state via the orthogonality of the excied 0⁺ state to the compact ground state. The orthogonality to the compact ground state prevents two α 's in the excied 0⁺ state from approaching close to each other. This implies the appearance

Fig. 2.5 Change of α - α relative wave function from 2α cluster state to 3α compact state



of the "effective repulsive force" between two α 's in the excited 0^+ state. Thus in the excited 0^+ state there is a combined repulsive interaction; one is this "effective repulsive force" and the other is the repulsive effect due to the inner oscillation of 2α relative wave function originating from the Pauli-forbidden states. This combined repulsive interaction now overwhelms the strengthened attractive force and expel each α from other α 's, which explains the formation of the weakly interacting gas-like 3α structure of the Hoyle state. We see thus that the formation of the 3α structure of the Hoyle state is governed by the orthogonality of the Hoyle state to the ground state.

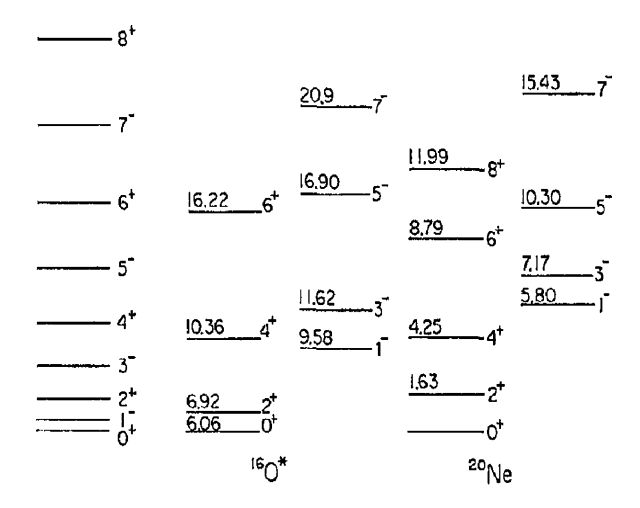
2.3.3 160 Case

The nucleus 16 O is a typical nucleus which shows that nuclear many-body system is rich. It has been long known that, while the ground state is described dominantly by double closed shell wave function, there exist many low-lying excited states which are well described by the 12 C + α cluster model around and above the 12 C + α threshold. Recently it is strongly suggested that there exist 4α condensate-like states around and above the 4α threshold. The formation of 4α condensate-like states is made by the activation of the α -clustering of the 12 C cluster of the 12 C + α structure and it is realized by the assistance of the orthogonality to the lower-lying 12 C + α states and the ground state.

2.3.3.1 12 C + α Clustering

The 16 O nucleus is a doubly magic nucleus and the ground state is described dominantly by double-closed shell structure. Thus this nucleus is a representative nucleus of the nuclear shell model. In spite of this fact, however, the first excited state is located at $E_x = 6.05$ MeV and has spin-parity $J^{\pi} = 0^+$. Since the value of $\hbar\omega$ in this mass region is about 15 MeV, the positive-parity excitation of the double-closed-shell ground state necessitates excitation energy around $2\hbar\omega \approx 30$ MeV if the mean-field (shell model) dynamics works soundly. Therefore the observed excitation energy 6.05 MeV means that this nucleus is not simply governed by the mean-field dynamics.

Fig. 2.6 Inversion doublet rotational bands in ¹⁶O and ²⁰Ne



In 1960s it was experimentally established that this 0_2^+ state is the head state of the positive-parity rotational band with K^{π} =0+ constituted by $J^{\pi}=0^+$, 2^+ , 4^+ , 6^+ states (Fig. 2.6). In correspondence with this experimental knowledge, an idea of the deformed mean field for this excited rotational band with $K^{\pi}=0^+$ prevailed [41, 42]. According to this idea, it is assumed that the ¹⁶O nucleus drastically changes its structure from the double closed shell configuration of the ground state into the largely deformed configuration of the $K^{\pi}=0^+_1$ rotational band whose dominant component is of four-particle four-hole nature. The small excitation energy of this $K^{\pi}=0^+_1$ band was attributed to the small energy gap between the deformed 0p-hole orbit and deformed 1s0d-particle orbit. Up to now, this interpretation of the 0^+_2 state as having deformed four-particle four-hole structure has remained unchanged in the mean-field model approaches.

Contrary to this deformed four-particle four-hole model which assumes a single common deformed mean field for both particles and holes, the weak coupling model of Ref. [43] considers that particles and holes move in their respective (noncommon) mean fields. Namely rotational motion of particles does not couple strongly with that of holes. When the coupling between particles and holes is weak, the 4 0*p*-holes take the configuration similar to the ground state of ¹²C and the four 1*s*0*d*-particles take the configuration similar to the ground rotational band of ²⁰Ne:

$$\Psi(K^{\pi} = 0_1^+, J) = |(0p)^{-4}(^{12}C, 0^+), (1s0d)^4(^{20}Ne, J^+)\rangle.$$
 (2.60)

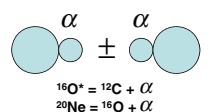
The configuration of four 1s0d-particles of ground rotational band states of 20 Ne is well approximated by the SU(3) configuration with the symmetry $(\lambda, \mu) = (8, 0)$. According to the Bayman–Bohr theorem[12], this SU(3) state is just equivalent to the cluster state with 16 O + α structure.

$$|(0s)^{4}, (0p)^{12}, (1s, 0d)^{4}; (8, 0)J\rangle = C_{J} \mathscr{A} \left\{ R_{8,J} \left(r_{O-\alpha}, \frac{16}{5} v \right) Y_{J} (\hat{r}_{O-\alpha}) \phi(\alpha) \phi(^{16}O) \right\} \times g(X_{G}, 20v).$$
(2.61)

Thus the weak-coupling model wave function has a relation to the ^{12}C + α cluster wave function.

The 12 C – α cluster model gives a very natural explanation of the observed small excitation energy 6.05 MeV of the first excited state (0^+_2) because the threshold energy of $^{12}\text{C} + \alpha$ breakup is located at $E_x = 7.16$ MeV. If this first excited state has a cluster structure of $^{12}C + \alpha$, the excitation energy 6.06 MeV is very reasonable because it means 1.1 MeV for the binding energy of the $^{12}\text{C} - \alpha$ relative motion. The assignment of $^{12}\text{C} + \alpha$ structure to the first excited state of ¹⁶O was suggested already around 1960 by Wildermuth and his coworkers [44, 45]. This work was an underlying knowledge for the weakcoupling model by Arima and his coworkers [43]. The 12 C + α cluster structure for the 0^+_2 state with definite idea of spatial localization of clusters was first proposed by Horiuchi and Ikeda [46]. They noticed the negative-parity rotational band states with $J^{\pi} = 1^{-}$, 3^{-} , 5^{-} , 7^{-} (Fig. 2.6) observed by α -particle resonant scattering on ¹²C by Davis and his coworkers [47–49]. The band head 1⁻ state is located at $E_r = 9.63$ MeV. The authors of Refs. [47–49] found that the α -widths of the rotational member states are large and comparable with Wigner-limit values and, from these large widths and from the value of the moment of inertia, they interpreted the rotational member states as consisting of an α-cluster rotating outside the ¹²C core nucleus. The authors of Ref. [46] argued that, if the intrinsic state of this negative-parity rotational band has a 12 C + α structure with spatial localization of clusters, the intrinsic state is of parity-asymmetric (parity-violating) shape and hence this intrinsic state should possess a parityinverted positive-parity rotational band which constitutes a parity doublet (inversion doublet) together with the negative-parity rotational band (Fig. 2.7). They concluded that this positive-parity rotational band is just the observed rotational band upon the 0^+_2 state as the band head state (Fig. 2.6). The main reason for this conclusion was firstly that, as we explained above, there already existed theoretical arguments of Refs. [43–45] which assign the 12 C + α structure to this positive parity band upon the 0^+_2 state. The other reason was that there is only this positive-parity band below the negative-parity band of Davis et al. [47–49].

Fig. 2.7 Inversion doublet intrinsic wave functions of core + α clustering



$2.3.3.2^{-12}C + \alpha OCM$

In 1970s an extensive study of 16 O was performed by Suzuki [50, 51] by using 12 C + α coupled-channel OCM [52] where the 12 C cluster can be excited to its ground band states with 2^+ and 4^+ . The equation of motion of the coupled-channel OCM for the 12 C + α system is given as;

$$(T_i(r) + (\Delta E_{\mathcal{C}})_i + E_r)\hat{\chi}_i(r) = -\sum_i U_{i,j}\hat{\chi}_j(r), \quad \sum_i \langle \chi_i^F(r)|\hat{\chi}_i(r)\rangle = 0, \quad (2.62)$$

$$T_{i}(r) = \left\langle Y_{\ell_{i}}(\hat{r}) \left| \frac{-\hbar^{2}}{2\mu} \frac{\partial^{2}}{\partial r^{2}} \right| Y_{\ell_{i}}(\hat{r}) \right\rangle, \quad (\triangle E_{\mathcal{C}})_{i} = E_{L_{i}}(\mathcal{C}) - E_{0}(\mathcal{C}),$$

$$E_{r} = E - E(\alpha) - E_{0}(\mathcal{C}), \tag{2.63}$$

where μ is the reduced mass of $^{12}\mathrm{C}$ and α and i is the index of a channel with total angular mementum J. $\{\chi_i^F(r)\}$ stand for the Pauli-forbidden states to which $\{\hat{\chi}_i(r)\}$ should be orthogonal. The wave function Ψ^J of the system is obtained from the solution of the relative wave function $\hat{\chi}_i(r)$ as follows,

$$\Psi^{J} = \mathscr{A} \left[\sum_{i} \chi_{i}(r) h_{i}^{J} \right], \quad \hat{\chi}_{i}(r) = \sum_{j} \int (N_{K}^{1/2})_{i,j}(r, r') \chi_{j}(r') r'^{2} dr', \qquad (2.64)$$

$$(N_K)_{i,j}(a,b) = \left\langle \frac{\delta(r-a)}{a^2} h_i^J \middle| \mathcal{A} \left[\frac{\delta(r-b)}{b^2} h_j^J \right] \right\rangle, \quad h_i^J = \left[Y_{\ell_i}(\hat{r}) \phi_{L_i}(\mathbf{C}) \right]_J \phi(\alpha).$$
(2.65)

The Pauli-forbidden states $\{\chi_i^F(r)\}$ are defined as those states that satisfy

$$\mathscr{A}\left[\sum_{i}\chi_{i}^{F}(r)h_{i}^{J}\right]=0. \tag{2.66}$$

The orthogonality requirement $\sum_{i}\langle\chi_{i}^{F}(r)|\hat{\chi}_{i}(r)\rangle=0$ means

$$0 = \sum_{i} \langle \chi_i^F(r) | \hat{\chi}_i(r) \rangle = \left\langle \sum_{i} \chi_i^F(r) h_i^J \middle| \sum_{j} \hat{\chi}_j(r) h_j^J \right\rangle. \tag{2.67}$$

The Pauli-forbidden configurations $\sum_i \chi_i^F(r) h_i^J$ are specified by SU(3) irreducible representations and are tabulated in Refs. [50–52].

According to the Bayman–Bohr theorem [12], the double closed shell wave function of ¹⁶O can be described with the cluster model wave function:

$$\det |(0s)^{4}(0p)^{12}| = c_{L} \mathscr{A} \Big[R_{4,L}(r_{C-\alpha}, 3v) \Big[Y_{L}(\hat{r}_{C-\alpha}) \phi_{L}(^{12}C) \Big]_{J=0} \phi(\alpha) \Big] \times g(X_{G}, 16v),$$
(2.68)

where $R_{4L}(r, 3v)$ is harmonic oscillator radial function with oscillator parameter 3v, angular momentum L and number of oscillator quanta 4, 4 = 2n + L. This equality holds for any L among L = 0, 2, and 4. Thus this OCM study could treat the ground state and accordingly the structure change between the shell-model-like structure and the cluster structure. The calculated results were very successful in reproducing almost all the observed data. The good reproduction of the energy spectra is shown in Fig. 2.8. Table 2.5 shows the good reproduction of electric transition data. The ground state was shown to be dominantly given by double closed shell wave function and the $K^{\pi} = 0^{+}_{1}$ and $K^{\pi} = 0^{-}_{1}$ bands were shown to have dominantly the $^{12}\text{C}(0_1^+) + \alpha$ cluster structure. Furthermore the negative parity states with $3_1^-, 1_1^-, 2_1^-$ were shown to have dominantly shell model structure with 1-particle 1-hole excitation although rather large mixture of cluster configuration is existent. Beside the good reproduction of energy spectra and electric transitions shown in Fig. 2.8 and Table 2.5, alpha-decay data are also well reproduced as shown in Table 2.6. The ${}^{12}C(2_1^+) + \alpha$ structure with S-wave of α motion is realized in the observed 2^+_2 state at 9.85 MeV.

The results of the $^{12}\text{C} + \alpha$ OCM deny the formation of single deformed structure composed of strong coupling of the rotational motion of ^{12}C cluster and the orbiting motion of α cluster around ^{12}C cluster. In the case of the 2^+_2 state at 9.85 MeV, as mentioned above, the dominant component of the 2^+_2 wave function is composed of $^{12}\text{C}(2^+)$ coupled with *S*-wave α cluster. This result is in

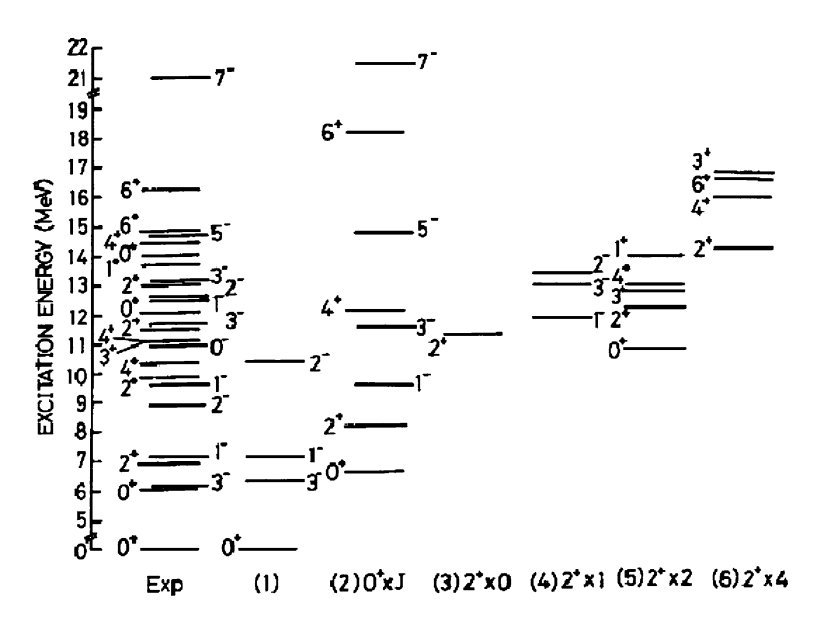


Fig. 2.8 Energy spectra by 12 C + α OCM [6, 50, 51] classified by dominant component $L^+ \times \ell(^{12}$ C(L^+) + $\alpha(\ell)$). Classification denoted as (1) is for the mean-field-type states including the ground state and 1p - 1h type states

Table 2.5 Electric transition rates in 16 O compared with 12 C + α OCM calculation [50, 51]

Transition	exp.	$^{12}\text{C} + \alpha$
$B(E2)(e^2 \text{fm}^4)$		_
$2_1^+ \to 0_1^+$	7.8 ± 0.3	2.20
$2_1^+ o 0_2^+$	76 ± 13	60.2
$1_1^- \to 3_1^-$	51 ± 10	25.5
$2_1^- \rightarrow 3_1^-$	14^{+3}_{-4}	13.8
$2^1 ightarrow 1^1$	36 ± 5	15.1
$2_2^+ \to 0_1^+$	0.082 ± 0.007	0.247
$2_2^+ ightarrow 0_2^+$	3.0 ± 0.7	9.68
$4_1^+ \rightarrow 2_1^+$	150 ± 18	102
$4_2^+ \rightarrow 2_1^+$	2.4 ± 0.6	0.0405
$2_3^+ \to 0_1^+$	3.7 ± 0.1	1.21
$2_3^+ \to 0_2^+$	7.6 ± 2	1.20
$M(E0)(fm^2)$		
0_1^+ - 0_2^+	3.55 ± 0.21	3.88
0_1^+ - 0_3^+	4.03 ± 0.09	3.50
$B(E3) (e^2 \text{fm}^6)$		
$3_1^- \rightarrow 0_1^+$	213 ± 11	130

accordance with the weak-coupling shell model of Ref. [43] which describes this 2_2^+ state as composed of the four-hole configuration $(0p)^{-4}(J_h=2)$ and the four-particle configuration $(1s0d)^4(J_p=0)$. In usual mean-field models, this state is

Table 2.6 Alpha decay 0data in 16 O compared with 12 C + α OCM calculation [50, 51]

$\overline{J^{\pi} (\text{Ex (MeV)})}$	Γ (keV)	Decay	$\theta_{\rm exp}^2$	$\theta_{\rm cal}^2$
1- (9.63)	510 ± 60	α_0	0.71	0.59
2 ⁺ ₂ (9.85)	0.9 ± 0.3	α_0	0.0019	0.0079
4 ⁺ ₁ (10.35)	27 ± 4	α_0	0.37	0.42
4 ⁺ ₂ (11.10)	0.28 ± 0.05	α_0	0.0011	0.047
2 ⁺ ₃ (11.52)	74 ± 4	α_0	0.033	0.048
3_2^- (11.60)	800 ± 100	α_0	0.63	0.51
0_3^+ (12.05)	1.5 ± 0.5	α_0	0.00037	0.097
1_3^- (12.44)	98 ± 7	α_0	0.024	0.000064
	0.025	α_1	0.084	0.18
2^{-}_{2} (12.53)	≤0.5	α_1	≤0.59	0.13
2 ⁺ ₄ (13.02)	150 ± 11	α_0	0.039	0.069
3_3^- (13.13)	90 ± 14	α_0	0.032	0.091
	≈20	α_1	≈ 0.36	0.41
1 ⁺ ₁ (13.66)	64 ± 3	α_1	0.54	0.54
5_1^- (14.67)	530 ± 71	α_{0}	0.38	0.30
	28 ± 4	α_1	0.10	0.074
6 ⁺ ₁ (14.82)	22	α_0	0.043	0.025
	48	α_1	0.62	0.41
6 ⁺ ₂ (16.29)	490 ± 40	α_{0}	0.42	0.42
7_{2}^{-} (20.88)	650 ± 75	α_0	0.27	0.34

Reduced widths θ^2 are at the channel radius a = 5.2 fm

regarded as the band-head state of the $K^{\pi} = 2^{+}$ side band with four-particle four-hole structure.

2.3.3.3 4\alpha OCM and 4\alpha-Gas Like States

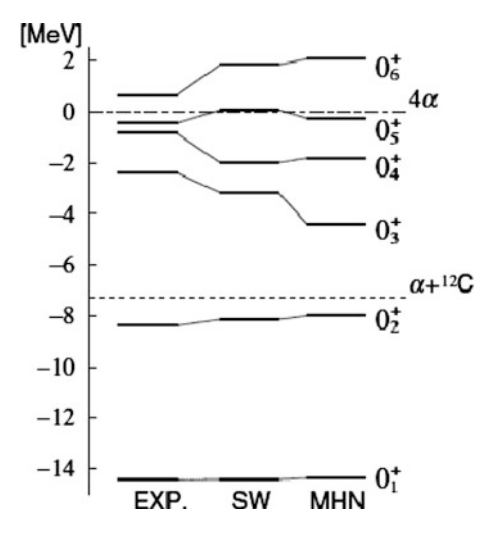
Recently Funaki and his coworkers have reported the results of the full four-body calculations in the framework of 4α OCM [53]. They claim that the calculated lowest six 0^+ states reproduce or well correspond to the observed six 0^+ states up to the 0_6^+ state at 15.1 MeV as shown in Fig. 2.9. The calculated 0_1^+ has, as its dominant component, the double closed shell wave function. From the calculation of the reduced width amplitudes y(r) of various $^{12}C + \alpha$ channels,

$$y(r) = \left\langle \frac{\delta(r_{C-\alpha} - r)}{r^2} \left[Y_L(\hat{r}_{C-\alpha}) \phi_L(^{12}C) \right]_0 | \Phi(^{16}O, 0_k^+) \right\rangle, \tag{2.69}$$

the calculated 0_2^+ and 0_3^+ states proved to have, as their dominant components, $^{12}\mathrm{C}(0_1^+) + \alpha$ and $^{12}\mathrm{C}(2_1^+) + \alpha$ cluster structures, respectively. In Eq. (2.69) $\phi_L(^{12}\mathrm{C})$ is the wave function of $^{12}\mathrm{C}$ given by the 3α OCM calculation [54] with the same effective inter- α interaction. One of the most important results of Ref. [53] is that the calculated 0_6^+ state has a structure of 4α -condensate-like state. The radius of the calculated 0_6^+ state has a very large value of about 5 fm. This large size suggests that the calculated 0_6^+ state is composed of a weakly interacting gas of α particles. The reduced width amplitudes y(r) of the calculated 0_6^+ state proved to have a large amplitude only in the $^{12}\mathrm{C}(0_2^+) + \alpha$ channel.

From the analyses of the reduced width amplitudes in various $^{12}C + \alpha$ channels, the calculated 0_4^+ and 0_5^+ states were found to have dominantly $^{12}C(0_1^+) + \alpha$ and

Fig. 2.9 Energy spectra by 4α OCM [53] with two kinds of effective nuclear force, SW and MHN



 12 C(1⁻) + α cluster structures, respectively. The widths of the calculated $0_4^+, 0_5^+$ and 0_6^+ states are $\sim 150, \sim 50$, and $\sim 50 \, \text{keV}$, respectively, while those of the observed $0_4^+, 0_5^+$ and 0_6^+ states are 600, 185, and 166 keV, respectively.

The full four-body calculation of alpha clusters of Ref. [53] shows us that nuclear many-body system undergoes actually drastic structure changes as the excitation energy increases, namely from compact shell-model-like structure to various $^{12}\text{C} + \alpha$ structures and furthermore to a 4α gas-like structure. Since the various $^{12}\text{C} + \alpha$ structures have been well confirmed to be realized in many excited states, the calculations of Ref. [53] which succeeded to reproduce these $^{12}\text{C} + \alpha$ states can be regarded as highly reliable.

2.3.4 ²⁰Ne Case

2.3.4.1 Ikeda Diagram and Transitional Character of the Ground Band Between Mean-Field Like Structure and Cluster Structure

As we mentioned in the previous section on ¹⁶O, Horiuchi and Ikeda proposed in ¹⁶O to regard the $K^{\pi} = 0^{+}$ band upon 6.05 MeV 0^{+} state and $K^{\pi} = 0^{-}$ band upon 9.63 MeV 1⁻ state as being inversion doublet bands with the parity-violating structure of 12 C + α [46]. In the same Ref. [46] the authors also proposed in 20 Ne to regard the $K^{\pi} = 0^{+}$ ground band and $K^{\pi} = 0^{-}$ band upon 5.78 MeV 1⁻ state as being inversion doublet bands with the parity-violating structure of $^{16}O + \alpha$ (Figs. 2.7, 2.8). One of the grounds of this proposal was the report given in Ref. [47–49] which reported on the resonant scattering of α particles on ¹⁶O together with that on 12 C. The authors of Refs. [47–49] found that the α -widths of the $K^{\pi} = 0^{-}$ band member states are large to be comparable with Wigner-limit values and, from these large widths and from the value of the moment of inertia, they interpreted the $K^{\pi} = 0^{-}$ band member states as having a structure of $^{16}O + \alpha$. Another ground of the proposal was the fact that the shell model study of the ²⁰Ne teaches us that the dominant component of the ground band is given by the SU(3) configuration with $(\lambda, \mu) = (8, 0), |(0s)^4, (0p)^{12}, (1s, 0d)^4; (8, 0)J\rangle$ [55, 56]. According to the Bayman-Bohr theorem this wave function is equivalent to the $^{16}O + \alpha$ cluster model wave function as was shown in Eq. (2.61). It was also important to note that below the $K^{\pi} = 0^{-}$ band upon 5.78 MeV 1⁻ state the ground band is the only band with $K^{\pi} = 0^{+}$.

Ikeda and his collaborators noticed the fact that the states in light nuclei which were assigned to have cluster structures are energetically located near or above the cluster-breakup thresholds corresponding to respective cluster structure. Typical examples are ground band states of ⁸Be, the Hoyle state of ¹²C, and the above-explained inversion doublet band states in ¹⁶O and in ²⁰Ne. Supported by this fact, they proposed the so-called Ikeda diagram which gives necessary conditions for the formation of cluster states [57] (Fig. 2.10). The first condition is the stability of

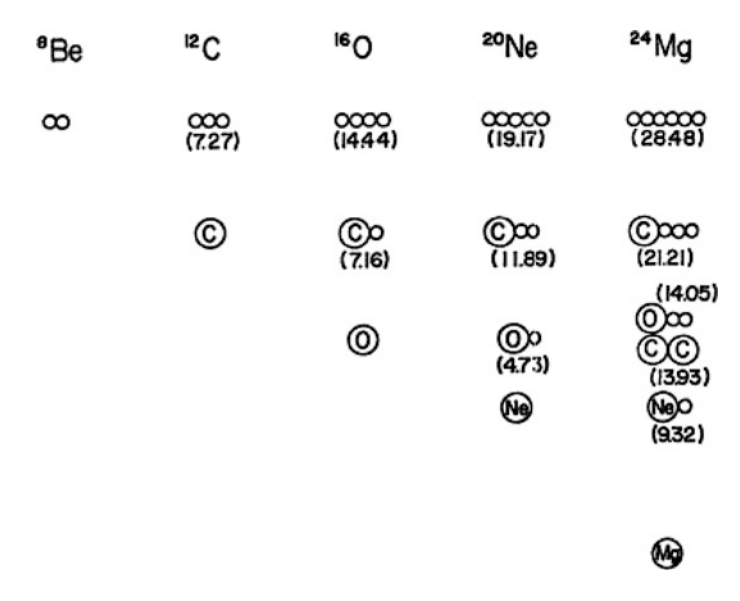


Fig. 2.10 Ikeda diagram [57]

the constituent clusters which is necessary for keeping the identity of the clusters. The second condition is the weakness of inter-cluster interaction. If the inter-cluster interaction is strongly attractive, the clusters will dissolve into mean-field-like structure. The weakness of the inter-cluster interaction results in the energy location of the cluster state near the breakup threshold into constituent clusters. Thus the Ikeda diagram says that the energy location of the cluster state is necessarily near the breakup threshold into constituent clusters. Usually ground states of nuclei are located well below the α breakup threshold and thus they have mean-field-like structure. A clear violation for this statement is the ground state of 8 Be which is located slightly above the α - α breakup threshold. The well-known fact that the ground state of 8 Be has an α - α cluster structure is in good accordance of the Ikeda diagram.

As mentioned above, the ground state is usually considered to have mean-field-like structure except the case of ^8Be . But in Ref. [46] the authors assigned the $^{16}\text{O} + \alpha$ cluster structure to the ground state of ^{20}Ne . Thus this assignment needs to be checked carefully. The ground state of ^{20}Ne is located below the $^{16}\text{O} + \alpha$ breakup threshold by 4.73 MeV. This value of 4.73 MeV is fairly smaller than the corresponding binding energies of the ground states measured from the α breakup threshold in other nuclei. For example in ^{12}C the ground state is located below the $^{8}\text{Be} + \alpha$ or 3α threshold by about 7.5 MeV and also in ^{16}O the ground state is located below the $^{12}\text{C} + \alpha$ threshold also by about 7.2 MeV. Hence it is conceivable that the ground state of ^{20}Ne does not have so good cluster structure of $^{16}\text{O} + \alpha$. At the same time it is conceivable that the ground state of ^{20}Ne does not have so good mean-field-like structure. This intermediate character of the ground band of ^{20}Ne was noticed from the beginning in Refs. [46, 57] and was

named [58, 6] "transitional character of the ground band of 20 Ne between mean-field like structure and cluster structure". In Refs. [46, 57] it was pointed out that, because of the transitional character of 20 Ne ground band, the magnitude of the gap energy between the band head states of the $K^{\pi} = 0^{+}$ band and the $K^{\pi} = 0^{-}$ band is much larger in 20 Ne (5.5 MeV) than in 16 O (3.0 MeV).

2.3.4.2 AMD Study of ²⁰Ne

AMD studies of ²⁰Ne [59–61] have made important contributions for the clarification of structural problems of ²⁰Ne, including the transitional character of the ground band. Figure 2.11 shows good reproduction of the observed energy spectra by the calculation of Ref. [60]. Table 2.7 shows that the E2 transitions inside the ground, $K^{\pi} = 0^{-}_{1}$, and $K^{\pi} = 2^{-}_{1}$ bands are also well reproduced by the calculation of Ref. [60] without use of any effective charge. The magnitudes of the deformations of the $K^{\pi} = 0^+_1$ (ground), $K^{\pi} = 0^-_1$, and $K^{\pi} = 2^-_1$ bands are shown in their energy curves with respect to the quadrupole deformation parameter β in Fig. 2.12. Here "deformed-basis AMD" means that the nucleon wave packets of AMD wave function are deformable while "spherical-basis AMD" means that the nucleon wave packets of AMD wave function are kept spherical. We note that for the $K^{\pi} = 0^{+}_{1}$ and $K^{\pi} = 2^{-}_{1}$ bands the deformation of nucleon wave packets makes the binding energies of these bands appreciably deeper while for the $K^{\pi} = 0^{-}_{1}$ band the nucleon wave packets favor spherical shape. The value of β at the minimum energy point is about 0.4 for both the $K^{\pi} = 0^{+}_{1}$ and $K^{\pi} = 2^{-}_{1}$ bands while it is about 0.5 for the $K^{\pi} = 0^{-}_{1}$ band. The $^{16}O + \alpha$ clustering features of these three bands can be seen in Fig. 2.13 which shows the position of centroids of the nucleon wave packets of the AMD wave function. This figure shows that

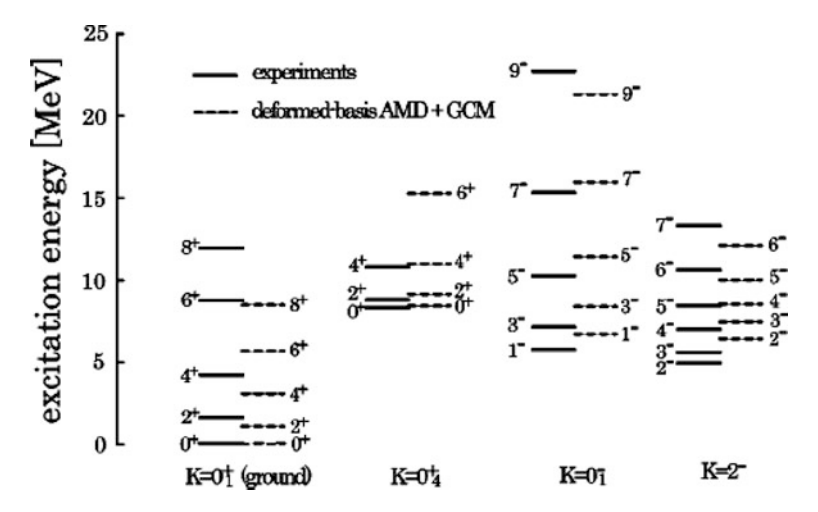


Fig. 2.11 Energy spectra of ²⁰Ne by AMD [60]

Table 2.7 B(E2) ($e^2 \text{fm}^2$) in ²⁰Ne compared with AMD calculation [60]

$\overline{J_i^\pi o J_f^+}$	EXP	AMD
$K^{\pi} = 0_1^+$		
$2_1^+ ightarrow 0_1^+$	65 ± 3	70.3
$4_1^+ \rightarrow 2_1^+$	71 ± 6	83.7
$6_1^+ \to 4_1^+$	64 ± 10	52.7
$8_1^+ \to 6_1^+$	29 ± 4	21.0
$[K^{\pi}=0^{-}]$		
$3^- ightarrow 1^-$	164 ± 26	151.2
$[K^{\pi}=2^{-}]$		
$3^1 ightarrow 2^-$	113 ± 29	102.8
$4^- \rightarrow 3^1$	77 ± 16	77.8
$4^- o 2^-$	34 ± 6	38.5
$5^1 ightarrow 4^-$	< 808	84.5
$5^1 \rightarrow 3^1$	84 ± 19	56.6
$6^1 \rightarrow 5^1$	32 ± 13	29.9
$6^- \rightarrow 4^-$	55^{+23}_{-13}	64.0

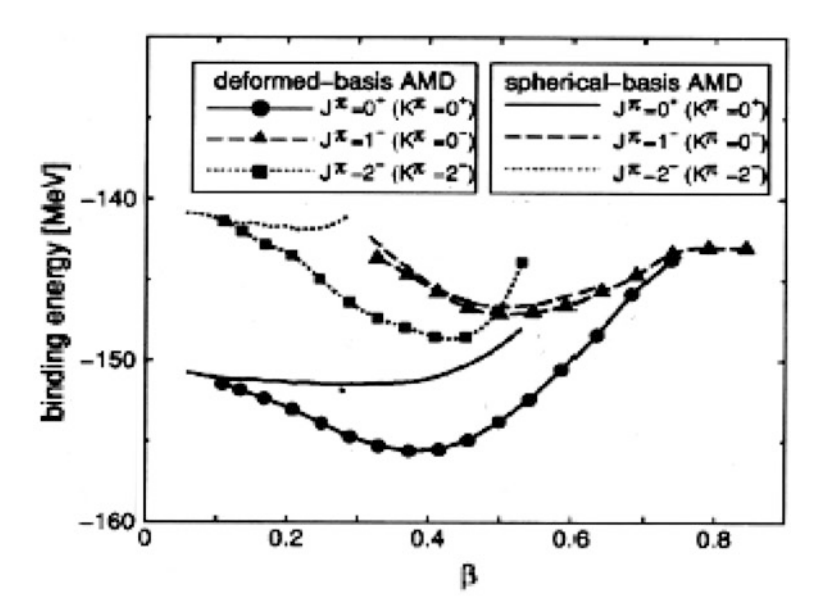


Fig. 2.12 Energy curves of ²⁰Ne with respect to quadrupole deformation by AMD [60]

the $K^\pi=0^-_1$ wave function around $\beta=0.5$ has nucleon wave packets of an α cluster separated largely apart from other 16 nucleon wave packets. This means that the $K^\pi=0^-_1$ band has a clear cluster structure of $^{16}{\rm O}+\alpha$. On the contrary, the nucleon wave packets of the $K^\pi=2^-_1$ wave function around $\beta=0.4$ are all located close to one another. This means that the $K^\pi=2^-_1$ band has a mean-field-type structure. The wave function of the $K^\pi=0^+_1$ band at the minimum energy

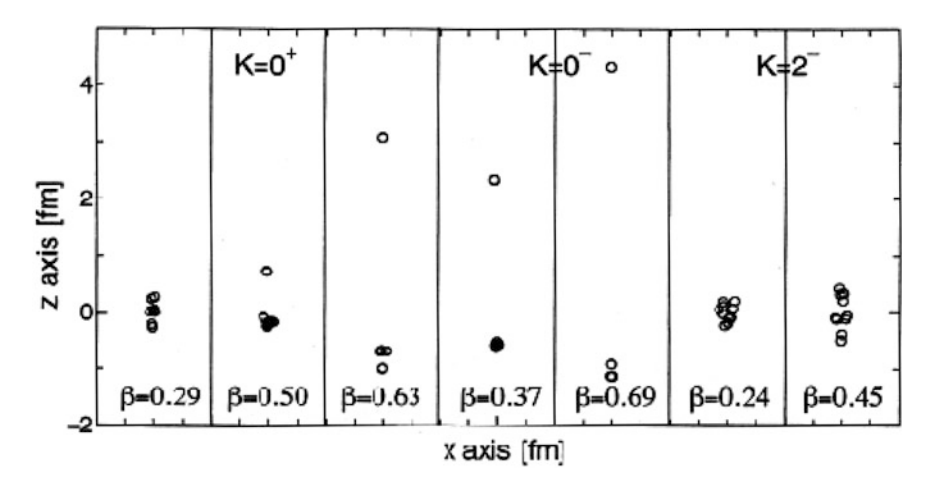


Fig. 2.13 Spatial positions of nucleon-wave-packet centroids of AMD wave functions of ²⁰Ne [60]

point around $\beta=0.4$ is seen to have rather similar spatial distribution of nucleon wave packets to that of the $K^\pi=2_1^-$ band. However it is also seen that the $K^\pi=0_1^+$ band wave function with slightly larger $\beta=0.5$ has a feature of weak clustering of $^{16}{\rm O}+\alpha$. Fig. 2.14 gives the density distributions of the intrinsic wave functions which have nucleon wave packet distributions shown in Fig. 2.13. We see in this figure that the density distribution of the $K^\pi=0_1^-$ intrinsic state around $\beta=0.5$ has a clear parity-violating shape due to the $^{16}{\rm O}+\alpha$ clustering while that of the $K^\pi=0_1^+$ intrinsic state in the region of $\beta=0.3$ ~0.5 does not show, just like the $K^\pi=2_1^-$ band with mean-field-type structure, clear parity-violating shape.

Although the density distribution of the intrinsic state of the ground band does not have a clear parity-violating shape due to the $^{16}\text{O} + \alpha$ clustering, the wave function of the ground band has a large component of $^{16}\text{O} + \alpha$ clustering. Table 2.8 shows that the squared amplitude of the $^{16}\text{O} + \alpha$ component W^J of the ground band is about 70% for low spin states and decreases to about 30% for high spin states. The magnitude W^J of the $^{16}\text{O} + \alpha$ component of a given wave function Φ^J is obtained as $W^J = |\alpha_I|^2$ with α_I defined as

$$\Phi^{J} = \alpha_{J} \Phi^{J}(^{16}O + \alpha) + \sqrt{1 - |\alpha_{J}|^{2}} \Phi_{R}^{J},$$
 (2.70)

$$\Phi^{J}(^{16}\mathrm{O} + \alpha) = n_{J} \mathscr{A} \Big\{ \chi_{J}(r_{\mathrm{O}-\alpha}) Y_{J}(\hat{r}_{\mathrm{O}-\alpha}) \phi(^{16}\mathrm{O}) \phi(\alpha) \Big\}, \tag{2.71}$$

where $\Phi^{J}(^{16}\mathrm{O}+\alpha)$ is normalized wave function in the functional space of $^{16}\mathrm{O}+\alpha$ and Φ^{J}_{R} is normalized component orthogonal to the $^{16}\mathrm{O}+\alpha$ functional space. A detailed explanation how to calculate W^{J} is given in Sect. 2.3.4.3. For the large value of $W^{J}=70\%$, the fact due to the Bayman–Bohr theorem given in Eq. (2.61), $|(0s)^{4},(0p)^{12},(1s,0d)^{4};(8,0)J\rangle=C_{J}\mathscr{A}\{R_{8,J}(r_{O-\alpha},(16/5)\nu)Y_{J}(\hat{r}_{O-\alpha})\}$

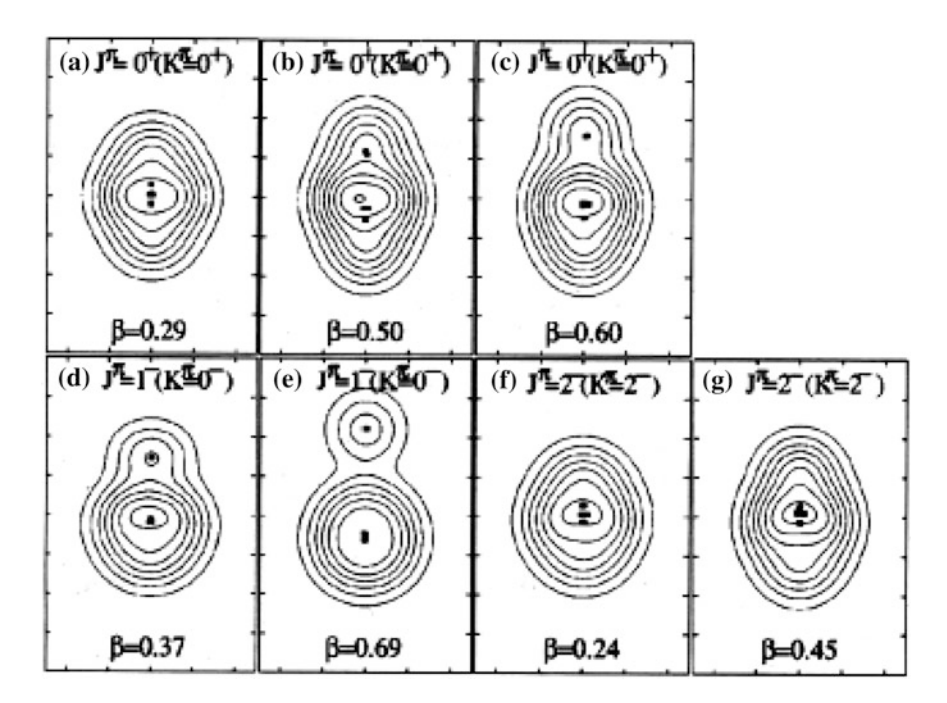


Fig. 2.14 Density distributions of AMD intrinsic wave functions with various quadrupole deformation [60]

 $\phi(\alpha)\phi(^{16}{\rm O})\}g(X_G,20\nu)$, makes a large contribution. The percentage of the $^{16}{\rm O}+\alpha$ component of the $K^\pi=0^-_1$ band is much larger than the ground band and is about 95% for low spin states but it again decreases to about 70% for high spin states. We can regard that the magnitude of $W^J=70\%$ for the ground band is large enough to allow the inversion doublet picture for the ground band and $K^\pi=0^-_1$ band.

AMD calculation reproduces the $K^{\pi}=0_4^+$ band which has the band head 0^+ state at 8.3 MeV. This band has been known by many cluster model studies [6] to have an $^{16}{\rm O}$ + α structure which has one more nodal points in their relative wave functions of $^{16}{\rm O}$ - α compared with the ground band. In terms of the quantum number N=2n+L with n standing for the number of nodes, the $K^{\pi}=0_4^+$ band has N=10, while for the ground and $K^{\pi}=0_1^-$ bands N=8 and 9, respectively. Table 2.8 shows the magnitude of W^I of the $K^{\pi}=0_4^+$ band is about 80% for low spin states and it decreases to about 60% for high spin states. The $^{16}{\rm O}$ + α clustering character is reflected in the α decay strength. Table 2.9 shows that the observed α decay strengths of the ground, $K^{\pi}=0_1^-$, and $K^{\pi}=0_4^+$ bands are well reproduced by the AMD calculations.

In all three bands of $K^{\pi}=0^+_1$, $K^{\pi}=0^-_1$, and $K^{\pi}=0^+_4$, the magnitude W^I of the $^{16}{\rm O}+\alpha$ component decreases from low spin to high spin states. An important reason of this decrease is the nucleon spin alignment which is against the formation of α cluster [59]. Figure 2.15 shows the expectation value of the intrinsic spin

Table 2.8 Squared amplitudes of $^{16}\text{O} + \alpha$ component W^I and expectation values of two-body spin-orbit force $\langle \bar{V}_{ls} \rangle$ by AMD [60]

K^{π}	J^{π}	W^{J}	$\langle ar{V}_{ls} angle$
01+	01+	0.70	-5.2
	21+	0.68	-5.3
	41+	0.54	-5.9
	6_{1}^{+}	0.34	-8.4
	81	0.28	-10.9
0_{4}^{+}	0_{4}^{+}	0.82	-3.2
	2_{4}^{+}	0.81	-3.0
	4_{4}^{+}	0.79	-4.9
	64	0.67	-6.8
	84	0.55	-7.4
0_{1}^{-}	1_{1}^{-}	0.95	-0.8
	3_{2}^{-}	0.93	-0.8
	5_{2}^{-}	0.88	-0.7
	7_{2}^{-}	0.71	-0.9
	9_{2}^{-}	0.70	-1.3
2^{-}	2_{1}^{-}		-12.9
	3_{1}^{-}		-13.0
	4_1^-		-14.1
	5_{1}^{-}		-14.4
	6_{1}^{-}		-16.5

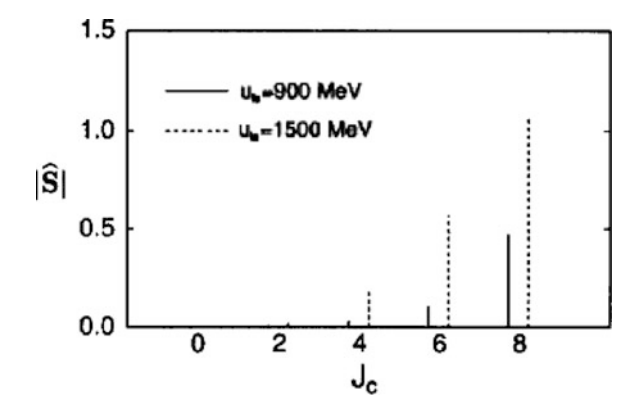
Table 2.9 α reduced widths θ^2 multiplied by 100 in ²⁰Ne compared with AMD calculations [60]

K^{π}	J^{π}	EXP	AMD
01+	61	1.0 ± 0.2	0.53
	81	0.094 ± 0.027	0.08
0_{4}^{+}	0_{4}^{+}	>50	69.0
	24	>59	68.0
	2 ₄ ⁺ 4 ₄ ⁺	23	35.5
0_{1}^{-}	1-	>16	31.0
	3_{2}^{-}	26	29.1
	5_{2}^{-}	30	28.8
	$ \begin{array}{r} 3_{2}^{-} \\ 5_{2}^{-} \\ 7_{2}^{-} \end{array} $	22 ± 5	11.5
	9-	17	8.9

Channel radius a is 6 fm

angular momentum (non orbital angular momentum) in the ground band which grows larger for high spin states. The nucleon spin alignment is reflected in the expectation value of the two-body spin-orbit force which, for the ground band, is $-5.2\,$ MeV for the $J^\pi=0^+_1$ state and increases to $-8.4\,$ MeV for the $J^\pi=8^+$ state. Since the $K^\pi=0^-_1$ band has very large component of $^{16}{\rm O}+\alpha$, the expectation value of the two-body spin-orbit force is small and is only $-0.8\,$ MeV for the $J^\pi=1^-$ state, but it still increases to $-1.3\,$ MeV the $J^\pi=9^-$ state. The effect of the nucleon spin alignment is reflected in the shape of the quadrupole

Fig. 2.15 Expectation values of intrinsic spin angular momentum for the ground band states of ²⁰Ne by AMD [59]



deformation [60]. Figure 2.16 shows that the ground band intrinsic wave function of AMD changes its shape from prolate deformation for low spin states to the oblate deformation of the $J^{\pi}=8^+$ state. This effect was discussed in detail in Ref. [59]. It is quite interesting that the nucleon spin alignment which is a mean-field-like dynamics is coexistent together with the clustering dynamics in the ground band and also even in the typical cluster band of $K^{\pi}=0^-_1$.

In this lecture we do not discuss the $K^{\pi}=0^+_2$ and $K^{\pi}=0^+_3$ bands whose bandhead $J^{\pi}=0^+$ states are located between the ground state and the $K^{\pi}=0^+_4$

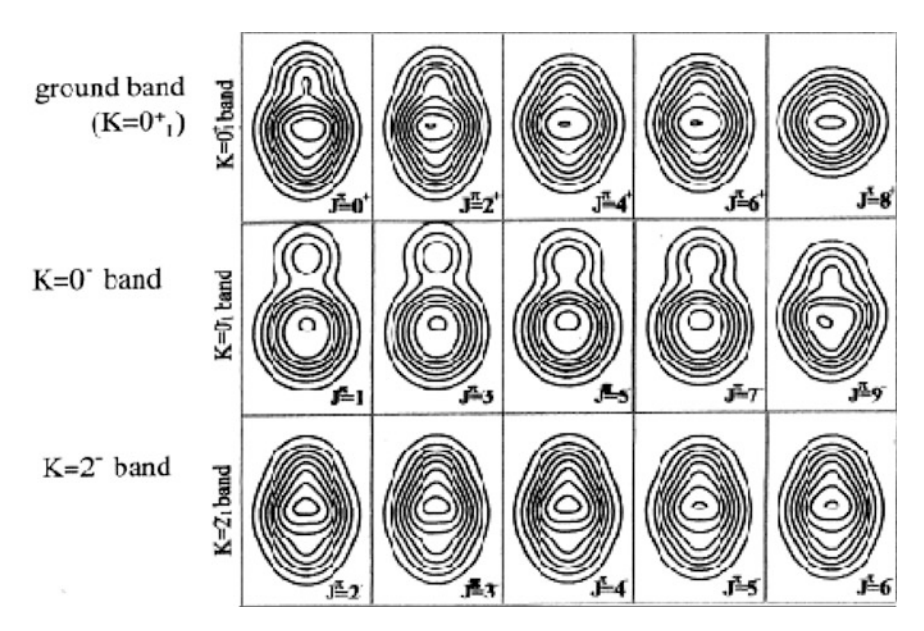


Fig. 2.16 Change of deformation with increase of angular momentum for ground, $K^{\pi} = 0^{-}$, and $K^{\pi} = 2^{-}$ bands of ²⁰Ne [60]

band-head $J^{\pi}=0^+$ state. The $K^{\pi}=0^+_2$ band has a shell-model-like structure with less collectivity than the ground band [6]. The $K^{\pi}=0^+_3$ band has been discussed to have a $^{12}\text{C}+2\alpha$ structure [6] which has been recently supported by an AMD calculation [61].

2.3.4.3 Projection Operator onto the Cluster Model Space

The projection operator onto the cluster model space can be constructed by using the eigenvalues and eigenfunctions of the RGM norm kernel N_K [63]. Here we explain a practical method of numerical construction of the projection operator onto the cluster model space spanned by the wave functions of the form $\mathscr{A}\{\chi_L(r)Y_L(\hat{r})\phi(C_1)\phi(C_2)\}$ with r standing for the relative coordinate between clusters C_1 and C_2 . We first prepare sufficient number of Brink wave functions $\{\Psi_L(R_i), (i=1\sim N)\}$,

$$\Psi_L(R) = D(R)P_L \mathcal{A}\{\psi(C_1, n_1r)\psi(C_2, n_2r)\} = \Phi_L(R)g(X_G, A\nu),$$
 (2.72)

$$\Phi_L(R) = D(R)P_L \mathcal{A}\{g(r-r, A_r \nu)\phi(C_1)\phi(C_2)\}$$
(2.73)

$$n_1 = \frac{A_2}{A}, \quad n_2 = -\frac{A_1}{A}, \quad A_r = \frac{A_1 A_2}{A}, \quad A = A_1 + A_2,$$
 (2.74)

where P_L is the projection operator of angular momentum, D(R) is normalization constant, and A_1 and A_2 are mass numbers of the clusters C_1 and C_2 , respectively. The functional space spanned by $\{\Phi_L(R_i), (i=1 \sim N)\}$ is intended to be approximately the same as the cluster model space under consideration. The orthonormal basis wave functions $\{\hat{\Phi}_L^i, (i=1 \sim N)\}$ of this functional space are obtained by diagonalizing the overlap matrix $\{A_{ij}\}$ with orthogonal matrix $\{e_{ij}\}$,

$$\hat{\Phi}_L^i = \frac{1}{\sqrt{\mu_i}} \sum_{i=1}^N e_{ij} \Phi_L(R_j), \quad \sum_{i=1}^N A_{ij} e_{kj} = \mu_k e_{ki}, \tag{2.75}$$

$$A_{ij} = \langle \Phi_L(R_i) | \Phi_L(R_j) \rangle = \langle \Psi_L(R_i) | \Psi_L(R_j) \rangle. \tag{2.76}$$

The desired projection operator P onto the cluster model space and the percentage W^I of the $C_1 + C_2$ cluster component of a given wave function Φ are approximately calculated as

$$P = \sum_{i=1}^{N} |\hat{\Phi}_L^i\rangle\langle\hat{\Phi}_L^i| = \sum_{i,j=1}^{N} (A^{-1})_{ij} |\Phi_L^i\rangle\langle\Phi_L^j|, \qquad (2.77)$$

$$W^{J} = \langle \Phi | P | \Phi \rangle = \sum_{i,i=1}^{N} (A^{-1})_{ij} \langle \Phi | \Phi_{L}^{i} \rangle \langle \Phi_{L}^{i} | \Phi \rangle. \tag{2.78}$$

2.4 Coexistence of Cluster Structure and Superdeformation in Heavy sd-Shell and Light pf-Shell Nuclei

Studies of cluster states in heavy *sd*-shell and light *pf*-shell nuclei have been pursued by many authors but microscopic studies have not been so extensive as in light *sd*-shell and *p*-shell nuclei. One of the characteristic features of the studies of clustering in this mass number region is the study of molecular resonances in somewhat high excitation energy region [64–66]. Recently a new stimulation has been brought to this subject by the accumulation of the experimental knowledge of superdeformed and hyperdeformed states in this mass number region which is by the use of powerful gamma detectors used in heavier mass regions. Representative examples are for nuclei like ³⁶Ar [67], ³⁸Ar [68], ⁴⁰Ca [69], and ⁴⁴Ti [70]. For the study of the coexistence of cluster states and mean-field-type states, the study of the interrelation between superdeformed states and cluster states including molecular resonances is a very important new subject to be investigated more in future. In this lecture we discuss this subject in two nuclei, ⁴⁴Ti and ³²S.

2.4.1 44Ti Case

2.4.1.1 ⁴⁰Ca + α Cluster States and Superdeformed States

The ⁴⁴Ti nucleus is the *pf*-shell analogue of the nucleus ²⁰Ne and several studies by using microscopic ⁴⁰Ca + α cluster wave function were performed [71–73]. An important knowledge on the ⁴⁰Ca + α structure in ⁴⁴Ti was obtained by using the unique ⁴⁰Ca + α potential which was derived by fitting the anomalous large angle scattering (ALAS) and nuclear rainbow phenomena of ⁴⁰Ca + α elastic scattering [66, 74]. The lowest 0⁺ state of this potential was found to be located about 4 MeV below the ⁴⁰Ca + α threshold which is near the experimental ground state located about 5 MeV below the threshold ($E_{th} = 5.14$ MeV). This result suggested that the ground state contains large component of ⁴⁰Ca + α cluster structure [75–77]. Similar conclusion was obtained by the ⁴⁰Ca + α RGM study of Ref. [78]. In this RGM study the parameters of the effective nuclear force were chosen so as to reproduce the observed elastic scattering cross sections in a wide energy range by using the same imaginary potential as Ref. [74]. Then this RGM calculation proved to give the lowest 0⁺ state near the experimental ground state.

An important experimental finding which supports the existence of the $^{40}\text{Ca} + \alpha$ cluster structure in ^{44}Ti was obtained by the α transfer experiment on ^{40}Ca [80]. This transfer experiment confirmed the existence of the negative-parity rotational band with $K^{\pi} = 0^{-}$ which has the $^{40}\text{Ca} + \alpha$ cluster structure. The band head 1^{-} level was found at \sim 7 MeV and band member states were found to have large α spectroscopic factors. As are the cases of the $^{12}\text{C} + \alpha$ structure in ^{16}O and the $^{16}\text{O} + \alpha$ structure in ^{20}Ne , the existence of the negative-parity rotational band with

 $K^{\pi}=0^{-}$ is a necessary condition in order for the $^{40}{\rm Ca}$ + α cluster structure to exist.

The two low-lying rotational bands, one with $K^{\pi}=0^+_2$ upon 0^+_2 state at 1.90 MeV and the other with $K^{\pi}=2^+$ upon 2^+ state at 2.89 MeV, are now suggested to be a superdeformed band and its side band, respectively [70]. The low spin members of these bands have been known since long [81, 82] and recently their high spin members were found to extend up to $J^{\pi}=12^+$ states. Shell model calculation assigned 8-particle four-hole configuration to this superdeformed band [83], and mean-field-type calculations confirmed the appearance of low-lying 8-particle four-hole band [84, 85] with superdeformation. On the other hand some cluster model studies assume $^{40}\text{Ca}^*+\alpha$ cluster structure to this band [77, 86, 87] with $^{40}\text{Ca}^*$ standing for the 0^+_2 and 2^+_1 states assumed to have $^{36}\text{Ar}+\alpha$ cluster structure.

2.4.1.2 AMD Study of ⁴⁴Ti

AMD study of ⁴⁴Ti in Ref. [8] has contributed for the clarification of the actual coexistence features of ⁴⁰Ca + α cluster states and mean-field-type states including superdeformed states.

Figure 2.17 shows good reproduction of the observed energy spectra by the calculation of Ref. [88]. Table 2.10 shows that the E2 transitions, intra-band transitions inside the ground band and two superdeformed bands with $K^{\pi}=0^{+}_{2}$ and $K^{\pi}=2^{+}$ and also the inter-band transitions between $K^{\pi}=0^{+}_{2}$ and $K^{\pi}=2^{+}$ bands, are well reproduced by the calculation of Ref. [88] without use of any effective charge.

Table 2.10 B(E2) (e^2 fm²) in ⁴⁴Ti compared with AMD calculation [88]

$J_i^\pi o J_f^\pi$	EXP	AMD
$[K^{\pi}=0_1^+]$		
$2_1^+ ightarrow 0_1^+$	120 ± 30	142
$4_1^+ \rightarrow 2_1^+$	280 ± 60	222
$6_1^+ \rightarrow 4_1^+$	160 ± 30	167
$8_1^+ \to 6_1^+$	14>	172
$10_1^+ \to 8_1^+$	140 ± 30	99
$12_1^+ \rightarrow 10_1^+$	40 ± 8	69
$K^{\pi}=2^{+}\rightarrow K^{\pi}=0$	0_{2}^{+}]	
$2^+_3 ightarrow 0^+_2$	43<	24
$[K^{\pi}=0_2^+]$		
$2_2^+ ightarrow 0_2^+$	220 ± 50	320
$4_2^+ \rightarrow 2_2^+$	268 ± 50	361
$K^{\pi} = 2^{+}$		
$3_3^+ ightarrow 2_3^+$	< 590	298
$4_3^+ \rightarrow 2_3^+$	175^{+100}_{-60}	220
$4_3^+ \to 3_1^+$	$< 785 \pm 650$	302

Figure 2.18 gives positive-parity energy curves with respect to the quadrupole deformation parameter β . We see, in addition to the minimum-energy point near $\beta = 0.2$ which corresponds to the ground band, the existence of the minimumenergy points near $\beta = 0.5$ which correspond to two superdeformed bands with $K^{\pi} = 0^{+}_{2}$ and $K^{\pi} = 2^{+}$. The calculated superdeformed bands have the wave function with $4\hbar\omega$ excitation (four particle jump from deformed sd to pf). The superdeformed state is triaxially deformed ($\gamma = 0.25$). In the case of the negativeparity energy curves, we see three minimum-energy points for $J^{\pi} = 1^{-}$ states with $K^{\pi} = 0^{-}$ in the low excitation energy region. The highest minimum-energy point is located near $\beta = 0.27$ and corresponds to the 40 Ca + α cluster state. The other two minimum-energy points around $\beta = 0.25$ and 0.4 correspond to structures with dominantly $1\hbar\omega$ and $3\hbar\omega$ excitations, respectively. In Fig. 2.18 we give the density distributions of the intrinsic wave functions of the $J^{\pi} = 1^{-}$ state with $K^{\pi} = 0^{-}$ near $\beta = 0.27$. This density distribution clearly shows the 40 Ca + α structure of this state. In this density distribution, the black points show the spatial positions of the centroids of the single-nucleon wave packets of AMD Slater determinant. While the nucleon wave packet centroids are divided clearly into two spatial groups for the $K^{\pi} = 0^{-}$ band, we do not see clear division of the nucleon wave packet centroids for the ground and $4\hbar\omega$ -jump bands. Thus the superdeformed states in ⁴⁴Ti are mean-field-type states and do not have clear clustering structure. It is reported in Ref. [88] that, if nucleon wave packets are not allowed to deform, the AMD wave function around the superdeformed deformation β has 36 Ar + 2 α structure.

In Table 2.11 we show the squared amplitudes W^{J} of the 40 Ca + α component of the ground band states. The definition of W^{J} is given in Sect. 2.3.4.3. W^{J} values of the ground band are about 40% for low spin members which are fairly smaller

Table 2.11 Squared amplitudes of 40 Ca + α component W^{J} and α spectroscopic factor S_{α} by AMD calculation [88]

J^{π}	W^{J}	S_{α}	$(S_{\alpha})_{exp}$	J^{π}	W^{J}	S_{α}
[ground]				[N = 14]	.]	,
0+	0.39	0.14	0.20	0+	0.46	0.22
2+	0.34	0.12	0.20	2+	0.42	0.23
4+	0.32	0.12	0.18	4+	0.38	0.19
6+	0.25	0.09	0.16	6+	0.30	0.17
8+	0.21	0.08	0.13	8+	0.21	0.13
10 ⁺	0.06	0.01		10 ⁺	0.12	0.08
12+	0.06	0.00				
[N = 13]				[N = 15]]	
1-	0.56	0.20	0.25	1-	0.63	0.34
3-	0.50	0.18	0.37	3-	0.59	0.32
5^{-}	0.43	0.16	0.30	5^-	0.56	0.31
7^{-}	0.38	0.12		7-	0.48	0.28
9-	0.32	0.10		9-	0.35	0.20

For ground and N = 13 bands S_{α} are compared with experiments

than the W^I values of the $^{16}{\rm O}$ + α component in the low spin members of the ground band of $^{20}{\rm Ne}$. But still they are of sizable magnitude in view of the density distributions of the ground band states which do not show clear clustering feature. For this sizable magnitude of W^I of the ground band, the following relation due to the Bayman–Bohr theorem makes a large contribution:

$$|^{40}\text{Ca}, (0f, 1p)^{4}; (12, 0)L\rangle = D_{L} \mathscr{A} \left\{ R_{12,L}(r_{\text{Ca}-\alpha}, (40/11)\nu) Y_{L}(\hat{r}_{\text{Ca}-\alpha}) \phi(\alpha) \phi(^{40}\text{Ca}) \right\} \times g(X_{G}, 40\nu).$$
(2.79)

The smaller W^J value of the 40 Ca + α component in 44 Ti than the W^J value of the 16 O + α component in 20 Ne is reasonable because the spin-orbit effect is much stronger than in 20 Ne and the core nucleus 40 Ca is much larger than the 16 O core in 20 Ne. As seen in the above equality due to the Bayman–Bohr theorem, the 40 Ca – α relative wave functions contained in the ground band states have the value 12 for the quantum number N = 2n + L with n standing for the number of nodes.

The percentage W^J of the $^{40}\text{Ca} + \alpha$ component of the $K^\pi = 0^-$ band which has $^{40}\text{Ca} + \alpha$ density distribution is larger than the ground band and is about 56% for the band head 1^- state but it decreases to about 32% for the 9^- state. The expectation value of the two-body spin-orbit force is -9.5 MeV for the ground state while it is -4.3 MeV for the band head 1^- state of the $K^\pi = 0^-$ band, which is the reflection of the smaller breaking of the spatial symmetry of the $K^\pi = 0^-$ band. The $^{40}\text{Ca} - \alpha$ relative wave functions contained in the $K^\pi = 0^-$ band states have the value 13 for the quantum number N = 2n + L, and hence in Table 2.11 this band is called the N = 13 band. In Table 2.11 we see good reproduction of the observed spectroscopic factor of $^{40}\text{Ca} + \alpha$ by AMD for the ground and N = 13 bands.

The AMD calculation gives excited bands with $K^{\pi}=0^+$ and $K^{\pi}=0^-$ which have $^{40}\text{Ca}+\alpha$ component with respective percentage numbers 46 and 63% for the band head 0^+ and 1^- states. The $^{40}\text{Ca}+\alpha$ components of these $K^{\pi}=0^{\pm}$ bands have one more nodal points than the lower $K^{\pi}=0^{\pm}$ bands in their $^{40}\text{Ca}-\alpha$ relative wave functions, namely N=14 and 15, respectively. Therefore, in Table 2.11 these bands are called the N=14 and 15 bands, respectively. The N=14 and 15 bands are called higher nodal $K^{\pi}=0^{\pm}$ bands. In Ref. [80] the higher nodal $K^{\pi}=0^{\pm}$ bands are reported to be observed experimentally, and they are shown in Fig. 2.17.

In the ground state of ⁴⁴Ti, the ⁴⁰Ca + α component is contained by only about 40%. But the AMD calculation does not give any other 0⁺ state which has larger percentage of ⁴⁰Ca + α component with N=12 below the higher nodal 0⁺ state. Thus we are allowed to say that the parity inversion partner of the observed $K^{\pi}=0^{-}$ band built upon the 1⁻ state around 7 MeV is the ground band. The higher nodal $K^{\pi}=0^{\pm}$ bands can be regarded as the excited bands which are formed by the activation of the ⁴⁰Ca - α clustering degree of freedom embedded in the ground band.

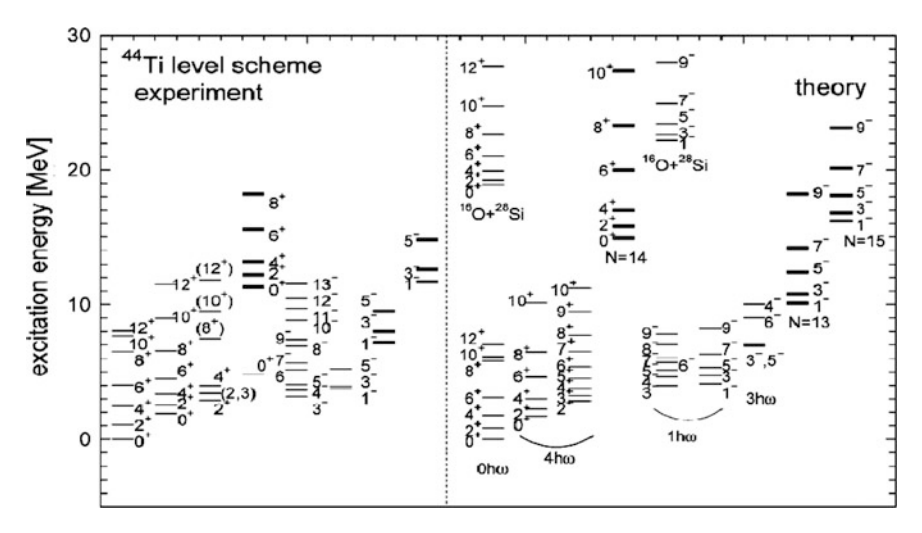


Fig. 2.17 Energy spectra of ⁴⁴Ti by AMD [88]. $(E_{th})_{exp}$ for ⁴⁰Ca + α breakup is 5.14 MeV

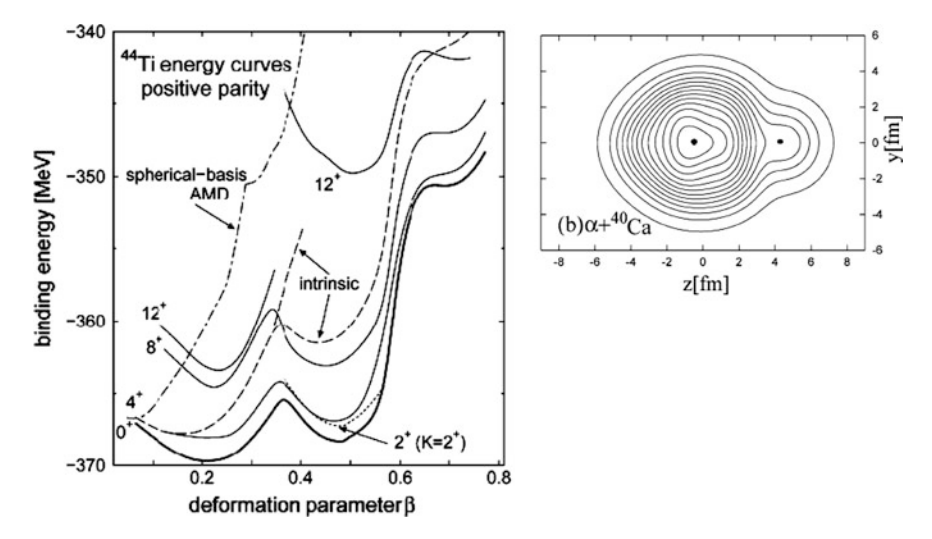


Fig. 2.18 Energy curves of positive-parity AMD states of 44 Ti with respect to quadrupole deformation and the density distribution of the intrinsic AMD wave function of the $J^{\pi}=1^-$ state of $K^{\pi}=0^-$ band [88]

2.4.2 ³²S Case

2.4.2.1 Superdeformed States and ¹⁶O + ¹⁶O Molecular Resonance States

In 32 S, many mean-field calculations predict the presence of the band with doubly superdeformed magic structure whose band head 0^+ state is located near

 $E_x=10$ MeV [89–91], although no definite experimental information has been obtained until now. The intrinsic state has a configuration with four nucleons raised into the deformed intruder orbit coming down from pf shell. The density distribution of this intrinsic state wave function looks like that of $^{16}O + ^{16}O$ molecular configuration. The microscopic study of the $^{16}O + ^{16}O$ molecular structure has been made by many authors [92–98], which is partly because the cluster system of two double-closed-shell nuclei is of fundamental importance and partly because the $^{16}O + ^{16}O$ molecular resonances were experimentally observed [99]. However, it was not easy to give any definite suggestion from microscopic theory to the $^{16}O + ^{16}O$ molecular resonance phenomena.

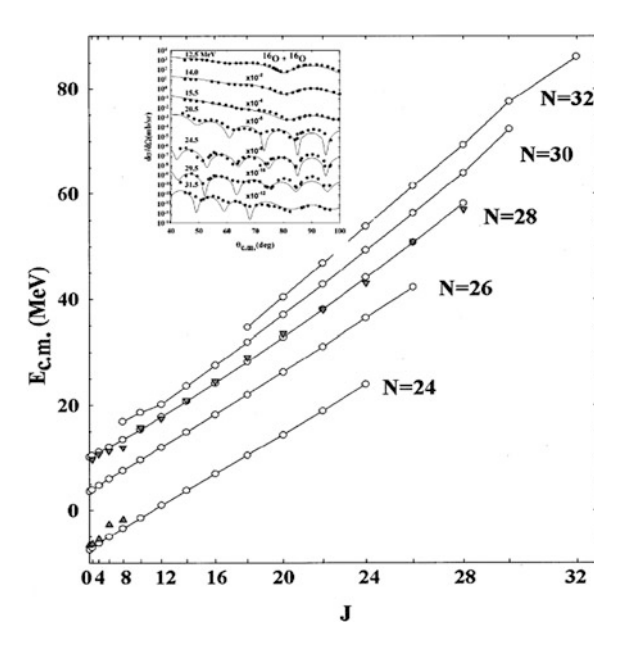
An important progress in the study of $^{16}O + ^{16}O$ system was made at the end of 80's, which was the discovery of the nuclear rainbow phenomena in the $^{16}O + ^{16}O$ elastic scattering [100]. This discovery made possible the derivation of unique $^{16}O - ^{16}O$ potential by Kondo and his coworkers [101, 102]. This unique potential proved to be deep contrary to the very shallow potentials long used to describe low energy scattering [99]. Additional measurements and calculations reinforced this deep potential picture for this $^{16}O - ^{16}O$ system [103–105] and neighboring systems like $^{12}C - ^{12}C$ and $^{12}C - ^{16}O$ [106]. Thus after years of controversy about the nature of the inter-nucleus potential, it is now definitely agreed that the potential is deep [17, 106, 107].

Recently it was argued, by calculating the eigenstates of the unique $^{16}O - ^{16}O$ potential, that the band of observed $^{16}O - ^{16}O$ molecular resonance states corresponds to the calculated rotational band having the number of N = 2n + L = 28 of the $^{16}O - ^{16}O$ relative motion with respect to the excitation energy [108] as shown in Fig. 2.19. Here n and L are the number of nodes and angular momentum of the relative wave function, respectively. Furthermore it was argued that the lowest rotational band having the lowest Pauli-allowed number of N = 2n + L = 24 has its band head 0^+ state at about 10 MeV in excitation energy (Fig. 2.19).

2.4.2.2 AMD Study of ³²S

AMD study of 32 S [109] teaches us how superdeformed states can be related to the molecular states. The AMD calculation by the use of the Gogny D1S force gives almost the same answer for the superdeformed excited rotational band as the Hartree–Fock calculations (Fig. 2.20). It is here to be noted that the minimum energy by the 16 O + 16 O Brink wave function is calculated to be higher by about 10 MeV than the superdeformed 0^+ . The Hill-Wheeler calculation by superposing the states on the AMD energy curve gives the refined superdeformed band and other two higher-lying rotational bands in addition to the ground state and low-lying excited states as shown in Fig. 2.21. The 16 O + 16 O component contained in the superdeformed band head state is about 42% and those contained in other two higher-lying rotational band head states

Fig. 2.19 Several lowest molecular bands calculated with unique $^{16}O - ^{16}O$ potential (circle points) [108]. Filled triangle points are averaged energy positions of observed $^{16}O + ^{16}O$ resonances. Observed angular distributions (dots) in the inset are from Ref. [99]



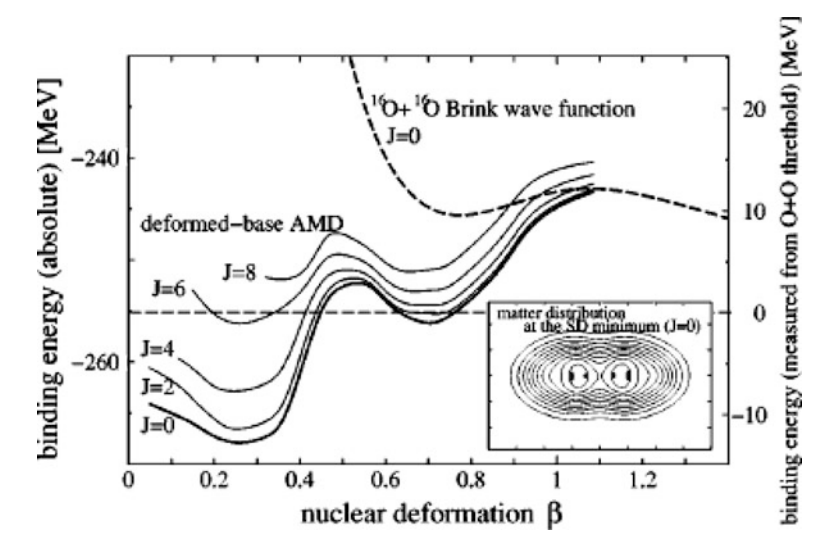
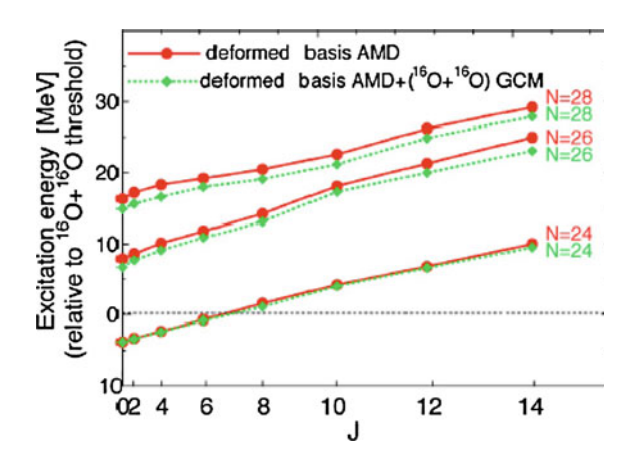


Fig. 2.20 Energy curves of ³²S with respect to quadrupole deformation by AMD [109]

are 71 and 73%. The expectation values of the two-body spin-orbit force are -4.5, -3.2, and -2.8 MeV for the superdeformed and two higher-lying band head states, respectively. The $^{16}O + ^{16}O$ components contained in the

98 H. Horiuchi

Fig. 2.21 Superdeformed rotational band and two excited bands in ³²S by AMD [109]



superdeformed and high-lying bands have the $^{16}O - ^{16}O$ relative wave functions whose number of N = 2n + L are 24, 26, and 28, respectively.

For the magnitude, about 42%, of the $^{16}O + ^{16}O$ component in the superdeformed band head state, the following relation due to the Bayman–Bohr theorem makes a large contribution:

$$(0,0,0)^{4}(1,0,0)^{4}(0,1,0)^{4}(0,0,1)^{4}(1,0,1)^{4}(0,1,1)^{4}(0,0,2)^{4}(0,0,3)^{4}$$

$$= n\mathscr{A}\left\{X_{(0,0,24)}(r_{O-O},8\nu)\phi(^{16}O)\phi(^{16}O)\right\}g(X_{G},32\nu).$$
(2.80)

In Ref. [109] the Hill-Wheeler calculation was made in wider basis space by adopting $^{16}O + ^{16}O$ Brink wave functions in addition to the basis states on the AMD energy curve (Fig. 2.21). This improved Hill-Wheeler calculation gave only little change to the superdeformed band; the energy gain was very small and the percentage of the $^{16}O + ^{16}O$ component contained in the superdeformed band head state changed from about 42 to about 44%. However the improved Hill-Wheeler calculation gave rather large change to the two higher-lying bands, namely the percentages of the $^{16}O + ^{16}O$ components contained in these two band head states changed from about 71 and 73% to about 90 and 98%, respectively, although the energy gains for these two bands were rather small. The higher band with N=28 is thus almost pure $^{16}O + ^{16}O$ molecular band.

When we compare three bands of AMD with N=24, 26, and 28 with the three bands of unique $^{16}O-^{16}O$ potential, we see good correspondence between them in excitation energies. Especially we can regard the AMD band with N=28 as corresponding to the band of observed molecular resonances of $^{16}O+^{16}O$. The AMD study teaches us that the $^{16}O+^{16}O$ molecular resonance band is formed by the activation of the $^{16}O-^{16}O$ clustering degree of freedom embedded in the super-deformed band.

2.5 Structure Change Between Cluster States and Mean-Field-Type States

2.5.1 Dual Character of Nuclear Wave Function

In previous sections we discussed the Bayman–Bohr theorem for the wave functions of the ground states of ⁸Be, ¹²C, ¹⁶O, ²⁰Ne, and ⁴⁴Ti, and for that of the superdeformed excited state of ³²S. This theorem says that the nuclear many-body wave function possesses two faces, face of 'mean-field-type structure' and face of 'cluster structure'. This fact may look like only a mathematical feature of the wave function. But it also represents a physical feature. It is because there do exist two kinds of excitation modes on the basis of this dual nature of the wave function. We below summarize what we discussed in previous sections in this lecture from this viewpoint.

In ${}^8\text{Be}$ we discussed Bayman–Bohr theorem for the ground state, but the ground state is a 2α cluster state rather than a mean-field-type state. In this nucleus, beyond the Bayman–Bohr theorem which compares the SU(3) shell model wave function with the cluster model wave function, the deformed Hartree–Fock wave functions for several types of Skyrme forces were compared with the 2α cluster wave function [111]. The result showed that the Hartree–Fock wave functions contain a large amount of the 2α component (W^I of Sect. 2.3.4.3) more than 97%. It is desirable to compare the Hartree–Fock wave functions with the optimum (minimum energy) 2α cluster wave function.

In ¹²C, the ground state wave function is known to contain large amount of the SU(3) shell model wave function $|(0s)^4(0p)^8, (\lambda, \mu) = (04)J = 0\rangle$. According to the Bayman–Bohr theorem, this wave function is equivalent to a 3α cluster wave function as follows,

$$|(0s)^{4}(0p)^{8}, (\lambda, \mu) = (04)J = 0\rangle$$

$$= N_{0} \mathscr{A} \left\{ R_{4,0}(\xi_{1}, (8/3)\nu) R_{4,0}(\xi_{2}, 2\nu) \phi(\alpha_{1}) \phi(\alpha_{2}) \phi(\alpha_{3}) \right\} \quad (2.81)$$

$$\times g(X_{G}, 12\nu),$$

where $\xi_1 = X_1 - (X_2 + X_3)/2$, $\xi_2 = X_2 - X_3$, and X_i stands for the center-of-mass coordinate of ith α cluster. Since the Hoyle state can be well described by the wave function $\mathscr{A}\{P_A \exp(-(4/(3B^2))\xi_1^2 - (1/B^2)\xi_2^2)\phi(\alpha_1)\phi(\alpha_2)\phi(\alpha_3)\}$ with P_A standing for the projection operator onto the functional space having the number of oscillator quanta larger than 8, the formation of the Hoyle state can be regarded to be the excitation of the 3α relative wave function from $R_{4,0}(\xi_1, (8/3)\nu) R_{4,0}(\xi_2, 2\nu)$ of the ground state to $P_A \exp(-(4/(3B^2))\xi_1^2 - (1/B^2)\xi_2^2)$ of the Hoyle state. On the other hand, there is, of course, mean-field-type excitation of the ground state as is typically seen in the formation of the 1^+ excited state at 12.7 MeV having non-zero intrinsic spin S=1.

100 H. Horiuchi

In ¹⁶O, it has been long known that the excited states of 3_1^- , 1_1^- , 2_1^- , 0_1^- , are dominantly of the structure of 1-particle 1-hole, namely they are the excited states due to the mean-field-type excitation mode. At the same time, as we described in section 3, it is now well known that lot of excited states including 0_2^+ , 2_1^+ , 2_2^+ , 4_1^+ , 6_1^+ , 1_2^- , 3_2^- , 5_1^- , 7_1^- , are dominantly of the cluster structure of ¹²C + α described by the wave function of the form $\mathscr{A}\{\chi_{\ell,L,J}(r_{C-\alpha})[Y_{\ell}(\hat{r}_{C-\alpha}) \phi_L(^{12}C)]_J\phi(\alpha)\}$. Since the Bayman–Bohr theorem assures that the double-closed-shell wave function of the ground state is equivalent to ¹²C + α cluster wave function as,

$$\det |(0s)^{4}(0p)^{12}| = c_{L} \mathscr{A} \Big[R_{4,L}(r_{C-\alpha}, 3\nu) \Big[Y_{L}(\hat{r}_{C-\alpha}) \phi_{L}(^{12}C) \Big]_{J=0} \phi(\alpha) \Big] \times g(X_{G}, 16\nu),$$
(2.82)

where L is arbitrary among L=0, 2, and 4, the formation of $^{12}\mathrm{C}+\alpha$ cluster states can be regarded to be the excitation of the $^{12}\mathrm{C}-\alpha$ relative motion from $R_{4,L}(r_{\mathrm{C}-\alpha},3\nu)Y_L(\hat{r}_{\mathrm{C}-\alpha})$ of the ground state to $\chi_{\ell,L,J}(r_{\mathrm{C}-\alpha})Y_\ell(\hat{r}_{\mathrm{C}-\alpha})$ of the cluster states.

In ²⁰Ne, the ground band states contain the ¹⁶O + α component at most 70%. This ¹⁶O + α component is mostly equivalent to SU(3) shell model wave function with $(\lambda, \mu) = (8, 0)$ due to Bayman–Bohr theorem (Eq. (2.61)):

$$|(0s)^{4}(0p)^{12}(1s,0d)^{4};(8,0)L\rangle = C_{L}\mathscr{A}\left\{R_{8,L}(r_{O-\alpha},(16/5)\nu)Y_{L}(\hat{r}_{O-\alpha})\phi(^{16}O)\phi(\alpha)\right\} \times g(X_{G},20\nu).$$
(2.83)

We saw in Sect. 2.3 that the excitations of $^{16}{\rm O}-\alpha$ clustering degree of freedom imbedded in the ground band states give rise to the excited cluster bands, $K^\pi=0^-$ and $K^\pi=0^+_4$ bands which are described by the wave functions of the form $\mathscr{A}\{\chi_L(r_{\rm O-\alpha})Y_L(\hat{r}_{\rm O-\alpha})\phi(^{16}{\rm O})\phi(\alpha)\}$. On the other hand, in $^{20}{\rm Ne}$ there exists the low-lying $K^\pi=2^-$ band having mean-field-type structure. This band is dominantly formed by 1-particle 1-hole excitation of the ground state.

In ⁴⁴Ti, the ground band states contain the ⁴⁰Ca + α component at most 40%. This ⁴⁰Ca + α component is mostly equivalent to SU(3) shell model wave function with $(\lambda, \mu) = (12, 0)$ due to Bayman–Bohr theorem :

$$|^{40}\text{Ca}, (0f, 1p)^{4}; (12, 0)L\rangle = D_{L} \mathscr{A} \Big\{ R_{12,L}(r_{\text{Ca}-\alpha}, (40/11)\nu) Y_{L}(\hat{r}_{\text{Ca}-\alpha}) \phi(^{40}\text{Ca}) \phi(\alpha) \Big\}$$

$$\times g(X_{G}, 40\nu).$$
(2.84)

We saw in Sect. 2.4 that the excitations of $^{40}\text{Ca} - \alpha$ relative motion imbedded in the ground band give rise to the excited cluster bands, $K^{\pi} = 0^{-}$, and N = 14, 15 higher nodal bands which are described by the wave functions of the form $\mathscr{A}\{\chi_L(r_{\text{Ca}-\alpha})Y_L(\hat{r}_{\text{Ca}-\alpha})\phi(^{40}\text{Ca})\phi(\alpha)\}$. On the other hand, in ^{44}Ti there exists the low-lying $K^{\pi} = 3^{-}$ band having mean-field-type structure. This band is

dominantly formed by 1-particle 1-hole excitation of the ground state. Furthermore, there exist two low-lying superdeformed bands with mean-field-type structure formed by four-particle jump.

In 32 S we showed that the superdeformed band contains 16 O + 16 O component by about 44%. This 16 O + 16 O component is mostly equivalent to shell model wave function with 4p - 4h excitation due to Bayman–Bohr theorem :

$$(0,0,0)^{4}(1,0,0)^{4}(0,1,0)^{4}(0,0,1)^{4}(1,0,1)^{4}(0,1,1)^{4}(0,0,2)^{4}(0,0,3)^{4}$$

$$= n\mathscr{A}\left\{X_{(0,0,24)}(r_{\mathrm{O-O}})\phi(^{16}\mathrm{O})\phi(^{16}\mathrm{O})\right\}g(X_{G},32\nu).$$
(2.85)

We explained that the excitation of $^{16}O - ^{16}O$ relative motion imbedded in the superdeformed band gives rise to the $^{16}O + ^{16}O$ molecular resonance band.

From these actual features of the coexistence of cluster states and mean-field-type states in ¹²C, ¹⁶O, ²⁰Ne, ⁴⁴Ti, and ³²S, one may say that the coexistence of cluster structure and mean-field-type structure is rather of logical necessity of the dual character of nuclear wave function. Recently this point has been argued by H. Horiuchi, K. Ikeda, K. Kato, and T. Yamada, who have called this dual nature of nuclear states the Janus nature of nuclei [110]. Of course this mechanism of the coexistence of mean-field type and cluster type states is based on the nature of nuclear force. Nuclear force has strong tensor force which gives rise to tightly bound alpha cluster and it is of course responsible to the formation of the mean field which is close to the harmonic oscillator field.

2.5.2 E0 Transitions Between Ground State and Cluster States in ¹⁶O and ¹²C

An important observable quantity which directly verifies the dual nature of the nuclear wave function expressed by the Bayman–Bohr theorem is the large strength of the monopole transition between shell model type ground state and the excited cluster states. *E*0 transition strengths between ground state and cluster states in light nuclei are actually strong in general with their order of magnitude comparable with single-nucleon strength [112, 113]. This looks strange because cluster states are many-particle many-hole states in the shell model description which implies *E*0 strengths from the ground state are much smaller than the single-nucleon strength.

Below we explain that the above problem of the E0 transition strength can be answered quite naturally by applying the Bayman–Bohr theorem to the ground state wave functions, by explicitly analysing the E0 transitions in ^{16}O and ^{12}C [113]. The observed strengths M(E0) of the E0 transition in ^{16}O are 3.55, 4.03, and 3.3 fm² for $0_2^+ \leftrightarrow 0_1^+, 0_3^+ \leftrightarrow 0_1^+$, and $0_5^+ \leftrightarrow 0_1^+$, respectively, while the observed M(E0) in ^{12}C for $0_2^+ \leftrightarrow 0_1^+$ is 5.4 fm². A rough estimation of the single-nucleon strength $\langle u_f(r)|r^2|u_i(r)\rangle$ is given by $(3/5)R^2$ with R standing for

102 H. Horiuchi

the nuclear radius. This estimation is obtained under the uniform-density approximation of $u(r) \sim \sqrt{3/R^3}$ for $u_i(r)$ and $u_f(r)$. For $R \sim 3$ fm, we have $\langle u_f(r)|r^2|u_i(r)\rangle \sim 5.4$ fm². Another strange point, from shell model viewpoint, about the observed values of M(E0) is the fact that the three excited 0⁺ states of ¹⁶O have very similar magnitude of M(E0) although they have different complicated configurations of many-particle many-hole. The explanation given below also answers to this question.

2.5.2.1 E0 Transitions in ¹⁶O

As we explained in Sect. 2.3, the 0_2^+ and 0_3^+ states can be dominantly described by $^{12}\text{C} + \alpha$ cluster model wave functions, $\mathscr{A}[\chi_0(r_{\text{C}-\alpha})[Y_0(\hat{r}_{\text{C}-\alpha})\phi_0(^{12}\text{C})]_{J=0}\phi(\alpha)]$ and $\mathscr{A}[\chi_2(r_{\text{C}-\alpha})[Y_2(\hat{r}_{\text{C}-\alpha})\phi_2(^{12}\text{C})]_{J=0}\phi(\alpha)]$, respectively. On the other hand, the ground state is dominantly described by the double-closed-shell wave function Φ_{DCS} which is equivalent to $\mathscr{A}[R_{4,L}(r_{\text{C}-\alpha},3\nu)[Y_L(\hat{r}_{\text{C}-\alpha})\phi_L(^{12}\text{C})]_{J=0}\phi(\alpha)]$ with arbitrary L=0,2,4. Therefore the E0 transition between the ground state and a $^{12}\text{C}+\alpha$ cluster state is the transition between the relative wave function $R_{4,L}(r_{\text{C}}-\alpha,3\nu)$ and $\chi_L(r_{\text{C}}-\alpha)$. Actually, in spite of the presence of the antisymmetrization, the E0 transition strength comes only from the relative motion part of the wave function. It means that the E0 transition strength comes only from the E0 operator O(E0, rel.) of the relative motion. In order to verify this, we decompose the total E0 operator O(E0) between zero isospin states as

$$O(E0) = \frac{1}{2} \sum_{i=1}^{16} (r_i - X_G)^2 = O(E0, {}^{12}\text{C}) + O(E0, \alpha) + O(E0, \text{rel.}), \qquad (2.86)$$

$$O(E0,^{12} C) = \frac{1}{2} \sum_{i \in I/C} (r_i - X_C)^2, \quad O(E0,^{12} C) = \frac{1}{2} \sum_{i \in \alpha} (r_i - X_\alpha)^2,$$
 (2.87)

$$O(E0, \text{rel.}) = \frac{1}{2} \frac{12 \times 4}{16} r_{C-\alpha}^2.$$
 (2.88)

We then note the fact that the relative wave function $\chi_L(r_C - \alpha)$ has the harmonic oscillator components whose number of the oscillator quanta is larger than 4 of $R_{4.L}$ ($r_C - \alpha$, 3 ν). From this fact we obtain the following equations,

$$\left\langle \Phi_{\mathrm{DCS}} \middle| \mathscr{A} \left\{ \chi_L(r_{\mathrm{C}-\alpha}) \left[Y_L(\hat{r}_{\mathrm{C}-\alpha}) O(E0,^{12}\,\mathrm{C}) \phi_L(^{12}\mathrm{C}) \right]_{J=0} \phi(\alpha) \right\} \right\rangle = 0, \qquad (2.89)$$

$$\left\langle \Phi_{\rm DCS} | \mathscr{A} \left\{ \chi_L(r_{\rm C-\alpha}) \left[Y_L(\hat{r}_{\rm C-\alpha}) \phi_L(^{12}{\rm C}) \right]_{J=0} O(E0, \alpha) \phi(\alpha) \right\} \right\rangle = 0. \tag{2.90}$$

In these equations use is made of the fact that the numbers of the oscillator quanta of $O(E0, {}^{12}\text{C})$ $\phi_L({}^{12}\text{C})$ and $O(E0, \alpha)$ $\phi(\alpha)$ are not smaller than those of $\phi_L({}^{12}\text{C})$ and

 $\phi(\alpha)$, respectively, because both $\phi_L(^{12}\text{C})$ and $\phi(\alpha)$ have minimum numbers of oscillator quanta for ^{12}C and α nuclei, respectively. We thus obtain for the M(E0)

$$\begin{split} \left\langle \Phi_{\mathrm{DCS}} | O(E0) | \mathscr{A} \left\{ \chi_L(r_{\mathrm{C}-\alpha}) \left[Y_L(\hat{r}_{\mathrm{C}-\alpha}) \phi_L(^{12}\mathrm{C}) \right]_{J=0} \phi(\alpha) \right\} \right\rangle \\ &= \left\langle \Phi_{\mathrm{DCS}} | O(E0) | \mathscr{A} \left\{ O(E0, \mathrm{rel.}) \chi_L(r_{\mathrm{C}-\alpha}) \left[Y_L(\hat{r}_{\mathrm{C}-\alpha}) \phi_L(^{12}\mathrm{C}) \right]_{J=0} \phi(\alpha) \right\} \right\rangle. \end{split}$$

$$(2.91)$$

In Ref. [113], exact analytical formulas of $M(E0,0_2^+\to 0_1^+)$ and $M(E0,0_3^+\to 0_1^+)$ are obtained as

$$M(E0, 0_2^+ \to 0_1^+) = \frac{1}{2} \sqrt{\frac{\tau_{0,4}}{\tau_{0,6}}} \eta_6 \langle R_{40}(r, \nu) | r^2 | R_{60}(r, \nu) \rangle, \qquad (2.92)$$

$$M(E0, 0_3^+ \to 0_1^+) = \frac{1}{2} \sqrt{\frac{\tau_{2,4}}{\tau_{2,6}}} \zeta_6 \langle R_{42}(r, \nu) | r^2 | R_{62}(r, \nu) \rangle, \qquad (2.93)$$

$$\tau_{L,N} = \langle \Psi_{L,N} | \mathcal{A} \{ \Psi_{L,N} \} \rangle, \quad \Psi_{L,N} = R_{N,L}(r_{C-\alpha}, 3\nu) \Big[Y_L(\hat{r}_{C-\alpha}) \phi_L(^{12}C) \Big]_{J=0} \phi(\alpha),$$

$$(2.94)$$

$$|0_{2}^{+}\rangle = \sum_{N=6}^{\infty} \eta_{N}(C_{N} \mathscr{A}\{\Psi_{0,N}\}), \quad ||C_{N} \mathscr{A}\{\Psi_{0,N}\}|| = 1,$$
 (2.95)

$$|0_3^+\rangle = \sum_{N=6}^{\infty} \zeta_N(D_N \mathscr{A}\{\Psi_{2,N}\}), \quad ||D_N \mathscr{A}\{\Psi_{2,N}\}|| = 1,$$
 (2.96)

The quantity $\tau_{L,N}$ represents the effect of the antisymmetrization and actually is fairly smaller than unity in general for non large N. However, in the above analytical formulas, quantities $\tau_{L,N}$ appear in the form of ratio, $\tau_{0,4}/\tau_{0,6}$ and $\tau_{2,4}/\tau_{2,6}$, and the magnitudes of these ratios are close to unity, which implies that the effect of antisymmetrization has only little influence on the M(E0) values. The quantities η_6 and ζ_6 are the coefficients of the $2\hbar\omega$ - jump component contained in $|0_2^+\rangle$ and $|0_3^+\rangle$, respectively, and their magnitudes are around 0.4. Note that η_6 and ζ_6 are not percentage quantities, $(\eta_6)^2$ and $(\zeta_6)^2$. The E0 matrix elements of the relative motion, $\langle R_{40}(r,v)|r^2|R_{60}(r,v)\rangle$ and $\langle R_{42}(r,v)|r^2|R_{62}(r,v)\rangle$, are larger than the corresponding E0 matrix elements of the single-nucleon motion, $\langle R_{00}(r,v)|r^2|R_{20}(r,v)\rangle$ and $\langle R_{11}(r,v)|r^2|R_{31}(r,v)\rangle$, by about 50%. We thus see that the order of magnitude of $M(E0,0_2^+\to 0_1^+)$ and $M(E0,0_3^+\to 0_1^+)$ are the same as the single-nucleon strength. Also we see that $M(E0,0_2^+\to 0_1^+)$ and $M(E0,0_3^+\to 0_1^+)$ should have similar magnitude because their analytical formulas are very similar each other.

The numerical values of $M(E0,0_2^+ \to 0_1^+)$ and $M(E0,0_3^+ \to 0_1^+)$ calculated with the above formulas with suitable parameter values are 1.97 fm² and 3.89 fm², respectively. These values are somewhat smaller than the observed values

104 H. Horiuchi

although the order of magnitudes are reproduced. This problem was investigated in Ref. [113], and it was shown that the inclusion of the ground state correlation into the ground state wave function makes the reproduction of the observed values by theory fairly satisfactory. The ground state correlation adopted is the one due to the inter-cluster relative motion, namely the $^{12}C - \alpha$ relative wave function embedded in the ground state is not simply $R_{4,L}$ ($r_C - \alpha$, 3v) but has contributions from higher N components, $R_{N,L}$ ($r_C - \alpha$, 3v), with N > 4. The important point of this result is that the clustering degree of freedom described by the Bayman–Bohr theorem induces the ground state correlation which affects the E0 matrix elements.

2.5.2.2 E0 Transitions in ¹²C

In Ref. [113] similar analytical formula of M(E0) was derived for the transition between the ground state and the 0_2^+ state of 12 C (Hoyle state) as follows

$$M(E0, 0_2^+ \to 0_1^+) = \sqrt{\frac{7}{6}} \sqrt{\frac{\langle F_4 \rangle}{\langle F_5 \rangle}} \sigma_5 \langle R_{40}(r, \nu) | r^2 | R_{60}(r, \nu) \rangle,$$
 (2.97)

$$\langle F_n \rangle = \langle Q_n | \mathscr{A} \{ Q_n \} \rangle, \quad Q_n = F_n(\xi_1, \xi_2) \phi(\alpha_1) \phi(\alpha_2) \phi(\alpha_3),$$
 (2.98)

$$F_n(\xi_1, \xi_2) = \frac{1}{4\pi} \sum_{n_1 + n_2 = n} \sqrt{\frac{(2n_1 + 1)!!(2n_2 + 1)!!}{2n_1!!2n_2!!}} R_{2n_1,0}(\xi_1, (8/3)\nu) R_{2n_2,0}(\xi_2, 2\nu),$$
(2.99)

$$|0_2^+\rangle = \sum_{n=5}^{\infty} \sigma_n(e_n \mathcal{A}\{Q_n\}), \quad ||e_n \mathcal{A}\{Q_n\}|| = 1,$$
 (2.100)

Here, as before, $|(0s)^4(0p)^8, (04)J = 0\rangle$ was adopted as the ground state wave function, and $\mathscr{A}\{P_A \exp(-(4/(3B^2))\xi_1^2 - (1/B^2)\xi_2^2)\phi(\alpha_1)\phi(\alpha_2)\phi(\alpha_3)\}$ was adopted for the Hoyle state. Applying the Bayman–Bohr theorem to the ground state, the *E*0 transition is shown to be the transition of the 3α relative wave function between $R_{4,0}(\xi_1, (8/3)\nu)$ $R_{4,0}(\xi_2, 2\nu)$ and $P_A \exp(-(4/(3B^2))\xi_1^2 - (1/B^2)\xi_2^2)$ by the *E*0 operator of relative motion $O(E0, \text{ rel.}) = (4/3)\xi_1^2 + \xi_2^2$.

The quantity $\langle F_n \rangle$ represents the effect of the antisymmetrization but in the above analytical formula, it appears in the form of ratio, $\langle F_4 \rangle / \langle F_5 \rangle$, whose magnitude is close to unity. Thus the effect of antisymmetrization has only little influence on the M(E0) value like in the case of ¹⁶O. The quantity σ_5 is the amplitude of the $2\hbar\omega$ -jump component contained in $|0_2^+\rangle$ and its magnitude is around 0.25. The E0 matrix element of the relative motion, $\langle R_{40}(r,v)|r^2|R_{60}(r,v)\rangle$, is the same as in ¹⁶O, and hence it is larger than the corresponding E0 matrix elements of the single-nucleon motion, $\langle R_{00}(r,v)|r^2|R_{20}(r,v)\rangle$ and $\langle R_{11}(r,v)|r^2|R_{31}(r,v)\rangle$, by about 50%. We thus

obtain the same result as in 16 O that the order of magnitude of $M(E0, 0_2^+ \to 0_1^+)$ is the same as the single-nucleon strength.

The numerical value of $M(E0,0^+_2\to0^+_1)$ calculated with the above formula with suitable parameter values is 1.3 fm². This value is smaller than the observed value although the order of magnitude is reproduced. In Ref. [113], there was given the same conclusion as in ^{16}O that the clustering degree of freedom described by the Bayman–Bohr theorem induces the ground state correlation which makes the magnitude of the calculated E0 matrix element close to the observed value.

2.6 Summary

(1) Actual features of coexistence of cluster states and mean-field-type states were discussed in six self-conjugate nuclei, ⁸Be, ¹²C, ¹⁶O, ²⁰Ne, ⁴⁴Ti, and ³²S. (2) In many cases detailed studies with AMD were utilized. The existence of the nucleon spin alignment in higher spin members of rotational bands even with prominent clustering character is one of the interesting features of coexistence of cluster dynamics and mean-field-type dynamics. (3) Rather large percentage of clustering components in the ground bands of ²⁰Ne and ⁴⁴Ti (about 70 and 40% for ground states of ²⁰Ne and ⁴⁴Ti, respectively) and the superdeformed bands in ³²S (about 40% for band-head), is largely due to the Bayman–Bohr theorem. (4) All the excited states with cluster structure discussed in this lecture can be considered to be formed by the excitation of the clustering degrees of freedom embedded in the ground states (superdeformed state in ³²S) which is described by the Bayman-Bohr theorem. (5) An important evidence of the dual nature of ground state wave function described by the Bayman-Bohr theorem was shown to be given by the fact that lots of E0 transitions between cluster states and ground state in ¹⁶O and ¹²C are rather strong comparable to the single-nucleon strength. (6) Coexistence of cluster states and mean-field-type states was discussed to be rather of logical necessity due to the dual character of nuclear wave function.

References

- 1. H. Horiuchi, J. Phys. Conf. Ser. 111, 012054 (2008)
- 2. Y. Kanada-En'yo, M. Kimura, H. Horiuchi, CDR Physique 4, 497 (2003)
- 3. K. Wildermuth, W. McClure, Springer Tracts in Modern Physics, vol. 41, (Springer, Berlin, 1966)
- 4. K. Wildermuth, Y.C. Tang, *Unified Theory of the Nucleus, Clustering Phenomena in Nuclei*, Vieweg, Braunschweig (1977)
- Y. Abe, Y. Akaishi, H. Bandō, J. Hiura, H. Horiuchi, K. Ikeda, M. Kamimura, T. Marumori, S. Nagata, F. Nemoto, Y. Suzuki, K. Takada, N. Takigawa, R. Tamagaki, H. Tanaka, Prog. Theor. Phys. Suppl. 52 (1972)

106 H. Horiuchi

 Y. Abe, Y. Fujiwara, H. Furutani, H. Horiuchi, K. Ikeda, M. Kamimura, K. Katō, H. Kanada, T. Kaneko, Y. Kondō, T. Matsuse, S. Nagata, H. Nishioka, S. Okabe, S. Saito, T. Sakuda, M. Seya, Y. Suzuki, A. Tohsaki-Suzuki, E. Uegaki, Prog. Theor. Phys. Suppl. 68 (1972)

- 7. H. Horiuchi, K. Ikeda, *International Review of Nuclear Physics*, vol.4, (World Scientific, Singapore, 1986), p. 1
- 8. W. von Oertzen, M. Freer, Y. Kanada-En'yo, Phys. Rep. 432, 43 (2006)
- 9. A. Doté, H. Horiuchi, Y. Kanada-En'yo, Phys.Rev. C 56, 1844 (1997)
- 10. Y. Kanada-En'yo, H. Horiuchi, Prog. Theor. Phys. Suppl. 142, 205 (2001)
- 11. D.M. Brink, *Proceedings of the International School of Physics Enrico Fermi* **36** (Academic Press, New York, 1966), p. 247
- 12. B.F. Bayman, A. Bohr, Nucl. Phys. 9, 596 (1958/1959)
- 13. S. Saito, Prog. Theor. Phys. 41, 705 (1969)
- 14. S. Saito, Prog. Theor. Phys. Suppl. 62, 11 (1977)
- 15. R. Tamagaki, H. Tanaka, Prog. Theor. Phys. 34, 191 (1965)
- 16. I. Shimodaya, R. Tamagaki, H. Tanaka, Prog. Theor. Phys. 27, 793 (1962)
- 17. H. Horiuchi, in *Trends in Theoretical Physics* vol. 2, eds. by P.J. Ellis, Y.C. Tang (Addison-Wesley, Redwood, 1991), p. 277
- Y. Funaki, H. Horiuchi, A. Tohsaki, P. Schuck, G. Röpke, Prog. Theor. Phys. 108, 297 (2002)
- 19. R.B. Wiringa, S.C. Pieper, J. Carlson, V.R. Pandharipande, Phys. Rev. C 62, 014001 (2000)
- 20. F. Hoyle, Astrophys. J. Suppl. 1, 121 (1954)
- 21. C.W. Cook, W.A. Fowler, C.C. Lauritzen, T. Lauritzen, Phys. Rev. 107, 508 (1957)
- 22. P. Navrátil, J.P. Vary, B.R. Barrett, Phys. Rev. Lett. 84, 5728 (2000)
- 23. P. Navrátil, J.P. Vary, B.R. Barrett, Phys. Rev. C 62, 054311 (2000)
- 24. H. Morinaga, Phys. Rev. 101, 254 (1956)
- 25. H. Morinaga, Phys. Lett. **21**, 78 (1966)
- 26. Y. Suzuki, H. Horiuchi, K. Ikeda, Prog. Theor. Phys. 47, 1517 (1972)
- 27. H. Horiuchi, Prog.Theor. Phys. **51**, 1266 (1974)
- 28. H. Horiuchi, Prog. Theor. Phys. 53, 447 (1975)
- 29. Y. Fukushima, M. Kamimura, Suppl. J. Phys. Soc. Jpn. 44, 225 (1978)
- 30. M. Kamimura, Nucl. Phys. A 351, 456 (1981)
- 31. E. Uegaki, S. Okabe, Y. Abe, H. Tanaka, Prog. Theor. Phys. 57, 1262 (1977)
- 32. E. Uegaki, Y. Abe, S. Okabe, H. Tanaka, Prog. Theor. Phys. 59, 1031 (1978)
- 33. E. Uegaki, S. Okabe, Y. Abe, H. Tanaka, Prog. Theor. Phys. 62, 1621 (1979)
- 34. Y. Kanada-En'yo, Phys. Rev. Lett. 81, 5291 (1998)
- 35. T. Neff, H. Feldmeier, Nucl. Phys. A 738, 357 (2004)
- 36. M. Chernykh, H. Feldmeier, T. Neff, P. von Neumann-Cosel, A. Richter, Phys. Rev. Lett. 98, 032501 (2007)
- 37. A. Tohsaki, H. Horiuchi, P. Schuck, G. Röpke, Phys. Rev. Lett. **87**, 192501 (2001)
- 38. G. Röpke, A. Schnell, P. Schuck, P. Nozièeres, Phys. Rev. Lett. 80, 3177 (1998)
- 39. Y. Funaki, A. Tohsaki, H. Horiuchi, P. Schuck, G. Röpke, Phys. Rev. C 67, 051306 (2003)
- 40. S. Ali, A.R. Bodmer, Nucl. Phys. 80, 99 (1966)
- 41. G.E. Brown, A.M. Green, Nucl. Phys. 75, 401 (1966)
- 42. W.H. Bassichis, G. Ripka, Phys. Lett. 15, 320 (1966)
- 43. A. Arima, H. Horiuchi, T. Sebe, Phys. Lett. B 24, 129 (1967)
- 44. B. Roth, K. Wildermuth, Nucl. Phys. 20, 10 (1960)
- 45. R.K. Sheline, K. Wildermuth, Nucl. Phys. 21, 196 (1960)
- 46. H. Horiuchi, K. Ikeda, Prog. Theor. Phys. **40**, 277 (1968)
- R.H. Davis, in *Proceedings of Third Conference on Reactions between Complex Nuclei*, eds. by A. Ghiorso, R.M. Diamond, H.E. Conzett (University of California Press, USA, 1963), p. 61
- 48. E.B. Carter, G.E. Mitchell, R.H. Davis, Phys. Rev. 133, B1421 (1964)
- 49. E.B. Carter, G.E. Mitchell, R.H. Davis, Phys. Rev. 133, B1434 (1964)
- 50. Y. Suzuki, Prog. Theor. Phys. 55, 1751 (1976)

- 51. Y. Suzuki, Prog. Theor. Phys. **56**, 111 (1976)
- 52. H. Horiuchi, Prog. Theor. Phys. **51**, 745 (1974)
- Y. Funaki, T. Yamada, H. Horiuchi, G. Röpke, P. Schuck, A. Tohsaki, Phys. Rev. Lett. 101, 082502 (2008)
- 54. T. Yamada, P. Schuck, Eur. Phys. J. A. 26, 185 (2005)
- 55. Y. Akiyama, A. Arima, T. Sebe, Nucl. Phys. A 138, 273 (1969)
- 56. T. Inoue, T. Sebe, H. Hagiwara, A. Arima, Nucl. Phys. A 59, 1 (1964)
- 57. K. Ikeda, N. Takigawa, H. Horiuchi, Prog. Theor. Phys. Suppl. 464 (1968)
- F. Nemoto, Y. Yamamoto, H. Horiuchi, Y. Suzuki, K. Ikeda, Prog. Theor. Phys. 54, 104 (1975)
- 59. Y. Kanada-En'yo, H. Horiuchi, Prog. Theor. Phys. 93, 115 (1995)
- 60. M. Kimura, Phys. Rev. C 69, 044319 (2004)
- 61. Y. Taniguchi, M. Kimura, H. Horiuchi, Prog. Theor. Phys. 112, 475 (2004)
- 62. A. Bohr, B.R. Mottelson, *Nuclear Structure*, vol. II. (Benjamin, New York, 1975)
- 63. H. Horiuchi, Prog. Theor. Phys. Suppl. **62**, 90 (1977)
- 64. R. Bock, Heavy Ion Collisions, vol.1 (North Holland, Amsterdam, 1979)
- 65. R. Bock, Heavy Ion Collisions, vol.2, (North Holland, Amsterdam, 1980)
- 66. P. Braun-Munzinger, J. Barrette, Phys. Rep. 87, 209 (1982)
- 67. C.E. Svensson, et al. Phys. Rev. Lett. 85, 2693 (2000)
- 68. D. Rudolph, et al. Phys. Rev. C 65, 034305 (2002)
- 69. E. Ideguchi, et al. Phys. Rev. Lett. 87, 222501 (2001)
- C.D. O'Leary, M.A. Bentley, B.A. Brown, D.E. Appelbe, R.A. Bark, D.M. Cullen, S. Ertürk, A. Maj, A.C. Merchant, Phys. Rev. C 61, 064314 (2000)
- 71. H. Friedrich, K. Langanke, Nucl. Phys. A 252, 47 (1975)
- H. Kihara, M. Kamimura, A. Tohsaki-Suzuki, Proceedings of International Conference on Nuclear Structure, Contributed Papers (International Academic Printing, Tokyo, 1977), p. 234
- 73. A. Arima, *Proceedings of Topical Conference on Physics of Medium Light Nuclei* (Editrice Compositori, Bologna, 1978), p. 19
- Th. Delbar, Gh. Grégoire, G. Paic, R. Ceuleneer, F. Michel, R. Vanderpoorten,
 A. Budzanowski, H. Dabrowski, L. Freindl, K. Garotowski, S. Micek, R. Planeta,
 A. Strzalkowski, K.A. Eberhard Phys. Rev. C 18, 1237 (1978)
- R. Ceuleneer, F. Michel, G. Reidemeister, Lect. Notes Phys. 156, p. 227, (Springer, Berlin, 1982)
- 76. F. Michel, G. Reidemeister, S. Ohkubo, Phys. Rev. Lett. **57**, 1215 (1986)
- F. Michel, S. Ohkubo, G. Reidemeister, Prog. Theor. Phys. Suppl. 132, 7 (1998), Chapter 2 and references therein
- 78. T. Wada, H. Horiuchi, Phys. Rev. C 38, 2063 (1988)
- 79. H. Horiuchi, Prog. Theor. Phys. **73**, 1172 (1985)
- 80. T. Yamaya, K. Katori, M. Fujiwara, S. Kato, S. Ohkubo, Prog. Theor. Phys. Suppl. **132**, 73 (1998), (Chapter 3 and references therein)
- 81. J.J. Simpson, W.R. Dixon, R.S. Storey, Phys. Rev. Lett. 31, 946 (1973)
- 82. J.J. Kolata, J.W. Olness, E.K. Warburton, Phys. Rev. C 10, 1663 (1974)
- 83. A. Arima, V. Gillet, J. Ginocchio, Phys. Rev. Lett. 25, 16043 (1970)
- 84. D.C. Zheng, D. Berdichevsky, L. Zamick, Phys. Rev. C 38, 437 (1988)
- 85. T. Inakura, S. Mizutori, M. Yamagami, K. Matsuyanagi, Nucl. Phys. A 710, 261 (2002)
- 86. T. Yamada, S. Ohkubo, Z. Phys. A 349, 363 (1994)
- 87. S. Ohkubo, Y. Hirabayashi, T. Sakuda, Phys. Rev. C **57**, 2760 (1998)
- 88. M. Kimura, H. Horiuchi, Nucl. Phys. A 767, 58 (2006)
- 89. M. Yamagami, K. Matsuyanagi, Nucl. Phys. A **672**, 123 (2000)
- 90. H. Molique, J. Dobaczewski, J. Dudek, Phys. Rev. C 61, 044304 (2000)
- 91. R.R. Rodríguez-Guzmán, J.L. Egido, L.M. Robledo, Phys. Rev. C 62, 054308 (2000)
- 92. H. Friedrich, Nucl. Phys. A 224, 537 (1974)
- 93. A. Tohsaki, F. Tanabe, R. Tamagaki, Prog. Theor. Phys. **53**, 1022 (1975)

108 H. Horiuchi

- 94. T. Ando, A. Tohsaki, K. Ikeda, Prog. Theor. Phys. 64, 1608 (1980)
- 95. D. Baye, G. Reidemeister, Nucl. Phys. A 258, 157 (1976)
- 96. D. Baye, P.-H. Heenen, Nucl. Phys. A 276, 354 (1977)
- 97. T. Wada, H. Horiuchi, Prog. Theor. Phys. 80, 488 (1988)
- 98. T. Wada, H. Horiuchi, Prog. Theor. Phys. 80, 502 (1988)
- J.V. Maher, M.W. Sachs, R.H. Siemssen, A. Weidinger, D.A. Bromley, Phys. Rev. 188, 1665 (1969)
- 100. E. Stiliaris, H.G. Bohlen, P. Fröbrich, B. Gebauer, D. Kolbert, W. von Oertzen, M. Wilpert, Th. Wilpert, Phys. Lett. 223B, 291 (1989)
- 101. Y. Kondō, B.A. Robson, R. Smith, Phys. Lett. 227B, 310 (1989)
- 102. Y. Kondō, F. Michel, G. Reidemeister, Phys. Lett. 242B, 340 (1990)
- D.T. Khoa, W. von Oertzen, A. Faessler, M. Ermer, H. Clement, Phys. Lett. 260B, 278 (1991)
- 104. D.T. Khoa, W. von Oertzen, H.G. Bohlen, G. Bartnitzky, H. Clement, Y. Sugiyama, B. Gebaure, A.N. Ostrowski, Th. Wilpert, M. Wilpert, C. Langner, Phys. Rev. Lett. 74, 34 (1995)
- 105. M.P. Nicoli, F. Haas, R.M. Freeman, N. Aissaoui, C. Beck, A. Elanique, R. Noucier, A. Morsad, S. Szilner, Z. Basrak, M.-E. Brandan, G.R. Satchler, Phys. Rev. C 61, 064608 (1999)
- 106. M.-E. Brandan, G.R. Satchler, Phys. Rep. 285, 143 (1997)
- H. Horiuchi, in Proceedings of IV International Conference on Clustering Aspects on Nuclear Structure and Nuclear Reactions, eds. by J. S. Lilley and M. A. Nagarajan, (Reidel, Dordrecht, 1985), p. 35
- 108. S. Ohkubo, K. Yamashita, Phys. Rev. C 66, 021301 (2002)
- 109. M. Kimura, H. Horiuchi, Phys. Rev. C 69, 051304 (2004)
- 110. H. Horiuchi, Int. J. Mod. Phys. A 24(11), 2205 (2009)
- J.A. Maruhn, M. Kimura, S. Schramm, P.-G. Reinhard, H. Horiuchi, A. Tohsaki, Phys. Rev. C 74, 044311 (2006)
- 112. T. Kawabata, H. Akimune, H. Fujita, Y. Fujita, M. Fujiwara, K. Hara, K. Hatanaka, M. Itoh, Y. Kanada-En'yo, S. Kishi, K. Nakanishi, H. Sakaguchi, Y. Shimbara, A. Tamii, S. Terashima, M. Uchida, T. Wakasa, Y. Yasuda, H.P. Yoshida, M. Yosoi, Phys. Lett. B 646, 6 (2007)
- T. Yamada, Y. Funaki, H. Horiuchi, K. Ikeda, A. Tohsaki, Prog. Theor. Phys. 120, 1139 (2008)

Chapter 3 Alpha-cluster Condensations in Nuclei and Experimental Approaches for their Studies

Wolfram von Oertzen

3.1 Binding Energy of Alpha Particles

The binding energies of nuclei in their ground states as a function of mass number show a peculiar systematic behavior, explained by the liquid drop model. Deviations from a smooth curve are due to shell effects, and are some times discussed to be related to the formation of α -clusters. The specific properties of the nucleon–nucleon force, namely the saturation which occurs if the spin and isospin quantum numbers are both coupled to zero, produces a very strong binding of α -particles [1]. In addition, due to the internal structure of the α 's an increased (30%) central density is observed compared to the the usual central density in nuclei. The α -particle is therefore a unique cluster subsystem in nuclei.

This feature is well known from the early history of nuclear science, and there has been small but steady activity in the field of clustering in nuclei in the last decades. Recently more attention to clustering in nuclei has emerged due to the study of weakly bound nuclei at the drip lines. For these nuclei clustering is very important even for the properties of ground states. These are well reproduced in model independent approaches, like in the antisymmetrized fermionic molecular dynamics (FMD) which uses all degrees of freedom in the nuclear forces, in the approach by Feldmeier et al. [2, 3]. With a related approach, the antisymmetrized molecular dynamics (AMD) with effective N–N forces, Horiuchi and Kanada-En'yo [4–6] are able to reproduce the ground state properties and a large variety of excited nuclear states, in particular those with molecular structure. In these calculations the density distributions of the nucleons are obtained. Quite spectacular are the results for loosely bound nuclear systems [5, 6], where α -clusters

W. von Oertzen

Fachbereich Physik, Freie Universitaet, 14109, Berlin, Germany

W. von Oertzen (⊠)

Helmholtz-Zentrum Berlin, 14109, Berlin, Germany

e-mail: oertzen@helmholtz-berlin.de

appear naturally as dominant substructures. This work has established that α -clusters play a decisive role in the description of light nuclei, in particular for the loosely bound neutron-rich isotopes. For example the extra neutrons are found in covalent molecular orbitals around two α -particles forming bound molecular two-center systems for the beryllium isotopes [7].

Furthermore, the α -particle is the most important ingredient in the concept of the Ikeda-diagram [8–11], where highly clustered states (e.g. linear chains) are predicted at excitation energies around the energy thresholds for the decomposition into specific cluster channels.

In order to explore the dynamics of α -clustering in excited states of N=Z nuclei the systematics of binding energies per α -particle in nuclei $E_{B\alpha}/N_{\alpha}$, has been considered [12]. The experimental masses have been taken from Ref. [13], for 164 Pb from a theoretical study of the mass A=164 region [14]. With the total binding energy $E_B^t(N,Z)$, the binding energy of all α -particles in N=Z nuclei can be obtained, this will again follow the well known curve for the binding energy (per nucleon) properly rescaled. We are interested in the binding energy per α -particle, $E_{B\alpha}/N_{\alpha}$, determined from the experimental data, as shown in Fig. 3.1, there we show the quantity,

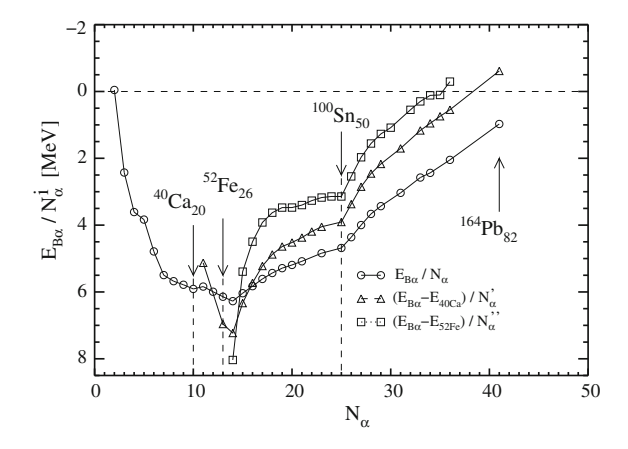
$$E_{B\alpha}/N_{\alpha} = \left[E_{B}^{t}(N,Z) - N_{\alpha} E_{B}^{\alpha} \right] / N_{\alpha}. \tag{3.1}$$

Here we have the typical maximum values around Fe-nuclei. The energy for the threshold states can be read from this figure. Searching for the alpha-condensed states we can also include states with a strongly bound core, e.g. a core of 16 O, a core of 40 Ca or 52 Fe, with the appropriate number N'_{α} of free α -particles outside. The binding energy with a core shown in Fig. 3.1 being:

$$E_{B\alpha}^{^{40}Ca}(N_{\alpha}')/(N_{\alpha}) = \left[E_{B}^{t}(N,Z) - E_{B}^{^{40}Ca}(N,Z) - (N_{\alpha} - 10)E_{B}^{\alpha} \right] / (N_{\alpha} - 10). \quad (3.2)$$

From this figure we can deduce that the excitation energy, where the value of $E_{B\alpha}/N_{\alpha}$ reaches zero, the threshold for complete decay, becomes lower with the

Fig. 3.1 The experimental binding energies per α -particle in N = Z nuclei, as function of the number of α -particles, N_{α} . The lines are drawn to connect the points. The same quantities are shown under the assumption with two different heavy clusters as cores: ⁴⁰Ca and ⁵²Fe, as indicated (adopted from [12])



inclusion of a core. For heavier nuclei around ¹⁰⁰Sn and masses approaching ¹⁶⁴Pb the nuclei become unstable relative to single (or multiple) proton or α-particle emission. The excitation energies, where the binding energy value for α 's approaches zero—these are the values where α-particle condensates can form will be discussed below, Sect. 3.2. Although these α -condensed states are at rather high excitation energies in the continuum of nucleonic states, they may have collective properties, which can give them a smaller observable width. We expect the decay into many α-particles, a decay not described by the Hauser–Fehsbach formalism for statistical compound nucleus decay (see below).

3.2 The Formation of Alpha Condensates

The α -particle condensates formed at the thresholds will be unbound states, their decay properties will be one of the most important points in the discussion of these boson states. In lighter nuclei, in particular for the second 0_2^+ state in 12 C, the *Hoyle* state [15], which can be considered as the first boson condensate, a gamma-decay is possible, here with the sequence $0_2^+ \rightarrow 2_1^+ \rightarrow 0_1^+$, a process most important for the formation of 12 C in stars. The recent proposal of an α -particle condensate wave function (THSR), by Tohsaki, Horiuchi, Schuck and Roepke [16], describes the properties of the Hoyle state very well, whereas even the largest shell model calculations fail completely to reproduce this state [17, 18], see also Refs. [20, 21] for the most recent discussion.

In medium size nuclei (Z < 20) the α -condensates, calculated using the known alpha-alpha-potential with a self-consistent approach (based on the Gross-Piatevski equation), will have Coulomb barriers [19] for the decay in to multiple α 's. With these barriers the states will have sufficiently small width for potential studies by inelastic scattering. However, the heaviest nucleus for which this barrier can create a quasi-bound state [19], is estimated to be around ⁴⁰Ca. In heavier nuclei these states will be embedded high in the continuum of the fermionic states, their decay is expected to be non statistical, the most characteristic property to study.

3.2.1 Second Order Phase Transition

The ground states of nuclei are well described by the shell model with a selfconsistent potential of all nucleons. If a cluster model with α -clusters is used, their strong spatial overlap, the anti-symmetrization of all nucleons destroys their original properties, a fact widely discussed in the literature (see Refs. [22] for the most recent discussion). The intrinsic structure of α -clusters in these cases are very different from that of free α -particles, still a large variety of molecular resonances connected to clusters are observed in N = Z nuclei [23].

We want to discuss the formation of an α -particle gas, where the average distance between α -particles is much larger with rather small spatial overlap. The corresponding nucleon density will be well below normal nuclear densities. In fact, in the theoretical investigation of Bose–Einstein condensates in nuclei Tohsaki et al. [16–19] find, that at the thresholds for multi α -particle decays, the states with α -clusters have a much larger radial extension than the ground states (larger α - α distances). From the view point of the nucleonic fermion gas the appearance of such states will depend on the temperature (i.e. excitation energy, E_x^*) of the nucleus. The concept of a second order phase transition as in a chemical reaction with two components can be used [12], a concept well established in thermodynamics of composite systems in statistical physics [24]. The basic equation is the "reaction" of four "free" nucleons (two protons and two neutrons coupled to total values of spin and isospin of zero) forming α -clusters:

$$(N_1 + N_2 + N_3 + N_4) \longleftrightarrow \alpha$$
-particle + 28.3 MeV.

The free nucleons, N_i , should have a definite volume and pressure, in order to define thermodynamic quantities and where the density allows the occurrence of the mentioned reaction. We can assume that the particles interact in a well defined volume created by a self consistent mean field for the nucleons (the Hartree–Fock approach) and for the α -clusters with the Gross–Piatevski approach for bosons. This latter has been used in the work of Yamada and Schuck [19].

In models like the AMD [6] a certain number of nucleons are confined in a volume with a positive kinetic energy, as suggested in Fig. 3.2. In this model a

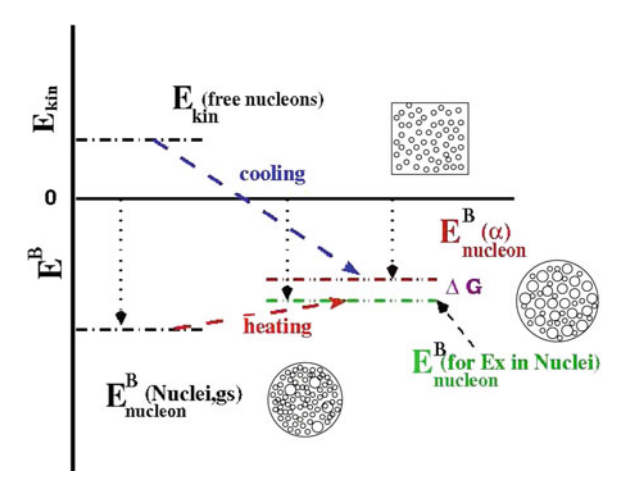


Fig. 3.2 Schematic illustration of the relative values of the energies of free nucleons and alternatively their binding energies in nuclei (8.2 MeV), the latter are generally larger than in α -clusters (7.07 MeV). The difference ΔG between these binding energies decreases with excitation energy ("heating") in nuclei. At a critical value the two binding energies become equal, $\Delta G=0$, a collective state of bosons (potentially mixed with fermions), the condensed α -particle gas can be formed. In the AMD this state is approached by "cooling" from a fermion gas

cooling method is applied to find the states of the lowest energy and higher density. The energy of the nucleons inside the nucleus is defined by their volume, and their Fermi-energy can be deduced from the nuclear radius, as described in text books [25]. In the AMD approach with the cooling process a certain α -cluster phase is observed, before the formation of the higher density states with bound fermions, and finally the ground states are reproduced. At the end the formation of normal nuclei with a binding energy per nucleon of 8.2 MeV or more is observed, a value which is higher than in the α -cluster (7.073 MeV). These two values define the difference in the chemical potentials in the two phases (Fig. 3.2). For less bound nuclei (binding energy per nucleon around 7.073 MeV), the α-clusters are obtained in a "natural" way. Starting from the ground states of normal nuclei the nucleons will form an α -cluster phase, with increasing temperature of the nucleus, e.g. with increasing excitation energy, see Fig. 3.2, ("heating"). This excitation energy becomes rather low in neutron-rich light exotic nuclei, where clustering may appear already in the ground states as the dominant structure [6], this may also happen potentially in very heavy N = Z nuclei.

For the nucleons confined in the nuclear volume we apply the concepts of statistical physics for the reaction $4N \longleftrightarrow \alpha$ -particle. The rate of the reaction is governed by the free energy, G, and the difference in the chemical potentials, μ_{α} and μ_n . The chemical potentials are defined as $\mu_i = \delta G/\delta N_i$, $i = n, \alpha$. The thermodynamic free energy depends on the number of nucleons, N_n and on N_α , with $G = G(N_n, N_\alpha)$. The change of the free energy becomes

$$\Delta G = \Delta N_{\alpha} \mu_{\alpha} + 4\Delta N_{n} \mu_{n}. \tag{3.3}$$

For the phase transition a minimum value of the free energy is needed, this gives the condition $\Delta G = 0$, this feature will be observed at a critical excitation energy E_x^{crit} . In the nuclear medium ΔG is the difference between the binding energy of the four nucleons in the free α -particle to that in the nuclear medium, as illustrated in Fig. 3.2.

The kinetic energy of the nucleons determines the temperature, T. However, we will use the temperature of the nucleus, t, related to its excitation energy. In the normal case of a mixed system of the two species, the relative abundance of N_{α} – N_n is a function of the temperature (in our case excitation energy) and is obtained through the expression

$$\frac{N_{\alpha}}{\left(N_{n}\right)^{4}} = K(t) = \exp\left(-\frac{\Delta G(t)}{RT(t)}\right) \tag{3.4}$$

The value of K is to be determined by experimental observation (the usual coefficient R appears as in statistical physics). For the case of negative $\Delta G(t)$, a decrease of the free energy (corresponding to a large value of the ratio K) gives a higher density of the α -particles as reaction products. A positive value of ΔG corresponds to an energetic disadvantage for the reaction creating α -particles, resulting in a smaller number N_{α} as reaction products. In the case of nuclei, the nucleons are embedded in the nuclear medium and are confined in the nuclear

potential created by the mean field of all nucleons. The binding energy per nucleon in nuclei is around 8 MeV (dependent on the size of the nucleus and its excitation energy). The nucleons have a larger binding energy in the nuclear medium (in the ground states of stable nuclei) compared to the value in the α -clusters. The relative positions of the relevant energies are illustrated in Fig. 2, from Ref. [7]. The change in the free energy of the nucleons in the medium is now in the difference between the binding energies in the nucleus and in the α -clusters. Actually, because the chemical potential of the nucleons will depend on the excitation energy in the nucleus (or on its temperature), we put this dependence in the expression for $\Delta G(t)$.

Alpha-cluster formation is expected if $4E_B^t/N_n$ is less than or equal to the total binding energy of four nucleons in the α -cluster. As the binding energy per nucleon becomes equal or smaller than in the α -particle, a new phase will be formed, a strongly interacting Bose gas. For binding energies of the nucleons close to (or larger) that in the α -particle it becomes possible to form a mixed phase of α -cluster states (liquid) and of nucleons. The binding energy of nucleons in the ground states of nuclei (see Fig. 3.2) $E_B^t/N_n = E_{nucleon}^B$, is usually larger than in the α -particle. The condition for the excitation (condensation) energies is $E_x^{cond} \geq E_x^{crit}$. The values for different nuclei relevant to this concept are given in Table 3.1.

We sumarize that the α -condensation condition is given by $E_B^t/N_n(E_x^{crit}) \ge 7.07$ MeV, The value of the critical excitation energy/(per nucleon) in a nucleus, E_x^{crit} , should be equal or larger than 7.07 MeV, which is the binding energy of

Table 3.1 Alpha-particle binding and critical excitation energies for the condensation condition in nuclei with N=Z

Nuclide	N_{lpha}	E_B^t	E_B^t/N_n	$E_{B\alpha}/N_{\alpha}$	E_x^{crit}	E_x^{crit}
⁴ He	1	28.3	7.073	_	_	(⁴⁰ Ca)
^{12}C	3	92.16	7.680	2.425	7.27	_
¹⁶ O	4	127.6	7.976	3.609	14.44	_
²⁰ Ne	5	160.7	8.032	3.83	19.17	-
24 Mg	6	197.2	8.260	4.787	28.72	-
²⁸ Si	7	236.5	8.447	5.495	38.47	-
^{32}S	8	271.8	8.493	5.677	45.41	_
³⁶ Ar	9	306.7	8.519	5.78	52.02	-
⁴⁰ Ca	10	342.0	8.551	5.910	59.10	-
⁵² Fe	13	447.7	8.609	6.143	79.86	-
⁵⁶ Ni	14	483.9	8.642	6.275	87.85	-
⁷² Kr	18	607.1	8.432	5.433	97.8	87.78
80 Zr	20	669.8	8.371	5.192	103.8	90.38
¹⁰⁰ Sn	25	824.5	8.244	4.684	117.1	97.65
¹¹² Ba	28	894.8	7.99	3.665	102.6	68.79
¹⁴⁴ Hf	36	1,090.9	7.577	2.074	74.6	19.68
¹⁶⁴ Pb	41	1,200.1	7.317	0.973	39.9	-25.21

The last column shows the values for the case of a 40 Ca-cluster core. All energies in MeV N_{α} , number of α -particles; E_B^i/N_n , binding energy per nucleon; $E_{B\alpha}/N_{\alpha}$, binding energy per α -particle; E_X^{crit} , condensation energy

nucleons in the α -particle. This statement is the same as the condition $\Delta G(t) = 0$. Alternatively, the phase transition will be achieved at excitation energies of the nucleus, E_x^* , corresponding to the thresholds where all clusters become unbound, the condition being that $E_{B\alpha}(N, Z) = 0$. This is the original concept of the Ikeda diagram. The Ikeda diagram [8, 9] gives a phenomenological condition for the appearance of clustered states (with the inclusion of other clusters like ¹²C, ¹⁶O, etc.) in nuclei. We can state that the Ikeda diagram with α-particles can be deduced from thermodynamic considerations. The level density for the fermionic phase space grows very fast with excitation energies, whereas those for the bosons will grow much slower.

Most important for the properties of the α -particle gas is, that they do not represent the "ideal" gas, they interact via an interaction which has similarities with a van der Waals interaction, with a strongly repulsive core due to the Pauli principle, see Fig. 3.3. Two α -particles form as the lowest state, the ground state of ${}^{8}\text{Be}$, a resonance at $E_x^* = 92 \text{ keV}$. We can calculate the de Broglie wave length, $\lambda = h/\sqrt{(2\mu E_x^*)}$ for this case and have $\lambda = 67$ fm (relative motion between the two α -particles). If for higher excitation we incorporate the 2⁺ at 3.04 MeV the value of λ is still 12.4 fm. Similarly three α -particles can form the Hoyle-state just above the three α -particle threshold in 12 C, the 0^+ at 7.654 MeV (288 keV above the threshold of 7.346 MeV). With these values for three α -particles we again get a similarly large de Broglie wave length of relative motion. Also the third 0_3^+ at 10.3 MeV excitation energy can participate in the formation of a multi- α -particle correlation.

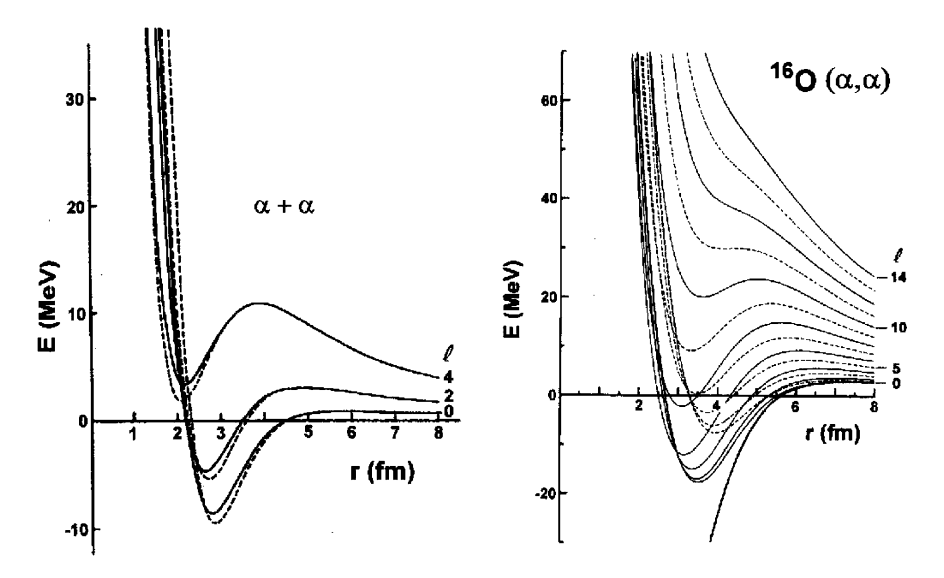


Fig. 3.3 The equivalent local potentials describing the $\alpha-\alpha$ and the $\alpha^{-16}O$ interaction. The resonant energies in 8 Be and the phase shifts are reproduced. With these interactions the α particle gas can be calculated. For the α - 16 O potential a similar van der Waals type of interaction is obtained, a potential suited for an α-particle gas with (and additional binding) by a core (adopted from [7])

Overall we have values for λ in the condensed state larger (by factors 2–5) then the radial extension of the nucleus. The multi- α -particle states will contain the α -particles mainly in their resonant states in ${}^8\text{Be}$. The condensed states at the binding energy threshold consisting of α -particles will form coherent super-fluid states. The resonant states in ${}^8\text{Be}$ and ${}^{12}\text{C}$ act in a similar way as the residual interaction in the formation of the superfluid neutron pairing states, see Ref. [1], volume II. The calculations of THSR based on a local α - α potential reproduce the states of ${}^8\text{Be}$, and the threshold states in other light nuclei. Inspecting the local potentials in Fig. 3.3 for the system of ${}^{16}\text{O} + \alpha$ -particle, we conclude that alpha-condensates with a ${}^{16}\text{O}$ -core can be formed, where this potential will create a common binding potential, for a larger number of alpha's (e.g. ${}^{40}\text{Ca} = {}^{16}\text{O} + 6\alpha$).

In Fig. 3.4 we illustrate the possible situation for an α -condensate in 100 Sn, with a core of 40 Ca and 15 α 's. These configurations can be formed in a reaction with a 72 Kr beam and a 28 Si target. At excitation energies of 97 MeV or more (excitation energies discussed earlier) many compound nuclear (CN) states will exist, consisting of different configurations of the α -particle gas plus a core. Here again the threshold rules apply with respect to excitation energies. We may expect many overlapping states (with a large decay width), which will interact coherently (see Ref. [28]), because the same compound states of the α -particle phase can be formed with a different number of α -particles. These will interact through the 0^+ and 2^+ resonances of 8 Be and 12 C*, depending on the excitation energy of the state. The decay of such a state (in the figure there is no barrier for the α -particles, in difference to the figure shown in Ref. [7]) can occur sequentially with different energies in each step, as in CN-decay. However, the most interesting case would be the simultaneous decay, with many α -particles with almost equal kinetic

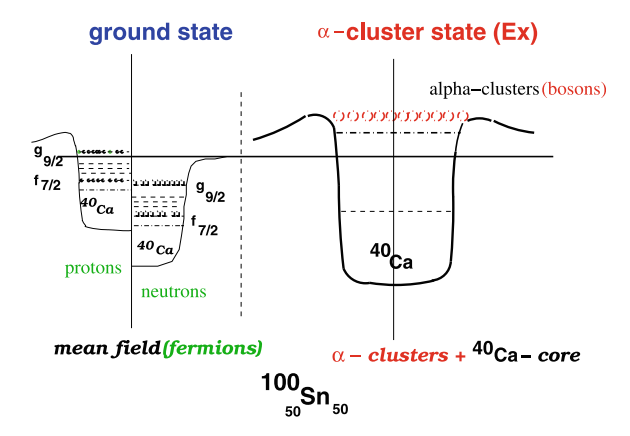


Fig. 3.4 Schematic illustration of the two models for states in 100 Sn. States of low excitation energy are formed by the mean field of nucleons, in this case the potentials for neutrons and protons are rather different due to the Coulomb interaction. Thus, the formation of α-particle structures is strongly suppressed. At the critical excitation energy of 97 MeV (for 100 Sn, see Fig. 3.1), a collective state of bosons with α-particles occupying the same orbit (relative S-states) outside a 40 Ca-core, will be energetically favored

energies, a process, which can also be considered as Coulomb explosion [41], see Sect. 3.3.

3.3 Experimental Observables

For the observation of states in nuclei, which have spin(parity) = 0(+) and the properties of α -particle condensates, there are several characteristic experimental features which we can propose for future studies.

- 1. The study of the radial extension, e.g. observed in inelastic α -scattering and in the form factors from electron scattering experiments.
- 2. Coherent emission of α-particles from compound nuclei in coincidence with large γ -detection arrays.
- 3. Fragmentation into multiple α -particle channels at GeV/nucleon energies.
- 4. α - α -correlations, for CN decay similar to 2.

A further approach which should be mentioned here is the detection of multi- α -clusters in a ternary cluster decay as described in Refs. [42, 43]. In these cases the coplanar detection of two heavier fragments as in a binary decay, shows missing mass and charge of multi-α-clusters. The study of these fission processes indicates that the missing α-clusters are emitted from the neck with very small intrinsic excitation and small angular momentum. These multi-α-clusters, will be emitted towards very small angles, where they should be detected with charged particle counter-telescopes.

3.3.1 Inelastic Scattering, Radial Extensions, Form Factors

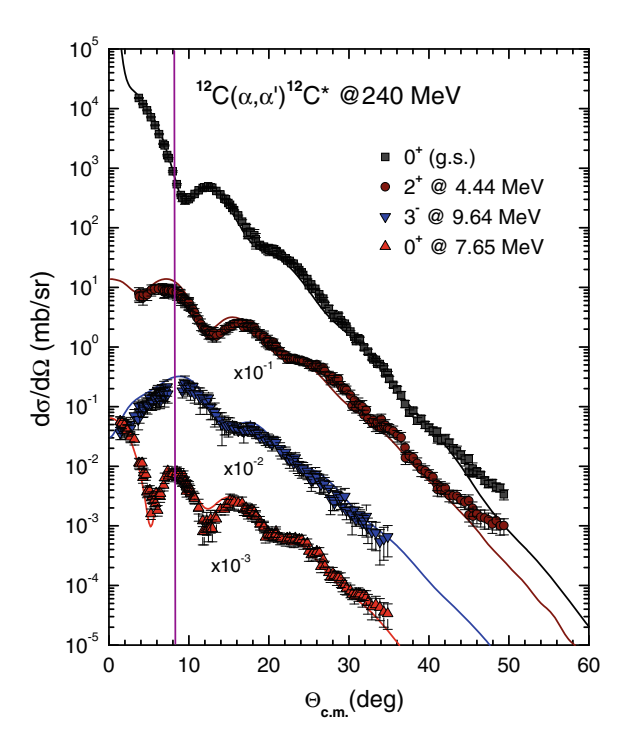
The threshold states in nuclei with condensed α -particles have spin/parity $J^{\pi} = 0^+$, these must be populated by monopole excitations (a collective radial density mode). In fact the most important predicted properties of these states, are the larger radial extensions. These can be manifested in inelastic electron and hadron scattering. The inelastic electron scattering on a ¹²C-target has been studied repeatedly. The form factor for the transition to the excited state at 7.65 MeV, the (Hoyle State), with $J^{\pi} = 0^{+}$ is thus well known see Refs. [33, 34] and earlier references therein.

Similarly there are extensive studies of inelastic hadron scattering on ¹²C using a large variety of projectiles. We concentrate here on the elastic and inelastic α-scattering at energies between 104 and 240 MeV, which has recently been analyzed with microscopic transition densities and the double folding approach for the scattering potential [32] and with a diffraction model [35]. The angular distributions exhibit at smaller angles strong diffraction patterns, and partially also a refractive maximum at larger angles. One feature, known from the early history of nuclear physics, is the Blair phase-rule established in α -particle scattering [34]. If states are populated in inelastic scattering and sufficiently high

energy, diffractive patterns (strong maxima and minima) are observed at forward angles, the structures of the elastic scattering and inelastic scattering are *out of phase if no parity change has occurred*. At higher energies the effect of *Q*-values, i.e. their influence on the position of the maxima and minima is small. The position of the diffractive minima depend on the radial extension (e.g. of the excited states).

The result at an incident energy of 240 MeV is shown in Fig. 3.5, the angular distributions show pronounced diffraction structures. Indeed the diffractive pattern for the inelastic excitation to the 2⁺ state at 4.43 MeV is clearly out of phase with that for the ground state. For the 0⁺ state at 7.65 MeV the diffractive pattern is more pronounced and is shifted by approximately 2° to forward angles, indicating a larger radius. The calculations, which were performed with the double folding model for the elastic scattering potential and for the transition densities [34], are also shown in Fig. 3.5. With this approach and a proper choice of the imaginary potential for the 0_2^+ state the absolute values are reproduced with a correct value for the E0-transition strength. The other inelastic transitions have been calculated, and are perfectly reproduced due to the choice of the transition densities obtained in the folding model. The analysis with a diffraction model [35] of such data gives the systematics of the diffraction radius over a large energy range and indicates a 10% larger radius for the 0_2^+ state compared to the ground state. Similar results will be expected for 0_6^+ at 15.1 MeV in $^{16}\mathrm{O}$, which is just above the four α -threshold (14.4 MeV), and has been searched for recently [36].

Fig. 3.5 The elastic and inelastic scattering of $\alpha + {}^{12}\text{C}$ at 240 MeV with the result of the analysis using the double folding model of Khoa et al. [34]. The *vertical line* illustrates the shift towards smaller angles for the transition to the 7.65 MeV (*Hoyle state*), due to its larger radial extension



3.3.2 Compound Nucleus Decay, Correlated Emission of Alpha's

In the formation of N=Z compound nuclei up to mass A=60–80, the heaviest combination of stable targets and projectiles is 40 Ca + 40 Ca giving 80 Zr compound states with appropriate excitation energy (see Table 3.1) and coherent α -particle states can be formed. For heavy N > Z compound nuclei with a small neutron excess, however, the features discussed below may also apply. For even heavier systems with N = Z, we will have to resort to beams of unstable nuclei, like e.g. a ⁷²Kr beam, which has a good chance of being produced in the future with usable intensities. The compound nucleus with a 40Ca-target will be 112 Ba (Q = -52.54 MeV). Because of the fact that the heavier compound nuclei are very far off-stability the reaction O value becomes very negative. With an incident energy close to the Coulomb barrier, the final excitation energy (Ex) can be well controlled and moderate values of Ex can be reached (see Table 3.1). These compound nuclei will have also favorable O values for the emission of several α-particles. Actually a new collective decay mode, where all alphaparticles share the same kinetic energy, as in Coulomb explosion, can be predicted. However, heavier compound nuclei will be unstable to charged-particle emission (protons and α 's) already in their ground states.

Further we may consider an excess of two or more neutrons (with an isotope with a more intense beam), this would most likely not destroy the special states discussed here. The excess neutrons will be placed in quantum orbits around the emitted clusters, for example as in the 9-10Be isotopes forming bound or metastable molecular states and configurations with low nucleon density [7].

We are interested in the multiple α -particle emission. Due to the coherent properties of the threshold states consisting of α-particles interacting coherently with a large de Broglie wave length, the decay of the CN will not follow the Hauser-Feshbach assumption of the statistical model: that all decay steps are statistically independent. If we consider a sequential process, after emission of the first α-particle, the residual nucleus contains the phase of the first emission process; the subsequent decays will follow with very short time delays related to nuclear reaction times (or their inverse, decays), favoring the formation of resonances like ${}^{8}\text{Be}(0^{+}, 2^{+})$ and the ${}^{12}\text{C}^{*}(0^{+}_{2}, 2^{+}_{2})$ states.

Another view for the α -gas in nuclei is the concept of a collective super-fluid state with a broken symmetry, the α -particle number, a concept much used for neutron pairing in superfluid states in nuclei [1, 37]. For the two-neutron pairing states in heavy nuclei, the transfer of neutron pairs between superfluid nuclei [37, 38] is strongly enhanced. The analogy to the enhancement of the transfer of correlated neutron-pairs, is the multiple emission of α -particles as a collective transition (changing the particle-number as a collective variable) from compound nuclei with superfluid properties (with α-condensates), i.e. between nuclei with different numbers of α -particles. This feature has been discussed for α -particle transfer between very heavy nuclei in the valley of stability in Ref. [39]. Thus the

observation of enhanced multiple emissions of α -particles from the compound state can be proposed as the signature for the observation of the collective Bosegas. The emission should be strongly enhanced, relative to the statistical model prediction. For the latter case the emission of several α -particles would be observed into different angles [27].

The coherent emission should occur into the same (identical) angle. This will lead to the situation that the observation of unbound resonances becomes possible, such as ${}^{8}\text{Be}(0^{+}, 2^{+})$ and the excited states of ${}^{12}\text{C}$, ${}^{12}\text{C}^{*}(0_{2}^{+}, 0_{3}^{+})$ -clusters. This feature in fact has been observed in the recent data [26–31] discussed in the next section.

3.3.3 Compound States with Multi-\alpha Decays

We are interested in the coherent multiple α -particle emission from excited compound nuclei (CN). Due to the coherent properties of the threshold states consisting of α -particles interacting with a large de-Broglie wave length [12], the decay of the CN will not follow the Hauser–Feshbach assumption of the statistical model: a sequential decay and that all decay steps are statistically independent.

After emission of the first α -particle, the residual α -particles in the nucleus contain the phase of the first emission process; the subsequent decays will follow with very short time delays related to nuclear reaction times, and possibly shorter then the 10^{-18} s of CN decay, actually a simultaneous decay can be considered. This fact should be responsible for the enhanced formation of resonances like ⁸Be and the $^{12}C^*(0_2^+, 2_2^+)$ states. An enhanced emission of multiple α -particles is predicted [12]. Most relevant, however, is the larger radial extension of the Boson condensate states, as discussed in Refs. [18, 19, 28].

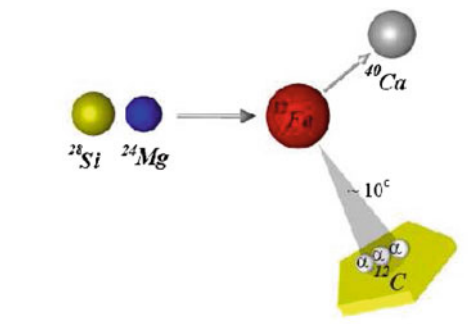
The best way to study such decays is the combination of multi-detector arrays for particle detection with ΔE -E detectors and a "calorimeter" to observe the remaining compound nucleus residue via its γ -decay. Such experiments have been performed with the large γ -detector array GASP at the Legnaro National Laboratory LNL at Padua (Italy), combined with the charged particle detector ball ISIS (details are given in Ref. [27]) consisting of 42 ΔE -E telescopes (see Fig. 3.6).

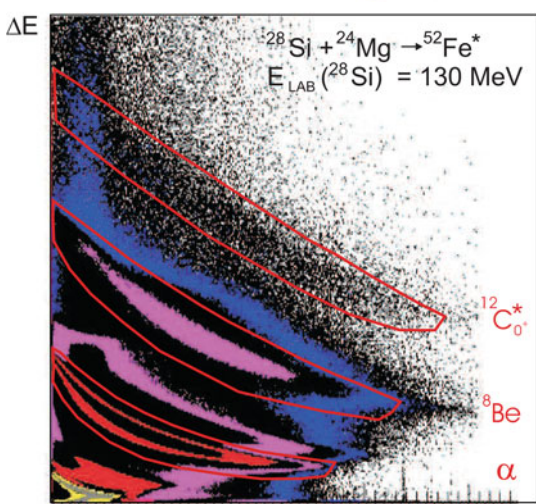
These experiments were performed in a study of γ -decays of compound nuclei selected with a particular particle decay [26]. The large opening angle of the individual ISIS- Δ E-E telescopes, which was 27°, allows to select the spontaneous decay of the weakly unbound states, namely of 8 Be into two α 's and the $^{12}C^*(0_2^+)$, into three α -particles. With the rather modest kinetic energy of these fragments and the small decay energies of a few 100 KeV the opening angles between the α 's are in the range of $10^\circ-25^\circ$, which fit into these solid angles. Therefore these prompt multiple α -decays are observed by the pile-up of the signals produced by individual alpha-particles in one of the Δ E-E telescopes. This is shown in Fig. 3.7. The corresponding coincident (particle gated) γ -decays are compared with the spectra obtained from statistical emission (with the same α -multiplicity) into different Δ E-E telescopes (see Fig. 3.8).

Fig. 3.6 Picture of the y-detector ball GASP, opened to give view on the detector ball ISIS with 42 ΔE -E telescopes. With these the emission of three α 's at different angles in different detectors (upper panel in Fig. 3.8), or the pile-up events for the three α 's from the decay of $^{12}C_{0+}^{*}$, see Fig. 3.7, are registered (courtesy of A. de Angelis, LNL)



Fig. 3.7 *Top* This part shows the kinematical situation for the triple pile-up of the signals for three α 's in one detector and the emission cone for α 's from the decay of $^{12}C^*(0_2^+)$. Bottom Plot of ΔE-E-signals as observed with the ISIS charged particle detector system. The events with the emission of single α 's, of ⁸Be and with three α 's from the state ${}^{12}C^*(0_2^+)$ are indicated. The reaction is 28 Si $+^{24}$ Mg \rightarrow 52 Fe \rightarrow 40 Ca +X at $E_{lab} = 130 \text{ MeV}$ (courtesy of Tz. Kokalova)





E

The comparison of the two γ -sprectra with different triggers is shown in Fig. 3.8 for the reaction $^{28}\text{Si} + ^{24}\text{Mg} \rightarrow ^{52}\text{Fe} \rightarrow ^{40}\text{Ca} + 3\alpha$, an experiment designed for the spectroscopy of ^{40}Ca . The spectrum gated with three α 's in one telescope shows additional γ -transitions in ^{36}Ar , connected with an emission of an additional α -particle, it is a dramatic effect, because these transitions are completely absent in the other spectrum gated by random directions of the three α 's. Initial attempts to explain these differences by parameters of the statistical compound nucleus decay failed, see Ref. [27]. A subsequent analysis [28], which

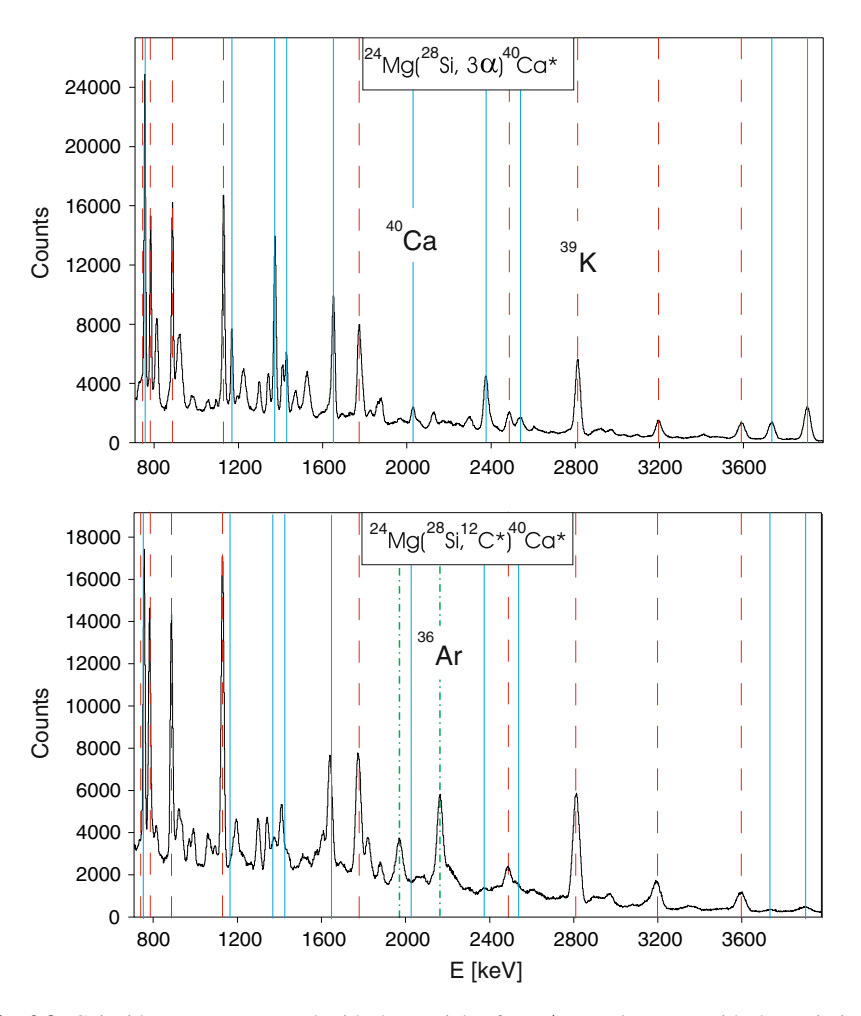


Fig. 3.8 Coincident γ-spectra gated with the particles from ΔE-E-telescopes with the emission of three random α's at different angles in different detectors (*upper panel*), in comparison with that obtained by the $^{12}C_{0_+}^*$ -gate (*lower panel*). The reaction is $^{28}\text{Si} + ^{24}\text{Mg} \rightarrow ^{52}\text{Fe} \rightarrow ^{40}\text{Ca} + 3\alpha$ at 130 MeV. Note the additional lines for ^{36}Ar in the lower panel (courtesy of Tz. Kokalova)

uses the the features of a α-condensed state, namely the larger diffuseness and the larger radial extension gave as an important effect a strong lowering by 10 MeV of the emission barrier for the emission of ${}^{12}C_{0+}^*$. This fact explains, that the energies of the ${}^{12}C_{0^+}^*$ are concentrated at much lower energies as compared to the summed energy of three α -particles under the same kinematical conditions. In this way the residual nucleus (⁴⁰Ca) attains a much higher residual excitation energy.

I also show the results of the previous study of the reactions $^{32}S + ^{24}Mg$ for the γ-spectroscopy of ⁴⁸Cr with ⁸Be-emission [29–31] performed with the same mentioned ISIS-GASP-combinations at the LNL in Legnaro. In Fig. 3.9 we show the identification of ⁸Be, and on the right side the comparison of the energy spectra, under the same kinematical conditions, for ⁸Be and the sum energy of the two α 's. We note that the energy spectrum of the ⁸Be is shifted to smaller energies, as in the previous case. This again must be explained by a larger diffuseness of the CN-state (an α-condensed state) and a lowered Coulomb barrier for the ⁸Be emission. The γ -spectra with the two possible particle gates are shown in Fig. 3.10. It shows the case of 8 Be-emission compared with the statistical emission of two α 's in two different detectors, the latter representing the usual statistically independent decay into two different detection angles. Again we found that the particular channel with ⁸Be carries less energy and less angular momentum, therefore more subsequent decays are observed. In this case a subsequent neutron and proton emission is observed, the ⁴⁶Ti-channel is strongly increased for the ⁸Be-gate. Attempts to explain these differences in terms of parameters of CN-decay,

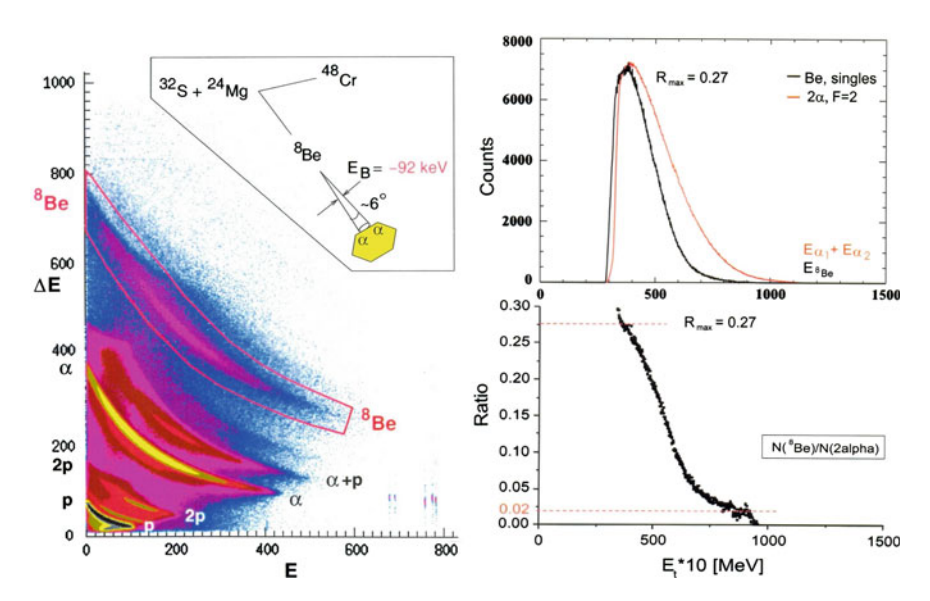
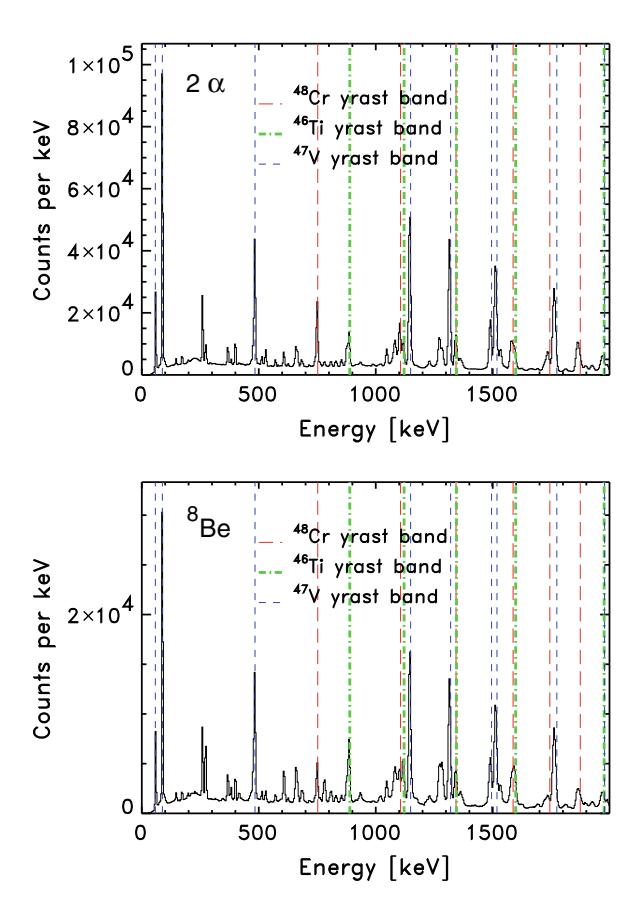


Fig. 3.9 The kinematics for 8 Be-observation, and comparison of the summed energies of two α 's with the energy of ⁸Be under the same kinematical conditions (courtesy of S. Thummerer)

Fig. 3.10 Coincident γ -spectra gated with the particles from ΔE-E-telescopes with the emission of two random α 's in different detectors (upper panel), in comparison with that obtained by the 8 Be-gate (lower panel). The reaction is 32 S + 24 Mg \rightarrow 56 Ni \rightarrow 48 Cr + 2 α at 130 MeV (courtesy of S. Thummerer)



(discussed in Ref. [30]) gave no conclusive result. At that time the concept of condensed α -particle states in the CN was not considered.

3.3.4 Inelastic Excitation and Fragmentation

The last entry in Table 3.1, the last column for the 40 Ca-core has a negative sign for 164 Pb, indicating that this nucleus, as well as lighter nuclei (actually above Z=72), are unstable in their ground state to single and multiple proton or multi- α -particle decay. For lighter N=Z nuclei, at excitation energies above E_{crit}^* another decay mode (as already mentioned) becomes possible, which we call Coulomb explosion. The condensed states are radial monopole excitations with respect to the ground state. The monopole states located at high excitation energies can best be excited by Coulomb excitation at the highest projectile energies. Coulomb excitations of the GQR (giant quadrupole resonance) or the GDR (giant dipole

resonance) have been studied [40] up to 300 MeV/nucleon. The highest cross sections are expected at projectile energies above 1 GeV/nucleon. Because of the larger step in excitation energy the increment for the dynamical matching becomes optimum at these highest energies. Such studies exist for some of the lighter N = Z nuclei (12 C, 16 O, 20 Ne) and heavier [44, 45]. In these studies nuclear emulsions have been used, the silver nuclei (Ag) acting as target nuclei for Coulomb excitation.

The results were obtained at the JINR in Dubna with beams from the nucletron accelerator [44, 45]. The reaction products are registered in nuclear emulsions, the Coulomb break-up being induced by the heavy target nuclei (Silver, Ag) of the material. In this way very characteristic multiple tracks after break-up have been observed (see Figs. 3.11, 3.12). In the case of ^{16}O we observe two α 's and a ^{8}Be , this fact points to the previous discussions of a coherent emission, two α 's must be emitted in a close correlation (in energy and space) in order to be able to form a ⁸Be resonance. We expect the formation of ⁸Be from the internal structure of the condensate state in ¹⁶O, but also in the case of a simultaneous (coherent) emission (and only in this case) the interaction of the two α 's can form ⁸Be.

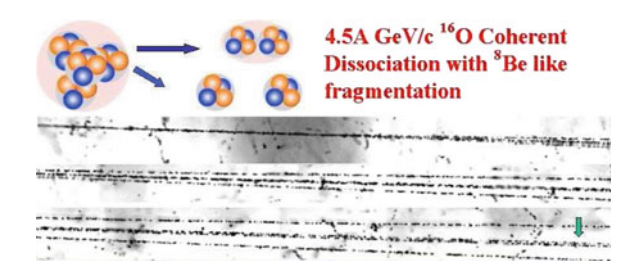
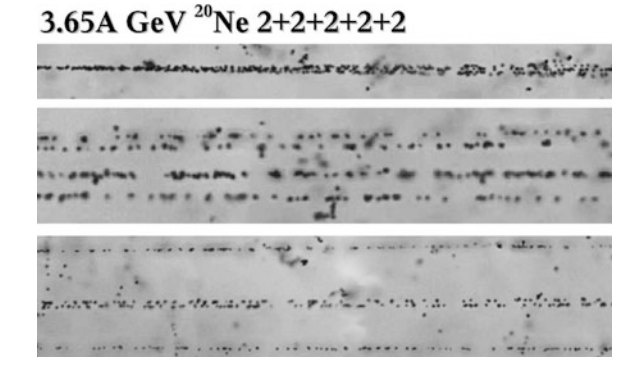


Fig. 3.11 Break-up of ^{16}O at 4.5 GeV/nucleon with the emission of four α 's, registered in an emulsion. Details of the decay can be seen, e.g. the more narrow cone of two α 's, due to the emission of ⁸Be. Different stages of the decay, registered down stream in the emulsion are shown in consecutive panels. P. Zarubin private communication and Refs. [44, 45]

Fig. 3.12 Break-up of ²⁰Ne at 3.65 GeV/nucleon with the emission of five α 's (again partially as 8Be), registered in an emulsion. Different stages of the decay, registered down stream in the emulsion are shown in three panels on top of each other. P. Zarubin private communication and [44, 45]



The result for the break-up of 20 Ne is shown in Fig. 3.12, among the different observed break-up's the emission of five α 's is observed with remarkable intensity. Again at least one pair of α 's is observed, indicating coherent emission with strong correlations, which allow the formation of the low lying 8 Be resonances.

In this context we mention that Coulomb explosion has been observed in highly charged atomic van der Waals clusters and is discussed by Last and Jortner [41]. In our case the simultaneous emission of many α -particles is expected, a decay process very different from standard statistical compound nucleus decay. In fact in this decay mode the α -particles must have all the same energy.

3.3.5 \(\alpha - \alpha\) Correlations

There have been numerous studies of particle-particle correlations in higher energy nuclear reactions around 50-100 MeV/nucleon [46], as well as for reactions at relativistic energies, where pion-pion correlations have been studied [47]. From this work we find that the spacial and time extension of the source can be studied in these correlations. A specific feature appears here, that the correlations of bosons will exhibit a maximum at the smallest angles and smallest relative momenta. However, with two α -particles the Coulomb interaction and the resonances in the α - α channel, states in the ⁸Be nucleus dominate the correlations [46]. With an experimental set-up consisting of ΔE -E telescopes like the detector ball EUROSIB, which contains sufficiently small angular resolution, and a γ -detector ball as in the experiments described in Sect. 3.3, the $\alpha-\alpha$ correlations should be studied in coincidence with γ -transitions of the residual N=Z compound nucleus (minus two α -particles). With the use of inverted kinematics, the heavier projectiles on a lighter target, the rather low energies of the α -particles in the cm system of the compound nucleus will have sufficiently high energy in the laboratory system to be registered in Δ E-E-telescopes (an absorber has to be used to block the heavy projectiles). A correlation matrix with $(E_{\alpha_1} - E_{\alpha_2})$, can be constructed. Such correlation matrices (for two γ -rays) have been constructed in γ -spectroscopy [48] with γ -detector balls. The correlations and the resonances can then be constructed over a wide range of momenta.

3.4 Conclusions

The data presented here show clearly experimental features, which point to the existence of α -condensed states giving rise to coherent multi α -particle states in excited N=Z nuclei. With the most recent experimental developments, we can expect that very new features of such states can be observed. These can potentially establish the existence of Bose–Einstein condensates in nuclei, a very promising field of research for future studies. The author is indebted to Peter Schuck for numerous discussions.

References

- 1. A. Bohr, B.R. Mottelson, *Nuclear Structure*, vol. I (Benjamin, Reading, 1975)
- 2. H. Feldmeier, K. Bieler, J. Schnack, Nucl. Phys. A 586, 493 (1995)
- 3. T. Neff, H. Feldmeier, R. Roth, Nucl. Phys. A 752, 94 (2005)
- 4. H. Horiuchi, K. Ikeda, Cluster Model of the Nucleus. International Review of Nuclear Physics, vol. 4 (World Scientific, Singapore, 1986), p. 1 and references therein
- 5. H. Horiuchi, Y. Kanada-En'yo, Nucl. Phys. A 616, 394c (1997)
- 6. Y. Kanada-En'yo, H. Horiuchi, Prog. Theor. Phys. Suppl. 142, 206 (2001)
- 7. W. von Oertzen, M. Freer, Y. Kanada-Enyo, Phys. Rep. 432, 43 (2006)
- 8. H. Horiuchi, K. Ikeda, Prog. Theor. Phys. (Jpn) A 40, 277 (1968)
- 9. K. Ikeda, N. Tagikawa, H. Horiuchi, Prog. Theor. Phys. (Jpn), Extra Vol. Suppl. 464 (1968)
- 10. H. Horiuchi, Prog. Theor. Phys. 43, 375 (1970)
- 11. H. Horiuchi, K. Ikeda, Y. Suzuki, Prog. Theor. Phys. (Jpn) Suppl. 52 Chap. 3 (1972)
- 12. W. von Oertzen Eur. Phys. J. A 29, 133 (2006)
- 13. G. Audi et al., Nucl. Phys. A 729, 3-128 (2003)
- 14. V.I. Isakov, et al., Part. Nucl. Lett. 5, 44 (2000)
- 15. F. Hoyle, Atrophys. J. Suppl. Ser. 1, 12 (1954)
- 16. A. Tohsaki, H. Horiuchi, P. Schuck, G. Röpke, Phys. Rev. Lett. 87, 192501 (2001)
- 17. P. Schuck, Y. Funaki, H. Horiuchi, G. Röpke, A. Tohsaki, T. Yamada, Nucl. Phys. A 738, 94 (2004)
- 18. Y. Funaki, H. Horiuchi, W. von Oertzen et al., Phys. Rev. C 80, 064326 (2009)
- 19. T. Yamada, P. Schuck, Phys. Rev. C 69, 024309 (2004)
- 20. P. Schuck, Y. Funaki, H. Horiuchi, G. Roepke, A. Tohsaki, T. Yamada, Prog.Part. Nucl. Phys. 59, 285 (2007)
- 21. P. Schuck, Y. Funaki, H. Horiuchi, G. Roepke, A. Tohsaki, T. Yamada, Nucl. Phys. News 17, 11 (2007)
- 22. Y. Funaki, et al., Phys. Rev. 80, 064326 (2009)
- 23. M. Freer, Rep. Prog. Phys. 70, 2149 (2007)
- 24. D.J. Amit, Y. Verbin, Statistical Physics: An Introductory Course (World Scientific, Singapore 1995)
- 25. H. Frauenfelder, E.M. Henley, Subatomic Physics. Physics Series (Prentice Hall, Englewood Cliffs, 1974), p. 546
- 26. S. Torilov, et al., Eur. Phys. J. A 19, 307 (2004)
- 27. T. Kokalova, et al., Eur. Phys. J. A 23, 19 (2005)
- 28. T. Kokalova, N. Itagaki, et al., Phys. Rev. Lett., 96, 192502 (2006)
- 29. S. Thummerer, et al., Phys. Scr. T 88, 114 (2000)
- 30. S. Thummerer, W. von Oertzen, B. Gebauer, S. Lenzi, A. Gadea, D.R. Napoli, C. Beck, M. Rousseau, J. Phys. G 27, 1405 (2001)
- 31. W. von Oertzen, Phys. Scr. T 88, 83 (2000)
- 32. D.T. Khoa, W. von Oertzen, H.G. Bohlen, S. Ohkubo J. Phys. G Nucl. Part. Phys. 34, R111-R164 (2007)
- 33. M. Chernych, et al., Phys. Rev. Lett. 98, 032501 (2007)
- 34. D.T. Khoa, D.C. Cuong, Phys. Lett. B 660, 331 (2008) and private communication
- 35. A.N. Danilov et al., Phys. Rev. C 80, 054603 (2009)
- 36. T. Wakasa, et al., Phys. Lett. B 653, 632 (2007)
- 37. R. Broglia, Ann. Phys. (New York), 80 60 (1973)
- 38. W. von Oertzen, A. Vitturi, Rep. Prog. Phys. 64, 1247 (2001)
- 39. W. von Oertzen, Phys. Lett. 61B, 223 (1976)
- 40. T. Glasmacher, Annu. Rev. Nucl. Part. Sci.48, 1 (1998)
- 41. I. Last, J. Jortner, Phys. Rev. A 62, 013201 (2000) and references therein
- 42. V. Zherebchevsky et al., Phys. Lett. **646 B**, 12 (2007)
- 43. W. von Oertzen et al., Eur. Phys. J. A 36, 279 (2008)

- 44. V. Bradnova et al., Nucl. Phys. A 734, E92 (2004)
- 45. P. Zarubin (2009). Private communication
- 46. J. Pochodzalla et al., Phys. Rev. C 35, 1695 (1987)
- 47. U.A. Wiedemann, U. Heinz, Phys. Rep. 319, 145 (1999)
- 48. F.S. Stephens, et al., Phys. Rev. Lett. 37, 2927 (1988)

Chapter 4 Cluster Structure of Neutron-Rich Nuclei Studied with Antisymmetrized Molecular Dynamics Model

Yoshiko Kanada-En'yo and Masaaki Kimura

4.1 Introduction

Following the progress in physics of unstable nuclei in these decades, a variety of novel cluster structures has been discovered. Theoretical studies has been revealed that valence neutrons play important roles to bring about such novel clustering phenomena. For description of clustering in unstable nuclei, various theoretical models have been developed. Among them, a method of antisymmetrized molecular dynamics (AMD) [1–8] is a powerful approach that successfully describes clustering and deformations of light unstable nuclei. Since the AMD method does not rely on specific cluster assumption and is applicable to general unstable nuclei, the method is useful for systematic study of various nuclei along isotope chains. In this chapter, we review formulation of the AMD and theoretical studies on structure of neutron-rich nuclei from Li to Mg isotopes.

4.2 Antisymmetrized Molecular Dynamics

4.2.1 Development of Theoretical Approaches for Cluster

Various exotic cluster structures has been discovered in the recent progress of unstable nuclear physics. For description of such novel structures in unstable nuclei, conventional cluster models for two- or three-body cluster systems are no longer

Yukawa Institute for Theoretical Physics, Kyoto University, Kyoto 606-8502, Japan e-mail: yenyo@ruby.scphys.kyoto-u.ac.jp

Creative Research Initiative "Sousei", Hokkaido University, Sapporo 001-0021, Japan e-mail: masaaki@nucl.sci.hokudai.ac.jp

Y. Kanada-En'yo (⊠)

M. Kimura

applicable because one often needs to solve more than three-body dynamics due to the degrees of freedom for excess nucleons. Therefore, various theoretical models have been developed for study of cluster phenomena in unstable nuclei. To describe many-body system consisting of cluster cores and valence nucleons, extended cluster models such as a stochastic variational method (SVM) [9–13], a molecular-orbital method (MO) [14–23], a generator coordinate method (GCM) [24–27], and an extended two-center model [28, 29] have been applied to unstable nuclei.

In these models, existence of clusters is a priori assumed. Although such cluster models are useful to describe detailed behavior of inter-cluster motion, the assumption of clusters is not necessarily obvious in real nuclear systems, because cluster states may have components of cluster breaking and they often coexist with the non-cluster states. Furthermore, for exotic nuclei with excess nucleons, another problem arises, i.e., it is unknown whether constituent clusters can be assumed.

To overcome this problem, it is important to take into account degrees of all single nucleons and construct new frameworks with no assumption of existence of specific clusters. In this point of view, a method of AMD [1–8] is one of the powerful approaches that do not rely on model assumption of constituent clusters. An AMD wave function is given by a Slater determinant of single-particle Gaussian wave functions, where all centers of the Gaussians are independently treated as variational parameters. Therefore, degrees of all single nucleons are independently treated in this framework. Moreover, because the AMD model space includes Bloch-Brink cluster wave functions, it can also describe cluster states. If a system favors a specific cluster channel, such cluster structure is naturally obtained by the energy variation.

A method of Fermionic molecular dynamics (FMD) [30, 31] is another promising approach whose model space is similar to that of the AMD but is a more generalized one. We should comment that, phenomenological effective nuclear forces with no hard core nor tensor term are used in the AMD method as well as in usual cluster models, while the effects of the hard core and the tensor force of *N*–*N* interactions are incorporated based on realistic nuclear forces in a recent version of the FMD [31] with unitary correlation operator method (UCOM).

After the first application of a simplest AMD method for structure study of unstable nuclei in 1995 [5, 6], the AMD framework has been developed to many versions (Refs. [4–7, 32–37] and references therein). In this section, we review the formulation of the simplest AMD and some advanced versions.

4.2.2 AMD Wave Function: Spherical Case

We set the model space for a wave function of a nuclear system as follows. In general, an A-nucleon system is given by a superposition of AMD wave functions,

$$\Phi = \Phi_{\text{AMD}}(\mathbf{Z}) + \Phi_{\text{AMD}}(\mathbf{Z}') + \Phi_{\text{AMD}}(\mathbf{Z}''). \tag{4.1}$$

Here, each AMD wave function is expressed by a Slater determinant of Gaussian wave packets;

$$\Phi_{\text{AMD}}(\mathbf{Z}) = \frac{1}{\sqrt{A!}} \mathcal{A}\{\varphi_1, \varphi_2, \dots, \varphi_A\},\tag{4.2}$$

where the *i*th single-particle wave function is written by a product of spatial (ϕ) , intrinsic spin (χ) , and isospin (τ) wave functions as,

$$\varphi_i = \phi_{\mathbf{X}_i} \chi_i \tau_i, \tag{4.3}$$

$$\phi_{\mathbf{X}_i}(\mathbf{r}_j) \propto \exp\left(-v\left(\mathbf{r}_j - \frac{\mathbf{X}_i}{\sqrt{v}}\right)^2\right),$$
 (4.4)

$$\chi_i = \left(\frac{1}{2} + \xi_i\right) \chi_{\uparrow} + \left(\frac{1}{2} - \xi_i\right) \chi_{\downarrow}. \tag{4.5}$$

The spatial part $\phi_{\mathbf{X}_i}$ of the *i*th single-particle wave function is represented by complex variational parameters, X_{i1} , X_{i2} , and X_{i3} , which indicate the center of the Gaussian wave packet. The spin part χ_i is parametrized by the complex number parameter, ξ_i . τ_i is isospin function which is fixed to be up (proton) or down (neutron). The width parameter v takes a common value for all nucleons, and is chosen to be an optimum value for each nucleus. Accordingly, an AMD wave function is expressed by a set of variational parameters, $\mathbf{Z} \equiv \{\mathbf{X}_1, \mathbf{X}_2, ..., \mathbf{X}_A, \xi_1, \xi_2, ..., \xi_A\}$. The parameters $\mathbf{Z} \equiv \{\mathbf{X}_1, \mathbf{X}_2, ..., \mathbf{X}_A, \xi_1, \xi_2, ..., \xi_A\}$ indicate the centroids of the localized Gaussians and the spin orientations, which are treated independently for all nucleons. Therefore, a system written by a single AMD wave function is specified by the configuration of single-nucleon wave packets in the phase space and their spin orientations. In the simplest AMD calculations, the spin part χ_i is sometimes fixed to be spin up or down. In this paper, the spin orientations are treated as free parameters in case of no explanation.

The AMD wave function can describe a Bloch-Brink cluster wave function if the parameters take a specific configuration (see Fig. 4.1a). Let us consider an example of an $\alpha + {}^{3}H$ cluster structure for ${}^{7}Li$. If Gaussian centers of singlenucleon wave packets for two protons and two neutrons are located at a same position and Gaussian wave packets for the other nucleons (one proton and two neutrons) are set at another position, the AMD wave function is equivalent to the Bloch-Brink cluster wave function consisting of α and ³H clusters which are written by the $(0s)^4$ and $(0s)^3$ configurations, respectively. With increase of the inter-cluster distance d, the spatial development of the corresponding cluster structure enhances. More generally, multi-cluster structure can be described by grouping of single-nucleon Gaussian wave packets in the spatial configuration. On the other hand, if centroids of Gaussians gather around the origin, the AMD wave function becomes equivalent to the harmonic oscillator shell-model wave function due to the effect of antisymmetrization (see Fig. 4.1b). Therefore, the model space of the AMD framework includes shell-model structure as well as various kinds of cluster structure. As we explain later, the optimum solution for complex number parameters **Z** is determined by energy variation. It means that if a system favors a specific cluster structure it is obtained automatically after the energy variation.

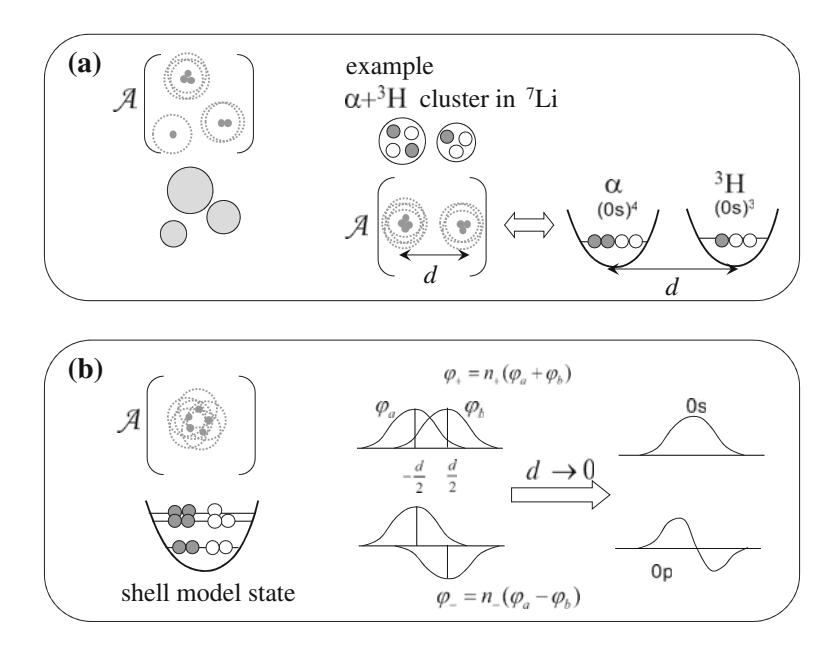


Fig. 4.1 Schematic figure of AMD wave functions. a Cluster structure. b H.O. shell-model structures are described with AMD wave functions. A indicates the antisymmetrizing operator

4.2.3 Deformed-Basis AMD

In the method of deformed-basis AMD [37, 38], triaxially deformed Gaussians are employed as the single-particle wave packets instead of spherical ones.

$$\phi_{\mathbf{X}_{i}}(\mathbf{r}_{j}) = \exp\left\{-\sum_{\sigma=x,y,z} v_{\sigma} (r_{j\sigma} - X_{i\sigma})^{2}\right\},\tag{4.6}$$

where the width parameters, v_x , v_y , and v_z , take different values for each direction, x, y, and z. They are determined in the energy variation to optimize energy of a system. By using this deformed basis, it is possible to describe sufficiently coexistence and mixing of the cluster and deformed mean-field structures that are essential in particular in medium-mass systems.

4.2.4 Parity and Angular-Momentum Projection

In calculation of expectation values for observable operators such as Hamiltonian, radii, moments, transitions, AMD wave functions are projected to parity and angular-momentum eigenstates. The parity-projected AMD wave function is given as

$$|\Phi_{\text{AMD}}^{\pm}\rangle \equiv P^{\pm}|\Phi_{\text{AMD}}\rangle = \frac{1\pm\hat{P}_x}{2}|\Phi_{\text{AMD}}\rangle,$$
 (4.7)

where $P^{\pm} = (1 \pm \hat{P}_x)/2$ is the parity projection operator. The angular-momentum projected AMD wave function is written as

$$|\Phi_{MK}^{J}\rangle = P_{MK}^{J}|\Phi_{\text{AMD}}\rangle = \int d\Omega D_{MK}^{J*}(\Omega)\hat{R}(\Omega)|\Phi_{\text{AMD}}\rangle,$$
 (4.8)

where $D^{J}_{MK}(\Omega)$ is Wigner's D function and $\hat{R}(\Omega)$ is a rotation operator with respect to Euler angle Ω . It is clear that the angular-momentum projected state is expressed by a linear combination of wave functions rotated from the intrinsic state $\Phi_{\rm AMD}$ with the weight function, D. For a tensor operator \hat{T}_q^k , where k is the rank and q is the z-component, the matrix element of the operator for $\langle P^{J}_{MK}\Phi_{\rm AMD}({\bf Z})|$ and $|P^{J'}_{M'K'}\Phi_{\rm AMD}({\bf Z}')\rangle$ can be calculated

$$\langle P_{MK}^{J} \Phi_{\text{AMD}}(\mathbf{Z}) | \hat{T}_{q}^{k} | P_{M'K'}^{J'} \Phi_{\text{AMD}}(\mathbf{Z}') \rangle = \frac{8\pi^{2}}{2J+1} \langle J'M'kq | JM \rangle \sum_{\mu\nu} \langle J'\mu k\nu | JK \rangle$$

$$\times \int d\Omega D_{\mu K'}^{J'*}(\Omega) \langle \Phi_{\text{AMD}}(\mathbf{Z}) | \hat{T}_{\nu}^{k} \hat{R}(\Omega) | \Phi_{\text{AMD}}(\mathbf{Z}') \rangle.$$
(4.9)

4.2.5 Hamiltonian and Energy Variation

The Hamiltonian consists of the kinetic energy, the nuclear and Coulomb potentials,

$$\hat{H} = \hat{T} + \hat{V}_{nuclear} + \hat{V}_{Coulomb} - \hat{T}_g. \tag{4.10}$$

Here the energy of the center-of-mass motion is subtracted. Since the single-particle wave functions are described by Gaussians with a common width parameter ν , the total wave function can be separated into the internal wave function and the center-of-mass wave function, and thus, the energy of the center-of-mass motion is calculated exactly.

For the effective nuclear potential $\hat{V}_{nuclear}$, finite-range forces are used as well as zero-range forces. For instance, Volkov [39], modified Volkov (MV1) [40], Gogny [41, 42], and Skyrme [43–45] forces have been used in the practical calculations. The Volkov force is the finite-range two-body force with no density dependent term, the Gogny force the finite-range two-body force with a zero-range density dependent force, the MV1 force the finite-range two-body force with a zero-range three-body force, while the Skyrme force is the zero-range density dependent force. Coulomb force is approximated by the seven-range Gaussian.

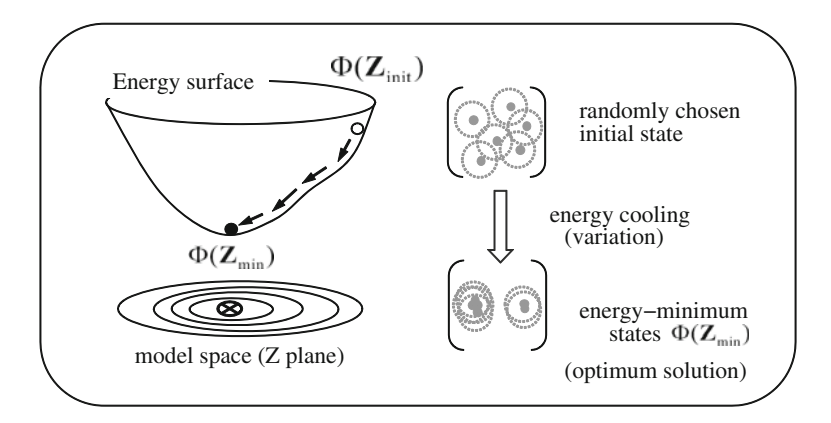


Fig. 4.2 Schematic figure of the frictional cooling method in the AMD model space

The AMD is a variational method. Namely, the variational parameters \mathbf{Z} are optimized to minimize the expectation value of the Hamiltonian within the AMD model space. The energy variation for the AMD wave function is performed by the frictional cooling method which is one of the imaginary time development methods. Here, we explain the frictional cooling method for a parity-projected AMD wave function. We introduce the following time development equation for the variational parameters \mathbf{X}_i and ξ_i ,

$$\frac{d\mathbf{Z}_{i}}{dt} = \frac{\mu}{\hbar} \frac{\partial}{\partial \mathbf{Z}_{i}^{*}} \frac{\langle \boldsymbol{\Phi}_{\text{AMD}}^{\pm} | \hat{H} | \boldsymbol{\Phi}_{\text{AMD}}^{\pm} \rangle}{\langle \boldsymbol{\Phi}_{\text{AMD}}^{\pm} | \boldsymbol{\Phi}_{\text{AMD}}^{\pm} \rangle}, \quad (i = 1, 2, ..., A).$$
(4.11)

Here, \mathbf{Z}_i indicates X_{i1} , X_{i2} , X_{i3} , and ξ_i . The value μ is an arbitrary negative real number. It is easily proved that the energy of the system,

$$E = \langle \Phi_{\text{AMD}}^{\pm} | \hat{H} | \Phi_{\text{AMD}}^{\pm} \rangle / \langle \Phi_{\text{AMD}}^{\pm} | \Phi_{\text{AMD}}^{\pm} \rangle, \tag{4.12}$$

decreases as time develops. We first start the energy variation from an initial AMD wave function which is given by randomly chosen parameters \mathbf{Z}_{init} . After enough cooling steps (iterations), we finally obtain the optimum set of parameters \mathbf{Z}_{min} which gives the AMD wave function for the minimum energy state in the model space (Fig. 4.2). In the deformed-basis AMD, the triaxial width parameters, also v_x , v_y , and v_z are optimized by the frictional cooling method.

4.2.6 GCM in **AMD**

In general, structures beyond the picture of independent single particles in a meanfield can be described by superposition of many Slater determinants. Superposition of Slater determinants is already done in the parity and/or angular-momentum projections of an AMD wave function. For excited states, it is useful to superpose many independent AMD wave functions. To adopt efficient AMD wave functions as basis wave functions for superposition, a constraint AMD method is applied. Let us consider the constraint on the nuclear quadrupole deformation parameter β . First, the energy variation after parity projection is performed with the constraint that the β value must be a given number $\bar{\beta}$. After the variation, the minimum energy state under the condition $\beta = \bar{\beta}$ is obtained. In more general, with a constraint of $\langle \hat{g} \rangle = \bar{g}$, the minimum energy state $\Phi^{\pm}_{AMD}(\bar{g}_k)$ is obtained by the constraint energy variation after parity projection for each constraint value $\bar{g} = \bar{g}_1, \bar{g}_2, \ldots, \bar{g}_k, \ldots$ Then, the angular-momentum projection is performed for the obtained states $\Phi^{\pm}_{AMD}(\bar{g}_k)$, and finally, the projected states of are superposed

$$|\Phi_n^{J\pm}\rangle = \sum_{kK} c_{kK} |P_{MK}^J \Phi_{\text{AMD}}^{\pm}(\bar{g}_k)\rangle.$$
 (4.13)

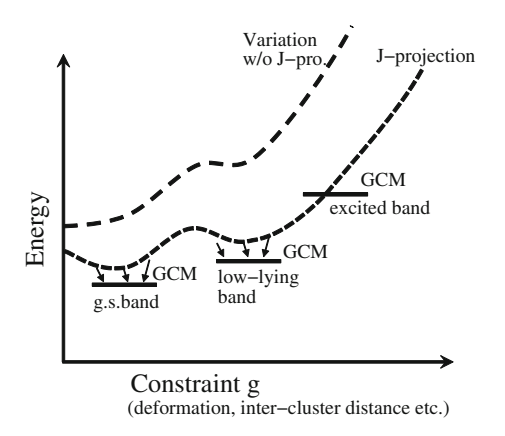
Here the values for the coefficients c_{kK} are determined by the variational principle,

$$\delta \left\{ \langle \Phi_n^{J\pm} | \hat{H} | \Phi_n^{J\pm} \rangle - \varepsilon_n \langle \Phi_n^{J\pm} | \Phi_n^{J\pm} \rangle \right\} = 0, \tag{4.14}$$

which is equivalent to diagonalization of the norm and the Hamiltonian matrices. The sum for the K quanta stands for the K-mixing. When an enough number of the basis wave functions with respect to the constraint value \bar{g}_k are taken into account, the superposition of different \bar{g}_k wave functions corresponds to the GCM, and \bar{g} is regarded as the generator coordinate. Many excited states can be described by superposing the parity and angular-momentum projected wave functions (GCM calculation). As the constraint $\langle \hat{g} \rangle$, principal oscillator quantum number $\langle a^\dagger a \rangle \equiv \langle \Phi^\pm | \sum_i^A \hat{\mathbf{a}}_i^\dagger \cdot \hat{\mathbf{a}}_i | \Phi^\pm \rangle / \langle \Phi^\pm | \Phi^\pm \rangle$ is sometimes employed as well as the quadrupole deformation β .

The practical procedure of the GCM calculations with the constraint AMD method is schematically illustrated in Fig. 4.3. First, the energy variation under the constraint is performed for a parity-projected AMD wave function. This means the constraint variation after parity projection but before angular-momentum

Fig. 4.3 Schematic figure of the procedure of the GCM calculations with the constraint AMD



projection (J-projection). After the variation for various constraint values, the parity and angular-momentum eigenstates projected from all the obtained AMD wave functions are superposed to construct the ground and excited states. Usually, the ground state wave functions are given by a linear combination of basis wave functions around the energy minimum state after the parity and angular-momentum projections. If there exists a local minimum on the parity and angularmomentum projected energy surface, the corresponding excited state may be obtained with the basis wave functions around the local minimum state in the GCM results. In case of the quadrupole deformation β constraint, it corresponds to the situation of shape coexistence where a low-lying deformed band appears in addition to the ground band. Moreover, in the GCM calculations, further excited bands might be obtained due to an excited mode in the generator coordinate. Thus, various excited states are obtained by a linear combinations of AMD wave functions in the GCM calculations. We note that, when a system has a cluster structure, the GCM calculation is also important to describe the detailed behavior of inter-cluster motion

4.2.7 Variation After Parity and Angular-Momentum Projections

For study of excited states, it is also efficient to perform variation after angular-momentum projection as well as parity projection. Namely, the energy expectation value for a parity and angular-momentum projected AMD wave function is minimized by the frictional cooling method,

$$\frac{d\mathbf{Z}_{i}}{dt} = \frac{\mu}{\hbar} \frac{\partial}{\partial \mathbf{Z}_{i}^{*}} \frac{\langle P_{MK}^{J\pm} \Phi_{\text{AMD}} | \hat{H} | P_{MK}^{J\pm} \Phi_{\text{AMD}} \rangle}{\langle P_{MK}^{J\pm} \Phi_{\text{AMD}} | P_{MK}^{J\pm} \Phi_{\text{AMD}} \rangle}.$$
(4.15)

Here $P_{MK}^{J\,\pm}$ is a spin-parity projection operator defined as $P_{MK}^{J\,\pm} \equiv P_{MK}^{J}P^{\,\pm}$. The lowest J^{\pm} state is denoted as $\Phi_{1}^{J\pm}(\{\mathbf{Z}\}_{1}^{J\pm}) = P_{MK}^{J\pm}\Phi_{\mathrm{AMD}}(\{\mathbf{Z}\}_{1}^{J\pm})$, where $\{\mathbf{Z}\}_{1}^{J\pm}$ stands for the parameter set $\{\mathbf{Z}\}$ which gives the energy minimum state for given spin and parity, $J^{\,\pm}$. The nth $J^{\,\pm}$ state is provided by varying $\{\mathbf{Z}\}$ to minimize the energy for the wave function $\Phi_{n}^{J\pm}(\{\mathbf{Z}\})$ orthogonalized to the already-obtained lower states $\Phi_{k}^{J\pm}(\{\mathbf{Z}\}_{k}^{J^{\pm}})(k=1,\ldots,n-1)$;

$$\Phi_{n}^{J\pm}(\{\mathbf{Z}\}) = P_{MK}^{J\pm}\Phi_{\text{AMD}}(\{\mathbf{Z}\}) - \sum_{k=1}^{n-1} \frac{\langle \Phi_{k}^{J\pm}(\{\mathbf{Z}\}_{k}^{J\pm}) | P_{MK}^{J\pm}\Phi_{\text{AMD}}(\{\mathbf{Z}\}) \rangle}{\langle \Phi_{k}^{J\pm}(\{\mathbf{Z}\}_{k}^{J\pm}) | \Phi_{k}^{J\pm}(\{\mathbf{Z}\}_{k}^{J\pm}) \rangle} \Phi_{k}^{J\pm}(\{\mathbf{Z}\}_{k}^{J\pm}).$$
(4.16)

After variation for various spins and parities, we superpose the intrinsic wave functions $\Phi_{AMD}(\{\mathbf{Z}\}_n^{J\pm})$ obtained by the variational calculations so as to get better wave functions. In the present paper, we call the variation after spin-parity

projection "VAP". Details of the VAP calculations are explained in Refs. [33, 46].

4.2.8 HF Single-Particle Orbits in an AMD Wave Function

In order to study the mean-field character of an intrinsic state given by an AMD wave function, it is useful to analyze the HF single-particle orbit contained in the AMD wave function [32] instead of the spatial configuration of single-nucleon wave packets. First, we transform the single-particle wave packets $|\varphi_i\rangle$ of the AMD wave function to an orthonormalized basis $|\alpha\rangle$,

$$B_{ij} = \langle \varphi_i | \varphi_j \rangle, \quad \sum_{i=1}^A B_{ij} d_{j\alpha} = \mu_{\alpha} d_{i\alpha}, \quad |\alpha\rangle = \frac{1}{\sqrt{\mu_{\alpha}}} \sum_{i=1}^A d_{j\alpha} |\varphi_j\rangle.$$
 (4.17)

From this orthonormalized basis $|\alpha\rangle$, we construct the HF single-particle Hamiltonian as follows. When Hamiltonian consists of the kinetic term and the two-body interaction, HF single-particle Hamiltonian is given as follows;

$$h_{\alpha\beta} = \langle \alpha | \hat{t} | \beta \rangle + \sum_{\gamma} \langle \alpha \gamma | \nu | \beta \gamma - \gamma \beta \rangle. \tag{4.18}$$

Then we diagonalize $h_{\alpha\beta}$ and obtain the single-particle energy e_p and single-particle orbit $|p\rangle$.

$$h_{\alpha\beta}g_{\beta\rho} = e_p g_{\alpha\rho},\tag{4.19}$$

$$|p\rangle = \sum_{\alpha} g_{\alpha p} |\alpha\rangle \tag{4.20}$$

It is easily proved that the Slater determinant of $|p\rangle$ is equivalent to that of $|\varphi_i\rangle$ except for a normalization.

4.2.9 Projection and Variation

As we mentioned before, an AMD wave function is expressed by a Slater determinant, however, the parity and angular-momentum projected wave function is no longer a Slater determinant but it is given by a linear combination of Slater determinants. Therefore, higher correlations beyond mean field may be incorporated in such projected states. Because of such correlation effects, clustering and deformation tend to enhance in the variation after projections in general.

For an example, we describe the results of ${}^{9}\text{Li}$ calculated by variation before parity and angular-momentum projections and that after parity and angular-momentum projections as well as the results of the β -constraint variation and the

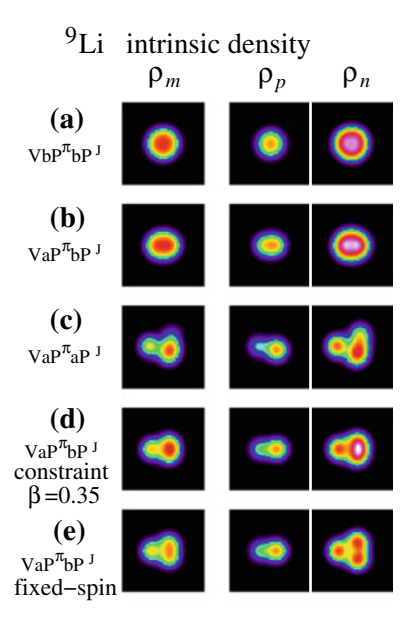


Fig. 4.4 Intrinsic density distributions of the AMD wave functions for ${}^9\mathrm{Li}$ obtained by a variation before parity projection $(P^{n=-})$ and before angular-momentum projection $(P^{J=3/2})$, **b** variation after parity projection and before angular-momentum projection, **c** variation after parity projection and after angular-momentum projection, **d** variation with the constraint $\beta=0.35$ after parity projection and before angular-momentum projection, **e** variation of an AMD wave function with fixed intrinsic spins after parity projection and before angular-momentum projection. The distribution of proton density (ρ_p) , neutron density (ρ_n) , and matter density (ρ_m) of the intrinsic AMD wave functions are illustrated. In the illustration, axes are chosen to be $\langle x^2 \rangle \leq \langle y^2 \rangle \leq \langle z^2 \rangle$, and the density is integrated along the x direction and shown on the z-y plane. The size of squares is 10 fm \times 10 fm. The adopted interaction consists of the Volkov No. 2 force with m=0.60, b=h=0.125 and the spin-orbit term from the G3RS interaction with $u_{ls}=u_I=-u_{II}=1,600 \text{ MeV}$

variation with fixed nucleon spins. Density distributions of the intrinsic states, each of which are written by a single AMD wave function, are illustrated in Fig. 4.4.

The intrinsic density of the AMD wave functions obtained by variation before parity and angular-momentum projections, that after parity projection but before angular-momentum projection, and that after parity and angular-momentum projections are shown in Fig. 4.4a–c, respectively. The state calculated by variation before projections (Fig. 4.4a) is the true energy minimum in a single AMD wave function and it corresponds to the Hartree–Fock solution within the AMD model space. This state has the most spherical shape due to an effect of the $p_{3/2}$ neutron shell closure. The variation after only parity projection yields a small deformation (Fig. 4.4b), however, a largely deformed state is obtained by the variation after parity and angular-momentum projections (Fig. 4.4c). The energies for the 3/2-states projected from these AMD wave functions (a), (b) and (c) are -29.9, -30.7 and -35.1 MeV, respectively. The energy gain in the VAP calculation

(c) is as much as 5 MeV in a ⁹Li system, and it originates in many-body correlations. These results indicates that the state with mean-field features is favored in the variation without projections while many-body correlations beyond mean-field are incorporated in the variation after parity and spin projections.

Many-body correlations can be contained also in the state obtained by the constraint variation before projections. We perform the variation after parity projection but before angular-momentum projection under the β constraint of quadrupole deformation. After the variation, we project the obtained AMD wave functions to the parity and angular-momentum eigenstates and calculate the $J^{\pm}=3/2^-$ -projected energies. The energy minimum in the projected energy curve is at $\beta=0.35$, and the corresponding intrinsic state is a deformed state shown in Fig. 4.4d. The $J^{\pm}=3/2^-$ energy for this state is -33.7 MeV which is much lower than -30.7 MeV of state (b) for the energy minimum solution without the β constraint. This energy gain is considered to come from the beyond mean-field correlations incorporated in the angular-momentum projection after the constraint variation.

We also show the AMD wave function obtained by variation after parity projection but before angular-momentum projection with fixed nucleon spins (χ_i) in Fig. 4.4e. The model space with fixed nucleon spins is rather restricted and it is included in the free spin model space. However, surprisingly, the $J^{\pm} = 3/2^-$ -projected energy for the state (e) with fixed spins is -32.2 MeV, and it is lower than -30.7 MeV for state (b) with free spins. This is naturally understood because the correlations between spin-up and spin-down neutrons may be enhanced in the restricted model space of fixed spins while they are smeared out in the free spin model space due to mean-field features in the variation of a single Slater determinant.

In this paper, we show mainly the results calculated by the variation after parity projection but before angular-momentum projection with AMD wave functions having free spins.

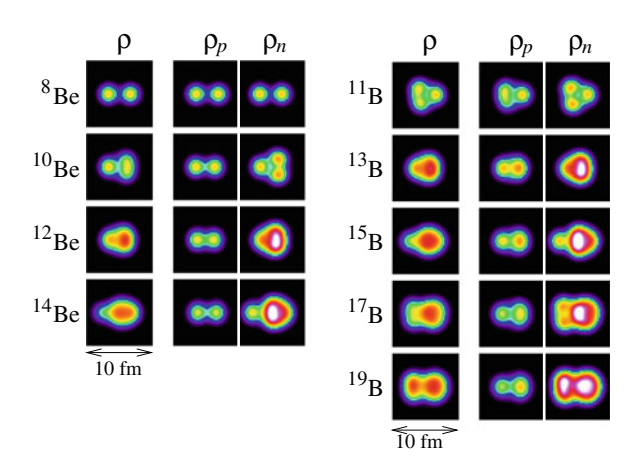
4.3 Properties of Low-Lying States in Light Nuclei

In this section, we briefly review structures of ground states in Li, Be, B, C isotopes based on studies with the AMD. We present the results obtained by the AMD calculations of variation after parity projection but before spin projection with fixed nucleon spins. More details are shown in Refs. [5–8] and references therein.

4.3.1 Structure Changes in Li, Be, B, C Isotopes

In 1990's, the AMD method has been applied for structure study of light neutron-rich nuclei such as Li, Be, B and C isotopes [5–8]. The AMD calculations succeed to reproduce various experimental data for structure properties.

Fig. 4.5 Density distributions of the normal-parity states of Be and B isotopes calculated with the AMD with fixed spins by using MV1 force with m = 0.576, b = h = 0 complemented by the spin-orbit term of G3RS with $u_{ls} = 900$ MeV. The figures are taken from Ref. [8]

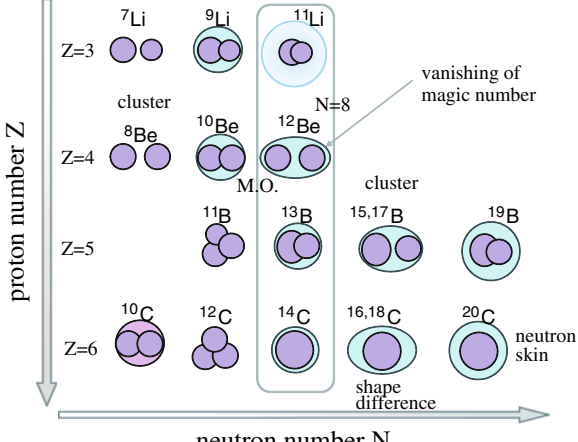


The results of the AMD calculations for Li, Be, B and C isotopes show that structures of ground states rapidly change depending on the neutron and proton numbers. Density distributions of the intrinsic wave functions for Be and B isotopes are shown in Fig. 4.5. Interestingly, various deformed states arise accompanying developed cluster structures in these isotopes.

Because of recent progress of theoretical and experimental investigations, structures of light neutron-rich nuclei have been revealed. We briefly summarize a current understanding of structure changes in Li, Be, B and C isotopes (Fig. 4.6) mainly based on the AMD calculations.

In the intrinsic states of Li isotopes, ⁷Li has the largest prolate deformation with a well-developed $\alpha + t$ cluster structure. As the neutron number N increases, the cluster structure becomes less prominent, and finally disappears in ¹¹Li with a spherical shape. We should comment that ¹¹Li is known to have an extremely large radius because of the two-neutron halo structure [47, 81–88], though it is difficult

Fig. 4.6 Schematic figure of structure change of the ground states in Li, Be, B and C isotopes



neutron number N

to describe such halo structure in the simple AMD framework because a singlenucleon wave function is written by a Gaussian in the model.

In Be isotopes, it is well-known that the 2α cluster structure is prominent in 8 Be [89]. The AMD results indicate that the 2α cluster core is formed also in neutron-rich Be isotopes as seen in the dumbbell shape of proton density in Fig. 4.5. As the neutron number increases from 8 Be, the 2α cluster structure becomes less developed in 10 Be. In 12 Be, which has the neutron magic number N=8, a spherical $0\hbar\omega$ state and a deformed $2\hbar\omega$ coexists in the low energy region. Although the spherical state with the neutron p-shell closure is the lowest state in the simple AMD calculations as shown in Fig. 4.5, this state may correspond to the excited state experimentally observed at 2.1 MeV. Instead, the improved AMD calculations suggested that the deformed $2\hbar\omega$ state with developed 2α clusters comes down due to the molecular-orbital structure and it dominates the real 12 Be ground state [90]. This phenomena is called "breaking of neutron magic number". The details of 10 Be, 11 Be will be explained in the next section.

In the case of B isotopes, the structure changes as a function of N is similar to that in Be isotopes except for the $N \sim 8$ region. ¹³B with N=8 has the most spherical shape because it is dominated by the neutron p-shell closed configuration. As the neutron number increases, a cluster feature develops with enhancement of the prolate deformation. For ¹⁹B at a neutron drip line, the improved AMD calculations suggested that shape coexistence may occur, i.e., the prolate state shown in Fig. 4.5 may be an excited state whereas an oblate state becomes the ground state in ¹⁹B [91].

In contrast to development of the cluster structures in neutron-rich Be and B isotopes, neutron-rich C isotopes are suggested not to have prominent cluster structures at least in ground states. In light C isotopes, cluster aspects are seen as in 12 C with an oblate deformation because of the 3α cluster feature. On the other hand, in neutron-rich C isotopes, even though the neutron structure rapidly varies as N increases, proton density remains in an inner compact region. As a result, the neutron skin structure may remarkably grow near the drip line.

It should be pointed out that the cluster features found in neutron-rich Be and B isotopes differ from the standard cluster structure consisting of weakly coupling clusters. They are regarded as new-type cluster structures, which are composed by a few cluster cores with surrounding neutrons.

4.3.2 Magnetic Moments of Li and B Isotopes

The AMD calculations show good reproductions for the electric and magnetic moments and transitions such as the magnetic dipole moments μ , electric quadrupole moments Q, and the E2 transition strength [5–8]. The experimental data for such magnetic and electric properties are successfully reproduced by the AMD calculations with the bare charges and the bare g-factors of nucleons instead of the phenomenological effective values that are usually used in shell model

calculations. It owes to flexibility of the AMD approach which can explicitly treat such structure aspects as large deformation, core excitation, development of cluster structure, and many-body correlations due to developed cluster structures.

It is helpful to investigate experimental data such as the moments along a chain of isotopes and discuss their neutron number dependence in relation with intrinsic structure changes. In Refs. [5–7], the structure of light neutron-rich nuclei were discussed by connecting experimental data of magnetic and electric moments with the cluster structures. We here discuss the magnetic moments of Li and B isotopes and effects of the cluster structure on them.

The nuclear magnetic moment is defined as

$$\mu \equiv \langle JM | \hat{\mu}_0 | JM \rangle_{M=J} \tag{4.21}$$

$$\hat{\mu}_0 = g_s^p S_z^p + g_I^p L_z^p + g_s^n S_z^p, \tag{4.22}$$

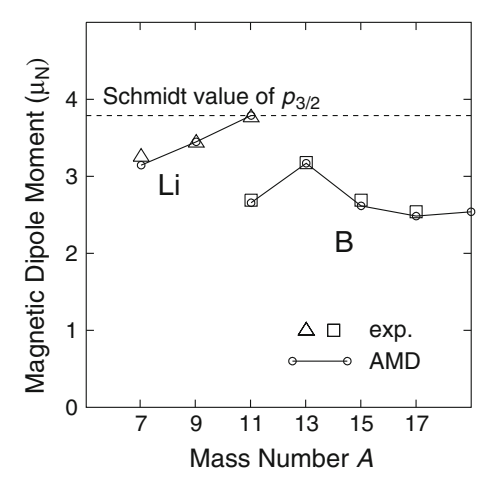
where g_s^p and g_s^n are the g-factors of a proton and a neutron, $g_s^p = 5.58$ and $g_s^n = -3.82$, and $g_l^p = 1$ is the factor for proton orbital angular momentum. S_z^p and S_z^n are the z-components of the total intrinsic spins for protons and neutrons, respectively, and L_z^p is that of the total orbital angular momentum for protons. Thus, the magnetic moment reflects components carrying the total angular momentum J in the highest M state.

Let us consider the magnetic moments of odd-even Li and Be isotopes which have $J=3/2^-$ ground states. In the simplest picture that all spins for even nucleons couple to be zero spin and gives no contribution to the total angular momentum, the total angular momentum is simply given by a single valence proton in the $p_{3/2}$ orbit. In this limit, the μ value can be simply estimated to be $\mu=g_s^p\times 0.5+g_l^p\times 1=3.79$ from the $p_{3/2}$ proton component (Fig. 4.8a). This value is called the Schmidt value. In reality, even nucleons do not necessarily pair off but may give non-zero spin contributions. In particular, a state with cluster structure may contain strong correlations in coupling of orbital angular momenta of nucleons, or in other words, much orbital excitations. As a result of such manybody correlations, non-zero spin contributions arise from even nucleons, and therefore the μ moment may deviate from the Schmidt value for the ideal case.

The values of μ moments for odd-even Li and B isotopes calculated by the AMD are shown in Fig. 4.7 as well as the experimental data. The theoretical values are in good agreement with the experimental data. In each series of isotopes, one can find the neutron number (N) dependence of the μ moment. This N dependence can be understood by cluster structures in Li and B isotopes. It is useful to discuss the deviation of μ moments from the Schmidt value $\mu = 3.79$ for the $p_{3/2}$ proton orbit.

In ^{11}Li , the μ value is almost equal to the Schmidt value. This is because ^{11}Li has no cluster structure and 8 neutrons give no contribution to the magnetic moment. As the neutron number decreases in Li isotopes, the μ value becomes small and the deviation from the Schmidt value grows up following the development of cluster structure. That is to say that, because of cluster structure,

Fig. 4.7 Magnetic dipole moments μ of odd-even Li and B isotopes. The calculations are same as those for Fig.4.5. The figure is taken from Ref. [5]



neutrons give non-zero component of finite orbital angular momentum $L^n \neq 0$ for neutron which causes the tilted proton orbital angular momentum L^p and reduction of the L^p_z component in the highest M state (Fig. 4.8). As a result, the term $\langle L^p_z \rangle$ becomes smaller than 1 and the μ value decreases.

The behavior of μ moments in B isotopes can be understood in a similar scenario. Also in B isotopes, ¹³B with N=8 shows the smallest deviation from the Schmidt value because it has the least cluster structure. In such non-cluster state,

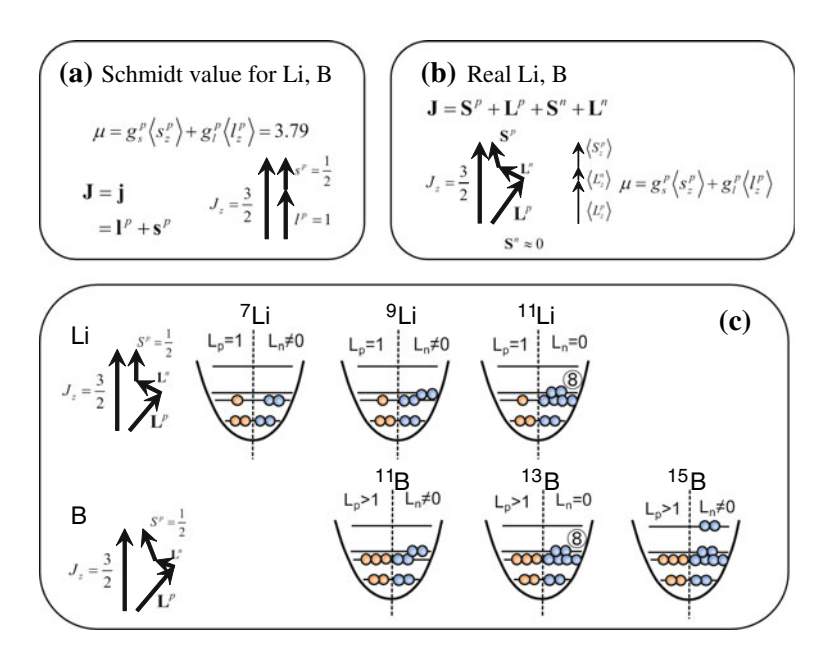


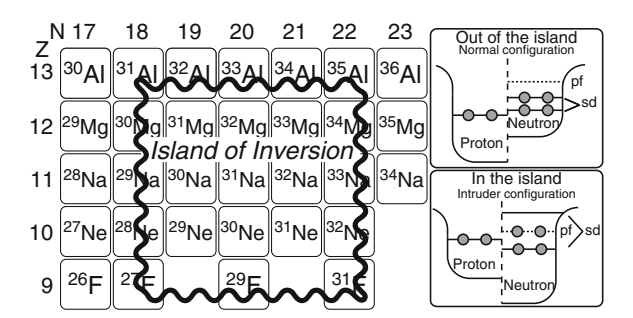
Fig. 4.8 Schematic figure for components in magnetic moments of Li and B isotopes

the neutron part with the p-shell closed configuration gives no contribution to the μ moment. As described before, the cluster structure develops in ^{15}B and ^{17}B with the increase of the neutron number. In such cluster structure, neutrons give non-zero orbital-angular-momentum $L^n \neq 0$ bringing the reduction of L^p_z component in the highest M state. Consequently, the deviation from the Schmidt value is larger in ^{15}B and ^{17}B than that in ^{13}B . It is also interesting that the μ values of B isotopes are systematically smaller than those in Li isotopes. This is because, in case of B isotopes, correlations of three protons in p-shell yields additional quenching of the μ moments of B.

4.4 Properties of Nuclei in the Island of Inversion

Several neutron-rich $N \sim 20$ nuclei are known to have anomalous properties in the binding and excitation energies, spin-parity and electro-weak transitions. These anomalies originate in large nuclear deformation and the resultant inversion of sdand pf-shells (breakdown of the magic number N = 20). Experimentally, it was firstly pointed out from the observation of the anomalous binding energy and spinparity of ³¹Na [48, 49]. More convincing evidence was given by the observation of the small excitation energy [50, 51] and the large E2 transition probability [52] of the 2⁺ state of ³²Mg. Theoretically, the Hartree–Fock calculation [53] showed that shape transition from spherical to prolate shapes possibly took place in neutronrich N = 20 nuclei. Shell model calculations [54–56] that allowed particle hole excitations across the N = 20 shell gap explained these abnormal properties and suggested strong deformation of ³¹Na and neighboring nuclei caused by the inversion between the normal and intruder configurations. Since then, many experimental [57–64] and theoretical [65–76] studies have been made and now the systematic breaking of N = 20 magic number is theoretically investigated and the large deformation is observed in ^{31,32,34}Mg [52, 61, 64], ^{30,31,32}Na [49, 77, 78] and ^{30,32}Ne [63, 79]. Thus, our knowledge of the breakdown of the neutron magic number N = 20 in the neutron-rich nuclei has been increasing rapidly in this decade. This domain of the nuclear chart is called "Island of Inversion" (Fig. 4.9).

Fig. 4.9 Island of inversion in the nuclear chart. The ground state is dominated by the intruder configuration in which the magic number N = 20 is broken. Note that the border of the island is still unclear and being investigated



In this section, we briefly discuss the properties of nuclei in the island of inversion and try to illustrate the landscape of the island based on the deformed-basis AMD. For more detail, readers are directed to the references [74–76].

4.4.1 Deformation, Particle-Hole Configuration and Spectrum

To make clear the onset of nuclear deformation in and around the island of inversion, it is most convenient to see the energy curve as function of nuclear quadrupole deformation, which indicates the β dependence of the expectation value of Hamiltonian obtained by β -constraint calculations. Fig. 4.10 shows the energy curves of Ne, Mg and Al isotopes with N=18, 20, 22, calculated by the deformed-basis AMD. For a moment, let us focus on the energy curves of 32 Mg that is located at the middle of the island. There are three minima in the positive-parity energy curve and two in the negative-parity. These minima have different single-particle configurations. Fig. 4.11a shows the single-particle orbitals occupied by the last 12 neutrons in the positive-parity state. We can see the Nilsson-model-like behavior of the orbitals. In the spherical region, the last two neutrons occupy the orbital originates in sd-shell. Therefore, the system has the closed shell (0p0h) configuration at small deformation (hereafter, we denote particle hole

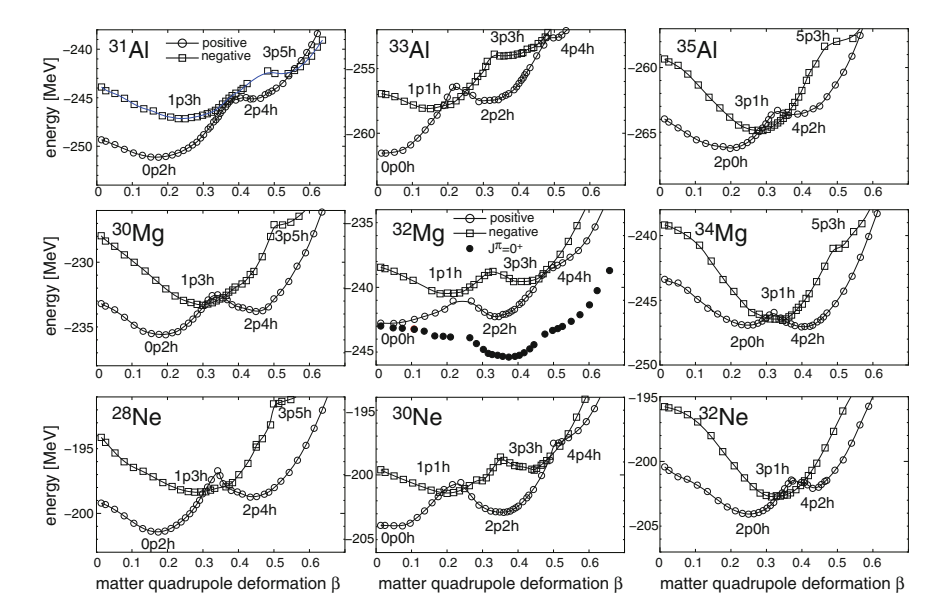


Fig. 4.10 Energy curves of Ne, Mg and Al isotopes as function of nuclear quadrupole deformation. *Open circles (open boxes)* show the energy curves for the positive-parity (negative-parity) states before the angular momentum projection. *Filled circles* in 32 Mg show the energy curve after the angular momentum projection to $J^{\pi} = 0^{+}$

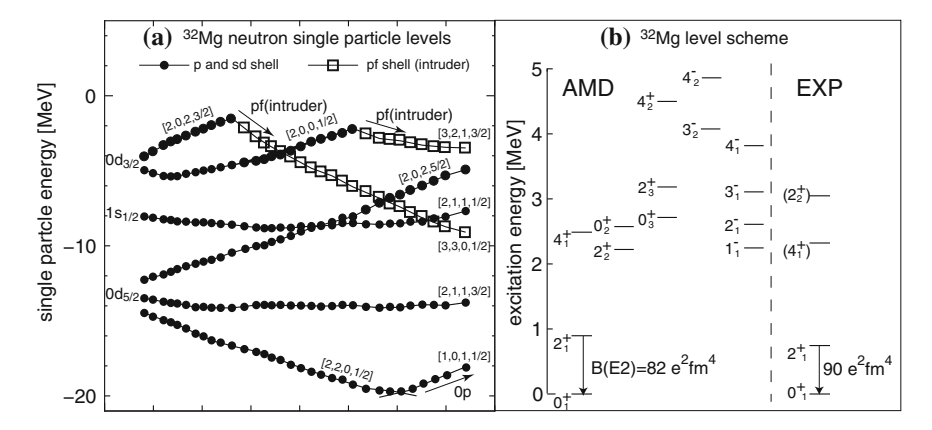


Fig. 4.11 a Single-particle levels for last 12 neutrons. *Filled circles* show the orbitals originates in the *p*- or *sd*-shell, while *open boxes* show the intruder orbital from *pf*-shell. **b** Calculated and observed low-lying level spectrum of 32 Mg. Experimental data are taken from Ref. [52]. It also shows the B($E2; 2_1^+ \rightarrow 2_1^+$)

configurations with respect to N=20 shell closure). Around $\beta=0.3$ an orbital intrudes from pf-shell into sd-shell. Two neutrons occupy this intruding orbital and the system has 2p2h configuration. Around $\beta=0.5$, another orbital comes down from pf-shell and the system has the 4p4h configuration. Thus, the minima on the positive-parity energy curve are understood to have 0p0h, 2p2h and 4p4h configurations in ascending order of deformation. In the same way, the minima on the negative-parity energy curve have 1p1h and 3p3h configurations.

After the angular momentum projection, the 2p2h configuration around $\beta=0.4$ has the smallest energy. By superposing those wave functions with different configurations and performing the GCM calculation, we have obtained the low-lying level spectrum (Fig. 4.11b). The ground band is dominated by the 2p2h configurations and strongly deformed. It is confirmed by the calculated and observed large $B(E2; 2_1^+ \rightarrow 0_1^+)$ and small excitation energy of the 2_1^+ state. It is notable that the calculation predicts the low-lying excited bands dominated by different particle-hole configurations in both positive- and negative-parity. Since the particle-hole configurations changes bustlingly as function of deformation, the low-lying bands with different configurations appear at small excitation energy. This is peculiar to the nuclei in the island of inversion and discussed later.

Now, let us move on the Ne, Mg and Al isotopes. These are several striking features in their energy curves and they are related to the mechanism of the breaking of the magic number N = 20; (a) there are several minima (shoulders) on the surface, (b) number of minima depends on neutron number but not on proton number, (c) relative energy between minima strongly depends on proton number.

The particle-hole configuration of each minimum shown in Fig. 4.10 tells that up to four particle or four hole configurations (from np4h to 4pnh) appear at small excitation energy. It is consistent with the behavior of neutron single-particle orbital in which two orbitals originates in the pf-shell and two from sd-shell cross

as deformation becomes larger. Since the states on the energy curve is dominated by the neutron particle-hole configurations, (a) minima with different neutron configurations appear, and (b) the single-particle configurations of each minimum depends on the neutron number. As proton number decreases, the binding energy of the spherical (or small deformed) states become smaller. It reduces the relative energy between different particle hole configurations and, in some case as ³²Mg, strongly deformed configuration becomes the ground state. From energy curve and the angular momentum projection, we will also see that ^{30,32}Ne and ^{32,34}Mg are in the island of inversion and other nuclei are out of the border of the island.

4.4.2 Probing the Particle Hole Configuration

We have seen that many particle hole configurations dominates the island of inversion. Since the neutron single-particle orbital is difficult to observe directly, an alternative way to confirm deformation and the neutron particle configuration is required. As an illustrative example, we discuss the spin-parity and β decay of ^{31}Mg . Here, ^{31}Mg is in the island of inversion [64] and dominated by the 2p1h configurations, while ^{31}Al is out of the island [80]. The spectrum of ^{31}Mg (Fig. 4.12a) confirms it. ^{31}Mg has odd neutron number, and hence, the orbital occupied by the last neutron determines the spin-parity of the system. From the Nilsson-model-like behavior, we can conclude that there is no other way to explain

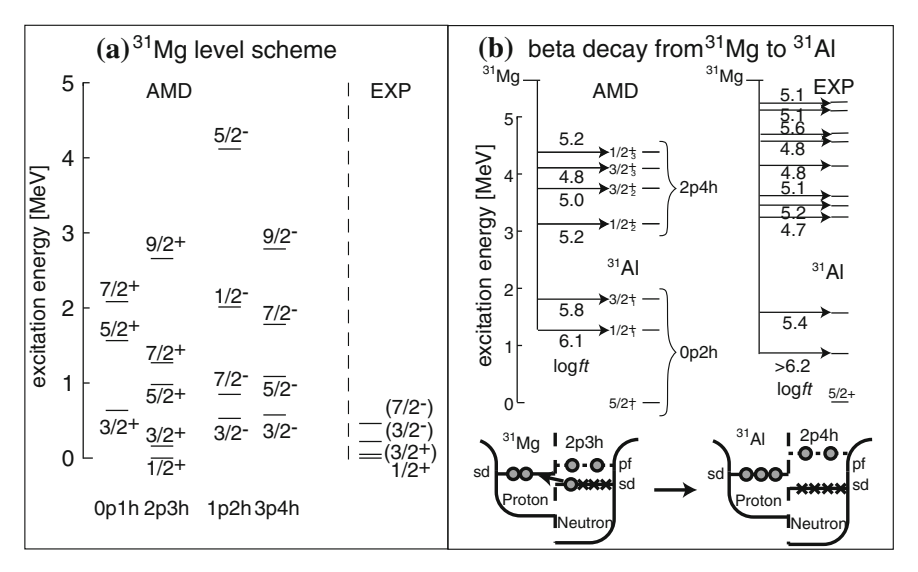


Fig. 4.12 a Calculated and observed low-lying level spectrum of 31 Mg. Dominating particle-hole configuration is shown in each band for the calculation. **b** Low-lying spectrum of 31 Al and logft of 31 Mg β decay. **a** Taken from Ref. [75]

the observed and calculated ground state spin $1/2^+$ [64] except for the 2p3h configuration associated with the strong deformation.

The β decays also sensitive to the particle hole configurations of 31 Mg as illustrated in Fig. 4.12b. Since the ground state of 31 Mg has the 2p3h configuration, it will most strongly feed the 2p4h configuration of 31 Al. Here, 31 Al is located at out of the island and its ground state is dominated by the 0p2h configuration and the intruder 2p4h configuration appear as the excited band around 3 MeV. Both the observation [51, 57] and the calculation shows the strong decays to the excited states of 31 Al and weaker decays to the low-lying states.

4.5 Cluster Structure in Excited States

4.5.1 Be Isotopes

4.5.1.1 Outline of Structure in Neutron-Rich Be

Cluster structure in neutron-rich Be isotopes is one of the interesting topics on cluster phenomena in unstable nuclei. Low-lying states of neutron-rich Be isotopes are understood by a molecular-orbital picture based on the structure with a 2α core and surrounding valence neutrons [8, 11–23, 32].

In the molecular–orbital picture, neutron-rich Be isotopes are considered to consist of a 2α core and valence neutrons. The molecular orbitals are formed by a linear combination of atomic orbitals around each cluster, and then valence neutrons occupy the molecular orbitals. In case of Be systems, so-called π and σ orbitals in the 2α system are considered for molecular orbitals of valence neutrons. The idea of the molecular orbitals surrounding a 2α core was suggested in 9 Be with a 2α + n cluster model [14–16] in 1970's. The molecular–orbital model was applied to neutron-rich Be isotopes by Seya et al. [17] in 1980's. In 1990's, in the works by von Oertzen et al. [18–20] and Itagaki et al. [21, 22], molecular–orbit models for the 2α + Xn cluster structure have been extended for systematic study on neutron-rich Be isotopes.

Recently, cluster structures of neutron-rich Be isotopes were theoretically investigated by many groups by using extended cluster models and molecular–orbital models, where the existence of 2α clusters are a priori assumed in the models. In contrast to these cluster models, the AMD method relies on neither existence of the cluster cores nor formation of the molecular orbitals, and therefore, it is suitable to check whether the molecular–orbital structure appears in real neutron-rich Be systems. The results of the AMD calculations suggested that the molecular–orbital structures with the 2α core and surrounding valence neutrons actually appear in low-lying states of Be isotopes, while di-cluster states with two-body He + He cluster structures arise in highly excited states of 12 Be.

In this section, we report the cluster structures of neutron-rich Be isotopes based on the AMD calculations [8, 23, 46, 90, 92]. The ground and excited states of

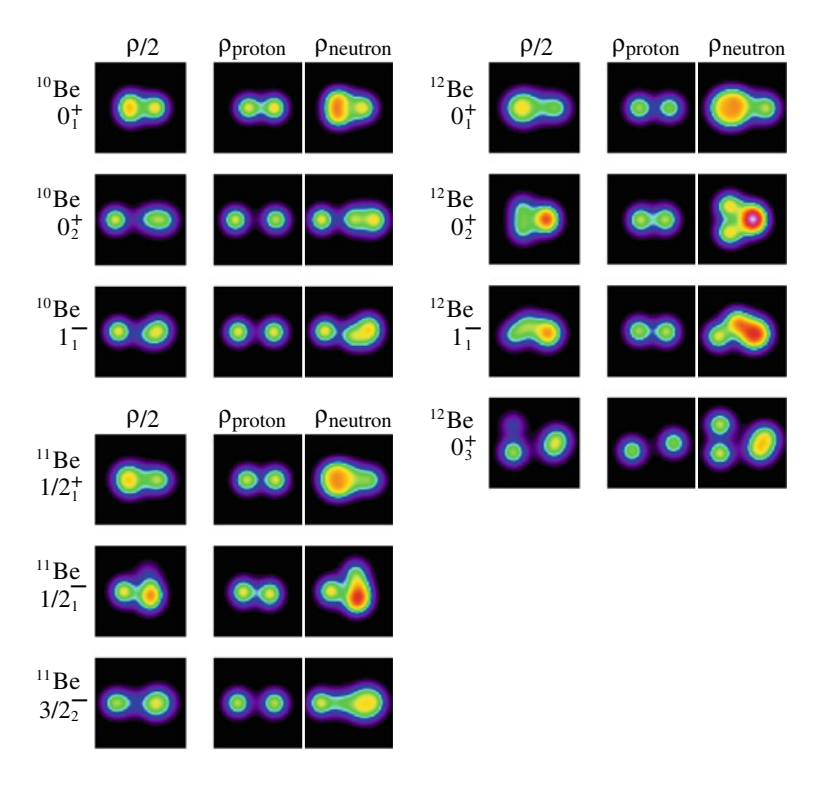
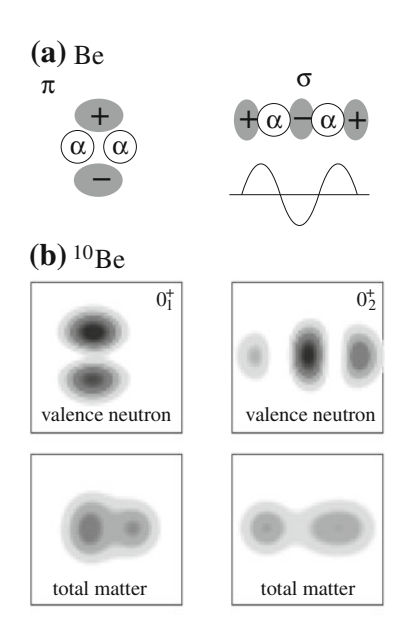


Fig. 4.13 Density distributions of the intrinsic states for the band-head states of ¹⁰Be, ¹¹Be and ¹²Be obtained by the VAP calculations. Distributions for matter, proton, and neutron densities are illustrated in the *left, middle* and *right* panels. The figures are taken from Ref. [8]

Be isotopes were calculated with the VAP method in the AMD framework [46, 90, 92]. The calculated results suggested that many rotational bands with the 2α core structure appear in Be isotopes. Fig. 4.13 shows the density distribution of the intrinsic wave functions for the band-head states of 10 Be, 11 Be and 12 Be. One can see that the proton-density distribution indicates the formation of the 2α -cluster core, while the neutron density distribution displays the feature of valence neutrons surrounding the 2α core.

By analyzing the single-particle behavior of the valence neutrons, it was found that the single-particle wave functions of the valence neutrons in the low-lying states of Be isotopes are associated with the molecular orbitals around the 2α core. As described before, in the molecular-orbital picture, valence neutrons occupy the molecular orbital formed by a linear combination of neutron orbits surrounding each cluster. In case of a 2α system, the lowest allowed neutron orbit around a single α cluster is the p orbit. Therefore, the molecular orbitals (π and σ) in a 2α system are expressed by a linear combination of p orbits around the two α cores as displayed in Fig. 4.14a. Let us analyze the HF single-particle orbits for the valence neutron in the intrinsic states of 10 Be. As shown in Fig. 4.14b, the valence neutron

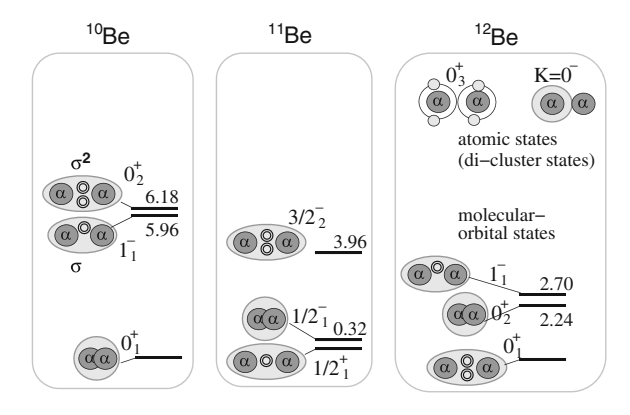
Fig. 4.14 Schematic figure for molecular orbitals, **a** *left* The π and *right* σ orbitals around a 2α core. **b** *Upper panels* Density distributions of the HF single-particle wave functions for valence neutrons in $^{10}\text{Be}(0^+_1)$ (*left*) and $^{10}\text{Be}(0^+_2)$ (*right*). *Lower panels* Distributions of total matter density in the $^{10}\text{Be}(0^+_1)$ and $^{10}\text{Be}(0^+_2)$ states



wave functions in the $^{10}Be(0_1^+)$ state is associated with the π orbital, while those in the $^{10}Be(0_2^+)$ state can be regarded as the σ orbital in terms of molecular orbitals. Therefore, the structure of the $0_1^+(0_2^+)$ is interpreted as the molecular–orbital structure where two valence neutrons occupy the $\pi(\sigma)$ orbitals around the 2α core. It is interesting that the cluster structure in the excited state, $^{10}Be(0_2^+)$, is prominent, while it is weaker in the ground state. The reason is that the σ orbital has nodes along the $\alpha-\alpha$ direction and therefore it gains its kinetic energy if the distance between two α clusters becomes large. This enhancement of the 2α cluster is consistent with the discussions of Refs. [18–23]. In a similar way, also the low-lying states in ^{11}Be and ^{12}Be can be understood in terms of the molecular orbitals. For instance, $^{11}Be(1/2^+)$, $^{11}Be(1/2^-)$, and $^{11}Be(3/2_2^-)$ correspond to $\pi^2\sigma$, π^3 , and $\pi\sigma^2$ configurations, respectively, and the $^{12}Be(0_1^+)$, $^{12}Be(0_2^+)$, and $^{12}Be(1_1^-)$ states are dominated by the $\pi^2\sigma^2$, π^4 , and $\pi^3\sigma^1$ configurations, respectively, in terms of the molecular orbitals occupied by the valence neutrons.

We show a schematic figure of the cluster states suggested in 10 Be, 11 Be and 12 Be in Fig. 4.15, where neutrons occupying the σ -type molecular orbital are explicitly drawn. The experimental values of excitation energies for the corresponding states are also shown in the figures. One of interesting features is that the degree of cluster development strongly correlates with the number of valence neutrons in the σ orbital. Namely, the 2α cluster structure develops with the increase of the number of σ -orbital neutrons. As we already mentioned, it is because the σ orbital gains its single-particle kinetic energy in a developed 2α system. On the other hand, as the number of π -orbital neutrons increases, the cluster structure tends to weaken.

Fig. 4.15 Schematic figures for cluster states suggested in 10 Be, 11 Be and 12 Be. We illustrate 2 α clusters and the valence neutrons in the σ orbital. The experimental data of the excitation energies for the corresponding states are also shown



Another interesting feature is that the ground states of ^{11}Be and ^{12}Be are the intruder states with σ -orbital neutron(s) instead of the normal states with $0\hbar\omega$ configurations. In terms of molecular orbitals, the ground $1/2^+$ state of ^{11}Be corresponds to the $\pi^2\sigma$ configuration, and $^{12}\text{Be}(0_1^+)$ is dominated by the intruder $\pi^2\sigma^2$ configurations. In the one-center limit where two α cores are close to each other, the π orbital becomes equivalent to the p orbit and the σ orbital becomes the corresponding sd orbit of the spherical harmonic oscillator basis. Therefore, in terms of shell model configurations, the $^{11}\text{Be}(1/2_1^+)$ and $^{12}\text{Be}(0_1^+)$ states are dominated by the neutron excited configurations of $1\hbar\omega$ with a sd-shell neutron and $2\hbar\omega$ with two sd-shell neutrons, respectively. In other words, the energy gain of the σ orbital in the deformed system with the developed 2α structure plays an important role for the breaking of the N=8 neutron magic number in ^{11}Be and ^{12}Be [7, 90, 92]. In highly excited states of ^{12}Be , well-developed di-cluster structures with He + He clustering have been theoretically suggested above the low-lying molecular-orbital states. More details of band structures in ^{10}Be and ^{12}Be are explained below.

4.5.1.2 ¹⁰Be

The calculated energy levels of 10 Be are shown in Fig. 4.16. The calculations well reproduce the level structure of the experimental data and also give theoretical suggestion for some new excited states. Moreover the experimental values for transition strength such as E2 and E1 transitions and β decays for 10 Be are reproduced well by the calculations [46].

By analyzing intrinsic structures, we can classify the excited states into four rotational bands, $K^{\pi}=0^+_1,2^+,0^+_2$, and 1^- , whose members are $(0^+_1,2^+_1,4^+_1)$, $(2^+_2,3^+_1),(0^+_2,2^+_3,4^+_2,6^+_1)$, and $(1^-,2^-,3^-,4^-,5^-)$, respectively. Various kinds of cluster structures are found in these bands. As mentioned before, the 2α core and 2n structure is found in most of the intrinsic states in the low-energy region. In particular, the $K^{\pi}=0^+_2$ and 1^- bands have the structure with well-developed 2α clusters. As seen in Fig. 4.13, the development of clusters is larger in the 1^- band

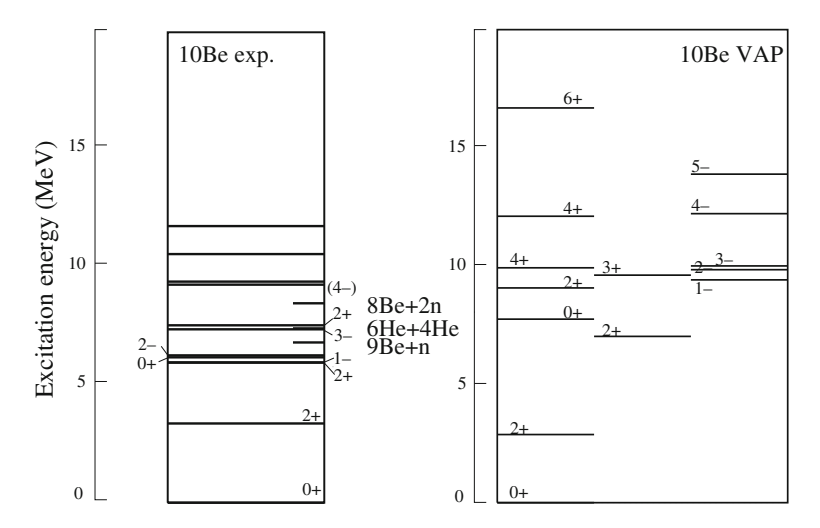


Fig. 4.16 Level schemes of 10 Be. Theoretical results are calculated with the VAP calculations using the MV1 force and the spin-orbit term of the G3RS force with the parameter set m=0.62, b=h=0, and $u_{ls}=3$, 000 MeV. The figures are taken from Ref. [8]

than the 0_1^+ band, and it is most prominent in the 0_2^+ band. On the other hand, the $K^\pi=2^+$ band is regarded as the side-band of the ground band. Cluster features in the present results are consistent with the results by extended cluster models of 2α clusters and surrounding neutrons [12, 21, 22]. An important point is that the AMD calculations [5–7, 32, 46] actually have confirmed formation of the 2α core in 10 Be in the framework without assuming existence of any clusters. As mentioned before, in the analysis of the HF single-particle orbits, the $0_1^+, 2_2^+, 1^-$, and 0_2^+ states are interpreted as the π^2 , π^2 , $\pi\sigma$, σ^2 molecular–orbital configurations, respectively (Fig. 4.14).

4.5.1.3 ¹²Be

In the recent past years, experimental and theoretical investigations of ¹²Be has been progressing, and properties of low-lying states and also those of highly excited states are being revealed [20, 23, 26, 29, 90, 94–102].

The ground and excited states of 12 Be have been calculated with VAP by adjusting the effective nuclear interactions to reproduce the parity inversion in 11 Be [90, 92]. The calculated energy levels of 12 Be are shown in Fig. 4.17 with the experimental data. We can classify the calculated positive-parity states with natural spins into three rotational bands, $K^{\pi} = 0^+_1, 0^+_2$ and 0^+_3 . The ground band consists of the intruder states ($2\hbar\omega$ excited configurations), which are well-deformed states with a 2α core and surrounding neutrons. On the other hand, the normal neutron p-shell closed states belong to the $K^{\pi} = 0^+_2$ band whose band-head state is assigned to the experimental second 0^+ state at 2.1 MeV [100]. It means

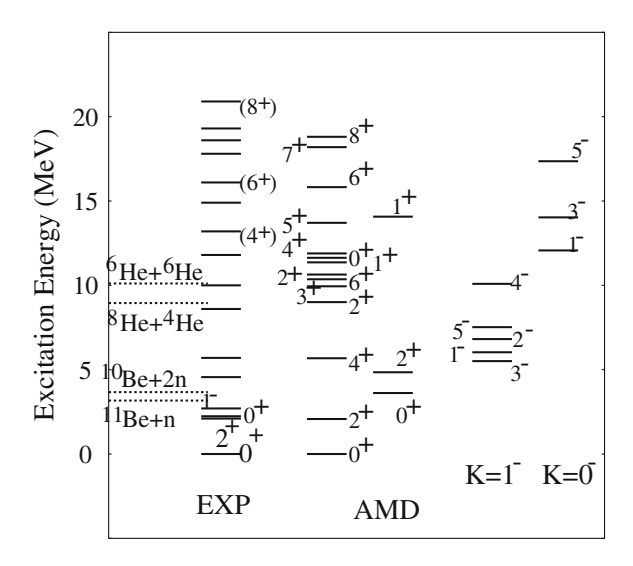


Fig. 4.17 Level schemes of ¹²Be calculated by the VAP calculations. The MV1 force and the spin-orbit term of the G3RS force with the parameter set m = 0.65, b = h = 0, and $u_{ts} = 3,700$ MeV are adopted in the calculations. The details of the calculations are explained in [90]. The figures are taken from Ref. [93]

that breaking of the neutron magic number N=8 occurs in ¹²Be. As mentioned before, these low-lying states are understood by the molecular-orbital picture. It should be stressed again that the valence neutrons in the σ orbital play an important role in the breaking of the N=8 magic number. In the $K^{\pi}=0^+_3$ band, a di-cluster structure of ⁶He + ⁶He clustering are suggested. The experimental 0^+ , 2^+ , 4^+ and 6^+ states above the He+He threshold energy measured in He+He break-up reactions [95–97] are candidates of these di-cluster states.

The breaking of the N=8 magic number in 12 Be has been also suggested in experimental investigations. One of the experimental evidence for the intruder $2\hbar\omega$ configurations of the 12 Be ground state is weak β decays to 12 B as discussed in the early works [103–105]. It has been also supported by recent observations of the 1^- and 0_2^+ excited states a few MeV above the ground state [98–100]. Recently, the neutron configurations of the ground state of 12 Be have been investigated in more details by neutron removal reactions, which indicate the dominant $(sd)^2$ components in 12 Be (0_1^+) [101, 102]. These experimental reports are consistent with the theoretical suggestions by the AMD calculations [90] that show the dominant σ^2 molecular—orbital structure in the ground state.

Next, let us explain negative-parity states of $^{\bar{1}2}$ Be. For the negative-parity states, the AMD calculations suggest two bands, $K^{\pi}=1^-$ and $K^{\pi}=0^-$. The lower band $K^{\pi}=1^-$ consists of the 1^- , 2^- , 3^- , 4^- and 5^- states. These states are interpreted as the molecular–orbital states, which can be described by the $\pi^3\sigma^1$ (three neutrons in the π orbitals and one neutron in the σ orbital) configuration for four valence neutrons around the 2α -cluster core. This $K^{\pi}=1^-$ band is consistent

with the molecular–orbital band predicted by von Oertzen et al. [20, 23]. On the other hand, we also obtain the higher negative-parity band ($K^{\pi}=0^{-}$) than the $K^{\pi}=1^{-}$ band. This $K^{\pi}=0^{-}$ band is formed by a parity asymmetric neutron structure with ${}^{4}\text{He} + {}^{8}\text{He-like}$ component in the intrinsic state, and it is consistent with the negative-parity band suggested in the GCM calculations with coupled channels of ${}^{6}\text{He} + {}^{6}\text{He}$ and ${}^{4}\text{He} + {}^{8}\text{He}$ by Descouvemont and Baye [26]. This band is associated with the well-known parity doublet $K^{\pi}=0^{-}$ band in ${}^{20}\text{Ne}$.

Thus, the AMD calculations suggested two negative-parity bands, the $K^{\pi}=1^-$ band with the molecular-orbital structure and the $K^{\pi}=0^-$ one formed by the parity asymmetric intrinsic state. As mentioned, these two bands have developed cluster structure in a sense, however, they have different origins for negative parity. In the $K^{\pi}=1^-$ band, the negative parity originates from one-particle excitation in molecular-orbital neutrons. However, in the $K^{\pi}=0^-$ band, it arises from parity asymmetry of the intrinsic structure. The experimentally observed $K^{\pi}=1^-$ state [99] may correspond to the band-head state of the $K^{\pi}=1^-$ band, while the $K^{\pi}=0^-$ band member has not been experimentally established yet.

Thus, it is concluded that low-lying states of 12 Be can be systematically understood by the molecular-orbital picture, while di-cluster resonant states with 6 He + 6 He and 8 He + α clusters were suggested in highly excited states of 12 Be (Fig. 4.15).

4.5.2 F and Ne Isotopes

We have seen that the low-lying states of Be isotopes are dominated by the molecular-orbital structure, while as excitation energy increases, the di-cluster resonant states such as ${}^{6}\text{He} + {}^{6}\text{He}$ appears. This picture suggests a new binding mechanism and a new type of clustering peculiar to $N \neq Z$ nuclei. At present, such phenomena is experimentally confirmed only in Be isotopes. Therefore, the exploration of clustering in heavier $N \neq Z$ system is of interest and importance for the understanding of the clustering of atomic nuclei.

O, F and Ne isotopes will be the promising candidate of such clustering in $N \neq Z$ nuclei, since the clustering of their N=Z isotopes are well established [106]. For example, in 22 Ne (Z=10, N=12) it is reported based on the α scattering on 18 O [107–109] that there are several $\alpha+^{18}$ O molecular bands at high excitation energy. These bands correspond to the predicted $\alpha+^{18}$ O molecular resonances [110–112]. Furthermore, by the α transfer reaction to 18 O, several candidates of α cluster states are reported below the α threshold energy [113, 114] whose structure has not established yet. Recently, similar situation is also reported in 18 O. Namely, many candidates of α cluster state are reported in highly excited region [115–119] by the α scattering and several are observed around the α threshold energy [120]. Thus, many α cluster states in $N \neq Z$ nuclei are reported in two energy region, at high excitation energy and around the α threshold energy suggesting much more complicated α clustering systematics than those of N=Z nuclei.

Theoretically, these nuclei have been studied in detail by Dufour, Descouvement and Baye based on the cluster model [110–112, 121]. Some of the α cluster states in high excitation energy are well understood as the di-cluster states such as α + 18 O, but the structure of the cluster states around the threshold energy are still uncertain. As a possible interpretation of these low-lying cluster states, Oertzen [122] has proposed the possible existence of the molecular–orbital structure in Ne isotopes and suggested a new assignment of the rotational bands of 21 Ne.

In this subsection, we discuss the clustering phenomena below the α threshold and at high excitation energy in $Z \neq N$ nuclei based on AMD study. The systematics of the clustering in ²²Ne is discussed in detail and the evolution of the cluster states toward the neutron drip-line is shown in F isotopes.

4.5.2.1 Feature of the Cluster States in F and Ne Isotopes

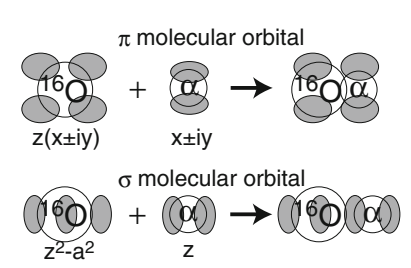
Before the detailed results, we first discuss the molecular orbitals occupied by valence neutrons in O, F and Ne isotopes. Here, as an example, we assume α + 16 O as the inert core and neglect the nucleon spin (Fig. 4.18). We consider three atomic orbitals around α (p-shell) and six orbitals around 16 O (sd-shell). By taking the linear combination of them and assuming the axial symmetry, we can construct six independent molecular orbitals. Two of them which we shall call the π and σ orbitals will appear at smaller excitation energy. The most striking difference from Be isotope is the parity asymmetry originates in the asymmetry of the core, that will lead to the parity doublet band.

Another difference exists in the assumption of the cluster core. In the case of the Be isotopes, we may be able to justify the assumption of the 2α inert core. However, the assumption of the cluster core is not trivial in the case of *sd*-shell nuclei. For example, in the case of ²⁰Ne, the shell and cluster structure mix in the ground band and they coexist in the excited bands [38]. Therefore, we can expect more dynamical structure change between the shell and cluster structure depending on the motion of valence neutrons.

4.5.2.2 ²²Ne

To investigate the structure change and clustering depending on the motion of valence neutrons, we have performed the variational calculation with the

Fig. 4.18 Schematic figure of the π and σ molecular orbitals around the α + 16 O cluster core



constraint on the valence neutron orbitals. Practically, we have added the constraint potential,

$$V_N = \nu_N (\langle \hat{N}_{val} \rangle - N_0)^2, \quad \nu_N > 0,$$
 (4.23)

to the total energy. \hat{N}_{val} is the principal quantum number of valence neutrons defined as the difference between the principal quantum numbers of protons and neutrons,

$$\hat{N}_{val} = \hat{N}_n - \hat{N}_n, \tag{4.24}$$

$$\hat{N}_{\tau} = \sum_{i \in \tau} \hat{\mathbf{a}}_{i}^{\dagger} \hat{\mathbf{a}}_{i} = \sum_{i \in \tau} \sum_{\sigma = x, y, z} \frac{1}{\hbar \omega_{\sigma}} \left(\frac{\hat{p}_{i\sigma}^{2}}{2m} + \frac{1}{2} m \omega_{\sigma}^{2} \hat{r}_{\sigma}^{2} \right) - \frac{3}{2}, \quad \tau = p \text{ or } n, \qquad (4.25)$$

where the oscillation numbers are defined by the width parameters of the single particle wave packet, $\omega_{\sigma}=2\hbar v_{\sigma}/m$. For example, if N_0 is set to 4, two valence neutrons occupy the *sd*-shell, while $N_0=6$ generates the states in which two neutrons occupy the *pf*-shell.

Figure 4.19a shows the energy curves with different valence neutron configuration obtained by this method. In this figure, energy curve (I) has two valence neutrons in sd-shell, energy curves (II) and (III) have those in pf-shell and energy curve (IV) has one valence neutron in sd-shell and another in pf-shell. Depending on the valence neutron configuration, energy curves have energy minima with different energy and deformation. Hereafter, we shall call those minima the state (I)–(IV). Figure 4.20 shows the density distribution of the core and valence neutrons in the state (I)–(IV) where the most weakly bound two neutron orbitals are

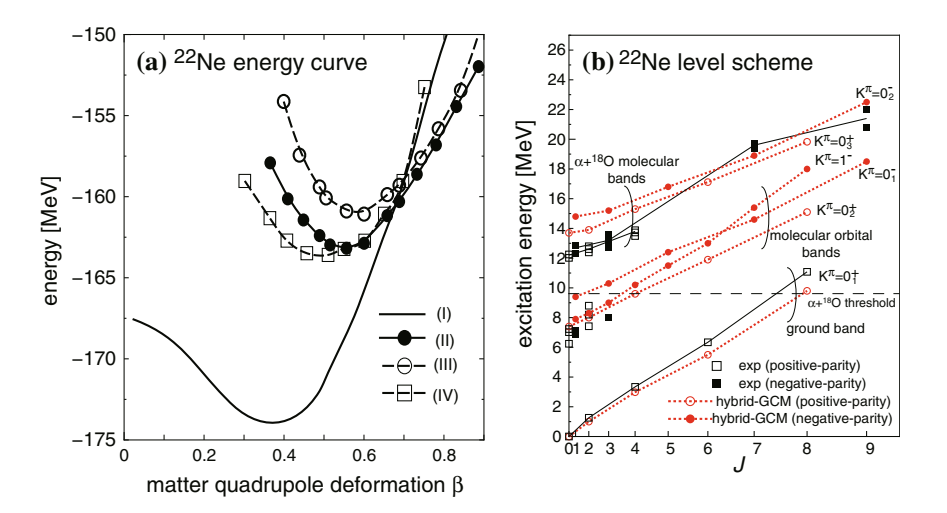


Fig. 4.19 a Energy curves of 22 Ne with different valence neutron configurations. b Calculated and observed cluster bands (plus ground band) of 22 Ne

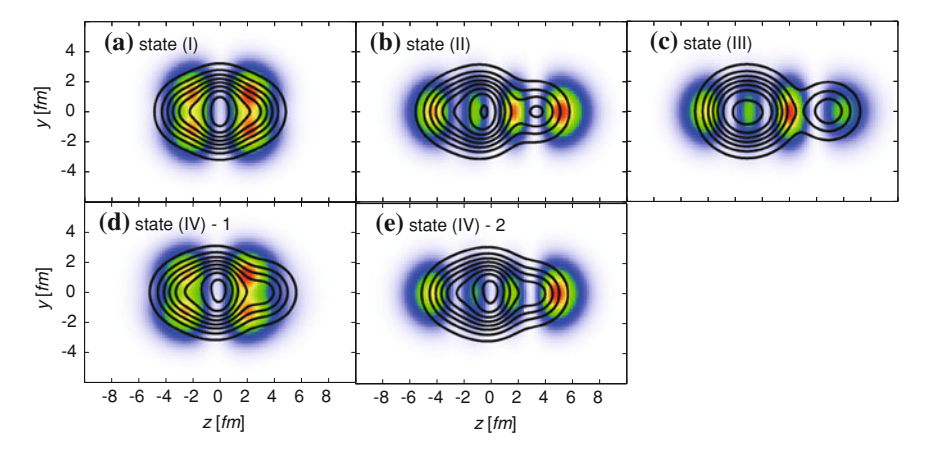


Fig. 4.20 Density distribution of the core (*solid line*) and valence neutrons (*color plot*) at the minima of energy curves (Fig. 4.19a)

defined as valence neutrons and the remaining nucleons as the core. There are two different kinds of valence neutron orbitals. First one has a node along the symmetry axis and sd-shell nature, while another has three nodes and pf-shell nature. These neutron orbitals can be regarded as π and σ molecular orbitals explained in Fig. 4.18. We can see that the α + 16 O clustering of the core develops in the state (II), (III) and (IV) in which one or two valence neutrons occupy the σ molecular orbital. Therefore, we can conjecture that the σ orbital induces the core clustering. On the contrary, the state (I) that corresponds to the ground state and have two valence neutrons in π orbital does not show the core clustering. Different form Be isotopes, valence neutrons in π orbital demolishes the core clustering.

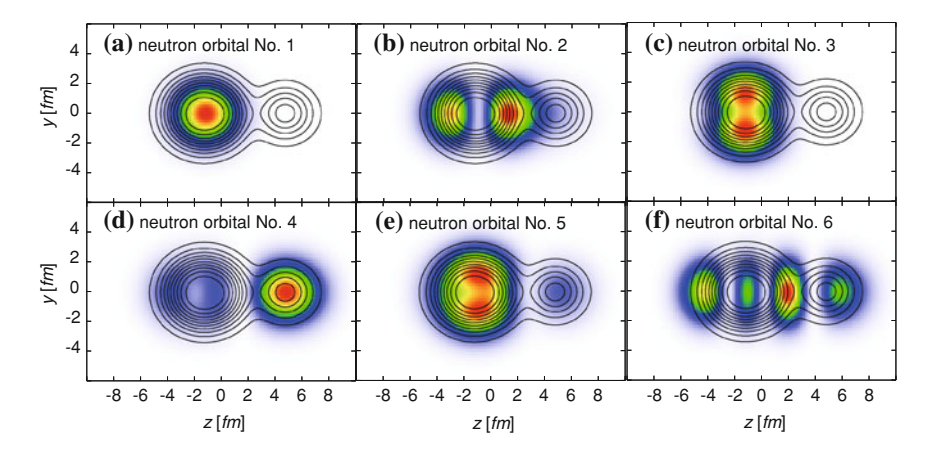


Fig. 4.21 Density distribution of the core (*solid line*) and all neutron single particle orbitals (*color plot*) for the state (III)

Experimentally, we can confirm this effect from the reduction of $B(E2; 0_1^+ \to 2_1^+)$ compared to ²⁰Ne that have α + ¹⁶O clustering.

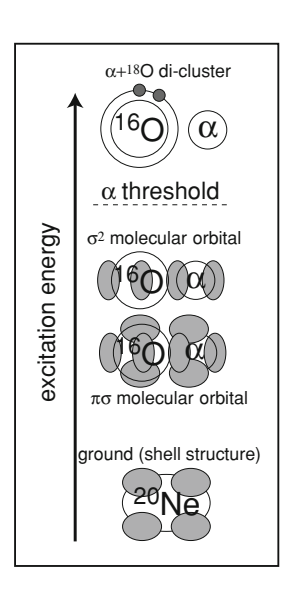
As a typical example of the molecular–orbital structure, Fig. 4.21 shows the neutron single-particle orbitals in the state (III). There are six neutron orbitals with different density distribution and two neutrons occupy each orbital in this state. The orbital (1)–(5) are well confined within the α or ^{16}O clusters and corresponds to the single-particle orbitals inside of clusters. It means the pronounced clustering of this state and the weak interaction between clusters. Only the most weakly bound neutrons (σ orbital) orbit around the entire system and bound two weakly interacting clusters.

Figure 4.19b shows the spectrum of the 22 Ne obtained by the angular momentum projection and Hybrid-GCM calculation (see Ref. [123] for the detail). We have obtained five rotational bands with the pronounced clustering (plus the ground band without $\alpha + ^{16}$ O clustering). Among them, $K^{\pi} = 0^{+}_{2}$, 0^{-}_{1} and 1^{-} bands have the molecular-orbital structure in which $\alpha + ^{16}$ O cluster core is surrounded by two covalent neutrons. The $K^{\pi} = 0^{+}_{2}$ and 0^{-}_{1} bands are dominated by the state (II) and (III) in which two valence neutrons occupy the σ molecular orbital. We note that the state (II) and (III) have quite similar structure to each other as seen in Fig. 4.20. Therefore, the $K^{\pi} = 0^{+}_{2}$ and 0^{-}_{1} bands are regarded as the parity doublet. This is the unique character of the molecular-orbital states in which the cluster core has the parity asymmetry. The $K^{\pi} = 1^{-}$ band is dominated by the state (III) that have neutrons in π and σ orbitals. Similar to the case of Be isotopes, the combination of the molecular orbital generates the various cluster structures. We can consider that the $K^{\pi} = 0^{+}_{2}$ and 0^{-}_{1} bands are the analog of the $K^{\pi} = 0^{+}_{2}$ band of 10 Be and the $K^{\pi} = 1^{-}$ corresponds to that of 10 Be.

Compared to the Be isotopes, experimental information is rather poor. Here we point out that several states below the α threshold energy are reported as the candidates of the α cluster states of ²²Ne based the α transfer reaction on ¹⁸O [113, 114]. They have tens times larger α reduced width amplitude (α RWA) than the ground state. Since the α RWA of the molecular–orbital states by AMD shows the qualitative agreement with the observation, the observed α cluster states will correspond to the molecular-orbital states discussed here. They will also have large ⁶He reduced width amplitude to be confirmed by the experiment, because of covalent nature of the valence neutrons.

Above these molecular-orbital state, we have also obtained the di-cluster bands ($K^{\pi}=0_3^+$ and 0_2^- bands) as similar to the α + 8 He state in 12 Be. In these bands, two valence neutrons orbit only around the 16 O cluster, and hence, they are regarded as the α + 18 O di-cluster bands. Because of the different motion of the valence neutrons, they have hundreds times larger α RWA than the molecular-orbital bands but smaller 6 He reduced width amplitude. Experimentally, this di-cluster bands are confirmed by the α scattering. AMD results shows a good agreement with the observed energies, moment of inertia and α RWA [107–109] and also with the cluster model calculation [111, 112].

Fig. 4.22 Schematic figure showing the clustering systematics in ²²Ne. As excitation energy increases, molecular–orbital structure and di-cluster structure manifest their selves



Thus, we have seen that even in the case of the heavier system, the molecular-orbital state will exist. The clustering systematic in 22 Ne is summarized as shown in Fig. 4.22. There are σ^2 ($K^{\pi}=0^+$ and 0^-) and $\pi\sigma$ ($K^{\pi}=1^-$) bands that are quite analogous to 10 Be. Different from the Be isotopes, π^2 configuration demolishes the clustering in the ground state. Another difference appears as the parity doublet. The parity asymmetry of the core generates the positive- and negative-parity doublet with the same intrinsic configuration (σ^2). In the highly excited states, di-cluster bands with the $\alpha + {}^{18}$ O clusters appear. We also comment that similar molecule-like structure is also predicted in 18,20 O by AMD study [124] and the experimental candidates are observed [125].

4.5.2.3 Neutron-Rich F Isotopes

If we add more neutrons to the molecular-orbital states, what will happen? To illustrate what we can expect in neutron-rich nuclei, we discuss the cluster states in F isotopes. ¹⁹F (N~Z stable nucleus) has a famous cluster state $1/2_1^-$ at very small excitation energy. It is known that this state has the α + ¹⁵N cluster structure, while the ground state has the shell structure with the $(sd)^3$ configuration. It is reminded that we need to promote at least a proton from p-shell to sd-shell to have the α clustering in F isotopes. This proton excitation changes the parity from positive to negative.

By performing the same AMD calculation, we have found that F isotopes also have the molecular–orbital states. The σ molecular orbital plays the central role for the clustering again. Namely, if one or two neutrons occupies the σ molecular orbital, the α clustering occurs in the core nucleus. It is also noted that a proton must

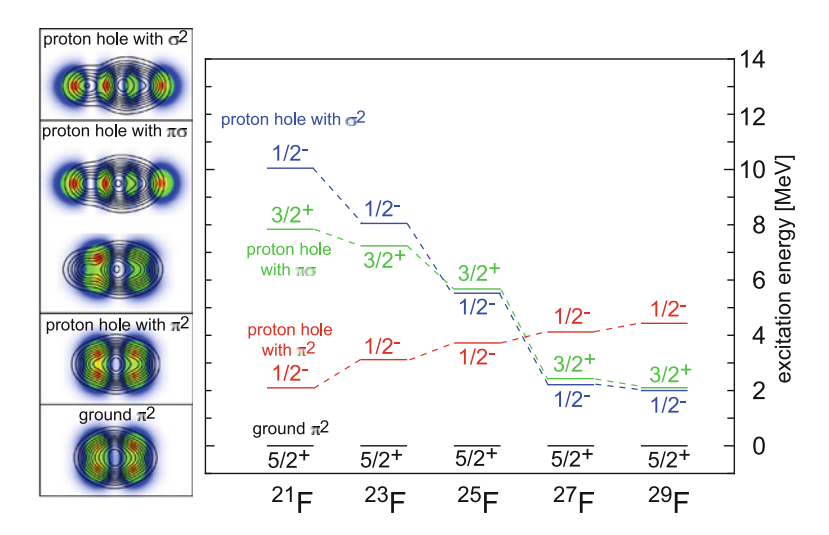


Fig. 4.23 Calculated excitation energies of the proton hole states in F isotopes. Only the band head states with different neutron configuration are shown. The density distribution of these states in 21 F are shown in the *left*

be excited into sd-shell from p-shell for the clustering as explained above. Figure 4.23 shows the band head states with a proton excitation into sd-shell. As the density distribution of 21 F shows, if no neutrons occupies the σ molecular orbital, $\alpha + {}^{15}N$ clustering is diminished, while σ neutrons enhances the α clustering. The most striking feature is that the excitation energies of the σ^2 and $\pi\sigma$ bands greatly reduce toward the neutron drip-line. Since the σ^2 configuration is the $3\hbar\omega$ excitation (proton $1\hbar\omega$ and neutron $2\hbar\omega$ excitation) from the normal configuration, its excitation energy in ^{27,29}F is abnormally small. This great reduction is closely related to the breaking of neutron magic number N = 20 discussed in Sect. 4.4. Readers are reminded that the breaking of the magic number N=20 is caused by the intruder orbital from pf-shell and ^{27,29}F are located in or on the border of the island of inversion. The point is that the σ molecular orbital discussed here is nothing but the intruder orbital in the island. Therefore, we can understand the reduction of excitation energy as follows. Since 27,29 F have much excess neutrons, the energy of the σ molecular orbital (intruder orbital) is small and it does not cost much energy to excite neutrons into this orbital from sd-shell. As explained in the case of ²²Ne, neutrons in this orbital induces the clustering of the core that leads to the large deformation of the system. Then, deformation of the core also reduces the single particle energy of σ molecular orbital. Due to this cooperative effect of clustering and intruder orbital, the reduction of excitation energy is achieved. It is also noted that this mechanism is similar to that of the breaking of neutron magic number N=8 in ¹²Be discussed in the previous subsection.

Experimentally, these molecular states in F isotopes have not been identified yet, though there are several candidates reported in ²³F [126] and ^{25,27}F [127]. It will be very important and interesting to explorer these states.

4.6 Conclusions

Cluster structures and deformations of neutron-rich nuclei from Li to Mg isotopes were reported based on theoretical studies with the AMD method. In Li, Be, B and C isotopes, it was shown that clusterings and deformations rapidly change as a function of the proton and neutron numbers. For neutron-rich Be, O, F and Ne isotopes, the structure of ground and excited states were discussed focusing on cluster phenomena. Island of inversion around ³²Mg was also described.

It has revealed that various exotic cluster structures appear in neutron-rich nuclei where excess neutrons play important roles. One of the key aspects for understanding the structure of Be isotopes is formation of a 2α -cluster core surrounded by valence neutrons. Around the ground state, molecular–orbital structure with covalent neutrons manifests, while the pronounced two-body cluster structures dominate as the excitation energy increases. Also in O, F and Ne isotopes, quite analogous molecular–orbital and two-body cluster structure is suggested in excited states.

These results suggest that cluster is one of the essential features in unstable nuclei as well as in stable nuclei. Even a nucleus has non-cluster ground state, developed cluster states are expected to exist in excited states. In the excited states of neutron-rich nuclei, various cluster structures such as molecular orbital structure may emerge because of a variety of neutron configurations.

Acknowledgements We would like to thank all the collaborators for fruitful discussions. The computational calculations in this work were performed by the supercomputers in KEK, RCNP, and YITP. This work was supported by the JSPS grant (Kakenhi).

References

- 1. H. Horiuchi, Nucl. Phys. A 522, 257c (1991)
- 2. A. Ono, H. Horiuchi, T. Maruyama, A. Ohnishi, Phys. Rev. Lett. 68, 2898 (1992)
- 3. A. Ono, H. Horiuchi, T. Maruyama, A. Ohnishi, Prog. Theor. Phys. 87, 1185 (1992)
- 4. Y. Kanada-En'yo, H. Horiuchi, Prog. Theor. Phys. 93, 115 (1995)
- 5. Y. Kanada-En'yo, H. Horiuchi, A. Ono, Phys. Rev. C 52, 628 (1995)
- 6. Y. Kanada-En'yo, H. Horiuchi, Phys. Rev. C 52, 647 (1995)
- 7. Y. Kanada-En'yo, H. Horiuchi, Prog. Theor. Phys. Suppl. 142, 205 (2001)
- 8. Y. Kanada-En'yo, M. Kimura, H. Horiuchi, C. R. Physique 4 497 (2003)
- 9. K. Varga, Y. Suzuki, R.G. Lovas, Nucl. Phys. A 571, 447 (1994)
- K. Varga, Y. Suzuki, I. Tanihata, Nucl. Phys. A 588, 157c (1995)
- 11. K. Arai, Y. Ogawa, Y. Suzuki, K. Varga, Phys. Rev. C 54, 132 (1996)
- 12. Y.Ogawa, K. Arai, Y. Suzuki, K. Varga, Nucl. Phys. A 673, 122 (2000)
- 13. K. Arai, Y. Ogawa, Y. Suzuki, K. Varga, Prog. Theor. Phys. Suppl. 142, 97 (2001)
- 14. S. Okabe, Y. Abe, H. Tanaka, Prog. Theory. Phys. 57, 866 (1977)
- 15. S. Okabe, Y. Abe, Prog. Theor. Phys. **59**, 315 (1978)
- 16. S. Okabe, Y. Abe, Prog. Theory. Phys. 61, 1049 (1979)
- 17. M. Seya, M. Kohno, S. Nagata, Prog. Theor. Phys. 65, 204 (1981)
- 18. W. von Oertzen, Z. Phys. A 354, 37 (1996)

- 19. W. von Oertzen, Z. Phys. A 357, 355 (1997)
- 20. W. von Oertzen, Nuovo Cimento 110, 895 (1997)
- 21. N. Itagaki, S. Okabe, Phys. Rev. C 61, 044306 (1999)
- 22. N. Itagaki, S. Okabe, K. Ikeda, Phys. Rev. C 62, 034301 (2000)
- 23. W. von Oertzen, M. Freer, Y. Kanada-En'yo, Phys. Rep. 432, 43 (2006)
- 24. D. Baye, P. Descouvemont, N.K. Timofeyuk, Nucl. Phys. A 577, 624 (1994)
- 25. P. Descouvemont, Nucl. Phys. A **626**, 647 (1997)
- 26. P. Descouvemont, D. Baye, Phys. Lett. B 505, 71 (2001)
- 27. P. Descouvemont, Nucl. Phys. A 699, 463 (2002)
- 28. M. Ito, K. Kato, K. Ikeda, Phys. Lett. B 588, 43 (2004)
- 29. M. Ito, N. Itagaki, H. Sakurai, K. Ikeda, Phys. Rev. Lett. 100, 182502 (2008)
- 30. H. Feldmeier, K. Bieler, J. Schnack, Nucl. Phys. A 586, 493 (1995)
- 31. T. Neff, H. Feldmeier, Nucl. Phys. A 713, 311 (2003)
- 32. A. Doté, H. Horiuchi, Y. Kanada-En'yo, Phys. Rev. C 56, 1844 (1997)
- 33. Y. Kanada-En'yo, Phys. Rev. Lett. **81**, 5291 (1998)
- 34. N. Itagaki, S. Aoyama, Phys. Rev. C 61, 024303 (2000)
- 35. Y. Sugawa, M. Kimura, H. Horiuchi, Prog. Theor. Phys. 106, 1129 (2001)
- 36. M. Kimura, Y. Sugawa, H. Horiuchi, Prog. Theor. Phys. 106, 1153 (2001)
- 37. M. Kimura, H. Horiuchi, Prog. Theor. Phys. 107, 33 (2002)
- 38. M. Kimura, Phys. Rev. C 69, 044319 (2004)
- 39. A.B. Volkov, Nucl. Phys. 74, 33 (1965)
- 40. T. Ando, K. Ikeda, A. Tohsaki, Prog. Theory. Phys. 64, 1608 (1980)
- 41. J. Decharge, D. Gogny, Phys. Rev. C 21, 1568 (1980)
- 42. J.F. Berger, M. Girod, D. Gogny, Comp. Phys. Commun. **63**, 365 (1991)
- 43. M. Beiner, H. Flocard, N. van Giai, P. Quentin, Nucl. Phys. A 238, 29 (1975)
- 44. E. Chabanat, P. Bonche, P. Haensel, J. Meyer, R. Schaeffer, Nucl. Phys. A 635, 231 (1998)
- E. Chabanat, P. Bonche, P. Haensel, J. Meyer, R. Schaeffer, Erratum Nucl. Phys. A 643, 441 (1998)
- 46. Y. Kanada-En'yo, H. Horiuchi, A. Doté, Phys. Rev. C 60, 064304 (1999)
- 47. I. Tanihata et al., Phys. Rev. Lett. **55**, 2676 (1985)
- 48. C. Thibault et al., Phys. Rev. C 12, 644 (1975)
- 49. G. Huber et al., Phys. Rev. C 18, 2342 (1978)
- 50. C. Détraz et al., Phys. Rev. C 19, 164 (1979)
- 51. D. Guillemaud-Mueller et al., Nucl. Phys. A 426, 37 (1984)
- 52. T. Motobayashi et al., Phys. Lett. B **490**, 9 (1995)
- 53. X. Campi, H. Flocard, A.K. Kerman, S. Koonin, Nucl. Phys. A 251 193 (1975)
- 54. A. Poves, J. Retamosa, Phys. Lett. B 184, 311 (1986)
- 55. E.K. Warburton, J.A. Becker, B.A. Brown, Phys. Rev. C 41, 1147 (1990)
- 56. N. Fukunishi, T. Otsuka, T. Sebe, Phys. Lett. B **296**, 279 (1992)
- 57. G. Klotz et al., Phys. Rev. C 47, 2502 (1993)
- 58. B.V. Pritychenko et al., Phys. Lett. B 461, 322 (1999)
- 59. B.V. Pritychenko et al., Phys. Lett. B 467, 309 (1999)
- 60. M. Keim et al., Eur. Phys. J. A 8, 31 (2000)
- 61. K. Yoneda et al., Phys. Lett. B 499, 233 (2001)
- 62. S. Nummela et al., Phys. Rev. C 64, 054313 (2001)
- 63. Y. Yanagisawa et al., Nucl. Phys. A **734**, 374 (2004)
- 64. G. Neyens et al., Phys. Rev. Lett. 94, 022501 (2005)
- 65. F. Marechal et al., Phys. Rev. C 72, 044314 (2005)
- 66. B.H. Wildenthal, M.S. Curtin, B.A. Brown, Phys. Rev. C 28, 1343 (1983)
- 67. A. Poves, J. Retamosa, Nucl. Phys. A **571**, 221 (1994)
- 68. Y. Utsuno, T. Otsuka, T. Mizusaki, M. Honma, Phys. Rev. C 60, 054315 (1999)
- Y. Utsuno, T. Otsuka, T. Glasmacher, T. Mizusaki, M. Honma, Phys. Rev. C 70, 044307 (2004)
- 70. D.J. Dean et al., Phys. Rev. C **59**, 2474 (1999)

- 71. R.R. Rodrguez-Guzmn, J.L. Egido, L.M. Robledo, Phys. Rev. C 62, 054319 (2000)
- 72. E. Caurier, F. Nowacki, A. Poves, J. Retamosa, Phys. Rev. C 58, 2033 (1998)
- 73. E. Caurier, F. Nowacki, A. Poves, Nucl. Phys. A 693, 374 (2001)
- 74. M. Kimura, H. Horiuchi, Prog. Theor. Phys. (Kyoto) **111**, 841 (2004)
- 75. M. Kimura, H. Horiuchi, Prog. Theor. Phys. (Kyoto) **107**, 33 (2002)
- 76. M. Kimura, Phys. Rev. C 75, 041302 (2007)
- 77. V. Tripathi et al., Phys. Rev. C 76, 021301 (2007)
- 78. C.M. Mattoon et al., Phys. Rev. C 75, 017302 (2007)
- 79. P. Doomenbal et al., Phys. Rev. Lett. 103, 032501 (2009)
- 80. D. Nagae et al., Phys. Rev. C 79, 027301 (2009)
- 81. P.G. Hansen, B. Jonson, Europhys. Lett. 4, 409 (1987)
- 82. G.F. Bertsch, H. Esbensen, Ann. Phys. 209, 327 (1991)
- M.V. Zhukov, B.V. Danilin, D.V. Fedorov, J.M. Bang, I.J. Thompson, J.S. Vaagen, Phys. Rep. 231, 151 (1993)
- 84. H. Esbensen, G.F. Bertsch, K. Hencken, Phys. Rev. C 56, 3054 (1997)
- 85. K. Ikeda. Nucl. Phys. A 538, 355c (1992)
- 86. S. Aoyama, K. Kato, K. Ikeda, Prog. Theor. Phys. Suppl. 142, 35 (2001)
- 87. T. Myo, S. Aoyama, K. Kato, K. Ikeda, Prog. Theor. Phys. 108, 133 (2002)
- 88. K. Ikeda, T. Myo, K. Kato, H. Toki (to be published in this series of lecture notes)
- 89. H. Horiuchi (to be published in this series of lecture notes)
- 90. Y. Kanada-En'yo, H. Horiuchi, Phys. Rev. C 68, 014319 (2002)
- 91. Y. Kanada-En'yo, Phys. Rev. C 71, 014303 (2005)
- 92. Y. Kanada-En'yo, H. Horiuchi, Phys. Rev. C **66**, 024305 (2002)
- 93. Y. Kanada-En'yo, M. Kimura, H. Horiuchi, Eur. Phys. J. A 25(Suppl. 1), 305 (2005)
- 94. A.A. Korsheninnikov et al., Phys. Lett. B **343**, 53 (1995)
- 95. M. Freer et al., Phys. Rev. Lett. **82**, 1383 (1999)
- 96. M. Freer et al., Phys. Rev. C 63, 034301 (2001)
- 97. A. Saito et al., Nucl. Phys. A 738, 337 (2004)
- 98. H. Iwasaki et al., Phys. Lett. B **481**, 7 (2000)
- 99. H. Iwasaki et al., Phys. Lett. B **491**, 8 (2000)
- 100. S. Shimoura et al., Phys. Lett. B **560**, 31 (2003)101. A. Navin et al., Phys. Rev. Lett. **85**, 266 (2000)
- 102. S.D. Pain et al., Phys. Rev. Lett. **96**, 032502 (2006)
- 103. F.C. Barker, J. Phys. G Nucl. Part. Phys. 2, L45 (1976)
- 104. H.T. Fortune, G.-B. Liu, D.E. Alburger, Phys. Rev. C 50, 1355 (1994)
- 105. T. Suzuki, T. Otsuka, Phys. Rev. C 56, 847 (1997)
- 106. Y. Fujiwara, H. Horiuchi, K. Ikeda, M. Kamimura, K. Kato, Y. Suzuki, E. Uegaki, Prog. Theor. Phys. Suppl. 68, 29 (1980)
- 107. G.V. Rogachev et al., Phys. Rev. C 64, 051302(R) (2001)
- N. Curtis, D.D. Caussyn, C. Chandler, M.W. Cooper, N.R. Fletcher, R.W. Laird, J. Pavan, Phys. Rev. C 66 024315 (2002)
- 109. V.Z. Goldberg et al., Phys. Rev. C 69, 024602 (2004)
- 110. P. Descouvemont, Phys. Rev. C 38, 2397 (1988)
- 111. M. Dufour, P. Descouvemont, Nucl. Phys. A 726, 53 (2003)
- 112. M. Dufour, P. Descouvemont, Nucl. Phys. A 738, 447 (2004)
- 113. W. Scholz, P. Neogy, K. Bethge, R. Middleton, Phys. Rev. Lett. 22, 949 (1969)
- 114. W. Scholz, P. Neogy, K. Bethge, R.Middleton, Phys. Rev. C 6, 893 (1972)
- 115. V.Z. Goldberg et al., Phys. At. Nucl. **68**, 1079 (2005)
- 116. N. Curtis et al., Phys. Rev. C 66, 024315 (2002)
- 117. N.I. Ashwood et al., J. Phys. G 32, 463 (2006)
- 118. S. Yildiz et al., Phys. Rev. C 73, 034601 (2006)
- 119. E.D. Johnson et al., Eur. Phys. J. A 42, 135 (2009)
- 120. W. von Oertzen et al., Eur. Phys. J A 43, 17 (2010)
- 121. P. Descouvemont, D. Baye, Phys. Rev. C 31, 2274 (1985)

- 122. W. von Oertzen, Eur. Phys. J A 11, 403 (2001)
- 123. M. Kimura, Phys. Rev. C 75, 034312 (2007)
- 124. N. Furutachi, M. Kimura, A. Dote, Y. Kanada-En'yo, S. Oryu, Prog. Theor. Phys. 119, 403 (2008)
- 125. W. von Oertzen et al., Eur. Phys. J. A 43, 17 (2010)
- 126. S. Michimasa et al., Phys. Lett. B 638, 146 (2006)
- 127. Z. Elekes et al., Phys. Lett. B **599**, 17 (2004)

Chapter 5 Di-Neutron Clustering and Deuteron-like Tensor Correlation in Nuclear Structure Focusing on ¹¹Li

Kiyomi Ikeda, Takayuki Myo, Kiyoshi Kato and Hiroshi Toki

5.1 Unstable Nuclei and the Halo Structure of ¹¹Li

We are in the era of being able to study experimentally unstable nuclei up to the drip lines and even up to super-heavy nuclei. We are able now to provide precious informations for astrophysics and cosmo-physics directly from experiment. All these activities started with the discovery of the halo structure of ¹¹Li [1]. Hence, there are many experimental data on ¹¹Li and surrounding nuclei. First of all, we would like to discuss the characteristics of ¹¹Li found by various experiments. We should present all the existing experimental facts about the Li-isotopes, in particular ⁹Li and ¹⁰Li

The formation of the halo structure in ¹¹Li is a difficult subject to understand theoretically. The fact that the binding energy is extremely small urges us to develop a theory to handle continuum states as precisely as bound states. This fact of small binding energy of the last two neutrons forces us to consider the pairing

K. Ikeda (⊠)

RIKEN Nishina Center, Wako, Saitama 351-0198, Japan

e-mail: k-ikeda@postman.riken.go.jp

T Myo

General Education, Faculty of Engineering, Osaka Institute of Technology,

Osaka 535-8585, Japan e-mail: myo@ge.oit.ac.jp

K. Kato

Division of Physics, Graduate School of Science, Hokkaido University,

Sapporo 060-0810, Japan

e-mail: kato@nucl.sci.hokudai.ac.jp

H. Tok

Research Center for Nuclear Physics (RCNP), Osaka University, Ibaraki,

Osaka 567-0047, Japan

e-mail: toki@rcnp.osaka-u.ac.jp

C. Beck (ed.), *Clusters in Nuclei*, Lecture Notes in Physics, 818, DOI: 10.1007/978-3-642-13899-7_5, © Springer-Verlag Berlin Heidelberg 2010

166 K. Ikeda et al.

interaction at low density, which leads to the concept of the di-neutron clustering phenomenon. Most fascinating physics necessary for the quantitative understanding of the halo structure turned out to be the discovery of the deuteron-like correlation caused by the strong tensor interaction. Theoretically we have experienced these conceptual developments on the theoretical framework to treat the Li isotopes. We discuss first the experimental facts on the Li isotopes and then discuss the theoretical tools for the understanding of ¹¹Li. All these theoretical tools developed for the Li isotopes are to be used for many new phenomena found in unstable nuclei.

5.1.1 Experimental Facts on ^{9,10}Li and ¹¹Li

There are many experimental data indicating that the ¹¹Li nucleus has a halo structure. A schematic picture of the halo structure is shown in Fig. 5.1. The halo structure of ¹¹Li was discovered as an anomalously large reaction cross section of this nucleus with target nuclei. The matter radii extracted from the reaction cross sections and other standard methods are shown in Fig. 5.2. We can see from this figure that the matter radius of ¹¹Li is much larger than that of the neighboring nucleus ⁹Li. The matter radius of ¹¹Li corresponds to those of medium mass nuclei. If we were to pick up nuclei, whose radii are suddenly increased from the

Fig. 5.1 A schematic image of halo structure in ¹¹Li

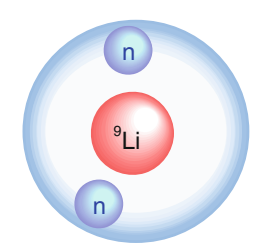
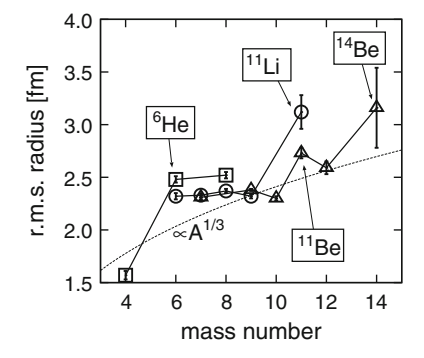


Fig. 5.2 Observed rms matter radii of He, Li and Be isotopes. Shown by the *dashed curve* is the one proportional to $A^{1/3}$. Those *points marked by arrows* are the ones with extraordinary large radii. Data are taken from Ref. [1]

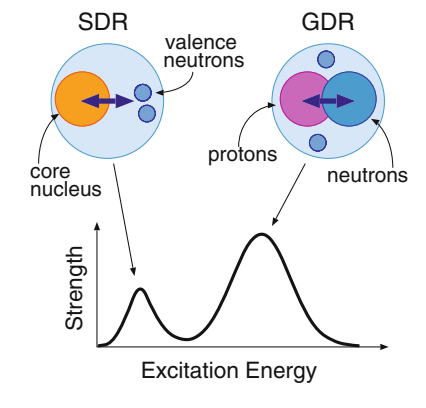


neighboring nuclei, they are ⁶He, ¹¹Be and ¹⁴Be in addition to ¹¹Li. Detailed studies on these sudden jumps of the matter radii made these phenomena as caused by the halo formation.

There are many experiments performed on the halo structure of unstable nuclei. Out of all these experiments, those of ¹¹Li are very interesting due to important nuclear many body physics behind the experimental data. In order to find the reason of the sudden increase, experiments were performed for the neutron separation momentum distributions. The momentum distributions of neutron separation were measured experimentally by Kobayashi et al. [2] by bombarding unstable nuclei on some stable target nuclei. The momentum distribution for the case of ¹¹Li is much narrower than other cases. The narrowness of the momentum distribution is related with large extension of the neutron distributions due to the uncertainty principle. Hence, this is a data showing directly the halo structure or at least a large spatial extension of the neutron distribution in 11Li. As for the structure of 11Li, there was an experiment performed by Simon et al. [3], who bombarded ¹¹Li on a carbon target and measure the momentum distribution of the ¹⁰Li fragments. From the shape of the distribution, the $(1s_{1/2})^2$ contribution to the mixture of $(1s_{1/2})^2$ and $(0p_{1/2})^2$ components was determined to be $(45 \pm 10)\%$.

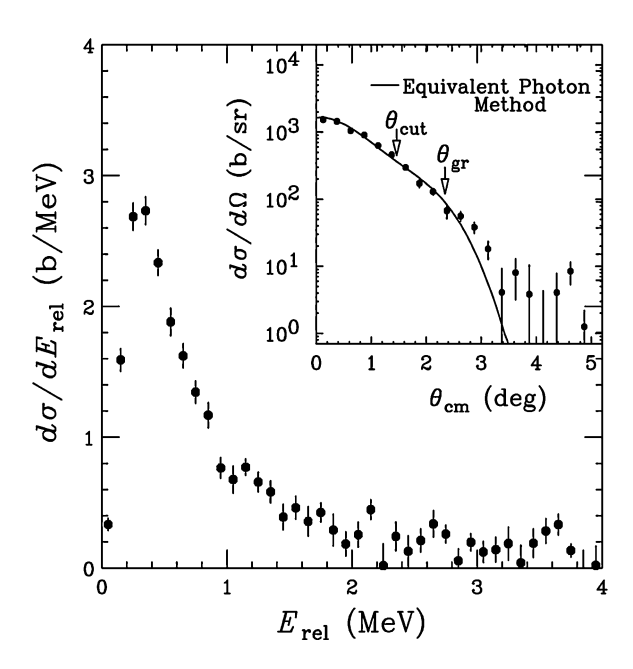
If there is a halo structure, we may expect an interesting excitation mode of ¹¹Li. If the core nucleus ⁹Li is surrounded by neutrons in the nuclear halo region, there is a possibility of making oscillation of the core nucleus in the neutron sea. This is called a soft dipole resonance to be excited by photo-disintegration as shown in Fig. 5.3 [4, 5]. The excitation energy is expected around a few MeV as compared to the standard giant *E*1 resonance of a few tens MeV. There are several experiments of Coulomb excitation of ¹¹Li. We show the most recent experimental data on Coulomb excitation taken by Nakamura et al. in Fig. 5.4 [6]. There is a bump structure just above the threshold energy. However, it is still debated if the bump structure is caused by the soft dipole resonance or not due to the complicated nuclear structure of ¹¹Li.

Fig. 5.3 A schematic spectrum of E1 excitation of soft dipole resonance and giant dipole resonance modes of halo nuclei. Shown above in the *left* is a schematic view of the soft dipole resonance (SDR) and the one in the *right* is that of the giant dipole resonance (GDR)



168 K. Ikeda et al.

Fig. 5.4 Coulomb excitation of ${}^{11}\text{Li}$ in ${}^{11}\text{Li}+\text{Pb}$ at 70 MeV/nucleon as a function of the ${}^{9}\text{Li} + n + n$ relative energy. Details are explained in the original papar [6]



There are many other experimental data on ¹¹Li as the magnetic moment and quadrupole moment. These experimental data will be presented together with theoretical results later.

We should also see experimental data for 10 Li, which is the neighboring nucleus, although this nucleus is unbound. We list the neutron single and double separation energies in 9,10,11 Li in Table 5.1. The two neutron separation energy in 11 Li is very small as 0.32 MeV. The separation energies in 9 Li are large and this nucleus should be considered as a standard shell model type nucleus. In 10 Li, the single neutron separation energy is -0.3 MeV, indicating this nucleus is not stable. This resonance structure seems to have positive parity and is assigned to have the $(p_{3/2})_{\pi}(p_{1/2})_{\nu}$ structure. At the same time, there are few informations on virtual states. There is an experimental data on neutron scattering with 9 Li at the threshold energy [7]. The scattering length comes out to be $a \sim -20$ fm, which is comparable with the one of neutron-neutron scattering $a = -18.5 \pm 0.4$ fm [8]. Hence, the large scattering length indicates the existence of strong attraction in the *s*-wave channel, which is close to the condition

Table 5.1 Single and double neutron separation energies in unit of MeV in 9,10,11 Li

Nucleus	S_{2n} [MeV]	S_n [MeV]
¹¹ Li ¹⁰ Li	0.32	0.62
¹⁰ Li	-	-0.3
⁹ Li	6.10	4.07

of forming a bound state in the free space. This means that the s-state structure appears close to the threshold energy of ${}^{9}\text{Li} + n$.

5.1.2 Theoretical Studies on the Halo Structure in ¹¹Li

The halo structure was completely new in nuclear physics community. Hence, there were many theoretical studies to describe this interesting phenomenon. We have recognized immediately that the standard shell model approach badly fails due to the fact that the two additional neutrons in 11 Li ought to enter in the $p_{1/2}$ neutron orbit but not in the $s_{1/2}$ orbit due to the N=8 magic structure. Hence, most of theoretical studies introduce some phenomenology to bring down the $s_{1/2}$ orbit. For example, in the work of Thompson and Zhukov [9], they treat 9 Li as a core and add two neutrons by taking state dependent neutron-core interactions. The additional attraction for s-wave component makes the $(s_{1/2})^2$ state energetically close to the $(p_{1/2})^2$ state. In this case, the $(s_{1/2})^2$ state has a large component in the ground state, which provides the halo structure for 11 Li.

There is a theoretical study on the pairing property and the E1 excitation in 11 Li by Esbensen and Bertsch [10]. In their study, it is essential to bring down the $s_{1/2}$ orbit to reproduce the experimental E1 excitation spectrum. As for the pairing correlation, there are many studies to describe 11 Li as the BCS state. In the study of Meng and Ring [11], they describe 11 Li in terms of a relativistic Hartree–Bogoliubov model. In this study, they can include the continuum effect in their pairing correlations. In the relativistic Hartree–Bogoliubov model, the s-wave contribution comes out to be about a quarter of the p-wave contribution for the paired two neutrons. We need more participation of the s-wave component as compared to the finding of the experimental data of Simon et al. [3].

There is another interpretation on the halo structure as due to deformation. In the work of Varga et al. [12], they try to break the 9 Li core and introduce the cluster structure. The wave function of 11 Li is written as 4 He + t + 4n and takes the interaction among them by a phenomenological central interaction. In this way, they can introduce the effect of the deformation and pairing correlations among the nucleons. The deformation effect provides a large matter radius and some s-wave component in the wave function.

The theoretical challenge on the halo structure is therefore summarized as follows. There are many indications that the *s*-wave component is very large in the ground state wave function. Hence, we have to find a mechanism to bring down the $s_{1/2}$ orbit with the amount to wash out the N=8 magic structure. The pairing properties are also very important to cause admixture of $(p_{1/2})^2$ and $(s_{1/2})^2$ states. In the halo nucleus, we ought to consider the di-neutron pairing correlation in a small nuclear matter density. All these new phenomena should be understood in terms of the many body framework with the nucleon–nucleon interaction.

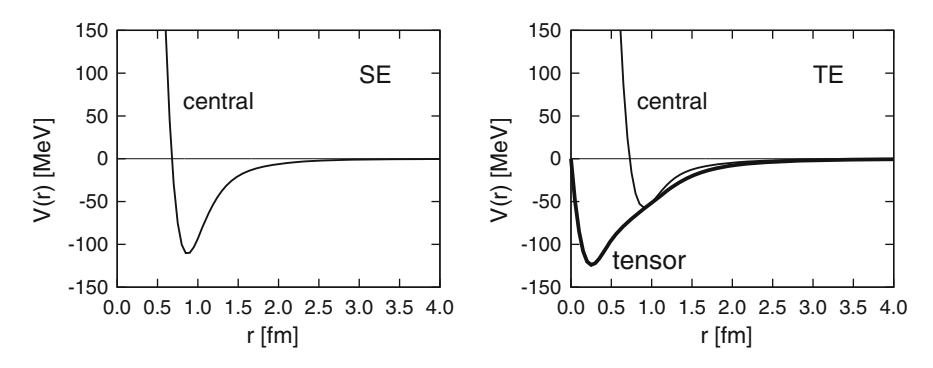


Fig. 5.5 Central and tensor interactions of the AV8' potential [13] in singlet even (SE) and triplet even (TE) channels

5.1.3 Nucleon–Nucleon Interaction and the Deuteron and the Di-Neutron System

We should learn the properties of the nucleon–nucleon interaction in order to understand the halo structure in 11 Li. To this end, we would like to show the central and the tensor interactions in the 3S_1 channel of the AV8' potential [13], which are shown in Fig. 5.5. In the central interaction, there are strong hard core (short range repulsive interaction) and intermediate range attraction of moderate strength. As for the tensor interaction, the long range part drops with the pion range, while the short range part increases until 0.2 fm and goes to zero at the origin due to the form-factor coming from the nucleon finite size. On the other hand, we have the similar structure for the central interaction in the 1S_0 channel, where there is a strong hard core due to the short range quark dynamics. In this channel, there is no tensor contribution due to zero total spin. The deuteron-like tensor correlation is produced by the *NN* interaction in the 3S_1 channel, while the di-neutron clustering is produced by the *NN* interaction in the 1S_0 channel.

In order to understand the role of the hard core and the tensor interaction, let us solve the Schrödinger equation for the deuteron by using the AV8' nucleon-nucleon interaction. The wave function of the deuteron is written as

$$\Psi_d = u(r)[Y_0(\hat{r}) \otimes \chi_1(\sigma_1\sigma_2)]_{1M} + w(r)[Y_2(\hat{r}) \otimes \chi_1(\sigma_1\sigma_2)]_{1M}. \tag{5.1}$$

The deuteron wave function is written by the s-wave and d-wave components. The tensor interaction mixes these two components. In Fig. 5.6 and Table 5.2, we show the deuteron properties for the wave functions and the various energy contributions and radii. In the wave function, the s-wave component is dominant and shows the long-tail due to the weak binding of 2 MeV. In the short-range part less than the 0.5 fm region, the s-wave function is largely reduced due to the short-range repulsion in the central interaction. Looking at the d-wave component, its amplitude starts from the origin, because of the centrifugal barrier in the L=2

Fig. 5.6 Deuteron *s*-wave and *d*-wave functions obtained using the AV8' nucleon–nucleon potential

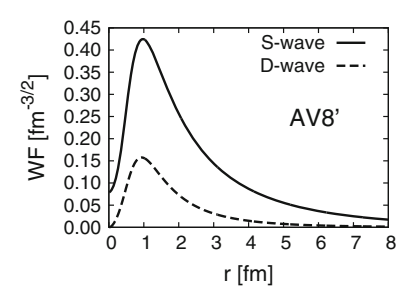


Table 5.2 Deuteron properties using the AV8' nucleon–nucleon potential

Energy	-2.24 [MeV]
Kinetic	19.88
(SS)	11.31
(DD)	8.57
Central	-4.46
(SS)	-3.96
(DD)	-0.50
Tensor	-16.64
(SD)	-18.93
(DD)	2.29
LS	-1.02
P(D)	5.78 [%]
Radius	1.96 [fm]
(SS)	2.00 [fm]
(DD)	1.22 [fm]

partial wave, which is absent in the *s*-wave case. These features of the *s*-wave and *d*-wave components have to be expressed using the shell model framework in finite nuclei as the deuteron-like tensor correlation. These features will be treated for finite nuclei by using the tensor optimized shell model (TOSM) and the unitary correlation operator method (UCOM) to be discussed later.

Among the expectation values of all the two-body interactions in the deuteron, the tensor interaction has the largest contribution of about -17 MeV. This expectation value is four times of that of the central interaction. This tensor interaction is the origin of the d-wave mixing in the wave function. From these results, it is found that the dominant energy contribution comes from the coupling of the s- and d-wave components by changing the relative orbital angular momentum by 2, $\Delta L = 2$. As for the radius of the deuteron, we decompose the radius into the s-wave and d-wave components and normalize them by using the corresponding amplitudes. It is interesting to see the size difference between two angular components, where the d-wave size is much smaller than the s-wave size. This compact d-wave structure produces high momentum component caused by the tensor interaction, namely the pion exchange effect. Hence, we can learn the role and the properties of the tensor interaction in finite nuclei from the deuteron. That is, the tensor interaction creates the relative d-wave component in the wave

function, which is spatially compact and involves high momentum components. These features should appear in finite nuclei as the deuteron-like tensor correlation. We shall treat this correlation in terms of the tensor optimized shell model (TOSM) in finite nuclei.

As for the di-neutron correlation, we have a moderate intermediate attraction with a short range repulsion as shown in Fig. 5.5. There is no tensor interaction and the relative motion is completely described by the central interaction. We are aware that there is no bound state in the 1S_0 channel, but that the scattering length is negatively very large $a=-18.5\pm0.4$ fm [8]. This negatively large scattering length indicates that the di-neutron system is close to develop a bound state. Hence, for a system like 11 Li, we expect a strong di-neutron clustering phenomenon in the halo region. For the quantitative account we ought to use the *NN* interaction for this phenomenon.

5.1.4 Wave Functions for ^{9,10}Li and ¹¹Li

We write the wave functions of the Li isotopes in order to understand the standard shell model state, the di-neutron clustering and the deuteron-like tensor correlation. It is illustrative to start writing the ⁹Li wave function.

$$|^{9}Li\rangle = C_{1}|(s_{1/2})_{\pi}^{2}(s_{1/2})_{\nu}^{2}(p_{3/2})_{\pi}(p_{3/2})_{\nu}^{4}\rangle_{J=3/2} + C_{2}|(s_{1/2})_{\pi}^{2}(s_{1/2})_{\nu}^{2}(p_{3/2})_{\pi}(p_{3/2})_{\nu J=0}^{2}(p_{1/2})_{\nu J=0}^{2}\rangle_{J=3/2} + C_{3}|[(s_{1/2})_{\pi}(s_{1/2})_{\nu}]_{J=1}(p_{3/2})_{\pi}(p_{3/2})_{\nu}^{4}[(p_{1/2})_{\pi}(p_{1/2})_{\nu}]_{J=1}\rangle_{J=3/2} + \cdots$$

$$(5.2)$$

We have written here only the dominant components explicitly where π and ν for each configuration denote proton and neutron, respectively. The term with the amplitude C_1 corresponds to the standard shell model state. The term with the amplitude C_2 corresponds to the main component of the two neutron pairing states, where a two-neutron pair couples to $J^{\pi} = 0^+$. The term with the amplitude C_3 corresponds to the main component of the deuteron-like tensor correlation states, where a proton-neutron pair couples to $J^{\pi} = 1^+$.

The di-neutron clustering correlation, which is associated with the C_2 amplitude component, should involve further particle states in sd and higher shells. As for $^9\mathrm{Li}$, the di-neutron clustering correlation provides a similar structure as the BCS state due to the fact that the nuclear density of the surface neutrons is ordinary as expected from the standard size of neutron separation energies listed in Table 5.1. With the increase of the neutron number, the nuclear density of the surface neutrons becomes very small and hence the di-neutron clustering correlation should show up. This change of the di-neutron clustering correlation due to the nuclear density is related with the BCS-BEC crossover. On the other hand, the deuteron-like tensor correlation, which is associated with the C_3 amplitude component,

needs excitation of a proton-neutron pair with $J^{\pi}=1^+$ from occupied states to unoccupied states. We have to include each particle state of the proton-neutron pair up to very high angular momentum state.

We write the ¹⁰Li wave function in terms of the ⁹Li wave function.

$$|^{10}Li\rangle = \mathscr{A}[|^{9}Li\rangle \times |\chi_{n}\rangle] \tag{5.3}$$

The additional neutron may enter the $p_{1/2}$ orbit in the shell model state. The addition of one more neutron to the pair correlated state has an effect to weaken the pairing correlation due to the blocking effect of the neutron. The addition of one more neutron to the deuteron-like configuration is very interesting, since the additional neutron may go into the $p_{1/2}$ orbit or into the $s_{1/2}$ orbit in the shell model state. If the last neutron goes into the $p_{1/2}$ orbit, the deuteron-like correlation is weakened by the additional neutron. Instead, if the last neutron goes into the $s_{1/2}$ orbit, the deuteron-like correlation is not weakened, because 2p-2h states with the use of $s_{1/2}$ orbit are not important for the deuteron-like correlation. Hence, there should appear the competition of the neutron $s_{1/2}$ and $p_{1/2}$ configurations in $s_{1/2}$

We write the ¹¹Li wave function in terms of ⁹Li wave function.

$$|^{11}Li\rangle = \mathcal{A}[|^{9}Li\rangle \times |\chi_{nn}\rangle] \tag{5.4}$$

In this case, there is an important physics to be added in addition to all the interesting phenomena in 10 Li As for the pair correlated state, two neutrons block the pair correlated state by entering in the $p_{1/2}$ orbit. More interesting is the case of the two neutrons going into the higher shell orbits. In this case, the two neutrons stay in a low density region far from the 9 Li core and hence the dineutron clustering phenomenon is expected. How large is the attraction due to the dineutron clustering effect for the 11 Li binding energy needs full account of all the effects. As for the C_3 component, two neutrons going into the $p_{1/2}$ orbit generate a strong blocking effect of the deuteron-like correlation and this configuration is disfavored by the tensor interaction. On the other hand, when the two neutrons go into the $s_{1/2}$ orbit, the deuteron-like correlation is not disturbed and therefore this configuration is favored. Hence, as the consequence of these di-neutron clustering correlation and the deuteron-like tensor correlation, these two correlations cooperate to wash out the N=8 magic structure and provide the interesting halo phenomenon in 11 Li.

5.2 Di-Neutron Clustering and the Hybrid-VT Model

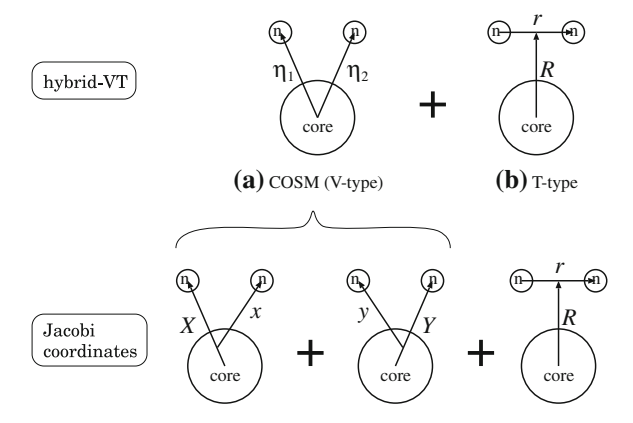
In ¹¹Li [14] and ⁶He [15], abnormally large matter radii were observed experimentally. This phenomenon was interpreted as a result of the halo structure, where two valence neutrons are spatially extended around the core nucleus due to their weak binding. It is important to investigate the dynamics of the motion of valence neutrons for the understanding of the halo structure. In such a situation, it is

necessary to develop a theoretical method to handle spatially extended structure of the Borromean system consisting of core nucleus and two neutrons. For this purpose, we have developed the hybrid-VT model as the most suitable model to describe the halo structure. In the hybrid-VT model for two-neutron halo nuclei, shown in Fig. 5.7, the mean field nature of each valence neutron can be described in the V-type basis states (the cluster orbital shell model (COSM), Fig. 5.7a). Further, the explicit neutron–neutron correlation is treated in the T-type (Fig. 5.7b) basis states. Here, the basic idea of this hybrid-VT model is presented, and in the next sub-section we explain the formulation of the hybrid-VT model in detail.

In the weak binding system it is necessary to consider the large spatial extension of single particle wave functions of valence neutrons. This situation corresponds to the coupling of the valence neutrons to continuum states. Suzuki and Ikeda [16] proposed the cluster orbital shell model (COSM, V-type), and applied to ⁶He and ¹¹Li [17–23]. The COSM is one extension of the shell model, in which the spatially extended character of valence neutrons can be treated. The V-type coordinates in the COSM are the suitable coordinates to express the mean field property of the valence neutrons, and therefore can express the shell model properties of ^{5,6}He and ^{10,11}Li most effectively. However, from the analysis of neutron-rich nuclei with the COSM, it was shown that the binding energies of the Borromean nuclei can not be described quantitatively. Furthermore, it was found that in a weakly bound system, the n-nclustering correlation, namely the di-neutron clustering correlation, becomes important to provide an extra binding energy. This is characterized by the participation of many $J^{\pi} = 0^{+}$ pair configurations with large single particle orbital angular momenta [24, 25].

Hence, it is important to include the physical effect of di-neutron clustering correlation explicitly in two-neutron halo nuclei, and the T-type wave function is suitable for this purpose [18, 19, 23, 24, 26]. We combine the T-type basis functions with the V-type ones as shown in Fig. 5.7. It has been shown that this hybrid-VT model describes the di-neutron clustering correlation with full

Fig. 5.7 The coordinates of the hybrid-*VT* model and their relation with those of the Jacobi coordinates. The *V*-type coordinates in (a) and the *T*-type coordinates in (b) are shown in the upper figures and the corresponding ones in the Jacobi coordinates are shown in the lower figures



convergence of the binding energy and radius as will be discussed in the following sub-sections. Hence, the hybrid-VT model wave function involves two-kinds of physical correlations as the mean-field and di-neutron clustering correlations, in the two-neutron halo nuclei. The hybrid-VT model is also a special case of few-body systems; a three-body system is generally described by using the Jacobi-coordinates [27] as shown in Fig. 5.7. In the case of core + n + n, the core nucleus has a large mass in comparison with that of valence neutrons. Therefore, as shown in Fig. 5.7, the V-type coordinates (η_1, η_2) correspond to the symmetric Y-type Jacobi coordinates, (X, X) and (X, X) and (X, X).

In this section, we explain the construction of the COSM and the hybrid-*VT* model [24–26, 28–37] and its application to the three-body systems: ⁶He and ¹¹Li. The subject of the di-neutron clustering is discussed in terms of BCS-BEC cross over in recent literature [38, 39, 40].

5.2.1 Formulation of Hybrid-VT Model

We consider the hybrid-VT model for a spatially extended core + n + n system. Here, we derive the three-body Hamiltonian from the A-nucleon system. This consideration is useful when we extend this model to include the core excitation in the halo nuclear system. The A-body Hamiltonian is given as

$$H = \sum_{i=1}^{A} t_i - T_{\rm cm} + \sum_{i>i}^{A} v_{ij} = T + V, \tag{5.5}$$

where $T=\sum t_i-T_{\rm cm}$ is the kinetic energy operator of the system after removing the center-of-mass motion $(T_{\rm cm})$ and $V=\sum v_{ij}$ is the two-body potential energy. We decompose the Hamiltonian of an A-nucleon system into a core part with A_c nucleons and $N(=A-A_c)$ valence neutrons. The relative coordinates between the core and the valence nucleons are given as $\eta_i=r_i-\frac{1}{A_c}\sum_{i=1}^{A_c}r_i$, as shown in Fig. 5.7. The kinetic energy term T is rewritten as

$$T = \sum_{i=1}^{A} t_i - T_{cm}$$

$$= T_c + \sum_{i=1}^{N} \frac{\mathbf{p}_i^2}{2\mu} + \sum_{i< j}^{N} \frac{\mathbf{p}_i \cdot \mathbf{p}_j}{(A_c + 1)\mu},$$
(5.6)

Here, $T_c = \sum_{i=1}^{A_c} t_i - T_{\rm cm}^c$ is the kinetic energy with $T_{\rm cm}^c$ being the center of mass motion of the core nucleus. The operator $\boldsymbol{p} = -i\hbar\nabla_{\boldsymbol{\eta}}$ is the momentum conjugate to $\boldsymbol{\eta}$ and $\boldsymbol{\mu} = A_c I(A_c + 1)m$ is the reduced mass between the core and a single neutron. The term of $\boldsymbol{p}_i \cdot \boldsymbol{p}_j$ is the recoil motion from the center of mass system. The potential term is similarly decomposed as

$$V = \sum_{i < j}^{A_c} v_{ij} + \sum_{i=1}^{N} \sum_{j=1}^{A_c} v_{ij} + \sum_{i < j}^{N} v_{ij},$$

= $V_c + \sum_{i=1}^{N} V_i + \sum_{i < i}^{N} v_{ij},$ (5.7)

where the mean field potential V_i for each valence neutron is given as

$$V_i = \sum_{j=1}^{A_c} v_{ij}.$$
 (5.8)

Here, V_c are the potential term of the core nucleus, and the Hamiltonian is rewritten as

$$H = \left[T_c + \sum_{i=1}^{N} \frac{\mathbf{p}_i^2}{2\mu} + \sum_{i < j}^{N} \frac{\mathbf{p}_i \cdot \mathbf{p}_j}{(A_c + 1)\mu} \right] + \left[V_c + \sum_{i=1}^{N} V_i + \sum_{i < j}^{N} v_{ij} \right],$$

$$= H_c + \sum_{i=1}^{N} \left[\frac{\mathbf{p}_i^2}{2\mu} + V_i \right] + \sum_{i < j}^{N} \left[v_{ij} + \frac{\mathbf{p}_i \cdot \mathbf{p}_j}{(A_c + 1)\mu} \right],$$
(5.9)

where the first term $H_c = T_c + V_c$ is the Hamiltonian of the core and the second and third terms are for valence neutrons. The second term is the single particle Hamiltonian for the relative motion between the single neutron and the core. This defines the orbitals for the valence nucleons. The third term is the two-body operator between the valence neutrons, which produces the coupling between valence neutrons, such as the di-neutron correlation.

We start with the core part $\Phi(A_c)$ and write the Schrödinger equation as

$$\Phi(A_c) = \sum_{\alpha} C_{\alpha} \phi_{\alpha}(A_c), \qquad (5.10)$$

$$H_c\Phi(A_c) = E_c\Phi(A_c), \tag{5.11}$$

where the index α is the label to distinguish various configurations of the core nucleus and the amplitudes C_{α} are those used in Eq. (5.2). They are determined by the variational equations obtained by the energy minimization of E_c . We employ the shell model like basis wave function for $\phi_{\alpha}(A_c)$.

The wave function of the two valence neutrons $\chi(nn)$ in the hybrid-VT model of two neutron halo nuclei (N=2) is expressed as the superposition of the COSM (V-type) and T-type wave functions as

$$\chi(nn) = \chi_V(\xi_V) + \chi_T(\xi_T). \tag{5.12}$$

Here, the coordinate sets ξ_V and ξ_T represent V-type and T-type ones, respectively, as shown in Fig. 5.7. We take antisymmetrization between two neutrons, explicitly. The radial components of the relative wave functions are expanded with a

finite number of Gaussian functions centered at the origin with various length parameters [41, 42].

In the hybrid-VT model, the total wave function of the A-nucleon system and the corresponding Schrödinger equation are given as

$$\Psi(A) = \mathscr{A}\left\{\sum_{\alpha} \phi_{\alpha}(A_c)\chi_{\alpha}(nn)\right\},\tag{5.13}$$

$$H\Psi(A) = E\Psi(A), \tag{5.14}$$

where the total Hamiltonian H is given in Eq. (5.9). We omit the angular momentum coupling between the core nucleus and the valence neutrons for simplicity. The operator \mathscr{A} is the antisymmetrizer between core nucleons and valence neutrons. The mixing amplitudes of the core configurations α are included in the wave functions $\chi_{\alpha}(nn)$. Equation (5.13) is useful to understand the asymptotic condition of the wave function, in which some of the valence neutrons are located far away from the core, such as the tail part of halo structure and the scattering states. This will be discussed later in the numerical results of ^{11}Li .

In order to solve Eq. (5.14), we employ the orthogonality condition model (OCM) [43–46] instead of the resonating group method (RGM) [47]. In the OCM, the antisymmetrizer $\mathscr A$ between core nucleons and valence nucleons is replaced by introducing the projection operator to remove the Pauli forbidden states from the relative motion of the valence neutrons. The projection is expressed by introducing the following one-body term in the original Hamiltonian in Eq. (5.9).

$$v_i^{\rm PF} = \lambda \sum_{k}^{N_i} |\phi_k^{\rm PF}\rangle \langle \phi_k^{\rm PF}|, \qquad (5.15)$$

where the indices i and k are the labels representing each valence neutron and each Pauli-forbidden state for one valence neutron. N_i is the number of Pauli-forbidden states for one valence neutron. We take a sufficiently large value for λ in the numerical calculation.

In the calculation of the matrix element of the Hamiltonian in Eq. (9), we fold the Hamiltonian by using the wave function of the core nucleus. In the coupled channel OCM with the hybrid-VT model, we obtain the following equation for the valence neutrons $\chi_{\alpha}(nn)$,

$$\sum_{\beta} \left[H_{\alpha\beta}^{c} + \sum_{i=1}^{2} \left\{ \frac{\boldsymbol{p}_{i}^{2}}{2\mu} \delta_{\alpha\beta} + V_{i,\alpha\beta}^{F} + v_{i}^{PF} \delta_{\alpha\beta} \right\} + \sum_{i < i}^{2} \left\{ v_{ij} + \frac{\boldsymbol{p}_{i} \cdot \boldsymbol{p}_{j}}{(A_{c} + 1)\mu} \right\} \delta_{\alpha\beta} \right] \chi_{\beta}(nn) = E \chi_{\alpha}(nn), \tag{5.16}$$

where

$$H_{\alpha\beta}^{c} = \langle \phi_{\alpha}(A_{c}) | H_{c} | \phi_{\beta}(A_{c}) \rangle, \tag{5.17}$$

$$V_{i,\alpha\beta}^{F} = \langle \phi_{\alpha}(A_c) | V_i | \phi_{\beta}(A_c) \rangle = \langle \phi_{\alpha}(A_c) | \sum_{j=1}^{A_c} v_{ij} | \phi_{\beta}(A_c) \rangle.$$
 (5.18)

We explain here the Gaussian expansion method to describe the wave functions of valence neutrons $\chi_{\alpha}(nn)$ in the hybrid-VT model. The spatial part of the basis functions for one relative motion r is given by the following Gaussian wave functions,

$$\psi_l^b(\mathbf{r}) = N_l(b) \, r^l \exp(-\frac{r^2}{2b^2}) \, Y_l(\hat{\mathbf{r}}), \tag{5.19}$$

$$N_l(b) = \left[\frac{2b^{-(2l+3)}}{\Gamma(l+3/2)}\right]^{\frac{1}{2}},\tag{5.20}$$

where l is the orbital angular momentum. The set of the length parameter b is usually chosen in geometric progression [48]. In V- and T-type basis functions, we commonly use these basis states. We expand each relative motion of the hybrid-VT model with a finite number of the above basis functions. The Gaussian expansion method is able to describe the halo structure very nicely.

For the coupling with intrinsic spin of neutrons, in the COSM (V-type), we adopt the j–j coupling scheme in a sense of the shell model. This representation is suitable to express the motion of each valence neutron in the mean field potential provided by the core nucleus. In the T-type basis function, we take the L–S coupling scheme. This is because the di-neutron pair is considered to have the dominant component of the 0^+ state with spin singlet state. In the T-type basis, we directly take into account the 1S_0 component of the two neutrons. Actually, the analysis of 6 He provides more than 80% in the spin singlet states. In the COSM (V-type basis), its basis wave function corresponding the configuration of the core nucleus ϕ_{α} is given as

$$\chi_{\alpha,V}^{J}(nn) = \sum_{p} C_{\alpha,V}^{p} \mathcal{A}_{12} \left[[\psi_{l_{1}}^{b_{1}}(\eta_{1}), \chi_{1/2}^{\sigma}]_{j_{1}}, [\psi_{l_{2}}^{b_{2}}(\eta_{1}), \chi_{1/2}^{\sigma}]_{j_{2}} \right]_{J}$$

$$p = \{b_{1}, b_{2}, l_{1}, l_{2}, j_{1}, j_{2}, J\},$$
(5.21)

where \mathscr{A}_{12} is an antisymmetrizer between two valence neutrons, and $C^p_{\alpha,V}$ are variational coefficients for the basis set.

The *T*-type basis function is similarly described as

$$\chi_{\alpha,T}^{J}(nn) = \sum_{q} C_{\alpha,T}^{q} \mathcal{A}_{12} [[\psi_{l}^{b_{r}}(\mathbf{r}), \psi_{L}^{b_{R}}(\vec{R})]_{I} \chi_{S}]_{J},
q = \{b_{r}, b_{R}, l, L, S, J\}, \qquad \chi_{S} = [\chi_{1/2}^{\sigma}, \chi_{1/2}^{\sigma}]_{S}.$$
(5.22)

In the calculation of the hybrid-VT model, we take various sets of orbital angular momenta and spins until we reach the convergence of the solutions. The variation of the total energy E with respect to the total wave function $\Psi(A)$ is given by

$$\delta \frac{\langle \Psi | H | \Psi \rangle}{\langle \Psi | \Psi \rangle} = 0, \tag{5.23}$$

which leads to the following equations:

$$\frac{\partial \langle \Psi | H - E | \Psi \rangle}{\partial C_{\alpha V}^{p}} = 0, \qquad \frac{\partial \langle \Psi | H - E | \Psi \rangle}{\partial C_{\alpha T}^{q}} = 0. \tag{5.24}$$

5.2.2 Application of the Hybrid-VT Model to ⁶He

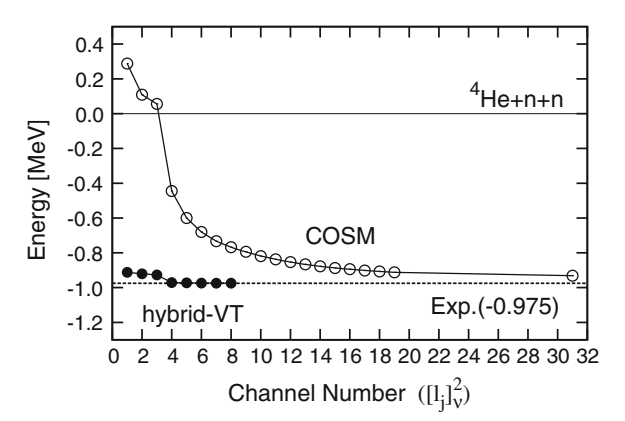
We discuss the results of the hybrid-VT model for the two-neutron halo nuclei 6 He as 4 He + n + n and 11 Li as 9 Li + n + n. An extension to a core plus many valence neutrons (e.g. 7 He = 4 He + n + n + n) is straightforward [49, 50]. For 6 He case, we take a single configuration for the 4 He core. The Hamiltonian in Eq. (16) can be written as

$$H = H_c + \sum_{i=1}^{2} \left\{ \frac{\mathbf{p}_i^2}{2\mu} + V_{cn}^F(\eta_i) + v_i^{PF} \right\} + v_{nn} + \frac{\mathbf{p}_1 \cdot \mathbf{p}_2}{(A_c + 1)\mu}.$$
 (5.25)

Here, H_c can be replaced by the observed energy of 4 He (-28.3 MeV) and we can discuss only the relative motion of valence two neutrons in 6 He. For the 4 He-n potential V_{cn}^F we adopt the microscopic KKNN potential [24, 51], which reproduces the observed phase shift between 4 He and n. The Minnesota interaction [52] is used for v_{nn} between two valence neutrons, where the exchange mixture u is chosen to be 0.95. These choices are the same as those in Refs. [26, 32] and [53].

It is important to understand the model performance for 6 He as a simple system for the description of more complicated systems as 11 Li. The binding energy of the 6 He ground state is shown as a function of the channel number in Fig. 5.8. The calculated results in the COSM and the hybrid-VT model are shown by the open and solid circles, respectively. In both cases, the convergence was achieved and it is found that the hybrid-VT model converges much faster than the COSM. In the hybrid-VT model, it is sufficient to take shell model states up to the $d_{5/2}$ -shell orbit (Channel number is five) using the V-type coordinates and add the di-neutron channel of l = L = 0 states in Eq. (5.22) using the T-type coordinates. Thus, the di-neutron correlation is very important for the ground state of 4 He. The hybrid-VT model is an efficient framework to treat the di-neutron correlation in the shell model basis.

Fig. 5.8 The binding energy of the ⁶He ground state as a function of the channel number [24]. The *open circles* are the results of the COSM model and the *solid circles* are those of the hybrid-*VT* model



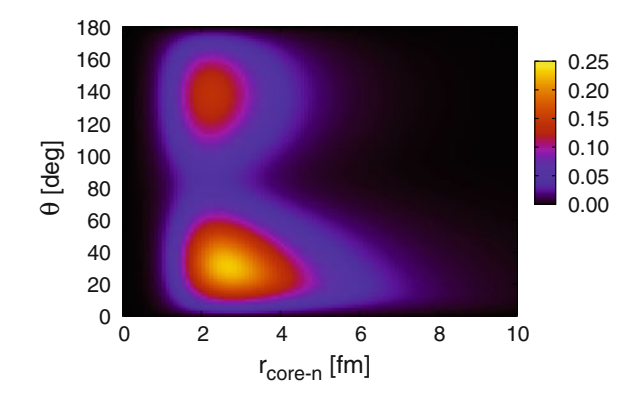
The radii of ⁶He are converged as 2.46 and 2.06 fm for matter and charge rms radii, respectively. These values agree with the recent observations [1, 55]. The core-n and n-n mean distances are obtained as 3.42 and 4.90 fm, respectively. In addition to the radius, the spatial correlations of the halo neutrons in ⁶He are interesting [10, 38, 56, 57] and the calculated results are shown in Fig. 5.9. We show the density distribution of halo neutrons $\rho_{nn}(r, \theta)$ in ⁶He as a contour in the plane of ⁴He-n distance r and the opening angle between two neutrons θ with the following definition [54, 62];

$$\rho_{nn}(r,\theta) = \int_{0}^{\infty} dr' \rho_{nn}(r,r',\theta)$$
 (5.26)

$$\rho_{nn}(r, r', \theta) = 8\pi^{2} r^{2} r'^{2} \sin \theta \, \langle \Psi^{J}(^{6}\text{He}, r, r', \theta) | \delta(r - r'') \delta(r' - r''') \\
\times \delta(\theta - \theta') | \Psi^{J}(^{6}\text{He}, r'', r''', \theta') \rangle,$$
(5.27)

where the total wave function of ${}^{6}\text{He}$ has three variables, the ${}^{4}\text{He-}n$ distances with r and r' for each neutron and their opening angle θ in Eq. (5.27). We integrate out only the variables of the ket part. It is confirmed that the di-neutron type

Fig. 5.9 The two neutron correlation density $\rho_{nn}(r_{\rm core}-n,\theta)$ in $^6{\rm He}$ in the r and θ plane [54]. Here, r_{core-n} denotes the relative distance between the core and one of the two neutrons and θ the opening angle between the two neutrons



configuration (a large r and a small θ) gives a maximum value of the density, although the density of neutrons is widely distributed. There is another component of the cigar type configuration (a small r and a large θ), which coexists with the di-neutron type configuration. The characteristics of these two structures in the density distribution come from the $p_{3/2}^2$ configuration of two neutrons in 6 He, which is the dominant component by 90.2% in the ground state wave function. The mixing of the higher orbital configurations makes a spatial extension of the distribution and enhances the di-neutron component, such as $p_{1/2}^2$ with 4.3%, $1s_{1/2}^2$ with 1.2%, $d_{5/2}^2$ with 2.6% and $d_{3/2}^2$ with 0.9%. The results indicate that the j-j coupling scheme is well established in 6 He.

5.2.3 Hybrid-VT Model on Di-Neutron Clustering in 11Li

We consider the three-body problem of ${}^9\mathrm{Li} + n + n$ using the orthogonality condition model (OCM). The Hamiltonian consists of the similar form as given in Eq. (5.25) for ${}^6\mathrm{He}$. The difference from the ${}^6\mathrm{He}$ model is the configuration mixing for the ${}^9\mathrm{Li}$ core nucleus, because of the small neutron separation energy of ${}^9\mathrm{Li}$ in comparison with ${}^4\mathrm{He}$. This means that we take into account the core excitation in ${}^{11}\mathrm{Li}$. In this section, we first take into account the neutron 0^+ pairing correlation of the ${}^9\mathrm{Li}$ core and examine this effect on the structures of ${}^{11}\mathrm{Li}$ and ${}^{10}\mathrm{Li}$. Later, we include the tensor correlation in ${}^9\mathrm{Li}$.

Before showing the numerical results, we generally formulate the coupled ${}^9\mathrm{Li} + n + n$ model of ${}^{11}\mathrm{Li}$, in which the configuration mixing is performed for the ${}^9\mathrm{Li}$ core. This framework is straightforward to apply when the tensor correlation is included in the core part, later. In the coupled hybrid-VT model of ${}^9\mathrm{Li} + n + n$, we consider the Pauli forbidden (PF) states in the ${}^9\mathrm{Li} - n$ relative motion [60]. In this model, PF states removed from the relative motion depend on the configuration of ${}^9\mathrm{Li}$, namely the orbits occupied by neutrons in the ${}^9\mathrm{Li}$ core. The main configurations are given in Eq. (5.2) and the amplitudes are written as C_1 , C_2 and C_3 . The PF states corresponding to those wave functions are given as

$$\phi_{PF} = \begin{cases} 0s_{1/2}, 0p_{3/2} & \text{for } C_1\\ 0s_{1/2}, 0p_{3/2}, (0p_{1/2})_{\nu\nu} & \text{for } C_2\\ 0s_{1/2}, 0p_{3/2}, (0p_{1/2})_{\pi\nu} & \text{for } C_3. \end{cases}$$
(5.28)

In case of C_2 the PF $p_{1/2}$ orbit is used by the pairing state and indicated as $(p_{1/2})_{\nu\nu}$, while in case of C_3 the PF $p_{1/2}$ orbit is used by the deuteron-like tensor correlation and indicated as $(p_{1/2})_{\pi\nu}$. From Eq. (5.13), the wave function of ¹¹Li is given as

$$\Psi^{J}(^{11}\text{Li}) = \sum_{\alpha}^{N_{\alpha}} \mathscr{A} \Big\{ [\phi_{\alpha}^{3/2^{-}}, \chi_{\alpha}^{j}(nn)]^{J} \Big\}.$$
 (5.29)

Here, $\chi_{\alpha}^{j}(nn)$ represents the wave functions of two valence neutrons, and j and J are the spin of two valence neutrons and the total spin of ¹¹Li, respectively. The three-body eigenstates are obtained by solving the eigenvalue problem for the coupled-channel Hamiltonian given in Eq. (5.9).

$$H(^{11}\text{Li})\Psi(^{11}\text{Li}) = E(^{11}\text{Li})\Psi(^{11}\text{Li})$$
 (5.30)

We discuss the coupling between the ^9Li configurations $\phi_{\alpha}^{3/2^-}$ and the motion of valence neutrons. In ^{11}Li , the amplitudes C_{α} of each configuration of ^9Li in Eq. (5.10) are determined variationally. Asymptotically, when the two valence neutrons are far away from ^9Li , the wave function of ^{11}Li becomes

$$\chi^{j}_{\alpha}(nn) \xrightarrow[\eta_{1},\eta_{2}\to\infty]{} C_{\alpha} \cdot \chi^{j}(nn),$$
 (5.31)

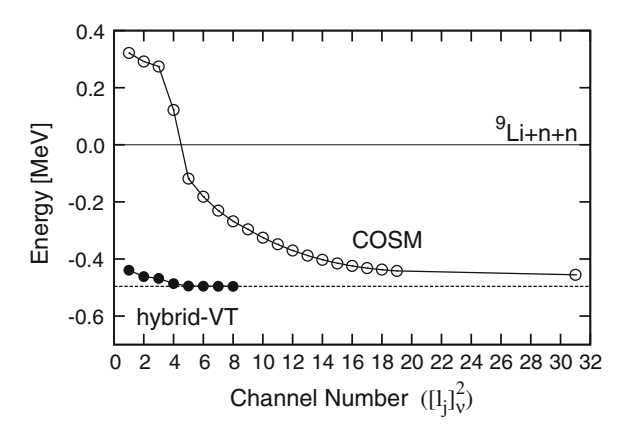
$$\Phi^{J}(^{11}\text{Li}) \underset{\eta_{1}, \eta_{2} \to \infty}{\longrightarrow} \left[\left(\sum_{\alpha}^{N_{\alpha}} C_{\alpha} \phi_{\alpha}^{3/2^{-}} \right), \chi^{j}(nn) \right]^{J}. \tag{5.32}$$

The first equation implies that the asymptotic wave function of the two valence neutrons is decomposed into the internal amplitude C_{α} of the ${}^{9}\text{Li}$ configuration and the relative wave function $\chi^{j}(nn)$, which is independent of the ${}^{9}\text{Li}$ configuration. This means that the coupling between the valence neutrons and ${}^{9}\text{Li}$ disappears. As for the di-neutron wave function $\chi^{j}(nn)$, the correlation between the two neutrons disappears also at far distance, because the two neutrons do not form bound state in the free space. The mixing amplitudes $\{C_{\alpha}\}$ of ${}^{9}\text{Li}$ in Eq. (5.32) are the same as those of the isolated ${}^{9}\text{Li}$ in Eq. (5.10). Contrastingly, when the two valence neutrons are close to the ${}^{9}\text{Li}$ core, the motions of the two valence neutrons dynamically couple to the configuration of ${}^{9}\text{Li}$ in order to satisfy the Pauli principle, which changes the mixing amplitudes $\{C_{\alpha}\}$ in ${}^{9}\text{Li}$ from those of the isolated ${}^{9}\text{Li}$ core.

We now carry out the coupled-channel three-body calculation for ^{11}Li . In the model, the $^{9}\text{Li}-n$ interaction $V_{c\,n}$ is taken as a folding-type potential with the MHN interaction [46, 58, 59], which is constructed from the G-matrix using the bare nucleon–nucleon interaction. The folding potential for $^{9}\text{Li}-n$ includes the coupling between intrinsic spins of the valence neutron and ^{9}Li (3/2 $^{-}$). This coupling produces splittings of the energy levels, for instance 1^{+} – 2^{+} (for the $p_{1/2}$ -neutron) and 1^{-} – 2^{-} (for the $s_{1/2}$ -neutron) in the ^{10}Li spectra.

The important points we wish to study in this calculation are whether the present model can solve the under-binding problem and describe the halo structure. This is because the three-body model of 11 Li by using only the inert core model of 9 Li, which corresponds to the use of the C_1 term alone in Eq. (5.2), does not make a bound state [26]. We also want to see how the pairing correlations act on the binding mechanism. The results are shown in Fig. 5.10. The binding energy of the 11 Li ground state measured from the three-body threshold is obtained as 0.5 MeV by considering the pairing correlation in 9 Li. The matter radius is obtained as 2.69 fm, which is smaller than the experimental value [1, 61].

Fig. 5.10 Convergence of the ¹¹Li ground state energy with respect to the channel number in the COSM (*open circles*) and in the hybrid-*VT* model (*solid circles*) [25]. The *dotted line* represents energy to which the calculation converges (-0.50 MeV) in the present model setting



We discuss the role of the pairing correlation between valence neutrons in ¹¹Li. In Fig. 5.10 two kinds of the energy convergence of ¹¹Li are plotted as functions of the channel number of the $j^{\pi} = 0^{+}$ pairing configuration for valence neutrons. One of them is the calculation employing only the COSM basis and the other is that with the hybrid-VT basis. In the calculation, we take the first channel as $(p_{1/2})^2$, and the order in which channels are added to the first one is $(s_{1/2})^2$, $(p_{3/2})^2$, $(d_{5/2})^2$, $(d_{5/2})^2$, $(d_{3/2})^2$,..., $(l_j)^2$. The maximum number of channel is 31, where the orbital angular momentum and the spin of one valence neutron are l=15 and $j = \frac{31}{2}$. We see rapid convergence of the energy in the hybrid-VT model. This result indicates that the pairing correlation between valence neutrons is important to reproduce the weak binding state of ¹¹Li. This result is similar to the ⁶He case shown in Fig. (5.8). We comment here that the binding energy comes out to be 0.5 MeV, which is larger than the experimental value of 0.3 MeV. At the same time, the s-wave component is less than 10% as compared with the experimental value $\sim 50\%$. In the present analysis, we determine the $^9\text{Li}-n$ interaction to reproduce the 1 $^+$ state at 0.42 MeV and the virtual s-wave state just at the 9 Li+n threshold energy in the ¹⁰Li spectrum. In this case, two neutrons of ¹¹Li are slightly overbound, which indicate that the pairing correlation of ⁹Li partially solves the problem of ^{10,11}Li. This over-binding property together with other problems will be removed consistently by considering the deuteron-like tensor correlation, which pushes up the $(p_{1/2})^2$ state energetically close to the $(s_{1/2})^2$ state, as will be shown later.

We also discuss the di-neutron correlation in ^{11}Li . The spatial correlations of the halo neutrons in ^{11}Li are interesting [10, 38, 56, 57] and they are shown in Fig. 5.11. We calculate the density distribution of halo neutrons $\rho_{nn}(r,\theta)$ in ^{11}Li as functions of the $^{9}\text{Li}-n$ distance r and the opening angle θ between two neutrons. In order to present the realistic case, which reproduce the large s^2 component of halo neutrons [3], we show here the result of calculations with the tensor optimized shell model (TOSM), which includes both the pairing and deuteron-like tensor correlations in ^{9}Li [62]. This TOSM wave function contains the s-wave component

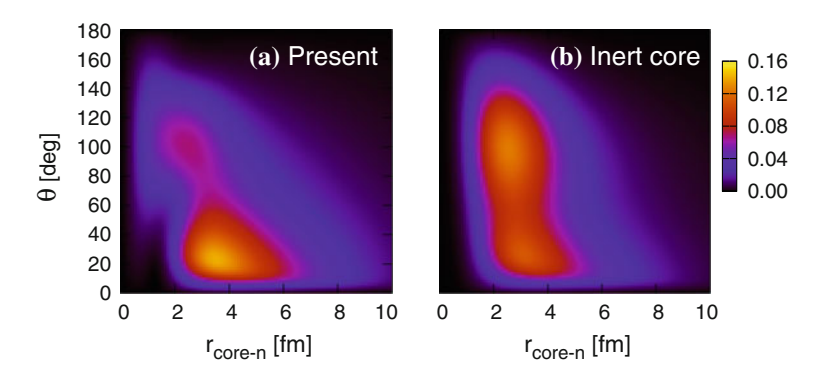


Fig. 5.11 Two neutron correlation density $\rho_{nn}(r_{core} - n, \theta)$ for ¹¹Li [62]. The case (**a**) is the calculation with the TOSM of ⁹Li and (**b**) is the Inert Core case of ⁹Li, respectively

in 11 Li by a large amount 47%. We will discuss the details of the TOSM in the following section. In the TOSM case (a), it is confirmed that the di-neutron clustering configuration gives a maximum value of the density, although the density of neutrons is widely distributed. Contrastingly, the Inert Core case (b) with a small s^2 component of 4%, does not show much enhancement of the di-neutron clustering configuration and the cigar type configuration coexists with the di-neutron clustering configuration. This feature of the case (b) is similar to 6 He [56]. These two results indicate the role of the s^2 component on the formation of the di-neutron clustering configuration as follows: The s^2 component in 11 Li increases the amplitude of the tail region of two neutrons far from 9 Li, and these neutrons tend to come close to each other to gain the interaction energy between them. As a result, the di-neutron clustering configuration is enhanced, although the spatial distribution of neutrons is still wide. The spatial distribution of two neutrons also affects the opening angle θ , where the TOSM case having large di-neutron component, shows a smaller θ value (65°) than the Inert Core one (73°).

5.3 Continuum and Resonance States in Complex Scaling Method

The halo nuclei have extremely small binding energies and it is very important to take into account the continuum and resonance states for quantitative account of the halo nuclei. At the same time, neighboring nuclei have odd numbers of neutrons and often those nuclei do not have bound states. Hence, in order to obtain precious informations on the neutron-core potentials, it is important to describe resonance states of the neighboring nuclei. In this section, we would like to develop a powerful method of treating continuum and resonance states as if they are bound states. This method is called the complex scaling method (CSM). We can also apply the CSM for excitation functions of halo nuclei. We would like to

emphasize here that there has not been any method to treat three-body unbound systems. In particular, there is a case where two-body system out of the three-body system may be in the resonance state. We can treat these interesting possibilities in the CSM.

5.3.1 Formulation of CSM

We explain the CSM, which describes resonances and non-resonant continuum states of a many-body system. Hereafter, we refer to non-resonant continuum states as simply continuum states. In the CSM, we transform every relative coordinates $\{r_i\}$ of the system such as core+ n + n model, by the operator U_θ as

$$U_{\theta}: \mathbf{r}_i \to \mathbf{r}_i e^{i\theta} \quad \text{for } i = 1, \dots, N,$$
 (5.33)

where θ is a scaling angle and N the total number of particles in the system. The Hamiltonian H is transformed into the complex-scaled Hamiltonian $H_{\theta} = U_{\theta}HU_{\theta}^{-1}$, and the corresponding complex-scaled Schrödinger equation is given as

$$H_{\theta}\Psi_{\theta}^{J} = E\Psi_{\theta}^{J},\tag{5.34}$$

$$\Psi_{\theta}^{J} = e^{(3/2)i\theta X} \Psi^{J}(\{r_{i}e^{i\theta}\}),$$
(5.35)

where X stands for the number of degrees of freedom. The phase factor $e^{(3/2)i\theta X}$ is attached here due to the phase freedom of wave function and originates from the Jacobian in the integral over the coordinates. In the three-body model of ^{11}Li , X=2. The eigenstates Ψ^J_{θ} are obtained by solving the eigenvalue problem of H_{θ} in Eq. (5.34). In the CSM, we obtain all the energy eigenvalues E of bound and unbound states on a complex energy plane, governed by the ABC theorem [63, 64]. In this theorem, it is proved that the boundary condition of Gamow resonances is transformed to the damping behavior at the asymptotic region. The Gamow resonance is a pole of S-matrix and has an complex energy eigenvalue of $E=E_r-i\Gamma/2$, where E_r and Γ are the resonance energies measured from the lowest threshold and the decay widths, respectively.

For simple understanding of this theorem, we consider the asymptotic wave functions for Gamow states in the two-body case. The Gamow states with complex wave number k_p are described by the outgoing waves $\exp(ik_p r e^{i\theta})$. It is easily understood that the bound state wave functions maintain the damping behavior for $\theta < \pi/2$. The wave functions of resonances, which had divergent behavior originally as $e^{ik_R \cdot r} = e^{i(\kappa_r - i\gamma_r)r} = e^{\gamma_r r} \cdot e^{i\kappa_r r}$, behave as

$$e^{ik_R \cdot re^{i\theta}} = e^{i(\kappa_r - i\gamma_r)re^{i\theta}} = e^{ir(\kappa_r - i\gamma_r)(\cos\theta + i\sin\theta)}$$

= $e^{(-\kappa_r \sin\theta + \gamma_r \cos\theta)r} \cdot e^{i(\kappa_r \cos\theta + \gamma_r \sin\theta)r}$. (5.36)

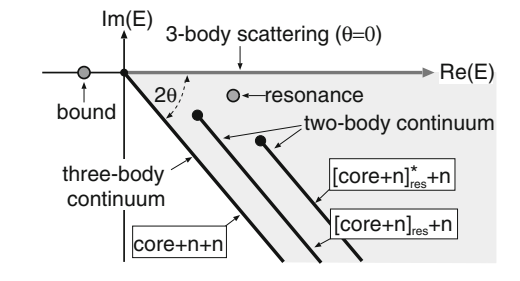
This equation shows that the divergent behavior of the resonant wave functions is regularized when we take the scaling angle θ to be larger than the angle $\theta_r = \tan^{-1}(\frac{\gamma_r}{\kappa_r})$ of the resonance position $\kappa_r - i\gamma_r$. This damping condition enables us to use the same theoretical method to obtain many-body resonance states as those used for bound states. For a finite value of θ , every Riemann branch cut is commonly rotated down by 2θ . We can identify the resonance poles of complex eigenvalues without any ambiguities.

In the wave function, the θ dependence is included in the variational coefficients in Eqs. (21) and (22) as $\{C_{\alpha,V}^{p,\theta}\}$ and $\{C_{\alpha,T}^{p,\theta}\}$, respectively. The wave functions are expanded with the finite number of the L^2 basis functions, so that all the obtained states are discretized on the complex energy plane. The stability of the calculated matrix elements of resonant and continuum states using the CSM has been shown in many works [28, 46, 65]. For continuum states, we adopt the discretized representation using the L^2 integrable basis functions. This discretization has been checked to reproduce the genuine continuum states by using the CSM [66–68].

In the study, we use the CSM not only to search for the resonance positions, but also to calculate the strength functions, such as *E1* responses. This is related to the continuum level density of the scattering states. We have shown that the CSM provides us with the accurate continuum level density even if the states are discretized. This fact means that the continuous strength function into scattering states can be obtained in the CSM, which is performable in the many-body case. So far, we have succeeded to apply this characteristics of the CSM to calculate the electric responses, Gamow–Teller strengths, nucleon-removal strength and so on.

In the calculation of the strength function, we need a complete set of the core+ n+n system including bound, resonant, and continuum states. We express this complete set using the complex-scaled eigenstates Ψ^J_{θ} obtained in the core+n+n model. We briefly explain the extended completeness relation (ECR) using the CSM [28, 65, 69]. When we take a large θ like in Fig. 5.12, three-body scattering states are decomposed into three categories of discrete three-body resonances, three-body continuum states of core+n+n, and two-body continuum states of [core + n]_{res} + n. Here, the [core + n]_{res} + n two-body continuum states are obtained on the branch cuts, whose origins are resonance positions of the core+n system, as shown in Fig. 5.12. Using all the unbound states, we introduce

Fig. 5.12 A schematic distribution of energy eigenvalues of the Borromean core + n + n system in the CSM, where the origin of energy is chosen as the three-body threshold energy [46]



the extended three-body completeness relation (ECR) of the complex-scaled Hamiltonian H_{θ} as

$$\mathbf{1} = \sum_{\nu} |\Phi_{\nu}^{\theta}\rangle\langle\widetilde{\Phi}_{\nu}^{\theta}|$$

$$= \{\text{three-body boundstate}\}$$

$$+ \{\text{three-body resonance}\}$$

$$+ \{\text{three-body continuum states of core} + n + n\}$$

$$+ \{\text{two-body continuum states of } [\text{core} + n]_{\text{res}} + n\},$$

$$(5.37)$$

where $\{\Phi_{\nu}^{\theta}, \widetilde{\Phi}_{\nu}^{\theta}\}$ are the complex-scaled wave functions and form a set of biorthogonal bases. This relation is an extension of the two-body ECR [46, 65]. Because the detailed definition of the biorthogonal bases is written in the previous works [28, 65], we only briefly explain it here. When the wave number k_{ν} of Φ_{ν} is for discrete bound and resonance states, the adjoint wave number \widetilde{k}_{ν} of $\widetilde{\Phi}_{\nu}$ is defined as $\widetilde{k}_{\nu} = -k_{\nu}^*$, which leads to the relation $\widetilde{\Phi}_{\nu} = (\Phi_{\nu})^*$ [65, 69, 70]. For continuum states, the same relation of the bi-orthogonal states of resonances is adopted, because we use a discretized representation. In the core+n+n model, the core+n+n system, because two neutrons do not have any bound states or physical resonances.

We explain how to calculate the strength function S(E) using the ECR model. The strength S(E) is a function of the real energy of the whole system E. We first introduce the Green's function $\mathcal{G}(E, \eta, \eta')$, which is used in the derivation of the strength [28, 29]. The coordinates, η and η' , represent the set of r_i (i = 1, ..., X) in Fig. 5.7. Here, we introduce the complex-scaled Green's function $\mathcal{G}^{\theta}(E, \eta, \eta')$ as

$$\mathscr{G}(E, \eta, \eta') = \left\langle \eta \left| \frac{1}{E - H} \right| \eta' \right\rangle \tag{5.38}$$

In the derivation from Eq. (5.38) to Eq. (5.39), we insert the ECR of the whole system given in Eq. (5.37). The total energy E_{ν}^{θ} corresponds to the eigen wave function Φ^{θ}_{ν} . The θ dependence of E_{ν}^{θ} appears only in the continuum spectra.

The strength function $S(E)_{\alpha}$ for the arbitrary operator O_{α} , in which α is the quantum number for the operator, is defined using the ordinary Green's function as

$$S_{\alpha}(E) = \sum_{\nu} \langle \widetilde{\Psi}_{0} | O_{\alpha}^{\dagger} | \Phi_{\nu} \rangle \langle \widetilde{\Phi}_{\nu} | O_{\alpha} \rangle \Psi_{0} \, \delta(E - E_{\nu})$$

$$= -\frac{1}{\pi} \operatorname{Im} \left[\int d\boldsymbol{\eta} d\boldsymbol{\eta}' \widetilde{\Psi}_{0}^{*}(\boldsymbol{\eta}) O_{\alpha}^{\dagger} \mathscr{G}(E, \boldsymbol{\eta}, \boldsymbol{\eta}') O_{\alpha} \Psi_{0}(\boldsymbol{\eta}') \right]. \tag{5.40}$$

For simplicity, we omit the labels of the angular momenta and their z components of the wave functions and of the operators. The wave function Ψ_0 is the initial state. We also consider the sum rule value of the strength $S_{\alpha}(E)$ in Eq. (5.40), which is defined by the integration of $S_{\alpha}(E)$ over the real energy E. Using the completeness relation of the final states of ⁶He, the sum rule value is given as

$$\int dE \, S_{\alpha}(E) = \sum_{\nu} \langle \widetilde{\Psi}_{0} | O_{\alpha}^{\dagger} | \Phi_{\nu} \rangle \langle \widetilde{\Phi}_{\nu} | O_{\alpha} | \Psi_{0} \rangle
= \langle \widetilde{\Psi}_{0} | O_{\alpha}^{\dagger} O_{\alpha} | \Psi_{0} \rangle.$$
(5.41)

Thus, it is also confirmed that the energy integrated value of $S_{\alpha}(E)$ satisfies the expectation value of the operator O_{α} for the initial state. In the case of the E1 transition of halo nuclei, the sum rule value corresponds to the relative distance between core and the center of mass of valence neutrons. When O_{α} is an annihilation operator, for example, ⁷He into ⁶He + n, the integrated value satisfies the associated particle number of ⁷He, namely the number of three valence neutrons.

To calculate the strength function $S_{\alpha}(E)$ in Eq. (5.40), we operate the complex scaling on $S_{\alpha}(E)$, and use the complex-scaled Green's function of Eq. (5.39) as

$$S_{\alpha}(E) = -\frac{1}{\pi} \operatorname{Im} \left[\int d\boldsymbol{\eta} d\boldsymbol{\eta}' [\widetilde{\Psi}_{0}^{*}(\boldsymbol{\eta})]^{\theta} (O_{\alpha}^{\dagger})^{\theta} \mathscr{G}^{\theta}(E, \boldsymbol{\eta}, \boldsymbol{\eta}') O_{\alpha}^{\theta} \Psi_{0}^{\theta}(\boldsymbol{\eta}') \right]$$

$$= \sum_{\nu} S_{\alpha,\nu}(E), \qquad (5.42)$$

$$S_{\alpha,\nu}(E) = -\frac{1}{\pi} \operatorname{Im} \left[\frac{\langle \widetilde{\Psi}_0^{\theta} | (O_{\alpha}^{\dagger})^{\theta} | \Phi_{\nu}^{\theta} \rangle \langle \widetilde{\Phi}_{\nu}^{\theta} | O_{\alpha}^{\theta} | \Psi_0^{\theta} \rangle}{E - E_{\nu}^{\theta}} \right]. \tag{5.43}$$

In Eq. (5.43), the strength function is calculated using the matrix elements $\langle \widetilde{\Phi}_{\nu}^{\theta} | O_{\alpha}^{\theta} | \Psi_{0}^{\theta} \rangle$. It is noted that the function $S_{\alpha,\nu}(E)$ is independent of θ [28, 50, 65, 68]. This is because any matrix elements are obtained independently of θ in the complex scaling method, and also because the state ν is uniquely classified according to the ECR defined in Eq. (5.37). As a result, the decomposed strength $S_{\alpha,\nu}(E)$ is uniquely obtained. Thus, the strength $S_{\alpha}(E)$ is calculated as a function of the real energy E of the nucleus of interest. When we discuss the structures appearing in $S_{\alpha}(E)$, it is useful to decompose $S_{\alpha}(E)$ into each component $S_{\alpha,\nu}(E)$ by using the complete set of the final state ν of the whole system. We can categorize ν using the ECR in Eq. (5.37). Because of this decomposition of unbound states, we can unambiguously investigate how much each resonant and continuum state

of the whole system exhausts the strength. This can be performed in the Coulomb breakup strengths of ⁶He, ¹¹Li and ¹¹Be and many other three-body systems.

5.3.2 Three Body Resonance and Continuum States in ⁶He

We discuss the results of the complex scaling method (CSM) for the halo system 6 He. We describe 6 He as a 4 He + n + n system in the hybrid-VT model [23, 27]. Here, we briefly recapitulate the important properties of the CSM. The Hamiltonian of the model is the same as the one in Ref. [24] except for an introduction of a three-body interaction;

$$H = \sum_{i=1}^{3} t_i - T_G + \sum_{i=1}^{2} (V_{\alpha n,i} + v_i^{PF}) + v_{nn} + V_{\alpha nn}^3,$$
 (5.44)

where t_i and T_G are kinetic energies of each particle and the center-of-mass of the three-body system, respectively. The ⁴He core cluster is assumed to have the $(0s)^4$ -closed configuration with the length parameter $b_c = 1.4$ fm, which reproduces the experimental charge radius of ⁴He. The Pauli-forbidden PF state is the 0s orbit in the relative motion. The two-body interactions $V_{\alpha}n$ and v_{nn} are given by the microscopic KKNN potential [51] for ⁴He-n and the Minnesota potential [51] for n-n, respectively. These potentials well reproduce the low-energy scattering data of each two-body system.

A phenomenological three-body ${}^4\text{He-}n-n$ interaction V_{znn}^3 is introduced to fit the binding energy of the ${}^6\text{He}$ ground state. This is introduced to overcome the small underbinding (few hundreds keV) of the ${}^6\text{He}$ ground state with a frozen ${}^4\text{He}$ core assumption. By taking into account the excitation or the dissociation of the ${}^4\text{He}$ core, this underbinding problem in ${}^6\text{He}$ is believed to be solved [71, 72]. We include effectively the excitation of the ${}^4\text{He}$ core inside ${}^6\text{He}$ by this three-body interaction term. We introduce the three-body interaction assuming a single Gaussian function

$$V_{onn}^3 = V_3 e^{-\nu(\mathbf{r}_1^2 + \mathbf{r}_2^2)}, \tag{5.45}$$

$$V_3 = -0.218 \text{MeV}, \quad v = (0.1/b_c)^2 \text{fm}^{-2}.$$
 (5.46)

Using this Hamiltonian, the present hybrid-VT model reproduces the observed energies and decay widths of ^{5,6}He, simultaneously [73], namely, the threshold energies of the particle emissions for the He isotopes.

The three-body eigenstates are obtained by solving the eigenvalue problem of the complex-scaled Hamiltonian. We use 30 Gaussian basis functions for 1 radial component in order to achieve stabilization of the calculated results for the position of resonances, distributions of continuum states and their transition matrix elements. The maximum range of Gaussian basis functions is about 40 fm.

In Fig. 5.13, we show the eigenvalue distribution for 1^- states of ${}^6\text{He}$. This result is obtained by diagonalization of the complex-scaled Hamiltonian of the ${}^4\text{He} + n + n$ model with $\theta = 35$ deg. From Fig. 5.13, we see that all eigenvalues are obtained along three lines of rotated Riemann cuts corresponding to two two-body and one three-body continuum channels. There is no 1^- resonance. Therefore, these results indicate that the 1^- unbound states above the ${}^4\text{He} + n + n$ threshold are classified into two-body continuum states of ${}^5\text{He}(3/2^-, 1/2^-) + n$ and three-body continuum states of ${}^4\text{He} + n + n$.

In Fig. 5.14, we show the obtained $2^+_{1,2}$ resonances and continuum solutions which are decomposed into two- and three-body continuum states, similar to the 1^- spectra. The whole energy levels of 6 He are displayed in Fig. 5.15. We can see a good agreement between our calculation and experimental data. The present calculation does not predict any 1^- resonance in the low excitation energy region. This result is consistent with the experimental results [73, 74].

Fig. 5.13 Energy eigenvalues of 1^- states calculated with the CSM where θ is 35 deg. [28]. Squares and triangles indicate the two-body continuum states of ${}^5\text{He}(3/2^-) + n$ and ${}^5\text{He}(1/2^-) + n$, respectively. Circles indicate the three-body continuum states of ${}^4\text{He} + n + n$

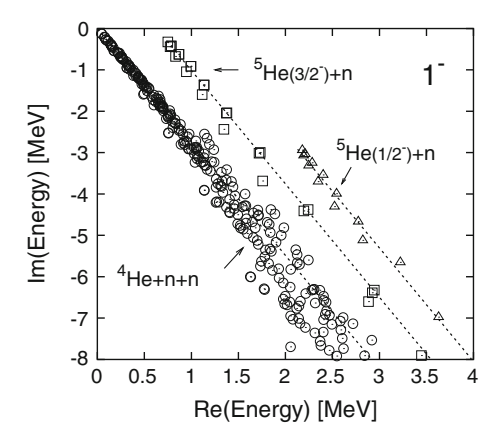


Fig. 5.14 Energy eigenvalues of 2⁺ states calculated with the CSM [28], where two *solid circles* are 2⁺_{1,2} resonances and other *marks* indicate the same meanings as those in Fig. 5.13

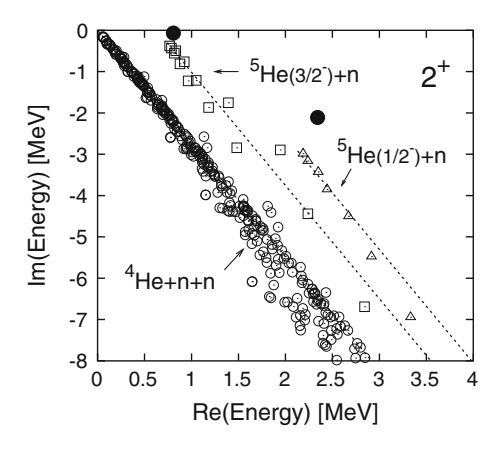
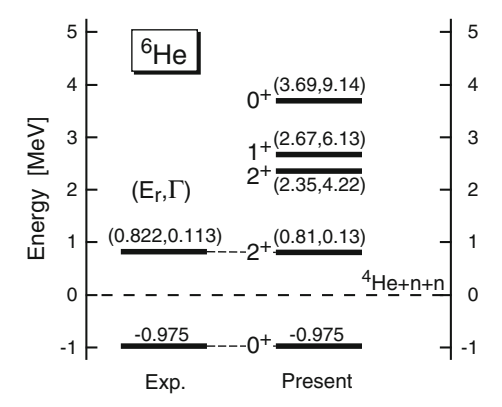


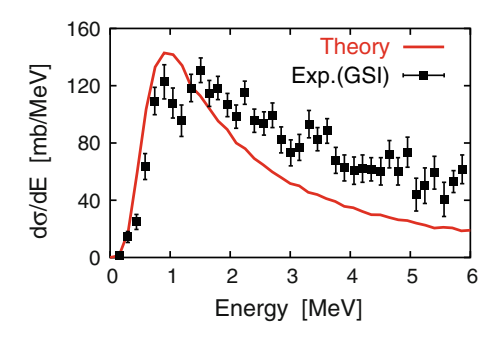
Fig. 5.15 Energy levels of ⁶He. Unit of energies and resonance widths is MeV [28]



In Fig. 5.16, we show the Coulomb breakup cross section with respect to the excitation energy of 6 He. This cross section is calculated using the E1 strength with the equivalent photon method, considering the experimental resolution [75]. The target is Pb and the incident energy of the 6 He projectile is 240 MeV/nucleon. It is found that there is a low energy enhancement in the strength at around 1 MeV measured from the three-body threshold energy. This energy is just above the two-body threshold (0.74 MeV) of the 5 He $(3/2^-) + n$ system [24], and the cross section gradually decreases with the excitation energy. This structure of the strength indicates the sequential breakup process via the 5 He $(3/2^-) + n$ channel [28]. We also compare the strength with experiments [75]. The obtained result fairly reproduces the trend of the observed cross section, especially in the low excitation energy region below $E \sim 2$ MeV. The height and position of the low-energy enhancement in the strength agree well with the experimental data.

In this section, we have discussed the complex scaling method (CSM) in order to treat resonance and continuum states in nuclear composite systems. As an example of the usefulness of the CSM, we have discussed the case of 6 He as a core + n + n three-body system. We can interpret the calculated results nicely and can distinguish any structure in the continuum spectrum. As for the application of the CSM to the Li isotopes, we defer the detailed discussions after the introduction of the deuteron-like tensor correlation. The interpretation of the experimental

Fig. 5.16 Coulomb breakup cross section of ⁶He [54]



results further need the participation of the $s_{1/2}$ orbit in the wave functions of the Li isotopes. For this, we have to introduce the deuteron-like tensor correlation, which is the subject of the next section.

5.4 Deuteron-like Tensor Correlation and Tensor Optimized Shell Model (TOSM)

In this section, we would like to discuss the role of the deuteron-like tensor correlation on the nuclear structure in ⁴He before applying the developed method to the halo nucleus ¹¹Li. The tensor interaction is one of the most important ingredients of the bare nucleon–nucleon interaction and plays the central role for the formation of finite nuclei and nuclear matter. In this lecture note, we have shown explicitly the case of the deuteron in Sect. 2, where the tensor interaction plays the central role to provide a strong binding energy through coupling of the *s*-wave component with the *d*-wave component. Although the tensor interaction is known to be important, the standard approach of nuclear many-body problems is to obtain the effective interaction (G-matrix) by solving the Brueckner equation to include the high momentum components in the effective G-matrix interaction. Hence, we are used to treat a well behaved central effective interaction and have not faced to treat the tensor interaction explicitly for shell model states. This is the reason why we have not developed a method of treating the tensor interaction explicitly in nuclear physics.

Recently it became possible to calculate nuclei up to mass around $A \sim 12$ [13, 76, 77] using the realistic nucleon–nucleon interaction. The method used for the calculation is the Green's function Monte-Carlo method (GFMC) with the use of relative nucleon coordinates. This method introduces various correlation functions with many variational parameters in the nuclear wave function. In the GFMC, the nuclear structures and binding energies were successfully reproduced by including the three-body interaction. One big surprise is extremely a large contribution of the one pion exchange interaction, which is about 70–80% of the whole nucleon–nucleon interaction. In principle, they can extend this method to calculate heavier nuclei. As for the tensor interaction, it contributes about 50% of the whole two-body matrix element. It is however extremely time consuming even with the present computer power. Hence, it is strongly desired to develop a new method to calculate nuclei with large nucleon numbers by using the nucleon–nucleon interaction.

The nucleon–nucleon interaction has distinctive features that there exists the strong tensor interaction at intermediate distance caused by pion exchange and strong short range repulsive interaction at short distance caused by quark dynamics. The explicit form of the nucleon–nucleon interaction is presented in Sect. 2. Although these two interactions have totally different characters, it is customary to adopt the Brueckner Hartree–Fock theory to integrate out the high momentum components on the same footing and use the resulting *G*-matrix as an

effective interaction in the shell model. In this way, we lose information of the tensor correlation and the short range correlation in the shell model wave function. Hence, we search for a powerful method to treat explicitly both the tensor interaction and the short range interaction for the study of not only light nuclei but also medium and heavy nuclei.

There have been two important developments for this purpose. One is to find out that the tensor interaction is of intermediate range and hence we are able to express the tensor correlation in a reasonable shell model space [78, 79]. We name this method as the Tensor Optimized Shell Model (TOSM), where the nuclear wave function is written in terms of the standard shell model state and enough amount of two-particle two-hole (2p2h) states. This TOSM formalism is based on the success of the parity and charge projection in the treatment of the pion exchange interaction [80, 81]. We have shown that the tensor interaction could be treated properly by taking a reasonable amount of multipoles (l < 5) in the 2p2hwave functions with the optimization of the radial parts of the particle states. The other is the Unitary Correlation Operator Method (UCOM) for the treatment of the short range correlation [82, 83]. The short range repulsive interaction is of very short range and it is suited to treat the short range correlation using a unitary transformation and take the approximation to use only up to the two-body operators. This approximation is justified because the volume associated with the short range correlation is extremely small, where more than three nucleons rarely enter into the small volume. This is not the case for the tensor correlation, since the tensor interaction is of intermediate and long range as discussed by Neff and Feldmeier [83].

Our idea is to combine these two methods, TOSM and UCOM, for our purpose to develop a theoretical framework to describe furthermore medium and heavy nuclei beyond the light nuclei using the realistic nucleon-nucleon interaction. We can use the TOSM for the strong tensor interaction utilizing the intermediate nature caused by finite angular momentum of the relative wave function and the UCOM for the strong short range interaction utilizing the short range nature. We use completely different methods for these two distinctive characters of the nucleon-nucleon interaction. After demonstrating its power we hope to apply a newly developed method, which we name TOSMU, to many nuclei. Using the TOSMU, we aim at understanding the roles of the tensor and short range correlations in nuclei using the bare nucleon-nucleon interaction. As a good start, we would like to apply the TOSMU to ⁴He. Hence, there are two purposes for this study. One is to see how this method works for the treatment of the bare nucleonnucleon interaction. The other is to compare with rigorous calculations to check the accuracy of the results obtained in the TOSMU. From this comparison, we can see how far we can describe the short range and tensor correlations and find what we are supposed to do for further improvement of the TOSMU in order to solve the nucleus as precisely as possible.

On the other hand, we would like to develop a theoretical framework to describe wave functions in terms of single particle coordinates, which we call a V-coordinate method. This V-coordinate method has ability to describe nuclei

with many nucleons relatively easier than the T-coordinate method. Furthermore, we are able to describe the wave function based on the shell model picture and hence it is easier to interpret the calculated results in the shell model sense. The difficulty, on the other hand, is to express the correlations of the relative motion between two nucleons, which are caused by the short range repulsive interaction and the tensor interaction in the nucleon–nucleon interaction. We overcome this problem by developing the TOSMU to describe the short range and the tensor correlations simultaneously.

5.4.1 Formulation of TOSM

We explain the formulation of the Tensor optimized shell model (TOSM). We shall begin with the many-body Hamiltonian with mass number A.

$$H = \sum_{i}^{A} T_{i} - T_{cm} + \sum_{i < i}^{A} V_{ij}$$
 (5.47)

with

$$V_{ij} = v_{ij}^{C} + v_{ij}^{T} + v_{ij}^{LS} + v_{ij}^{Clmb}.$$
 (5.48)

Here, T_i is the kinetic energy of all the nucleons with $T_{\rm cm}$ being the center of mass kinetic energy. We take the bare nucleon–nucleon interaction for V_{ij} such as the AV8' consisting of central (v_{ij}^C) , tensor (v_{ij}^T) and spin-orbit (v_{ij}^{LS}) terms. The $v_{ij}^{\rm Clmb}$ is the Coulomb term. We describe the many-body system with many-body wave function, Ψ , by solving the Schrödinger equation $H \Psi = E\Psi$. In the TOSM, we take the V-coordinates to express Ψ .

We have discussed the property of the deuteron, whose wave function is expressed in terms of the s-wave and d-wave components. We ought to express the deuteron-like tensor correlation in finite nuclei. We show the deuteron-like structure is expressed in terms of 2p-2h configurations in the shell model framework by taking the case of ${}^{4}\text{He}$. The two nucleons in the s-orbit have two components. One is the ${}^{3}S_{1}$ pair and the other is the ${}^{1}S_{0}$ pair. The ${}^{3}S_{1}$ pair can be expressed as

$$|[(0s_{1/2})^2]_{1M}\rangle \sim \Psi_{L=0}(R)\psi_{l=0}(r)[Y_0(\hat{r})\otimes \chi_1(\sigma_1\sigma_2)]_{1M}. \tag{5.49}$$

Hence, the relative wave function is in the s-state. On the other hand, when two nucleons are in the p-orbit, we can write the wave function of the relative motion being in the triplet even channel as

$$|[(0p_{1/2})^2]_{1M}\rangle \sim \Psi_{L=0}(R)\psi_{l=2}(r)[Y_2(\hat{r})\otimes\chi_1(\sigma_1\sigma_2)]_{1M}.$$
 (5.50)

Hence, the relative wave function is in the d-state. As discussed for the deuteron wave function being written in terms of the s and d wave components, we are able

to express the deuteron-like wave function in the shell model framework by taking both the above two components. Hence, we have to introduce 2p-2h wave functions to express the deuteron-like tensor correlation in the shell model basis. There is the other p-wave component, $(p_{3/2})^2$. In this case, the spin and the angular momentum have a stretched configuration and this state is not mixed by the tensor interaction. This consideration naturally leads us to introduce the tensor optimized shell model (TOSM). It remains for us to check if we can express the deuteron-like tensor correlation within reasonable amount of multipoles in the TOSM [78]. As for the short range correlation appearing in the s-wave component in the deuteron wave function, we ought to take a clever method. For this problem, Feldmeier et al. have demonstrated that the unitary correlation operator method (UCOM) can be used to treat the short-range correlation [82, 83].

In the TOSM, the total wave function Ψ is written in terms of a linear combination of 0p–0h and 2p–2h wave functions.

$$\Psi = C_0|0\rangle + \sum_p C_p|2p2h\rangle_p. \tag{5.51}$$

Here, the wave function $|0\rangle$ is a shell model wave function and $|(0s)^4\rangle$ for ⁴He. $|2p2h\rangle$ represents a 2p2h state with various ranges for the radial wave functions of particle states. We can write $|2p2h\rangle$ as

$$|2p2h\rangle_{p} = \left| \left[\left[\Psi_{\alpha_{1}}^{n_{1}}(\mathbf{x}_{1}) \Psi_{\alpha_{2}}^{n_{2}}(\mathbf{x}_{2}) \right]^{J} \otimes \left[\tilde{\Psi}_{\alpha_{3}}^{n_{3}}(\mathbf{x}_{1}) \tilde{\Psi}_{\alpha_{4}}^{n_{4}}(\mathbf{x}_{2}) \right]^{J} \right]^{0} \right\rangle_{A}.$$
 (5.52)

The suffix A of the wave function indicates anti-symmetrization of the wave functions. Here, p denotes a set of quantum numbers of 2p2h states, which are expressed with particle (hole) wave functions $\Psi_{\sigma}^{n}(\tilde{\Psi}_{\sigma}^{n})$. The index n is to distinguish the different radial components of the single-particle wave function Ψ. The index α is a set of three quantum numbers, l, j and t_z , to distinguish the singleparticle orbits, where l and j are the orbital and total angular momenta of the single-particle states, respectively, and t_z is the projection of the nucleon isospin. The normalization factors of the two particle states are included in the wave functions given in Eq. (5.52). For ⁴He, the coupled spin, J, of two nucleons is J = 0 or J = 1. We omit writing the coupled isospin, which should be either 0 or 1 depending on the value of J. We have used Gaussian functions for radial wave functions to express more effectively compressed radial wave functions [78]. The shell model technique is used to calculate all the necessary matrix elements, which are expressed explicitly in Ref. [84]. In more heavier nuclei, such as ¹²C and ¹⁶O, the dominant configuration |0| can be extended to the superposed ones, which includes the few $\hbar\omega$ configurations such as $2\hbar\omega$. This part describes the low-momentum component of the wave function and the tensor force contribution is not so decisive to determine the nuclear structure. The high momentum part is treated by considering the 2p2h excitations $|2p2h\rangle_p$ from the each lowmomentum configurations. In that case, the spatial shrinkage of particle states becomes important.

We explain the Gaussian expansion technique for single-particle orbits [46, 48]. Each Gaussian basis function has the form of a nodeless harmonic oscillator wave function (HOWF), except for the 1s orbit. When we superpose a sufficient number of Gaussian bases with appropriate length parameters, we can fully optimize the radial component of every orbit of every configuration with respect to the total Hamiltonian in Eq. (5.47). We construct the following ortho-normalized single-particle wave function ψ^n_{α} with a linear combination of Gaussian bases $\{\phi_{\alpha}\}$ with length parameters $b_{\alpha,m}$.

$$\Psi_{\alpha}^{n}(r) = \sum_{m=1}^{N_{\alpha}} d_{\alpha,m}^{n} \phi_{\alpha}(r, b_{\alpha,m}) \quad \text{for } n = 1, ..., N_{\alpha}.$$
(5.53)

Here, N_{α} is the number of basis functions for α , and m is an index that distinguishes the bases with different values of $b_{\alpha,m}$. The explicit form of the Gaussian basis function is expressed as

$$\phi_{\alpha}(r, b_{\alpha,m}) = N_l(b_{\alpha,m}) r^l e^{-(r/b_{\alpha,m})^2/2} [Y_l(\hat{\mathbf{r}}), \chi_{1/2}^{\sigma}]_j \chi_{t_z},$$
 (5.54)

$$N_l(b_{\alpha,m}) = \left[\frac{2 b_{\alpha,m}^{-(2l+3)}}{\Gamma(l+3/2)}\right]^{\frac{1}{2}}.$$
 (5.55)

The coefficients $\{d_{\alpha,m}^n\}$ are determined by solving the eigenvalue problem for the norm matrix of the non orthogonal Gaussian basis set in Eq. (5.54) with the dimension N_{α} . Following this procedure, we obtain new single-particle wave functions $\{\psi_{\alpha}^n\}$ using Eq. (5.53).

We choose the Gaussian bases for the particle states to be orthogonal to the occupied single-particle states, which is $0s_{1/2}$ in the ⁴He case. For $0s_{1/2}$ states, we employ one Gaussian basis function, namely, the HOWF with the length parameter $b_{0s_{1/2},m=1}=b_{0s}$. For $1s_{1/2}$ states, we introduce an extended 1s basis function orthogonal to the $0s_{1/2}$ states and possessing a length parameter $b_{1s,m}$ that differs from b_{0s} [78]. In the extended 1s basis functions, we change the polynomial part from the usual 1s basis states to satisfy the conditions of the normalization and the orthogonality to the 0s state.

Two-body matrix elements in the Hamiltonian are analytically calculated using the Gaussian bases [46, 48], whose explicit forms are given in Ref. [84]. In the numerical calculation of following, we prepare 9 Gaussian functions at most with parameters of various ranges to obtain a convergence of the energy. Furthermore, we have to take care of the center-of-mass excitations. For this purpose, we use the well-tested method of introducing a center-of-mass term in the many-body Hamiltonian [85, 86].

$$H_{\rm cm} = \lambda \left(\frac{P_{\rm cm}^2}{2A \, m} + \frac{1}{2} \, A \, m \, \omega^2 \, R_{\rm cm}^2 - \frac{3}{2} \, \hbar \omega \right), \tag{5.56}$$

$$\mathbf{P}_{\rm cm} = \sum_{i=1}^{A} \mathbf{p}_i, \qquad \mathbf{R}_{\rm cm} = \frac{1}{A} \sum_{i=1}^{A} \mathbf{r}_i, \qquad \omega = \frac{\hbar}{m b_{0s}^2}. \tag{5.57}$$

Here, m and A are the nucleon mass and the mass number, respectively, and b_{0s} is the length parameter of the HOWF for the hole 0s state. We take a sufficiently large coefficient, λ , to project out only the lowest HO state for the center-of-mass motion. In the numerical calculation, the excitation of the spurious center-of-mass motion is suppressed to be less than 10 keV.

The variation of the energy expectation value with respect to the total wave function $\Psi(^4\text{He})$ is given by

$$\delta \frac{\langle \Psi | H | \Psi \rangle}{\langle \Psi | \Psi \rangle} = 0, \tag{5.58}$$

which leads to the following equations:

$$\frac{\partial \langle \Psi | H - E | \Psi \rangle}{\partial b_{\alpha,m}} = 0, \quad \frac{\partial \langle \Psi | H - E | \Psi \rangle}{\partial C_p} = 0.$$
 (5.59)

Here, E is a Lagrange multiplier corresponding to the total energy. The parameters $\{b_{\alpha,m}\}$ for the Gaussian bases appear in non linear forms in the energy expectation value. We solve two types of variational equations in the following steps. First, fixing all the length parameters $b_{\alpha,m}$, we solve the linear equation for $\{C_p\}$ as an eigenvalue problem for H with partial waves up to L_{\max} . We thereby obtain the eigenvalue E, which is a function of $\{b_{\alpha,m}\}$. Next, we try to search various sets of the length parameters $\{b_{\alpha,m}\}$ to find the solution that minimizes the total energy. In this wave function, we can describe the spatial shrinkage with an appropriate radial form, which is important for the tensor correlation [78].

5.4.2 Formulation of UCOM

We employ the UCOM for the short-range correlation. Feldmeier et al. [82, 83] worked out a unitary correlation operator in the form,

$$C = \exp\left(-i\sum_{i < j} g_{ij}\right) = \prod_{i < j} c_{ij}$$
 (5.60)

with $c_{ij} = \exp(-i \ g_{ij})$. Here, i and j are the indices to distinguish particles. Here, the two-body operator g_{ij} is a Hermite operator, and hence C is a unitary operator. We express the full wave function Ψ in terms of less sophisticated wave function Φ as $\Psi = C\Phi$. Hence, the Schrödinger equation, $H\Psi = E\Psi$ becomes $\hat{H}\Phi = E\Phi$, where $\hat{H} = C^{\dagger}HC$. If we choose properly the unitary correlator C we are able to solve more easily the Schrödinger equation. Moreover, once we obtain Φ , we can

then obtain the full wave function, Ψ , by the unitary transformation $\Psi = C\Phi$. Since C is expressed with a two-body operator in the exponential, it is a many-body operator. In the case of the short-range correlation, we are able to truncate modified operators at the level of two-body operators [82].

In the actual calculation of the UCOM, we define the operator g_{ij} as

$$g_{ij} = \frac{1}{2} \{ p_{r,ij} s(r_{ij}) + s(r_{ij}) p_{r,ij} \},$$
 (5.61)

where the momentum $p_{r,ij}$ is the radial component of the relative momentum, which is conjugate to the relative coordinate r_{ij} . $s(r_{ij})$ is the amount of the shift of the relative wave function at the relative coordinate r_{ij} for each nucleon pair. Hereafter, we omit the indices i and j for simplicity. We also introduce $R_+(r)$ as

$$\int_{r}^{R_{+}(r)} \frac{d\xi}{s(\xi)} = 1, \tag{5.62}$$

which leads to the following relation,

$$\frac{dR_{+}(r)}{dr} = \frac{s(R_{+}(r))}{s(r)}. (5.63)$$

In the UCOM, we use $R_+(r)$ instead of s(r) to use the UCOM prescription. $R_+(r)$ represents the correlation function to reduce the amplitude of the short-range part of the relative wave function in nuclei and can be determined for four spin-isospin channels independently. The explicit form of the transformation of the operator for the relative motion is given as

$$c^{\dagger}rc = \mathbf{R}_{+}(r), \qquad c^{\dagger}p_{r}c = \frac{1}{\sqrt{\mathbf{R}'_{+}(r)}}p_{r}\frac{1}{\sqrt{\mathbf{R}'_{+}(r)}}, \qquad c^{\dagger}\mathbf{l}c = \mathbf{l},$$
 (5.64)

$$c^{\dagger} \mathbf{s} c = \mathbf{s}, \qquad c^{\dagger} S_{12} c = S_{12}, \qquad c^{\dagger} v(r) c = v(\mathbf{R}_{+}(r)),$$
 (5.65)

where the operators \mathbf{l} , \mathbf{s} and S_{12} are the relative orbital angular momentum operator, the intrinsic spin operator and the tensor operator, respectively. v(r) is the arbitrary function depending on r, such as potential.

In the calculation using the UCOM, we parametrize $R_{+}(r)$ in the same manner as proposed by Neff-Feldmeier and Roth et al. [82, 83, 87]. We assume the following forms for even and odd channels, respectively.

$$R_{+}^{\text{even}}(r) = r + \alpha \left(\frac{r}{\beta}\right)^{\gamma} \exp[-\exp(r/\beta)],$$
 (5.66)

$$R_{+}^{\text{odd}}(r) = r + \alpha (1 - \exp(-r/\gamma)) \exp[-\exp(r/\beta)]. \tag{5.67}$$

Here, α , β , γ are the variational parameters to optimize the function $R_+(r)$ and minimize the energy of the system. They are independently determined for four channels of the spin-isospin pair. In the actual procedure of the variation, once we fix the parameters included in $R_+(r)$, we solve the eigenvalue problem of the Hamiltonian using Eq. (5.59) and determine the configuration mixing of the shell model-type bases. Next, we try to search various sets of the $R_+(r)$ parameters to minimize the obtained energy.

In the present framework of the UCOM, we introduce the UCOM function $R_+(r)$ for each spin-isospin channel and ignore the partial wave dependence of $R_+(r)$. It is generally possible to introduce the partial wave dependence in the UCOM and then $R_+(r)$ functions are determined in each relative partial wave in the two-body matrix elements. Here, we consider the specific case of this extension of the UCOM by taking care of the characteristics of the short-range correlation. One of the simplest cases of this extension is the UCOM for only the s-wave relative motion, since all the other partial waves l except for s-wave (l=0) have r^l behavior near the origin, where the short-range hard core is extremely large. Hence, this r^l behavior largely cuts down the effect of the short-range hard core. However, only the s-wave function is finite at the origin, and the behavior in the origin is determined by the hard core dynamics. In fact, the method used by Feldmeier et al. [82] is to determine the unitary operator to reproduce the short-range behavior of the s-wave relative wave function.

When we incorporate the S-wave UCOM (S-UCOM, hereafter) into the TOSM, we extract the relative s-wave component in all the two-body matrix elements in the TOSM using the V-type basis expanded by the Gaussian functions. For numerical calculations, we prepare the completeness relation consisting of the T-type basis functions $|T\rangle$ as

$$1 = \sum_{i} |T_{i}\rangle\langle T_{i}|, \qquad |T_{i}\rangle = |[[\mathbf{\Psi}_{l}^{\mathbf{r}}\mathbf{\Psi}_{L}^{\mathbf{R}}]_{L'}, \mathbf{\chi}_{S}]_{J}\mathbf{\chi}_{T}\rangle, \tag{5.68}$$

where the T-type basis is expanded by the two coordinates of the relative part \mathbf{r} and the center of mass part \mathbf{R} of two nucleons, which are the set of Jacobi coordinates. The orbital angular momenta of each coordinate, \mathbf{r} and \mathbf{R} , are l and L, respectively. It is easy to prepare the s-wave relative part by considering l as zero in the T-type basis. We construct the above completeness relation of the T-type basis states by diagonalizing the norm matrix expanded by the finite number of Gaussian basis functions for two coordinates. In the actual calculation, we use 12 bases for each coordinate, with which convergence is achieved.

We calculate the matrix elements of the arbitrary two-body operator \hat{O} including the S-UCOM correlator C_s using the V-type basis with indices α and β . Here, we insert the above T-type completeness relation in Eq. (5.68) as

$$\langle V_{\alpha}|C_{s}^{\dagger}\hat{O}C_{s}|V_{\beta}\rangle = \sum_{ij}\langle V_{\alpha}|T_{i}\rangle \cdot \langle T_{i}|C_{s}^{\dagger}\hat{O}C_{s}|T_{j}\rangle \cdot \langle T_{j}|V_{\beta}\rangle. \tag{5.69}$$

The matrix element using the T-type base, $\langle T_i | C_s^\dagger \hat{O} C_s | T_j \rangle$, is calculated for the two-body kinetic part and the central and tensor interactions. For the kinetic part and the central interaction, the matrix elements conserve the relative angular momentum, and then we can easily calculate the matrix elements of the transformed operator $C_s^\dagger \hat{O} C_s$. For the tensor interaction, the sd coupling matrix elements are properly treated, in which C_s is operated on only the s-wave part of the relative motion. In this case, the operator C_s acts on the s-wave relative Gaussian basis function $\phi_{l=0}(r)$, which is transformed as

$$C_S \phi_{l=0}(r) = \frac{R_-(r)}{r} \sqrt{R'_-(r)} \phi_{l=0}(R_-(r)), \tag{5.70}$$

where $R_{-}(r)$ is the inverse transformation of $R_{+}(r)$, namely, $R_{-}(R_{+}(r)) = r$. The matrix elements of the *T*-type basis function are calculated using the above transformed wave function.

5.4.3 Numerical Results of TOSM for ⁴He

It is important to understand the origin of the large binding energy of ⁴He for the study of the Li isotopes. Particularly, it is important to develop a method to describe the source of the large binding energy in the shell model language. Hence, we describe in detail the structure of ⁴He in the TOSM and also the role of the UCOM. First of all, we determine the UCOM functions $R_{+}(r)$ for the calculation of the TOSMU. In the UCOM, we optimize the $R_{+}(r)$ function by changing the three parameters of α , β and γ to search for the energy minimum in the TOSMU. In Table 5.3, the optimized three parameters in the S-UCOM are listed. In Fig. 5.17, $R_{+}(r)$ functions used in the present study are plotted in comparison with the case in Ref. [87]. For the odd channel, in accordance with the discussion in Refs. [83] and [87], we cannot find the optimum value of $R_{+}(r)$ in the two-body cluster approximation of the UCOM transformation for the Hamiltonian. Hence, we decide to fix the range of $R_{+}(r)$, namely, β as the same one adopted in Ref. [87] and optimize α and γ , while the variation of $R_+(r)$ for the odd channel does not have significant effects on the energy and other properties of ⁴He in comparison with the original case [83, 87]. Essentially, two types of parameter set of $R_{+}(r)$ in the present study and Ref. [87] give the similar form of $R_{+}(r)$ for even channels, in which we omitted the correlation function for the even channels except for s-waves. This result indicates that the correlation functions for the short-range repulsion are uniquely determined for each channel.

Table 5.3 Optimized parameters in $R_+(r)$ in TOSM+UCOM for four channels in fm in the present work

	α	β	γ
singlet even	1.32	0.88	0.36
Triplet even	1.33	0.93	0.41
Singlet odd	1.57	1.26	0.73
Triplet odd	1.18	1.39	0.53

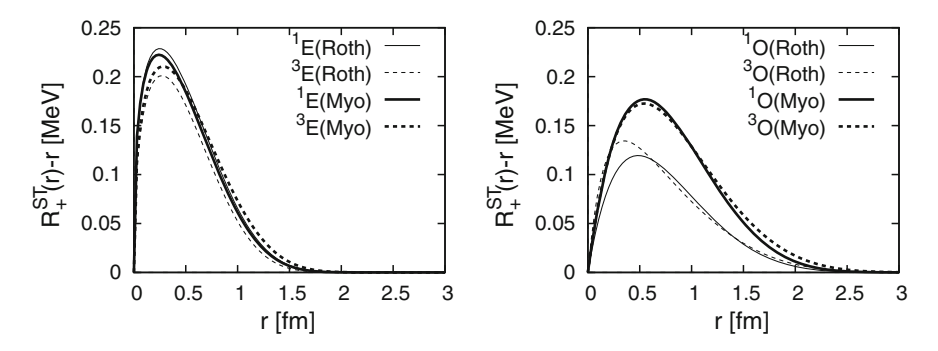
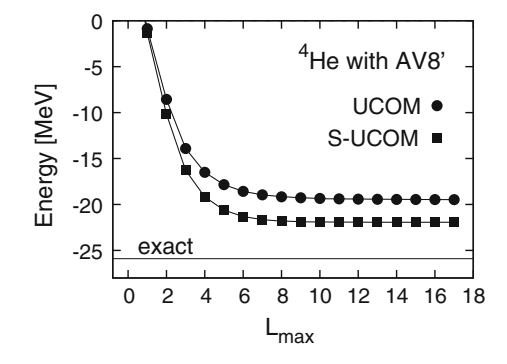


Fig. 5.17 The short range correlation functions, $R_+(r)$, for the UCOM in even and odd channels. The *thin curves* are for the $R_+(r)$ function of Roth et al. and the *thick curves* are those of Myo et al.

Next, we show the calculated results of the energy of 4 He as a function of $L_{\rm max}$ in Fig. 5.18. We shall then compare the obtained results with the benchmark calculation given in Ref. [89]. To start with, we show the ordinary UCOM case where the UCOM is used for all the partial waves. The calculated results of the energy are indicated in Fig. 5.18 by circles as a function of the maximum angular momentum L_{max} . The results show good convergence to reach -19 MeV, while the exact value of the few-body calculations is approximately -26 MeV as indicated in Fig. 5.18. Although the binding energy is small, we point out here that we can calculate the binding energy directly using the nucleon-nucleon interaction in the TOSMU. The tensor interaction matrix element is approximately -50 MeV. On the other hand, in the previous study [78], we obtained approximately -60 MeV for the tensor interaction matrix element to check the validity of the TOSM, when we used the G-matrix for the central interaction to renormalize the short-range repulsion and retained the bare tensor interaction of AV8' in our previous calculation. This fact indicates that the treatment of the short-range repulsive interaction is interfering with the contribution of the tensor interaction. This is due to a large removal of the short-range part of the relative wave functions in the UCOM, in particular, in the d-wave part of the sd coupling of the tensor interaction matrix element, where the tensor interaction possesses some amount of

Fig. 5.18 The energy of 4 He in the TOSMU as a function of the maximum angular momentum L_{max} . The *circles* are the results where the UCOM is used for all the partial waves. The squares are the results using *S*-UCOM in the tensor interaction matrix elements

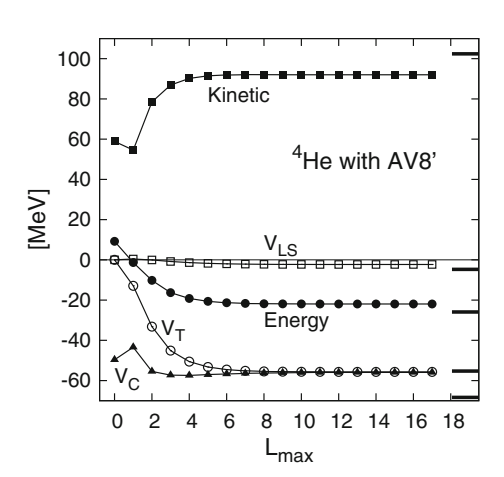


strength. We have also calculated the contributions beyond the 2p2h configurations in the TOSM such as 3p3h and 4p4h configurations. When we include the 4p4h configurations within the p-shell, their contribution to the binding energy is approximately 50 keV. This fact denotes that these more complicated wave functions contribute very little in the total 4 He wave function.

We have decided to restrict the use of the UCOM to the relative s-wave only for the even channel (S-UCOM), where the treatment of the short-range repulsion is absolutely necessary. In other partial waves, we have the centrifugal potential that cuts out the short-range part from the wave functions of the higher partial waves. In this case, we can use the modified interaction and the kinetic energy only for the relative s-wave component in the even channels. Since the use of the UCOM for the odd partial wave is slightly better, we use the UCOM for all odd partial waves. As a starting calculation, we have neglected the S-UCOM correlation in the calculation of the tensor interaction matrix elements. The energy converges to -24 MeV, which is now very close to the exact one as shown in Fig. 5.18. In this case, the tensor interaction matrix element is -61 MeV, which becomes close to the exact value of -68 MeV. This improvement mainly comes from the increase in the sd coupling of the tensor interaction matrix element, however, this calculation is still not yet perfect. We have to treat the effects of the short-range repulsion on the tensor interaction matrix element. Hence, we have worked out the formulation to treat the rigorous s-wave function with the effect of the short-range repulsion for the calculation of the tensor interaction matrix elements as explained in the previous section.

The numerical calculation is quite involved in the S-UCOM case, since the s-wave relative wave function with the effect of short-range repulsion should be used for the tensor interaction matrix element. We show the calculated results for the total energy by the squares in Fig. 5.18. We see quite a satisfactory result for the total energy, which is approximately -22 MeV. We show now all the components of the energy for ⁴He in Fig. 5.19. All the energy components show the saturation behavior as function of L_{max} . In the tensor component, the saturation is

Fig. 5.19 Matrix elements of the central interaction (V_C) , tensor interaction (V_T) and the spin-orbit interaction (V_{LS}) together with the kinetic energy (Kinetic) and total energy (Energy) in the Hamiltonian for 4He as function of $L_{\rm max}$. We observe good convergence for all the matrix elements. These values are compared with the benchmark results of Ref. [88], which are indicated by the thick short solid lines on the right-hand side of the figure



obtained at around L_{max} being 8. For the other components, their saturation points are seen at the similar L_{max} . A very interesting feature is the kinetic energy, which goes up to a large value as the tensor interaction matrix element becomes large. As for the comparison with the rigorous calculation, we see that V_c satisfies the rigorous value, which is approximately -55 MeV. On the other hand, the tensor interaction matrix element, V_T converges to -55 MeV, while the rigorous one is -68 MeV. The kinetic energy is approximately 90 MeV, while the rigorous one is 102 MeV. The LS matrix element is also smaller than the rigorous value. As the net value, the total energy, E, is -22 MeV and the rigorous value is -26 MeV. A detailed comparison is performed in Table 5.4, in which the converged energies in the TOSMU are shown with the rigorous calculations. One of the possibilities for the lack of the energy in the TOSMU is due to the separate treatment of the short-range and tensor correlations. Although the dominant part of the tensor interaction is of intermediate and long range, there may remain some small strength in the short-range part of the tensor interaction, which can couple with the short-range correlations. This effect can be included by extending the truncation of the UCOM transformation in the Hamiltonian to more than the two-body level. Three-body term of the UCOM transformation is one of the possibilities to overcome the lack of energy in the TOSMU [82].

In Table 5.5, we list the mixing probabilities of the dominant configurations in 4 He. The subscripts 00 and 10 represent J and T, the spin and isospin quantum numbers, respectively. It is found that the 2p2h configurations with (J, T) = (1, 0) for the particle pair state are significantly mixed. These spin and isospin are the same as those for the deuteron, and thus, this two-nucleon coupling can be understood as a deuteron-like correlation [78].

Table 5.4 Total energy, matrix elements of the Hamiltonian and radius of ⁴He are compared with the benchmark results denoted by FY

	Energy	Kinetic	Central	Tensor	LS	Radius	
Present (UCOM)	-19.46	88.64	-56.81	-50.05	-1.24	1.555	
Present (S-UCOM)	-22.30	90.50	-55.71	-54.55	-2.53	1.546	
FY	-25.94	102.39	-55.26	-68.35	-4.72	1.485	

Units are in MeV for the total energy and the matrix elements, and fm for the radius of 4 He

Table 5.5 Mixing probabilities in the ⁴He ground state in %

$(0s)_{00}^4$	82.48
$(0s)_{10}^{-2}(0p_{1/2})_{10}^2$	2.54
$(0s)_{10}^{-2}[(1s_{1/2})(0d_{3/2})]_{10}$	2.34
$(0s)_{10}^{-2}[(0p_{3/2})(0f_{5/2})]_{10}$	1.90
$(0s)_{10}^{-2}[(0p_{1/2})(0p_{3/2})]_{10}$	1.55
$(0s)_{10}^{-2}[(0d_{5/2})(0g_{7/2})]_{10}$	0.79
$(0s)_{10}^{-2}(0d_{3/2})_{10}^{2}$	0.44
remaining part	7.96

We have been describing ⁴He as an example of the TOSMU for the strong tensor correlation with the use of the UCOM for the short range correlation. This method is able to describe the ⁴He system almost precisely with the use of the bare nucleon–nucleon interaction. We are working out further the small difference present between the TOSM and the few body many body methods. We believe now that the difference comes from the competition of the short range repulsion and the tensor attraction in the very short range part of the relative wave function. However, we believe that the TOSM is able to describe the deuteron-like tensor correlation and we shall apply this method for the description of the Li isotopes.

5.5 Di-Neutron Clustering and Deuteron-like Tensor Correlation in Li Isotopes

The biggest puzzle from the theory side is the large s-wave component for the halo neutrons in 11 Li. If we interpret this fact in the shell model, the shell gap at N=8 has to disappear. However, the mean field treatment of a central force is not able to provide the disappearance of the N=8 shell gap. So far, there were many theoretical studies for 11 Li [9, 10, 12, 20, 25, 26, 89–94] and essentially all the theoretical works of 11 Li had to accept that the $1s_{1/2}$ single particle state is brought down to the $0p_{1/2}$ state without knowing its reason [9, 92]. It is therefore the real challenge for theoretician to understand this disappearance of the N=8 shell gap, to be called s-p shell gap problem, which is discussed in this section by developing a framework to treat the deuteron-like tensor correlation explicitly using the nucleon–nucleon interaction. The halo structure of 11 Li is also related with the 1s-state and the 0p-state in 10 Li. Several experiments suggest the dual states of the $s_{1/2}$ -state coupled to the $3/2^-$ proton state appears close to the threshold energy of 9 Li + n together with the dual states of the $p_{1/2}$ -state [95, 96].

The tensor interaction, on the other hand, plays an important role in the nuclear structure. For example, the contribution of the tensor interaction in the binding of 4 He is comparable to that of the central force [88, 97]. The tensor correlation induced by the tensor interaction was demonstrated important for the 4 He+n system [98–101]. We treated there the tensor interaction in the shell model basis by 2p-2h excitations, and found that the $(0s_{1/2})^{-2}(0p_{1/2})^{2}$ excitation of the protonneutron pair has a special importance in describing the tensor correlation in 4 He [80, 101]. This 2p-2h excitation causes the strong Pauli-blocking in the 4 He + n system for the $p_{1/2}$ -orbit of the last neutron, which contributes to the p-wave doublet splitting in 5 He [101]. The same effect of the deuteron-like tensor correlation with the Pauli-blocking of the additional two neutrons in the $p_{1/2}$ orbit is expected in 11 Li. The occupation of the two neutrons in the $p_{1/2}$ orbit interferes with the deuteron-like tensor correlation, which is used to provide a large binding effect of 4 He in 9 Li.

Hence, it is important to study the effect of the deuteron-like tensor correlation together with the pairing correlation for the s–p shell gap problem in 11 Li. This is the purpose of this section. We shall perform the configuration mixing based on the shell model framework for 9 Li to describe the tensor and pairing correlations explicitly. In particular, we pay attention to the special features of the tensor correlation. For 11 Li, we shall solve the coupled 9 Li + n + n problem which treats both correlations and investigate further the Coulomb breakup strength of 11 Li and other observables to see the effect of these correlations.

5.5.1 Model of Li Isotopes

We shall begin with the introduction of the model for ⁹Li, whose Hamiltonian is given as

$$H(^{9}\text{Li}) = \sum_{i=1}^{9} t_i - t_G + \sum_{i < i}^{9} v_{ij}.$$
 (5.71)

Here, t_i , t_G , and v_{ij} are the kinetic energy of each nucleon, the center-of-mass (c.m.) term and the two-body *NN* interaction consisting of central, spin-orbit, tensor and Coulomb terms, respectively. The wave function of ${}^9\text{Li}(3/2^-)$ is described in the tensor-optimized shell model [78, 101]. We express ${}^9\text{Li}$ by a multi-configuration,

$$\Psi(^{9}\text{Li}) = \sum_{i}^{N} C_{i} \Phi_{i}^{3/2^{-}}, \qquad (5.72)$$

where we consider up to the 2p-2h excitations within the 0p shell for $\Phi_i^{3/2^*-}$ in a shell model type wave function, and N is the configuration number. Based on the previous study of the tensor-optimized shell model [78, 101], we adopt the spatially modified harmonic oscillator wave function (Gaussian function) as a single particle orbit and treat the length parameters b_{α} of every orbit α of 0s, $0p_{1/2}$ and $0p_{3/2}$ as variational parameters. This variation is shown to be important to optimize the tensor correlation [78, 80, 81, 101].

Following the procedure of the tensor-optimized shell model, we solve the variational equation for the Hamiltonian of ${}^9\text{Li}$ and determine $\{C_i\}$ in Eq. (5.72) and the length parameters $\{b_\alpha\}$ of three orbits. The variation of the energy expectation value with respect to the total wave function $\Psi({}^9\text{Li})$ is given by

$$\delta \frac{\langle \Psi | H(^{9}\text{Li}) | \Psi \rangle}{\langle \Psi | \Psi \rangle} = 0, \tag{5.73}$$

which leads to the following equations:

$$\frac{\partial \langle \Psi | H(^{9}\text{Li}) - E | \Psi \rangle}{\partial h_{\alpha}} = 0, \quad \frac{\partial \langle \Psi | H(^{9}\text{Li}) - E | \Psi \rangle}{\partial C_{i}} = 0.$$
 (5.74)

Here, E is the total energy of ${}^9\text{Li}$. The parameters $\{b_\alpha\}$ for the Gaussian bases appear in non-linear forms in the total energy E. We solve two kinds of variational equations in the following steps. First, fixing all the length parameters b_α , we solve the linear equation for $\{C_i\}$ as an eigenvalue problem for $H({}^9\text{Li})$. We thereby obtain the eigenvalue E, which is a function of $\{b_\alpha\}$. Next, we try various sets of the length parameters $\{b_\alpha\}$ to find the solution which minimizes the energy of ${}^9\text{Li}$. In this wave function, we can optimize the radial form of single particle orbit appropriately so as to describe the spatial shrinkage of the particle state, which is important for the tensor correlation [78, 80, 81, 101].

For ¹¹Li and ¹⁰Li, their Hamiltonians are written in terms of ⁹Li + n + n and ⁹Li + n, respectively, and are given as

$$H(^{11}\text{Li}) = H(^{9}\text{Li}) + \sum_{k=0}^{2} T_k - T_G^{(3)} + \sum_{k=1}^{2} V_{cn,k} + V_{nn},$$
 (5.75)

$$H(^{10}\text{Li}) = H(^{9}\text{Li}) + \sum_{k=0}^{1} T_k - T_G^{(2)} + V_{cn},$$
 (5.76)

where $H(^9\text{Li})$, T_k , $T^{(3)}{}_G$ and $T^{(2)}{}_G$ are the internal Hamiltonian of ^9Li given by Eq. (5.71), the kinetic energies of each cluster (k=0 for ^9Li) and the c.m. terms of three or two cluster systems, respectively. $V_{cn,k}$ are the ^9Li core-n interaction (k=1,2) and V_{nn} is the interaction between last two neutrons. The wave functions of ^{11}Li and ^{10}Li with the spin J and J', respectively, are given as

$$\Psi^{J}(^{11}\text{Li}) = \sum_{i}^{N} \mathscr{A}\left\{ \left[\Phi_{i}^{3/2^{-}}, \chi_{i}^{J_{0}}(nn)\right]^{J} \right\}, \tag{5.77}$$

$$\Psi^{J'}(^{10}\text{Li}) = \sum_{i}^{N} \mathscr{A}\left\{ \left[\Phi_{i}^{3/2^{-}}, \chi_{i}^{J'_{0}}(n)\right]^{J'}\right\}.$$
 (5.78)

We obtain the coupled differential equations for the neutron wave functions $\chi^{J_0}(nn)$ and $\chi''_0(n)$, where J_0 and J'_0 are the spins of the additional neutron part of 11 Li and 10 Li, respectively. To obtain the total wave function $\Psi^{J}(^{11}$ Li) and $\Psi^{J''}(^{10}$ Li), we actually use the orthogonality condition model (OCM) [20, 25, 46] to treat the antisymmetrization between last neutrons and neutrons in 9 Li. In OCM, the neutron wave functions χ are imposed to be orthogonal to the occupied orbits by neutrons in 9 Li, which depend on the configuration $\Phi_i^{3/2^{\wedge}-}$ in Eq. (5.72). We obtain the following coupled Schrödinger equations with OCM for the set of the wave functions $\{\chi_i^{J_0}(nn)\}$ for 11 Li and $\{\chi_i^{J'_0}(n)\}$ for 10 Li, where i=1,...,N:

$$\sum_{i=1}^{N} \left[\left(T_{\text{rel}}^{(3)} + \sum_{k=1}^{2} V_{cn,k} + V_{nn} + \Lambda_{i} \right) \delta_{ij} + h_{ij}(^{9}\text{Li}) \right] \chi_{j}^{J_{0}}(nn) = E \chi_{i}^{J_{0}}(nn), \quad (5.79)$$

$$\sum_{i=1}^{N} \left[\left(T_{\text{rel}}^{(2)} + V_{cn} + \Lambda_i \right) \delta_{ij} + h_{ij} {}^{(9}\text{Li}) \right] \chi_j^{J_0'}(n) = E \, \chi_i^{J_0'}(n), \tag{5.80}$$

$$\Lambda_{i} = \lambda \sum_{\alpha \in \Phi_{i}({}^{9}\text{Li})} |\phi_{\alpha}\rangle\langle\phi_{\alpha}|, \tag{5.81}$$

where $h_{ij}(^9{\rm Li}) = \langle \Phi_i^{3/2^-} | H(^9{\rm Li}) | \Phi_j^{3/2^-} \rangle$. $T_{\rm rel}^{(3)}$ and $T_{\rm rel}^{(2)}$ are the total kinetic energies consisting of the relative motions for $^{11}{\rm Li}$ and $^{10}{\rm Li}$, respectively. Λ_i is the projection operator to remove the Pauli forbidden states ϕ_α from the relative wave functions [53, 60], where ϕ_α is the occupied single particle wave function of the orbit α in $^9{\rm Li}$ defined in Eq. (5.28). This Λ_i depends on the neutron occupied orbits in the configuration $\Phi_i^{3/2^-}$ of $^9{\rm Li}$ and plays an essential role to produce the Pauli-blocking in $^{11}{\rm Li}$ and $^{10}{\rm Li}$, explained later. This Pauli blocking term Λ_i reduces the pairing and the deuteron-like tensor correlations depending on the occupation of the additional neutrons in shell model single particle orbits. In $^{10}{\rm Li}$ and $^{11}{\rm Li}$, the term is particularly effective when the neutron or neutrons occupy the $p_{1/2}$ single particle orbit. The value of λ is taken large as 10^6 MeV in the present calculation in order to project out the components of the Pauli forbidden states into an unphysical energy region. Here, we keep the length parameters $\{b_\alpha\}$ of the single particle wave functions as those obtained for $^9{\rm Li}$.

We explain the method of treating the orthogonality condition including the particle-hole excitations of ${}^{9}\text{Li}$ in more detail [25, 101]. When the neutron orbit in ${}^{9}\text{Li}$ is fully occupied, the orthogonality condition for the last neutrons to this orbit is given by Λ_i in Eqs. (79) and (80). When neutron orbits in ${}^{9}\text{Li}$ are partially occupied, such as in the 2p-2h states, the last neutrons can occupy these orbits with particular probabilities, which are determined by the fractional parentage coefficients of the total wave functions of ${}^{10,11}\text{Li}$ consisting of ${}^{9}\text{Li}$ and the last neutrons.

We describe the two neutron wave functions $\chi(nn)$ in Eq. (5.79) for ¹¹Li precisely in a few-body approach of the hybrid-VT model [20, 24, 25];

$$\chi_i^{J_0}(nn) = \chi_i^{J_0}(\xi_V) + \chi_i^{J_0}(\xi_T), \tag{5.82}$$

where ξ_V and ξ_T are V-type and T-type coordinate sets of the three-body system, respectively, as shown in Fig. 5.7.

Here, we discuss the coupling between ^9Li and the last neutrons, whose details were already explained in the pairing-blocking case [25, 29, 53, 102]. We consider the case of ^{11}Li . In the present three-body model, the Pauli forbidden states for the relative motion provides the Pauli-blocking effect caused by the last two neutrons [25, 53]. This blocking depends on the relative distance between ^9Li and the two neutrons, and change the structure of ^9Li inside ^{11}Li , which is determined variationally to minimize the energy of the ^{11}Li ground state. Asymptotically, when the last two neutrons are far away from ^9Li ($\xi_{V,T} \to \infty$), the effects of antisymmetrization and the interaction between ^9Li and two neutrons vanish in Eq. (5.79). Therefore, any coupling between ^9Li and two neutrons disappears and ^9Li becomes

its ground state. Namely, the mixing coefficients $\{C_i\}$ are the same as those obtained in Eq. (5.72). Contrastingly, when the two neutrons are close to ${}^9\text{Li}$, the two neutrons dynamically couple to the configuration $\Phi_i^{3/2^{-}}$ of ${}^9\text{Li}$ satisfying the Pauli principle. This coupling changes $\{C_i\}$ of ${}^9\text{Li}$ from those of the ${}^9\text{Li}$ ground state, and makes the tensor and pairing correlations to be different from those in the isolated case. For ${}^{10}\text{Li}$, the similar coupling scheme is considered. The dynamical effect of the coupling arising from the Pauli-blocking is explained in the results in detail.

5.5.2 Effective Interactions

We explain here the interactions employed in Hamiltonians in Eqs. (71), (75) and (76). Before explaining the present interactions, we give a brief review of the situation of the treatment of the effective interactions for the study of ^{9,10,11}Li. As was mentioned, most theoretical studies based on the three-body model of 11Li employ the state-dependent ⁹Li-*n* potential where only the *s*-wave potential is made deeper than other partial waves [9], while the ⁹Li core is described as inert. This state-dependence in the ⁹Li-*n* potential is phenomenologically determined in order to satisfy the experimental observations of a large s^2 component and a twoneutron-separation energy of ¹¹Li, and a virtual s-state in ¹⁰Li, simultaneously. On the other hand, for the *nn* part, the interaction having a mild short-range repulsion [26, 90] or the density-dependent one are often used [10]. However, even in the microscopic cluster models using an unique effective NN interaction consisting of the central and LS forces [12, 89], the s-p shell gap problem in ¹¹Li and ¹⁰Li cannot be solved simultaneously. From these results, we consider that the usual approach based on the effective central and LS interactions may be insufficient to explain the exotic structures of ^{10,11}Li. For this problem, even the so-called abinitio calculations using the realistic NN interactions, such as Green's function Monte Calro [103], do not provide good results for ¹¹Li.

In this study, we focus on the tensor correlation, which is newly considered to figure out the s–p shell gap problem. To do this, we extend the three-body model of 11 Li to incorporate the tensor correlation fully, in particular, for the 9 Li part. In the present study, our policy for the study of 11 Li is to use the experimental informations and the corresponding theoretical knowledge for 9 Li and 10 Li as much as possible. Following this policy, we explain our interactions in three terms; v_{ij} of $H(^{9}$ Li) in Eq. (5.71), core-n V_{cn} and n–n V_{nn} of the Hamiltonians in Eqs. (75) and (76).

For the potential V_{nn} between the last two neutrons, we take a realistic interaction AV8' in Eq. (5.75). Our interest is to see the n-n correlation in the two-neutron halo structure, and therefore it is necessary to solve two-neutron relative motion without any assumption. For this purpose, our model space of two neutrons using the hybrid-VT model shown in Eq. (5.82) has no restriction and wide enough to describe the short range correlation under the realistic nuclear interaction AV8'. Therefore, there is no parameter in the potential V_{nn} .

The ${}^{9}\text{Li}-n$ potential, $V_{c,n}$, in Eqs. (75) and (76) is given by folding an effective interaction, the MHN interaction [59, 104], which is obtained by the G-matrix calculation and frequently used in the cluster study of light nuclei [20, 37, 46, 53, 59]. In the 9 Li + n system, the folding potential for the 9 Li density calculated by using H.O. wave function has been discussed to reproduce the proper energies of the ¹⁰Li spectra [20, 25, 53]. Furthermore, considering the small one-neutronseparation energy of ⁹Li and a long-range exponential tail of the density, we improve the tail behavior of the folding potential to have a Yukawa type form [25, 29]. Any state-dependence is not used in the present ⁹Li-n potential, such as a deeper potential for the s-wave. This is possible because the Pauli blocking effect of the single particle state is in action and the state with the $p_{1/2}$ orbit is pushed up in energy and becomes close to the state with the $s_{1/2}$ orbit [25, 53]. We will discuss the results on ¹⁰Li after the discussion on ¹¹Li. We introduce one parameter δ , which is the second-range strength of the MHN G-matrix interaction in the calculation of the ${}^{9}\text{Li}-n$ potential as shown in Table 5.9. The parameter δ is to describe the starting energy dependence dominantly coming from the tensor interaction in the G-matrix calculation [46, 59]. In the present calculation, we chose this δ parameter to reproduce the two-neutron-separation energy of $^{11}{\rm Li}$ as 0.31 MeV after working out the tensor and the pairing correlation effects as explained later. It is found that this folding potential also reproduces the positions of the p-wave resonances in ${}^{10}Li$, just above the ${}^{9}Li + n$ threshold energy [100], as shown in the results.

Now we discuss the choice of the interaction between nucleons in the ⁹Li core; v_{ii} in $H(^{9}\text{Li})$, where we use the limited shell model wave functions up to the p shell for the 9 Li core in Eq. (5.72). Since our main interest in this work is to investigate the role of the tensor interaction and the Pauli blocking effect on the two-neutron halo formation, we describe the tensor correlation in addition to the pairing correlation in the ⁹Li core. Along this line, recently we have many interesting works [80, 81, 105-107]. We have also studied the role of the tensor interaction in the shell model framework, and proposed the tensor-optimized shell model [78, 101]. As a reliable effective interaction considered from those studies, in this calculation, we use GA proposed by Akaishi [101, 106, 107] for v_{ii} in Eqs. (71), (75) and (76). This effective interaction GA has a term of the tensor interaction obtained from the G-matrix calculation using the AV8' realistic potential keeping the large momentum space [106, 107]. Since we limit the shell model space, we increase the tensor strength by 50%. This increase of the tensor strength has been studied in the full TOSM to provide a quantitative account of the tensor correlation in the limited shell model space. In GA, the obtained ⁹Li wave function in Eq. (5.72) shows smaller matter radius than the observed one due to the high momentum component produced by the tensor correlation [80, 81, 101]. Hence, we have to adjust the central force, which is done by changing the second range of the central force by reducing the strength by 21.5% and increasing the range by 0.185 fm to reproduce the observed binding energy and the matter radius of ⁹Li in the same manner as done for ⁴He [78, 101].

5.5.3 ⁹Li

We first show the results of the ⁹Li properties, which give a dynamical influence on the motion of last neutrons above the ⁹Li core in ^{11,10}Li. In Fig. 5.20, we display the energy surface of 9Li as functions of the length parameters of two 0p orbits, where b_{0s} is already optimized as 1.45 fm. There are two energy minima, (a) and (b), which have almost a common $b_{0p_{3/2}}$ value of 1.7-1.8 fm, and a small (0.85 fm) and a large (1.8 fm) $b_{0p_{1/2}}$ values, respectively. The properties of two minima are listed in Table 5.6 with the dominant 2p-2h configurations and their probabilities. It is found that the minimum (a) shows a large tensor contribution, while the minimum (b) does not. Among the 2p-2h configurations, the largest probabilities are given by $(0s)_{10}^{-2}(0p_{1/2})_{10}^2$ for (a), similar to the results in Ref. [101], and $(0p_{3/2})_{01}^{-2}(0p_{1/2})_{01}^{2}$, namely the 0p shell pairing correlation for (b). These results indicate that the minima (a) and (b) represent the different correlations of the tensor and pairing characters, respectively. The spatial properties are also different from each other; the tensor correlation is optimized with spatially shrunk excited nucleons for (a) and the pairing correlation is optimized when two Op orbits make a large spatial overlap for (b). In Table 5.6, we show the results of

Fig. 5.20 (Color online) Energy surface of 9 Li with respect to the length parameters b_{α} of 0p orbits [79]. The two minima indicated by (a) and (b) in the contour map correspond to the states due to the tensor correlation and the paring correlation, respectively

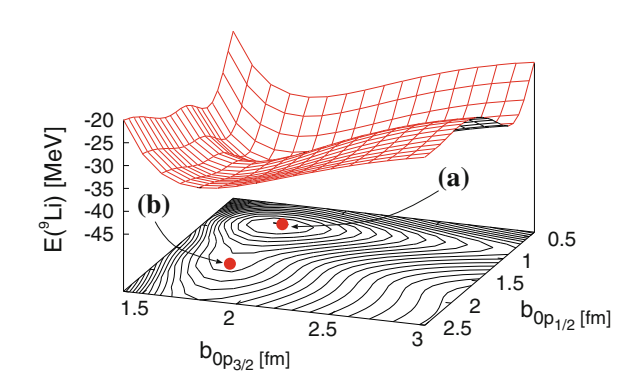


Table 5.6 Properties of ⁹Li with configuration mixing

-	Present			Expt.
	(a)	(b)	(c)	
E [MeV]	-43.8	-37.3	-45.3	-45.3
$\langle V_T \rangle$ [MeV]	-22.6	-1.8	-20.7	_
R_m [fm]	2.30	2.32	2.31	$2.32 \pm 0.02[1]$
0p– $0h$	91.2	60.1	82.9	_
$(0p_{3/2})^{-2}_{01}(0p_{1/2})^{2}_{01}$	0.03	37.1	9.0	_
$(0s_{1/2})^{-2}{}_{10}(0p_{1/2})^{2}{}_{10}$	8.2	1.8	7.2	_

The states (a) and (b) correspond to the each energy minimum shown in Fig. 5.20, respectively. The states (c) is obtained by superposing (a) and (b)

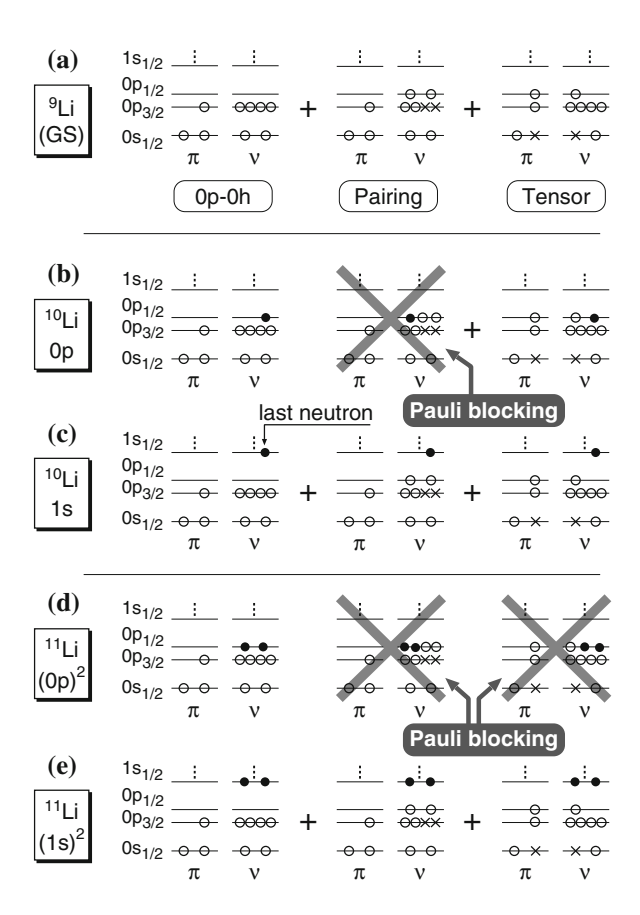
the superposition of minima (a) and (b), named as (c), to obtain a 9 Li wave function including the tensor and pairing correlations, simultaneously. For (c), the favored two configurations in each minimum (a) and (b) are still mixed with the 0p-0h one, and the property of the tensor correlation is kept in (c). The superposed 9 Li wave function possesses both the tensor and pairing correlations.

5.5.4 Pauli-Blocking Effect in ¹¹Li

We discuss here the Pauli-blocking effect in 11 Li and 10 Li. Considering the properties of the configuration mixing of 9 Li, we discuss the Pauli-blocking effects in 10 Li and 11 Li and their difference as shown in Fig. 5.21. For (a) in Fig. 5.21, the 9 Li ground state (GS) is strongly mixed, in addition to the 0p-0h state, with the 2p-2h states caused by the tensor and pairing correlations.

Let us add one neutron to ${}^{9}\text{Li}$ for ${}^{10}\text{Li}$. For (b) in Fig. 5.21, when a last neutron occupies the $0p_{1/2}$ orbit for the *p*-state of ${}^{10}\text{Li}$, the 2p-2h excitation of the pairing

Fig. 5.21 Schematic illustration for the Pauli-blocking in ¹¹Li. Details are described in the text



correlation in ${}^{9}\text{Li}$ are Pauli-blocked. The tensor correlation is also blocked partially, but not fully by the Pauli principle because the $0p_{1/2}$ orbit is not fully occupied by a last neutron. Accordingly, the correlation energy of ${}^{9}\text{Li}$ is partially lost inside ${}^{10}\text{Li}$. Contrastingly, for (c) in Fig. 5.21, the 1s state of ${}^{10}\text{Li}$, the Pauliblocking does not occur and ${}^{9}\text{Li}$ gains its correlation energy fully by the configuration mixing with the 2p-2h excitations. Hence, the energy difference between p and s states of ${}^{10}\text{Li}$ becomes small to explain the inversion phenomenon [25, 53].

For ¹¹Li, let us add two neutrons to ⁹Li. The similar blocking effect is expected for ¹¹Li, whose important properties were given in the previous paper [79]. For (d) in Fig. 5.21, when two neutrons occupy the $0p_{1/2}$ -orbit, the 2p-2h excitations of the tensor and pairing correlations in ⁹Li are Pauli-blocked. In particular, the blocking of the tensor correlation in ¹¹Li is expected to work stronger than the ¹⁰Li case, due to the presence of the last two neutrons in the $p_{1/2}$ orbit. Accordingly, the correlation energy of ⁹Li is lost inside ¹¹Li stronger than the ¹⁰Li case. For (e) in Fig. 5.21, $(1s)^2$ of two neutrons, the Pauli-blocking does not occur, similar to the 1s state of ${}^{10}\text{Li}$. Hence, the relative energy distance between $(0p)^2$ and $(1s)^2$ configurations of ¹¹Li becomes small to break the magicity in ¹¹Li. It is found that there is a difference in the blocking effects between ¹¹Li and ¹⁰Li. It is interesting to examine how this difference affects the s-p shell gap problem in these nuclei. For the pairing correlation, we already pointed out the different blocking effects between ¹⁰Li and ¹¹Li in the previous study [25]. We further consider the blocking effect in the dipole excited states of ¹¹Li later, which is also different from the ground state case. In the previous paper [79], we examined that the configuration mixing of the sd-shell for ⁹Li would give a small influence on the blocking effect on the $(1s)^2$ configuration of 11 Li.

5.5.5 ¹⁰Li

We solve ^{10}Li in a coupled $^9\text{Li} + n$ model, in which the $^9\text{Li}-n$ folding potential is determined to reproduce the two-neutron separation energy S_{2n} of ^{11}Li as 0.31 MeV. The resonant states are described using the complex scaling method. On this condition, we investigate the spectroscopic properties of ^{10}Li . In Table 5.7, it is shown that using the TOSM for ^9Li , the dual p-state resonances are obtained near the $^9\text{Li} + n$ threshold energy. The dual states come from the coupling of $[(0p_{3/2})_\pi(0p_{1/2})_\nu]_{1^+/2^+}$, while the experimental uncertainty is still remaining including the spin assignment [7]. The 1^+ state is predicted at a lower energy than the 2^+ state due to the attractive effect of the triplet-even 3E channel in the pn interaction.

For the s-wave states, their scattering lengths a_s of the ${}^9\text{Li} + n$ system show negative values. In particular, the 2^- state shows a large negative value of a_s , which is comparable to that of the nn system (-18.5 fm) with the 1S_0 channel [8], and indicates the existence of the virtual s-state near the ${}^9\text{Li} + n$ threshold energy. Therefore the inversion phenomenon in ${}^{10}\text{Li}$ is reasonably explained in the

(1 and 2 states) of Britaint of the v, measured from the Britain and						
	TOSM	Inert Core				
$(E_r, \Gamma)(1^+)$ [MeV]	(0.22, 0.09)	(0.03, 0.005)				
$(E_r, \Gamma)(2^+)$ [MeV]	(0.64, 0.45)	(0.33, 0.20)				
$a_s(1^-)$ [fm]	-5.6	1.4				
$a_s(2^-)$ [fm]	-17.4	0.8				

Table 5.7 The resonance energies E_r and the decay widths Γ of the *p*-wave resonance states (1⁺ and 2⁺ states) of 10 Li in unit of MeV, measured from the 9 Li + *n* threshold

The scattering lengths a_s of the s-states (1⁻ and 2⁻ states) are shown in unit of fm. We show here the two kinds of the results using TOSM and Inert Core for 9 Li

present model. The order of 2^- and 1^- also comes from the attractive 3E component in the pn interaction.

For comparison, we calculate 10 Li without the core excitations of 9 Li ("Inert Core"), namely, we adopt only the single 0p-0h configuration for 9 Li without the Pauli blocking effect explained in Fig. 5.21d. In this case, we adjust the δ parameter of the potential strength $(1 + \delta)V_{cn}$ to be 0.066. In Table 5.7, the p-wave resonances are obtained just above the 9 Li + n threshold energy, and a_s values show small positive values for both 1^- and 2^- states, which means that the virtual s-states are not located near the 9 Li + n threshold, and the s-p shell gap is large. These results mean that the Pauli-blocking nicely describes the spectroscopic properties of 10 Li.

The *d*-wave resonance states of ¹⁰Li are also predicted using the TOSM case of ⁹Li, as shown in Table 5.8, whose excitation energies are higher than those of the *p*-states. The whole spectra of ¹⁰Li is summarized in Fig. 5.22 in comparison with the experimental data [108].

5.5.6 ¹¹Li

We solve 11 Li in a coupled 9 Li + n + n model and show the detailed properties of 11 Li in Table 5.9, the partial wave components $P((nlj)^2)$ for halo neutrons, the various rms radius, the relative distance between halo neutrons (R_{n-n}) and the core-2n distance (R_{c-2n}) , and the expectation value of the opening angle between two neutrons θ measured from the 9 Li core, respectively. The case using TOSM for 9 Li gives a large $P((1s)^2)$ value, comparable to $P((p_{1/2})^2)$ for halo neutrons and a large matter radius R_m for 11 Li, which are enough to explain the observations.

Table 5.8 The resonance energies E_r and the decay widths Γ of the *d*-wave resonance states in ¹⁰Li in unit of MeV

	TOSM
$(E_r, \Gamma)(1^-)$	(5.84, 5.16)
$(E_r, \Gamma)(2^-)$	(5.81, 5.20)
$(E_r, \Gamma)(3^-)$	(6.57, 6.31)
$(E_r, \Gamma)(4^-)$	(5.30, 3.84)

Fig. 5.22 ¹⁰Li spectrum using TOSM and Inert core for ⁹Li description [62]. Experimental data is taken from Ref. [108]

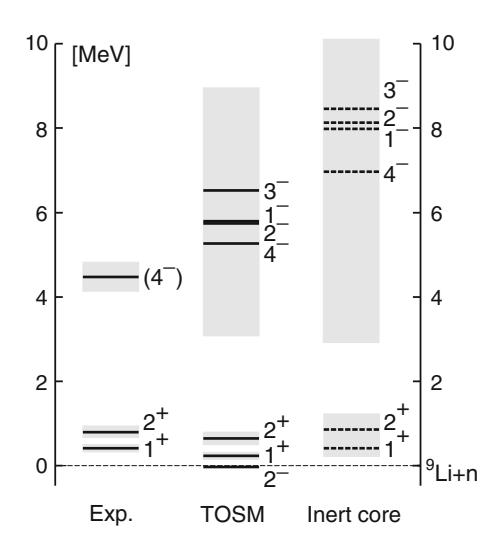


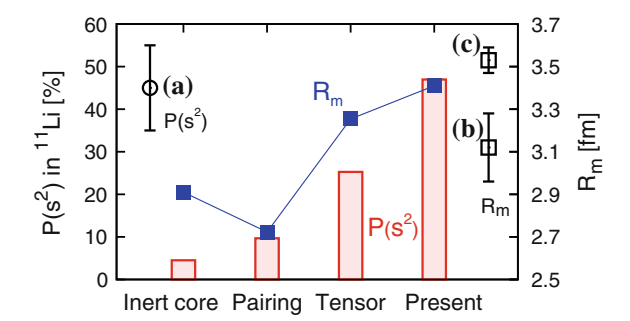
Table 5.9 Ground state properties of ${}^{11}\text{Li}$ with $S_{2n} = 0.31$ MeV, where two kinds of the ${}^{9}\text{Li}$ descriptions of TOSM and Inert Core are shown, respectively

	TOSM	Inert Core	Expt.
$P((p_{1/2})^2))$ [%]	42.7	90.6	_
$(1s_{1/2})^2$	46.9	4.3	$45 \pm 10[3]$
$(p_{3/2})^2$	2.5	0.8	_
$(d_{3/2})^2$	1.9	1.3	-
$(d_{5/2})^2$	4.1	2.1	_
$(f_{5/2})^2$	0.5	0.2	_
$(f_{7/2})^2$	0.6	0.3	_
R_m [fm]	3.41	2.99	$3.12 \pm 0.16[1]$
			3.53 ± 0.06 [61]
			$3.71 \pm 0.20[109]$
R_p	2.34	2.24	$2.88 \pm 0.11[1]$
R_n	3.73	3.23	$3.21 \pm 0.17[1]$
R_{ch}	2.44	2.34	$2.467 \pm 0.037[110]$
			2.423 ± 0.034 [111]
R_{n-n}	7.33	6.43	
R_{c-2n}	5.69	4.26	
θ [deg.]	65.3	73.1	

Details are described in the text

The case of "Inert Core" gives small $P((1s)^2)$ and small R_m values, which disagree with the experiments. From the difference between two models, it is found that the tensor and pairing correlations in ${}^9\text{Li}$ play important roles to break the magicity and make the halo structure of ${}^{11}\text{Li}$, in addition to the s-p inversion phenomenon in ${}^{10}\text{Li}$. As was shown in the previous study [79], the Pauli blocking effect from the tensor correlation is stronger than the pairing one to break the magicity of ${}^{11}\text{Li}$.

Fig. 5.23 (Color online) $(1s)^2$ probability $P(s^2)$ and matter radius R_m of 11 Li with four models in comparison with the experiments (**a** [3], **b** [1] and **c** [61]). The scale of $P(s^2)$ (R_m) is right (*left*) hand side



In Fig. 5.23, "Present" is found to give a large amount of the $(1s)^2$ probability $P(s^2)$, 46.9% for the last two neutrons and a large matter radius R_m , 3.41 fm for ¹¹Li, which are enough to explain the observations. The probabilities of $(p_{1/2})^2$, $(p_{3/2})^2$, $(d_{5/2})^2$ and $(d_{3/2})^2$ for the last two neutrons are obtained as 42.7%, 2.5%, 4.1% and 1.9%, respectively. In Fig. 5.23, when we individually consider the tensor and pairing correlations for ⁹Li, $P(s^2)$ is larger for the tensor case than for the pairing case. Finally, both blocking effects furthermore enhance $P(s^2)$ and provide almost equal amount of $(1s)^2$ and $(0p)^2$ configurations. Hence, two correlations play important roles to break the magicity and make the halo structure for ¹¹Li.

In Table 5.10, we also estimate the relative energy difference ΔE between $(1s)^2$ and $(0p)^2$ configurations for ¹¹Li using the mixing probabilities of these configurations and the coupling matrix element between them as 0.5 MeV obtained in Ref. [25]. The present model is found to give the degenerated energies enough to cause a large coupling between the $(0p)^2$ and $(1s)^2$ configurations by the pairing interaction between the last neutrons.

In addition to the matter radius, the halo structure also affects the proton radius of 11 Li, because of the recoil effect of the c.m. motion. In the three-body model of 11 Li, its proton radius (R_p) consisting of the proton radius of 9 Li and the relative distance between 9 Li and the c.m. of two neutrons (R_{c-2n}) with the following relation

$$\langle R_p^2(^{11}\text{Li})\rangle = \langle R_p^2(^9\text{Li})\rangle + \left(\frac{2}{11}\right)^2 \langle R_{c-2n}^2\rangle,$$
 (5.83)

where the second term represents the recoil effect. When the halo structure develops, $\langle R_{\text{c-2n}}^2 \rangle$ is expected to be large. Experimentally, considering the nucleon

Table 5.10 δ used in the ⁹Li–n potential, and the energy differences ΔE between the $(1s)^2$ and $(0p)^2$ configurations of ¹¹Li in MeV

	Inert core	Pairing	Tensor	Present
δ	0.066	0.143	0.1502	0.1745
ΔE	2.1	1.4	0.5	-0.1

radius, the charge radius of 11 Li was measured recently and its value is 2.467 ± 0.037 fm, which is enhanced from the one of 9 Li, 2.217 ± 0.035 fm [110]. The improved calculation for the isotope shift determination [111] shows that 2.423 ± 0.037 fm and 2.185 ± 0.033 fm for 11 Li and 9 Li, respectively. The present wave functions provide 2.44 and 2.23 fm for 11 Li and 9 Li, respectively, which are in a good agreement with the experimental values. This enhancement is mainly caused by the large value of $\sqrt{\langle R^2_{-2n} \rangle}$ obtained as 5.69 fm. For comparison, the distance between last two neutrons is 7.33 fm, which is larger than the core-2n case.

5.5.7 Electromagnetic Properties of Li Isotopes

We show the Q and μ moments of $^9\mathrm{Li}$ and $^{11}\mathrm{Li}$ in Tables 5.11 and 5.12, where only the absolute value of the Q moment of $^{11}\mathrm{Li}$ is reported in the experiments [11]. The present model describes reasonably those values for $^9\mathrm{Li}$ and $^{11}\mathrm{Li}$. For Q moments, the values of $^9\mathrm{Li}$ and $^{11}\mathrm{Li}$ do not differ so much to each other. This result is similar to that of the anti-symmetrized molecular dynamics (AMD) model [113] and different from the stochastic variational method (SVM) based on the multi-cluster model [12]. Here, similar to the charge radius, we discuss the recoil effect in the Q moment of $^{11}\mathrm{Li}$ by expanding its operator $Q(^{11}\mathrm{Li})$ into the core part ($Q(^9\mathrm{Li})$), the last neutron part and their coupling part as

$$Q(^{11}\text{Li}) = Q(^{9}\text{Li}) + \sqrt{\frac{16\pi}{5}} 3e \left(\frac{2}{11}\right)^{2} \mathcal{Y}_{20}(\mathbf{R}_{c-2n}) - 8\pi \sqrt{\frac{2}{3}} [O_{1}(^{9}\text{Li}), \mathcal{Y}_{1}(\mathbf{R}_{c-2n})]_{20},$$
(5.84)

Table 5.11 Q moments of 9 Li and 11 Li in units of e fm²

	⁹ Li	¹¹ Li
TOSM	-2.65	-2.80
AMD[113]	-2.66	-2.94
SVM[12]	-2.74	-3.71
Expt.[112]	-2.74 ± 0.10	3.12 ± 0.45
		(Q)
Expt.[114]	-3.06 ± 0.02	_

Table 5.12 μ moments of 9 Li and 11 Li in units of μ_N

_	⁹ Li	¹¹ Li
TOSM	3.69	3.77
AMD[113]	3.42	3.76
SVM[12]	3.43	3.23
Expt.[112]	3.44	3.67

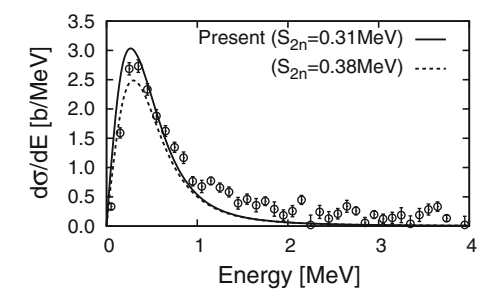
$$O_{1m}(^{9}\text{Li}) = e \sum_{i \in \text{proton}} \mathscr{Y}_{1m}(\mathbf{a}_i), \tag{5.85}$$

where $\mathcal{Y}_{lm}(\mathbf{r}) \equiv r^l Y_{lm}(\hat{\mathbf{r}})$ and $\{\mathbf{a}_i\}$ are the internal coordinates of protons in ${}^9\mathrm{Li}$. In our wave function of ${}^{11}\mathrm{Li}$, last two neutrons almost form the 0^+ state with the probability of around 99%. In that case, the Q moment for the relative motion part of ${}^9\mathrm{Li}-2n(c-2n)$ having the relative coordinate \mathbf{R}_{c-2n} almost vanishes because of the non-zero rank properties of the Q moment operator. This means that the recoil effect from the clusterization is negligible. Therefore, the Q moment of ${}^{11}\mathrm{Li}$ is caused mainly by the ${}^9\mathrm{Li}$ core part inside ${}^{11}\mathrm{Li}$. In our wave function, the spatial properties of the proton part of ${}^9\mathrm{Li}$ inside ${}^{11}\mathrm{Li}$ do not change so much. Hence, the Q moment of ${}^{11}\mathrm{Li}$ is similar to the value of the isolated ${}^9\mathrm{Li}$. Small enhancement from ${}^9\mathrm{Li}$ to ${}^{11}\mathrm{Li}$ mainly comes from the lacking of the high momentum component of the tensor correlation due to the Pauli-blocking in ${}^{11}\mathrm{Li}$, which extends the radial wave function of ${}^{11}\mathrm{Li}$. The experimental information of the Q moment is important to understand the structure of ${}^{11}\mathrm{Li}$. It is highly desired that further experimental data are available for the Q moment of ${}^{11}\mathrm{Li}$.

For the μ moment, the value observed in ^{11}Li is almost the Schmidt value of 3.79 μ_N of the $0p_{3/2}$ proton. In ^{9}Li , the $p_{1/2}$ proton is slightly mixed, which decreases the μ moment. In ^{9}Li , this $p_{1/2}$ proton is excited from the $0p_{3/2}$ -orbit in a pair with the $p_{1/2}$ neutron and the 2p-2h excitation is Pauli-blocked in ^{11}Li due to the additional neutrons. As a result, the excitation of $p_{1/2}$ is suppressed, which makes the μ moment of ^{11}Li close to the Schmidt value of the $p_{3/2}$ orbit. The tendency of the increase of the μ moment from ^{9}Li to ^{11}Li can be obtained also in the shell model analysis using various effective interactions [115].

We further calculate the three-body Coulomb breakup strength of 11 Li into the 9 Li + n + n system to investigate the properties of the dipole excited states and compare the strength with the new data from the RIKEN group [6]. We use the Green's function method combined with the complex scaling method [46] to calculate the three-body breakup strength [29] using the dipole strength and the equivalent photon method, where the experimental energy resolution is taken into account [6]. We do not find any resonances with a sharp decay width enough to make a resonance structure. In Fig. 5.24, it is found that the present model well reproduces the experiment, in particular, for low energy enhancement and its

Fig. 5.24 Calculated Coulomb breakup cross section of ¹¹Li into ⁹Li + n + n measured from the ⁹Li + n + n threshold energy. Data are taken from Ref. [6]



magnitude. Seeing more closely, however, our results seem to underestimate the cross section at E > 1 MeV, while overestimate at low energy peak region slightly. As a result, the integrated dipole strength for $E \le 3$ MeV gives 1.35 e^2 fm², which agrees with the experimental value of $1.42 \pm 0.18e^2$ fm² [6]. We also slightly change the two neutron separation energy of the ground state of 11 Li, which is close to the recent observation [116, 117].

Summarizing this section, we have considered newly the tensor correlation in 11 Li based on the extended three-body model. We have found that the tensor and pairing correlations play important roles in 9 Li with different spatial characteristics, where the tensor correlation prefers a shrunk spatial extension. The tensor and pairing correlations in 9 Li inside 11 Li are then Pauli-blocked by additional two neutrons, which makes the $(1s)^2$ and $(0p)^2$ configurations close to each other and hence activates the pairing interaction to mix about equal amount of two configurations. As a result we naturally explain the breaking of magicity and the halo formation for 11 Li. We also reproduce the recent results of the Coulomb breakup strength and the charge radius of 11 Li. For 10 Li, the inversion phenomenon is explained from the Pauli-blocking effect.

5.6 Conclusion

We have presented the physics of the di-neutron clustering and the deuteron-like tensor correlations by focusing on the halo structure of 11 Li. The halo structure provides an ideal platform for the di-neutron clustering to play an important role. This di-neutron clustering phenomenon is strongly related with the central interaction in the 1 S₀ channel, where the large scattering length in the nucleon–nucleon scattering suggests the appearance of the bound state by changing slightly the environment. On the other hand, in order to produce the halo structure, there should be an active participation of the $s_{1/2}$ configuration in the neutron wave function. This participation of the $s_{1/2}$ orbit was very difficult in the standard shell model framework. We had to invoke the deuteron-like tensor correlation in 11 Li, which blocks the two neutrons to enter the $p_{1/2}$ orbit and hence provides a mechanism to put neutrons in the $s_{1/2}$ orbit.

The theoretical description of these two new correlations to realize in ¹¹Li was very difficult. In fact, we had to develop the cluster orbit shell model (COSM) to handle an extended object and further the hybrid-VT model (Hybrid-VT) to treat the di-neutron clustering correlation in finite nuclei. We had to deal with unbound and resonance states quantitatively, since the halo structure appears when the binding energy of the last neutrons is very small. The excitation function of several MeV forces us to treat the spectral function in the continuum region. At the same time, the neighboring nuclei are also unbound. Hence, we had to develop the complex scaling method (CSM) to treat the continuum and resonance states. All these theoretically involved methods have been developed for the quantitative description of the halo nucleus ¹¹Li. The most essential mechanism to bring down

the $s_{1/2}$ configuration for the halo formation came from the deuteron-like tensor correlation in nuclei. The strong binding energy of ⁴He comes from the strong tensor interaction. We had to develop the tensor optimized shell model (TOSM) to describe the deuteron-like tensor correlation in the shell model basis. The TOSM provided a clear key to push up the configuration involving the $p_{1/2}$ orbit, since the strong binding of the ⁴He nucleus requires the use of the $p_{1/2}$ orbit. Hence, naturally the $s_{1/2}$ configuration is energetically favored for the halo structure formation.

We are used to treat the central interaction with the spin-orbit interaction in the shell model basis to treat many body systems. In the theoretical challenge to describe the halo structure of 11 Li, we had to face to treat the strong tensor interaction for the important role of the deuteron-like tensor correlation in many body systems. We have seen that the deuteron-like correlation worked out in the shell model basis is able to treat the Pauli blocking effect due to the $(p_{1/2})^2$ neutrons to wash away the N=8 shell gap. This effect allows the participation of the $(s_{1/2})^2$ configuration to provide a platform to develop the di-neutron clustering correlation in the halo structure of 11 Li. Hence, we expect many interesting many-body phenomena in unstable nuclei to be found in near future, where the deuteron-like tensor and/or di-neutron clustering correlations play important roles.

In this lecture note, we have gone through all these theoretical materials in details. We have tried to make the motivation of the development of the theoretical tools in each step to describe the halo nucleus quantitatively. These theoretical frameworks are not only for use of the halo structure, but should play a very important role for the description of finite nuclei. In fact, the TOSM is essential to describe the deuteron-like tensor correlation, which should be the most important ingredient to provide large binding energies for all the nuclei.

Acknowledgments We are grateful to all the collaborators for fruitful collaborations and continuous discussions. We would like to thank Prof. Hisashi Horiuchi for continuous support and encouragement. This work is supported by the JSPS grant: No. 18540269, 21540267 and 21740194.

References

- 1. I. Tanihata, et al., Phys. Lett. **B206**, 592 (1988)
- 2. T. Kobayashi, Nucl. Phys. A538, 343c (1992)
- 3. H. Simon, et al., Phys. Rev. Lett. 83, 496 (1999)
- 4. P.G. Hansen, B. Jonson, Europhys. Lett. 4, 409 (1987)
- 5. K. Ikeda, INS Report JHP-7(1988), in Japanese
- 6. T. Nakamura, et al., Phys. Rev. Lett. 96, 252502 (2006)
- 7. H.B. Jeppesen, et al., Phys. Lett. B642, 449 (2006), and the references therein
- 8. G.F. de Téramond, B. Gabioud, Phys. Rev. C **36**, 691 (1987)
- 9. I.J. Thompson, M.V. Zhukov, Phys. Rev. C 49, 1904 (1994)
- 10. H. Esbensen, G.F. Bertsch, Nucl. Phys. **A542**, 310 (1992)
- 11. J. Meng, P. Ring, Phys. Rev. Lett. 77, 3963 (1996)
- 12. K. Varga, Y. Suzuki, R.G. Lovas, Phys. Rev. C 66, 041302 (2002)
- B.S. Pudliner, V.R. Pandharipande, J. Carlson, S.C. Pieper, R.B. Wiringa, Phys. Rev. C 56, 1720 (1997)

- 14. I. Tanihata, et al., Phys. Rev. Lett. **55**, 2676 (1985)
- 15. I. Tanihata, et al., Phys. Lett. **B160**, 380 (1985)
- 16. Y. Suzuki, K. Ikeda, Phys. Rev. C 38, 410 (1988)
- 17. Y. Suzuki, J.J. Wang, Phys. Rev. C 41, 736 (1990)
- 18. Y. Tosaka, Y. Suzuki, K. Ikeda, Prog. Theor. Phys. 83, 1140 (1990)
- 19. Y. Tosaka, Y. Suzuki, Nucl. Phys. A512, 46 (1990)
- 20. Y. Suzuki, Y. Tosaka, Nucl. Phys. A517, 599 (1990)
- 21. Y. Suzuki, K. Ikeda, H. Sato, Prog. Theor. Phys. 83, 180 (1990)
- 22. Y. Suzuki, Nucl. Phys. A528, 395 (1991)
- 23. K. Ikeda, Nucl. Phys. A538, 355c (1992)
- 24. S. Aoyama, S. Mukai, K. Kato, K. Ikeda, Prog. Theor. Phys. 93, 99 (1995)
- 25. T. Myo, S. Aoyama, K. Kato, K. Ikeda, Prog. Theor. Phys. 108, 133 (2002)
- 26. S. Mukai, S. Aoyama, K. Kato, K. Ikeda, Prog. Theor. Phys. 99, 381 (1998)
- 27. S. Funada, H. Kameyama, Y. Sakuragi, Nucl. Phys. A575, 93 (1994)
- 28. T. Myo, K. Kato, S. Aoyama, K. Ikeda, Phys. Rev. C 63, 054313 (2001)
- 29. T. Myo, S. Aoyama, K. Kato, K. Ikeda, Phys. Lett. **B576**, 281 (2003)
- 30. S. Aoyama, S. Mukai, K. Kato, K. Ikeda, Prog. Theor. Phys. 94, 343 (1995)
- 31. K. Kato, S. Aoyama, S. Mukai, K. Ikeda, Nucl. Phys. **A588**, 29c (1995)
- 32. S. Aoyama, K. Kato, K. Ikeda, Phys. Rev. C 55, 2379 (1997)
- 33. S. Aoyama, K. Kato, K. Ikeda, Phys. Lett. **B414**, 13 (1997)
- 34. S. Aoyama, K. Kato, K. Ikeda, Prog. Theor. Phys. 99, 623 (1998)
- 35. S. Aoyama, Phys. Rev. C 59, 531 (1999)
- 36. S. Aoyama, K. Kato, K. Ikeda, Prog. Theor. Phys. Suppl. **142**, 35 (2001)
- 37. S. Aoyama, K. Kato, T. Myo, K. Ikeda, Prog. Theor. Phys. 107, 543 (2002)
- 38. K. Hagino, H. Sagawa, Phys. Rev. C 72, 044321 (2005)
- 39. M. Matsuo, K. Mizuyama, Y. Serizawa, Phys. Rev. C 71, 064326 (2005)
- 40. B.Y. Sun, H. Toki, J. Meng, Phys. Lett. **B683**, 134 (2010)
- 41. M. Kamimura, Phys. Rev. A 38, 621 (1988)
- 42. H. Kameyama, M. Kamimura, Y. Fukushima, Phys. Rev. C 40, 974 (1989)
- 43. S. Saito, Prog. Theor. Phys. Suppl. **62**, 11 (1977)
- 44. T. Yamada, K. Ikeda, H. Bando, T. Motoba, Phys. Lett. **B172**, 149 (1986)
- 45. T. Yamada, K. Ikeda, H. Bando, T. Motoba, Phys. Rev. C 38, 854 (1988)
- 46. S. Aoyama, T. Myo, K. Kato, K. Ikeda, Prog. Theor. Phys. 116, 1 (2006)
- 47. H. Horiuchi, Prog. Theor. Phys. Suppl. **62**, 90 (1977)
- 48. E. Hiyama, Y. Kino, M. Kamimura, Prog. Part. Nucl. Phys. 51, 223 (2003)
- 49. H. Masui, K. Kato, K. Ikeda, Phys. Rev. C 73, 034318 (2006)
- 50. T. Myo, K. Kato, K. Ikeda, Phys. Rev. C 76, 054309 (2007)
- 51. H. Kanada, T. Kaneko, S. Nagata, M. Nomoto, Prog. Theor. Phys. 61, 1327 (1979)
- 52. Y.C. Tang, M. LeMere, D.R. Thompson, Phys. Rep. 47, 167 (1978)
- 53. K. Kato, T. Yamada, K. Ikeda, Prog. Theor. Phys. **101**, 119 (1999)
- 54. Y, Kikuchi, T. Myo, M. Takashina, K. Kato, K. Ikeda, Prog. Theor. Phys. 122, 499 (2009)
- 55. P. Mueller, et al., Phys. Rev. Lett. **99**, 252501 (2007)
- M.V. Zhukov, B.V. Danilin, D.V. Fedorov, J.M. Bang, I.J. Thompson, J.S. Vaagen, Phys. Rep. 231, 151 (1993)
- 57. E. Nielsen, D.V. Fedorov, A.S. Jensen, E. Garrido, Phys. Rep. 347, 373 (2001)
- 58. K. Kato, K. Ikeda, Prog. Theor. Phys. 89, 623 (1993)
- H. Furutani, H. Kanada, T. Kaneko, Si. Nagata, H. Nishioka, S. Okabe, S. Saito, T. Sakuda, M. Seya, Prog. Theor. Phys. Suppl. 68, 193 (1980)
- V.I. Kukulin, V.M. Krasnopol'sky, V.T. Voronchev, P.B. Sazonov, Nucl. Phys. A453, 365 (1986)
- 61. J.A. Tostevin, J.S. Al-Khalili, Nucl. Phys. **A616**, 418c (1997)
- 62. T. Myo, Y. Kikuchi, K. Kato, H. Toki, K. Ikeda, Prog. Theor. Phys. 119, 561 (2008)
- 63. J. Aguilar, J.M. Combes, Commun. Math. Phys. 22, 269 (1971)
- 64. E. Balslev, J.M. Combes, Commun. Math. Phys. 22, 280 (1971)

- 65. T. Myo, A. Ohnishi, K. Kato, Prog. Theor. Phys. 99, 801 (1998)
- 66. A.T. Kruppa, R. Suzuki, K. Kato, Phys. Rev. C 75, 044602 (2007)
- 67. R. Suzuki, A.T. Kruppa, B.G. Giraud, K. Kato, Prog. Theor. Phys. 119, 949 (2008)
- 68. R. Suzuki, T. Myo, K. Kato, Prog. Theor. Phys. 113, 1273 (2005)
- 69. T. Berggren, Nucl. Phys. A109, 265 (1968)
- 70. N. Moiseyev, P.R. Certain, F. Weinhold, Mole. Phys. 36, 1613 (1978)
- 71. A. Csótó, Phys. Rev. C 48, 165 (1993)
- 72. K. Arai, Y. Suzuki, R.G. Lovas, Phys. Rev. C 59, 1432 (1999)
- 73. F. Ajzenberg-Selove, Nucl. Phys. **A506**, 1 (1989)
- 74. J. Jänecke, et al., Phys. Rev. C 54, 1070 (1996)
- 75. T. Aumann, et al., Phys. Rev. C 59, 1252 (1999)
- 76. S.C. Pieper, R.B. Wiringa, Annu. Rev. Nucl. Part. Sci. **51**, 53 (2001)
- 77. S.C. Pieper, K. Varga, R.B. Wiringa, Phys. Rev. C 66, 044310 (2002)
- 78. T. Myo, S. Sugimoto, K. Kato, H. Toki, K. Ikeda, Prog. Theor. Phys. 117, 257 (2007)
- 79. T. Myo, K. Kato, H. Toki, K. Ikeda, Phys. Rev. C 76, 024305 (2007)
- 80. S. Sugimoto, K. Ikeda, H. Toki, Nucl. Phys. A740, 77 (2004)
- 81. Y. Ogawa, H. Toki, S. Tamenaga, S. Sugimoto, K. Ikeda, Phys. Rev. C 73, 034301 (2006)
- 82. H. Feldmeier, T. Neff, R. Roth, J. Schnack, Nucl. Phys. A632, 61 (1998)
- 83. T. Neff, H. Feldmeier, Nucl. Phys. A713, 311 (2003)
- 84. T. Myo, H. Toki, K. Ikeda, Prog. Theor. Phys. 121, 511 (2009)
- 85. T. Otsuka, Y. Utsuno, M. Honma, T. Mizusaki, Prog. Part. Nucl. Phys. 46, 155 (2003)
- 86. D.H. Gloeckner, R.D. Lawson: Phys. Lett. **B53**, 313 (1974)
- R. Roth, P. Papakonstantinou, N. Paar, H. Hergert, T. Neff, H. Feldmeier, Phys. Rev. C 73, 044312 (2006)
- 88. H. Kamada, et al., Phys. Rev. C 64, 044001 (2001)
- 89. P. Descouvemont, Nucl. Phys. A626, 647 (1997)
- 90. D. Baye, Nucl. Phys. **A627**, 305 (1997)
- 91. N. Vinh Mau, J.C. Pacheco, Nucl. Phys. A607, 163 (1996)
- 92. E. Garrido, D.V. Fedorov, A.S. Jensen, Nucl. Phys. A700, 117 (2002)
- 93. E. Garrido, D.V. Fedorov, A.S. Jensen, Nucl. Phys. A708, 277 (2002)
- 94. G. Blanchon, A. Bonaccorso, D.M. Brink, N. Vinh Mau, Nucl. Phys. A791, 303 (2007)
- 95. M. Thoennessen, et al., Phys. Rev. C 59, 111 (1999)
- 96. M. Chartier, et al., Phys. Lett. B510, 24 (2001)
- 97. Y. Akaishi, Int. Rev. Nucl. Phys. 4, 259 (1986)
- 98. T. Terasawa, Prog. Theor. Phys. 23, 87 (1960)
- 99. A. Arima, T. Terasawa, Prog. Theor. Phys. 23, 115 (1960)
- 100. S. Nagata, T. Sasakawa, T. Sawada, R. Tamagaki, Prog. Theor. Phys. 22, 274 (1959)
- 101. T. Myo, K. Kato, K. Ikeda, Prog. Theor. Phys. 113, 763 (2005)
- 102. H. Sagawa, B.A. Brown, H. Esbensen, Phys. Lett. B309, 1 (1993)
- 103. S.C. Pieper, R.B. Wiringa, J. Carlson, Phys. Rev. C 70, 054325 (2004)
- 104. A. Hasegawa, S. Nagata, Prog. Theor. Phys. 45, 1786 (1971)
- 105. H. Toki, S. Sugimoto, K. Ikeda, Prog. Theor. Phys. 108, 903 (2002)
- 106. Y. Akaishi, Nucl. Phys. A738, 80 (2004)
- 107. K. Ikeda, S. Sugimoto, H. Toki, Nucl. Phys. A738, 73 (2004)
- 108. H. G. Bohlen, et al., Z. Phys. A344, 381 (1993)
- 109. A.V. Dobrovolsky, et al., Nucl. Phys. A766, 1 (2006)
- 110. R. Sánchez, et al., Phys. Rev. Lett. 96, 033002 (2006)
- 111. M. Puchalski, A.M. Moro, K. Pachucki, Phys. Rev. Lett. 97, 133001 (2006)
- 112. E. Arnold, et al., Z. Phys. A349, 337 (1994)
- 113. Y. Kanada-En'yo, H. Horiuchi, A. Ono, Phys. Rev. C 52, 628 (1995)
- 114. D. Borremans, et al., Phys. Rev. C 72, 044309 (2005)
- 115. T. Suzuki, R. Fujimoto, T. Otsuka, Phys. Rev. C 67, 044302 (2003)
- 116. C. Bachelet, Eur. Phys. J. A25, 31 (2005)
- 117. C. Bachelet, Phys. Rev. Lett. 100, 182501 (2008)

Chapter 6 Collective Clusterization in Nuclei and Excited Compound Systems: The Dynamical Cluster-Decay Model

Raj K. Gupta

6.1 Introduction

Clustering is a general feature of light, N = Z, α -like stable nuclei for both the ground and (intrinsic) excited states. This phenomenon is observed in spontaneous decays of heavy radioactive nuclei, and seems to play an important role in the decay of excited compound systems formed in heavy ion reactions. It is also shown to be present in exotic light-halo, super-heavy and super-superheavy nuclei.

In these Lecture Notes, we propose to analyze the clustering phenomenon first very briefly within the relativistic (and, also non-relativistic) mean field approach, and then develop a collective clusterization model for both the spontaneous (ground-state) and excited-state decay of nuclei. Thus, a dynamical collective clusterization model, called the dynamical cluster-decay model (DCM), is developed for the decay of a hot and rotating compound nucleus, which contains the spontaneous ground-state decay as its special case in terms of, so-called, preformed cluster model (PCM). The concept of preformed clusters in nuclei will be introduced, which leads to a non-statistical description for the decay of a compound nucleus to light particles $(n, p, \alpha$ -particle and γ -rays), the intermediate mass fragments (both light and heavy), fusion-fission and quasi-fission (equivalently, capture) processes. Hence, a model, alternative to the well known Hauser-Feshbach analysis (statistical evaporation code) and statistical fission models, will be developed. For the ground-state decay of a nucleus, we get the phenomena of α -decay and exotic cluster radioactivity. In other words, the PCM for ground-state decays, and the DCM for decay of excited compound nuclei, consider all decay

Physics Department, Panjab University, Chandigarh 160014, India e-mail: rajkgupta.chd@gmail.com

R. K. Gupta (⊠)

products as dynamical mass motion of preformed fragments or clusters through the interaction barrier, thereby including the structure effects of nuclei and/or compound nuclei explicitly.

The DCM calls for the introduction of temperature-dependent binding energies, and the deformations and orientations degrees of freedom, together with the use of "optimum" or "compact" orientations, for incoming nuclei as well as out-going nuclei/fragments. The deformation and orientation effects of both the parent and decay products (daughter and cluster nuclei) are also found essential in the PCM for ground-state, spontaneous decays. Applications of the model (PCM/DCM) will be discussed for illustrative decays from various mass regions of the Periodic Table.

6.2 Clustering in Light, Medium-Mass, Heavy, Super-Heavy, and Super-Superheavy Nuclei: Mean Field Approach

In this section, we first look for the possible existence of clusters in the groundand intrinsic excited states of various nuclei, in a mean field approach. If clusters are found in the mean-field description of nuclei, this will give strength to the concept of "pre-formed clusters" in nuclei and the compound systems formed in heavy ion reactions, which is used in the next section on dynamical cluster-decay model (DCM) for hot and rotating compound nuclei, and its ground-state version, the preformed cluster model (PCM), for spontaneous decays of radioactive nuclei.

The first place to look for clustering structure in nuclei is the light N=Z, α -like stable nuclei which are a multiple of α -particles. Cluster structure of light nuclei is very well studied on the basis of cluster models, but then the existence of clusters is assumed a priori. A major drawback of such a model is that it could not be applied to, say, "exotic" (unstable) nuclei, where structural information is not that abundant.

When cluster structures are prominent, like in light, N=Z, α -nuclei, the description by conventional mean field models based on the shell-model-like picture becomes insufficient. Examples of frameworks which could explain both the mean-field and clustering properties of nuclei are the methods of Fermionic molecular dynamics (FMD) [1] and antisymmetrized molecular dynamics (AMD) [2–4], which describe well the structural properties of several nuclei, and their excited states, in the lighter mass region [5–9]. In the following, however, we discuss another model, the relativistic mean field (RMF) model, which is recently shown to be capable of explaining the clustering shapes in light, stable and exotic nuclei [10, 11]. The RMF model seems to work well for light-mass regime, including also the light-halo nuclei, in-spite of several arguments put forth to its shortcomings related to the inadequacy of the mean-field approximation itself, the RMF parameters, the shape degrees of freedom, and the lack of proper pairing correlations, etc. Further applications of the RMF model to medium-mass nuclei [12],

the heavy radioactive nuclei [13–15], the super-heavy nuclei [12, 16], and a super-superheavy nucleus [17] seem to establish the cluster picture in both the ground and excited states of nuclei, *without* any a priori assumption of clustering interaction in the formalism. Here, in the following, after presenting a very brief description of the formalism itself, we discuss some of these above stated applications.

6.2.1 Relativistic Mean Field Method

In RMF model, we begin with the relativistic Lagrangian density for a nucleon-meson many-body system [18, 19–24]

$$L = \bar{\psi}_{i}(i\gamma^{\mu}\partial_{\mu} - M)\psi_{i}$$

$$+ \frac{1}{2}\partial^{\mu}\sigma\partial_{\mu}\sigma - \frac{1}{2}m_{\sigma}^{2}\sigma^{2} + \frac{1}{3}g_{2}\sigma^{3} + \frac{1}{4}g_{3}\sigma^{4} - g_{s}\bar{\psi}_{i}\psi_{i}\sigma$$

$$- \frac{1}{4}\Omega^{\mu\nu}\Omega_{\mu\nu} + \frac{1}{2}m_{\omega}^{2}V^{\mu}V_{\mu} + \frac{1}{4}c_{3}(V_{\mu}V^{\mu})^{2} - g_{\omega}\bar{\psi}_{i}\gamma^{\mu}\psi_{i}V_{\mu}$$

$$- \frac{1}{4}\mathbf{B}^{\mu\nu} \cdot \mathbf{B}_{\mu\nu} + \frac{1}{2}m_{\rho}^{2}\mathbf{R}^{\mu} \cdot \mathbf{R}_{\mu} - g_{\rho}\bar{\psi}_{i}\gamma^{\mu}\tau\psi_{i} \cdot \mathbf{R}^{\mu}$$

$$- \frac{1}{4}F^{\mu\nu}F_{\mu\nu} - e\bar{\psi}_{i}\gamma^{\mu}\frac{(1 - \tau_{3i})}{2}\psi_{i}A_{\mu}.$$

$$(6.1)$$

The field for the σ -meson is denoted by σ , that of the ω -meson by V_{μ} and of the isovector ρ -meson by ρ_{μ} . A^{μ} denotes the electromagnetic field. ψ_i are the Dirac field for the nucleons, whose third component of isospin is denoted by τ_{3i} . Here g_s , g_w , g_{ρ} and $e^2/4\pi = 1/137$ are the coupling constants for σ , ω , ρ mesons and photon, respectively. M is the mass of the nucleon and m_{σ} , m_{ω} and m_{ρ} are the masses of the σ , ω and ρ -mesons, respectively. $\Omega^{\mu\nu}$, $\mathbf{B}^{\mu\nu}$ and $F^{\mu\nu}$ are the field tensors for the V^{μ} , ρ^{μ} and the photon fields, respectively, and are defined as:

$$\Omega^{\mu\nu} = \partial^{\mu} \mathbf{V}^{\nu} - \partial^{\nu} \mathbf{V}^{\mu}
\mathbf{B}^{\mu\nu} = \partial^{\mu} \boldsymbol{\rho}^{\nu} - \partial^{\nu} \boldsymbol{\rho}^{\mu} - g_{\rho} (\boldsymbol{\rho} \times \boldsymbol{\rho})
F^{\mu\nu} = \partial^{\mu} \mathbf{A}^{\nu} - \partial^{\nu} \mathbf{A}^{\mu}.$$
(6.2)

The meson and electromagnetic fields are assumed to be static, time-independent classical fields, whereas the nucleon wavefunctions oscillate with a single particle energy ε_i . From the above Lagrangian, using equation of motion, the mean-field equations for mesons and nucleons are obtained as:

$$(-\Delta + m_{\sigma}^{2})\sigma(r) = -g_{s}\rho_{s}(r) - g_{2}\sigma^{2}(r) - g_{3}\sigma^{3}(r)$$
(6.3)

$$(-\Delta + m_{\omega}^2)V_0(r) = g_{\omega}\rho(r) - c_3(V_0(r))^3$$
(6.4)

$$(-\Delta + m_o^2)R_0^0(r) = g_\rho \rho_3(r) \tag{6.5}$$

$$-\Delta A^0(r) = e \rho_n(r) \tag{6.6}$$

$$\epsilon_{i}\psi_{i}(r) = \left[\gamma_{0}(-i\gamma \cdot \nabla + M_{B} + g_{\sigma}\sigma(r) + g_{\omega}V_{0}\omega_{0}(r) + g_{\rho}\gamma_{0}\tau_{3}R_{0}^{0}(r) + e\left(\frac{1-\tau_{3}}{2}\right)\gamma_{0}A_{0}(r)\right]\psi_{i}(r),$$

$$(6.7)$$

with the scalar, baryon (vector), isovector, and proton densities defined, respectively, as

$$\rho_s(r) = \sum_{i=1}^{A} \bar{\psi}_i(r)\psi_i(r) \tag{6.8}$$

$$\rho(r) = \sum_{i=1}^{A} \psi_i^{\dagger}(r)\psi_i(r) \tag{6.9}$$

$$\rho_3(r) = \sum_{i=1}^{A} \psi_i^{\dagger}(r) \tau_{3i} \psi_i(r)$$
 (6.10)

$$\rho_{p}(r) = \sum_{i=1}^{A} \psi_{i}^{\dagger}(r) \left(\frac{1 - \tau_{3i}}{2}\right) \psi_{i}(r). \tag{6.11}$$

Here we get bosonic equation for σ , ω and ρ mesons and Dirac equation for the nucleons. The σ -field gives the attractive and the ω -field the repulsive component of the nuclear potential. However, the ρ meson field takes care of the protonneutron asymmetric energy. This set of coupled partial differential equations is solved by expanding the upper and lower components of the Dirac spinors and the wavefunctions of the boson fields in an axially deformed harmonic oscillator potential basis, taking volume conservation into account [20, 25, 26], and with an initial quadrupole deformation parameter $\beta_2 = \beta_0$. The frequencies $\hbar\omega_\perp$ and $\hbar\omega_z$ of the harmonic oscillator potential can be expressed in terms of the deformation parameter β_2 [20, 25, 26]. A large number of parameter sets are obtained by different authors to fit the ground state properties of a small number of nuclei, listed in Table 1 of Ref. [27]. The most commonly used parameter sets are the NL3 [28] and NL-SH [29].

In numerical calculations, the wavefunctions for the bosons and fermions are expanded in a fairly large basis with the number of oscillator shells N_B for bosons and N_F for fermions. The coupled equations are solved iteratively to obtain convergent self-consistent solutions. The β_2 is obtained from the calculated quadrupole moments for the protons and neutrons through

$$Q = Q_n + Q_p = \sqrt{\frac{9}{5}}\pi A R^2 \beta_2, \tag{6.12}$$

Nucleus	BE (MeV)		β_2		Probable structure	Similar	
	RMF	Expt.	RMF	Expt.		predictions	
¹² C	89.74	92.16	-0.29	0.58	3α-Equilateral triangle	[2-4, 6, 39, 40]	
	89.63		0.00		Spherical		
	72.55		2.33		3α-Linear chain	[41]	
¹⁶ O	128.84	127.62	0.00		4α-Tetrahedron	[6, 39, 42]	
	112.95		0.95		4α-Kite	[40]	
	92.28		3.79		4α-Linear chain	[41]	
²⁰ Ne	156.70	160.64	0.54	0.73	5α-Trigonal bipyramid	[5, 39, 42]	
	151.96		-0.24		$^{10}\text{B} + ^{10}\text{B}$		
	108.24		7.76		¹⁰ B + ¹⁰ B (fragments)		
^{24}Mg	194.37	198.26	0.50	0.61	¹² C + ¹² C -(Central bishpenoid)	[39]	
_	186.82		-0.26		¹² C + ¹² C-Trigonal biprism		
²⁸ Si	232.08	236.54	-0.34	0.41	D_{3d} symmetry	[39]	
	231.18		0.00		Hollow sphere (Pentagonal bipyramid)		
	224.11		0.60		12 C + α + 12 C Trigonal biprism	[9, 39, 42]	
^{32}S	265.96	271.78	0.25	0.31	¹⁶ O + ¹⁶ O (Kite)		
	256.38		1.03		¹⁶ O + ¹⁶ O (Tetrahedron)		

Table 6.1 Calculated binding energies (BE) and deformation parameters $β_2$ for α-nuclei from 12 C to 32 S, together with the experimental data

The (interpreted) probable structures obtained from the RMF calculated density distributions are also shown, along with the references where similar structures were predicted (see, e.g., Figs. 4.5 and 4.6 in Ref. [3], or Fig. 2.1 for ⁸Be in Ref. [4]). Some of the structures proposed are rather speculative due to the symmetry conservation and other limitations of our RMF calculations, put in braces. The Table is taken from our published work in Ref. [10]

where $R=1.2A^{1/3}$ fm and Q are the quadrupole moments. The charge radius is given by $r_c=\sqrt{r_p^2+0.64}$ (considering the radius of proton as 0.8 fm), while the root mean square (rms) matter radius is defined as

$$\langle r_m^2 \rangle = \frac{1}{A} \int \rho(r_\perp, z) r^2 d\tau,$$
 (6.13)

with A as the mass number, and $\rho(r_\perp,z)$, the deformed density. Analogous definitions of protons and neutrons distribution radii are $\langle r_p^2 \rangle = \frac{1}{Z} \int \rho_p r_p^2 \, d\tau$ and $\langle r_n^2 \rangle = \frac{1}{N} \int \rho_n r_n^2 \, d\tau$, respectively. The total binding energy of the system is given by $-E_{total}$, where

$$E_{total} = E_{part} + E_{\sigma} + E_{\omega} + E_{\rho} + E_{c} + E_{pair} + E_{CM}. \tag{6.14}$$

The E_{part} is the sum of the single-particle energies of the nucleons and E_{σ} , E_{ω} , E_{ρ} , E_{c} , and E_{pair} are the contributions of the meson fields, the Coulomb field and the pairing energy, respectively. The effects of pairing interaction can be added in the

BCS formalism with a constant pairing gap, wherever necessary. Note that for very light nuclei, the effects of pairing are not known in all necessary details. For light systems, since the number of protons and neutrons is very small, the pairing correlations can be neglected. However, these correlations get more and more important with the increase of nucleon number in the nucleonic system. The center-of-mass energy correction $E_{CM} = -\frac{3}{4}(41A^{-\frac{1}{3}})$, in the non-relativistic harmonic oscillator approximation.

As outputs of the above equations, we obtain different potentials, densities, single-particle energy levels, radii, quadrupole deformations and the binding energies. For a given nucleus, the maximum binding energy corresponds to the ground state and other solutions are obtained as various excited intrinsic states, provided the nucleus does not undergo fission. However, when a nucleus undergoes fission [30–32], in most cases, depending on the total number of nucleons in a nucleus, the total energy of the nuclear system (of, say, two fragments) is more than its own binding energy as a single nucleus. Thus, after the scission point, when a nucleus is in a process of fission, the total energy is more than the ground state binding energy. For example, for the highly deformed solutions (scission states) of 112 Ba and 114 Ba isotopes with $\beta_2 = 10.71$ and 10.58, respectively, the energies of the systems at scission are 897.33 and 920.61 MeV, which are more than the ground state solutions 895.38 and 920.13 MeV, respectively [12].

In these Lecture Notes, we present our results only on the calculated neutron, proton and total (neutrons + protons)-matter density distributions, and the neutron-proton asymmetry variable $\alpha = \frac{\rho_n - \rho_p}{\rho_n + \rho_p}$. For other properties, like the binding energies (BE), quadrupole deformation parameters (β_2), and the root-mean-square (rms) matter radii (r_m), we refer the reader to our publications [10–17] and earlier references there in them. It is apparent that $|\alpha| = 1$ means only one type of nucleons (protons or neutrons), and $|\alpha| = 0$ refers to a N = Z, α -like matter. The matter densities are obtained in the positive quadrant of the plane parallel to the symmetry z-axis, i.e., in the $r_\perp - z$ plane where $x = y = r_\perp$. As the space reflection symmetry about z-axis, as well as about r_\perp axes, is conserved in our formalism, the results obtained in the positive quadrant are suitably reflected in other quadrants so as to have a complete picture in the $r_\perp - z$ plane. Such unbroken symmetries of our numerical procedure lead to several limitations, which are discussed in Ref. [10].

The density distribution of nucleons also plays the prominent role for studying the internal or cluster structure of a nucleus. For a differently quadrupole deformed nucleus, the density distribution $\rho(r_{\perp},z)$ inside the nucleus must vary. For example, the $\rho(r_{\perp},z)$ for a spherical nucleus is symmetrical in (r_{\perp},z) -plane. However, it is highly asymmetric for a largely deformed nucleus. Knowing the density distribution of the spherical or (oblate/prolate) deformed configuration, we can calculate the number of nucleons for each configuration, defined in [12] as

$$n = \int_{z_{\perp}}^{z_{2}} \int_{r_{1}}^{r_{2}} \rho(r_{\perp}, z) d\tau, \tag{6.15}$$

with n as number of neutrons N, protons Z or mass A. Though a straight forward calculation, this gives an important information about the internal or sub-structure of the cluster configuration in the ground or intrinsic excited states of a nucleus.

Furthermore, having obtained the density distributions ρ_c and ρ_d in RMF method for the emitted cluster (c) and remaining daughter (d) nucleus, the nuclear interaction potential $V_n(R)$ can be obtained by folding [33], say, the M3Y nucleon–nucleon interaction plus the zero-range pseudo-potential representing the single-nucleon exchange effects [34], denoted M3Y + Ex, without including the Pauli blocking effect, i.e., the density-dependence [35–37] in the interaction,

$$V_n(\mathbf{R}) = \int \rho_c(\mathbf{r_c}) \rho_d(\mathbf{r_d}) \nu(|\mathbf{r_c} - \mathbf{r_d} + \mathbf{R}| \equiv s) d^3 r_c d^3 r_d, \qquad (6.16)$$

where the well known M3Y + Ex interaction [34] is given as

$$v(s) = 7,999 \frac{e^{-4s}}{4s} - 2,134.25 \frac{e^{-2.5s}}{2.5s} + J_{00}(E)\delta(s), \tag{6.17}$$

with the zero-range pseudo-potential (exchange term) given by

$$J_{00}(E) = -276(1 - 0.005E/A_{\alpha(c)}) \text{ MeV fm}^3.$$

Here $A_{\alpha(c)}$ is the α -particle (cluster) mass, and E, the energy measured in the centre-of-mass of the α - or cluster-daughter nucleus system, is equal to the released Q value. Compared to, say, the energies involved in high energy α -scattering, practically $J_{00}(E)$ is independent of energy for the α - or cluster-decay process and hence can be taken as -276 MeV fm³, an approximation also used by other authors [38].

Adding to $V_n(R)$ the Coulomb interaction $V_c(R)$, we get the total interaction potential $V(R) = V_n(R) + V_c(R)$ between the cluster and daughter nuclei, which can be used to calculate, say, the cluster penetration probability for determining its decay constant, etc., as discussed below.

6.2.2 Applications of the RMF Model

6.2.2.1 Light α- and Exotic-Nuclei

RMF calculations for light nuclei are made [10, 11] for the stable and exotic $^{6-14}$ Be, odd-mass $^{11-19}$ B, and the even N=Z, α -nuclei 12 C to 32 S and 56 Ni, using the NL3 (NL-SH for 12 C) parameter set with no pairing effects included. In the following, we first present our results for the N=Z, α -nuclei, showing α -particle and α -nucleus clustering structures in both the ground and excited intrinsic states. The non-relativistic Skyrme Hartree Fock (SHF) calculation for light nuclei is made for 56 Ni only [11], which supports the RMF result, discussed below.

Fig. 6.1 Contour plots of neutron, proton and matter density distributions in ⁸Be, using RMF(NL3). This figure is based on Fig. 2 of our published work in Ref. [10]

RMF(NL3)

8Be ρ_n ρ_p ρ ρ ρ ρ

Fig. 6.2 Contour plots of matter density distributions in a spherical ground-state with hollowness at the center due to a regular 4α-Tetrahedron clustering in three dimensions, b A highly deformed first excited-state at $\beta_2 = 0.95$ forming a 4α Kite-like structure, and c the highest deformed second excited-state at $\beta_2 = 3.79$ of a linear 4α -chain, in ^{16}O . using RMF(NL3). This figure is taken from our published work in Ref. [10]

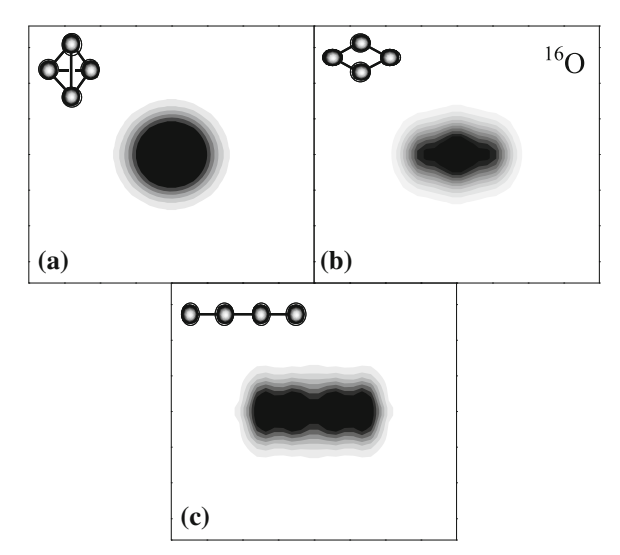


Figure 6.1 shows in x(=y)-z plane, the $\alpha-\alpha$ clustering in ⁸Be, which serves as a benchmark nucleus of the formalism. The next two α -nuclei, ¹²C and ¹⁶O, show several known ground-state (g.s.) structures such as the 3α -equilateral triangle (co-existing with spherical shape) and 4α -tetrahedron or kite-like, plus the 3α - and 4α -linear chains for excited states [10]. This is illustrated in Fig. 6.2 for ¹⁶O, and listed in Table 6.1 for all the α -nuclei from ¹²C to ³²S. For α -nuclei beyond ¹⁶O, i.e., from ²⁰Ne up to ³²S, both α and non- α cluster structures, like ¹⁰B + ¹⁰B, ¹²C + ¹²C, ¹²C + α + ¹²C and ¹⁶O + ¹⁶O, are seen. Also, 5- α -trigonal bipyramid and pentagonal bipyramid (hollow sphere) are obtained, but *no* 5- α , 6- α chains, etc., for ²⁰Ne, ²⁴Mg, etc., in agreement with other known results (for more details, see Ref. [10]).

For other Be and B nuclei, we get [10] the α -clustering and "halo" structures of $(\alpha + \alpha)$ -core or $(\alpha + \alpha + p)$ -core plus xn, i.e., xn playing the role of "halo" neutrons. Some interesting observations for Be-nuclei, heavier than ⁸Be, are (i) the clustering in proton matter remains undisturbed, and (ii) the α clustering in proton density distribution of ^{9,10}Be are more closely packed, i.e., the smallest distance between two α clusters occurs for ¹⁰Be which, according to some authors [43], may be due to the strong pairing effects (for further details of the calculation, we refer

the reader to Ref. [10]). Finally, ⁵⁶Ni shows [11] a preferred N=Z, α -nucleus clustering for states with deformations up to hyper-deformation ($\beta \le 2.45$). The SHF calculation for ⁵⁶Ni nucleus is also made [11], which supports the above result, and shows a two cluster or symmetric fission for the hyper-hyperdeformed ($\beta \ge 4.87$) state (for more details, see Ref. [11]).

6.2.2.2 Medium Mass Nuclei

In the medium mass region, we have studied the clustering structure of various $Z=56^{-112-122}$ Ba nuclei, within the RMF model, with an additional attempt to determine for the first time the number of protons and neutrons in a cluster, i.e., the internal structure(s) of the cluster(s) [12]. In our earlier calculations [13, 17], only the N/Z (= ρ_n/ρ_p) ratios were calculated which are indeterminate up to $\sim 20\%$ since only average densities were obtained.

Decay of such "stable" nuclei, specifically, the neutron-deficient and neutron-rich isotopes of Z=54-64 nuclei, against exotic cluster decays were first studied by us [44–47] on the basis of the preformed cluster model (PCM) of Gupta and collaborators [48–54] (see, also the works of other authors [55, 56, 57]). From the neutron-deficient parents, the N=Z, α -nuclei 8 Be, 12 C, 16 O, 20 Ne, 24 Mg, and 28 Si are predicted to be the most probable clusters emitted with a much smaller decay half-life compared to N>Z clusters predicted preferably or observed from neutron-rich parents (e.g., 14 C from 146 Ba or 222 Ra with 132 Sn or 208 Pb as the daughter, respectively). Thus, other than the α particle, 12 C decay of $^{112-120}$ Ba nuclei is shown to be the most probable one with 100 Sn, and its heavier isotopes, as the daughter nuclei.

The ground-state decay of Ba, however, could not be established as yet [58, 59], and a new phenomenon of intermediate mass fragments (IMFs) with $3 \le Z \le 9$, also referred to as 'clusters' or 'complex fragments', is observed to be emitted from the compound nucleus ¹¹⁶Ba* formed in ⁵⁸Ni + ⁵⁸Ni \rightarrow ¹¹⁶Ba* reactions at both the high [60, 61] and medium energies [62, 63]. The measured IMF cross-section σ_{IMF} for the ¹¹⁶Ba* decay at all the above mentioned medium and high energies are so far understood only on the preformed-clusters (PCM) based dynamical cluster-decay model (DCM) of Gupta and collaborators [64], to be discussed in next section. In this subsection, we are interested to see if the RMF model supports a clustering structure for the ground and/ or excited states of Ba nuclei.

Analyzing the clustering configurations of the density distributions for both the ground and excited state solutions of $^{112-122}$ Ba nuclei (illustrated in Fig. 6.3 for the prolate-deformed ground-state solutions), we determine the number of nucleons by using the general formula in (6.15), for both the protons and neutrons (using individual density distributions), which are listed in Table 6.2. For this calculation, we first find the range of the integral (marked in Fig. 6.3 for the clusters formed in 112 Ba, and listed in Table 6.2, i.e., the lower and the upper limits of the (r and z) axes from the plotted density distributions like in Fig. 6.3,

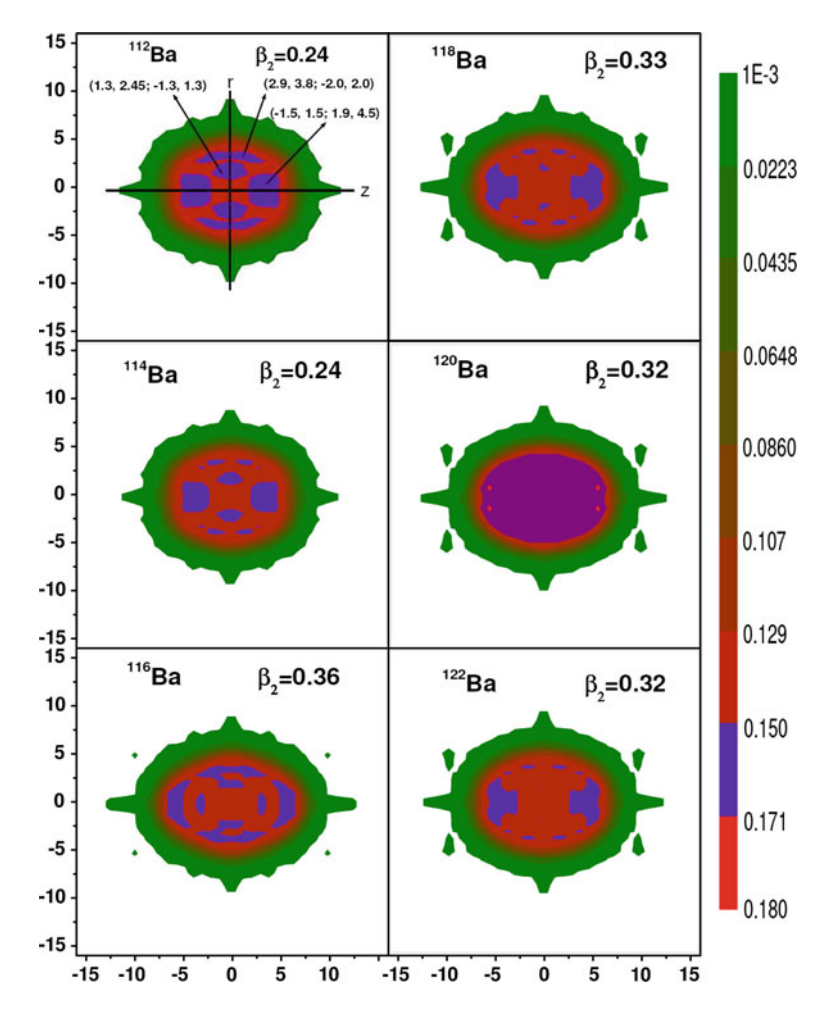


Fig. 6.3 Contour plots of matter density distributions in prolate deformed ground-state solutions of $^{112-122}$ Ba nuclei, using RMF(NL3). For one nucleus, the ranges of integration in (6.15), i.e., r_1 , r_2 ; z_1 , z_2 (in fm), are marked for all the clusters formed. This figure is taken from our work in Ref. [12]

and then evaluate the integral for each case. Note that, due to un-even shapes of the clusters formed, the ranges can be determined to the extent of the $Z_{clus.}$ and $N_{clus.}$ being correct within one unit, i.e., the obtained $Z_{clus.}$ and $N_{clus.}$ give $A_{clus.}$ within $A_{clus.}$ ± 2 .

We notice from Table 6.2 that the prolate-deformed ground-states (g.s.) of ¹¹²Ba, ¹¹⁴Ba and ¹¹⁶Ba nuclei, and the first excited oblate-deformed states (e.s. I) of ¹¹⁸Ba and ¹²⁰Ba, show the presence of ¹²C cluster configuration. Note that ¹²C cluster refers to ¹⁰⁰Sn daughter, and its existence inside the Ba nuclei has been of interest both from experimental and theoretical points of views. The g.s. of

Table 6.2 The number of protons $Z_{clus.}$ and neutrons $N_{clus.}$, and their sum, the nucleons $A_{clus.}$, in clusters inside the $^{112-122}$ Ba nuclei for different solutions of deformations β_2 obtained from the RMF(NL3) formalism

Nucleus	State	β_2	Cluster range $(r_1, r_2; z_1, z_2)$	$Z_{clus.}$	N _{clus} .	$A_{clus.}$	Cluster
¹¹² Ba	g.s.	0.24	(-1.5, 1.5; 1.9, 4.5)	17.7	18.3	36.0	36 Ar
			(1.3, 2.45; -1.3, 1.3)	5.8	6.2	13.0	¹² C
			(2.9, 3.8; -2.0, 2.0)	7.1	7.4	14.5	¹⁴ N
	e.s. I	-0.39	(-3.45, 3.45; -1.7, 1.7)	50.4	52.9	103.3	103 Sn
	e.s. II	1.24	(-1.0, 1.0; -6.4, 6.4)	46.5	48.8	95.3	⁹⁵ Pd
	e.s. III	10.71	(-3.5, 3.5, -6.3, 6.3)	0.7	0.8	1.6	^{2}H
¹¹⁴ Ba	g.s.	0.24	(-1.5, 1.5; 2.1, 4.6)	16.9	17.9	34.7	35Cl
	_		(1.25, 2.5; -1.1, 1.1)	5.8	6.2	12.0	¹² C
			(3.3, 3.7; 0.7, 2.0)	1.1	1.2	2.3	^{2}H
	e.s. I	-0.39	(-3.35, 3.35; -1.5, 1.5)	49.9	54.7	104.6	105 Sn
	e.s. II	1.19	(-0.7, 0.7; 3.9, 5.4)	4.1	4.3	8.4	⁸ Be
	e.s. III	10.58	(-3.8, 3.8; -6.6, 6.3)	1.1	1.1	2.2	^{2}H
¹¹⁶ Ba	g.s.	0.36	(-1.6, 1.6; 4.4, 6.2)	12.3	13.1	25.3	25 Mg
			(-0.9, 0.9; 2.6, 3.4)	2.8	3.4	6.1	⁶ Li
			(2.9, 3.6; -2.0, 2.0)	5.74	6.10	11.95	¹² C
			(1.6, 2.3; -1.1, 1.1)	3.07	3.36	6.43	⁶ Li
	e.s. I	-0.39	(-3.3, 3.3; -1.5, 1.5)	48.8	54.9	103.7	¹⁰⁴ In
	e.s. II	1.20	(-1.0, 1.0; -6.7, 6.7)	47.8	52.5	103.3	103 Cd
	e.s. III	10.40	(-0.8, 0.8; 11.0, 12.2)	3.7	3.8	7.5	⁸ Be
			(2.3, 2.9; 9.9, 12.8)	3.2	3.4	6.6	⁶ Li
			(-3.4, 3.4; -6.1, 6.1)	0.9	1.0	1.9	^{2}H
¹¹⁸ Ba	g.s.	0.33	(-1.6, 1.6; 2.5, 5.5)	19.9	22.2	42.0	⁴² Ca
			(3.3, 3.6; 0.7, 2.0)	0.8	0.9	1.7	^{2}H
			(1.6, 2.1; -0.4, 0.4)	0.7	0.8	1.6	^{2}H
	e.s. I	-0.24	(-1.1, 1.1; -0.6, 0.6)	5.6	6.4	12.0	¹² C
	e.s. III	10.24	(-3.7, 3.7; -6.2, 6.2)	1.2	1.6	2.8	^{3}H
¹²⁰ Ba	g.s.	0.32	(0.7, 1.2; 5.0, 5.5)	0.3	0.6	0.9	^{1}H
	e.s. I	-0.23	(-1.1, 1.1; -0.6, 0.6)	5.9	6.3	12.2	¹² C
	e.s. III	10.97	(-4.3, 4.3; -6.3, 6.3)	1.6	2.1	3.8	⁴ He
¹²² Ba	g.s.	0.32	(-1.7, 1.7; 2.5, 5.3)	19.7	22.8	42.6	⁴³ Ca
			(3.4, 3.7; 0.8, 2.0)	0.7	0.8	1.6	^{2}H
	e.s. I	-0.22	(-1.5, 1.5; -1.0, 1.0)	11.2	13.2	24.4	²³ Na
	e.s. III	9.96	(-3.7, 3.7; -6.1, 6.1)	1.0	1.4	2.4	^{2}H

The clusters are listed as the ground state (g.s.), and first excited state (e.s. I) and second excited state (e.s. II), etc., solutions. The ranges of integration in (6.15), i.e., r_1 , r_2 ; z_1 , z_2 (in fm), for each cluster are also given. The Table is taken from our work in Ref. [12]

^{112–116}Ba also show the presence of other lighter and relatively heavier clusters, like ⁶Li, ¹⁴N, ²⁵Mg and ³⁵Cl, ³⁶Ar, respectively, whereas the same for the g.s. of ^{118,122}Ba are predicted to be only the relatively heavier ones like ⁴²Ca and ⁴³Ca. The g.s. of ¹²⁰Ba, e.s.II of ¹¹⁴Ba and e.s.III of ¹¹⁶Ba seem to present isolated cases each of a relatively higher density (red color) ¹H, ⁸Be and ⁶Li cluster, respectively.

Furthermore, the oblate state in 122 Ba also shows the presence of a lighter cluster 23 Na, whereas the oblate states of $^{112-116}$ Ba show only very heavy clusters of mass $A_{clus.} \sim 100$. The important point to note here is that 12 C cluster is formed inside the Ba nuclei and, as noted below, are *not* from the neck region where 2,3 H or 4 He nuclei are shown to exist. In other words, 12 C does constitute the cluster structure both in ground and excited states of some Ba isotopes, particularly in $^{112-116}$ Ba and 118,120 Ba, respectively, and other lighter clusters of masses below the Ca nucleus are also predicted.

Next, the hyper-deformed ($\beta_2 \sim 1.2$) solutions exist only in $^{112-116}$ Ba isotopes, and 114 Ba shows the 8 Be cluster configuration, the only nucleus showing clustering configuration at such large deformations. Finally, for very large $\beta_2 \sim 10.5$ (the fission state), the internal configurations of the isotopic chain $^{112-122}$ Ba are of the form of two separated (identical) nuclei which are connected by a neck like configuration. The neck configurations contain simply the hydrogen isotopes 2,3 H or 4 He nucleus.

Concluding, the results of 12 C constituting the cluster configuration in both the prolate-deformed ground-state and oblate-deformed excited states of some Ba nuclei, together with clusters such as 6 Li, 8 Be, 14 N, and in the neighborhood of N=Z, 22 Na, 24 Mg, 34 Cl, 36 Ar and 40 Ca, with the scission stage of all $^{112-122}$ Ba nuclei constituting of 2,3 H and 4 He as the neck between two symmetrical fragments, are of interest, respectively, for observed intermediate mass fragments (IMFs), fusion–fission and the so far unobserved evaporation residues from the decaying Ba* compound nuclei formed in heavy ion reactions. In other words, the clusters are shown to be formed inside the Ba nuclei, and the evaporation residues seem to come from the neck region. This is an important result of the RMF(NL3) method for nuclear structure physics.

6.2.2.3 Heavy Mass Radioactive Nuclei

For the known (g.s.) spontaneous cluster-emitting heavy actinides [54, 65], such as 222 Ra, 232 U, 236 Pu and 242 Cm, we have first looked for the possible cluster configurations in the ground and intrinsic excited states of these nuclei, and then calculated the interaction potential $V_n(R)$ by using (6.16) for the experimentally observed cluster-daughter configuration, which is then used to calculate the decay half-life within the PCM. We analyze the cluster configurations here in the following, and calculate the decay half-lives in next section after the PCM is introduced.

Figure 6.4 shows that the RMF(NL3) densities predict [13] not only the $N \approx Z$, α -like matter or clustering in the ground state, but also the $N \approx Z$ matter and exotic $N \neq Z$ clustering in excited intrinsic states of the above said radioactive nuclei. On the other hand, clustering is not so general for the SHF(SkI4), as is illustrated in Fig. 6.5 for both the ground and excited states. Note that the BCS pairing is included here for heavy (superheavy and super-superheavy) nuclei, in an axially deformed harmonic oscillator basis.

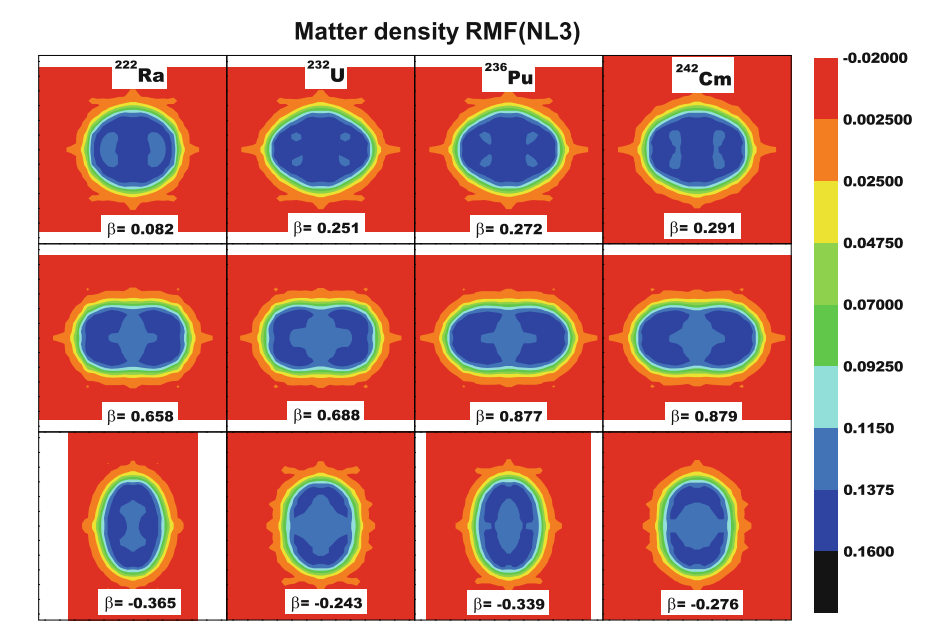


Fig. 6.4 Matter density distributions for the ground- and intrinsic excited-states of ²²²Ra, ²³²U, ²³⁶Pu and ²⁴²Cm nuclei, using RMF(NL3). This figure is taken from our published work in Ref. [13]

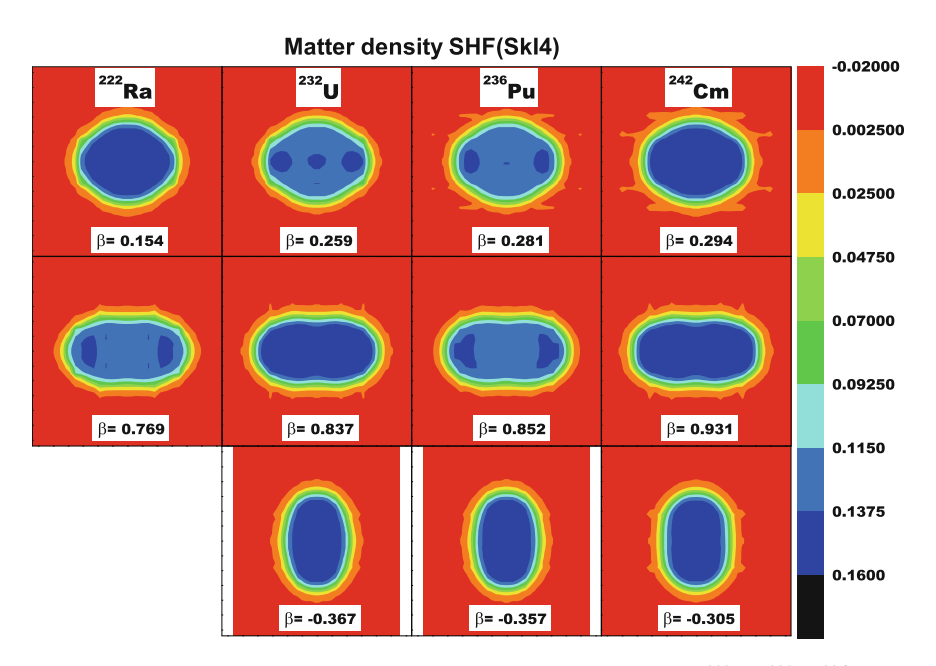


Fig. 6.5 Matter density distributions for Skyrme–Hartree–Fock model of ²²²Ra, ²³²U, ²³⁶Pu and ²⁴²Cm nuclei, using SkI4 parameter set [SHF(SkI4)]. This figure is taken from our published work in Ref. [13]

6.2.2.4 Superheavy Nuclei

Our density distribution calculations [13, 16] for superheavy Z = 114 and 120, N = 172-184 nuclei, using the RMF(NL3), show cases of non-clustering, bubble-like (hollow sphere) structures as signatures of doubly closed shell nuclei in the (spherical) ground and normal-(oblate)-deformed states, as well as the exotic $N \neq Z$ clusters at the centre of their superdeformed ground state (co-existing with spherical shape), as is illustrated in Fig. 6.6 for Z = 114 nuclei [13] and in Fig. 6.7 for the three solutions of Z = 120, N = 172, O(N = 172) nucleus [16] (see also, O(N = 172)) asymmetry distribution plots in Figs. 5 and 6 of Ref. [16]). Specifically, O(N = 172) are shown as the doubly magic nuclei. Also, we obtain O(N = 184) as a two cluster configuration. In fact, the clustering in to two large and some small pieces is universal for all superdeformed ground states in O(N = 184) nuclei for RMF(NL3), the number and size of smaller pieces (fragments) decreasing as the neutron number increases, becoming zero for O(N = 184) (see Fig. 4 in [16]).

6.2.2.5 Super-Superheavy Nuclei

Clustering structures of the various resonance states of the compound nucleus $^{476}184^*$ formed in ^{238}U + ^{238}U reaction are also studied within both the

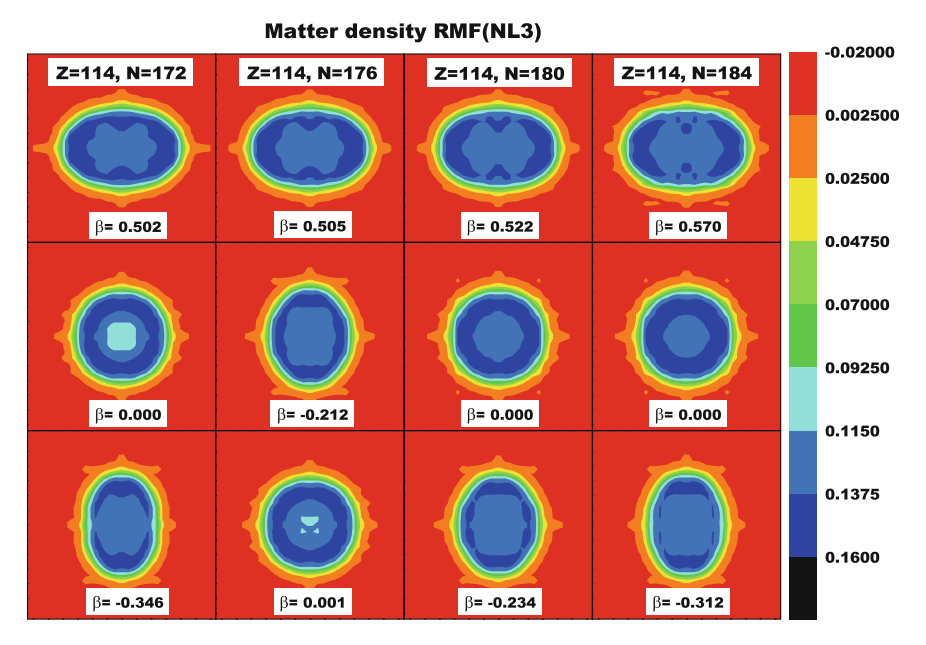
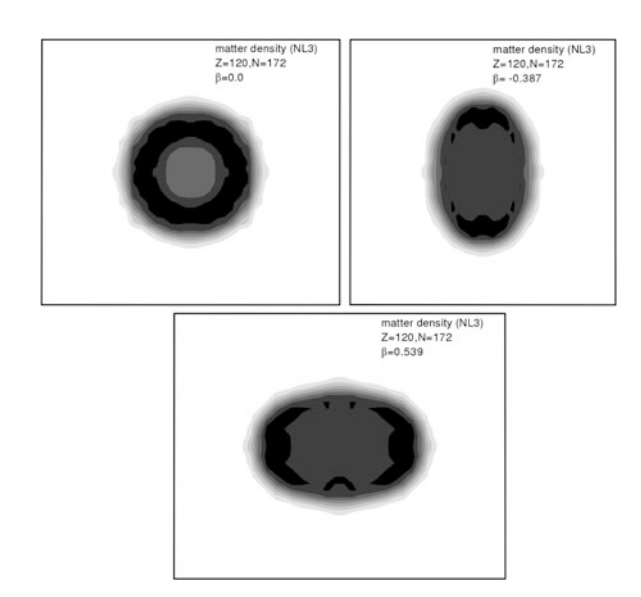


Fig. 6.6 Matter density distributions for superheavy nuclei ^{286,290,294,298}114, taken from our published work in Ref. [13]

Fig. 6.7 Matter density distributions for the superheavy nucleus ²⁹²120, taken from our published work in Ref. [16]



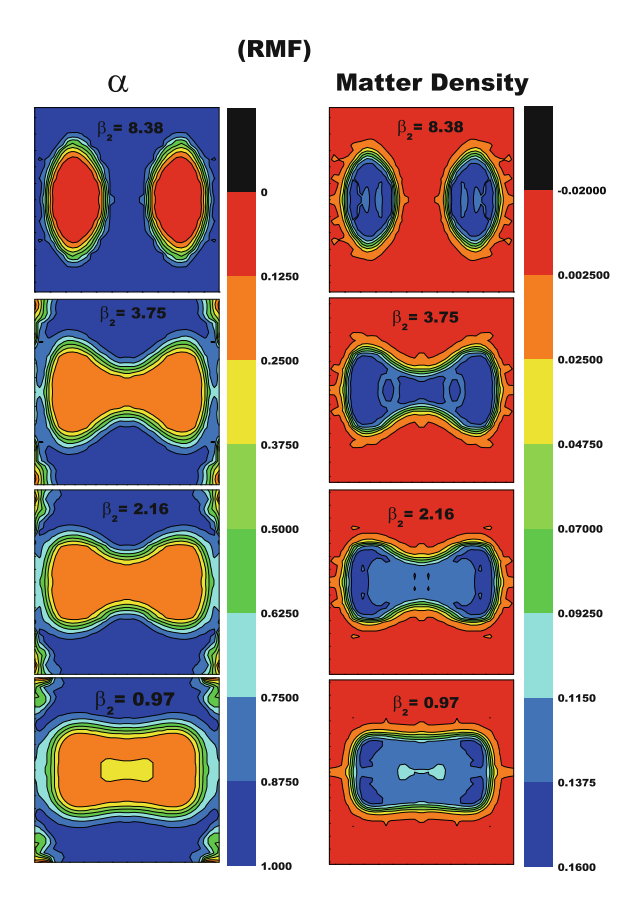
RMF(NL3) and SHF(SkI4) formalism [17]. Figure 6.8 illustrates our results for the RMF(NL3). Interesting enough, the super-superheavy nucleus $^{476}184^*$ also supports the clustering phenomenon, more so for RMF, with a kind of triple fission of an exotic cluster in the neck region of two equal fragments of N = Z matter [17].

Concluding this section, the clustering phenomenon, observed in spontaneous decay of heavy radioactive nuclei, is shown to be a general feature of nuclei throughout the Periodic Table, and hence should play an important role for the decay of compound systems formed in heavy ion reactions.

6.3 The Preformed-Cluster Based Dynamical Cluster-Decay Model for the Decay of Hot and Rotating Compound Nucleus

Historically, the preformed cluster model (PCM) [48–54] was given first for the ground-state, spontaneous emission of clusters from the radioactive nuclei. It was then extended to the decay of hot and rotating compound nucleus formed in heavy ion reactions, in terms of the so-called dynamical cluster-decay model (DCM) [64, 66–74]. In the following, we discuss the DCM in detail, showing that the PCM is a special case of DCM for temperature T=0. The applications of PCM to observed cases of spontaneous cluster emission are then discussed in the next section. Finally, the applications of the DCM, in the section following the application of the PCM, show how the cluster preformation factor is important for the decay process in both the radioactive nuclei and the nuclei formed in heavy ion reactions.

Fig. 6.8 The matter density distribution (*right*) and the neutron–proton asymmetry variable $\alpha = \frac{\rho_n - \rho_p}{\rho_n + \rho_p}$ (*left*) for different solutions of compound nucleus ⁴⁷⁶184, using the RMF(NL3) formalism, taken from our published work in Ref. [17]



A compound nucleus (CN), formed in low energy (<15 MeV/A) heavy-ion reactions, in general, decays by emitting the multiple light-particles (LPs; n, p, α and γ -rays), resulting in evaporation residue cross section σ_{ER} , the intermediate mass fragments (IMFs) of masses $5 \le A \le 20$, charges 2 < Z < 10 ($\sigma_{IMFs} = 5-10\%$ σ_{ER}), and the symmetric fission (SF) and near symmetric fission (nSF), the fusion–fission process (σ_{ff}). Different mass regions of the Periodic Table show different combinations of these processes or any one of them as a dominant mode. In addition, there are effects of non-compound nucleus decays, like the quasifission (qf), pre-equilibrium or deep-inelastic collisions (DIC), occurring mostly at higher incident center of mass (c.m.) energies. These effects could be small or large enough to compete with CN decays. Within the CN decay model, an empirical estimate of, say, σ_{qf} can be obtained from the measured and calculated fusion cross sections as

$$\sigma_{qf} = \sigma_{fus}^{Expt} - \sigma_{fus}^{Cal}, \text{ where } \sigma_{fus}^{Cal} = \sigma_{ER} + \sigma_{IMFs} + \sigma_{ff}.$$
 (6.18)

As an alternative of the well known [75] Hauser–Feshbach analysis for LPs (statistical evaporation codes) and the statistical fission model treatment of IMFs

and ff, in the DCM we treat all of these processes within one and the same formalism, as the dynamical collective mass motion of preformed clusters through the interaction barrier. The cluster-decay model is in fact also a fission-model where the structure effects of CN are included via the preformation probability of the (decay or fission) fragments.

The DCM is based on the dynamical (or quantum mechanical) fragmentation theory of fission process and cold fusion phenomenon in heavy ion reactions [76–80], whose collective coordinates are:

(i) the mass and charge asymmetries

$$\eta = (A_1 - A_2)/(A_1 + A_2)$$
 and $\eta_z = (Z_1 - Z_2)/(Z_1 + Z_2)$,

1 and 2 represent, respectively, the heavy (H) and light (L) fragments.

- (ii) relative separation R.
- (iii) neck parameter ε , and
- (iv) the multi-pole deformations $\beta_{\lambda i}(\lambda=2,3,4,\ldots;\ i=1,2)$, orientations θ_i of two nuclei or fragments and the azimuthal angle ϕ between their principal planes.

In DCM, the above coordinates characterize, respectively,

- (i) the nucleon-division (or -exchange) between the outgoing fragments, and
- (ii) the transfer of kinetic energy of incident channel $E_{c.m.}$ to internal excitation (total excitation energy TXE and/ or total kinetic energy TXE) of the outgoing channel, since the fixed $R = R_a$ (defined later), at which the process is calculated, depends on temperature T as well as on η , i.e., $R(T, \eta)$. This energy transfer process, for negative Q_{out} , illustrated in Fig. 6.9 (see also Fig. 1 in [66]), follows the relation

$$E_{CN}^* = E_{c.m.} + Q_{in} = |Q_{out}(T)| + TKE(T) + TXE(T).$$
(6.19)

Here Q_{in} is positive (or negative) and hence would add to (or subtract from) entrance channel energy $E_{c.m.}$. If Q_{out} were positive, it would instead add on left hand side of (6.19) to the CN excitation energy E_{CN}^* . The E_{CN}^* is related to CN temperature T (in MeV) as

$$E_{CN}^* = (A/a)T^2 - T, (6.20)$$

with a = 8 - 10, depending on mass A of the CN.

- (iii) the neck parameter $\varepsilon = 1$ for touching configurations ($R = R_1 + R_2$), and hence a neck length parameter ΔR (defined later) is introduced (see Fig. 6.9).
- (iv) both the coplanar ($\phi = 0^{\circ}$) and non-coplanar ($\phi \neq 0^{\circ}$) nuclei are considered [81–83].

For the de-coupled η - and R-motions, in terms of partial waves, the DCM defines the fragment formation or CN-decay cross section as [64, 66–74].

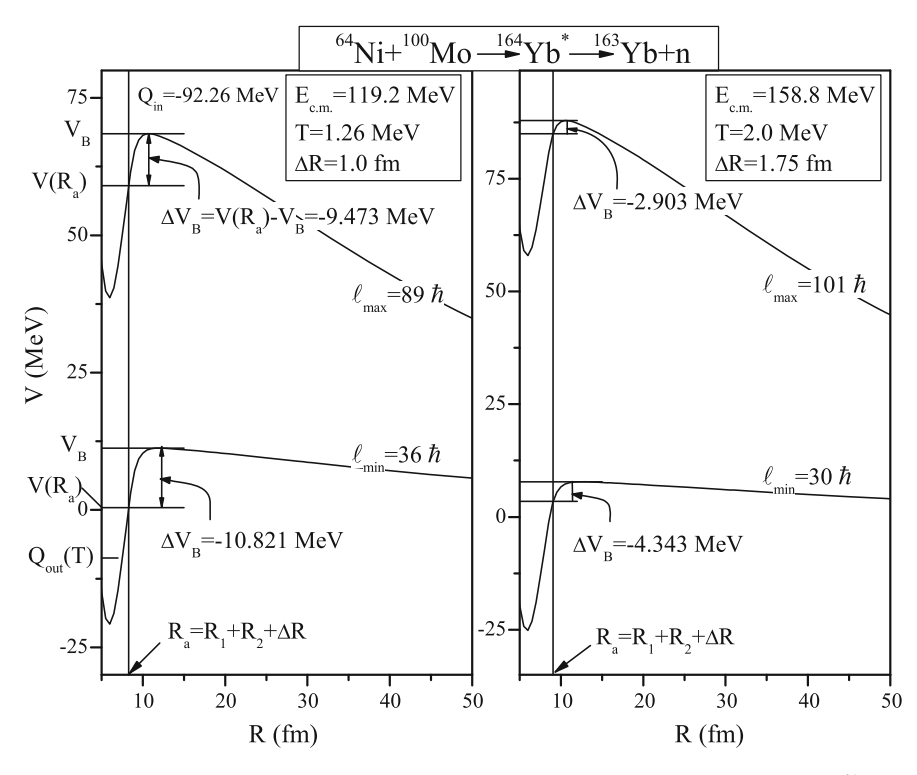


Fig. 6.9 The T and ℓ dependent scattering potentials V(R), illustrated for $^{64}\text{Ni} + ^{100}\text{Mo} \rightarrow ^{164}\text{Yb}^* \rightarrow ^{163}\text{Yb} + n$, at two different ℓ and T (equivalently, $E_{c.m.}$) values. The potential for each ℓ is calculated by using $V(R, T, \ell) = V_c(T) + V_P(T) + V_\ell(T)$, normalized to exit channel T-dependent binding energies $B_L(T) + B_H(T)$, each defined as $B(T) = V_{LDM}(T) + \delta U(T)$. The decay path, defined by $V(R_a, \ell) = Q_{eff}(T, \ell)$ for each ℓ is shown to begin at $R_a = R_1 + R_2 + \Delta R$ for the ℓ_{min} value. The definition of "barrier lowering" $\Delta V_B = V(R_a) - V_B$ is also shown in this figure for both the ℓ_{min} and ℓ_{max} values. This figure is taken from our published work in Ref. [73]

$$\sigma = \sum_{\ell=0}^{\ell_{max}} \sigma_{\ell} = \frac{\pi}{k^2} \sum_{\ell=0}^{\ell_{max}} (2\ell+1) P_0 P; \quad k = \sqrt{\frac{2\mu E_{c.m.}}{\hbar^2}}.$$
 (6.21)

Here, the penetrability P refers to R-motion, and the pre-formation probability P_0 to η -motion, both depending on ℓ , T, $\beta_{\lambda i}$, θ_i and ϕ . Here, $\mu = [A_1A_2/(A_1+A_2)]m = \frac{1}{4}Am(1-\eta^2)$ is the reduced mass with m as the nucleon mass, and ℓ_{max} , the maximum angular momentum, to be defined later.

Apparently, for s-wave ($\ell = 0$ case),

$$\sigma_0 = \frac{\pi}{k^2} P_0 P,\tag{6.22}$$

equivalently, the g.s. (T = 0) decay constant

$$\lambda = v_0 P_0 P$$
 or decay half-life $T_{1/2} = ln2/\lambda$, (6.23)

with v_0 as the barrier assault frequency, giving the g.s. decay constant or decay half-life in PCM. In other words, σ_0 in DCM and λ in PCM differ through a constant only. Thus, both the cluster-daughter system in PCM and the complex fragments (like LPs, IMFs and ff) in DCM are treated as the dynamical collective mass motion of the *preformed clusters or fragments* through the barrier. The structure information of the CN enters the model via the preformation probabilities P_0 (also known as the spectroscopic factors) of the fragments.

Furthermore, the same formula (6.21) is also applicable [68] to the (competing) non-compound, quasi-fission decay channel σ_{qf} or, equivalently [84], the capture cross-section $\sigma_{capture}$, where $P_0=1$ for the *incoming channel* since the target and projectile nuclei can be considered to have not yet lost their identity [85]. Let me remind here that (6.21) for $P_0=1$ is the well known (ℓ summed up explicitly) Wong formula [86] where, in its approximately ℓ -summed form, the barrier position R_B and barrier height $V(R_B)$ refer to the $\ell=0$ values. The role of explicit ℓ -summation in Wong formula is also studied recently by the author and collaborators [87].

 P_0 is the solution of stationary Schrödinger equation in η , at a fixed $R = R_a$, the first turning point(s) of the penetration path(s) shown in Fig. 6.9 for different ℓ values,

$$\left\{ -\frac{\hbar^2}{2\sqrt{B_{\eta\eta}}} \frac{\partial}{\partial \eta} \frac{1}{\sqrt{B_{\eta\eta}}} \frac{\partial}{\partial \eta} + V(R, \eta, T) \right\} \psi^{\nu}(\eta) = E^{\nu} \psi^{\nu}(\eta), \tag{6.24}$$

with v = 0, 1, 2, 3... referring to ground-state (v = 0) and excited-states solutions. Then, the probability

$$P_0(A_i) = |\psi(\eta(A_i))|^2 \sqrt{B_{\eta\eta}} \frac{2}{A},$$
 (6.25)

where for a Boltzmann-like function

$$|\psi|^2 = \sum_{v=0}^{\infty} |\psi^v|^2 \exp(-E^v/T).$$
 (6.26)

For the position $R = R_a$, the first turning point where P_0 is calculated, in the case of the decay of a hot CN, we use the postulate [88–92],

$$R_{a}(T) = R_{1}(\alpha_{1}, T) + R_{2}(\alpha_{2}, T) + \Delta R(\eta, T),$$

= $R_{t}(\alpha, \eta, T) + \Delta R(\eta, T),$ (6.27)

with radius vectors

$$R_i(\alpha_i, T) = R_{0i}(T) \left[1 + \sum_{\lambda} \beta_{\lambda i} Y_{\lambda}^{(0)}(\alpha_i) \right]$$
 (6.28)

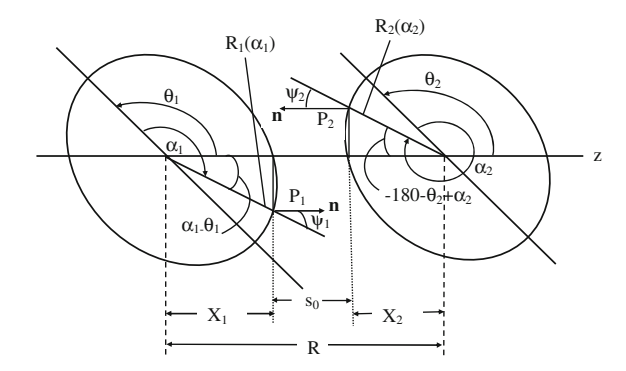


Fig. 6.10 Schematic configuration of two unequal axially symmetric deformed, oriented nuclei, lying in the same plane (azimuthal angle $\phi = 0^{\circ}$) for various θ_1 and θ_2 values in the range 0° –180°. The θ_i are measured anti-clockwise from the colliding axis and the angle α_i in the clockwise from the symmetry axis. This figure is taken from our published work in Ref. [83]

and the temperature-dependent nuclear radii $R_{0i}(T)$ for the equivalent spherical nuclei [93],

$$R_{0i} = [1.28A_i^{1/3} - 0.76 + 0.8A_i^{-1/3}](1 + 0.0007T^2).$$
 (6.29)

For the definition of angles α_i , θ_i , etc., see Fig. 6.10. In R_a above, $\Delta R(\eta, T)$ is the neck-length parameter that assimilates the deformation and neck formation effects between two nuclei, introduced within the extended model of Gupta and collaborators [50, 94, 95]. This method of introducing a neck-length parameter ΔR is similar to that used in both the scission-point [96] and saddle-point [97, 98] statistical fission models. Also, we use the Süsmann central radii $C_i = R_i - b^2/R_i$ (in fm), where the surface thickness parameter (in fm) [93] is

$$b(T) = 0.99(1 + 0.009T^2). (6.30)$$

The choice of parameter R_a [equivalently, ΔR in (6.27)], for the best fit to the data (on emission of LPs), allows us to relate in a simple way the $V(R_a, \ell)$ to the top of the barrier $V_B(\ell)$ for each ℓ , by defining their difference $\Delta V_B(\ell)$ as the effective "lowering of the barrier"

$$\Delta V_R(\ell) = V(R_a, \ell) - V_R(\ell). \tag{6.31}$$

Note, ΔV_B for each ℓ is defined as a negative quantity since the actually used barrier is effectively lowered. This is illustrated in Fig. 6.9 for ℓ_{min} and ℓ_{max} values, whose values are fixed for the light-particles (here xn, x=1-4) cross section $\sum_x \sigma_{xn}(\ell) \to 0$ and the penetrability starts to contribute, i.e., $\sigma_{ER} > 10^{-9}$ mb and $P_{xn} > 10^{-9}$ for the example studied [73]. Thus, fitting parameter ΔR controls "barrier lowering" ΔV_B .

Note from Fig. 6.9 (or, from Fig. 1 in [66]), that $\Delta R(\eta, T)$ depends on the total kinetic energy TKE(T). The corresponding potential $V(R_a)$ acts like an effective

Q value, Q_{eff} , for the decay of the hot CN at temperature T, to two exit-channel fragments observed in g.s. (T = 0), defined by

$$Q_{eff}(T) = B(T) - [B_1(T=0) + B_2(T=0)]$$

= $TKE(T) = V(R_a(T)).$ (6.32)

Here B's are the respective binding energies.

Equation (6.32) above, could apparently be achieved only by emitting some light particle(s), like n, p, α , or γ -rays, of energy

$$E_x = B(T) - B(0) = Q_{eff}(T) - Q_{out}(T=0)$$

= $TKE(T) - TKE(T=0)$ (6.33)

which is zero for the g.s. (T=0) decay, the case of exotic Cluster Radioactivity, treated within PCM. Note that the second equality in (6.33) is not defined for a negative $Q_{out}(T=0)$ system since the negative TKE(T=0) has no meaning. Apparently, (6.33) w.r.t (6.32) suggests that the emission of light-particles starts early in the decay process. The fact that exit channel fragments in (6.32) are obtained in the ground-state with TKE(T=0), can be seen by calculating $E_{CN}^* - E_x$:

$$E_{CN}^* - E_x = |Q_{out}(T)| + TKE(T = 0) + TXE(T),$$
 (6.34)

where, excitation energy TXE(T) is used in the secondary emission of light particles from the fragments, which are otherwise in their g.s. with TKE(T=0) in the radial motion, not treated here. Instead, we compare our calculations with the primary pre-secondary-evaporation fragment emission data [98, 99]. Thus, by defining $Q_{eff}(T)$ as in (6.32), via T-dependent binding energies, DCM becomes a parameter free [66], non-statistical dynamical treatment of the complete decay of hot and rotating CN, where the LPs emission are treated at par with the IMFs and ff decays.

The collective fragmentation potential $V(R, \eta, T)$ in (6.24), that brings in the structure effects of the CN in to the formalism, is calculated according to the Strutinsky renormalization procedure $(B = V_{LDM} + \delta U)$, using the T-dependent liquid drop model energy $V_{LDM}(T)$ of Davidson et al. [100], and the "empirical" shell corrections δU of Myers and Swiatecki [101], denoted $\delta U(MS)$, for spherical nuclei, also made T-dependent to vanish exponentially with $T_0 = 1.5$ MeV [102]. Then, including also the T-dependence in nuclear proximity V_P , Coulomb V_C , and ℓ -dependent potential V_ℓ ,

$$V(R, \eta, T) = \sum_{i=1}^{2} [V_{LDM}(A_i, Z_i, T)] + \sum_{i=1}^{2} [\delta U_i] exp\left(-\frac{T^2}{T_0^2}\right) + V_P(R, A_i, \beta_{\lambda i}, \theta_i, \phi, T) + V_C(R, Z_i, \beta_{\lambda i}, \theta_i, \phi, T) + V_\ell(R, A_i, \beta_{\lambda i}, \theta_i, \phi, T).$$
(6.35)

where V_P , V_C and V_ℓ are also for deformed, oriented nuclei. The $V_{LDM}(T)$ of [100] in Eq. (6.35), based on the semi-empirical mass formula of Seeger [103], is

$$V_{LDM}(A, Z, T) = \alpha(T)A + \beta(T)A^{\frac{2}{3}} + \left(\gamma(T) - \frac{\eta(T)}{A^{\frac{1}{3}}}\right) \left(\frac{I^{2} + 2 \mid I \mid}{A}\right) + \frac{Z^{2}}{r_{0}(T)A^{\frac{1}{3}}} \left(1 - \frac{0.7636}{Z^{\frac{2}{3}}} - \frac{2.29}{\left[r_{0}(T)A^{\frac{1}{3}}\right]^{2}}\right) + \delta(T)\frac{f(Z, A)}{A^{\frac{3}{4}}},$$
(6.36)

where

$$I = a_a(Z - N), \quad a_a = 1,$$

and, respectively, for even-even, even-odd, and odd-odd nuclei,

$$f(Z,A) = (-1,0,1).$$

Seeger [103] fitted the constants from ground-state (T = 0) binding energies of some 488 nuclei available at that time (in 1961) and obtained:

$$\begin{array}{ll} \alpha(0) = -16.11\, {\rm MeV}, & \beta(0) = 20.21\, {\rm MeV}, & \gamma(0) = 20.65\, {\rm MeV}, \\ \eta(0) = 48.00\, {\rm MeV}, & \end{array}$$

with the pairing energy term $\delta(0) = 33.0 \text{ MeV}$, from Ref. [104]. These constants, however, are now readjusted by some of us [68, 89, 90] to give the new experimental binding energies, by defining $B_{Expt} = V_{LDM}(T=0) + \delta U$. This was first done [89, 90] for the 1995 Audi Wapstra Tables [105] of binding energies, and more recently [68] for the 2003 Tables [106]. (Note: In the Appendix of [89] and Eq. (8) of [90], a_a =0.5, instead of a_a =1 used in [68]). Whenever the B_{Expt} were not available, the theoretical estimates of Möller et al. [107] are used. Since the aim here was simply to include the T-dependence on experimental binding energies, and not to obtain the new parameter set of V_{LDM} , simply the bulk constant $\alpha(0)$ and the proton–neutron asymmetry constant a_a are readjusted to obtain B_{Expt} within <1.5 MeV. The temperature dependencies of the constants of V_{LDM} in (6.36) are given in Fig. 1 of [100]. Note that the missing deformation effects in spherical shell corrections δU (discussed below) are also included here to some extent in the V_{LDM} since we essentially use the experimental binding energies split in to two contributions, V_{LDM} and δU , for reasons of adding the T-dependence on it.

The above procedure is particularly useful for light nuclei where shell corrections δU could not be defined on any shell model basis, and is also applied to neutron- and proton-clusters, xn and xp, x=1, 2, 3,..., by defining [108, 109] the binding energy of a cluster with x-neutrons as x times the binding energy of one-neutron (equivalently, the mass excess $\Delta m_n = 8.0713$ MeV), i.e.,

$$B(A_2 = xn) = x\Delta m_n, (6.37)$$

and the same for proton-clusters, as

$$B(A_2 = xp) = x\Delta m_p - a_c A_2^{5/3}, \tag{6.38}$$

with $\Delta m_p = 7.2880$ MeV, the one-proton mass excess or equivalently the binding energy of one-proton. $a_c = 0.7053$ MeV [101], with the additional term due to a_c acting as the disruptive Coulomb energy $(=-a_c(Z_2^2/A_2^{1/3}))$ between the x protons (here $x = A_2 = Z_2$). Since it is difficult to define the volume and surface of n- or p-clusters, the T-dependence of their binding energy is included here only via the shell correction term δU , and not in V_{LDM} . The above definitions of n- or p-clusters mean that the nucleons in these clusters are taken to be unbound, following the model of Hansen and Jonson [110], the few-body theories [111] or as is suggested by some experiments [112, 113].

The shell effects δU , added to the liquid drop energy in (6.35), are the empirically obtained ones of Myers and Swiatecki [101], for spherical shapes, as

$$\delta U = C \left[\frac{F(N) + F(Z)}{(A/2)^{\frac{2}{3}}} - cA^{\frac{1}{3}} \right]$$
 (6.39)

with

$$F(X) = \frac{3}{5} \left(\frac{M_i^{\frac{5}{3}} - M_{i-1}^{\frac{5}{3}}}{M_i - M_{i-1}} \right) (X - M_{i-1}) - \frac{3}{5} \left(X^{\frac{5}{3}} - M_{i-1}^{\frac{5}{3}} \right),$$

where, X = N or Z, and $M_{i-1} < X < M_i$. M_i are the magic numbers 2, 8, 14 (or 20), 28, 50, 82, 126 and 184 for both neutrons and protons. The constants are C = 5.8 MeV and c = 0.26 MeV. The shell effects are also known to be strongly dependent on the deformation of the nucleus, but a similar prescription for deformed nuclei is not available. However, as already stated above, the missing deformation effects in spherical δU are included to some extent in the re-adjusted constants of V_{LDM} .

The proximity potential V_P for deformed and oriented nuclei in the same plane $(\phi=0^\circ)$ [81], including T-dependence, is

$$V_P(s_0(T)) = 4\pi \bar{R}(T)\gamma b(T)\Phi(s_0(T)),$$
 (6.40)

where the nuclear surface thickness b(T) is defined in (6.30), and the surface energy constant

$$\gamma = 0.9517 \left[1 - 1.7826 \left(\frac{N-Z}{A} \right)^2 \right] \text{MeV fm}^{-2}.$$

 $\Phi(s_0)$ in (6.40) is the universal function, which is independent of the shapes of nuclei or the geometry of nuclear system but depends on the minimum separation distance $s_0(T)$ (see Fig. 6.10), and is given as

$$\Phi(s_0) = \begin{cases} -\frac{1}{2}(s_0 - 2.54)^2 - 0.0852(s_0 - 2.54)^3 \\ -3.437exp(-\frac{s_0}{0.75}) \end{cases}$$
(6.41)

respectively, for $s_0(T) \le 1.2511$ and ≥ 1.2511 , with the s_0 (in units of b), given as (see Fig. 6.10)

$$s_0 = R - X_1 - X_2$$

= $R - R_1(\alpha_1, T)cos(\theta_1 - \alpha_1) - R_2(\alpha_2, T)cos(180 + \theta_2 - \alpha_2),$ (6.42)

minimized in α_i . The minimization conditions, known as normal vector conditions, are

$$\tan(\theta_1 - \alpha_1) = -\frac{R'_1(\alpha_1)}{R_1(\alpha_1)}$$

$$\tan(180 + \theta_2 - \alpha_2) = -\frac{R'_2(\alpha_2)}{R_2(\alpha_2)},$$
(6.43)

the $R'_i(\alpha_i)$ being the first order derivative of $R_i(\alpha_i)$ with respect to α_i . Finally, $\bar{R}(T)$, the mean curvature radius, characterizing s_0 , i.e., the points of closest approach for nuclei lying in the same plane ($\phi = 0^{\circ}$), is

$$\frac{1}{\bar{R}^2} = \frac{1}{R_{11}R_{12}} + \frac{1}{R_{21}R_{22}} + \frac{1}{R_{11}R_{22}} + \frac{1}{R_{21}R_{12}},\tag{6.44}$$

where R_{i1} and R_{i2} are the principal radii of curvatures at the points P_1 and P_2 in Fig. 6.10. For explicit expressions of R_{i1} and R_{i2} and other details on generalized proximity potential for co-planar nuclei, see Ref. [81].

Next, for non-coplanar nuclei ($\phi \neq 0^{\circ}$) we use the same formalism as for $\phi = 0^{\circ}$ above, but by replacing for the out-of-plane nucleus (i = 1 or 2) the corresponding radius parameter $R_i(\alpha_i)$ with the projected radius parameter $R_i^P(\alpha_i)$ in the definitions of both the mean curvature radius \bar{R} and the shortest distance s_0 [82]. The $R_i^P(\alpha_i)$ is determined by defining, for the out-of-plane nucleus, two principal planes X'Z' and Y'Z', respectively, with radius parameters $R_i(\alpha_i)$ and $R_j(\delta_j)$, such that their projections into the plane (XZ) of the other nucleus are (see Fig. 6.11)

$$R_i^P(\alpha_i) = R_i(\alpha_i) \cos \phi \quad i = 1 \text{ or } 2, \tag{6.45}$$

and

$$R_i^P(\delta_j) = R_j(\delta_j) \cos(\phi - \delta_j) \quad j = i = 1 \text{ or } 2.$$
 (6.46)

Then, maximizing $R_i(\delta_i)$ in angle δ_i , we get

$$R_{i}^{P}(\alpha_{i}) = R_{i}^{P}(\alpha_{i} = 0^{0}) + R_{i}^{P}(\alpha_{i} \neq 0^{0})$$

$$= R_{i}^{P}(\delta_{i}^{max}) + R_{i}(\alpha_{i} \neq 0^{0}) \cos \phi,$$
(6.47)

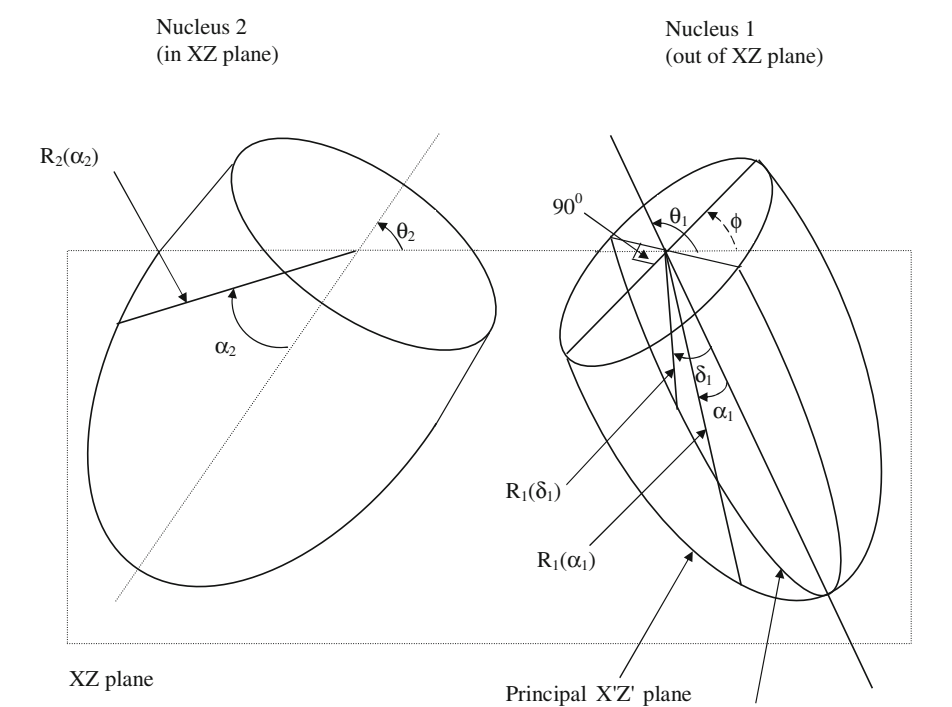


Fig. 6.11 Schematic configuration of two unequal nuclei, oriented at angles θ_1 and θ_2 , with their principal planes X'Z' and XZ making an azimuthal angle ϕ . The angle ϕ is shown by a dashed line, since it is meant to be an angle coming out of the plane XZ. Nucleus 2 is in XZ plane and for the out-of-plane nucleus 1, another principal plane Y'Z', perpendicular to X'Z', is also shown. The angles θ_i are measured anti-clockwise from the collision Z axis, and the angles α_i (and δ_i) are measured in the clockwise direction from the nuclear symmetry axis. Only lower-halves of the two nuclei are depicted. This figure is taken from our published work in Ref. [82]

with δ_i^{max} given by the condition (for fixed ϕ),

$$\tan(\phi - \delta_j) = -\frac{R'_j(\delta_j)}{R_i(\delta_j)}.$$
(6.48)

Principal Y'Z' plane

Thus, the ϕ -dependence of projected radius vector $R_i^P(\alpha_i)$ is also contained in maximized $R_j^P(\delta_j^{max})$. For further details, see [82]. Then, for nuclear proximity potential, denoting by V_P^{12} the potential for the nucleus 1 to be out-of-plane, and by V_P^{21} for the nucleus 2 to be out-of-plane, the effective nuclear proximity potential

$$V_P = \frac{1}{2} [V_P^{12} + V_P^{21}]. \tag{6.49}$$

The Coulomb potential for two non-overlapping nuclei, with higher multi-pole deformations included by following [86], is given as

$$V_{C} = \frac{Z_{1}Z_{2}e^{2}}{R} + 3Z_{1}Z_{2}e^{2} \sum_{\lambda,i=1,2} \frac{1}{2\lambda+1} \frac{R_{i}^{\lambda}(\alpha_{i},T)}{R^{\lambda+1}} Y_{\lambda}^{(0)}(\theta_{i}) \times \left[\beta_{\lambda i} + \frac{4}{7}\beta_{\lambda i}^{2} Y_{\lambda}^{(0)}(\theta_{i})\right],$$
(6.50)

and the angular momentum dependent potential,

$$V_{\ell}(T) = \frac{\hbar^2 \ell(\ell+1)}{2I(T)},\tag{6.51}$$

where, in complete sticking limit, the moment of inertia

$$I(T) = I_S(T) = \mu R^2 + \frac{2}{5} A_1 m R_1^2(\alpha_1, T) + \frac{2}{5} A_2 m R_2^2(\alpha_2, T).$$
 (6.52)

In general, the experimental numbers for ℓ are based on the moment of inertia calculated in non-sticking limit $I = I_{NS} = \mu R^2$. This use of reduced mass alone corresponds to the supposition of prompt emission of fragments, and there are also other possible hypotheses besides sticking limit as the rolling or sliding conditions. We find that the sticking limit I_S used here is more appropriate for the proximity potential (nuclear surfaces ≤ 2 fm apart) which has consequences for the limiting ℓ value to be much larger. For nuclear collisions, use of larger ℓ_{max} value due to relatively larger magnitude of I_S is shown [68, 72] to result in reduction of the nuclear surface separation distance ΔR , and vice-versa for I_{NS} .

The mass parameters $B_{\eta\eta}$, entering (6.24) for the P_0 calculations, are the smooth classical hydrodynamical masses [114], since at large T values the shell effects are almost completely washed out. For smaller T (<1.5 MeV), in principle, the shell corrected masses, like the Cranking masses, should be used, but for simplicity we use the smooth classical hydrodynamical masses. In the classical hydro-dynamical model, for touching spheres ($C_t = C_1 + C_2$),

$$B_{\eta\eta} = \frac{AmC_t^2(T)}{4} \left[\frac{v_t(T)(1+\beta(T))}{v_c(T)} - 1 \right]$$
 (6.53)

with

$$\beta(T) = \frac{R_c(T)}{2C_t(T)} \left[2 - \frac{R_c(T)}{C_1(T)} - \frac{R_c(T)}{C_2(T)} \right]$$

$$v_c(T) = \pi R_c^2(T) C_t(T) \quad R_c(T) = 0.4 C_2(T)$$

and $v_t = v_1 + v_2$, the total conserved volume. Also, $C_2 \ll C_1$ and $R_c(\neq 0)$ is the radius of a cylinder of length C_t , whose existence is assumed for a homogeneous radial flow of mass between the two spherical fragments. Note that here all radial or radial-dependent quantities are T-dependent.

The penetrability P in (6.21) is the WKB integral,

$$P = exp\left[-\frac{2}{\hbar} \int_{R_a}^{R_b} \left\{2\mu[V(R,T) - Q_{eff}]\right\}^{1/2} dR\right], \tag{6.54}$$

solved analytically [48, 49], with the second turning point R_b (see Fig. 6.9 or Fig. 1 in [66]) satisfying

$$V(R_a) = V(R_b) = Q_{eff} = TKE(T). \tag{6.55}$$

This means that $V(R_a, \ell)$ acts like an effective Q value, $Q_{eff}(T, \ell)$, given by the total kinetic energy TKE(T). As ℓ value increases, the $Q_{eff}(T)$ (=TKE(T)) increases and hence $V(R_a, \ell)$ increases. Thus, R_a acts like a parametriough $\Delta R(\eta, T)$, and we define that R_a is the same for all ℓ values, i.e., $V(R_a) = Q_{eff}(T, \ell = 0)$. This is required because we do not know how to add the ℓ -effects in binding energies. Alternatively, we define R_a and hence $\Delta R(\eta, T)$ in terms of the T-dependent binding energies B(T), as in (6.32).

Finally, the $\ell = \ell_{max}$ value in (6.21) is either the critical ℓ_c value, in terms of the bombarding energy $E_{c.m.}$, the reduced mass μ and the first turning point R_a of the entrance channel η_{in} , given by

$$\ell_c = R_a \sqrt{2\mu [E_{c.m.} - V(R_a, \eta_{in}, \ell = 0)]}/\hbar, \tag{6.56}$$

or, alternatively, it could be fixed for the vanishing of fusion barrier of the incoming channel, called ℓ_{fus} , or else the ℓ value where the light-particle cross section $\sigma_{LP} \rightarrow 0$. This could also be taken as a variable parameter [98, 99].

6.3.1 The Preformed Cluster Model for Exotic Cluster Radioactivity

After about three decades of its theoretical prediction [115] and a quarter of century of first experimental observation [116], the novel process of cluster radioactivity is now well established, and the experimental data on cluster-decay half-lives and its branching ratios *w.r.t.* α-decays up to the year 2007 are nicely reviewed in [65] (for an older review, see, e.g., [54], and for a discussion on fission model, see [56]). Spontaneous emissions of some thirteen to fourteen neutron-rich clusters, ranging from ¹⁴C up to ³⁴Si, are measured for the ground-state decays of certain parent nuclei in trans-lead region, specifically from ²²¹Fr to ²⁴²Cm. More recently, ¹⁴C and ¹⁵N decays of ²²³Ac and ³⁴Si decay of ²³⁸U are also observed [117, 118]. The study of ²²³Ac decays is interesting for the odd–even effects of both the daughter and the cluster, which were earlier observed for a few cases only, like ¹⁴C from ²²¹Fr and ²²⁵Ac or ²³F from ²³¹Pa. Since the cluster decay process is observed with a magic or near magic daughter

nucleus always (see, e.g., the review [54]), ¹⁵N decay of ²²³Ac is expected to be more favored because the daughter nucleus is a doubly magic ²⁰⁸Pb nucleus in this case, but only the upper limits are measured. Similarly, for ²³⁸U parent, ³⁴Si is the heaviest cluster observed to-date, but in this case with the longest decay half-life ever measured. Also, an un-successful attempt on decay of ¹¹⁴Ba is made [119], which was first proposed theoretically [45, 46, 55, 56, 57, 120] on the basis of doubly magic ¹⁰⁰Sn daughter. The cluster decay process is well understood by taking explicit contributions of shell effects in to account (see, e.g., the review [54]).

Recently, the PCM of Gupta and collaborators [48–51] has been extended to include the deformation and orientation effects of nuclei [52, 53]. In addition to shell effects, deformations and orientations of nuclei are also found to play important role in the cluster decay process. The calculated decay half-lives for the observed cluster decays are generally in good agreement with the measured values for calculations performed with quadrupole deformations β_2 alone and "optimum" orientations of cold elongated configurations [83]. In some cases, however, particularly for the observed ¹⁴C decays of ²²¹Fr, ^{221–224, 226}Ra, and ²²⁵Ac, the inclusion of multi-pole deformations up to hexadecapole β_4 is found essential for comparison with data. Note that the measured β_4 values are not available in general, and hence the available higher multi-pole deformations values from calculations [107], particularly for clusters in mass region $16 \le A \le 26$, need be used with caution. Another important result of this recent study [52, 53] is to show that the decay half-life depends strongly on the Q value of the decay process, and hence the two quantities (the decay half-life and Q value) should be measured together in the same experiment.

In the following, we first present some details of the PCM, with effects of deformation and orientation of nuclei included. Our calculations for ground-state decays of all the observed cases, illustrated mainly for newly observed ¹⁴C and ¹⁵N decays of ²²³Ac and ³⁴Si decay of ²³⁸U are then presented, first for the use of nuclear proximity potential, and then for the RMF-densities based folding potential.

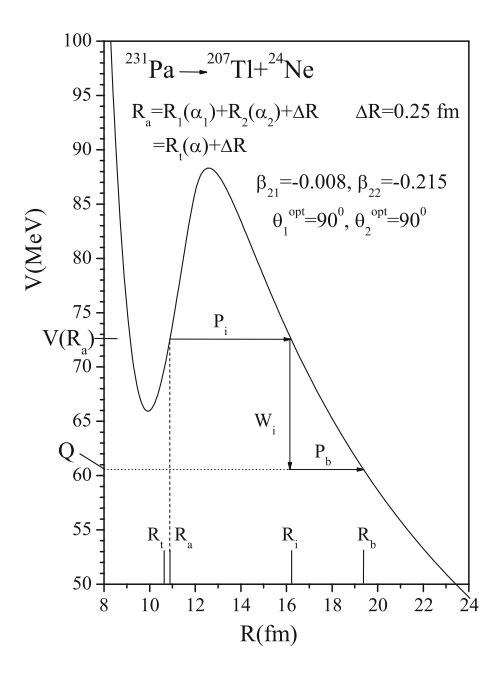
6.3.1.1 The Preformed Cluster Model

As per (6.23) above, the decay constant, and hence the decay half-life time, in PCM is defined as,

$$\lambda = v_0 P_0 P, \quad T_{1/2} = \frac{\ln 2}{\lambda},$$
(6.57)

which means to say that in PCM the clusters are taken to be preborn in the parent nucleus at $R = R_a$ with preformation probability P_0 , which hit the barrier with impinging frequency v_0 , and penetrate it with penetrability P, as is illustrated in Fig. 6.12. If R_0 is the radius of parent nucleus and $E_2 = \frac{1}{2}\mu v^2$ is the kinetic energy of the emitted cluster, v_0 is given by

Fig. 6.12 The scattering potential for the decay 231 Pa \rightarrow 207 Tl + 24 Ne, with both the daughter and cluster taken with quadrupole deformations β_{2i} alone, and with "optimum" cold orientation angles $\theta_i^{opt.}$ of Table 1 in Ref. [83]. For the decay path, note that the tunneling begins at $R = R_a$ and terminates at $R = R_b$, with $V(R_b) = Q$ value, since exotic cluster radioactivity is a ground-state decay. This figure is taken from our published work in Ref. [53]



$$v_0 = \frac{v}{R_0} = \frac{(2E_2/\mu)^{1/2}}{R_0}. (6.58)$$

 v_0 is nearly constant $\sim 10^{21} \, \mathrm{s}^{-1}$ for all the observed cluster decays. In terms of the (positive) Q value of decay, since both the emitted cluster and daughter nuclei are produced in ground state, the entire Q value is the total kinetic energy, $(Q = E_1 + E_2)$, available for the decay process, which is shared between the two fragments, such that for the emitted cluster (1 and 2 stand, respectively, for daughter and cluster),

$$E_2 = \frac{A_1}{A}Q (6.59)$$

and, $E_1(=Q-E_2)$ is the recoil energy of daughter nucleus. P_0 and P are calculated, as described above for the DCM, within the well-known quantum mechanical fragmentation theory (QMFT) [76, 77, 83], with effects of deformation and orientation degrees of freedom included. Apparently, the relative separation coordinate R refers to the transfer of positive Q value to the total kinetic energy $(E_1 + E_2)$ of two nuclei, determining the penetrability P, and the preformation factor P_0 , referring to mass asymmetry coordinate η , is determined only for the ground-state solution (v = 0, T = 0). Also, for ground-state decays, $\ell = 0$ is a good approximation [54].

6.3.1.2 Applications of the PCM Based on Nuclear Proximity Potential

The model is applied to all the measured cluster radioactive decays [54, 65], considering both the cases of spherical and deformed nuclei. A compilation of our results, together with the best fitted R_a values, is given in Table 6.3, taken mostly from our published work in Ref. [53]. The experimental data on decay half-life times are from Refs. [54, 65]. The frequency $v_0 \sim 10^{21} \, \mathrm{s}^{-1}$, fixed for each case. $Q_{M.N.}$ refers to Q value based on the calculated binding energies of Möller et al. [107], used to fit the R_a (equivalently, ΔR) value. The experimental Q value, $Q_{Expt.}$, is also given for comparison, calculated from the measured binding energies [106], wherever available. The limiting value of calculated $\log_{10}T_{1/2}(s) < 30$, in view of the present experiments.

Table 6.3 shows that the deformations and orientations of nuclei modify the decay half-life considerably, which is due to the change in both the preformation probability P_0 and tunneling probability P. As P_0 is a relative quantity, its calculation depends on all the possible fragmentations of the parent nucleus, whose potential is illustrated in Fig. 6.13 for ²²³Ac and ²³⁸U parent nuclei at $R = R_a$, for both the cases of all fragments taken as spheres (open circles) and with quadrupole deformation β_2 and optimum orientations (solid circles). The value of R_a (equivalently, the neck-length parameter ΔR) is for the best fit to the data in Table 6.3. Here, the case of higher multi-pole deformations, i.e., quadrupole, octupole and hexadecapole deformations $(\beta_2, \beta_3, \beta_4)$ taken in to account is not plotted since it leads to deeper minima for many un-observed clusters (like in Figure 2(b) of [52]), which get ruled out by the calculated penetrability P (small P). The important point to note in Fig. 6.13 is that, with deformation and orientation effects included, many new minima are predicted in ²²³Ac for cluster mass $A_2 > 25$, and in ²³⁸U for $A_2 > 40$. The changes in fragmentation potentials are evident even for lighter mass clusters, which would change the relative P_0 significantly, as is illustrated in Fig. 6.14 for the 238 U parent. P_0 are, in general, larger for the case of deformations and orientations included. Furthermore, P_0 for clusters like ²⁶Ne, ³⁰Mg and ³²Mg are as large as for the observed cluster ³⁴Si. However, with the contribution of P included, all clusters other than ³⁴Si get ruled out due to their smaller penetrability P, or large calculated decay half-life times $T_{1/2}(s)$, as is shown in Table 6.4 where the $T_{1/2}(s)$'s are calculated for the four clusters (26 Ne, 30 Mg, 32 Mg and 34 Si) preformed in 238 U with larger P_0 in the neighborhood of the observed 34 Si cluster. Interesting enough, though P_0 for, say, 32 Mg is larger than for ³⁴Si (see Fig. 6.14) or the minimum in fragmentation potential is deeper for ³²Mg as compared to that for ³⁴Si (see Fig. 6.13, lower panel), the decay half-life time is the smallest for the ³⁴Si decay for ²³⁸U, in complete agreement with the experimental data for the case of quadrupole deformed nuclei. This happens because P for 32 Mg is much smaller than for 34 Si such that the product P_0P is smaller, and hence $T_{1/2}(s)$ larger for ^{32}Mg .

Finally, the role of Q value is illustrated in Fig. 6.15, which depicts the comparison of experimentally observed and our calculated $T_{1/2}(s)$ for ³⁴Si emitted from ²³⁸U parent nucleus, as a function of Q value, for both the cases of nuclei taken as

Table 6.3 Half-life times and other characteristic quantities for various cluster decays, calculated on PCM for spherical, β_2 alone and $\beta_2 - \beta_4$ deformed nuclei, and "optimum" orientations of cold decay process [83]

Decay	$Q_{Expt.}$	R_a	$Q_{M.N.}$	Half-lives $log_{10}T_{1/2}(s)$			Expt.
				PCM			
				Sph.	β_2	β_2 , β_3 , β_4	
$^{114}\text{Ba} \rightarrow {}^{12}\text{C} + {}^{102}\text{Sn}$	18.98	$R_t + 1.7$	21.4	5.43	6.89	6.83	>4.10
221 Fr $\rightarrow {}^{14}$ C + 207 Tl	31.29	$R_t + 1.21$	31.09	19.80	17.76	14.41	14.52
221 Ra $\rightarrow {}^{14}$ C + 207 Pb	32.40	$R_t + 1.18$	32.13	18.87	17.55	13.37	13.39
222 Ra $\rightarrow {}^{14}$ C + 208 Pb	33.05	$R_t + 1.26$	32.47	17.36	15.89	11.20	11.01
223 Ra $\rightarrow {}^{14}$ C + 209 Pb	31.83	$R_t + 1.15$	31.89	19.83	18.51	15.03	15.06
224 Ra $\rightarrow {}^{14}$ C + 210 Pb	30.54	$R_t + 1.23$	31.16	19.95	18.98	15.74	15.86
226 Ra $\rightarrow {}^{14}$ C + 212 Pb	28.20	$R_t + 1.01$	28.61	26.60	25.35	21.20	21.19
223 Ac $\rightarrow {}^{14}$ C + 209 Bi	33.07	$R_t + 0.65$	32.89	12.98	12.02		12.60
223 Ac $\rightarrow ^{15}$ N + 208 Pb	39.47	$R_t + 0.65$	38.97	15.54	14.73		>14.76
225 Ac $\rightarrow {}^{14}$ C + 211 Bi	30.48	$R_t + 1.1$	31.08	20.94	19.78	17.15	17.16
$^{226}\text{Th} \rightarrow {}^{14}\text{C} + {}^{212}\text{Po}$	30.55	$R_t + 0.65$	31.70	20.9	19.56	24.34	>15.3
$^{226}\text{Th} \rightarrow {}^{18}\text{O} + {}^{208}\text{Pb}$	45.73	$R_t + 0.65$	47.55	20.10	18.35		>15.3
$^{228}\text{Th} \rightarrow ^{20}\text{O} + ^{208}\text{Pb}$	44.72	$R_t + 0.5$	45.91	21.72	20.40		20.87
230 Th $\rightarrow {}^{24}$ Ne + 206 Hg	57.76	$R_t + 0.5$	58.57	24.06	24.19		24.61
231 Pa $\rightarrow ^{23}$ F + 208 Pb	51.84	$R_t + 0.25$	50.81	28.73	27.38	9.28	26.02
231 Pa $\rightarrow ^{24}$ Ne + 207 Tl	60.41	$R_t + 0.25$	60.59	25.86	23.07		23.23
$^{230}\text{U} \rightarrow ^{22}\text{Ne} + ^{208}\text{Pb}$	61.39	R_t	61.69	26.15	19.41	1.27	19.57
$^{230}\text{U} \rightarrow ^{24}\text{Ne} + ^{206}\text{Pb}$	61.35	R_t	61.81	25.35	23.07		>18.2
$^{232}\text{U} \rightarrow ^{24}\text{Ne} + ^{208}\text{Pb}$	62.31	R_t	62.03	24.04	22.88	11.19	21.05
$^{232}\text{U} \rightarrow ^{28}\text{Mg} + ^{204}\text{Hg}$	74.32	R_t	74.06	28.78	20.31	21.23	>22.26
$^{233}\text{U} \rightarrow ^{24}\text{Ne} + ^{209}\text{Pb}$	60.49	$R_t + 0.5$	60.55	24.06	24.57		24.84
$^{233}\text{U} \rightarrow ^{28}\text{Mg} + ^{205}\text{Hg}$	74.23	$R_t + 0.5$	74.42	24.06	19.22	15.02	>27.59
$^{234}\text{U} \rightarrow ^{24}\text{Ne} + ^{210}\text{Pb}$	58.83	$R_t + 0.5$	59.30	24.06	25.99		25.92
$^{234}\text{U} \rightarrow ^{26}\text{Ne} + ^{208}\text{Pb}$	59.47	$R_t + 0.5$	58.65	28.00	26.49	16.15	25.92
$^{234}\text{U} \rightarrow ^{28}\text{Mg} + ^{206}\text{Hg}$	74.11	$R_t + 0.5$	74.22	26.72	18.44	15.02	25.54
$^{235}U \rightarrow ^{28}Mg + ^{207}Hg$	72.16	R_t	72.62	30.08	26.19		> 28.09
$^{236}\text{U} \rightarrow ^{28}\text{Mg} + ^{208}\text{Hg}$	70.56	R_t	71.33	31.53	25.55		27.58
$^{238}\text{U} \rightarrow ^{34}\text{Si} + ^{204}\text{Pt}$	84.65 ^a	$R_t + 0.215$	85.82	30.37	29.04		29.04
$^{237}\text{Np} \rightarrow ^{30}\text{Mg} + ^{207}\text{Tl}$	74.82	R_t	75.18	28.12	26.44		>26.93
236 Pu $\rightarrow ^{28}$ Mg + 208 Pb	79.67	$R_t - 0.4$	78.75	28.7	21.57		21.67
238 Pu $\rightarrow ^{28}$ Mg + 210 Pb	75.91	$R_t - 0.4$	75.83	33.7	25.40		25.70
238 Pu $\rightarrow ^{30}$ Mg + 208 Pb	76.82	$R_t + 0.5$	76.82	24.77	21.87		25.70
238 Pu $\rightarrow ^{32}$ Si $+ ^{206}$ Hg	91.19	$R_t + 0.5$	90.03		25.16		25.27
$^{241}\text{Am} \rightarrow ^{34}\text{Si} + ^{207}\text{Tl}$	93.93	R_t	93.62	25.23	22.83		>22.71
$^{242}\text{Cm} \rightarrow ^{34}\text{Si} + ^{208}\text{Pb}$	96.51	R_t	95.78	23.59	21.47		23.24
252 Cf $\rightarrow {}^{46}$ Ar + 206 Hg	126.70	R_t	126.19	20.29	19.66	28.07	>15.89
252 Cf $\rightarrow {}^{48}$ Ca + 204 Pt		R_t	138.33	21.56			>15.89
$^{252}Cf \rightarrow {}^{50}Ca + {}^{202}Pt$	138.20	R_t	137.71	21.76	20.06		>15.89

The table is from [53], with improved calculations for various 14 C decays a Q value used by the authors of experimental work [118]

Fig. 6.13 The fragmentation potentials for the parent nuclei ²²³Ac and ²³⁸U, taking all possible fragments as spheres (*open circles*) and with quadrupole deformation $β_2$ and cold "optimum" orientations $θ_i^{opt.}$ of Table 1 in Ref. [83] (*solid circles*) at the best fitted ΔR values. This figure is taken from our published work in Ref. [53]

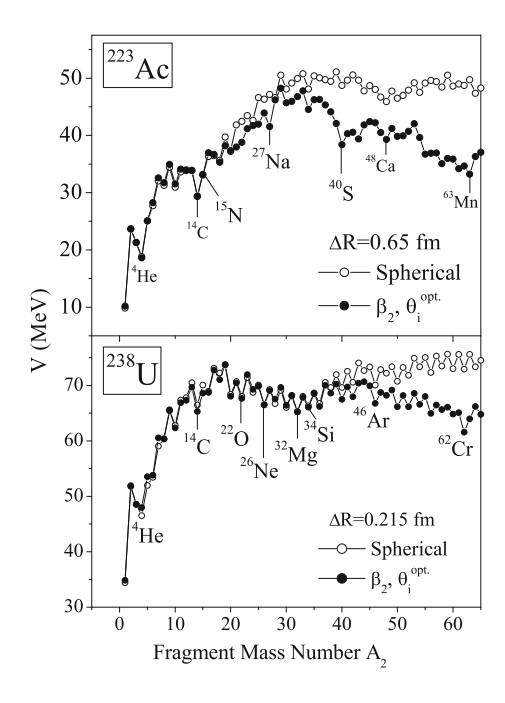
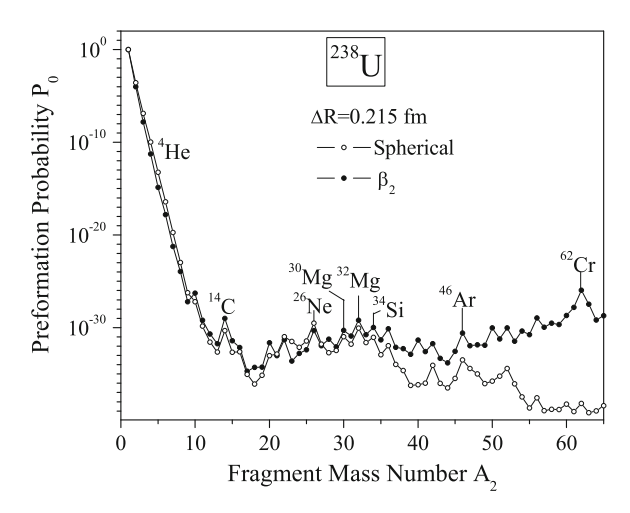


Fig. 6.14 The preformation probability P_0 for the parent nucleus 238 U alone taking all possible fragments as spheres (open circles) and with quadrupole deformation β_2 and cold "optimum" orientations $\theta_i^{opt.}$ of Table 1 in Ref. [83] (solid circles) at the best fitted ΔR value. This figure is taken from our published work in Ref. [53]



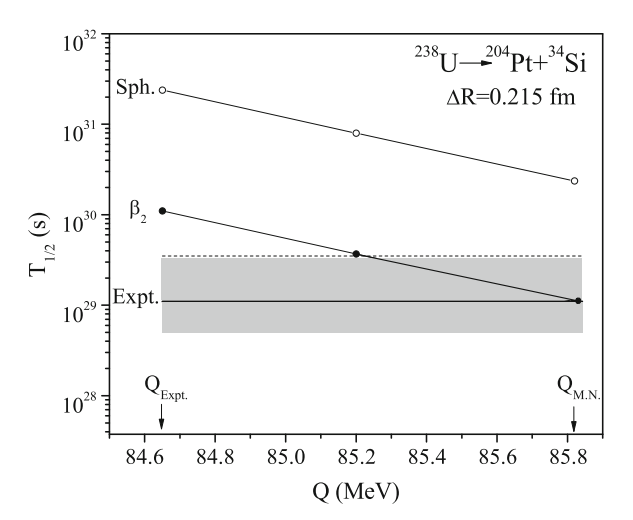
spherical or with β_2 deformation. Apparently, the ³⁴Si decay of ²³⁸U parent shows a clear preference for the case of quadrupole deformed nuclei. The only parameter of model is the neck-length ΔR , fitted for $Q_{M.N.}$, the Q value based on binding energies of Möller et al. [107]. We have also shown in Fig. 6.15, the Q value $(Q_{Expt.})$ used by the authors of the experimental work [118], indicating large differences with $Q_{M.N.}$ value.

51 Hom C, carculate	a on i civi					
Decay	$Q_{M.N.}$	Half-life time $T_{1/2}$ (s)				
		PCM		Expt.		
		Sph.	β_2			
$^{238}\text{U} \rightarrow ^{26}\text{Ne} + ^{212}\text{Pb}$	54.14	1.74×10^{38}	1.83×10^{37}	_		
$^{238}\text{U} \rightarrow ^{30}\text{Mg} + ^{208}\text{Hg}$	70.90	6.56×10^{32}	1.18×10^{31}	_		
$^{238}\text{U} \rightarrow ^{32}\text{Mg} + ^{206}\text{Hg}$	70.39	1.26×10^{33}	9.90×10^{31}	_		
$^{238}\text{U} \rightarrow ^{34}\text{Si} + ^{204}\text{Pt}$	85.82	2.36×10^{30}	1.09×10^{29}	$(1.1 \pm {}^{2.4}_{0.6}) \times 10^{29}$		

Table 6.4 The cluster-decay half-lives for some best preformed clusters in the neighborhood of ³⁴Si from ²³⁸U. calculated on PCM

The experimental data is known only for ³⁴ Si decay of ²³⁸ U [118]. This Table is taken from our published work in Ref. [53]

Fig. 6.15 Comparison between the experimentally observed and calculated half-life time for the 34 Si cluster emitted from the 238 U, as a function of the Q value. The $Q_{M.N.}$ and $Q_{Expt.}$ refer, respectively to Q values calculated by using the binding energies from Möller et al. [107] and used by the authors of experimental work [118]. This figure is taken from our published work in Ref. [53]

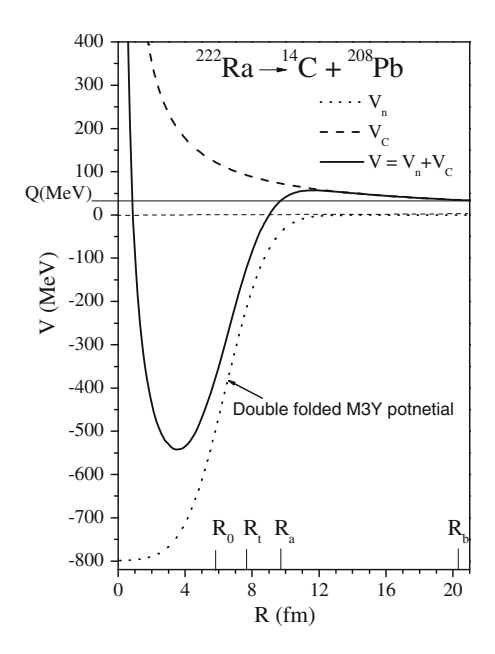


Summarizing the results of this section, in cluster radioactivity, not only the shell effects but also the deformations and orientations of decay fragments are found to be important. Except for the 14 C decays of 221 Fr, the $^{221-224,\ 226}$ Ra isotope, and 225 Ac, where higher multi-pole deformations up to β_4 are found essential, and the 25 Ne and 28 Mg decays of 234 U and 30 Mg emitted from 238 Pu, where spherical considerations seem to do better, the quadrupole deformation β_2 alone seem to give the results of experiments. Also, 34 Si decay of 242 Cm via 208 Pb daughter gives a better result for spherical nuclei since both the cluster and daughter are spherical nuclei. The cluster-decay process is shown to occur, in general, at or near the touching configuration (ΔR is zero or small).

6.3.1.3 Applications of the PCM using the RMF-Densities Based Folding Potential

We have applied these considerations [14, 15] to cluster radioactive decays having the doubly magic ²⁰⁸Pb as the daughter nucleus always. Figure 6.16 illustrates the

Fig. 6.16 The double-folded M3Y + Ex potential V_n based on RMF (spherical) densities, the Coulomb V_C and the total interaction potential V as a function of radial separation R between the cluster ¹⁴C and daughter nucleus ²⁰⁸Pb. The Q value is based on experimental binding energies [106]. This figure is from our publication in Ref. [14, 15], where by mistake M3Y + Ex is termed as DDM3Y



double-folded M3Y + Exchange term (M3Y + Ex) nuclear interaction potential $V_n(R)$ (dotted line), together with the the total interaction potential $V(R) = V_n(R) + V_C$ (solid line), using the RMF calculated densities for spherical cluster ¹⁴C and daughter ²⁰⁸Pb nuclei in the decay of ²²²Ra. The interaction potential V(R) is used to calculate the WKB penetration probability P, which in turn is used to calculate the "empirical" preformation factor P_0^{emp} by comparing within PCM the product Pv_0 with experimental value of decay constant λ_{expt} (or decay half-life T_{12}^{expt}), as follows

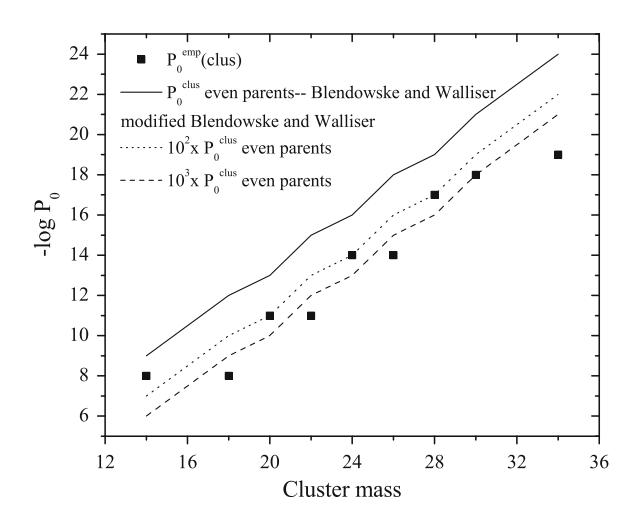
$$P_0^{emp} = \frac{\lambda_{expt}}{Pv_0} = \frac{1}{Pv_0} \frac{\ln 2}{T_{1/2}^{expt}}.$$
 (6.60)

The calculated $-\log P_0^{emp}$ as a function of cluster mass, for all the considered parents, is shown in Fig. 6.17, and compared with the simple phenomenological formula proposed by Blendowske and Walliser [121] for the light clusters $(A_2 \le 28)$, as

$$P_0^{clus} = \left(P_0^{\alpha}\right)^{\frac{A_{clus}-1}{3}},\tag{6.61}$$

with α -preformation factor $P_0^{\alpha}=6.3\times 10^{-3}$ for decay from even parents, since only even parents are considered here (solid line). For odd parents, $P_0^{\alpha}=3.2\times 10^{-3}$, not used here. Interesting enough, the two calculations match within two to three orders of magnitude (compare solid squares with dotted and dashed lines), which is a reasonable comparison. The important point is that the microscopic RMF formalism, combined with a realistic nucleon–nucleon

Fig. 6.17 The "empirically" estimated preformation probability $-\log P_0^{emp}$ on RMF-densities based folding potential (*solid squares*) as a function of cluster mass for even parents decaying in each case to 208 Pb daughter, compared with the predictions of Blendowske and Walliser [121] formula (*solid line*) and its scaled values (*dotted and dashed lines*). This figure is based on our publication [14, 15]



interaction, supports the concept of preformation of clusters in nuclei, introduced first by Gupta and collaborators in PCM for cluster radioactive decays [48, 49].

6.3.2 Applications of the DCM Using Nuclear Proximity Potential

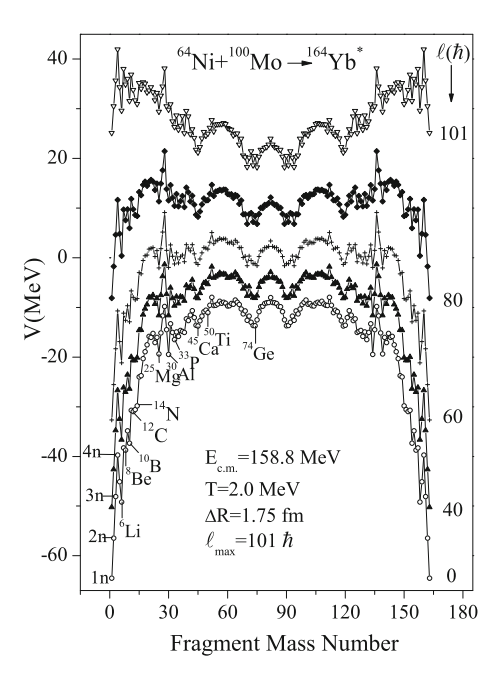
Applications of the DCM are successfully made to the emission of IMFs in light and medium mass compound systems, namely, $^{48}\text{Cr}^*$ [67], $^{56}\text{Ni}^*$ [66] and $^{58}\text{Ni} + ^{58}\text{Ni} \rightarrow ^{116}\text{Ba}^*$ [64], fission (and quasi-fission) of $^{246}\text{Bk}^*$ [68] formed in $^{11}\text{B} + ^{235}\text{U}$ and $^{14}\text{N} + ^{232}\text{Th}$ reactions. A small qf component in $^{11}\text{B} + ^{235}\text{U} \rightarrow$ ²⁴⁶Bk* decay at higher incident energies [68], and an additional ff window of $14 \le Z \le 28$ in 116 Ba* [64] are predicted. This later result is now supported by the recent IMFs and ff data [122] for decays of heavier 118,122Ba* nuclei studied via ^{78,82}Kr + ⁴⁰Ca reactions, and reasonably well interpreted more recently on DCM [71]. Also, the three processes of ER, ff and qf are well understood on DCM in reactions $^{48}\text{Ca} + ^{244}\text{Pu} \rightarrow ^{292}114^*$ [72] and $^{48}\text{Ca} + ^{154}\text{Sm} \rightarrow ^{202}\text{Pb}^*$ [74]. In the $^{48}\text{Ca} + ^{244}\text{Pu}$ reaction or, in general, $^{48}\text{Ca} + ^{48}\text{Ca} + ^{48}\text{Ca$ plus-actinide reactions, the ER cross-sections are very small (in pb) compared to σ_{ff} and σ_{af} (in mb), and that $\sigma_{qf} > \sigma_{ff}$ by at least one order of magnitude, almost independent of CN excitation energy E_{CN}^* . On the other hand, in the ⁴⁸Ca + ¹⁵⁴Sm reaction the three decay processes (ER, ff and qf) are quite comparable (all in mb) at low excitation energies, ER being the most dominant, but at higher excitation energies the ff becomes most probable followed by ER and qf. However, at (nearly) the same excitation energy, but at above barrier energies, no qf component is measured in another 48Ca + 144Sm reaction. perhaps because both the nuclei are then spherical. A divergent application of

the DCM to the ⁴⁸Ca + ²³⁸U reaction data is also made [123] for establishing the island of stability for superheavy elements to be at Z = 114, 120 or 126 with N = 184. This calculation, made for only the ER data, seems to support such an island to be centered around Z = 126, N = 184, though the preliminary results of the extended calculation to include the complete data on all the three processes (ER, ff and qf) prefer Z = 120, N = 184 a bit over Z = 126, N = 184. Both the calculations for 48 Ca-plus-actinide reactions [72, 123] are based on the "compact' orientations of nuclei [124, 125]. Furthermore, the dominant ER cross-sections for the $^{64}Ni + ^{100}Mo \rightarrow ^{164}Yb^*$ reaction are also nicely explained on the DCM [73] with the "barrier lowering" ΔV_R given in a straightforward way through the neck-length parameter ΔR for LPs (see, Fig. 6.9). Also, the ff cross-sections are predicted on DCM at above-barrier energies only, which are compatible with the statistical model (CASCADE) estimates. In the following, we illustrate our DCM results for σ_{ER} data [126, 127] on ⁶⁴Ni + ¹⁰⁰Mo and ⁶⁴Ni + ⁶⁴Ni reactions. A brief report on ⁶⁴Ni + ⁶⁴Ni reaction is recently published in Ref. [128, 129]. For ⁶⁴Ni + ¹⁰⁰Mo and ⁶⁴Ni + ⁶⁴Ni reactions (so also for ⁵⁸Ni + ⁵⁸Ni reaction),

at energies far below the Coulomb barrier, the unexpected behavior of the measured ER cross-sections σ_{ER} , has challenged the theoretical models to explain the, so called, fusion hindrance phenomenon in coupled-channels calculations (ccc) [126, 127]. In ccc, however, this phenomenon could simply be sensitive to the sofar unobserved, hence not-included, high-lying states. The only acceptable explanation so-far is the "modification of the shape of the inner part of the potential in terms of a thicker barrier and shallower pocket" [130, 131]. As already stated above, this property of "lowering of barriers" at sub-barrier energies is also supported by the DCM calculations [73, 128, 129], discussed below. Very recently, we have also shown [87] that the Wong formula, with its ℓ -summation carried out explicitly, also shows the necessity of "barrier modification" at subbarrier energies, which can be affected empirically in terms of either the "barrier lowering" ΔV_B^{emp} or "barrier narrowing" $\Delta \hbar \omega^{emp}$ via the curvature constant. In fact, the ℓ -summed Wong formula is shown [87] to be a special case of the DCM, more suitable for the capture or quasi-fission cross-sections where the incoming nuclei keep their identity ($P_0 = 1$).

In the following, first of all, we look for the energetically favored LPs ($A_2 \leq 4$), and the other, not yet observed, mass fragmentations (ff = IMFs + HMFs + SF, where HMFs are the heavy mass IMFs) predicted by the DCM for the compound nucleus 164 Yb* formed in 64 Ni + 100 Mo reaction. This is illustrated in Fig. 6.18 at different ℓ values, minimized in charge coordinate η_Z , calculated for a fixed T=2.0 MeV and $R=R_a=R_t+\Delta R, \Delta R=1.75$ fm, corresponding to the 64 Ni + 100 Mo reaction at the highest center-of-mass energy $E_{c.m.}=158.8$ MeV [126, 127]. The deformations $\beta_{\lambda i}$ of two fragments are included up to hexadecapole ($\lambda=2,3,4; i=1,2$), taken from [107], and the orientations are "optimum" orientations θ_i^{opt} of "hot fusion" process, taken from Table 1 of [83]. The R_a value (equivalently, ΔR) is chosen for the best fit to available ER data and ℓ_{min} and ℓ_{max}

Fig. 6.18 The fragmentation potential V(A) at different ℓ values, defined by (6.35), for the energetically favored fragmentation of the compound system ¹⁶⁴Yb*, formed in ⁶⁴Ni + ¹⁰⁰Mo reaction at a fixed temperature T = 2.0 MeV (equivalently, $E_{cm} = 158.8 \text{ MeV}$) and $\Delta R = 1.75$ fm. For mass four fragment, the binding energy of the energetically favored fragment ⁴H is replaced by that of the observed 4n in view of the experiments. This figure is from our earlier work published in Ref. [73]



values are 32 and 101 \hbar , respectively, for $\sigma_{ER}(\ell) > 10^{-9}$ mb or equivalently $P_0(\ell) > 10^{-7}$ and $P(\ell) > 10^{-9}$ (see, Figs. 4–6 in [73]).

Figure 6.19 depicts the results of both the neck-length parameter ΔR as a function of $E_{c.m.}$, and the fusion excitation functions, $\sigma_{ER}(E_{c.m.})$. We notice in Fig. 6.19a that $\Delta R(E_{c.m.})$ or, equivalently, $\Delta R(T)$ vary smoothly from abovebarrier to below-barrier energies, always remaining within the range of proximity potential (<2 fm). Figure 6.19b shows that the fitting of the data is rather very good for the case of LPs = 1n-4n, and the deformations and orientations of nuclei included. Similar results are obtained for the DCM calculations of ⁶⁴Ni + ⁶⁴Ni reaction [128, 129]. This means to say that the physics of problem, now contained in $\Delta R(T)$, suggest no new phenomenon, like the hindrance in ccc, at below barrier energies different from near and above barrier energies. However, the "barrier lowering" $\Delta V_B(T)$, associated with hindrance phenomenon [130, 131], is contained in fitted $\Delta R(T)$ values, and is again a smooth function, as is discussed below. In Fig. 6.19b, we have also plotted the cases of (i) LPs consisting of only 2n, 3n and 4n, and (ii) nuclei taken to be spheres, using in each case the same relative separation R_a as are obtained in Fig. 6.19a for deformed, oriented nuclei. Evidently, both the cases under-estimate σ_{ER} , thereby stressing the importance of including both the 1n-emission and the deformation and orientation effects of nuclei in the present study on DCM.

Figure 6.20 shows the DCM calculated index of "barrier lowering" ΔV_B as a function of $E_{c.m.}$ for the ⁶⁴Ni + ¹⁰⁰Mo and ⁶⁴Ni + ⁶⁴Ni reactions. The actual barrier height V_B at each ℓ and the barrier height $V(R_a)$ actually used for fitting the ER data are as marked in Fig. 6.9 with barrier position R_a obtained as in Fig. 6.19a (solid

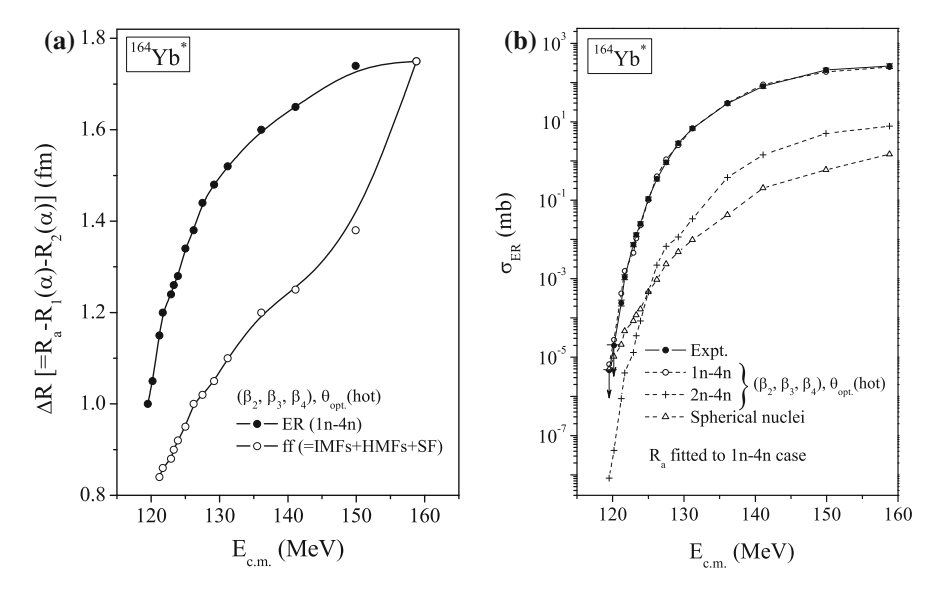


Fig. 6.19 a Variation of ΔR with $E_{c.m.}$ obtained for the best fit to fusion ER data [126, 127], taking LPs as xn (x = 1 - 4) (solid circles with solid line), and to fusion–fission CASCADE data [126, 127] (open circles with solid line, not discussed here). **b** Calculated σ_{ER} for 64 Ni + 100 Mo \rightarrow 164 Yb* reaction as a function of $E_{c.m.}$, compared with experimental data [126, 127]. Different cases of LPs as xn (x = 1 - 4 or 2–4), and of deformed, oriented and spherical shapes are considered. This figure is from our earlier work published in Ref. [73]

circles with solid line) at each c.m. energy. The ER is considered to be due to 1n-4n. Only the case of $\ell = \ell_{max}$ is shown here in Fig. 6.20, and an exactly the same result is evident from Fig. 6.9 at $\ell = \ell_{min}$. The interesting result of Fig. 6.20 is that barrier modification is minimum and nearly constant for the top two/three energies, and it becomes larger and larger as the c.m. energy decreases and goes below the barrier energy. In other words, at the above barrier energies, where barrier modification should be zero, we get a small (~2 MeV) constant value, and the modification is large of $\sim 8-10$ MeV for 64 Ni + 100 Mo, and $\sim 10-12$ MeV in the case of ⁶⁴Ni + ⁶⁴Ni, for below barrier energies. The important point is that the "lowering of barrier" at sub-barrier energies is obtained in a natural way by the fitting procedure of the DCM. It may be reminded here that in DCM, the ΔR and ℓ_{max} are related quantities, and our choice of ΔR is good within $\ell_{max} \pm 1$, fixed for LPs cross-section $\sigma_{ER}(\ell) \rightarrow 0$ at $\ell = \ell_{max}$ value. Another factor responsible for the success of DCM in fitting the ER cross-section is the varying preformation factor P_0 , not included in models such as the Statistical models and the Wong formula.

Summarizing the results of this section, the DCM gives a complete description of the fusion–evaporation (ER) cross-section, with additional contributions of intermediate mass fragments (IMFs), heavy mass fragments (HMFs), near symmetric fission (nSF) and symmetric fission (SF) processes, or the dominantly fission or quasi-fission decays of hot and rotating nuclei. The only parameter of the

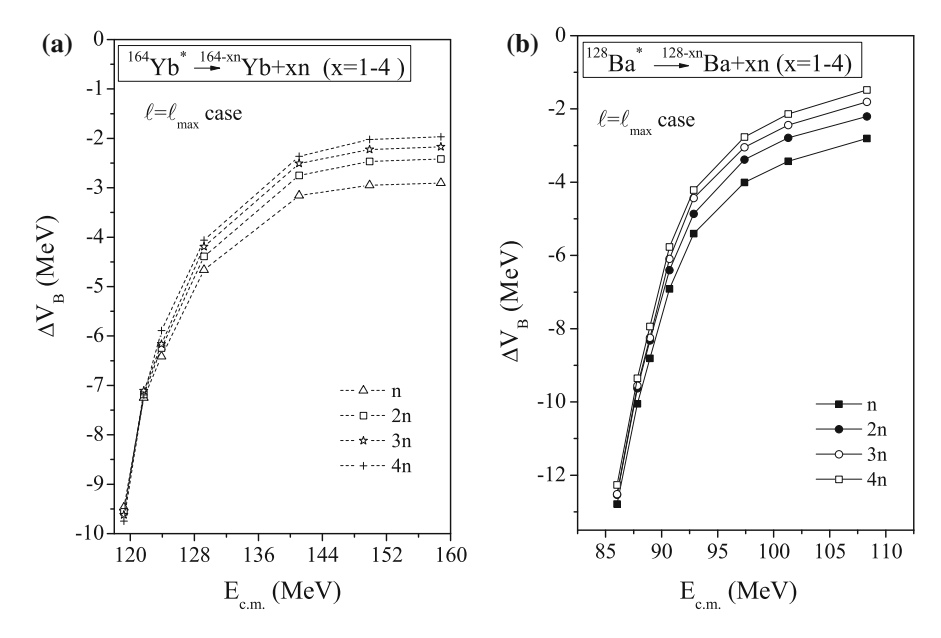


Fig. 6.20 The barrier lowering ΔV_B in DCM, as defined by (6.31), as a function of $E_{c.m.}$ for the case of $\ell = \ell_{max}$ in ${\bf a}^{64}{\rm Ni} + {}^{100}{\rm Mo} \rightarrow {}^{164}{\rm Yb}^*$, taken from our work published in Ref. [73], and ${\bf b}^{64}{\rm Ni} + {}^{64}{\rm Ni} \rightarrow {}^{128}{\rm Ba}^*$ reaction, taken from our work published in Ref. [128, 129]

model is the neck-length ΔR , shown to be related to "barrier lowering" of the proximity potential in the present calculations, similar to one in M3Y double-folding potential of Refs. [130, 131], for reactions known for the hindrance effect in coupled-channel calculations.

6.4 Conclusions

We have seen that clustering is a general characteristic of nuclei, and mean field approaches, without any extra clustering correlations, are suitable to study this phenomenon (more so for RMF than for SHF). Also, the dynamical collective clusterization process is shown to be an effective alternative to the statistical Hauser–Feshbach analysis and/or fission models for the decay of hot and rotating compound nucleus. The dynamical collective clusterization model, the DCM, is given as an extension of the preformed cluster model (PCM) propounded for exotic cluster radioactivity. Thus, the concept of preformed clusters in spontaneously decaying nuclei or excited compound systems was introduced, which seems to be supported now equally well by the rigorous RMF model.

Acknowledgments Thanks are due to many of my collaborators, such as Profs. W. Greiner, C. Beck, S.K. Patra, P. Arumugam and P.D. Stevenson, and many students who have helped me

in understanding much of the physics associated with the problem of Collective cluterization in stable and radioactive nuclei as well as in excited compound systems.

References

- 1. H. Feldmeier, J. Schnack, Rev. Mod. Phys. 72, 655 (2000)
- 2. Y. Kanada-En'Yo, H. Horiuchi, Prog. Theor. Phys. Suppl. 142, 205 (2001)
- 3. Y. Kanada-En'Yo, M. Kimura: Lecture Notes in Physics, Chapter in this Series
- 4. H. Horiuchi: Lecture Notes in Physics, Chapter in this Series
- 5. Y. Kanada-En'Yo, M. Kimura, H. Horiuchi, C. R. Physique 4, 497 (2003)
- 6. T. Neff, H. Feldmeier (2003). Arxiv:nucl-th/0312130; and references therein
- 7. Y. Kanada-En'Yo, H. Horiuchi, Phys. Rev. C 52, 628 (2004)
- 8. Y. Kanada-En'Yo, H. Horiuchi, Phys. Rev. C 52, 647 (2004)
- 9. Y. Kanada-En'Yo (2004). Arxiv:nucl-th/0409056
- 10. P. Arumugam, B.K. Sharma, S.K. Patra, R.K. Gupta, Phys. Rev. C 71, 064308 (2005)
- R.K. Gupta, S.K. Patra, P.D. Stevenson, C. Beck, W. Greiner, J. Phys. G Nucl. Part. Phys. 35, 075106 (2008)
- 12. M. Bhuyan, S.K. Patra, P. Arumugam, R.K. Gupta, Bhubaneswar-Chandigarh Preprint (2009), to be published
- S.K. Patra, R.K. Gupta, B.K. Sharma, P.D. Stevenson, W. Greiner, J. Phys. G Nucl. Part. Phys. 34, 2073 (2007)
- B.B. Singh, S.K. Patra, M. Bhuyan, R.K. Gupta, Proc. Indian Nuclear Science National Seminar on "Nuclear Technology for Sustainable Development", Thapar University, Patiala, Oct.10–11, 2009
- 15. B.B. Singh, S.K. Patra, M. Bhuyan, R.K. Gupta, *Proc. International Symp. on Nucl. Phys.* (isnp2009), BARC, Mumbai, December 8–12, 2009
- B.K. Sharma, P. Arumugam, S.K. Patra, P.D. Stevenson, R.K. Gupta, W. Greiner, J. Phys. G Nucl. Part. Phys. 32, L1 (2006)
- 17. R.K. Gupta, S.K. Patra, P.D. Stevenson, W. Greiner, Int. J. Mod. Phys. E 16, 1721 (2007)
- 18. P.-G. Reinhard, M. Rufa, J. Maruhn, W. Greiner, J. Friedrich, Z. Phys. A 323, 13 (1986)
- M. Rufa, P.-G. Reinhard, J.A. Maruhn, W. Greiner, M.R. Strayer, Phys. Rev. C 38, 390 (1988)
- 20. Y.K. Gambhir, P. Ring, A. Thimet, Ann. Phys. (N.Y.) 198, 132 (1990)
- 21. C.J. Horowitz, B.D. Serot, Nucl. Phys. A 368, 503 (1981)
- 22. B.D. Serot, J.D. Walecka, Adv. Nucl. Phys. 16, 1 (1986)
- 23. B.D. Serot, Rep. Prog. Phys. 55, 1855 (1992)
- 24. J. Boguta, A.R. Bodmer, Nucl. Phys. A 292, 413 (1977)
- 25. S.K. Patra, C.R. Praharaj, Phys. Rev. C 44, 2552 (1991)
- 26. D. Vautherin, D.M. Brink, Phys. Rev. C 5, 626 (1972)
- S.K. Patra, R.K. Gupta, W. Greiner, in *Heavy Elements and Related New Phenomena*, vol. II, ed. by W. Greiner, R.K. Gupta, (World Scientific, Singapore, 1999), p. 994
- 28. G.A. Lalazissis, J. König, P. Ring, Phys. Rev. C 55, 540 (1997)
- 29. M.M. Sharma, P. Ring, Phys. Rev. C 44, 2524 (1992)
- 30. K. Rutz, J.A. Maruhn, P.-G. Reinhard, W. Greiner, Nucl. Phys. A 590, 680 (1995)
- M. Bender, K. Rutz, P.-G. Reinhard, J.A. Maruhn, W. Greiner, Phys. Rev. C 58, 2126 (1998)
- 32. P.-G. Reinhard and J.A. Maruhn, in *Heavy Element and Related Phenomena*, vol. I, chap. 8, ed., by W. Greiner, R. K. Gupta, (World Scientific, Singapore, 1999), p. 332
- 33. D.T. Khoa, W. Oertzen, H.G. Bohlen, Phys. Rev. C 49, 1652 (1994)
- 34. G.R. Satchler, W.G. Love, Phys. Rep. 55, 183 (1979)
- 35. A.M. Kobos, B.A. Brown, P.E. Hodgson, G.R. Satchler, A. Budzanowski, Nucl. Phys. A 384, 65 (1982)

- A.M. Kobos, B.A. Brown, P.E. Hodgson, G.R. Satchler, A. Budzanowski, Nucl. Phys. A 425, 205 (1984)
- 37. A.K. Chaudhuri, Nucl. Phys. A 449, 243 (1986)
- 38. D.N. Basu, J. Phys. G Nucl. Part. Phys. 29, 2079 (2003)
- 39. B.R. Fulton, Contemp. Phys. 40, 299 (1999)
- 40. J. Zhang, W.D.M. Rae, Nucl. Phys. A 564, 252 (1993)
- 41. H. Horiuchi, K. Ikeda, Y. Suzuki, Prog. Theor. Phys. Suppl. 52, 89 (1972)
- 42. J. Zhang, W.D.M. Rae, A.C. Merchant, Nucl. Phys. A 575, 61 (1994)
- 43. M. Seya, M. Kohno, S. Nagata, Prog. Theor. Phys. 65, 204 (1981)
- 44. R.K. Gupta, S. Singh, R.K. Puri, W. Scheid, Phys. Rev. C 47, 561 (1993)
- 45. S. Kumar, R.K. Gupta, Phys. Rev. C 49, 1922 (1994)
- 46. S. Kumar, D. Bir, R.K. Gupta, Phys. Rev. C **51**, 1762 (1995)
- 47. S. Kumar, J.S. Batra, R.K. Gupta, J. Phys. G Nucl. Part. Phys. 22, 215 (1996)
- R.K. Gupta, in Proceedings of the 5th International Conference on Nuclear Reaction Mechanisms, Varenna, Italy, ed. by E. Gadioli (Ricerca Scintifica Educazione Permanente, Italy) (1988), p. 416
- 49. S.S. Malik, R.K. Gupta, Phys. Rev. C **39**, 1992 (1989)
- 50. S. Kumar, R.K. Gupta, Phys. Rev. C 55, 218 (1997)
- R.K. Gupta, in *Heavy Elements and Related New Phenomena*, vol. II, ed. by W. Greiner,
 R.K. Gupta (World Scientific, Singapore, 1999), p. 731
- S.K. Arun, R.K. Gupta, B.B. Singh, S. Kanwar, M.K. Sharma, Phys. Rev. C 79, 064616 (2009)
- S.K. Arun, R.K. Gupta, S. Kanwar, B.B. Singh, M.K. Sharma, Phys. Rev. C 80, 034317 (2009)
- 54. R.K. Gupta, W. Greiner, Int. J. Mod. Phys. E **3**(Suppl.), 335 (1994)
- D.N. Poenaru, D. Schnabel, W. Greiner, D. Mazilu, R. Gherghescu, At. Data. Nucl. Data. Tables 48, 231 (1991)
- 56. D.N. Poenaru and W. Greiner, Lecture Notes in Physics, Chapter in this Series
- 57. D.N. Poenaru, W. Greiner, E. Hourani, Phys. Rev. C 51, 594 (1995)
- Yu.Ts. Oganessian, Yu.A. Lazarev, V.L. Mikheev, Yu.A. Muzychka, I.V. Shirokovsky, S.P. Tretyakova, V.K. Utyonkov, Z. Phys. A 349, 341 (1994)
- A. Guglielmetti, B. Blank, R. Bonetti, Z. James, H. Keller, R. Kirchner, O. Klepper, A. Piechaczek, A. Plochocki, G. Poli, P.B. Price, E. Roeckl, K. Schmidt, J. Szerypo, A.J. Westphal, Nucl. Phys. A 583, 867 (1995)
- J. Campo del Gomez, J.L. Charvet, A. D'Onofrio, R.L. Auble, J.R. Beene, M.L. Halbert, H.J. Kim, Phys. Rev. Lett. 61, 290 (1988)
- J. Campo del Gomez, R.L. Auble, J.R. Beene, M.L. Halbert, H.J. Kim, A. D'Onofrio, J.L. Charvet, Phys. Rev. C 43, 2689 (1991)
- 62. J. Campo del Gomez, C. Baktash, H.-Q. Jin, D. Rudolph, A. D'Onofrio, F. Terrasi, G. de Angelis, M. de Poli, C. Fahlander, A. Gadea, D.R. Napoli, Q. Pan, P. Spolaore, L. de Acuna, D. Bazzacco, S. Lunardi, P. Pavan, C. Rossi-Alvarez, A. Buscemi, R. Zanon, A. de Rosa, L. Campajola, M. La Commara, G. Inglima, V. Roca, M. Romano, M. Sandoli, M. Romoli, A. Ordine, D. Pierroutsakou, Phys. Rev. C 57, R457 (1998)
- 63. M. La Commara, J. Campo del Gomez, A. D'Onofrio, A. Gadea, M. Glogowski, P. Jarillo-Herrero, N. Belcari, R. Borcea, G. de Angelis, C. Fahlander, M. Gorska, H. Grawe, M. Hellström, R. Kirchner, M. Rejmund, V. Roca, E. Roeckl, M. Romano, K. Rykaczewski, K. Schmidt, F. Terrasi, Nucl. Phys. A 669, 43 (2000)
- R.K. Gupta, M. Balasubramaniam, R. Kumar, D. Singh, S.K. Arun, W. Greiner, J. Phys. G Nucl. Part. Phys. 32, 345 (2006)
- 65. R. Bonetti, A. Guglielmetti, Romanian Rep. Phys. 59, 301 (2007)
- R.K. Gupta, M. Balasubramaniam, R. Kumar, D. Singh, C. Beck, W. Greiner, Phys. Rev. C 71, 014601 (2005); and earlier references there in it
- 67. B.B. Singh, M.K. Sharma, R.K. Gupta, W. Greiner, Int. J. Mod. Phys. E 15, 699 (2006)
- 68. B.B. Singh, M.K. Sharma, R.K. Gupta, Phys. Rev. C 77, 054613 (2008)

 R.K. Gupta, S.K. Arun, D. Singh, R. Kumar, Niyti, S.K. Patra, P. Arumugam, B.K. Sharma, Int. J. Mod. Phys. E 17, 2244 (2008)

- 70. R.K. Gupta, S.K. Arun, R. Kumar, Niyti, Int. Rev. Phys. (IREPHY) 2, 369 (2008)
- 71. R. Kumar, R.K. Gupta, Phys. Rev. C **79**, 034602 (2009)
- 72. R.K. Gupta, Niyti, M. Manhas, S. Hofmann, W. Greiner, Int. J. Mod. Phys. E 18, 601 (2009)
- 73. S.K. Arun, R. Kumar, R.K. Gupta, J. Phys. G Nucl. Part. Phys. 36, 085105 (2009)
- S. Kanwar, M.K. Sharma, B.B. Singh, R.K. Gupta, W. Greiner, Int. J. Mod. Phys. E 18, 1453 (2009)
- 75. S.J. Sanders, A. Szanto de Toledo, C. Beck, Phys. Rep. 311, 487 (1999)
- 76. J. Maruhn, W. Greiner, Phys. Rev. Lett. 32, 548 (1974)
- 77. R.K. Gupta, W. Scheid, W. Greiner, Phys. Rev. Lett. 35, 353 (1975)
- 78. R.K. Gupta, Sov. J. Part. Nucl. 8, 289 (1977)
- 79. J.A. Maruhn, W. Greiner, W. Scheid, in *Heavy Ion Collisions*, vol. 2, chap. 6 ed. by R. Bock (North Holland, Amsterdam, 1988)
- 80. R.K. Gupta, W. Greiner, in *Heavy Elements and Related New Phenomena*, vol. I, ed. by W. Greiner, R.K. Gupta, (World Scientific, Singapore, 1999), p. 397, 536
- 81. R.K. Gupta, N. Singh, M. Manhas, Phys. Rev. C 70, 034608 (2004)
- 82. M. Manhas, R.K. Gupta, Phys. Rev. C 72, 024606 (2005)
- 83. R.K. Gupta, M. Balasubramaniam, R. Kumar, N. Singh, M. Manhas, W. Greiner, J. Phys. G Nucl. Part. Phys. 31, 631 (2005)
- 84. Yu.Ts. Oganessian et al., Phys. Rev. C 70, 064609 (2004)
- 85. M.G. Itkis et al., J. Nucl. Radiochem. Sci. 3, 57 (2002)
- 86. C.Y. Wong, Phys. Rev. Lett. **31**, 766 (1973)
- 87. R. Kumar, M. Bansal, S.K. Arun, R.K. Gupta, Phys. Rev. C 80, 034618 (2009)
- 88. R.K. Gupta, M. Balasubramaniam, C. Mazzocchi, M. La Commara, W. Scheid, Phys. Rev. C 65, 024601 (2002)
- R.K. Gupta, R. Kumar, N.K. Dhiman, M. Balasubramaniam, W. Scheid, C. Beck, Phys. Rev. C 68, 014610 (2003)
- M. Balasubramaniam, R. Kumar, R.K. Gupta, C. Beck, W. Scheid, J. Phys. G Nucl. Part. Phys. 29, 2703 (2003)
- 91. R.K. Gupta, Acta Phys. Hung. (N.S.) Heavy Ion Phys. 18, 347 (2003)
- R.K. Gupta, M. Balasubramaniam, R. Kumar, D. Singh, C. Beck, Nucl. Phys. A 738, 479c (2004)
- 93. G. Royer, J. Mignen, J. Phys. G Nucl. Part. Phys. 18, 1781 (1992)
- 94. H.S. Khosla, S.S. Malik, R.K. Gupta, Nucl. Phys. A 513, 115 (1990)
- 95. R.K. Gupta, S. Kumar, W. Scheid, Int. J. Mod. Phys. E 6, 259 (1997)
- 96. T. Matsuse, C. Beck, R. Nouicer, D. Mahboub, Phys. Rev. C 55, 1380 (1997)
- 97. S.J. Sanders, Phys. Rev. C 44, 2676 (1991)
- S.J. Sanders, D.G. Kovar, B.B. Back, C. Beck, D.J. Henderson, R.V.F. Janssens, T.F. Wang, B.D. Wilkins, Phys. Rev. C 40, 2091 (1989)
- S.J. Sanders, D.G. Kovar, B.B. Back, C. Beck, B.K. Dichter, D. Henderson, R.V.F. Janssens, J.G. Keller, S. Kaufman, T.-F. Wang, B. Wilkins, F. Videbaek, Phys. Rev. Lett. 59, 2856 (1987)
- N.J. Davidson, S.S. Hsiao, J. Markram, H.G. Miller, Y. Tzeng, Nucl. Phys. A 570, 61c (1994)
- 101. W. Myers, W.J. Swiatecki, Nucl. Phys. **81**, 1 (1966)
- 102. A.S. Jensen, J. Damgaard, Nucl. Phys. A 203, 578 (1973)
- 103. P.A. Seeger, Nucl. Phys. 25, 1 (1961)
- 104. S. De Benedetti, Nuclear Interactions (Wiley, New York, 1964)
- 105. G. Audi, A.H. Wapstra, Nucl. Phys. A 595, 4 (1995)
- 106. G. Audi, A.H. Wapstra, C. Thibault, Nucl. Phys. A 729, 337 (2003)
- 107. P. Möller, J.R. Nix, W.D. Myers, W.J. Swiatecki, At. Nucl. Data Tables 59, 185 (1995)
- 108. R.K. Gupta, S. Kumar, M. Balasubramaniam, G. Münzenberg, W. Scheid, J. Phys. G Nucl. Part. Phys. 28, 699 (2002)

- 109. R.K. Gupta, M. Balasubramaniam, S. Kumar, S.K. Patra, G. Münzenberg, W. Greiner, J. Phys. G Nucl. Part. Phys. 32, 565 (2006)
- 110. P.G. Hansen and B. Jonson, Europhys. Lett. 4, 409 (1987)
- 111. I.J. Thompson, J.S. Vaagen, in *Heavy Elements and Related New Phenomena*, vol. II, ed. by W. Greiner, R.K. Gupta, (World Scientific, Singapore, 1999), p. 976
- 112. K. Ieki, A. Golansky, D. Sackett, J.J. Kruse, W.G. Lynch, D.J. Morrissey, N.A. Orr, B.M. Sherrill, J.A. Winger, F. Deak, A. Horvath, A. Kiss, Z. Seres, J.J. Kolata, R.E. Warner, D.L. Humphery, Phys. Rev. C **54**, 1589 (1996)
- 113. E. Sauvan et al., Phys. Rev. Lett., 87, 042501 (2001)
- 114. H. Kröger, W. Scheid, J. Phys. G 6, L85 (1980)
- 115. A. Săndulescu, D.N. Poenaru, W. Greiner, Sov. J. Part. Nucl. 11, 528 (1980)
- 116. H.J. Rose, G.A. Jones, Nature 307, 245 (1984)
- 117. A. Guglielmetti, D. Faccio, R. Bonetti, S.V. Shishkin, S.P. Tretyakova, S.V. Dmitriev, A.A. Ogloblin, G.A. Pik-Pichak, N.P. van der Meulen, G.F. Steyn, T.N. van der Walt, C. Vermeulen, D. McGee, J. Phys. Conf. Ser. 111, 012050 (2008)
- 118. R. Bonetti, A. Guglielmetti, V.L. Mikheev, S.P. Tretyakova, Private communication; and to be published
- 119. A. Guglielmetti, R. Bonetti, G. Poli, R. Collatz, Z. Hu, R. Kirchner, E. Roeckl, N. Gunn, P.B. Price, B.A. Weaver, A. Westphal, Phys. Rev. C 56, R2912 (1997)
- 120. W. Greiner et al., in *Treatise on Heavy Ion Science*, vol. **8** ed. by D.A. Bromley (Plenum, New York, 1989), p. 641
- 121. R. Blendowske, H. Walliser, Phys. Rev. Lett. 61, 1930 (1988)
- 122. E. Bonnet et al., Int. J. Mod. Phys. E 17, 2359 (2008)
- 123. R.K. Gupta, Niyti, M. Manhas, W. Greiner, J. Phys. G Nucl. Part. Phys. 36, 115105 (2009)
- 124. R.K. Gupta, M. Manhas, W. Greiner, Phys. Rev. C 73, 054307 (2006)
- 125. M. Manhas, R.K. Gupta, Q. Li, S.K. Patra, W. Greiner, Phys. Rev. C 74, 034603 (2006)
- 126. C.L. Jiang et al., Phys. Rev. C 71, 044613 (2005)
- 127. C.L. Jiang et al., Phys. Rev. Lett. 93, 012701 (2004)
- 128. R.K. Gupta, S.K. Arun, R. Kumar, M. Bansal, Nucl. Phys. A 834, 176c (2010)
- 129. R.K. Gupta, S.K. Arun, R. Kumar, M. Bansal, in *Proceedings NN2009: 10th International Conference on Nucleus–Nucleus Collisions*, Beijing, China, 16–21 August 2009
- 130. S. Misicu, H. Esbensen, Phys. Rev. C 75, 034606 (2007)
- 131. S. Misicu, H. Esbensen, Phys. Rev. Lett. 96, 112701 (2006)

Chapter 7 Giant Nuclear Systems of Molecular Type

Valery Zagrebaev and Walter Greiner

7.1 Introduction

Cluster structure is very often set off against the shell structure of light and medium nuclei. However the appearance of clusters themselves (compact pieces of nuclear matter) is conditioned just by the shell effects. In light nuclei these clusters are mainly alpha-particles. In heavy nuclear systems tightly packed nuclei (such as ¹³²Sn or ²⁰⁸Pb) may lead to energetically favorable two (and even three) center configurations. These cluster configurations play an important role both in the structure of heavy nuclear systems and in the low-energy nuclear dynamics. The asymmetric nuclear fission (see, for example, Ref. [1]), the heavy-ion radioactivity [2, 3], the shape isomeric states of heavy nuclei [4] and the true ternary fission of superheavy nuclei (see below) are the manifestations of such kind of clusterization. Our studies of fusion-fission reactions and multi-nucleon transfer processes in low-energy heavy ion collisions demonstrated that the shell effects have also a strong influence upon evolution of heavy nuclear systems. Low-energy nuclear dynamics is regulated mainly by the multidimensional potential energy surface in the space of collective variables. At low excitation energies the nuclear system creeps along the fission and quasi-fission valleys of the potential energy caused by the nascent cluster structure. It falls and delays in the local minima of this potential surface (shape isomeric states) and finally splashes out in the exit channels with formation of energetically favorable closed shell nuclei.

Flerov Laboratory of Nuclear Reactions, JINR, Dubna, Russia

e-mail: zagrebaev@jinr.ru

W. Greiner

Frankfurt Institute for Advanced Studies, Frankfurt am Main, Germany

e-mail: greiner@fias.uni-frankfurt.de

V. Zagrebaev (⊠)

7.2 Potential Energy of Heavy Nuclear System

The potential energy of any physics system is a key quantity which determines its properties and time evolution. At low excitation energies of a heavy nuclear system (consisting of many nucleons) only a few collective degrees of freedom play most important role. The proper choice of these degrees of freedom is essential and rather difficult. The number of the degrees of freedom should not be too large so that one is able to solve numerically the corresponding set of dynamic equations of motion and understand quite well the behavior of the nuclear system under study. On the other hand, however, with a restricted number of collective variables it is difficult to describe properly and simultaneously all the strongly coupled reaction channels and processes. The distance between the nuclear centers (corresponding to the elongation of a mono-nucleus), dynamic surface deformations, mutual orientations of deformed nuclei and charge and mass asymmetry are probably the most relevant degrees of freedom both for description of the fusion–fission dynamics and the deep inelastic scattering.

7.2.1 Diabatic Potential Energy

The interaction potential of two separated nuclei may be calculated rather easily within the folding procedure with effective (density dependent) nucleon–nucleon interaction or parameterized, e.g., by the proximity potential. Of course, some uncertainty remains here, but the heights of the Coulomb barriers obtained in these models coincide with the empirical Bass parametrization [5] within 1 or 2 MeV. After contact the mechanism of interaction of two colliding nuclei becomes more complicated. For fast collisions ($E/A \sim \epsilon_{\rm Fermi}$ or higher) the nucleus–nucleus potential, $V_{\rm diab}$, should reveal a strong repulsion at short distances preventing the "frozen" nuclei to penetrate each other and form a region of nuclear matter with double density (diabatic conditions, sudden potential [6]). For slow collisions (near-barrier energies, $v_{\rm rel} \ll v_{\rm Fermi}$), when nucleons have enough time to reach equilibrium distribution within a volume with a constant nuclear density (adiabatic conditions), the nucleus–nucleus potential energy, $V_{\rm adiab}$, is quite different (see Fig. 7.1. It is clear that for far separated nuclei in the entrance channel these potentials coincide.

Thus, at collision energies well above the Coulomb barrier we need to use a time-dependent potential [7], which after contact gradually transforms from a diabatic potential energy into an adiabatic one:

$$V = V_{\text{diab}}[1 - f(t)] + V_{\text{adiab}}f(t). \tag{7.1}$$

Here t is the time of interaction and f(t) is a smoothing function with parameter $\tau_{\rm relax} \sim 10^{-21}$ s [8, 9], f(t=0) = 0, $f(t \gg \tau_{\rm relax}) = 1$. Note that at slow near-barrier collisions the first (diabatic) term plays a minor role. It dissolves almost

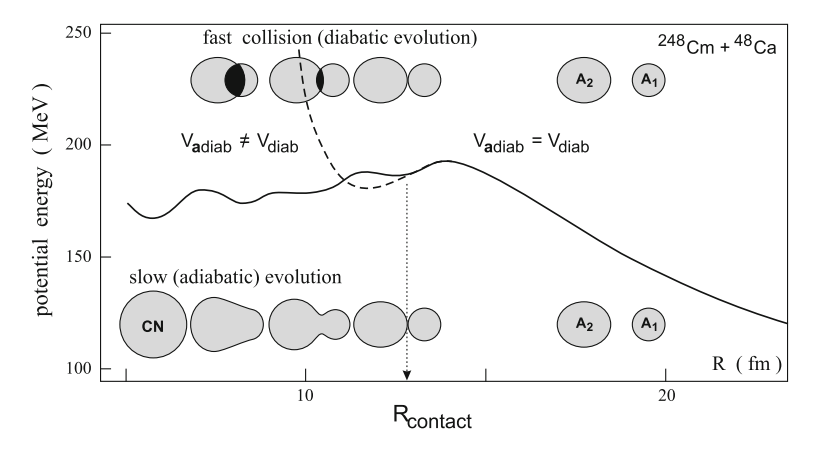


Fig. 7.1 Potential energy of the nuclear system formed in collision of 48 Ca + 248 Cm at diabatic (*dashed curve*) and adiabatic (*solid curve*) conditions depending on the distance between the nuclear centres

completely during slow motion from the Coulomb barrier to the contact configuration ($d = R_{\text{Barrier}} - R_{\text{cont}} \sim 1-2$ fm, $t \sim 10^{-21}$ s) and just the adiabatic potential energy regulates the whole process.

Nucleon exchange and rearrangement between the reaction fragments play an important role in low-energy dynamics of the heavy nuclear system. It is convenient to include the change in binding energies of the fragments (arising due to nucleon rearrangement) just into the potential energy which may be written as

$$V_{\text{diab}}(A, Z; R, \beta_1, \Omega_1, \beta_2, \Omega_2, \eta) = V_{12}(A_1, Z_1, A_2, Z_2; R, \beta_1, \Omega_1, \beta_2, \Omega_2) + M(A_1, Z_1; \beta_1) + M(A_2, Z_2; \beta_2) - M(A_P, Z_P; \beta_P^{\text{g.s.}}) - M(A_T, Z_T; \beta_T^{\text{g.s.}}).$$

$$(7.2)$$

Here V_{12} is the interaction potential of two nuclei, $M(A_i, Z_i) = Z_i m_p c^2 + N_i m_n c^2 - B(A_i, Z_i)$ is the mass of the fragment (B is the binding energy) and the constant $M(A_P, Z_P) + M(A_T, Z_T)$ (sum of the masses of initial nuclei) is subtracted to give a zero value of the potential energy at infinite distance of the colliding nuclei in the entrance channel. In all the other channels at infinite distance ($R \to \infty$) the potential energy (2) is equal to the Q-value of the corresponding two-body reaction $A_P + A_T \to A_1 + A_2$. $\beta_{1,2} = \{\beta_{1,2}^{\lambda}\}$ in (2) are the dynamic deformations of interacting nuclei ($\lambda = 2, 3, ...$ are the multipolarities of surface deformations), $\Omega_{1,2} = (\varphi_{1,2}, \psi_{1,2})$ are the orientations of deformed nuclei ($\varphi_{1,2}$ are the polar orientations of the symmetry axes relative to the beam direction and $\psi_{1,2}$ are the azimuthal orientations of the colliding nuclei, see Fig. 7.13), and $\eta = (A_2 - A_1)/(A_2 + A_1)$ is the mass asymmetry. The multi-dimensional potential energy surface written in the form (2) is named usually "driving potential".

The simplest and effective method for the calculation of the diabatic nucleusnucleus interaction potential is the use of some phenomenological model. In that case the interaction potential is written as a sum of nuclear and Coulomb energy, $V_{12} = V_{12}^{N} + V_{12}^{C}$. The Coulomb interaction of uniformly charged nuclei is usually defined in analytical form (decomposed over multipoles in the case of deformed nuclei [10]) and the short-range nuclear part, V_{12}^N , is simply parameterized. For example, the proximity forces [11], which practically have no free adjustable parameters, seems to be more convenient for estimation of the nuclear part of the diabatic potential energy of two interacting medium and heavy nuclei. The absence of adjustable parameters is the main advantage of the proximity potential. This interaction essentially depends only on a choice of matter radii of nuclei. Realistic results can be obtained choosing $r_0 \approx 1.16$ fm for heavy nuclei (A > 40) and $r_0 \approx 1.22$ fm for nuclei with $A \sim 16$. The following expression can be recommended for nuclei heavier than oxygen:

$$r_0(A) = 1.16 + \frac{16}{A^2}. (7.3)$$

For deformed nuclei dependence of the proximity interaction on the curvatures of their surfaces (i.e. on the area of touched surfaces) is rather important and should be also taken into account [12].

More sophisticated calculation of the diabatic interaction potential may be performed within the energy-density functional approach [13–16]. The interaction energy of two nuclei is defined here as the difference of the total system energy and those of the isolated nuclei V_{12} (R, β_1 , Ω_1 , β_2 , Ω_2) = E_{1+2} (R, β_1 , Ω_1 , β_2 , Ω_2) – $E_1(\beta_1) - E_2(\beta_2)$, where E_{1+2} is the energy of the system of two interacting nuclei and E_1 , E_2 are the energies of isolated nuclei. Also the "sudden" two-center shell model [17] may be utilized for the calculation of interaction potential for fast nucleus–nucleus collisions.

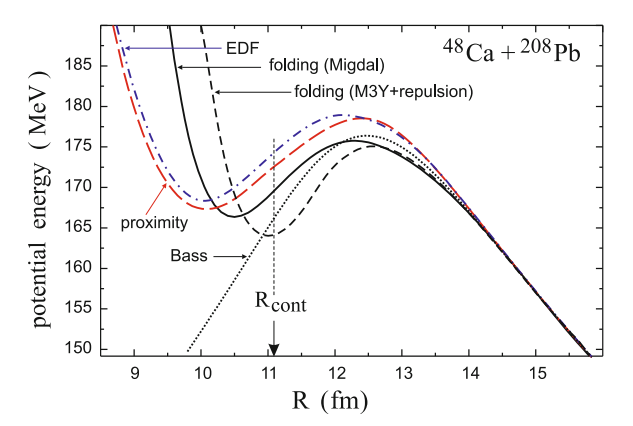
The double folding procedure (i.e. direct summation of two-body nucleon-nucleon forces averaged over density distributions) is the most natural method for the calculation of the diabatic nucleus–nucleus potential (see, for example [18])

$$V_{12}(R; \beta_1, \Omega_1, \beta_2, \Omega_2) = \int_{V_1} \rho_1(\mathbf{r}_1) \int_{V_2} \rho_2(\mathbf{r}_2) \nu_{\text{NN}}(\mathbf{r}_{12}) d^3 \mathbf{r}_1 d^3 \mathbf{r}_2.$$
 (7.4)

Here $v_{\rm NN}({\bf r}_{12}={\bf R}+{\bf r}_2-{\bf r}_1)$ is the nucleon–nucleon potential and $\rho_{i=1,2}({\bf r}_i)$ are the nuclear matter density distributions. A realistic nucleus–nucleus potential in this method is obtained only if one uses the "effective" density dependent nucleon–nucleon interactions $v_{\rm NN}$ with the extra term which simulates a repulsion for strongly overlapping nuclei. The M3Y nucleon–nucleon potential [19–21] with effective repulsion [22, 23] is usually used is this method. The zero-range density dependent Migdal nucleon–nucleon forces [24] combined with the properly parameterized nuclear densities may be also used for rather fast calculation of the folding potential [12]. In Fig. 7.2 the diabatic potential energy of ⁴⁸Ca + ²⁰⁸Pb nuclei is shown calculated within the different theoretical models mentioned above.

One can see from Fig. 7.2 that several methods give more or less close values of the height (within 2 or 3 MeV) and position (within 0.5 fm) of the Coulomb barrier. At the same time these potentials are quite different at contact point and in

Fig. 7.2 Diabatic potential energy of ⁴⁸Ca + ²⁰⁸Pb calculated within the folding procedure with the Migdal forces [12] (*solid curve*) and with M3Y + repulsion nucleon–nucleon potential [23] (*dashed curve*), energy–density functional potential [16] (*dash-dotted curve*), proximity potential [11] (*long dashed curve*) and the Bass potential [5] (*dotted curve*)



the region of overlapping of colliding nuclei. Available experimental data on heavy-ion induced nuclear reactions do not allow one to determine better the diabatic nucleus–nucleus potential energy at short distances. The main reason for that is a strong coupling of the nucleus–nucleus relative motion (coordinate R) with many other internal degrees of freedom and collective variables for such configurations.

Note finally that all the methods mentioned above may be used for calculation of the interaction diabatic potential (2) for deformed and arbitrary oriented nuclei. In Fig. 7.3 the calculated folding potential with the Migdal nucleon–nucleon forces is shown for two deformed nuclei, 64 Zn ($\beta_2^{\text{g.s.}} = 0.22$) + 150 Nd ($\beta_2^{\text{g.s.}} = 0.24$) depending on the orientation of their axes of symmetry [12]. One can see that just the mutual polar orientation of deformed nuclei (deviations of axes of symmetry φ_1 and φ_2 from the internuclear axis) strongly influences the interaction potential—for heavy statically deformed nuclei the Coulomb barrier for the "nose-to-nose" (tip) configuration may be 20 MeV less than for the side one. The azimuthal orientations change the Coulomb barrier within 1 or 2 MeV only, see Fig. 7.3a and b.

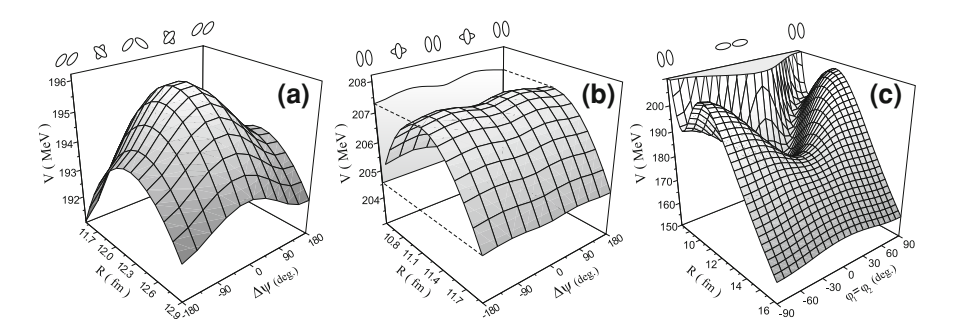


Fig. 7.3 Interaction potential of two deformed nuclei ⁶⁴Zn $(\beta_2^{\text{g.s.}} = 0.22) + ^{150}$ Nd $(\beta_2^{\text{g.s.}} = 0.24)$ depending on their azimuthal—**a** and **b**, and polar **c** orientations. **a** $\varphi_1 = \varphi_2 = \pi/4$, **b** $\varphi_1 = \varphi_2 = \pi/2$, **c** $\psi_1 = \psi_2$, i.e., $\Delta \psi = 0$. Schematic orientations of the nuclei are shown in *upper part* of the figure

In low-energy collisions (and decay) of heavy nuclei their dynamic deformations play a very important role due to a change of the distance between nuclear centers (change of V_{12}^C) and between nuclear surfaces (change of V_{12}^N). Thus the deformation energy itself should be also added to the diabatic interaction potential (2) (it is included by definition into the adiabatic potential energy, see below). For small deformations we may restrict ourselves by consideration of the deformation energy in the harmonic approximation

$$\frac{1}{2} \sum_{\lambda} C_{1,\lambda} (\beta_{1,\lambda} - \beta_{1,\lambda}^{g.s.})^2 + \frac{1}{2} \sum_{\lambda} C_{2,\lambda} (\beta_{2,\lambda} - \beta_{2,\lambda}^{g.s.})^2, \tag{7.5}$$

where $C_{i,\lambda}$ are the rigidities (stiffness parameters) of nuclear surfaces, which can be estimated within the liquid drop model [25] or derived from the experimental properties of vibrational states of a given nucleus, and $\beta_{i,\lambda}$ are the dynamic deformations of multipolarity λ . For large dynamic deformations the harmonic approximation (5) may be insufficient and more correct calculation of the deformation energy should be performed, for example, within the macro-microscopic model (see below).

As can be seen from Fig. 7.4 the diabatic nucleus–nucleus potential energy strongly depends on dynamic deformations of interacting nuclei. The Coulomb barrier of two heavy nuclei (spherical in their ground states) may decrease by more than 10 MeV due to their dynamic deformations. Thus, it is incorrect to keep in mind one specific value of the Coulomb barrier even for interaction of spherical

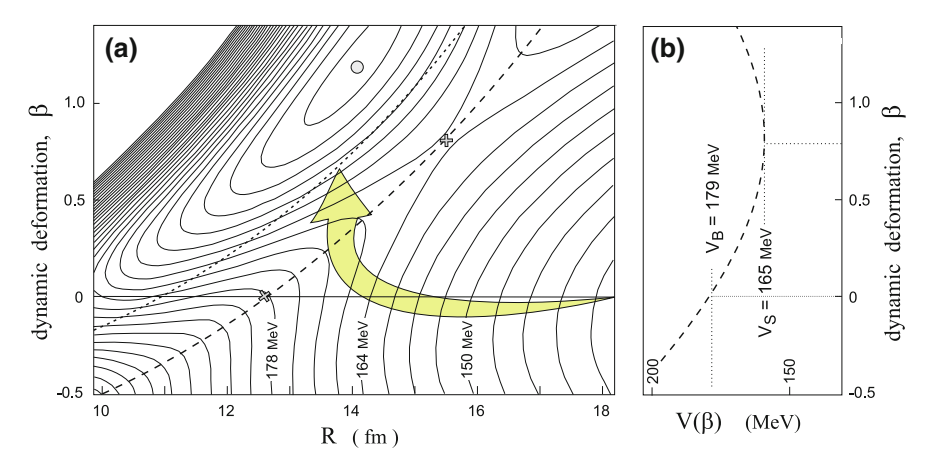


Fig. 7.4 a Landscape of the interaction potential of 48 Ca + 208 Pb depending on quadrupol dynamic deformations of both nuclei $\beta = \beta_1 + \beta_2$ (at $\beta_1 = \beta_2$). The *dashed curve* shows the ridge of the two-dimensional Coulomb barrier, whereas the *dotted* one corresponds to the contact configurations. The *crosses* indicate position of the Coulomb barrier at zero deformations and the minimal value of the barrier for dynamically deformed nuclei (fusion saddle point). The *circle* shows the minimum of the potential pocket and the *hatched arrow* indicates the most probable path for fusing nuclei at low energies. **b** Potential energy along the barrier ridge (*dashed curve* at the *left panel*)

nuclei. There is the multi-dimensional Coulomb barrier ridge and we have to use a concept of the barrier distribution function [26] describing nucleus–nucleus interaction. First, this effect significantly enhances the sub-barrier penetration probability in fusion reactions (the channel coupling and empirical model calculations give here similar results [27]). Second, as can be seen from Fig. 7.4, at contact configuration the potential energy has a minimal value (potential pocket) at non-zero dynamic deformations. Thus, at low collision energies even two magic nuclei (such as ⁴⁸Ca and ²⁰⁸Pb, spherical in their ground states) after overcoming the Coulomb barrier immediately acquire rather elongated shapes. This effect strongly influences subsequent evolution of the nuclear system (see below).

7.2.2 Adiabatic Potential Energy and the Two-Center Shell Model

The calculation of the multidimensional adiabatic potential energy (equilibrated over the fast single particle motion) remains a very complicated physical problem, which is not yet solved in full. For a heavy nuclear system the adiabatic potential energy may be defined as a difference between the mass of the whole nuclear system (the system could be either a mononucleus or two separated nuclei) and the ground-state masses of initial target and projectile

$$V_{\text{adiab}}(A, Z; R, \beta, \eta) = M(A, Z; R, \beta, \eta) - M(A_P, Z_P; \beta_P^{\text{g.s.}}) - M(A_T, Z_T; \beta_T^{\text{g.s.}}).$$
(7.6)

The constant $M(A_P, Z_P) + M(A_T, Z_T)$ provides as before a zero value of the potential energy at infinite distance of the fragments in the entrance channel.

The purely microscopic self-consistent methods of the Hartree–Fock type with effective density-dependent nucleon–nucleon interactions (see, e.g. [28, 29]) or the relativistic mean field approach [30, 31] may be used for a calculation of the mass of deformed nuclear system. These methods, however, are rather complicated and time-consuming. In the "macro-microscopical" approach the mass of deformed nucleus is composed of the two parts

$$M(A, Z; R, \beta, \eta) = M_{\text{mac}}(A, Z; R, \beta, \eta) + \delta E(A, Z; R, \beta, \eta). \tag{7.7}$$

The macroscopic part, $M_{\rm mac}$, smoothly depends on the proton and neutron numbers and may be calculated within the finite-range liquid-drop model [32–34]. The microscopic part, δE , describes the shell effects. It is constructed from the single-particle energy spectra by the Strutinsky procedure [35, 36].

At low dynamic deformations (ground state or saddle point masses) the Woods–Saxon mean-field potential may be used for a calculation of the single-particle energy spectra [34, 37]. For large dynamic deformations (up to configuration of two separated nuclei) the two-center shell model (TCSM) [38] seems to be most appropriate for calculation of the adiabatic potential energy. The mean-field potential of the TCSM consists of two axially symmetric harmonic oscillator

potentials with independent centers. This model describes correctly transition from the small ellipsoidal deformations near the ground state configuration (here it coincides with the well-known Nilsson model) to the strongly deformed shapes up to the configuration of two separated nuclei (giving the Nilsson model for each of the fragments). In [38] the model was extended for the case of mass-asymmetric shapes and the mean-field potential was smoothed at the contact point.

The mean-field potential [its momentum-independent part $V(\rho, z)$, where ρ and zare the cylindrical coordinates] determines the shape parametrization of the nuclear system—the nuclear surface is an equipotential surface of $V(\rho, z)$, see Fig. 7.5. The external parts of the shape are axially symmetric ellipsoids with semi-axes c_i and b_i (i = 1, 2). Internal part of the shape is more complicated. The shape parametrization of the TCSM has five independent parameters, that allows one to introduce five collective variables: (1) the elongation R of the system, which for separated nuclei is the distance between mass centers of the nuclei; (2, 3) the ellipsoidal deformations of the two parts of the system δ_1 and δ_2 , defined as $\delta_i = c_i/b_i - 1$ (at small values the quadrupole and ellipsoidal deformations are similar, $\beta_2 = 4/3\sqrt{\pi/5}\delta \approx 1.057\delta$); (4) the mass-asymmetry parameter $\eta = (A_2 - A_1)/(A_2 + A_1)$, where A_1 and A_2 are the mass numbers of the system halves; (5) the neck parameter ε smoothes the shape of overlapping nuclei (see Fig. 7.5b). Smaller values of ε correspond to a thicker neck at fixed values of other parameters. The details of calculation of the single particle energy spectra within the TCSM and the explanation of all the parameters used may be found in Refs [12, 38].

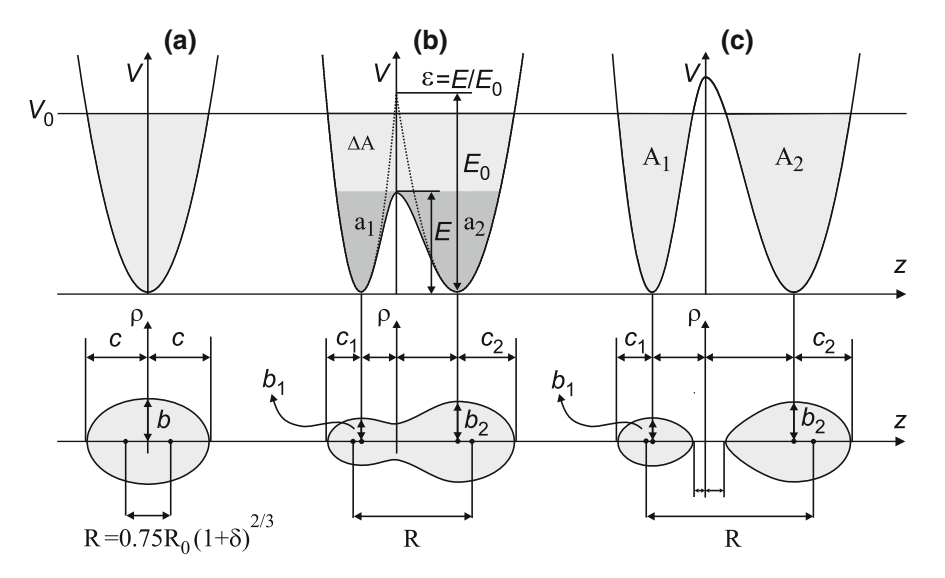
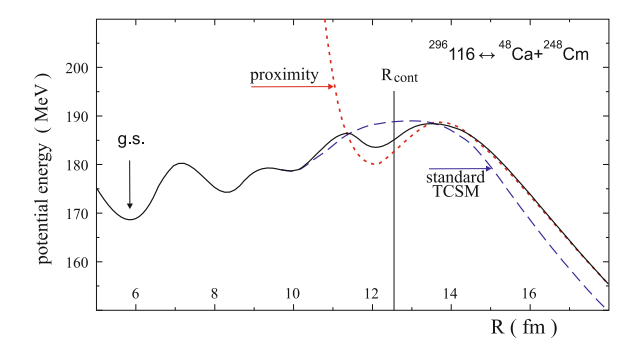


Fig. 7.5 Nuclear shape and the mean-field potential $V(\rho=0,z)$ of the TCSM shown for $\delta_1=\delta_2=\delta=0.5$ and $\epsilon=0.5$. The mass asymmetry parameter $\eta=0$ for ${\bf a}$ and $\eta=0.625$ for ${\bf b}$ and ${\bf c}$. Dark hatched areas marked by a_1 and a_2 in ${\bf b}$ denote two cores, whereas ΔA are the collectivized nucleons (Sect. 2.3)

Fig. 7.6 Potential energy of nuclear system $^{296}116 \leftrightarrow^{48}$ Ca $+^{248}$ Cm (g.s. masses and deformations of colliding nuclei) calculated within the standard (*dashed curve*) and extended (*solid curve*) versions of TCSM. The *dotted curve* shows the diabatic proximity potential. The contact point is indicated by the *vertical line*



The standard version of the TCSM (as well as any macro-microscopic model) meets some problems at the calculation of potential energy for contact (scission) configuration and for separated nuclei. In particular, it does not reproduce correctly the value of the Coulomb barrier and the depth of potential pocket at contact. Figure 7.6 shows the adiabatic potential energy calculated within the standard TCSM approach (dashed curve) in comparison with the diabatic proximity potential (dotted curve) for ⁴⁸Ca + ²⁴⁸Cm. As noted above, the adiabatic and diabatic potentials should give identical results for separated nuclei, for which the energy is known to be the sum of the experimental values of masses plus the Coulomb interaction energy. It is clear from Fig. 7.6 that the adiabatic potential energy, calculated in the standard macro-microscopic model, substantially differs from the "true" value in the asymptotic and contact regions of two nuclei.

The reason for this limitation of macro-microscopic model is the non-additive terms in the macroscopic part of the total mass (7) (i.e. nonadditivity of the Weizsäcker formula) and incorrect single particle energy spectra of two separated nuclei being calculated as for a mono-nucleus. However, this limitation has been overcome recently in the extended version of the two-center shell model [12]. The standard macro-microscopic model agrees well with the experimental data on the ground-state masses and fission barriers. On the other hand, the double-folding model reproduces the data on the fusion barriers and the potential energy in the region of separated nuclei (as mentioned above in this region the diabatic and adiabatic potential energies should coincide). In Ref. [12] it was proposed to use the correct properties of these two potentials and to construct the adiabatic potential energy as follows:

$$\begin{split} V_{\text{adiab}}^{\text{TCSM}}(A,Z;R,\delta,\eta) &= ([M_{\text{FRLDM}}(A,Z;R,\delta,\eta) + \delta E_{\text{TCSM}}(A,Z;R,\delta,\eta)] \\ &- [M_{\text{FRLDM}}(A_P,Z_P;\delta_P^{\text{g.s.}}) + \delta E_{\text{TCSM}}(A_P,Z_P;\delta_P^{\text{g.s.}})] \\ &- [M_{\text{FRLDM}}(A_T,Z_T;\delta_T^{\text{g.s.}}) + \delta E_{\text{TCSM}}(A_T,Z_T;\delta_T^{\text{g.s.}})])B(R,\delta_1,\delta_2,\eta) \\ &+ V_{\text{diab}}(A,Z;R,\delta_1,\delta_2,\eta)[1 - B(R,\delta_1,\delta_2,\eta)]. \end{split}$$

The "smoothing" function $B(R, \delta_1, \delta_2, \eta)$ defines the transition from the properties of two separated nuclei to those of the mono-nucleus. The function $B(R, \delta_1, \delta_2, \eta)$ is rather arbitrary. It should be unity for the ground state region of mono-nucleus and it should tend to zero for completely separated nuclei. The following simple expression for this function can be used: $B(R, \delta_1, \delta_2, \eta) = (1 + \exp[(R - R_{\text{cont}})/a])^{-2}$, where $R_{\text{cont}}(A_1, A_2; \delta_1, \delta_2)$ is the distance between the mass centers corresponding to the touching (scission) point of the nuclei, and a is the adjustable parameter. With the quite appropriate value of a = 0.5 fm the fusion barriers are reproduced quite well. The adiabatic potential energy calculated within the extended macro-microscopic Eq. (8) is shown in Fig. 7.6 by the solid curve. As can be seen the proposed improvement leads to the correct adiabatic potential energy which reproduces properly the ground state properties of mono-nucleus as well as the fission and fusion barriers and the asymptotic behavior of the potential energy for two separated nuclei.

The two-center parametrization has five free parameters (five collective degrees of freedom) which determine the shape of the nucleus: R, δ_1 , δ_2 , η and ε . This parametrization is quite flexible and gives reasonable shapes both for the fusion and fission processes. However, the use of all the five degrees of freedom in the dynamical equations of motion (see below) is beyond the present computational possibilities (mainly due to impossibility to keep in memory the five-dimensional potential energy and all its derivatives). First, we may decrease the number of collective variables assuming equality of the deformation forces acting onto the nuclear surfaces, i.e., $C_1\delta_1=C_2\delta_2$, where $C_{1,2}$ are the LDM stiffness parameters of the fragments, see Eq. (5). Using this ratio and the definition $\delta_1+\delta_2=2\delta$, the deformations of the fragments are easily derived from the common variable δ .

Evolution of the neck parameter ε (smoothing the single-particle mean field at the contact point, see Fig. 7.5b) may be also considered in an approximate way. Figure 7.7, shows the macroscopic potential energy in the space of (R, ε) and the map of the corresponding nuclear shapes. At scission configuration in the fission channel the nuclear shape has a large distance between mass centers and a well

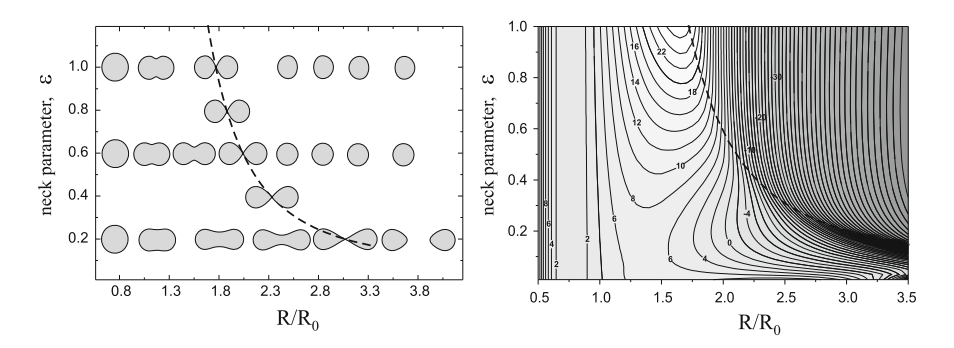


Fig. 7.7 The potential energy (*right panel*) and the corresponding shapes of nuclei (*left panel*) in the coordinates (R, ε) for the system ²²⁴Th calculated for $\eta = 0$ and $\delta_1 = \delta_2 = 0$. The potential energy is normalized to zero for the spherical compound nucleus. The *thick dashed curve* is the *scission* (contact) *line*

pronounced neck. On the contrary, at the contact point of the fusion channel the nuclear shape is rather compact and almost without neck, i.e., $\varepsilon=1$. For the exit fission channels the value of the neck parameter should be chosen to minimize the potential energy along the fission path. The value $\varepsilon_{\text{out}} \approx 0.35$ was recommended in [39] for the fission processes. One can see from Fig. 7.7, that the potential energy is practically independent of the neck parameter for separated nuclei. Therefore, the neck parameter keeps the constant value ($\varepsilon_{\text{in}}=1$) in the entrance channel, whereas the fission process (motion from the ground state configuration along the bottom of the potential energy surface to scission point) takes place at $\varepsilon<1$ and finishes at some ε_{out} for separated fission fragments.

It is clear that we should take into account somehow the difference of nuclear shapes in the entrance and exit channels. Nevertheless, to restrict ourselves by the three-dimensional configurational space (R, η, δ) , we may consider evolution of the neck parameter as a relaxation process with the characteristic time τ_{ϵ} which is evidently comparable with fission time $\sim 10^{-20}$ s. In that case the adiabatic potential energy calculated within the two-center shell model, second term in Eq. (1), becomes also time-dependent

$$V_{\text{adiab}}^{\text{TCSM}}(R, \eta, \delta; t) = V_{\text{adiab}}^{\text{TCSM}}(\varepsilon_{\text{in}}) \exp(-t/\tau_{\varepsilon}) + V_{\text{adiab}}^{\text{TCSM}}(\varepsilon_{\text{out}}) [1 - \exp(-t/\tau_{\varepsilon})], \quad (7.9)$$

where t is the interaction time (i.e., time after contact), $\varepsilon_{\rm in}=1$ and $\varepsilon_{\rm out}=1\approx0.35$ is the adjustable parameter found from the best fit of experimental energy distribution of the fission fragments.

Note finally that all the potentials discussed above (diabatic phenomenological and folding potentials as well as adiabatic ones) may be properly calculated depending on chosen degrees of freedom just in the Web window of the low-energy nuclear knowledge base [40].

7.2.3 Two-core Approximation for Adiabatic Potential

The calculation of the adiabatic driving potential within the TCSM is still rather difficult and time-consuming problem. To avoid complex numerical calculations of the shell correction term one may use the empirical two-core model [41, 42], in which the shell correction is taken into account by means of the use of the ground state masses of intermediate fragments (cores). This approximation is also based on the two-center shell model idea, in which the lowest single particle states of non-overlapping cores of two nuclei (see dark hatched areas in Fig. 7.5b) are rather close to the states of isolated core nuclei. It is assumed in this model that on the way from the initial configuration of two touching nuclei to the compound mononucleus (and back to fission or quasi-fission channel), the system consists of two cores, $a_1 = z_1 + n_1$ and $a_2 = z_2 + n_2$, and a number of common (collectivized) nucleons $\Delta A = A_{\rm CN} - a_1 - a_2$ occupying the quasi-molecular states and moving in the whole volume of the nuclear system, see the upper hatched area in Fig. 7.5b.

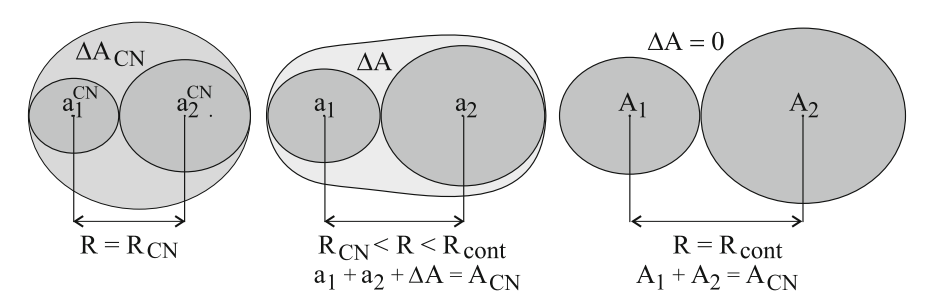


Fig. 7.8 Schematic picture of nuclear system in the two-core approximation. From *right* to *left*: the contact, intermediate and compound nucleus configurations are shown

Let us denote by $\Delta A_{\rm CN}$ such number of common (shared) nucleons at which the two cores a_1 and a_2 fit the volume of the compound nucleus (and are completely "dissolved" in it), i.e., $R(a_1, \delta_1) + R(a_2, \delta_2) = R(A_{\rm CN}, \delta_{\rm CN}^{\rm g.s.})$ (left part of Fig. 7.8). Apparently, $\Delta A_{\rm CN} < A_{\rm CN}$. The compound nucleus formation ($\Delta A \rightarrow \Delta A_{\rm CN}$), nuclear fission and quasi-fission ($\Delta A \rightarrow 0$) proceed in the space (z_1, n_1, δ_1 ; z_2, n_2, δ_2). The formation of the compound nucleus is assumed to be completed if the elongation of the system is less than that of the corresponding saddle configuration ($R < R(A_{\rm CN}, \delta_{\rm CN}^{\rm saddle})$). The adiabatic driving potential in the two-core approximation is defined as

$$V_{\text{adiab}}^{\text{TC}}(R; z_1, n_1, \delta_1; z_2, n_2, \delta_2) = \tilde{V}_{12}(R, z_1, n_1, \delta_1; z_2, n_2, \delta_2) - [\tilde{B}(a_1) + \tilde{B}(a_2) + \tilde{B}(\Delta A)] + B(A_P) + B(A_T).$$
(7.10)

Here $\tilde{B}(a_1) = \tilde{b}_1 \cdot a_1$, $\tilde{B}(a_2) = \tilde{b}_2 \cdot a_2$ and $\tilde{B}(\Delta A) = 0.5(\tilde{b}_1 + \tilde{b}_1)\Delta A$ are the binding energies of the two cores and of the common (shared) nucleons. These values depend on the number of collective nucleons. Let us define the degree of collectivization as $x = \Delta A/\Delta A_{\rm CN}$, then the reduced binding energies $\tilde{b}_{1,2}$ can be calculated as $\tilde{b}_i(a_i) = b_i^{\rm exp}(a_i)\varphi(x) + b_{\rm CN}^{\rm exp}[1-\varphi(x)]$. Here $b_i^{\rm exp}$ and $b_{\rm CN}^{\rm exp}$ are the reduced binding energies of the isolated fragments which are known experimentally. $\varphi(x)$ is a monotonic function constrained as $\varphi(x=0)=1$ and $\varphi(x=1)=0$. Therefore, the reduced binding energies of the cores gradually change from the values which correspond to the isolated nuclei to those of the compound nucleus as ΔA increases from zero to $\Delta A_{\rm CN}$. Thus all the shell effects are explicitly accounted for in (10) through the experimental binding energies $b_{1,2}^{\rm exp}$ and $b_{\rm CN}^{\rm exp}$.

The interaction potential \tilde{V}_{12} between two fragments is defined at $R \geq R_{\rm cont}$ as a usual diabatic potential (see Sect. 2.1). At $R < R_{\rm cont}$ the interaction between the two cores a_1 and a_2 weakens as the number of common nucleons ΔA increases and the cores are gradually dissolved in a compound nucleus, $\tilde{V}_{12}(x \to 1) \to 0$ (see details in [41, 42]). Thus, for the compound nucleus configuration ($\Delta A = \Delta A_{\rm CN}$) the total energy $V_{\rm adiab}^{\rm TC} = Q_{gg}^{\rm fus} = B(A_P) + B(A_T) - B(A_{\rm CN})$, as it should be if the zero value of the energy corresponds to configuration of initial nuclei A_P and A_T (in their ground states) at infinite distance.

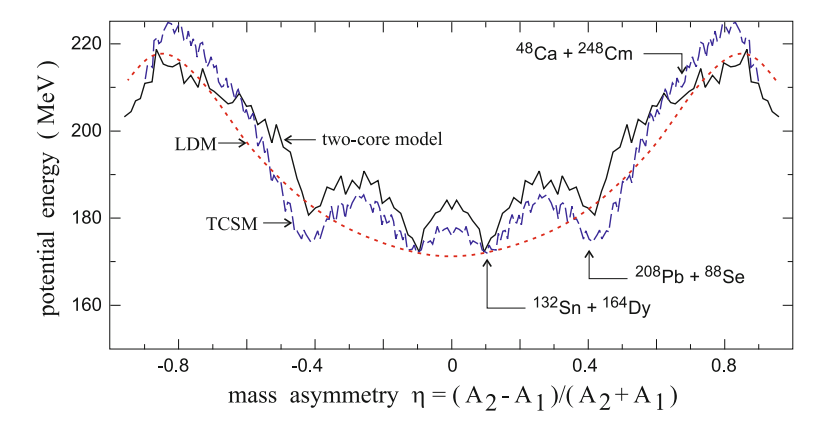


Fig. 7.9 Fusion–fission driving potential of the nuclear system formed in collision of $^{48}\text{Ca} + ^{248}\text{Cm}$ as a function of mass asymmetry. The potential energy was calculated at fixed distance between nuclear centers R=12 fm and zero deformation. *Dotted, dashed* and *solid curves* correspond to the liquid-drop model, two-center shell model and two-core model, respectively

In Fig. 7.9, the driving potentials calculated within the two-center shell model and within the two-core model are compared for the nuclear system formed in the collision of ⁴⁸Ca + ²⁴⁸Cm leading to a compound nucleus ²⁹⁶116. As can be seen, the results of the two calculations are rather close. At the same time, there are several advantages of the empirical approach. To get a reasonable value for the fission barrier one may use the shell corrections at zero and ground state deformations calculated according to [34] and the parametrization of the liquid drop energy proposed in [43]. Based on these values the adiabatic potential may be easily calculated for small values of elongation and deformation (up to the saddle point configuration). Then it is joined together with the potential of two touching nuclei as described above. The use of experimental binding energies of the two cores gives us the "true" values of the shell corrections. As a result, the two-core model gives automatically an explicit (experimental) value of the nucleus-nucleus interaction energy in the asymptotic region for well-separated nuclei where it is well known (the Coulomb interaction plus experimental reaction Q-value). This potential has quite realistic (diabatic) heights of the Coulomb barriers, which is important for the description of near-barrier heavy-ion reactions. It is defined in the whole region $R_{\rm CN} < R < \infty$ as a smooth and continuous function of R, δ , η and, thus, may be used for a simultaneous description of the whole fusion–fission process.

7.2.4 "Cold Valleys" within the Potential Energy Surface

A multi-dimensional character of the adiabatic potential (8) or (10) significantly complicates its visualization. In the case of the three collective variables

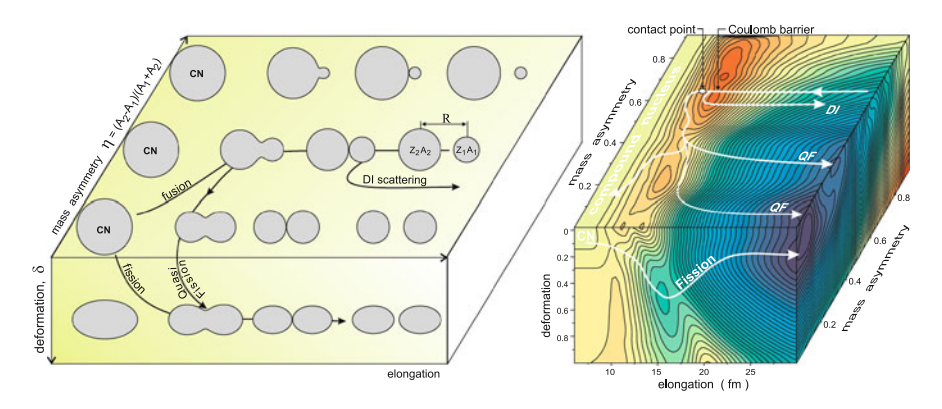


Fig. 7.10 *Left* schematic evolution of nuclear system in the space of "elongation–mass asymmetry–deformation". *Right* adiabatic driving potential for the nuclear system formed in 48 Ca + 248 Cm collision. The *solid lines* show schematically projections onto the plane of zero deformation of the trajectories corresponding to the deep inelastic scattering (DI), quasi-fission (QF) and fusion processes. Also shown is the projection of the regular fission path onto the plane of zero mass asymmetry ($\eta = 0$)

(elongation, deformation and mass asymmetry) evolution of the system in fission process and in a head-on collision of heavy ions occurs in the three-dimensional configurational space inside the cube shown in Fig. 7.10. Schematic views of the deep inelastic scattering (DI), quasi-fission (QF), fusion and regular fission are shown on the left panel of this figure. Only the landscapes of the driving potential may be drawn on the cube faces. Any real trajectory locates inside the cube (Fig. 7.15) and only its projections on a given plane may be shown here (right panel of Fig. 7.10).

Rather better view may be obtained by the two-dimensional plots of the driving potential. In Fig. 7.11a the potential energy is shown at fixed (zero) value of dynamic deformation depending on elongation and mass rearrangement. Schematic trajectories of DI, QF and fusion–fission processes are also shown. In Figs. 7.10 and 7.11 the deep valleys caused by the shell effects are distinctly visible. They correspond to the formation of doubly magic nuclei in the exit channel: 208 Pb (at $\eta \approx 0.4$) and 132 Sn (at $\eta \approx 0.1$).

The more symmetric valley with formation of well-bound nuclei around ¹³²Sn is well known and always reveals itself in regular fission processes (for example, in a preferable asymmetric spontaneous fission of uranium). Another deep valley caused by formation of the doubly magic nucleus ²⁰⁸Pb (biggest nuclear cluster) is more pronounced but hardly may be reached in normal fission of heavy nuclei (this valley is too far from the fission saddle point, see Figs. 7.10 and 7.11a. However it manifests quite distinctly in experimental mass distributions of the reaction fragments formed in collisions of heavy nuclei with actinide targets, see Fig. 7.11b.

The process, which is responsible for formation of lead-like fragments in collisions of such nuclei as 48 Ca + 248 Cm (rearrangement of more than 40 nucleons),

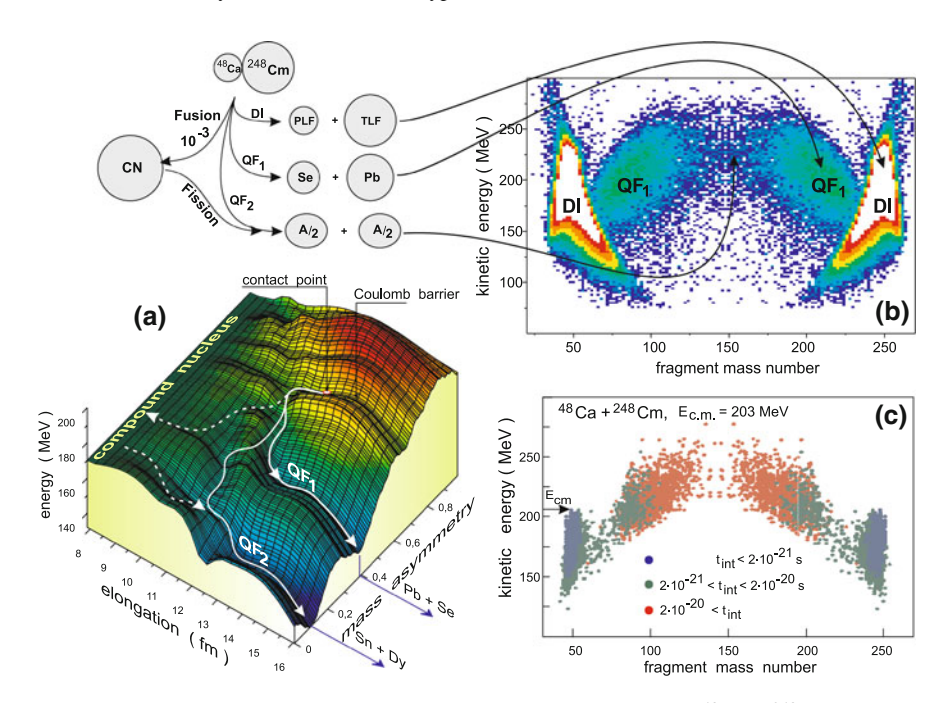


Fig. 7.11 a Adiabatic driving potential for the nuclear system formed in ⁴⁸Ca + ²⁴⁸Cm collision. The *solid lines* with *arrows* show schematically (without fluctuations) the quasi-fission trajectories going to the lead and tin valleys. The *dashed curves* correspond to fusion (CN formation) and fission processes. Experimental **b** [44] and calculated **c** [7] mass–energy distribution of reaction fragments in collision of ⁴⁸Ca with ²⁴⁸Cm at 203 MeV center-of-mass energy. *Different colors* in **c** indicate the interaction time of different events (longer for larger mass rearrangement)

was named "quasi-fission". It is qualitatively distinguished both from the deep inelastic scattering with formation of projectile-like and target-like fragments and from the more symmetric regular fission. This process, caused by the shell effects, dominates in collisions of heavy nuclei with actinide targets preventing them from fusion and, thus, reduces the yield of superheavy nuclei synthesized in such reactions. The quasi-fission process is observed also for lighter nuclear systems, in which the lighter closed shell nuclear clusters play the main role [44].

Note, that the heavy nuclear system, formed, for example, in the collision of 48 Ca with 248 Cm, may come also to the mass-symmetric exit channels without formation of compound nucleus—see the path marked by QF₂ in Fig. 7.11a. This quasi-fission process of second type cannot be distinguished from the regular fission of the compound nucleus and, thus, experimentally it is impossible to measure the fusion cross section for such heavy nuclear systems. Theoretical estimation of the fusion cross section for 48 Ca + 248 Cm collisions at 203 MeV center-of-mass energy (Bass barrier for this system is equal to 201 MeV) gives a very low value of 0.02 mb [7] (whereas the quasi-fission cross section is about 10 mb at this energy). It is the low value of the fusion cross section multiplied by low survival probability of the excited compound nucleus (about 10^{-7} at the

corresponding excitation energy $E_{\rm CN}^* \sim 40$ MeV) which leads to extremely low yield of superheavy elements in such reactions [41].

7.3 Local Potential Minima and Shape Isomeric States

Within the two-center shell model, after contact of colliding nuclei, the processes of compound nucleus formation, fission and quasi-fission may be described both in the space of $(R, \eta, \delta_1, \delta_2)$ and in the space $(a_1, \delta_1, a_2, \delta_2)$, because for a given nuclear configuration $(R, \eta, \delta_1, \delta_2)$ we may unambiguously determine the two deformed cores a_1 and a_2 surrounded with a certain amount of shared nucleons $\Delta A = A_{\rm CN} - a_1 - a_2$. This double choice of equivalent sets of coordinates is extremely important for clear understanding and interpretation of physical meaning of the intermediate local minima appearing on the multi-dimensional adiabatic potential energy surface.

The adiabatic driving potential for formation and decay of superheavy nucleus $^{296}116$ at fixed deformations of both fragments is shown in Fig. 7.12 as a function of elongation and mass asymmetry and also as a function of charge numbers z_1 and z_2 (minimized over neutron numbers n_1 and n_2) at $R \le R_{\rm cont}$. It is easy to see that the shell structure, clearly revealing itself at the contact of two nuclei, is also retained at $R < R_{\rm cont}$ (see the deep minima in the regions of $z_{1,2} \sim 50$ and $z_{1,2} \sim 82$ in Fig. 7.12b).

Following the fission path (dotted curves in Fig. 7.12a, b) the nuclear system passes through the optimal configurations (with minimal potential energy) and overcomes the multi-humped fission barrier (Fig. 7.12c). The intermediate minima located along this path correspond to the shape isomeric states. From the analysis of the driving potential one may unambiguously conclude that these isomeric states are nothing else but the two-cluster configurations with magic or semi-magic cores *surrounded with a certain amount of shared nucleons*. Thus, the shape isomeric states (discovered experimentally in Dubna many years ago [45]) are the most obvious and vivid manifestation of the clusterization of heavy nuclei. Note that these isomeric states are rather similar in physics to the light nuclear molecules consisting of two alpha-particles and extra neutrons in covalent binding orbits [46, 47].

In our case (fission of nucleus $^{296}116$) the second (after ground state) minimum on the fission path appears due to the two-cluster nuclear configuration consisting of tin-like and krypton-like cores and about 70 shared nucleons. The third minimum corresponds to the mass-symmetric clusterization with two magic 132 Sn cores (surrounded with about 30 common nucleons), which finally decay to the preferable asymmetric fission valley with 132 Sn and 164 Dy fragments. It is clear that the same interpretation of the shape isomeric states should be true also for lighter nuclei. Of course, if the compound nucleus is lighter than Fm ($Z_{\rm CN} \leq 100$) the second minimum caused by two tin cores cannot appear. Such nuclei should have in general two-humped fission barriers with one pronounced shape isomeric

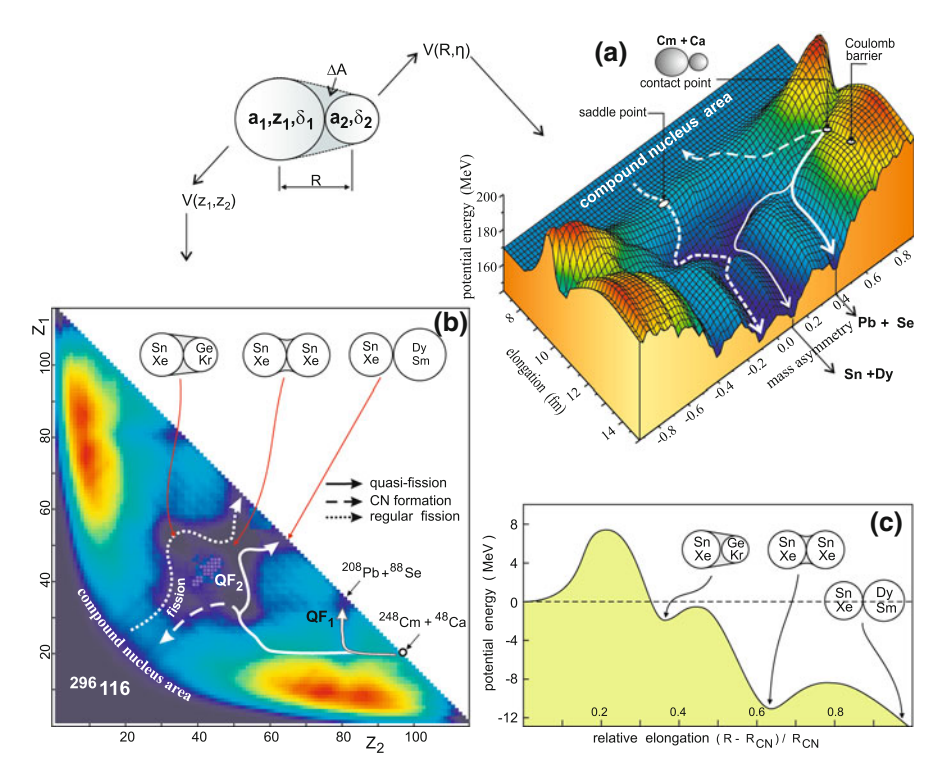


Fig. 7.12 Adiabatic driving potential of heavy nuclear system formed in collision of 48 Ca with 248 Cm. **a** Potential energy in the "elongation–mass asymmetry" space. **b** Topographical landscape of the same driving potential in the (z_1, z_2) plane. *Dashed, solid* and *dotted curves* show most probable trajectories of fusion, quasi-fission and regular fission, respectively. The *diagonal* corresponds to the contact configurations $(R = R_{\text{cont}}, z_1 + z_2 = Z_{\text{CN}}, \Delta A = 0)$. **c** The three-humped barrier calculated along the fission path $(dotted\ curve)$

state (the other minima may arise, in principle, due to deformed closed shell cores).

7.4 Cluster (Shell) Effects in Low Energy Heavy-Ion Collisions

Clustering phenomena should reveal themselves also in collisions of heavy ions. Of course, at high incident energies the nucleon degrees of freedom become to prevail over the collective ones. Large excitation energy of heavy nuclear system also destroy the shell effects. Under these conditions only small nuclear clusters (such as α -particles) may appear, but not so heavy as lead-like or tin-like fragments. The issue about maximal excitation energy, at which the shell effects are still important and heavy nuclear clusters play a noticeable role, remains open. In fact, there are not many experimental data on low-energy near-barrier collisions of

heavy nuclei (moreover, most of them are rather incomplete), and we are still far from a clear understanding and proper description of all the strongly coupled channels of such reactions.

7.4.1 Equations of Motion

A choice of dynamic equations for the description of low-energy deep inelastic scattering of heavy ions, fusion, quasi-fission and regular fission is not evident. For the collective coordinates R, δ various equations can be used, namely: classical Newtonian and Langevin type [48] or quantum Schrödinger coupled differential equations. The corresponding inertia parameters μ_R and μ_δ can be calculated, for example, within the Werner–Wheeler approach [49, 50] or within the cranking model [51]. However a proper description of the nucleon transfer and the change of the mass asymmetry η (which is a discrete variable by its nature) is not so simple. Moreover, the corresponding inertia parameter μ_η , being calculated within the Werner–Wheeler approach, becomes infinite at contact (scission) point and for separated nuclei. Thus the nucleon transfer and a change of the mass asymmetry requires a separate consideration.

The master-equation for the distribution function $\varphi(A, t)$

$$\frac{\partial \varphi}{\partial t} = \sum_{A' = A+1} \lambda(A' \to A) \varphi(A', t) - \lambda(A \to A') \varphi(A, t)$$
 (7.11)

seems to be good for the description of nucleon transfer in deep inelastic scattering [52, 53]. Here A is the number of nucleons in one of the fragments at time t and $\lambda(A' \leftrightarrow A)$ is the macroscopic transition probability. This equation was successfully used also for the description of CN formation in strong competition with the dominant quasi-fission channels in reactions leading to the synthesis of superheavy nuclei [41, 42].

Nevertheless, Eq. (11) defines the evolution of the distribution function $\varphi(A,t) \sim \varphi(\eta,t)$ and not of the coordinate η itself! Thus, it cannot be included directly in a common set of coupled differential equations for the coordinates R and δ . However, by certain rules (see, for example, Refs [54, 55]) this equation may be transformed first to the Fokker–Planck equation $\frac{\partial \varphi}{\partial t} = -\frac{\partial}{\partial A}(D^{(1)}\varphi) + \frac{\partial^2}{\partial A^2}(D^{(2)}\varphi)$ and then to the Langevin type equation $\frac{dA}{dt} = D^{(1)} + \sqrt{D^{(2)}}\Gamma(t)$, or (so far as $\eta = (2A - A_{\rm CN})/A_{\rm CN}$)

$$\frac{d\eta}{dt} = \frac{2}{A_{\rm CN}} D_A^{(1)}(\eta) + \frac{2}{A_{\rm CN}} \sqrt{D_A^{(2)}(\eta)} \Gamma(t), \tag{7.12}$$

where $\Gamma(t)$ is the normalized random variable with Gaussian distribution, $\langle \Gamma(t) \rangle = 0$, $\langle \Gamma(t) \Gamma(t') \rangle = 2\delta(t-t')$. This random variable is responsible for the fluctuations and, thus, for diffusion of nucleons between overlapping nuclei. The transport coefficients $D^{(1)}$ and $D^{(2)}$ are defined as follows

$$D^{(1)} = \int (A' - A)\lambda(A \to A')dA',$$

$$D^{(2)} = \frac{1}{2} \int (A' - A)^2 \lambda(A \to A')dA'.$$
(7.13)

Note that Eq. (12) describes an inertialess change of the mass asymmetry η , i.e., there is no kinetic energy connected with nucleon transfer (whereas the potential energy strongly depends on η).

Assuming that sequential nucleon transfers play a main role in mass rearrangement, i.e. $A' = A \pm 1$, we have

$$D^{(1)} = \lambda(A \to A + 1) - \lambda(A \to A - 1),$$

$$D^{(2)} = \frac{1}{2}\lambda(A \to A + 1) + \lambda(A \to A - 1).$$
(7.14)

For nuclei in contact the transition probability $\lambda(A'=A\pm 1)$ is defined by a change of nuclear level density [52, 53], $\rho\sim\exp[2\sqrt{aE^*(R,\delta,\eta)}]$ (which, in turn, depends on the local excitation energy)

$$\lambda^{(\pm)} = \lambda_0 \sqrt{\rho(A \pm 1)/\rho(A)} \approx \lambda_0 \exp[(V(R, \delta, A \pm 1) - V(R, \delta, A)/2T]. \quad (7.15)$$

Here $T=\sqrt{E^*/a}$ is the local nuclear temperature, E^* excitation energy, a level density parameter, and λ nucleon transfer rate, which is about $10^{22}~{\rm s}^{-1}$ as it was estimated in [52, 53]. The nucleon transfer rate may, in principle, depend on the excitation energy (the same hold for the transport coefficients $D^{(1,2)}$). This feature, however, is not completely clear. In [52] the mass diffusion coefficient was assumed to be independent of excitation energy, whereas the microscopic consideration gives a square root dependence of it on nuclear temperature [56]. A linear dependence of the mass diffusion coefficient on T can be also found in the literature [57]. For the moment, it looks much better to use the nucleon transfer rate λ_0 as an adjustable parameter of the model [7]. The temperature dependence of this parameter and its precise value may be derived from a systematic analysis of available experimental data on DI scattering of heavy ions.

Nucleon transfers for slightly separated nuclei are also rather probable. They are determined by extension of the tails of the single particle wave functions. This intermediate (before contact) nucleon exchange plays a very important role in sub-barrier fusion processes [58, 59] and has to be taken into account in Eq. (12). This can be done by using the following final expression for the transition probability

$$\lambda^{(\pm)} = \lambda_0 \sqrt{\frac{\rho(A \pm 1)}{\rho(A)}} P_{\text{tr}}(R, \delta, A \to A \pm 1). \tag{7.16}$$

Here $P_{\rm tr}(R, \delta, A \to A \pm 1)$ is the probability of one nucleon transfer depending on the distance between the nuclear surfaces and nucleon separation energy.

This probability goes exponentially to zero at $R \to \infty$ and it is equal to unity for overlapping nuclei. A rather simple semiclassical approximation for $P_{\rm tr}$ proposed in Ref. [58] can be used for this quantity. Equation (12) along with (16) defines a continuous change of the mass asymmetry in the whole space. It is clear that $\frac{d\eta}{dt} \to 0$ (no nucleon transfer) for far separated nuclei.

To describe properly the yield of different isotopes of a given element (including the extremely neutron-rich ones, see below) one needs to consider separately neutron and proton transfers. Thus, we should extend the model described above and (instead of only one mass-asymmetry variable η) take into consideration the neutron and proton asymmetries, $\eta_N = (2N - N_{\rm CN})/N_{\rm CN}$ and $\eta_Z = (2Z - Z_{\rm CN})/Z_{\rm CN}$, where N and Z are the neutron and proton numbers in one of the fragments, whereas $N_{\rm CN}$ and $Z_{\rm CN}$ refer to the compound nucleus. This noticeably complicates the problem because of the necessity to deal with the four-dimensional potential energy surface $V(R, \delta, \eta_N, \eta_Z)$ for overlapping nuclei. In that case, instead of Eq. (12), we have a set of two equations defining the proton and neutron rearrangement

$$\frac{d\eta_N}{dt} = \frac{2}{N_{\rm CN}} D_N^{(1)} + \frac{2}{N_{\rm CN}} \sqrt{D_N^{(2)}} \Gamma_N(t), \quad \frac{d\eta_Z}{dt} = \frac{2}{Z_{\rm CN}} D_Z^{(1)} + \frac{2}{Z_{\rm CN}} \sqrt{D_Z^{(2)}} \Gamma_Z(t). \quad (7.17)$$

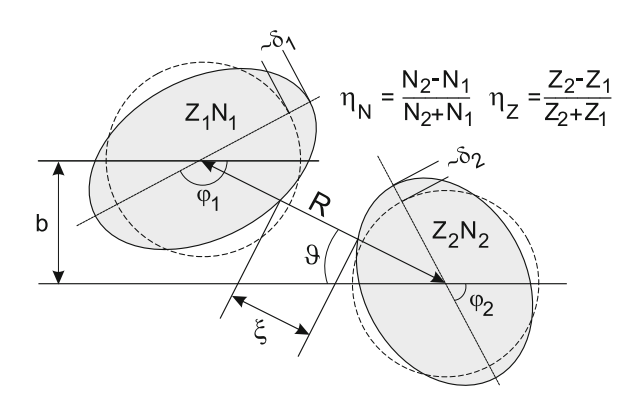
The transport coefficients $D_{N,Z}^{(1,2)}$ are defined by Eqs. (14) with the neutron and proton transition probability given by

$$\lambda_{N,Z}^{(\pm)} = \lambda_{N,Z}^{0} \sqrt{\frac{\rho(A\pm 1)}{\rho(A)}} P_{N,Z}^{\text{tr}}(R, \delta, A \to A \pm 1).$$
 (7.18)

There is no information in the literature on a difference between neutron and proton transfer rates, and for simplicity we assume here that $\lambda_N^0 = \lambda_Z^0 = \lambda^0/2$, where λ^0 is the nucleon transfer rate defined above.

Finally, we have the following set of 14 coupled Langevin type equations for 8 degrees of freedom $\{R, \vartheta, \delta_1, \delta_2, \varphi_1, \varphi_2, \eta_N, \eta_Z\} \equiv \mathbf{x}$ shown in Fig. 7.13.

Fig. 7.13 Degrees of freedom used in the model



$$\begin{split} \frac{dR}{dt} &= \frac{p_R}{\mu_R}, \quad \frac{d\vartheta}{dt} = \frac{\hbar\ell}{\mu_R R^2}, \quad \frac{d\varphi_1}{dt} = \frac{\hbar L_1}{\Im_1}, \quad \frac{d\varphi_2}{dt} = \frac{\hbar L_2}{\Im_2}, \\ \frac{d\delta_1}{dt} &= \frac{p_{\delta_1}}{\mu_{\delta_1}}, \quad \frac{d\delta_2}{dt} = \frac{p_{\delta_2}}{\mu_{\delta_2}}, \\ \frac{d\eta_N}{dt} &= \frac{2}{N_{\rm CN}} D_N^{(1)} + \frac{2}{N_{\rm CN}} \sqrt{D_N^{(2)}} \Gamma_N(t), \\ \frac{d\eta_Z}{dt} &= \frac{2}{Z_{\rm CN}} D_Z^{(1)} + \frac{2}{Z_{\rm CN}} \sqrt{D_Z^{(2)}} \Gamma_Z(t), \\ \frac{dp_R}{dt} &= -\frac{\partial V}{\partial R} + \frac{\hbar^2 \ell^2}{\mu_R R^3} + \left(\frac{\hbar^2 \ell^2}{2\mu_R^2 R^2} + \frac{p_R^2}{2\mu_R^2}\right) \frac{\partial \mu_R}{\partial R} + \frac{p_{\delta_1}^2}{2\mu_{\delta_1}^2} \frac{\partial \mu_{\delta_1}}{\partial R} + \frac{p_{\delta_2}^2}{2\mu_{\delta_2}^2} \frac{\partial \mu_{\delta_2}}{\partial R} \\ &- \gamma_R \frac{p_R}{\mu_R} + \sqrt{\gamma_R T} \Gamma_R(t), \\ \frac{d\ell}{dt} &= -\frac{1\partial V}{\hbar \partial \vartheta} - \gamma_{\rm tang} \left(\frac{\ell}{\mu_R R} - \frac{L_1}{\Im_1} a_1 - \frac{L_2}{\Im_2} a_2\right) R + \frac{R}{\hbar} \sqrt{\gamma_{\rm tang}} T \Gamma_{\rm tang}(t), \\ \frac{dL_1}{dt} &= -\frac{1}{\hbar \partial \Psi} + \gamma_{\rm tang} \left(\frac{\ell}{\mu_R R} - \frac{L_1}{\Im_1} a_1 - \frac{L_2}{\Im_2} a_2\right) a_1 - \frac{a_1}{\hbar} \sqrt{\gamma_{\rm tang}} T \Gamma_{\rm tang}(t), \\ \frac{dL_2}{dt} &= -\frac{1}{\hbar \partial \varphi_1} + \gamma_{\rm tang} \left(\frac{\ell}{\mu_R R} - \frac{L_1}{\Im_1} a_1 - \frac{L_2}{\Im_2} a_2\right) a_2 - \frac{a_2}{\hbar} \sqrt{\gamma_{\rm tang}} T \Gamma_{\rm tang}(t), \\ \frac{dp_{\delta_1}}{dt} &= -\frac{\partial V}{\hbar \partial \varphi_2} + \gamma_{\rm tang} \left(\frac{\ell}{\mu_R R} - \frac{L_1}{\Im_1} a_1 - \frac{L_2}{\Im_2} a_2\right) a_2 - \frac{a_2}{\hbar} \sqrt{\gamma_{\rm tang}} T \Gamma_{\rm tang}(t), \\ \frac{dp_{\delta_1}}{dt} &= -\frac{\partial V}{\partial \delta_1} + \frac{p_{\delta_1}^2}{2\mu_{\delta_1}^2} \frac{\partial \mu_{\delta_1}}{\partial \delta_1} + \frac{p_{\delta_2}^2}{2\mu_{\delta_2}^2} \frac{\partial \mu_{\delta_2}}{\partial \delta_1} + \frac{\hbar^2 L_1^2 \partial \Im_1}{2\Im_1^2} \partial \delta_1 + \left(\frac{\hbar^2 \ell^2}{2\mu_R^2 R^2} + \frac{p_R^2}{2\mu_R^2}\right) \frac{\partial \mu_R}{\partial \delta_1} \\ &- \gamma_{\delta_1} \frac{p_{\delta_1}}{\mu_{\delta_1}} + \sqrt{\gamma_{\delta_1}} T \Gamma_{\delta_1}(t), \\ \frac{dp_{\delta_2}}{dt} &= -\frac{\partial V}{\partial \delta_2} + \frac{p_{\delta_1}^2}{2\mu_{\delta_1}^2} \frac{\partial \mu_{\delta_1}}{\partial \delta_2} + \frac{p_{\delta_2}^2}{2\mu_{\delta_2}^2} \frac{\partial \mu_{\delta_2}}{\partial \delta_2} + \frac{\hbar^2 L_2^2 \partial \Im_2}{2\Im_2^2} \partial \delta_2} + \left(\frac{\hbar^2 \ell^2}{2\mu_R^2 R^2} + \frac{p_R^2}{2\mu_R^2}\right) \frac{\partial \mu_R}{\partial \delta_2} \\ &- \gamma_{\delta_2} \frac{p_{\delta_2}}{\mu_{\delta_1}} + \sqrt{\gamma_{\delta_2}} T \Gamma_{\delta_2}(t). \end{split}$$

Here φ_1 and φ_2 are the angles of rotation of the nuclei in reaction plane (their moments of inertia are $\Im_{1,2}(\delta_{1,2})=k_{\overline{5}}^2M_{1,2}R_{1,2}^0{}^2(1+\delta_{1,2}/3),\ k\approx 0.4),\ a_{1,2}=R/2\pm(R_1-R_2)/2$ are the distances from the centers of fragments up to the middle point between nuclear surfaces, and $R_{1,2}=R_{1,2}^0[1+\sqrt{5/4\pi}\delta_{1,2}\times P_2(\cos(\varphi_{1,2}-\vartheta))]$ are the nuclear radii. ℓ is the orbital angular momentum of relative motion and $L_{1,2}$ are the angular momenta of two fragments. γ_R , $\gamma_{\rm tang}$ and $\gamma_{\delta_{-1,2}}$ are the friction forces which depend generally on the coordinates ${\bf x}$. The random forces in the last eight equations (proportional to the friction forces and \sqrt{T}) are responsible for the fluctuations of all the degrees of freedom. These fluctuations (appearing when nuclei approach each other) increase with increasing excitation energy (temperature) of nuclear system.

For the moment we ignore the non-diagonal terms of the mass and friction parameters. The so called "sliding friction" (which is proportional to the relative

velocity of nearest nuclear surfaces $v_{\rm tang} = \frac{\hbar\ell}{\mu_R R} - \frac{\hbar L_1}{\Im_1} a_1 - \frac{\hbar L_2}{\Im_2} a_2$) is mainly responsible for the dissipation of the angular momentum (see, for example [5], p. 265 and [60]). The nucleus–nucleus potential energy depends on the distance between nuclear surfaces $\xi = R - R_{\rm cont}$, where $R_{\rm cont} = R_1(\eta, \delta_1, \varphi_1 - \theta) + R_2(\eta, \delta_2, \varphi_2 - \theta)$. Therefore $\frac{\partial V}{\partial \varphi_1} + \frac{\partial V}{\partial \varphi_2} = -\frac{\partial V}{\partial \theta}$ and the total angular momentum $\ell + L_1 + L_2$ is evidently conserved in the processes described by the set of Eqs. (19).

The unified set of dynamic equations of motion (19) may be used for simultaneous and continuous (not interrupted in time) description of the evolution of a heavy nuclear system starting from the approaching stage in the entrance channel and ending in the DI, QF and/or fusion–fission reaction channels. The double differential cross-sections of all the processes are calculated as follows:

$$\frac{d^2\sigma_{N,Z}}{d\Omega dE}(E,\theta) = \int_{0}^{\infty} bdb \frac{\Delta N_{N,Z}(b,E,\theta)}{N_{\text{tot}}(b)} \frac{1}{\sin(\theta)\Delta\theta \Delta E}.$$
 (7.20)

Here $\Delta N_{N,Z}(b, E, \theta)$ is the number of events at a given impact parameter b in which a nucleus (N, Z) is formed with kinetic energy in the region $(E, E + \Delta E)$ and center-of-mass outgoing angle in the region $(\theta, \theta + \Delta \theta)$, $N_{tot}(b)$ is the total number of simulated events for a given value of impact parameter. Expression (20) describes the mass, charge, energy and angular distributions of the excited *primary* fragments formed in a binary reaction. Subsequent de-excitation cascades of these fragments via emission of light particles and gamma-rays in competition with fission has to be taken into account for each event (for example, within the statistical model) leading to the *final* distributions of the detected reaction products. All the parameters of the model can be found in Refs [7, 61] and those needed for description of decay of excited primary fragments in Ref. [62]. The decay properties of excited nuclei (fission, light particle evaporation and gamma emission widths as well as the corresponding survival probabilities) may be easily calculated within the standard statistical model on the Web page [40].

The model described above allows one to perform also a time analysis of the studied reactions. Each tested event is characterized by the reaction time $\tau_{\rm int}$, which is calculated as a difference between re-separation (scission) and contact times. Those events, in which nuclei do not come in contact (e.g., for large impact parameters), are excluded from the analysis. In such a way, for all the channels we may calculate and analyze reaction-time distributions and the corresponding cross sections $d\sigma_n/d\tau_{\rm int}$ (see below).

7.4.2 Shell Effects in Low-Energy Damped Collisions

The most evident manifestation of the shell (cluster) effects in heavy ion collisions are the quasi-fission phenomena discussed above. These effects should reveal themselves also in transfer reactions at low collision energies. Damped collisions

of heavy nuclei were studied extensively about 30 years ago (see, for example, review [60] and references therein). Among others, there had been great interest in the use of heavy-ion transfer reactions with actinide targets to produce new nuclear species in the transactinide region [63–68]. The cross sections were found to decrease very rapidly with increasing atomic number of surviving target-like fragments, however, Fm and Md neutron-rich isotopes were produced at the level of $0.1~\mu b$. At the same time it was also observed that the nuclear structure might strongly influence the nucleon flow in the low-energy dissipative collisions of heavy ions. For example, in 238 U-induced reactions on 110 Pd at about 6 MeV/u bombarding energy an enhanced proton flow along the neutron shells $N_1 = 82$ and $N_2 = 126$ (reached almost simultaneously in target-like and projectile-like fragments) was observed in the distribution of binary reaction products [69]. Unfortunately, up to now, most experimental studies of damped collisions were performed at rather high incident energies (well-above the Coulomb barrier) and were not aimed at revealing the shell effects.

New interest in the damped collision of heavy nuclei is conditioned first of all by a search for new ways for production of neutron rich superheavy (SH) nuclei and isotopes. SH elements obtained in "cold" fusion reactions with Pb or Bi target [70] are situated along the proton drip line being very neutron-deficient with a short half-life. In fusion of transactinides with ⁴⁸Ca more neutron-rich SH nuclei were produced [71] with much longer half-life. But they are still far from the center of the predicted "island of stability" formed by the neutron shell around N=184 and proton shell at Z=114 and/or Z=120. In the "cold" fusion, the cross sections for formation of SH nuclei decrease very fast with increasing charge of the projectile and become less than 1 pb for Z > 112. On the other hand, heaviest transactinide, Cf, which can be used as a target in the second method, leads to the SH nucleus with Z = 118 being fused with 48 Ca. Using the next nearest elements instead of ⁴⁸Ca (e.g., ⁵⁰Ti, ⁵⁴Cr, etc.) in fusion reactions with actinides is expected less encouraging, though experiments of such a kind are already in progress. In this connection other ways for the production of SH elements in the region of the "island of stability" should be searched for [72].

In [61, 73] low-energy collisions of very heavy nuclei ($^{238}\text{U} + ^{238}\text{U}$, $^{232}\text{Th} + ^{250}\text{Cf}$, and $^{238}\text{U} + ^{248}\text{Cm}$) have been studied and a possibility for the formation of the surviving superheavy long-lived neutron-rich nuclei has been predicted as a matter of principle (see below). It was found that the charge and mass transfers strongly depend on the shell structure of the multi-dimensional potential energy surface and also on the values of the fundamental parameters of nuclear dynamics, such as nuclear viscosity and nucleon transfer rate, which are not well determined yet. In spite of the rather good agreement of recent experimental data on $^{238}\text{U} + ^{238}\text{U}$ collisions [74] with our predictions, more detailed experiments have to be performed in order to find out and to study the shell effects in multi-nucleon transfer reactions in low-energy damped collisions of heavy ions.

In this connection we proposed to explore the effect of the "inverse" (antisymmetrizing) quasi-fission process in experiments with less heavy nuclei, in particular, in collisions of ¹⁶⁰Gd with ¹⁸⁶W [75]. The choice of the projectile and

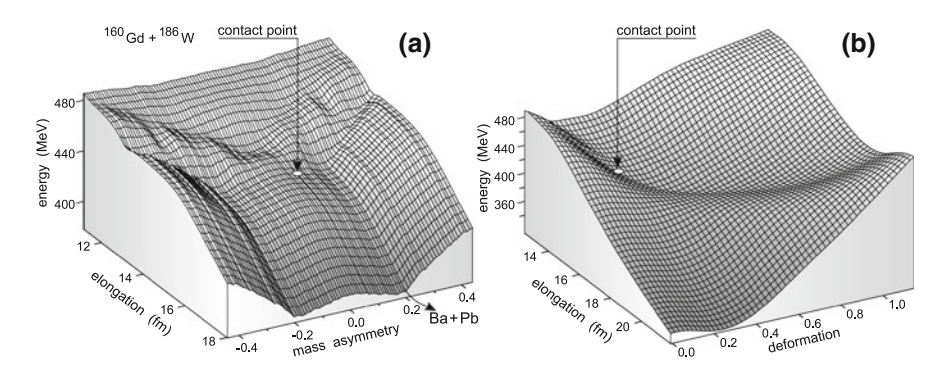


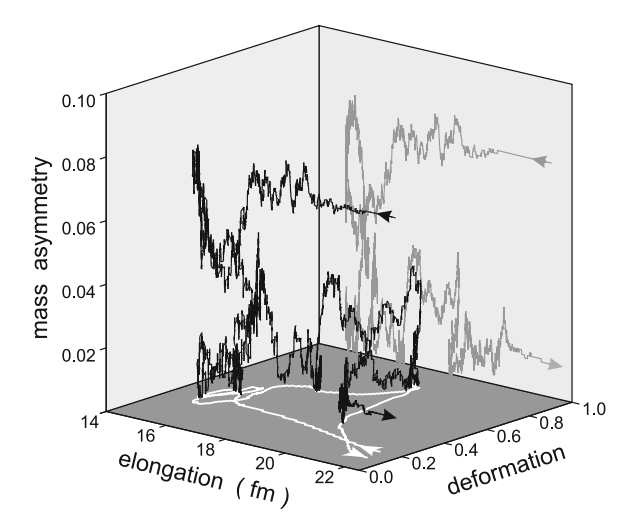
Fig. 7.14 Potential energy surface of the nuclear system formed in collision of $^{160}\text{Gd} + ^{186}\text{W}$ [75]. **a** Dependence on elongation and mass asymmetry (deformation is fixed at $\delta = 0.2$); **b** dependence on elongation and deformation at fixed value of the mass asymmetry $\eta = 0.075$ (entrance channel)

target nuclei is conditioned by the fact that these nuclei are located just between the closed shells ($Z_1 = 50$, $N_1 = 82$) and ($Z_2 = 82$, $N_2 = 126$), which, as we expect, play a significant role in the multi-nucleon transfer processes. Comparison of theoretical predictions with experimental probability for multi-nucleon transfer (which can be measured for this reaction much easier as compared to U + Cm collisions, for example) may be used then for a realistic estimation of a possibility for the synthesis of long-living neutron-rich SH nuclei in low-energy damped collisions of heavy ions (including those induced by the accelerated neutron-rich fission fragments).

In Fig. 7.14 the multi-dimensional adiabatic driving potential is shown in the spaces of "elongation–mass asymmetry" and "elongation–deformation" for the axially symmetric nuclear system formed in the collision of $^{160}\text{Gd} + ^{186}\text{W}$. The deep valley corresponding to formation of well bound nuclei ^{138}Ba and ^{208}Pb is clearly visible on the surface. There is no potential pocket for this heavy nuclear system. However, as can be seen from Fig. 7.14, the potential energy at contact point is rather flat (particularly along the deformation coordinate), which means that the nuclei may keep in touch a long time due to fluctuations and nucleon transfer. One of the "trajectories" showing evolution of the nuclear system formed in the collision of ^{160}Gd with ^{186}W at zero impact parameter and 460 MeV center-of-mass energy (corresponding to the Bass barrier [5] of this combination) is presented in Fig. 7.15. Moving along this trajectory the nuclear system was in contact during 0.5×10^{-20} s, the time from the moment when colliding nuclei (Gd + W, $\eta = 0.075$) came in touch in the entrance channel and up to the moment of scission (at $\eta = 0.013$) in the exit one.

In Fig. 7.16a the potential energy of this nuclear system is shown at contact configuration depending on mass asymmetry (mass transfer). As can be seen from Fig. 7.14b the potential energy depends strongly on deformations of touching fragments. However, even for rather large deformations the shell effects are still quite visible. In particular, the configuration of 138 Ba + 208 Pb has much lower

Fig. 7.15 Typical trajectory showing evolution of the nuclear system formed in collision of ¹⁶⁰Gd + ¹⁸⁶W at 460 MeV center-of mass energy (zero impact parameter) in the space of "elongation–deformation–mass asymmetry" [75]



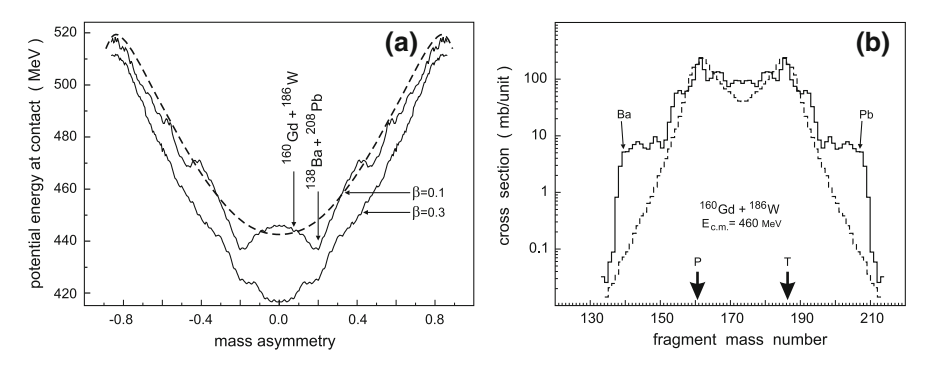


Fig. 7.16 a Potential energy at contact configuration of different fragments formed in collision of ^{160}Gd with ^{186}W . The deformation is fixed at $\delta=0.1$ (upper curves) and $\delta=0.3$ (lower curve). The dashed curve shows the potential energy without shell corrections at $\delta=0.1$. **b** Primary fragment mass distribution in the $^{160}\text{Gd}+^{186}\text{W}$ reaction at 460 MeV center-of mass energy calculated with (solid) and without (dashed histogram) shell corrections in potential energy [75]

potential energy as compared with nearest ones due to the influence of the neutron (N=82 and N=126) and proton (Z=82) shells. The mass distributions of the primary fragments in the $^{160}\text{Gd} + ^{186}\text{W}$ reaction calculated with and without the shell corrections to the potential energy are shown in Fig. 7.16b (mass distribution of the final fragments is rather close, see Ref. [75]). Only the events with energy loss higher than 15 MeV were taken into account to exclude a contribution from the quasi-elastic scattering. As can be seen at near barrier collision energies, the shell effects really play a very important role and may increase by two orders of magnitude the yield of the reaction products even for a transfer of 20 nucleons.

For more asymmetric combinations (such as Ca + Cm and so on) the shell effects, caused by the magic nuclei located between the masses of colliding partners (132 Sn and 208 Pb in the case of Ca + Cm collision), reveal themselves in the quasi-fission processes (see above Sect. 2.4). The process we discuss here is rather similar. However there are two important distinctions. First, CN is not formed at all in collision of very heavy nuclei. This is not a fusion–fission process as in the case of Ca + Cm collision but a deep inelastic (damped) reaction. Second, the magic nuclei (Z = 50, N = 82) and (Z = 82, N = 126) are located here from the outside of the colliding partners. Thus the shell effects drive the system to increase the initial mass asymmetry and decay in the two (light and heavy) massive clusters—that is why we name this process "inverse (antisymmetrizing) quasi-fission". Note that the macroscopic part of the adiabatic potential energy always drives heavy nuclear system to symmetric configuration (see, for example, Fig. 7.9).

This process has not yet been studied experimentally, even though experimental observation of the effect is quite important! First, it would give us a better understanding of the low-energy dynamics of heavy nuclear systems and clarify to what extend the shell effects (clusterization) influence the mass transfer in damped collisions of heavy ions. Second, the experimentally measured enhancement factor in the yield of closed shell nuclei might allow us to make more accurate predictions (or simple extrapolations) of this effect for other nuclear combinations, which are more difficult for experimental study. If experimental observations confirm our predictions, then the production of long-living neutron-rich SH nuclei in collisions of transuranium ions will be really possible due to a large mass and charge rearrangement in the inverse (anti-symmetrizing) quasi-fission process caused by the Z=82 and N=126 nuclear shells (see below).

7.4.3 Production of New Heavy Neutron Rich Nuclei at the "North-East" Part of Nuclear Map

During the last years the study of exotic nuclei located far from the stability line has been of increased interest from experimental and theoretical point of view and the progress in the investigation of these nuclei has been impressive. Nowadays, nuclei far from stability are accessible for experimental study in almost any region of the map of nuclides. The only exception is the north-east part where a vast "blank spot" is still unexplored. The present limits of the upper part of the nuclear map is very close to stability while the unexplored area of heavy neutron-rich nuclides (to the east of the stability line) is extremely important for nuclear astrophysics investigations and, in particular, for the understanding of the r-process of astrophysical nucleo-genesis.

According to a recent report by the National Research Council of the National Academy of Sciences (USA), the origin of heavy elements from iron to uranium remains one of the 11 greatest unanswered questions of modern physics (see, for example [76]), and it is likely to remain a hot research topic for the years to come.

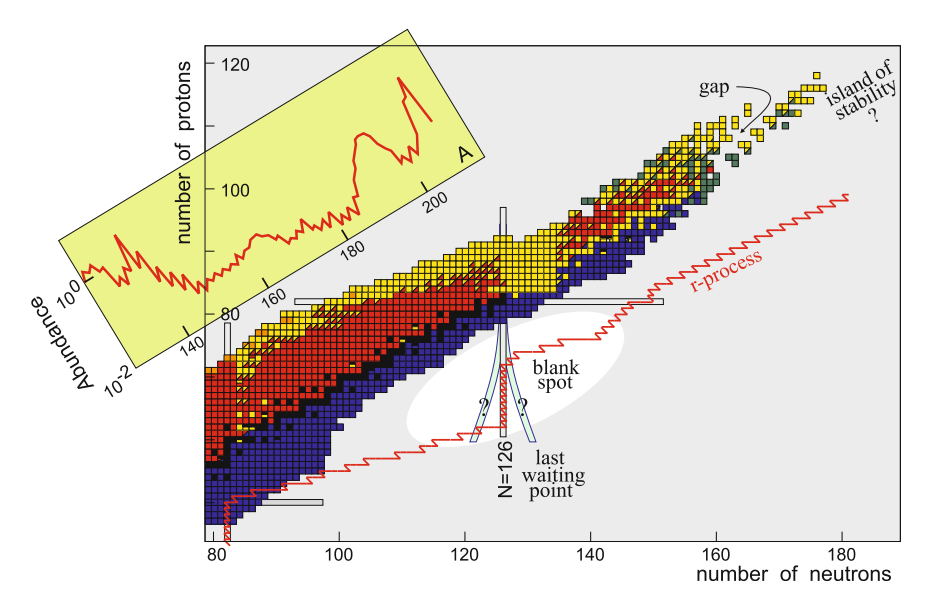


Fig. 7.17 Top part of the nuclear map. The r-process path is shown schematically. In the *inset* the abundance of the elements is shown

The r-process path is located (and interrupted by fission) just in the region of unknown heavy nuclei with a large neutron excess. The neutron shell N=126 (and $Z\sim70$) is the last "waiting point" on this path (see Fig. 7.17). The half-lives and other characteristics of these nuclei are extremely important for the r-process scenario of the nucleosynthesis [77]. Study of the structural properties of nuclei along the neutron shell N=126 could also contribute to the present discussion of the quenching of shell effects in nuclei with large neutron excess.

As a rule, new (neutron and proton rich) isotopes located far from the stability line are obtained in the fragmentation (spallation) processes at intermediate colliding energies, in fission of heavy nuclei and in low-energy fusion reactions. Two first methods are extensively used today for the production of new isotopes in the light and medium mass region including those which are close to the drip lines. Due to the "curvature" of the stability line, in the fusion reactions of stable nuclei we may produce only proton rich isotopes of heavy elements. For example, in fusion of neutron rich ¹⁸O and ¹⁸⁶W nuclei one may get only the neutron deficient ²⁰⁴Pb excited compound nucleus, which after evaporation of several neutrons shifts even more to the proton rich side. This is the main reason for the impossibility to reach the center of the "island of stability" ($Z \sim 114$, 120 and $N \sim 184$) in the superheavy mass region in fusion reactions with stable projectiles. Because of that we also have almost no information about neutron rich isotopes of heavy elements located in the north-east part of the nuclear map—for example, there are 19 known neutron-rich isotopes of cesium (Z = 55) and only 4 of platinum (Z = 78).

A novel idea was recently proposed in [78, 79] for the production of the heavy neutron-rich nuclei (located along the closed neutron shell N = 126) via the

multi-nucleon transfer processes of low-energy collisions of heavy ions. It is well known that in the deep inelastic (damped) collisions of heavy ions the relative motion energy is quickly transformed into internal excitation of the projectile-like and target-like reaction fragments which are de-excited then by evaporation of light particles (mostly neutrons). This seems not to give us a chance for production of nuclei with large neutron excess in such reactions. However, if the colliding energy is rather low and the reaction Q-value is not very high, the formed primary reaction fragments might be not very much excited and will descend to their ground states after evaporation of a few neutrons thus remaining far from the stability line. The questions are how big is the cross section for the multi-nucleon transfer reactions at low colliding energies and could these reactions be considered as an alternative way for the production of exotic nuclei.

For the production of heavy neutron rich nuclei located along the neutron closed shell N=126 we proposed to explore the multi-nucleon transfer reactions in low-energy collisions of 136 Xe with 208 Pb. The idea is to use the stabilizing effect of the closed neutron shells in both nuclei, N=82 and N=126, respectively (see the left panel of Fig. 7.18). The proton transfer from lead to xenon might be rather favorable here because the light fragments formed in such a process are well bound (stable nuclei) and the reaction Q-values are almost zero, for example, even for a transfer of six protons in the reaction 136 Xe + 208 Pb \rightarrow 142 Nd + 202 Os the Q-value is equal to -8.3 MeV.

The landscape of the calculated cross sections for the yield of the different reaction fragments in low-energy collision of 136 Xe with 208 Pb is shown in the right panel of Fig. 7.18, whereas the cross sections for production of final (after a few neutron evaporation) heavy neutron-rich nuclei in this reaction at the incident energy $E_{\rm c.m.} = 450$ MeV, which is very close to the Coulomb barrier (Bass barrier for this combination is about 434 MeV), is shown in Fig. 7.19.

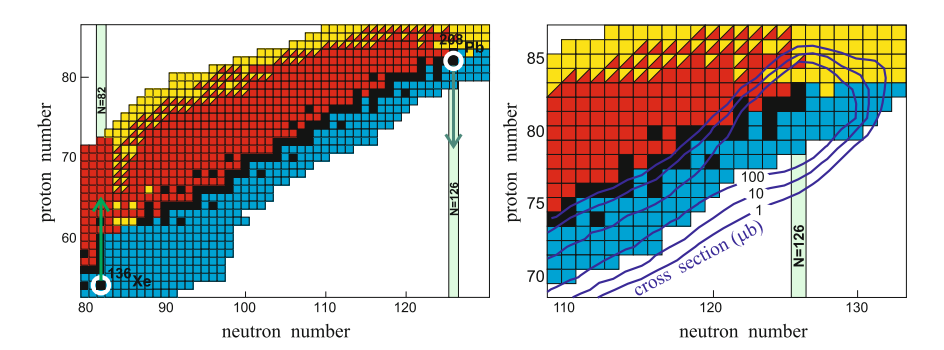


Fig. 7.18 Left panel schematic picture for preferable proton transfer reactions in low-energy collisions of 136 Xe with 208 Pb. Black rectangles indicate stable nuclei. Right panel landscape of the total cross section $d^2\sigma/dZdN$ (microbarns, numbers near the curves) for the production of heavy fragments in collisions of 136 Xe with 208 Pb at $E_{\rm c.m.}=450$ MeV. The contour lines are drawn over one order of magnitude

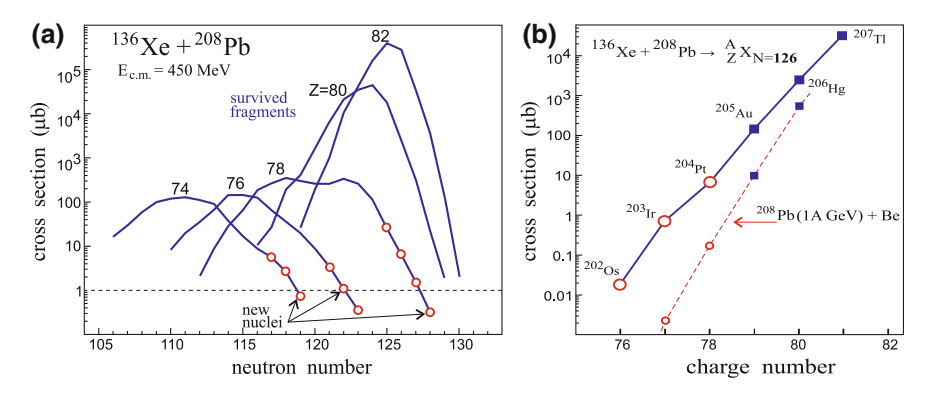


Fig. 7.19 a Cross sections for production of heavy neutron-rich nuclei in collisions of ¹³⁶Xe with ²⁰⁸Pb at $E_{\rm c.m.} = 450$ MeV. *Open circles* indicate unknown isotopes. **b** Yield of nuclei with neutron closed shell N = 126. The *dashed curve* shows the yield of the nuclei in high energy proton removal process [80]

Thus, we may conclude that the low-energy multi-nucleon transfer reactions can really be used for the production of heavy neutron rich nuclei. The estimated yields of neutron-rich nuclei are found to be rather high in such reactions (much larger than in high-energy proton-removal nuclear reactions [80], see Fig. 7.19b) and several tens of new nuclides can be produced, for example, in the near-barrier collision of ¹³⁶Xe with ²⁰⁸Pb. This finding may spur new studies at heavy-ion facilities and should have significant impact on future experiments. Similar reactions with uranium and thorium targets may be used for the production of new neutron rich isotopes with Z > 82. Accelerated neutron rich fission fragments (which hardly may be useful for the synthesis of superheavy nuclei in fusion reactions due to low cross sections [72]) look especially promising for production of new heavy neutron rich isotopes in low-energy multi-nucleon transfer processes. In the 132 Sn + 208 Pb reaction, for example, the nuclei 202 Os_{N=126} (six protons transferred) and $^{200}W_{N=126}$ (eight protons transferred) are produced with the Q-values of +4 and -3 MeV, correspondingly, which should significantly increase the cross sections. Note, that a possibility for the production of new heavy isotopes in the multi-nucleon transfer reactions with neutron-rich calcium and xenon beams at much higher energies (at which the shell effects do not play any role) has been discussed also in [81] within the semiclassical approach.

Cross sections of one microbarn are quite reachable at the available experimental setups. However the identification of new heavy nuclei obtained in the multi-nucleon transfer reactions is a rather complicated problem. Most of these nuclei undergo β^- decay. The atomic mass could be determined by the time-of-flight technique rather accurately. The identification of the atomic number of the heavy nucleus is more difficult. The same is true for the determination of its half-life, which is the most important property of the nuclei in the region of $N \sim 126$ (last waiting point in the r-process). In principle, it could be done by the registration of the electron cascade in the β^- -decay chain in coincidence with the

gamma-rays of the daughter nuclei. Anyhow, the synthesis and study of these nuclei (important for many reasons) is a challenge for low-energy nuclear physics now and in forthcoming years.

7.5 Low-Energy Collisions of Heavy Actinide Nuclei and Giant Nuclear Systems of Molecular Type

The idea to take advantage of the shell effects also for the production of SH nuclei in the multi-nucleon transfer processes of low-energy heavy ion collisions was proposed recently in [61, 73]. As shown above the shell effects play an important role in fusion of heavy ions with actinide targets driving the nuclear system to the quasi-fission channels (into the deep lead and tin valleys) and, thus, decreasing the fusion probability. On the contrary, in the transfer reactions the same effects may lead to enhanced yield of SH nuclei. It may occur if one of the heavy colliding nuclei, say ²³⁸U, gives away nucleons transforming to the double magic ²⁰⁸Pb nucleus (sui generis clustering), whereas another one, say ²⁴⁸Cm, accepts these nucleons becoming superheavy in the exit channel—the so called "inverse" (anti-symmetrizing) quasi-fission process (see Sect. 4.2). The time analysis of the damped collisions of actinide nuclei is also very interesting. If the system consisting of two very heavy nuclei holds in contact rather long time (forming a giant nuclear molecule), then the positron line structure (emerging on top of the background dynamical positron spectrum) may appear due to spontaneous $e^+e^$ production from the supercritical electric field of a giant atom. This fundamental QED process ("decay of the vacuum") was predicted many years ago [82–84] and was not observed yet experimentally.

7.5.1 Production of Superheavy Elements in Collisions of Actinide Nuclei

The use of multi-nucleon transfer from heavy-ion projectile to an actinide target nucleus for the production of new nuclear species in the transuranium region has a long history. Light (carbon [85], oxygen and neon [86]), medium (calcium [63, 87], krypton and xenon [67, 68]) and very heavy (238 U [64, 66]) projectiles were used and heavy actinides (up to Mendelevium) have been produced in these reactions. The cross sections were found to decrease very rapidly with increasing transferred mass and atomic number of surviving target-like fragments. The level of 0.1 μ b was reached for chemically separated Md isotopes [66]. These experiments seem to give not so great chances for production of new SH nuclei. However, we may expect that the shell structure of the driving potential (deep valleys caused by the double shell closure Z=82 and N=126) might

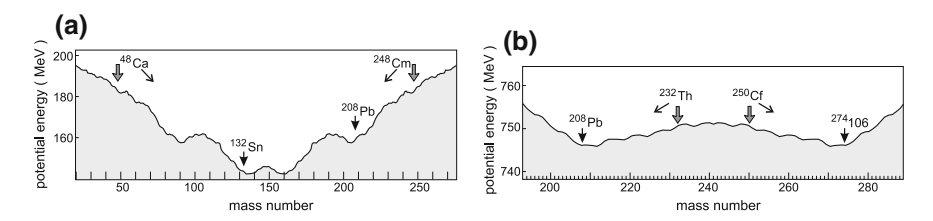


Fig. 7.20 Potential energy at contact "nose-to-nose" configuration for the two nuclear systems formed in ${}^{48}\text{Ca} + {}^{248}\text{Cm}$ **a** and ${}^{232}\text{Th} + {}^{250}\text{Cf}$ **b** collisions. The spheroidal deformation is equal to 0.2 for both cases. The *arrows* indicate initial configurations and possible clusterization of nuclear systems

significantly influence the nucleon rearrangement between primary fragments at low collision energies.

In Fig. 7.20, the potential energies are shown depending on mass rearrangement at contact configuration of the nuclear systems formed in ⁴⁸Ca + ²⁴⁸Cm and ²³²Th + ²⁵⁰Cf collisions. The lead valley evidently reveals itself in both cases (for ⁴⁸Ca + ²⁴⁸Cm system there is also a tin valley). In the first case (⁴⁸Ca + ²⁴⁸Cm), a discharge of the system into the lead valley (normal or symmetrizing quasi-fission) is the main reaction channel, which decreases significantly the probability of CN formation (see Sect. 2.4). In collisions of heavy nuclei (Th + Cf, U + Cm and so on), one may expect that the existence of this valley may notably increase the yield of surviving neutron-rich super-heavy nuclei complementary to the projectile-like fragments around ²⁰⁸Pb ("inverse" or anti-symmetrizing quasi-fission process).

Using the model described in Sect. 4 we calculated the yield of primary and surviving fragments formed in the ²³²Th + ²⁵⁰Cf collision at 800 MeV center-of mass energy. Low fission barriers of the colliding nuclei and of the most of the reaction products jointly with rather high excitation energies of them in the exit channel lead to very low yield of surviving heavy fragments. Indeed, sequential fission of the projectile-like and target-like fragments dominate in these collisions, see Fig. 7.21. At first sight, there is no chances to get surviving superheavy nuclei in such reactions.

However the results of much longer calculations (shown in Fig. 7.22, where the mass and charge distributions of surviving fragments obtained in the 232 Th + 250 Cf collision at 800 MeV are presented) demonstrate quite clear an appearance of the pronounced shoulder in the mass distribution of the primary fragments near the mass number A = 208. It is obviously explained by the existence of a deep valley in the potential energy surface [see Fig. 7.20b], which corresponds to the formation of doubly magic nucleus 208 Pb. If one fragment becomes lighter than lead, the potential energy sharply increases and the mass distribution of the primary fragments decreases rapidly at A < 208 (A > 274). The same is true for the charge distribution at Z < 82 (Z > 106). As a result, in the charge distribution of the surviving heavy fragments, Fig. 7.22b, there is also a shoulder at $Z \sim 106$ and the yield of nuclei with Z > 108 was found in this reaction at the level of less than 1 pb. This result differs sharply from those

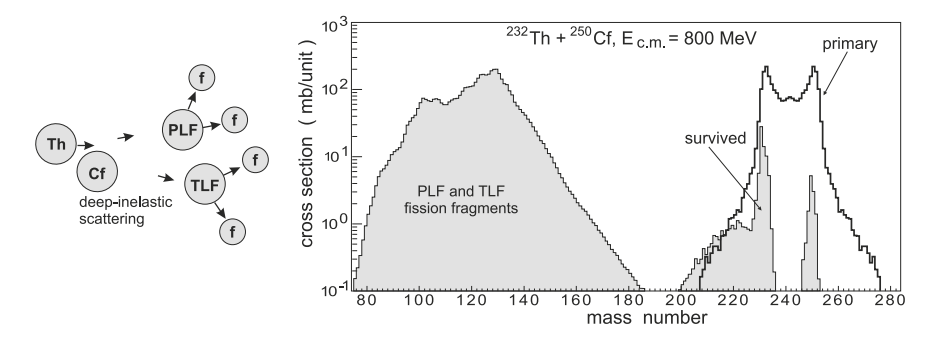


Fig. 7.21 Schematic view of DI scattering in the ²³²Th + ²⁵⁰Cf collision at 800 MeV center-of-mass energy and the calculated mass distributions of primary (*solid histogram*), survived and sequential fission fragments (*hatched areas*)

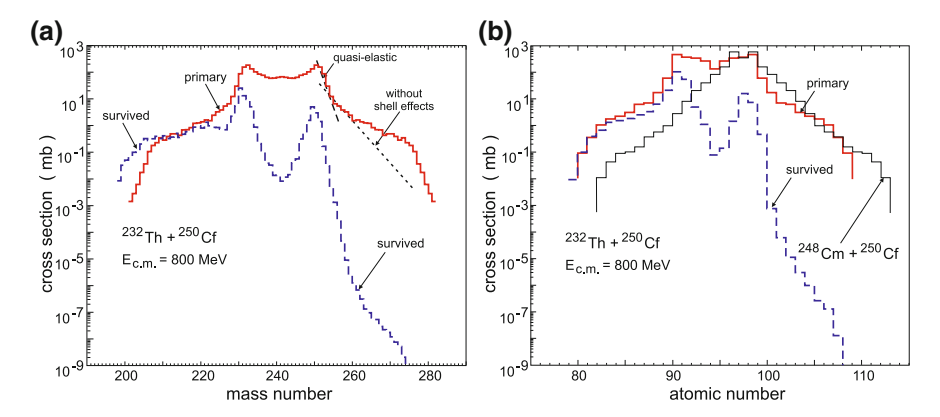


Fig. 7.22 Mass **a** and charge **b** distributions of primary (*solid histograms*) and surviving (*dashed histograms*) fragments in the 232 Th + 250 Cf collision at 800 MeV center-of-mass energy [61]. Thin solid histogram in **b** shows the primary fragment distribution in the hypothetical reaction 248 Cm + 250 Cf

obtained in Ref. [88], where the reactions of such kind have been analyzed within the parametrized diffusion model and the yield of heavy primary fragments was found to diminish monotonically with increasing charge number. The authors of Ref. [88] concluded, however, that the "fluctuations and shell effects not taken into account may considerably increase the formation probabilities". This is indeed the case.

A possibility for the production of more neutron rich SH isotopes is another advantage of using multi-nucleon transfer processes. As mentioned above, in the fusion reactions of stable nuclei we may produce only proton rich isotopes of heavy elements and cannot approach the center of the "island of stability" ($Z \sim 114, 120 \text{ and } N \sim 184$) in the superheavy mass region. At the same time, we know that in low-energy damped collisions of heavy ions just the potential

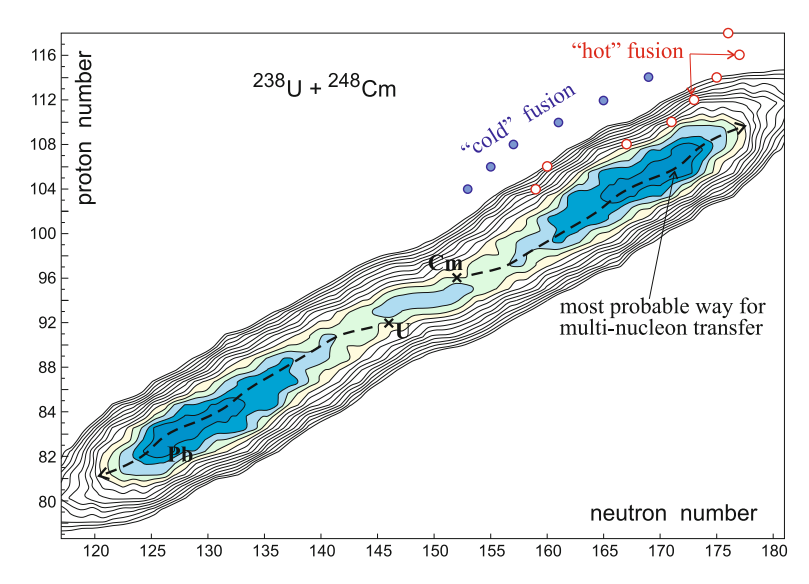


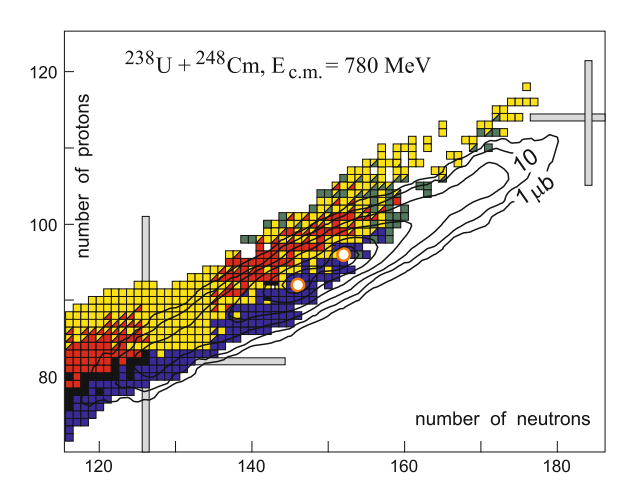
Fig. 7.23 Landscape of potential energy surface of the nuclear system formed in collision of 238 U with 248 Cm (contact configuration, dynamic deformation $\delta=0.2$, contour lines are drawn over 1 MeV energy interval) [72]. Open circles correspond to the most neutron-rich nuclei synthesized in 48 Ca induced fusion reactions while the filled ones show SH nuclei produced in the "cold" fusion with lead target. The dashed line shows the most probable evolution of the nuclear system in multi-nucleon transfer process

energy surface regulates to a great extent the evolution of the nuclear system driving it to the minimal values of potential energy in the multidimensional space of collective variables.

The potential energy surface of the giant nuclear system formed in collision of $^{238}\mathrm{U}$ and $^{248}\mathrm{Cm}$ nuclei is shown in Fig. 7.23. It is calculated within the two-center shell model for a configuration of two touching nuclei (with the fixed value of dynamic deformation $\delta=0.2$) depending on numbers of transferred protons and neutrons. The initial configuration of $^{238}\mathrm{U}$ and $^{248}\mathrm{Cm}$ touching nuclei is shown by the crosses. From this figure one sees that in the course of nucleon exchange the most probable path of the nuclear system formed by $^{238}\mathrm{U}$ and $^{248}\mathrm{Cm}$ lies along the line of stability with formation of SH nuclei which have many more neutrons as compared with those produced in the "cold" and "hot" fusion reactions. Due to fluctuations even more neutron rich isotopes of SH nuclei may be formed in such transfer reactions.

The calculated cross sections for formation of primary fragments in low-energy collisions of ²³⁸U with ²⁴⁸Cm target are shown in Fig. 7.24 by the counter lines in logarithmic scale. As can be seen, the superheavy nuclei located very close to the center of the island of stability may be produced in this reaction with rather high cross section of one microbarn. Note one again that this region of the nuclear map cannot be reached in any fusion reaction with stable projectiles and long-lived targets. Of course, the question arises whether these excited superheavy primary

Fig. 7.24 Landscape of the cross sections (microbarns, logarithmic scale) for production of primary fragments in collision of ²³⁸U with ²⁴⁸Cm at 780 MeV center-of-mass energy (contour lines are drawn over one order of magnitude). Vertical and horizontal strips indicate the magic proton and neutron numbers



fragments produced in the transfer reactions may survive in competition with fast fission which is a dominated decay channel for heavy nuclei.

Indeed, the yield of survived SH elements produced in the low-energy collisions of actinide nuclei is rather low, though the shell effects (see two double magic crossing in Fig. 7.24) give us a definite gain as compared to a monotonous exponential decrease of the cross sections with increasing number of transferred nucleons. In Fig. 7.25 the calculated EvR cross sections for production of SH nuclei in damped collisions of ²³⁸U with ²⁴⁸Cm at 800 MeV center-of-mass energy

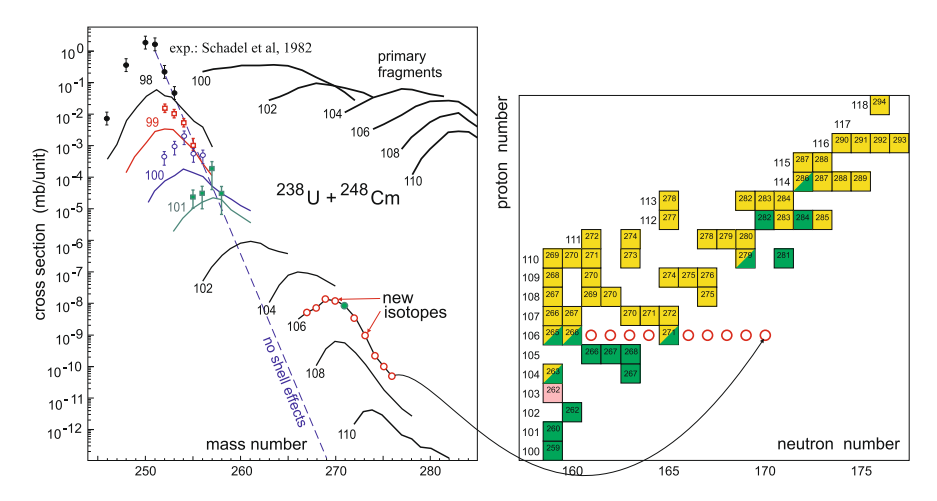


Fig. 7.25 Yield of primary and survived isotopes of SH nuclei produced in collisions of 238 U with 248 Cm at 800 MeV center-of-mass energy. Experimental data for Cf (*filled circles*), Es (*open rectangles*), Fm (*open circles*) and Md isotopes (*filled rectangles*) obtained in [66] are also shown. *Dashed line* shows the expected locus of transfer reaction cross sections without the shell effects. *Open circles* at the curve with Z=106 indicate unknown isotopes of Siborgium and their positions at the nuclear map (*right panel*)

are shown along with available experimental data. As can be seen, really much more neutron rich isotopes of SH nuclei might be produced in such reactions (new isotopes of Siborgium (Z=106) are shown in Fig. 7.25 by the open circles). Reactions of such kind can be also used to fill the gap between the SH nuclei produced in the "hot" fusion reactions with ⁴⁸Ca and the continent of known nuclei (see Fig. 7.17). This gap hinders one from obtaining a clear view of the properties of SH nuclei in this region.

Certainly, the reliability of our predictions for the production of neutron-rich superheavy nuclei in the processes with a transfer of several tens of nucleons is not very high. Up to now very few experiments were performed on heavy-ion multinucleon transfer reactions at energies close to the Coulomb barrier and the role of the shell effects in these reactions is unknown. In this connection more detailed experiments have to be done aimed on the study of the shell effects in the mass transfer processes in low-energy damped collisions of heavy ions. The effect of "inverse" quasi-fission may be studied also in experiments with less heavy nuclei (for example, in the collision of ¹⁶⁰Gd with ¹⁸⁶W as discussed above). The experimental observation of this effect and the measurement of the corresponding enhancement factor in the yield of closed shell nuclei might allow us to make better predictions (and/or simple extrapolations) for heavier nuclear combinations which are more difficult for experimental study.

7.5.2 Giant Nuclear Systems of Molecular Type and Spontaneous Positron Formation

Direct time analysis of the reaction dynamics within the model described above allows one to estimate also the lifetime of the composite system consisting of two touching heavy nuclei with total charge $Z \sim 180$. Such "long-living" configurations may lead to spontaneous positron emission from super-strong electric field of giant quasi-atoms by a static QED process (transition from neutral to charged QED vacuum) [82–84], see schematic Fig. 7.26. About 20 years ago an extended search for this fundamental process was carried out and narrow line structures in the positron spectra were first reported at GSI. Unfortunately these results were not confirmed later, neither at ANL [89], nor in the last experiments performed at GSI [90, 91] (see also hierarchical references therein). These negative findings, however, were contradicted by Jack Greenberg (private communication and supervised thesis at Wright Nuclear Structure Laboratory, Yale university). Thus the situation remains unclear, while the experimental efforts in this field have ended. The principal problem was that there has been no trigger for long lifetimes of the giant nuclear system involved! We hope that new experiments and new analysis, performed according to the predictions of our dynamical model (see below), may shed additional light on this problem and also answer the principal question: are there some reaction features (triggers) testifying long reaction delays? If they exist, new

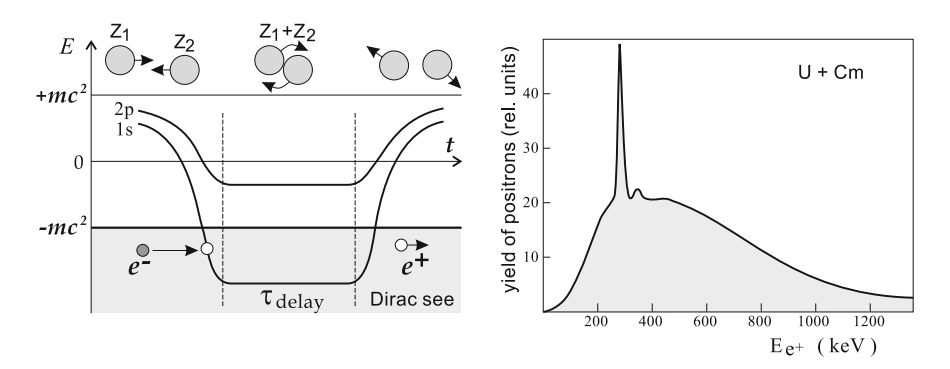


Fig. 7.26 Schematic picture for spontaneous positron formation in supercritical electric field of long-lived giant quasi-atom. Here a sharp lifetime distribution is assumed

experiments should be planned to detect the spontaneous positrons in the specific reaction channels.

Of course, for such heavy nuclei there is most likely no attractive potential pocket typical for lighter nuclear systems, the potential is repulsive everywhere. However, the potential energy is not very steep in the region of the contact point and two nuclei may keep in contact for a long time changing their deformations and transferring nucleons to each other. Projections of the multi-dimensional adiabatic potential energy surface onto the $(R - \eta)$ and $(R - \delta)$ planes are shown in Fig. 7.27 along with a typical "trajectory" for the nuclear system formed in collision of 232 Th + 250 Cf.

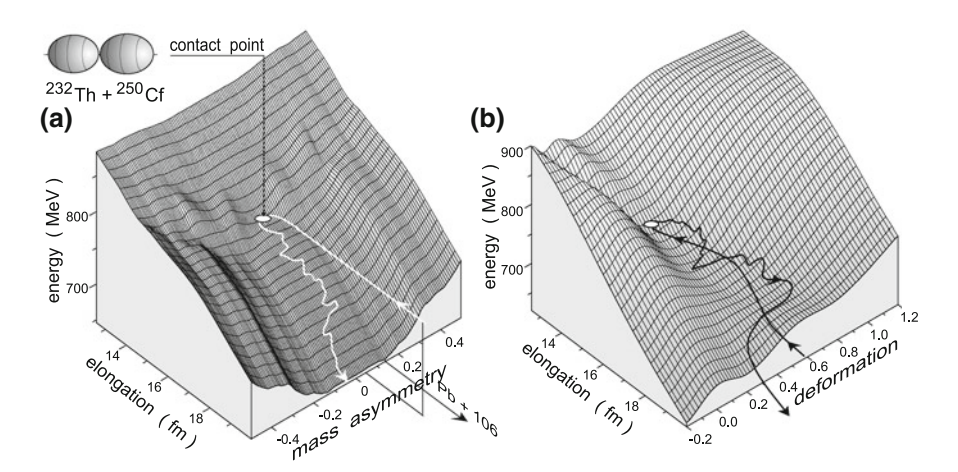


Fig. 7.27 Potential energy surface for the nuclear system formed by 232 Th + 250 Cf as a function of R and η ($\delta = 0.22$) (a), and R and $\delta(\eta = 0.037)$ (b) [73]. A typical trajectories are shown by the *thick curves* with *arrows*. Before nuclei reach the region of nuclear friction forces, they are in their ground states (zero temperature) and no fluctuations occur. However when nuclei come in contact they very quickly become well excited and fluctuations start to play a significant role

The time analysis of the damped collisions of actinide nuclei shows that in spite of non-existing attractive potential pocket the system consisting of two very heavy nuclei may hold in contact rather long in some cases. The exchange of nucleons forth and back between the colliding fragments and also the forth and back change of deformations of the fragments act like a "glue". During the interaction time the giant nuclear system moves over the multidimensional potential energy surface with almost zero kinetic energy (result of large nuclear viscosity).

The total reaction time distribution, $\frac{d\sigma}{d\log(\tau)}$ (τ denotes the time after the contact of two nuclei), is shown in Fig. 7.28 for the ²³⁸U + ²⁴⁸Cm collision. We found that the dynamic deformations are mainly responsible here for the time delay of the nucleus–nucleus collision. Ignoring the dynamic deformations in the equations of motion significantly decreases the reaction time, see Fig. 7.28a. With increase of the energy loss and mass transfer the reaction time becomes longer and its distribution becomes more narrow, see Fig. 7.28b.

The lifetime of a giant composite system more than 10^{-20} s is quite enough to expect positron line structure emerging on top of the dynamical positron spectrum due to spontaneous e^+e^- production from the supercritical electric fields [82–84]. The absolute cross section for long events ($\tau > 10^{-20}$ s) is found to be about half millibarn. It reaches the maximal value just at the beam energy ensuring the two nuclei to be in contact, see Fig. 7.28c. Note that the same energy is also optimal for the production of the most neutron-rich SH nuclei (see above). Of course, there are some uncertainties in the used parameters, mostly in the value of nuclear viscosity. However we found only a linear dependence of the reaction time on the strength of nuclear viscosity, which means that the obtained reaction time distribution is rather reliable, see logarithmic scale on both axes in Fig. 7.28a. Note also that the time distribution shown in Fig. 7.28 corresponds to the time intervals between contact and scission of reaction fragments. However the electron eigenstates of the quasi-atom are weakly sensitive to a re-separation of nuclei (and

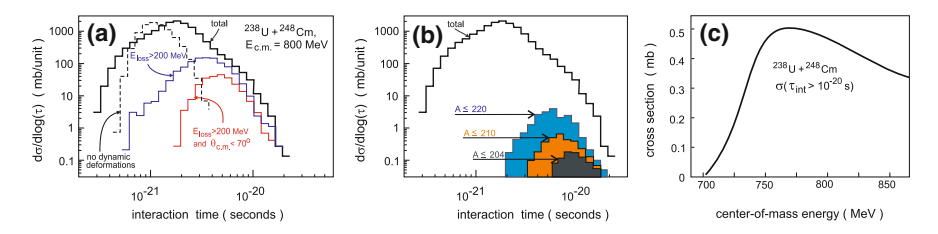
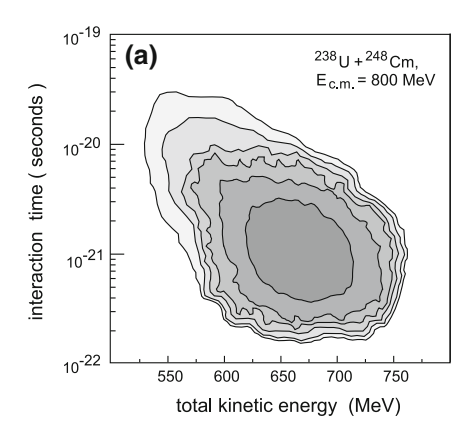


Fig. 7.28 Reaction time distributions for the 238 U + 248 Cm collision at 800 MeV center-of-mass energy. *Thick solid* histograms correspond to all events with energy loss more than 30 MeV. **a** *Dashed histogram* shows the effect of switching-off dynamic deformations. *Thin histograms* show the reaction time distributions in the channels with formation of primary fragments with $E_{loss} > 200$ MeV and $E_{loss} > 200$ MeV, $\theta_{c.m.} < 70^{\circ}$, correspondingly. **b** *Shaded histograms* show reaction time distributions in the channels with formation of primary fragments with $E_{loss} > 200$ MeV, $\theta_{c.m.} < 70^{\circ}$ and $A \le 220$, $A \le 210$ and $A \le 204$ (*numbers* near the histograms). **c** Cross section for events with interaction time longer than 10^{-20} s depending on beam energy



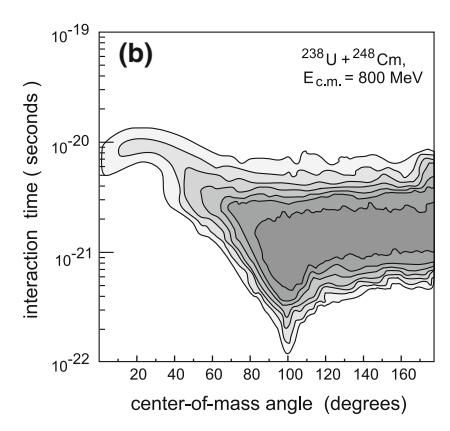


Fig. 7.29 Energy–time **a** and angular-time **b** distributions of primary fragments in the 238 U + 248 Cm collision at 800 MeV ($E_{loss} > 15$ MeV). Landscape is shown in logarithmic scalelines are drawn over one order of magnitude. Quasi-elastic peak is removed

depend on the total charge $Z_1 + Z_2$) as long as the distance between nuclear centers is shorter than the electron Compton wavelength (validating the monopole approximation for the Dirac orbits, see [83, 84]). Thus the lifetime distribution of giant quasi-atoms is even slightly wider than it is shown in Fig. 7.28a.

Formation of the background positrons in these reactions forces one to find some additional trigger for the longest events. Such long events correspond to the most damped collisions with formation of mostly excited primary fragments decaying by fission, see Figs. 29a. However there is also a chance for production of the primary fragments in the region of doubly magic nucleus 208 Pb, which could survive against fission due to nucleon evaporation. The number of the longest events depends weakly on impact parameter up to some critical value. On the other hand, in the angular distribution of all the excited primary fragments (strongly peaked at the center-of-mass angle slightly larger than 90°) there is the rapidly decreasing tail at small angles corresponding to the trajectories with non-zero impact parameters at which the sticking giant nuclear system rotates almost half-turn before scission, see Fig. 7.29b. Time distribution for the most damped events ($E_{loss} > 150$ MeV) in which a large mass transfer occurs and primary fragments with masses $A \sim 200$ scatter in forward angles ($\theta_{c.m.} < 70^{\circ}$) is rather narrow and really shifted to longer time delay, see hatched areas in Fig. 7.28b.

Thus, we learned that a long enough lifetime distribution should exist for making the vacuum decay in supercritical electrical fields possible for observation. For the considered case of $^{238}\text{U} + ^{248}\text{Cm}$ collision at 800 MeV center-of-mass energy, the detection of the surviving nuclei in the lead region at the laboratory angles of about 25° and at the low-energy border of their spectrum (around 1,000 MeV for Pb) could be a real trigger for longest reaction time. Because of the lifetime distribution the positron spectrum should not show a narrow line as indicated in Fig. 7.26, but, instead, a very strong and broad line structure as that in Fig. 7.30 should emerge.

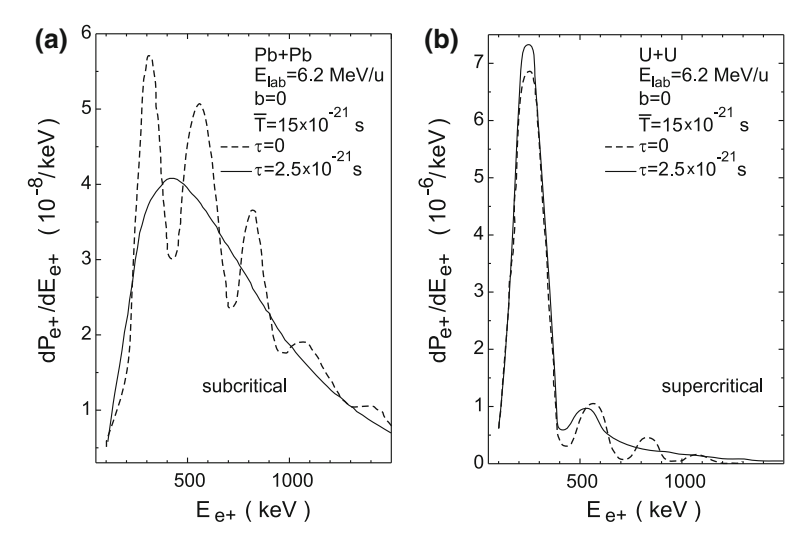
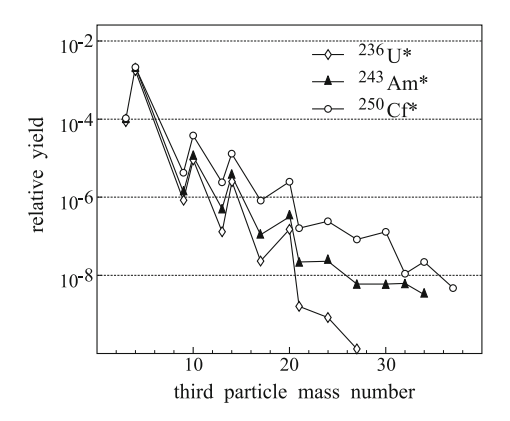


Fig. 7.30 The effect of a nuclear time delay distribution f(T), here a Gaussian distribution, on positron spectra. A mean time $\overline{T} = 15 \times 10^{-21}$ s have been assumed. **a** In the subcritical system Pb + Pb the interference pattern is damped out. **b** In the supercritical system U + U the spontaneous positron line is still present and will survive even for large deviations τ . The figure is taken from Ref. [92]

7.6 Three-Cluster Configurations of Giant Nuclear Systems

In this section we discuss briefly a possibility for a simultaneous formation of three heavy clusters in decay of heavy nuclear system (ternary fission). Today the term "ternary fission" is commonly used to denote the process of formation of light charged particle accompanied fission [93]. This is a rare process (less than 1%) relative to binary fission, see Fig. 7.31. As can be seen the probability of such a process decreases sharply with increasing mass number of accompanied third particle. These light particles are emitted almost perpendicularly with respect to

Fig. 7.31 Relative to binary fission yields of ternary particles in the (n_{th}, f) reactions with thermal neutrons [94]



the fission axis (equatorial emission) [93]. It is interpreted as an indication that the light ternary particles are emitted from the neck region and are accelerated by the Coulomb fields of both heavy fragments.

In contrast to such a process, the term "true ternary fission" is used for a simultaneous decay of heavy nucleus into three fragments of not very different mass [93]. Such decays of low excited heavy nuclei were not observed yet. The true ternary fission of atomic nuclei has a long history of theoretical and experimental studies. Early theoretical considerations based on the liquid drop model (LDM) [95] showed that for heavy nuclei ternary fission produces a larger total energy release in comparison to binary fission, but the actual possibility of ternary fission is decided, in fact, by barrier properties and not by the total energy release. It was found that the LDM ternary fission barriers for oblate (triangle) deformations are much higher as compared to the barriers of prolate configurations [96], and it seems that the oblate ternary fission may be excluded from consideration. Further study of this problem within the more sophisticated three-center shell model [97] showed that the shell effects may significantly reduce the ternary fission barriers even for oblate deformations of very heavy nuclei. However an overall study of the problem was not performed yet, and the question about a possibility for three-body clusterization of heavy nuclei remains unanswered both in theory and in experiment. In the meanwhile, today it becomes possible to study experimentally the properties and dynamics of formation and decay of superheavy nuclei, for which the ternary fission could be rather probable (see below).

A three-body clusterization might appear in a vicinity of the scission point of heavy nucleus (more exactly, on the path from the saddle point to scission), where the shared nucleons ΔA may form a third cluster located between the two heavy cores a_1 and a_2 (see Figs. 7.8, 7.12). In Fig. 7.32 schematic view is shown for normal (two-body) and ternary fission starting from the configuration of the last shape isomeric minimum of CN consisting of two magic tin cores and 36 extra nucleons shared between the two cores and moving in the whole volume of the mono-nucleus. In the two-body fission scenario these extra nucleons gradually spread between the two fission fragments (or pass into one of the fragments if the other is a magic nucleus) with formation of two nuclei in the exit channel (Sn and Dy in our case, see the fission path in Fig. 7.12, mass-symmetric fission of this CN is energetically less favorable). However there is a chance for these extra nucleons ΔA to concentrate in the neck region between the two cores and form finally the third fission fragment (36 S in our case).

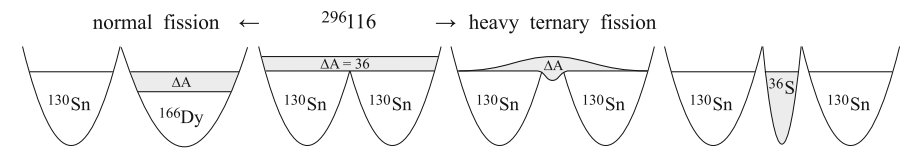
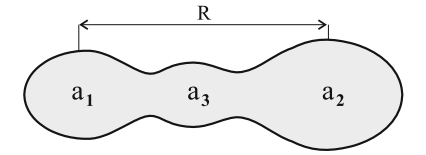


Fig. 7.32 Schematic view of the regular (with formation of ¹³⁰Sn and ¹⁶⁶Dy nuclei in accordance with Fig. 7.12) and ternary fission of superheavy nucleus ²⁹⁶116

Fig. 7.33 Three-body axially symmetric configuration of heavy nuclear system



It is clear that there are too many collective degrees of freedom needed for proper description of potential energy of a nuclear configuration consisting of three deformed heavy cores. Here we restricted ourselves by consideration of potential energy of a three-body axially symmetric configuration (shown in Fig. 7.33) as a function of three variables, a_1 , a_3 and elongation R at fixed dynamic deformations of the fragments ($\delta_1 = \delta_2 = \delta_3 = \delta$). Note that the third fragment may appear only when the elongation of the whole system is rather large to involve the two cores a_1 and a_2 , i.e. at $R > R(a_1) + R(a_2)$. Up to this distance the two-body and three-body potential energies coincide and $a_3 = \Delta A$ nucleons spread over the whole volume (see Figs. 7.5 and 7.32).

Potential energy of the three-body contact configuration at $R = R(A_1) + 2R(A_3) + R(A_2)$ is shown in Fig. 7.34 for ²⁴⁸Cm at fixed dynamic deformation $\delta = 0.1$. To make the result quite visible we minimized the potential energy over the neutron numbers of the fragments, N_1 and N_3 , and plot the energy as a function of Z_1 and Z_3 . As can be seen, this nucleus preferably decays in two (tin-like and palladium-like) fragments ($Z_3 \sim 0$). The potential energy smoothly increases with increasing charge of the third nucleus and no other local deep minima appear on the potential energy surface. Though the combinations like Te–O–Kr or Sn–O–Sr are located not so high up on the potential energy surface (10–20 MeV), and they are quite reachable due to fluctuations at several tens of MeV of excitation energy.

We calculated also the three-dimensional potential energy $V(R, \delta, A_3)$ for the three-body symmetric configuration with two equal cores $a_1 = a_2$ (and, thus, with two equal fragments $A_1 = A_2$ in the exit fission channels) trying to find a preferable path for ternary fission and estimate how larger is the barrier for three-body decay as compared to binary fission. For better visualization we plot the calculated

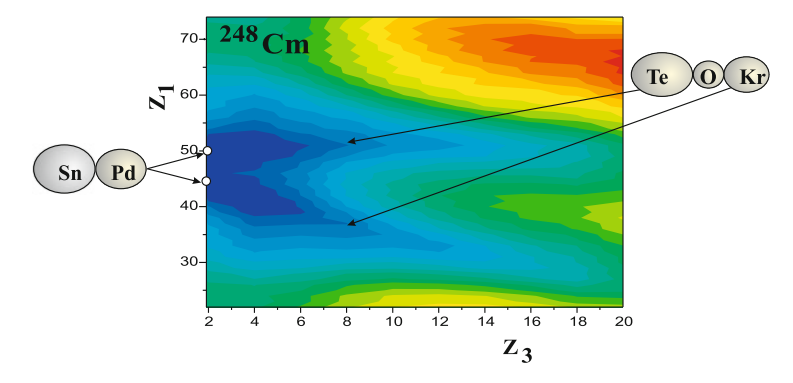


Fig. 7.34 Landscape of the potential energy surface for three-body clusterization of ²⁴⁸Cm

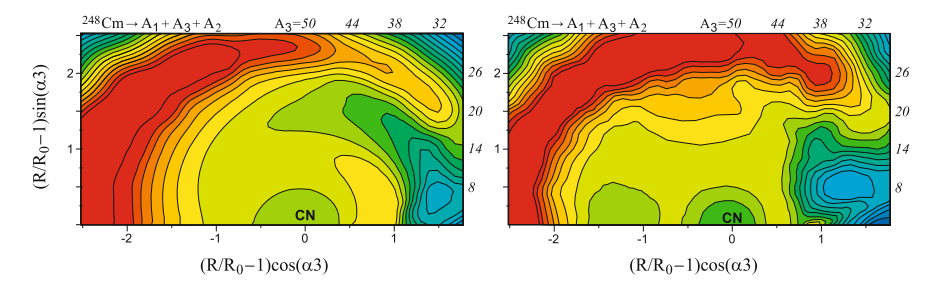


Fig. 7.35 Potential energy for ternary fission of 248 Cm. Macroscopic part of potential energy and the total one (LDM plus shell corrections) are shown at *left* and *right* panels, respectively, depending on elongation and mass of third fragment (*italic numbers*) at $A_1 = A_2$. Contour lines are drawn over 3 MeV

potential energy $V(R, \delta, A_3)$ as a function of $(R/R_0 - 1)\cos(\alpha_3)$ and $(R/R_0 - 1)\sin(\alpha_3)$ at fixed dynamic deformation δ , where $\alpha_3 = \pi A_3/100$ and R_0 is the radius of sphere of equivalent volume (CN).

The macroscopic (LDM) part of the potential energy for 248 Cm is shown in left panel of Fig. 7.35 at $\delta=0.2$. The binary fission of 248 Cm evidently dominates because after the barrier the potential energy is much steeper just in the binary exit channel (right bottom corner, $A_3 \sim 0$). Emission of light third particle is possible here but not the true ternary fission. The shell correction (which makes deeper the ground state of this nucleus by about 3 MeV) does not change distinctively the total potential energy (see the right panel of Fig. 7.35). Nevertheless the experiments aimed on observation of real ternary fission of actinide nuclei (with formation of heavy third fragment) are currently in progress [98, 99].

We found, however, that the situation changes for heavier transactinide nuclei. With increasing mass number of heavy nucleus more and more possibilities for its clusterization appear. In the case of superheavy nuclei the macroscopic potential energy does not lead to any barrier at all (neither in binary nor in ternary exit channel) and stability of these nuclei is determined completely by the shell corrections. In Fig. 7.36 the calculated potential energy is shown for superheavy

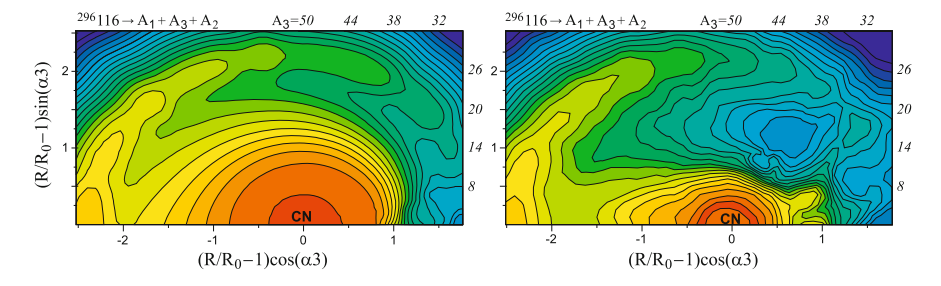


Fig. 7.36 Potential energy for ternary fission of superheavy nucleus $^{296}116$. Macroscopic part of potential energy and the total one are shown at *left* and *right* panels, respectively, depending on elongation and mass of third fragment (*italic numbers*) at $\delta = 0.2$. *Contour lines* are drawn over 5 MeV

nucleus $^{296}116$ in the space of "elongation– A_3 " at $A_1=A_2$. In contrast with 248 Cm, in this case a real possibility for ternary fission appears with formation of third fragment $A_3 \sim 30$ and two heavy fragments $A_1=A_2 \sim 130$. The ternary fission valley is quite well separated by the potential ridge from the binary fission valley. This means that the ternary fission of $^{296}116$ nucleus into the "tin–sulfur–tin" combination should dominate as compared with other true ternary fission channels of this nucleus.

More sophisticated consideration of the multi-dimensional potential energy surface is needed to estimate the "ternary fission barrier" accurately. However, as can be seen from Fig. 7.36, the height of the ternary fission barrier is not immensely high. It is quite comparable with the regular fission barrier because the ternary fission starts in fact from the configuration of the shape isomeric state which is located outside from the first (highest) saddle point of superheavy nucleus ²⁹⁶116 (see Fig. 7.12).

Conditions for the three-body fission (quasi-fission) are even better in the giant nuclear systems formed in low-energy collisions of actinide nuclei. In this case the shell effects significantly reduce the potential energy of the three-cluster configurations with two strongly bound lead-like fragments. In Fig. 7.37 the landscape of the potential energy surface is shown for a three-body clusterization of the nuclear system formed in collision of U + U. Here the potential energy was calculated as a function of three variables, Z_1 , Z_3 and R at fixed (equal) dynamic deformations of the fragments being in contact $(R_1 + 2R_3 + R_2 = R)$.

As can be seen, the giant nuclear system, consisting of two touching uranium nuclei, may split into the two-body exit channel with formation of lead-like fragment and complementary superheavy nucleus—the so-called anti-symmetrizing quasi-fission process which may lead to an enhanced yield of SH nuclei in multi-nucleon transfer reactions (see above). Beside the two-body Pb–No clusterization and the shallow local three-body minimum with formation of light intermediate oxygen-like cluster, the potential energy has the very deep minimum

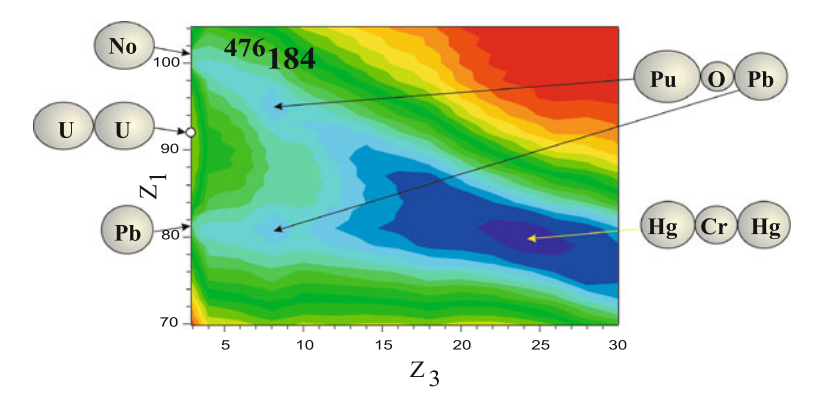
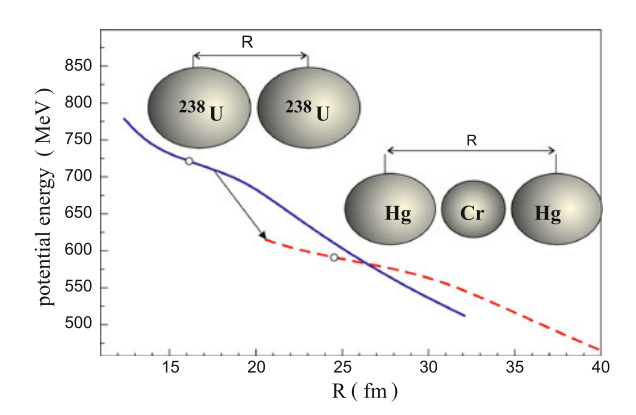


Fig. 7.37 Landscape of potential energy of three-body configurations formed in collision of $^{238}\mathrm{II} + ^{238}\mathrm{II}$

Fig. 7.38 Radial dependence of the potential energy of two uranium nuclei (*solid curve*) and of the three-body nuclear configuration formed in collision of ²³⁸U + ²³⁸U (*dashed curve*)



corresponding to the Pb–Ca–Pb-like configuration (or Hg–Cr–Hg) caused by the N=126 and Z=82 nuclear shells.

Thus we found that for superheavy nuclei the three-body clusterization (and, hence, real ternary fission with a heavy third fragment) is quite possible. The simplest way to discover this phenomena is a detection of two tin or xenon-like clusters in low energy collisions of medium mass nuclei with actinide targets, for example, in ⁶⁴Ni + ²³⁸U reaction. Note, that the experiments, in which the two-body quasi-fission processes have been studied in collisions of ⁴⁸Ca with ²⁴⁸Cm [44] (see Fig. 7.11), were not aimed originally on a search of the three-body reaction channels. This should be done with a new experimental procedure. These unusual ternary decays (a new type of radioactivity) could be searched for also among the spontaneous fission events of superheavy nuclei.

The extreme clustering process of formation of two lead-like double magic fragments in collisions of actinide nuclei is also a very interesting subject for experimental study. Such measurements, in our opinion, are not too difficult. It is sufficient to detect two coincident lead-like ejectiles (or one lead-like and one calcium-like fragments) in U + U collisions to conclude unambiguously about the ternary fission of the giant nuclear system (in this connection the combination of $^{233}\text{U} + ^{233}\text{U}$ is more preferable). More flat radial dependence of the potential energy (as compared with a two-body system) is another feature of the three body clusterization, see Fig. 7.38. This means that decay of U + U-like nuclear system into the energetically preferable (and more stable in some sense) three-body configurations may also significantly prolong the reaction time, which (among other things) could be important for spontaneous positron formation in superstrong electric field (see Sect. 5.2).

7.7 Conclusion

As we know clustering is a common feature of many body systems. In each case it is nothing else but formation of energetically favorable clusters of

particles: binding energy of particles inside the cluster is higher than in medium. As a result, due to conservation of total energy, the binding energy between clusters becomes lower. Due to the shell effects, inside the nuclear matter (depending on its size) the nucleons prefer to form the compact strongly bound double magic fragments, 4 He, 16 O, 48 Ca, 132 Sn, 208 Pb. In some cases the binding energy between these fragments becomes positive leading to a cluster decay of heavy nuclei (α -decay, heavy-ion radioactivity, fission). Bound (or long-lived) two-body cluster configurations of heavy actinide nuclei reveal themselves as the shape isomers which are the most obvious and vivid manifestation of the two-body clusterization of heavy nuclei.

The clustering phenomena caused by the shell effects play an important role also in low-energy dynamics of nuclear systems. Fission and quasi-fission are the most known processes of such kind. In damped multi-nucleon transfer reactions the shell effects might be also rather important. As shown above, the use of these effects may help us to synthesize new heavy neutron rich nuclei located at the "north-east" part of the nuclear map. The properties of these nuclei are extremely important for the understanding the r-process of astrophysical nucleosynthesis of heavy elements. The study of the structural properties of nuclei along the neutron shell N=126 would also contribute to the present discussion of the quenching of shell effects in nuclei with large neutron excess.

This "blank spot" of the nuclear map can be filled neither in fission reactions nor in fusion processes. Our calculations show that just the low-energy multinucleon transfer reactions can be used for the production of heavy neutron rich nuclei. Several tens of new isotopes of the elements with Z=70-80 (also those located along the closed neutron shell N=126) may be produced in the collision of 136 Xe with 208 Pb with cross sections higher than one microbarn. It is clear, that there are many other combinations of colliding nuclei. In particular, uranium and thorium targets may be used, for example, for the production of new neutron rich isotopes with $Z \geq 82$. Also the accelerated neutron rich fission fragments (which are most likely useless for the synthesis of superheavy nuclei in fusion reactions) can be used for the production of new heavy isotopes in low-energy multi-nucleon transfer processes.

A possibility for the production of long-lived neutron-rich SH nuclei in collisions of actinide ions is also very important finding. In these reactions a large mass and charge transfer due to the inverse (anti-symmetrizing) quasi-fission process is significantly enhanced by the Z=82 and N=126 nuclear shells, that is by the release of strongly bound lead-like cluster with formation of SH residue. At first stage, radiochemical identification of long-living 267,268 Db and/or 271,272 Bh isotopes, produced in the Th + Cf or U + Cm reactions, could be performed, for example, to test this conclusion. If the found cross sections were to be higher than several picobarns, then the subsequent experiments with such reactions could be planned aiming at the production of SH nuclei just in the region of the "island of stability".

The lifetime of a giant nuclear molecule (giant nuclear system) formed in lowenergy collision of two uranium-like nuclei may be in some cases rather long, more than 10^{-20} s. This time delay (in spite of absence of attractive potential pocket) is caused by the dynamic deformations and nucleon exchange between two fragments. The longest events correspond to higher energy loss and largest mass transfer. The absolute cross section for long events (> 10^{-20} s) was found to be about half millibarn. It reaches the maximal value just at the low beam energy ensuring two nuclei to be in contact. Thus, in such collisions one may really detect the process of spontaneous e^+e^- production from the strong electric field if the additional trigger for longest events will be used to decrease the contribution from the background positrons. The coincident with positrons detection of the nuclei in the lead region (30 nucleons transferred from uranium) with lowest kinetic energy at forward laboratory angles could be a definite witness of a long reaction time. The process of spontaneous positron formation in the strong electric field (appearance of a vacation in the Dirac see) is a most fundamental QED process which is not discovered yet experimentally.

We found that for superheavy nuclei the three-body clusterization (and, hence, a real ternary fission with formation of a heavy third fragment) is quite possible. The simplest way to discover this phenomena is a detection of two tin or xenon-like clusters in low energy collisions of medium mass nuclei (Ca-Ni) with actinide targets. The extreme clustering process of formation of two lead-like double magic fragments in collisions of actinide nuclei is also a very interesting subject for experimental study. Such measurements, in our opinion, are not too difficult. It is sufficient to detect two coincident lead-like ejectiles (or one lead-like and one calcium-like fragments) in U+U collisions to conclude unambiguously about the ternary fission (quasi-fission) of the giant nuclear system.

Acknowledgment The work was supported by the DFG-RFBR collaboration project under Grant No. 09-02-91334.

References

- 1. R. Vandenbosch, J.R. Huizenga, Nuclear Fission (Academic Press, New York, 1973)
- 2. A. Sandulescu, D.N. Poenaru, W. Greiner, Sov. J. Part. Nucl. 11, 528 (1980)
- 3. W. Greiner, D.N. Poenaru, see this volume of Lect. Notes Phys
- 4. V. Zagrebaev, W. Greiner, Int. J. Mod. Phys. E 17, 2199 (2008)
- 5. R. Bass, Nuclear Reactions with Heavy Ions (Springer, Berlin, 1980)
- 6. W. Scheid, R. Ligensa, W. Greiner, Phys. Rev. Lett. 21, 1479 (1968)
- 7. V. Zagrebaev, W. Greiner, J. Phys. G 31, 825 (2005)
- 8. G.F. Bertsch, Z. Phys. A289, 103 (1978)
- 9. W. Cassing, W. Nörenberg, Nucl. Phys. A 401, 467 (1983)
- 10. N. Takigawa, T. Rumin, N. Ihara, Phys. Rev. C 61, 044607 (2000)
- 11. J. Blocki, J. Randrup, W.J. Swiatecki, C.F. Tsang, Ann. Phys. (N.Y.) 105, 427 (1977)
- V.I. Zagrebaev, A.V. Karpov, Y. Aritomo, M. Naumenko, W. Greiner, Phys. Part.Nucl. 38, 469 (2007)
- 13. K.A. Brueckner, J.R. Buchler, M.M. Kelly, Phys. Rev. 173, 944 (1968)
- C. Ngô, B. Tamain, M. Beiner, R.J. Lombard, D. Mas, H.H. Deubler, Nucl. Phys. A252, 237 (1975)

- 15. M. Brack, C. Guet, H.-B. Høakansson, Phys. Rep. 123, 275 (1985)
- 16. V. Yu. Denisov, W. Nörenberg, Eur. Phys. J. A 15, 375 (2002)
- 17. K. Pruess, W. Greiner, Phys. Lett. B 33, 197 (1970)
- 18. G.R. Satchler, W.G. Love, Phys. Rep. 55, 183 (1979)
- 19. G. Bertsch, J. Borysowicz, H. McManus, W.G. Love, Nucl. Phys. A 284, 399 (1977)
- M. Lacombe, B. Loiseau, J.M. Richard, R. Vinh Mau, J. Côté, P. Pirès, R. de Tourreil, Phys. Rev. C 21, 861 (1980)
- 21. N. Anantaraman, H. Toki, G.F. Bertsch, Nucl. Phys. A 398, 269 (1983)
- 22. E. Uegaki, Y. Abe, Prog. Theor. Phys. 90, 615 (1993)
- 23. S. Misicu, H. Esbensen, Phys. Rev. Lett. 96, 112701 (2006)
- A.B. Migdal, Theory of Finite Fermi Systems and Applications to Atomic Nuclei (Wiley Interscience, New York, 1967)
- A. Bohr, B.R. Mottelson, Nuclear Structure, vol 2, Nuclear Deformations (W.A. Benjamin, New York, 1974)
- 26. N. Rowley, G.R. Satchler, P.H. Stelson, Phys.Lett. B 254, 25 (1991)
- 27. V. Zagrebaev, V. Samarin, Phys. Atom. Nucl. 67, 1462 (2004)
- 28. J. Dobaczewski, H. Flocard, J. Treiner, Nucl. Phys. A 422, 103 (1983)
- 29. J.F. Berger, M. Girod, D. Gogny, Nucl. Phys. A 428, 23 (1984)
- 30. P.-G. Reinhard, M. Rufa, J. Maruhn, W. Greiner, J. Friedrich, Z. Phys. A 323, 13 (1986)
- 31. M. Bender, P.-H. Heenen, P.-G. Reinhard, Rev. Mod. Phys. 75, 121 (2003)
- 32. H.J. Krappe, J.R. Nix, A.J. Sierk, Phys. Rev. C 20, 992 (1979)
- 33. A.J. Sierk, Phys. Rev. C 33, 2039 (1986)
- 34. P. Möller, J.R. Nix, W.D. Myers, W.J. Swiatecki, At. Data Nucl. Data Tables 59, 185 (1995)
- 35. V.M. Strutinsky, Nucl. Phys. A 95, 420 (1967)
- 36. V.M. Strutinsky, Nucl. Phys. A 122, 1 (1968)
- 37. A. Sobiczewski, A. Gyurkovich, M. Brack, Nucl. Phys. A 289, 346 (1977)
- 38. J. Maruhn, W. Greiner, Z. Phys. A **251**, 431 (1972)
- 39. S. Yamaji, H. Hofmann, R. Samhammer, Nucl. Phys. A 475, 487 (1988)
- 40. V.I. Zagrebaev et al., Low-energy Nuclear Knowledge Base, http://www.nrv.jinr.ru/nrv
- 41. V.I. Zagrebaev, Phys. Rev. C 64, 034606 (2001)
- 42. V.I. Zagrebaev, AIP Conf. Proc. **704**, 31 (2004)
- 43. W.D. Myers, W. Swiatecki, Ann. Phys. **84**, 186 (1974)
- 44. M.G. Itkis, J. Äystö, S. Beghini, A.A. Bogachev, L. Corradi, O. Dorvaux, A. Gadea, G. Giardina, F. Hanappe, I.M. Itkis, M. Jandel, J. Kliman, S.V. Khlebnikov, G.N. Kniajeva, N.A. Kondratiev, E.M. Kozulin, L. Krupa, A. Latina, T. Materna, G. Montagnoli, Y.T. Oganessian, I.V. Pokrovsky, E.V. Prokhorova, N. Rowley, V.A. Rubchenya, A.Y. Rusanov, R.N. Sagaidak, F. Scarlassara, A.M. Stefanini, L. Stuttge, S. Szilner, M. Trotta, W.H. Trzaska, D.N. Vakhtin, A.M. Vinodkumar, V.M. Voskressenski, V.I. Zagrebaev, Nucl. Phys. A 734, 136 (2004)
- S.M. Polikanov, V.A. Druin, V.A. Karnaukhov, V.L. Mikheev, A.A. Pleve, N.K. Skobelev, V.G. Subbotin, G.M. Ter-Akopian, V.A. Fomichev, JETP 42, 1464 (1962)
- 46. W. von Oertzen, Physics of atomic nuclei, 66, 1591 (2006)
- 47. W. von Oertzen, see this volume of Lect. Notes Phys
- 48. P. Fröbrich, I.I. Gonchar, Phys. Rep. 292, 131 (1998)
- 49. F.G Werner, J.A. Wheeler, unpublished
- 50. K.T.R. Davies, A.J. Sierk, J.R. Nix, Phys. Rev. C 13, 2385 (1976)
- J.M. Eisenberg, W. Greiner, Microscopic Theory of the Nucleus (North-Holland, Amsterdam, 1972)
- 52. W. Nörenberg, Phys. Lett. B 52, 289 (1974)
- 53. L.G. Moretto, J.S. Sventek, Phys. Lett. B 58, 26 (1975)
- 54. H. Risken, The Fokker Planck Equation (Springer, Berlin, 1984)
- 55. C.W. Gardiner, Stochastic Methods (Springer, Berlin, 1990)
- 56. S. Ayik, B. Schürmann, W. Nörenberg, Z. Phys. A 279, 174 (1976)
- 57. R. Schmidt, G. Wolschin, Z. Phys. A 296, 215 (1980)

- 58. V.I. Zagrebaev, Phys. Rev. C 67, 061601 (2003)
- 59. V.I. Zagrebaev, V.V. Samarin, W. Greiner, Phys. Rev. C 75, 035809 (2007)
- W.U. Schröder, J.R. Huizenga, Damped Nuclear Reactions, in Treatise on Heavy-Ion Science vol 2, ed. by D.A. Bromley (Plenum Press, New York, 1984), p.140
- 61. V. Zagrebaev, W. Greiner, J. Phys. G 34, 1 (2007)
- V.I. Zagrebaev, Y. Aritomo, M.G. Itkis, Yu.Ts. Oganessian, M. Ohta, Phys. Rev. C 65, 014607 (2002)
- 63. E.K. Hulet, R.W. Lougheed, J.F. Wild, J.H. Landrum, P.C. Stevenson, A. Ghiorso, J.M. Nitschke, R.J. Otto, D.J. Morrissey, P.A. Baisden, B.F. Gavin, D. Lee, R.J. Silva, M.M. Fowler, G.T. Seaborg, Phys. Rev. Lett. 39, 385 (1977)
- 64. M. Schädel, J.V. Kratz, H. Ahrens, W. Brüchle, G. Franz, H. Gäggeler, I. Warnecke, G. Wirth, G. Herrmann, N. Trautmann, M. Weis, Phys. Rev. Lett. 41, 469 (1978)
- H. Freiesleben, K.D. Hildenbrand, F. Pühlhofer, W.F.W. Scneider, R. Bock, D.V. Harrach, H.J. Specht, Z. Phys. A 292, 171 (1979)
- 66. M. Schädel, W. Brüchle, H. Gäggeler, J.V. Kratz, K. Sümmerer, G. Wirth, G. Herrmann, R. Stakemann, G. Tittel, N. Trautmann, J.M. Nitschke, E.K. Hulet, R.W. Lougheed, R.L. Hahn, R.L. Ferguson, Phys. Rev. Lett. 48, 852 (1982)
- 67. K.J. Moody, D. Lee, R.B. Welch, K.E. Gregorich, G.T. Seaborg, R.W. Lougheed, E.K. Hulet, Phys. Rev. C 33, 1315 (1986)
- 68. R.B. Welch, K.J. Moody, K.E. Gregorich, D. Lee, G.T. Seaborg, Phys. Rev. C 35, 204 (1987)
- W. Mayer, G. Beier, J. Friese, W. Henning, P. Kienle, H.J. Körner, W.A. Mayer, L. Müller, G. Rosner, W. Wagner, Phys. Lett. B 152, 162 (1985)
- 70. S. Hofmann, G. Münzenberg, Rev. Mod. Phys. **72**, 733 (2000)
- Y.T. Oganessian, V.K. Utyonkov, Y.V. Lobanov, F.S. Abdullin, A.N. Polyakov, I.V. Shirokovsky, Y.S. Tsyganov, G.G. Gulbekian, S.L. Bogomolov, B.N. Gikal, A.N. Mezentsev, S. Iliev, V.G. Subbotin, A.M. Sukhov, A.A. Voinov, G.V. Buklanov, K. Subotic, V.I. Zagrebaev, M.G. Itkis, J.B. Patin, K.J. Moody, J.F. Wild, M.A. Stoyer, N.J. Stoyer, D.A. Shaughnessy, J.M. Kenneally, P.A. Wilk, R.W. Lougheed, R.I. Il'kaev, S.P. Vesnovskii, Phys. Rev. C 70, 064609 (2004)
- 72. V.I. Zagrebaev, W. Greiner, Phys. Rev. C 78, 034610 (2008)
- 73. V.I. Zagrebaev, Yu.Ts. Oganessian, M.G. Itkis, W. Greiner, Phys. Rev. C 73, 031602 (2006)
- 74. A.C.C. Villari, C. Golabek, W. Mittig, S. Heinz, S. Bhattacharyya, D. Boilley, R. Dayras, G. De France, A. Drouart, L. Gaudefroy, L. Giot, A. Marchix, V. Maslov, M. Morjean, G. Mukherjee, A. Navin, Yu. Penionzkevich, F. Rejmund, M. Rejmund, P. Roussel-Chomaz, C. Stodel, M. Winkler, in *Tours Symposium on Nuclear Physics VI, Tours, France*, 2006, AIP Conf. Proc. 891, 60 (2007)
- 75. V. Zagrebaev, W. Greiner, J. Phys. G 34, 2265 (2007)
- 76. E. Haseltine, http://www.discovermagazine.com/2002/feb/cover
- 77. C.E. Rolfs, W.S. Rodney, *Cauldrons in the Cosmos* (The University of Chicago Press, Chicago, 1988) 469
- 78. V. Zagrebaev, W. Greiner, Phys. Rev. Lett. 101, 122701 (2008)
- 79. V. Zagrebaev, W. Greiner, J. Phys. G 35, 125103 (2008)
- 80. T. Kurtukian Nieto, Ph.D. Thesis, Universidade de Santiago de Compostela, 2007
- 81. C.H. Dasso, G. Pollarolo, A. Winther, Phys. Rev. Lett. 73, 1907 (1994)
- 82. J. Reinhardt, U. Müller, W. Greiner, Z. Phys. A 303, 173 (1981)
- 83. W. Greiner (ed.), Quantum Electrodynamics of Strong Fields (Plenum Press, New York, 1983)
- 84. W. Greiner, B. Müller, J. Rafelski, *QED of Strong Fields*, 2nd edn (Springer, Berlin, 1985)
- 85. R.L. Hahn, P.F. Dittner, K.S. Toth, O.L. Keller, Phys. Rev. C 10, 1889 (1974)
- D. Lee, H. von Gunten, B. Jacak, M. Nurmia, Y.F. Liu, C. Luo, G.T. Seaborg, D.C. Hoffman, Phys. Rev. C 25, 286 (1982)
- 87. A. Türler, H.R. von Gunten, J.D. Leyba, D.C. Hoffman, D.M. Lee, K.E. Gregorich, D.A. Bennett, R.M. Chasteler, C.M. Gannett, H.L. Hall, R.A. Henderson, M.J. Nurmia, Phys. Rev. C 46, 1364 (1992)

- 88. C. Riedel, W. Nörenberg, Z. Phys. A 290, 385 (1979)
- 89. I. Ahmad, S.M. Austin, B.B. Back, R.R. Betts, F.P. Calaprice, K.C. Chan, A. Chishti, C.M. Conner, R.W. Dunford, J.D. Fox, S.J. Freedman, M. Freer, S.B. Gazes, A.L. Hallin, Th. Happ, D. Henderson, N.I. Kaloskamis, E. Kashy, W. Kutschera, J. Last, C.J. Lister, M. Liu, M.R. Maier, D.M. Mercer, D. Mikolas, P.A.A. Perera, M.D. Rhein, D.E. Roa, J.P. Schiffer, T.A. Trainor, P. Wilt, J.S. Winfield, M. Wolanski, F.L.H. Wolfs, A.H. Wuosmaa, A.R. Young, J.E. Yurkon (APEX collaboration), Phys. Rev. C 60, 064601 (1999)
- R. Ganz, R. Bär, A. Balanda, J. Baumann, W. Berg, K. Bethge, A. Billmeier, H. Bokemeyer, H. Fehlhaber, H. Folgera, J. Foryciara, O. Fröhlich, O. Hartung, M. Rhein, M. Samek, P. Salabura, W. Schön, D. Schwalm, K.E. Stiebing, P. Thee (EPoS II collaboration), Phys. Lett. B 389, 4 (1996)
- U. Leinberger, E. Berdermanna, F. Heine, S. Heinz, O. Joeres, P. Kienle, I. Koenig, W. Koenig, C. Kozhuharov, M. Rhein, A. Schröter, H. Tsertos, (ORANGE Collaboration), Phys. Lett. B 394, 16 (1997)
- U. Müller, G. Soff, T. deReus, J. Reinhardt, B. Müller, W. Greiner, Z. Phys. A 313, 263 (1983)
- 93. C. Wagemans, *Ternary Fission* in *The Nuclear Fission Process*, Chap. 12, ed. by Cyriel Wagemans (CRC Press, Boca Raton, 1991)
- 94. F. Gönnenwein, M. Wöstheinrich, M. Hesse, H. Faust, G. Fioni, S. Oberstedt, in *Seminar on Fission*, Pont d'Oye IV, Belgium, 1999, edited by Cyriel Wagemans et al., (World Scientific, Singapore, 1999) p. 59
- W.J. Swiatecki, Second UN Int. Conf. on the Peaceful Uses of Atomic Energy, Geneva, 1958,
 p. 651
- 96. H. Diehl, W. Greiner, Nucl. Phys. **A229**, 29 (1974)
- 97. A.R. Degheidy, J.A. Maruhn, Z. Phys. A 290, 205 (1979)
- 98. Y.V. Pyatkov, D.V. Kamanin, W.H. Trzaska, W. Von Oertzen, S.R. Yamaletdinov, A.N. Tjukavkin, V.G. Tishcenko, V.G. Lyapin, Y.E. Penionzhkevich, A.A. Alexandrov, S.V. Khlebnikov, Rom Rep Phy, **59**(2), 569 (2007)
- D.V. Kamanin, Yu.V. Pyatkov, A.N. Tyukavkin, Yu.N. Kopatch, Int. J. Mod. Phys. E17, 2250 (2008)